IntechOpen

Molecular Dynamics

Theoretical Developments and Applications in Nanotechnology and Energy

Edited by Lichang Wang

WEB OF SCIENCE™

MOLECULAR DYNAMICS – THEORETICAL DEVELOPMENTS AND APPLICATIONS IN NANOTECHNOLOGY AND ENERGY

Edited by **Lichang Wang**

Molecular Dynamics - Theoretical Developments and Applications in Nanotechnology and Energy
http://dx.doi.org/10.5772/2383
Edited by Lichang Wang

Contributors

Gaotsiwe Joel Rampho, Rang-Su Liu, Kin-Yiu Wong, Yuto Komeiji, Kah Chun Lau, Brett. I Dunlap, Takashi Tokumasu, Dan Mu, Jian-Quan Li, Victor M. Rosas-Garcia, Isabel Sáenz-Tavera, Yasemin Ciftci, Seda Keskin, Ewa Hawlicka, Eldin Wee Chuan Lim, Lichang Wang, Tomoaki Togashi, Konstantinos Termentzidis, Samy Merabia, Kien Ling Khoo, Victor Chentsov, Eduard Pastukhov, Nicolay Sidorov, Andrej Vostrjakov, Ikuo Fukuda, Gonzalo Gutierrez, Sergio Davis, Claudia Loyola, Felipe González-Cataldo, Yasmin Navarrete, Felipe Gonzalez-Wasaff, Joaquin Peralta

Notice

First published in Croatia, 2012 by INTECH d.o.o.
eBook (PDF) Published by IN TECH d.o.o.
Place and year of publication of eBook (PDF): Rijeka, 2019.
IntechOpen is the global imprint of IN TECH d.o.o.
Printed in Croatia

Legal deposit, Croatia: National and University Library in Zagreb

Additional hard and PDF copies can be obtained from orders@intechopen.com

Molecular Dynamics - Theoretical Developments and Applications in Nanotechnology and Energy
Edited by Lichang Wang

p. cm.

ISBN 978-953-51-0443-8

eBook (PDF) ISBN 978-953-51-4306-2

Meet the editor

Lichang Wang, Ph.D., is Professor of Chemistry and Biochemistry at Southern Illinois University Carbondale and the founder and president of MASIS, Inc. Her research activities encompass the area of molecular modeling, such as developing molecular dynamics simulation tools for complex systems and performing dynamics simulations and electronic structure calculations to study various systems of chemical and energy interests: (a) Transition metal nanoparticles, their toxicity to humans, and their catalytic activities for dehydrogenation of CH4, reduction of O2, direct conversion of coal to liquid fuel, and reactions of ethanol; and (b) Organic dyes for solar cell applications. Details of her research can be found on the website: http://www.chem.siu.edu/wang. The ultimate goal of her research activities is to replace as many bench top R & D experiments as possible by molecular modeling in order to achieve a greener, as well as economically better, R & D in Chemical and Energy Industries.

Contents

Preface

Molecular dynamics (MD) simulations have played increasing roles in our understanding of physical and chemical processes of complex systems and in advancing science and technology. Over the past forty years, MD simulations have made great progress from developing sophisticated theories for treating complex systems to broadening applications to a wide range of scientific and technological fields. The chapters of *Molecular Dynamics* are a reflection of the most recent progress in the field of MD simulations.

This is the first book of *Molecular Dynamics* which focuses on the theoretical developments and the applications in nanotechnology and energy. This book is divided into five parts. The first part deals with the development of molecular dynamics theory. Komeiji et al. summarize, in Chapter 1, the advances made in fragment molecular orbital based molecular dynamics, which is the *ab inito* molecular dynamics simulations, to treat large molecular systems with solvent molecules being treated explicitly. In Chapter 2, Wang & Hudson present a new meta-molecular dynamics method, i.e. beyond the conventional MD simulations, that allows monitoring the change of electronic state of the system during the dynamical process. Fukuda & Queyroy discuss in Chapter 3 two numerical techniques, i.e. phase space time-invariant function and numerical integrator, to enhance the MD performance. In Chapter 4, Rosas-García & Sáenz-Tavera provide a summary of MD methods to perform a configurational search of clusters of less than 100 atoms. In Chapter 5, Termentzidis & Merabia describe MD simulations in the calculation of thermal transport properties of nanomaterils.

The second part consists of three chapters that describe MD theory beyond a classical treatment. In Chapter 6, Wong describes a practical ab inito path-integral method, denoted as $\psi\pi\phi$ method, for macromolecules. Chapters 7 and 8, by Rampho and Togashi & Katō, respectively, deal with the asymmetric molecular dynamics simulations of nuclear structures.

Part III is on nanoparticles. In Chapter 9, Liu et al. provide a detailed description of MD simulations to study liquid metal clusters consisting of up to 10^6 atoms. In Chapter 10, Çiftci & Özgen provide a MD study of Au clusters on the melting, glass formation, and crystallization processes. Lim provides a MD study of gelation of

magnetic nanoparticles in Chapter 11. Chapter 12 by Gutiérrez et al. provides a MD simulation of a nanoparticle colliding inelastically with a solid surface.

The fourth part is about diffusion of gas molecules in solid, an important research area related to gas storage, gas separation, catalysis, and biomedical applications. In Chapter 13, Keskin describes MD simulations of the gas diffusion in molecular organic framework (MOF). In Chapter 14, Pastukhov et al. provide the MD results on the H_2 dynamics on various solid surfaces. In Chapter 15, Tokumasu provides a summary of MD results on H_2 dissociation on Pt(111). In Chapter 16, Mu & Li discuss MD simulation of the adsorption and diffusion of polydimethylsiloxane (PDMS) on a Si(111) surface.

In the last part of the book, ionic conductivity in solid oxides is discussed. Solid oxides are especially important materials in the field of energy, including the development of fuel cells and batteries. In Chapter 17, Lau & Dunlap describe the dynamics of O^{2-} in Y_2O_3 and in Y_2O_3 doped crystal and amorphous ZrYO. Khoo & Dissado provide a study of the mechanism of Na^+ conductivity in hollandites in Chapter 18. The last chapter of this part deals with the ion solvation in methanol/water mixture. Hawlicka and Rybicki summarize the Mg^{2+}, Ca^{2+}, and Cl^- solvation in the liquid mixture and I hope the readers can find connections between the liquid and solid ionic conductivities.

With strenuous and continuing efforts, a greater impact of MD simulations will be made on understanding various processes and on advancing many scientific and technological areas in the foreseeable future.

In closing I would like to thank all the authors taking primary responsibility to ensure the accuracy of the contents covered in their respective chapters. I also want to thank my publishing process manager Ms. Daria Nahtigal for her diligent work and for keeping the book publishing progress in check.

Lichang Wang
Department of Chemistry and Biochemistry
Southern Illinois University
Carbondale
USA

Part 1

Molecular Dynamics Theory and Development

1

Recent Advances in Fragment Molecular Orbital-Based Molecular Dynamics (FMO-MD) Simulations

Yuto Komeiji[1], Yuji Mochizuki[2], Tatsuya Nakano[3] and Hirotoshi Mori[4]
[1]*National Institute of Advanced Industrial Science and Technology (AIST)*
[2]*Rikkyo University*
[3]*National Institute of Health Sciences*
[4]*Ochanomizu University*
Japan

1. Introduction

Fragment molecular orbital (FMO)-based molecular dynamics simulation (MD), hereafter referred to as "FMO-MD," is an *ab initio* MD method (Komeiji *et al.*, 2003) based on FMO, a highly parallelizable *ab initio* molecular orbital (MO) method (Kitaura *et al.*, 1999). Like any *ab initio* MD method, FMO-MD can simulate molecular phenomena involving electronic structure changes such as polarization, electron transfer, and reaction. In addition, FMO's high parallelizability enables FMO-MD to handle large molecular systems. To date, FMO-MD has been successfully applied to ion-solvent interaction and chemical reactions of organic molecules. In the near future, FMO-MD will be used to handle the dynamics of proteins and nucleic acids.

In this chapter, various aspects of FMO-MD are reviewed, including methods, applications, and future prospects. We have previously published two reviews of the method (Komeiji *et al.*, 2009b; chapter 6 of Fedorov & Kitaura, 2009), but this chapter includes the latest developments in FMO-MD and describes the most recent applications of this method.

2. Methodology of FMO-MD

FMO-MD is based on the Born-Oppenheimer approximation, in which the motion of the electrons and that of the nuclei are separated (Fig. 1). In FMO-MD, the electronic state is solved quantum mechanically by FMO using the instantaneous 3D coordinates of the nuclei (**r**) to obtain the energy (E) and force (**F**, minus the energy gradient) acting on each nucleus, which are then used to update **r** classical mechanically by MD. In the following subsections, software systems for FMO-MD are described, and then the FMO and MD aspects of the FMO-MD methodology are explained separately.

2.1 Software systems for FMO-MD

FMO-MD can be implemented by using a combination of two independent programs, one for FMO and the other for MD. Most of the simulations presented in this article were

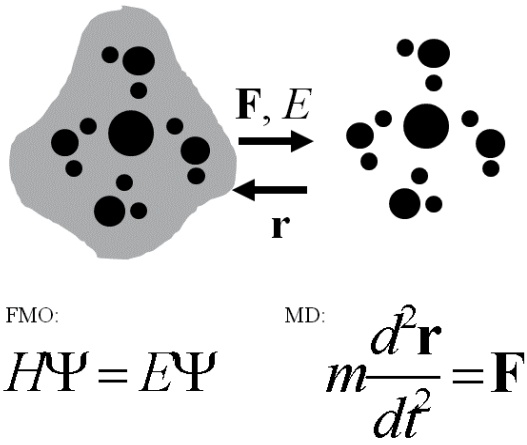

Fig. 1. Schematics of the FMO-MD method exemplified by an ion solvation with four water molecules. The atomic nuclei are represented by black circles (the large one for the ion, medium ones for Oxygens, and small ones for Hydrogens) and the electron cloud by a grey shadow. The electronic structure is calculated by FMO to give force (**F**) and energy (*E*), which are then used to update the 3D coordinates of nuclei (**r**) by MD, i.e., by solving the classical equation of motion.

performed by the PEACH/ABINIT-MP software system composed of the PEACH MD program (Komeiji *et al*., 1997) and the ABINIT-MP [1] (F)MO program (Nakano *et al*., 2000). We have revised the system several times (Komeiji *et al*., 2004, 2009a), but here we describe the latest system, which has not yet been published. In the latest system, the PEACH program prepares the ABINIT-MP input file containing the list of fragments and 3D atomic coordinates, executes an intermediate shell script to run ABINIT-MP, receives the resultant FMO energy and force, and updates the coordinates by the velocity-Verlet integration algorithm. This procedure is repeated for a given number of time steps.

The above implementation of FMO-MD, referred to as the PEACH/ABINIT-MP system, has both advantages and disadvantages. The most important advantage is the convenience for the software developers; both FMO and MD programmers can modify their programs independently from each other. Also, if one wants to add a new function of MD, one can first write and debug the MD program against an inexpensive classical force field simulation and then transfer the function to FMO-MD, a costly *ab initio* MD. Nonetheless, the PEACH/ABINIT-MP system has several practical disadvantages as well, mostly related to the use of the systemcall command to connect the two programs. For example, frequent invoking of ABINIT-MP from PEACH sometimes causes a system error that leads to an abrupt end of simulations. Furthermore, use of the systemcall command is prohibited in many supercomputing facilities. To overcome these disadvantages, we are currently

[1] Our developers' version of ABINIT-MP is named ABINIT-MPX, but it is referred to as ABINIT-MP throughout this article.

implementing FMO-MD directly in the ABINIT-MP program. This working version of ABINIT-MP is scheduled to be completed within 2012.

Though not faultless, the PEACH/ABINIT-MP system has produced most of the important FMO-MD simulations performed thus far, which will be presented in this article. Besides the PEACH/ABINIT-MP system, a few FMO-MD software systems have been reported in the literature, some using ABINIT-MP (Ishimoto *et al.*, 2004, 2005; Fujita *et al.*, 2009, 2011) and others GAMESS (Fedorov *et al.*, 2004a; Nagata *et al.*, 2010, 2011c; Fujiwara *et al.*, 2010a). Several simulations with these systems are also presented.

2.2 FMO

FMO, the essential constituent of FMO-MD, is an approximate *ab initio* MO method (Kitaura *et al.*, 1999). FMO scales to $N^{1\text{-}2}$, is easy to parallelize, and retains chemical accuracy during these processes. A vast number of papers have been published on the FMO methodology, but here we review mainly those closely related to FMO-MD. To be more specific, those on the FMO energy gradient, Energy Minimization (EM, or geometry optimization), and MD are preferentially selected in the reference list. Thus, those readers interested in FMO itself are referred to Fedorov & Kitaura (2007b, 2009) for comprehensive reviews of FMO. Also, one can find an extensive review of fragment methods in Gordon *et al.* (2011), where FMO is re-evaluated in the context of its place in the history of the general fragment methods.

2.2.1 Hartree-Fock (HF)

We describe the formulation and algorithm for the HF level calculation with 2-body expansion (FMO2), the very fundamental of the FMO methodology (Kitaura *et al.*, 1999). Below, subscripts *I, J, K*... denote fragments, while *i*, *j*, *k*,... denote atomic nuclei.

First, the molecular system of interest is divided into N_f fragments. Second, the initial electron density, $\rho_I(r)$, is estimated with a lower-level MO method, e.g., extended Hückel, for all the fragments. Third, self-consistent field (SCF) energy, E_I, is calculated for each fragment monomer while considering the electrostatic environment. The SCF calculation is repeated until all $\rho_I(r)$'s are mutually converged. This procedure is called the self-consistent charge (SCC) loop. At the end of the SCC loop, monomer electron density $\rho_I(\mathbf{r})$ and energy E_I are obtained. Finally, an SCF calculation is performed once for each fragment pair to obtain dimer electron density $\rho_{IJ}(\mathbf{r})$ and energy E_{IJ}. Total electron density $\rho(\mathbf{r})$ and energy E are calculated using the following formulae:

$$\rho(\mathbf{r}) = \sum_{I>J} \rho_{IJ}(\mathbf{r}) - (N_f - 2)\sum_I \rho_I(\mathbf{r}) \tag{1}$$

$$E = \sum_{I>J} E_{IJ} - (N_f - 2)\sum_I E_I \,. \tag{2}$$

In calculation of the dimer terms, electrostatic interactions between distant pairs are approximiated by simple Coulombic interactions (dimer-ES approximation, Nakano *et al.*, 2002). This approximation is mandatory to reduce the computation cost from $O(N^4)$ to $O(N^2)$.

The total energy of the molecular system, U, is obtained by adding the electrostatic interaction energy between nuclei to E, namely,

$$U = \sum_{I>J} E_{IJ} - (N_f - 2)\sum_{I} E_I + \sum_{i>j} \frac{Z_i Z_j}{r_{ij}} \tag{3}$$

where r_{ij} denotes the distance between nuclei i and j and Z_i and Z_i their charges, respectively.

Force ($\mathbf{F}_i$) acting on atomic nucleus i can be obtained by differenciation of eq. (3) by $\mathbf{r}_i$ as follows:

$$\mathbf{F}_i = -\nabla_i U \tag{4}$$

Analytical formulation of eq. (4) was originally derived for the HF level by Kitaura *et al.* (2001) and used in several EM calculations (for example, Fedorov *et al.*, 2007a) and in the first FMO-MD simulation (Komeiji *et al.,* 2003). Later on, the HF gradient was made fully analytic by Nagata *et al.* (2009, 2010, 2011a).

2.2.2 FMO*n*

The procedure described in the previous subsection is called FMO2, with "2" indicating that the energy is expanded up to 2-body terms of fragments. It is possible to improve the precision of FMO by adding 3-body, 4-body, ..., and n-body terms (FMOn) at the expense of the computation cost of $O(1)$. FMO3 has been implemented in both GAMESS and ABINIT-MP. The improvement by FMO3 is especially apparent in FMO-MD, as exemplified by a simulation of proton transfer in water (Komeiji *et al.*, 2010). Recently, FMO4 was implemented in ABINIT-MP (Nakano *et al.,* 2012), which will presumably make it possible to regard even a metal ion as a fragment.

2.2.3 Second-order Moeller-Plesset perturbation (MP2)

The HF calculation neglects the electron correlation effect, which is necessary to incorporate the so-called dispersion term. The electron correlation can be calculated fairly easily by the second-order Moeller-Plesset perturbation (MP2). Though the MP2/FMO energy formula was published as early as 2004 (Fedorov *et al.,* 2004b; Mochizuki *et al.*, 2004ab), the energy gradient formula for MP2/FMO was first published in 2011 by Mochizuki *et al.* (2011) and then by Nagata *et al.* (2011). In Mochizuki's implementation of MP2 to ABINIT-MP, an integral-direct MP2 gradient program module with distributed parallelism was developed for both FMO2 and FMO3 levels, and a new option called "FMO(3)" was added, in which FMO3 is applied to HF but FMO2 is applied to MP2 to reduce computation time, based on the relatively short-range nature of the electron correlation compared to the range of the Coulomb or electrostatic interactions.

The MP2/FMO gradient was soon applied to FMO-MD of a droplet of water molecules (Mochizuki *et al.*, 2011). The water was simulated with the 6-31G* basis set with and without MP2, and the resultant trajectories were subjected to calculations of radial distribution functions (RDF). The RDF peak position of MP2/FMO-MD was closer to the experimental

value than that of HF/FMO-MD was. This result indicated the importance of the correlation energy incorporated by MP2 to describe a condensed phase.

2.2.4 Configuration Interaction Singles (CIS)

CIS is a useful tool to model low-lying excited states caused by transitions among near HOMO-LUMO levels in a semi-quantitative fashion (Foresman *et al.*, 1992). A tendency of CIS to overestimate excitation energies is compensated for by CIS(D) in which the orbital relaxation energy for an excited state of interest as well as the differential correlation energy from the ground state correlated at the MP2 level (Head-Gordon *et al.*, 1994). Both CIS and CIS(D) have been introduced to multilayer FMO (MFMO; Fedorov *et al.*, 2005) in ABINIT-MP (Mochizuki *et al.*, 2005a, 2007a). Very recently, Mochizuki implemented the parallelized FMO3-CIS gradient calculation, based on the efficient formulations with Fock-like contractions (Foresman *et al.*, 1992). The dynamics of excited states is now traceable as long as the CIS approximation is qualitatively correct enough. The influence of hydration on the excited state induced proton-transfer (ESIPT) has been attracting considerable interest, and we have started related simulations for several pet systems such as toropolone.

2.2.5 Unrestricted Hartree-Fock (UHF)

UHF is the simplest method for handling open-shell molecular systems, as long as care for the associated spin contamination is taken. The UHF gradient was implemented by preparing α- and β-density matrices. Simulation of hydrated Cu(II) has been underway at the FMO3-UHF level, and the Jahn-Teller distortion of hexa-hydration has been reasonably reproduced (Kato *et al.*, in preparation). The extension to a UMP2 gradient is planned as a future subject, where the computational cost may triple the MP2 gradient because of the three types of transformed integrals, (αα,αα), (ββ,ββ), and (αα,ββ) (Aikens *et al.*, 2003).

2.2.6 Model Core Potential (MCP)

Heavy metal ions play major roles in various biological systems and functional materials. Therefore, it is important to understand the fundamental chemical nature and dynamics of the metal ions under physiological or experimental conditions. Each heavy metal element has a large number of electrons to which relativistic effects must be taken into account, however. Hence, the heavy metal ions increase the computation cost of high-level electronic structure theories. A way to reduce the computation is the Model Core Potential (MCP; Sakai *et al.*, 1987; Miyoshi *et al.*, 2005; Osanai *et al.*, 2008ab; Mori *et al.*, 2009), where the proper nodal structures of valence shell orbitals can be maintained by the projection operator technique. In the MCP scheme, only valence electrons are considered, and core electrons are replaced with 1-electron relativistic pseudo-potentials to decrease computational costs. The MCP method has been combined with FMO and implemented in ABINIT-MP (Ishikawa *et al.*, 2006), which has been used in the comparative MCP/FMO-MD simulations of hydrated *cis*-platin and *trans*-platin (see subsection 3.6). Very recently, the 4f-in-core type MCP set for trilvalent lanthanides has been developed and made available (Fujiwara *et al.*, 2011).

2.2.7 Periodic Boundary Condition (PBC)

PBC was finally introduced to FMO-MD in the TINKER/ABINIT-MP system by Fujita *et al.* (2011). PBC is a standard protocol for both classical and *ab intio* MD simulations.

Nonetheless, partly due to the complexity of PBC in formulation but mostly due to its computation cost, FMO-MD simulations reported in the literature had been performed under a free boundary condition, usually with a cluster solvent model restrained by a harmonic spherical potential. This spherical boundary has the disadvantage of exposing the simulated molecular system to a vacuum condition and altering the electronic structure of the outer surface (Komeiji *et al.*, 2007). Hence, PBC is expected to avoid the disadvantage and to extend FMO-MD to simulations of bulk solvent and crystals. For PBC simulations to be practical, efficient approximations in evaluating the ESP matrix elements will need to be developed. A technique of multipole expansion may be worth considering.

2.2.8 Miscellaneous

Analytic gradient formulae have been derived for several FMO methods and implemented in the GAMESS software, including those for the adaptive frozen orbital bond detachment scheme (AFO; Fedorov *et al.*, 2009), polarizable continuum model method (PCM; Li *et al.*, 2010), time-dependent density functional theory (TD-DFT; Chiba *et al.*, 2009), MFMO with active, polarisable, and frozen sites (Fedorov *et al.*, 2011), and effective fragment potential (EFP; Nagata *et al.*, 2011c). Also, Ishikawa *et al.* (2010) implemented partial energy gradient (PEG) in their software PACIS. These gradients have been used for FMO-EM calculations of appropriate molecules. Among them, the EFP gradient has already been applied successfully to FMO-MD (Nagata *et al.*, 2011c), and the others will be combined with FMO-MD in the near future.

2.3 MD

The MD portion of FMO-MD resembles the conventional classical MD method, but several algorithms have been introduced to facilitate FMO-MD.

2.3.1 Dynamic Fragmentation (DF)

DF refers to the redefinition of fragments depending on the molecular configuration during FMO-MD. For example, in an H^+-transfer reaction ($AH^+ + B \rightarrow AHB^+ \rightarrow A + BH^+$), AH^+ and B can be separate fragments before the reaction but should be unified in the transition state AHB^+, and A and BH^+ may be separated after the reaction. The DF algorithm handles this fragment rearrangement by observing the relative position and nuclear species of the constituent atoms at each time step of a simulation run.

The need for DF arose for the first time in an FMO-MD simulation of solvated H_2CO (Mochizuki *et al.* 2007b; see subsection 3.1). During the equilibration stage of the simulation, an artifactual H^+-transport frequently brought about an abrupt halt of the simulation. To avoid the halt by the H^+-transport, T. Ishikawa developed a program to unite the donor and acceptor of H^+ by looking up the spatial formation of the water molecules. This program was executed at each time step of the simulation. This was the first implementation of the DF algorithm (see Komeiji *et al.*, 2009a, for details). A similar *ad hoc* DF program was written for a simulation of hydrolysis methyl-diazonium (Sato *et al.*, 2008; see subsection 3.2). Thus, at the original stage, different DF programs were needed for different molecular systems.

The DF algorithm was generalized later to handle arbitrary molecular systems (Komeiji *et al.*, 2010). The algorithm requires each atom's van der Waals radius and instantaneous 3D coordinate, atomic composition and net charge of possible fragment species, and certain threshold parameters.

Presently, PEACH has four fragmentation modes, as follows:

Mode 0: Use the fragmentation data in the input file throughout the simulation.
Mode 1: Merge covalently connected atoms, namely, those constituting a molecule, into a fragment.
Mode 2: Fragments produced by Mode 1 are unified into a larger fragment if they are forming an H-bond.
Mode 3: Fragments produced by Mode 2 are unified if they are an ion and coordinating solvent molecules.

The modes are further explained as follows. Heavy atoms located significantly close to each other are united as a fragment, and each H atom is assigned to its closest heavy atom (Mode 1). Then, two fragments sharing an H atom are unified (Mode 2). Finally, an ion and surrounding molecules are united (Mode 3). See Figure 2 for typical examples of DF. Usually, Mode 1 is enough, but Mode 2 or 3 sometimes become necessary.

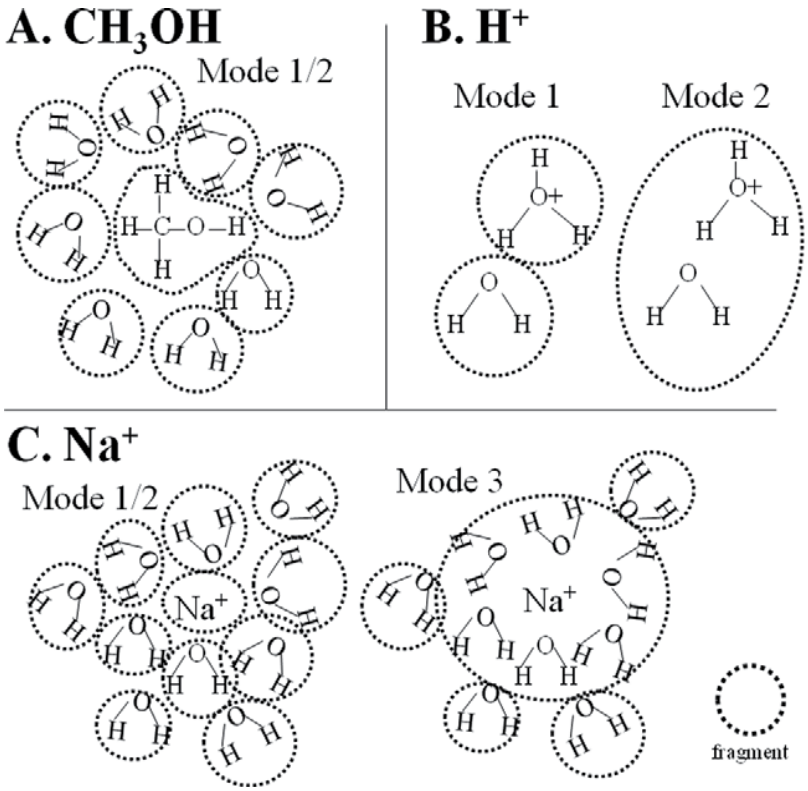

Fig. 2. Typical examples of fragment species generated by the generalized DF scheme. Expected fragmentation patterns are drawn for three solute molecules, A–C. Reproduced from Komeiji *et al.* (2010) with permission.

The DF algorithm gracefully handles molecular systems consisting of small solute and solvent molecules, but not those containing large molecules such as proteins and DNA, which should be fragmented at covalent bonds. Currently, Mode 0 is the only choice of fragmentation for these large molecules, in which the initial fragmentation should be used throughout and no fragment rearrangement is allowed (Nakano *et al.*, 2000; Komeiji *et al.*, 2004). This limitation of the DF algorithm will be abolished soon by the introduction of a mixed algorithm of DF and a static fragmentation.

2.3.2 Blue moon ensemble

The blue moon ensemble method (Sprik & Ciccotti, 1998) is a way to calculate the free energy profile along a reaction coordinate (RC) while constraining RC to a specified value. The method was implemented in FMO-MD (Komeiji, 2007) and was successfully applied to drawing a free energy profile of the Menschutkin reaction (Komeiji *et al.*, 2009a).

2.3.3 Path Integral Molecular Dynamics (PIMD)

The nuclei were handled by the classical mechanics in most of the FMO-MD simulations performed to date (Fig. 1), but PIMD (Marx & Parrinello, 1996) has been introduced into FMO-MD to incorporate the nucleic quantum effect (Fujita *et al.*, 2009). FMO-PIMD consumes tens of times more computational resource than the classical FMO-MD does but is necessary for a better description of, for example, a proton transfer reaction.

2.3.4 Miscellaneous

Miscellaneous MD methods implemented in the PEACH/ABINIT-MP system include the Nosé-Hoover (chain) thermostat, RATTLE bond constraint, RC constraint, spherical solvent boundary, and so on (Komeiji *et al.*, 2009a). Another research group has implemented the Hamiltonian Algorithm (HA) to FMO-MD to enhance conformation sampling of, for example, polypeptides (Ishimoto *et al.*, 2004, 2005; Tamura *et al.*, 2008).

3. Applications of FMO-MD

FMO-MD has been extensively applied to hydrated small molecules to simulate their solvation and chemical reactions. Some benchmark FMO-MD simulations were described briefly in the previous section. In this section, we review genuine applications of FMO-MD in detail.

3.1 Excitation energy of hydrated formaldehyde

FMO-MD and MFMO-CIS(D) were combined to evaluate the lowest $n\pi^*$ excitation energy of hydrated formaldehyde (H_2CO) molecules (Mochizuki *et al.*, 2007b). The shift of excitation energy of a solute by the presence of a solvent, known as solvatochronism, has drawn attention of both experimentalists and theorists and has been studied by various computational methods, mostly by the quantum mechanics and molecular mechanics (QM/MM) method. Alternatively, Mochizuki *et al.* (2007b) tried a fully *ab initio* approach, in which FMO-MD sampled molecular configurations for excited calculations.

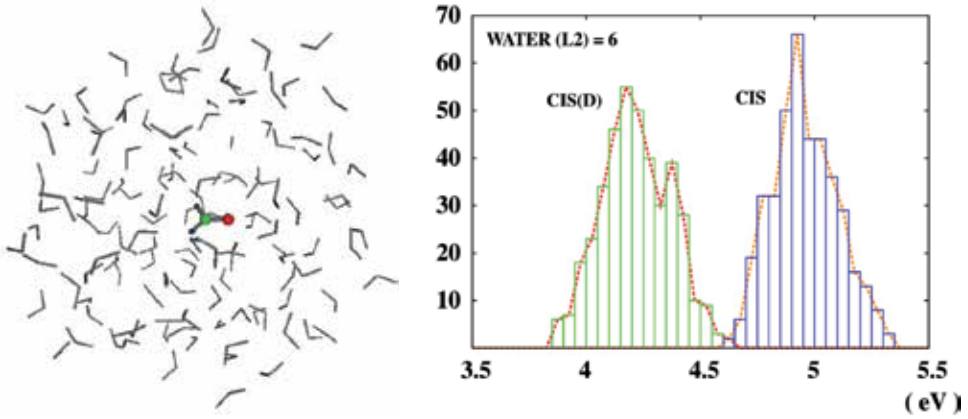

Fig. 3. An FMO-MD snapshot of the solvated H_2CO (left). Histogram of excitation energies for CIS and CIS(D) calculations (right). Reproduced from Mochizuki *et al.* (2007b) with permission.

In the configuration sampling, H_2CO was solvated within a droplet of 128 water molecules (Fig. 3 left), and the molecular system was simulated by FMO-MD at the FMO2-HF/6-31G level to generate a 2.62-ps trajectory at 300 K. From the last 2-ps portion of the trajectory, 400 conformations were chosen and were subjected to MFMO-CIS(D) calculations at the FMO2/HF/6-31G* level. In MFMO, the chromophore region contained H_2CO and several water molecules and was the target of CIS(D) calculation. The calculated excitation energy was averaged over the 400 configurations (Fig. 3 right). A similar protocol was applied to an isolated H_2CO molecule to calculate the excitation energy in a vacuum. The blue-shift by solvatochromism thus estimated was 0.14 eV, in agreement with preceding calculations.

The solvatochromism of H_2CO is frequently challenged by various computational methods, but this study distinguishes itself from preceding studies in that all the calculations were fully quantum, without classical force field parameters.

3.2 Hydrolysis of a methyl diazonium ion

The hydrolysis of the methyl-diazonium ion ($CH_3N_2^+$) is an S_N2-type substitution reaction that proceeds as follows:

$$H_2O + CH_3N_2^+ \rightarrow [H_2O...CH_3^+...N_2]‡ \rightarrow {}^+H_2OCH_3 + N_2. \quad (5)$$

Traditionally, this reaction is believed to occur in an enforced concerted mechanism in which a productive methyl cation after N_2 leaving is too reactive to have a finite lifetime, and consequently the attack by H_2O and the bond cleavage occur simultaneously. This traditional view was challenged by Sato *et al.* (2008) using FMO-MD. The FMO-MD simulations exhibited diverse paths, showing that the chemical reaction does not always proceed through the lowest energy paths.

This reaction was simulated as follows. FMO-MD simulations were conducted at the FMO2/HF/6-31G level. CH_3-N_2^+ was optimized in the gas phase and then hydrated in a sphere of 156 water molecules. The water was optimized at 300 K for 0.5 ps with the RATTLE bond constraint. The temperature of the molecular system was raised to 1000 K,

and the simulation was continued for 5 ps. From the 1000 K trajectory, 15 configurations were taken and subjected to a further run at 700 K without any constraint. Ten trajectories out of fifteen produced the final products (CH_3-OH_2^++N_2). The ten productive trajectories were classified into three groups: tight S_N2, loose S_N2, and intermediate.

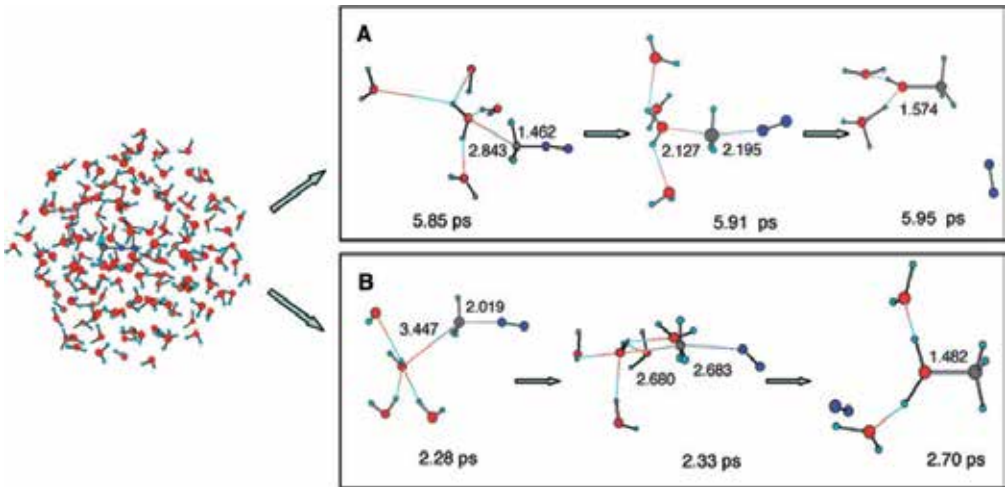

Fig. 4. Initial droplet structure and structures of substrate and nearby water molecules along type A and B trajectories. Numbers are atomic distances in Å. Reproduced from Sato *et al.* (2008) by permission.

Trajectory A in Fig. 4 is of the tight S_N2 type, in which the attack by H_2O and C-N bond cleavage, i.e. release of N_2, occur concertedly. Trajectory B is of the loose S_N2 type, which shows a two-stage process in which C-N bond cleavage precedes the attack by H_2O.

The difference between trajectories A and B was further analyzed by the configuration analysis for fragment interaction (CAFI; Mochizuki *et al.*, 2005b), and the results are plotted in Fig. 5. Charge-transfer (CT) interaction between the two fragments increases rapidly when the C-N distance increases to 1.6 Å for trajectory A, but for trajectory B the CT increased only when R_{CN} was 2.4 Å or longer. In trajectory B, the C-N bond cleavage and O-C bond formation events take place in a two-stage fashion. The CT interaction energy is larger for trajectory B than for A at $R_{C\text{-}O}$ = 2.6 Å, because at the same C-O distance the C-N bond is cleaved to a larger extent, and hence the CH_3 moiety has more positive charge for trajectory B than for trajectory A.

Most of the other productive trajectories exhibited intermediate characteristics between those of trajectories A and B. The diversity of the reaction path can be illustrated by the two-dimensional $R_{C\text{-}N}$-$R_{O\text{-}C}$ plot (Fig. 6). The existence of different paths indicates that the reaction does not always proceed through the lowest energy pathway with optimal solvation.

In summary, this series of simulations illustrated for the first time how the atoms in reacting molecules, from reactant to product, behave in solution at the molecular level. This was made possible by the advent of the full *ab initio* FMO-MD method.

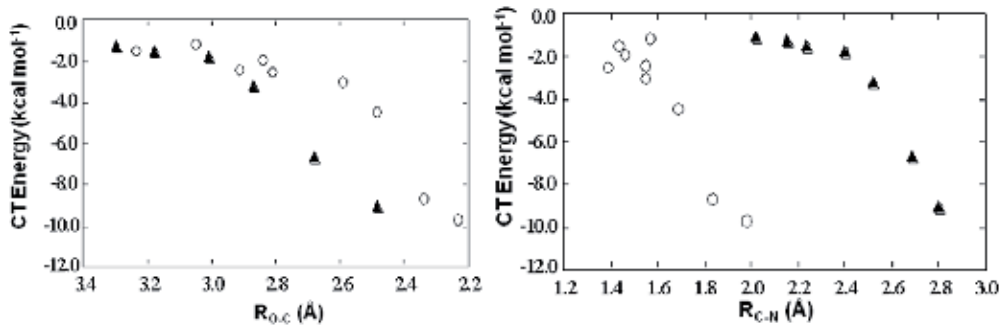

Fig. 5. Charge transfer interaction energy between attacking H_2O and $CH_3N_2^+$ as functions of $R_{O\text{-}C}$ (left) and $R_{C\text{-}N}$ (right). The open circles show trajectory A, and the filled triangles show trajectory B. Reproduced from Sato *et al*. (2008) by permission.

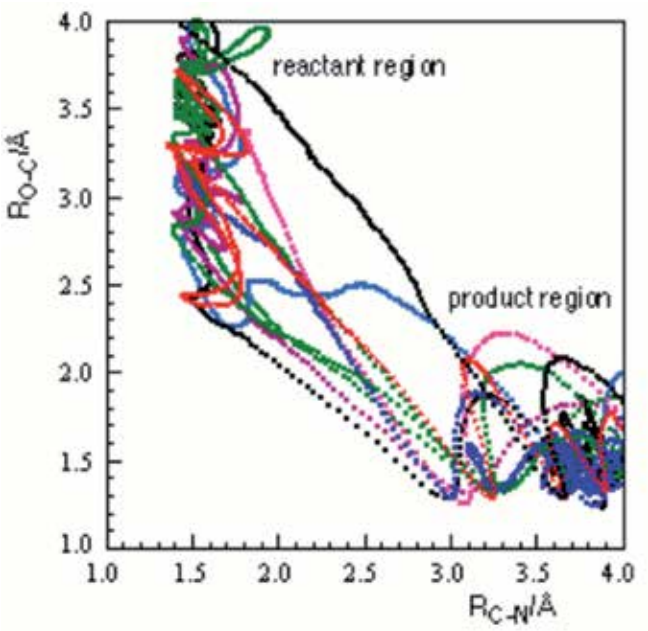

Fig. 6. $R_{C\text{-}N}$-$R_{O\text{-}C}$ plot of the ten trajectories that resulted in product formation. Those trajectories that proceeded along the diagonal line are regarded as tight S_N2, in which attack by water and the exit of N_2 occurred simultaneously, while a trajectory that deviated from the diagonal line is regarded as loose S_N2, in which N_2 left before the attack by water. Reproduced from Sato *et al.* (2008) by permission.

3.3 Amination of formaldehyde

Sato *et al*. (2010) tackled the reaction mechanism of the amination of H_2CO by FMO-MD simulations. In particular, they focused on whether the reaction proceeds via a zwitterion (ZW) intermediate (Fig. 7). The results indicated that the reaction proceeds through a stepwise mechanism with ZW as a stable intermediate.

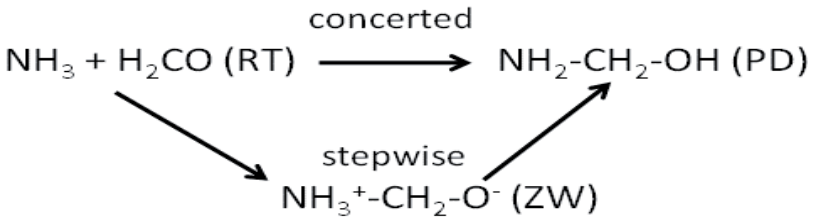

Fig. 7. Two contradictory schemes of H_2CO amination. RT: reactant; ZW: zwitterion; PD: product.

The FMO-MD simulations were designed as follows. RC was defined as $R_{N\text{-}C}$-$R_{N\text{-}H}$. With RC constrained, structural changes of the reactant (RT) molecules in MD simulations are confined to the line that has the slope=1 and intercept=RC in a More O'Ferrall–Jencks-type diagram (Fig. 8). This diagram allows the reader to distinguish between the stepwise process and the concerted one.

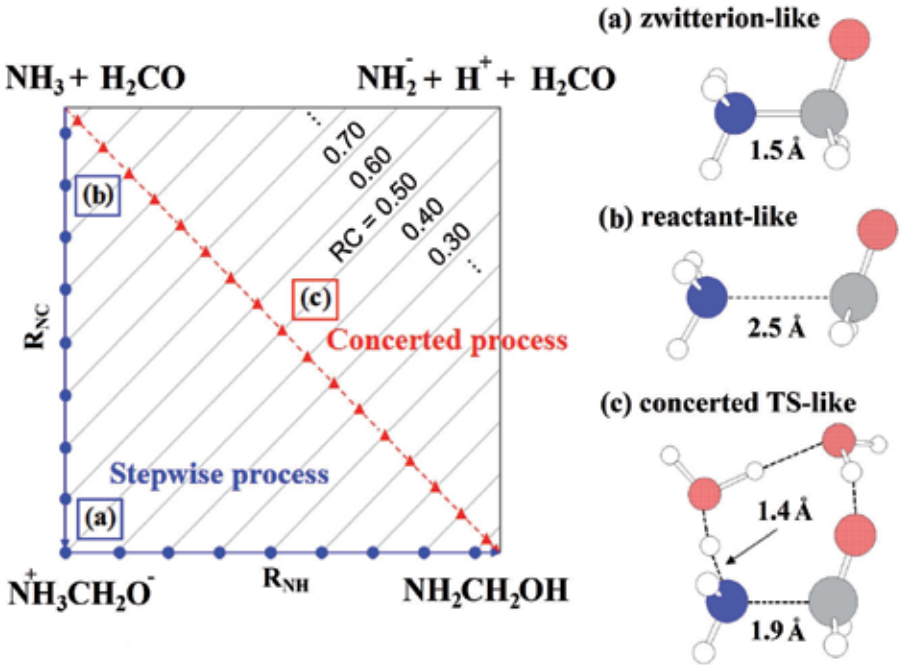

Fig. 8. Schematic representation of the More O'Farrall-Jencks-type diagram of carbinolamine formation of formaldehyde and ammonia (left). Three optimized initial configurations (right). Reproduced from Sato *et al.* (2010) by permission.

By FMO-MD, a More O'Ferrall–Jencks-type diagram was drawn for the H_2CO amination. Three initial configurations were prepared, (A) zwitterion-like, (B) reactant-like, and (C) concerted TS-like (Fig. 8), each solvated with ca. 200 water molecules. After appropriate optimization and equilibration by classical and FMO-EM/MD methods, average R_{NH} and R_{NC} were calculated at 300 K for RC = -0.4, -0.3,..., 0.9 Å starting from configuration A and

for RC = 0.9, 1.0,..., 1.8 Å starting from configuration B. For each RC value the configuration was equilibrated for 0.3 ps and sampled for a further 0.3 ps.

The diagram thus obtained clearly favored the stepwise mechanism over the concerted mechanism (Fig. 9). Nevertheless, there remained a possibility of the MD trajectory being trapped in a local minimum. To investigate the possibility, we conducted additional FMO-MD simulations starting from configuration C, the concerted TS-like one. These additional trajectories all diverted from the TS-like structure toward the trajectory of the stepwise path (see Sato *et al.*, 2010, for details), thus confirming the validity of the stepwise mechanism.

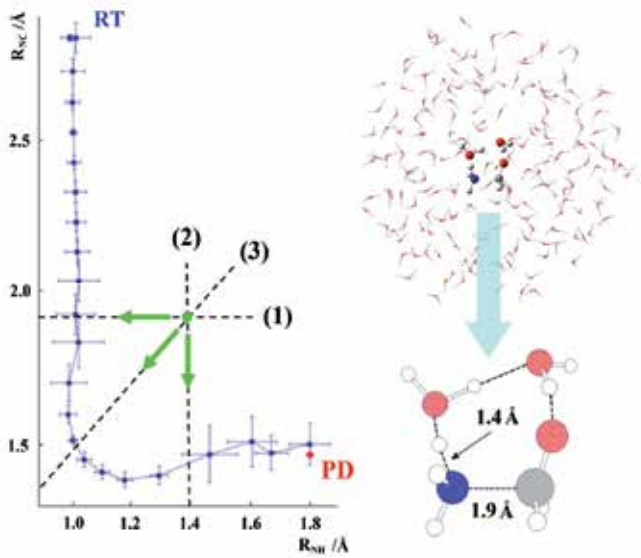

Fig. 9. Reaction profile obtained by FMO-MD simulations (left). The concerted TS-like structure (right). Reproduced from Sato *et al.* (2010) by permission.

In summary, the constraint FMO-MD simulations indicated that the H_2CO amination in water solvent occurs by the stepwise mechanism, not by the concerted one.

3.4 Hydration of Zn(II)

The divalent zinc ion, Zn(II), plays bio-chemically relevant roles, e.g., as the reaction center of superoxide dismutase. By using a droplet model of the Zn(II) ion with 64 water molecules, FMO2- and FMO3-MD simulations were performed at the HF/6-31G level, supposing that the electrostatic and coordination interactions are dominant in this system (Fujiwara *et al.*, 2010b). The Zn-O peak positions at the first hydration shell were investigated, and a better accuracy of FMO3-MD than that of FMO2-MD was demonstrated, where the FMO3 value of 2.05 Å agreed well with the experimental value of 2.06±0.02 Å (Fig. 10). The coordination number of the first hydration shell was 6 consistently. Additionally, the charge fluctuations on the Zn atom were evaluated by the natural population analysis (NPA) as well as the conventional Mulliken population analysis (MPA). The NPA results showed a consistent picture with the coordination bond with reasonable fluctuation (around a net charge of 1.8), while MPA yielded an artificially enhanced

fluctuation with a larger extent of electron donation (net charge of 1.3-1.4). Discussion with NPA was found to be preferable for hydrated metal ions.

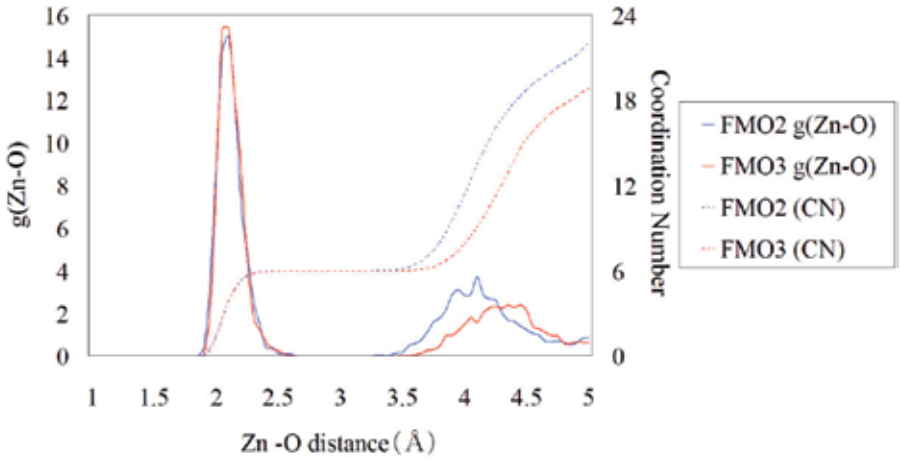

Fig. 10. Zn-O RDFs and coordination numbers (CN) calculated by FMO2/3-MD simulations. Reproduced from Fujiwara *et al.* (2010b) by permission.

3.5 Hydration of Ln(III)

The lanthanide contraction and the gadolinium break have attracted considerable attention in the inorganic chemistry. As an application of the 4f-in-core MCP (Fujiwara *et al.*, 2011), a series of FMO3-MD simulations on droplet model of Ln(III) plus 64 water molecules have been underway at the HF level (Fujiwara *et al.*, in preparation). The RDF peal positions for La(III) (nona-hydration) and Lu(III) (octa-hydration) were estimated to be 2.59 Å and 2.31 Å, respectively, and they were comparable to the corresponding experimental values of 2.54 Å and 2.31 Å. Interestingly, the octa- and nona-hydration results for Gd(III) were evaluated as 2.46 Å and 2.53 Å, respectively. The former value is in closer agreement with the experimental value of 2.42 Å, suggesting that the octa-hydration is preferable.

3.6 Comparison on hydration dynamics of *cis*- and *trans*-platin

FMO-MD has also given important insight into the difference in the hydration dynamics of *cis*- and *trans*-platin (Mori *et al.*, 2012). Since *cis*-platin (*cis*-$[Pt^{II}Cl_2(NH_3)_2]$) is recognized as an anticancer substance, quite a few studies have been devoted to the biochemical functions of its derivatives. Particularly interesting in the pharmaceutical research field of Pt-based anticancer drugs is the behaviour of its geometrical isomer, *trans*-platin, which only shows very low anticancer activity (Fig. 11). *Trans*-platin had not been considered to form DNA adducts that lead to anticancer activity. However, *trans*-type Pt-complexes that shows antitumor activities was found recently. Despite the extensive research on both *cis*- and *trans*-platin, the origin of their difference in biochemical activity still remains unclear. The final step of the antitumor treatment is the combination of *cis*-platin and DNA leading modifications of the DNA structure. Meanwhile, some earlier steps, such as solvation before reaching the final target, are also believed to play important roles in the efficacy of drugs.

Their hydration should be investigated to understand the difference in the medical application between *cis*- and *trans*-platins.

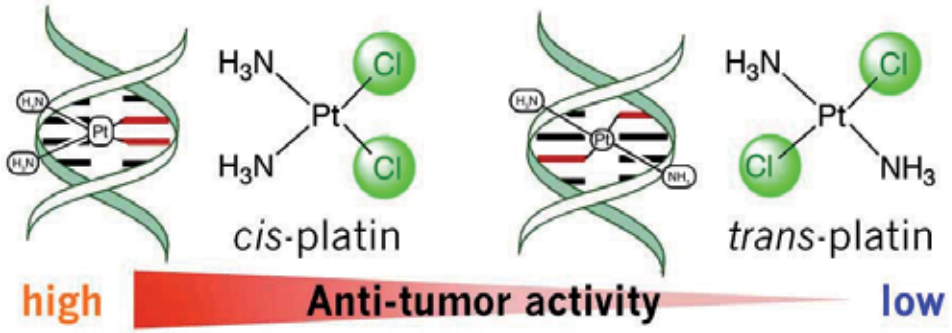

Fig. 11. Structures of *cis*- and *trans*-platins and schematic representations of DNA adducts. Reproduced from Mori *et al.* (2012) by permission.

FMO-MD simulations were performed for hydrated *cis*- and *trans*-platins. The simulation conditions were set as described below. Each platin complex was hydrated with a spherical droplet of water centred at the Pt atom with a diameter of 10.5 Å. This diameter was determined to include up to the second solvation shell, so that the physicochemical properties of the first shell should be reproduced. In the FMO-MD simulations, the electronic states of the hydrated platin complexes were described by FMO(3)-MP2. The basis sets were MCPdz for Pt, MCPdzp for Cl, and 6-31G(d) for the others, respectively. The MCP basis sets were applied for heavy elements (see subsection 2.2.6). The central platin and each of the water molecules were regarded as independent fragments. DF was applied to allow for the generation of proton-transferred species during the production MD runs. For each *cis*- and *trans*-platin system, a 1-ps equilibration and a subsequent 2-ps production MD run were performed using the Nose-Hoover Chains NVT ensemble at 300 K. NPA was also performed during the FMO-MD run to analyze the differences in charge fluctuations between *cis*- and *trans*-platin, illuminating the differences in the hydration environment around polarized $Pt^{\delta+}$-$Cl^{\delta-}$ bonds, which should be cleaved by the nucleophilic attack of a solvent water molecule.

The time evolution of the natural charge on each ligand in *cis*- and *trans*-platin, and that of Pt-Cl bond lengths are shown in Fig. 12. Relatively larger charge fluctuations were observed on the Pt/Cl sites than on the NH_3 sites in both platins. This difference among the sites was attributable to the fact that NH_3 has no amplitude in the highest occupied molecular orbital. A close comparison of the left and right graphs in Fig. 12 revealed a correlation between fluctuation of the Pt/Cl sites and that of the Pt-Cl bond. By applying the Fourier transform technique to the charge fluctuation, we calculated the frequency of the fluctuation to be 334 cm^{-1}. This frequency can also be assigned to the Pt-Cl stretching mode coupled with intermolecular vibrations between the solute platin and solvent water molecules. The correlation observed in charge fluctuation on Pt and Cl sites means that there is a CT interaction between them. Since the frontier MO that participates in the CT process is a Pt-Cl antibonding orbital, the CT interaction coupled with the fluctuation of the solvent water should induce a Pt-Cl bonds fluctuation. Since *trans*-platin has inversion symmetry, the

dipole moment of *trans*-platin is much smaller than that of *cis*-platin. This means that the number of water molecules which coordinates to the platin complex is larger for *cis*-platin than for *trans*-platin. Thus, the CT interaction coupled with the solvent motion is stronger in *cis*-platin than in *trans*-platin. As a result, the Pt-Cl bonds are easier to elongate for the cleavage in the hydrated *cis*-platin than in the hydrated *trans*-platin. Thus, by using FMO-MD simulations, we obtained new quantum chemical insight into the solvation of platin complexes.

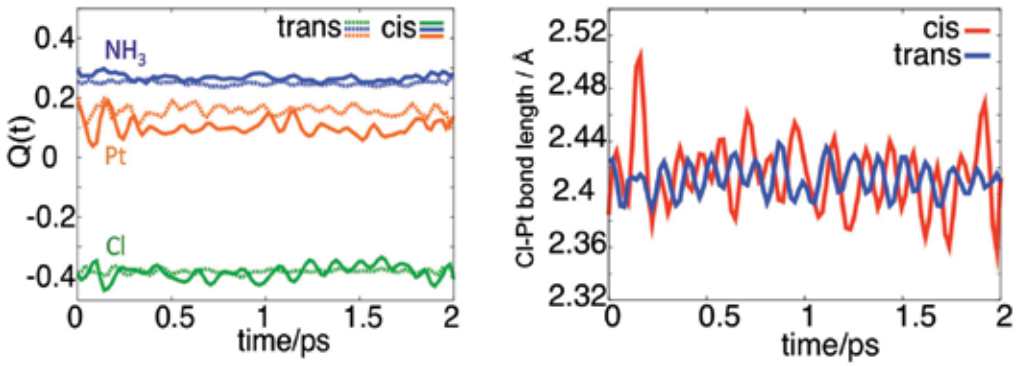

Fig. 12. (Left) Time evolution of natural charge on the Pt, NH_3, and Cl sites in the *cis*- and *trans*-platin. Solid and dotted lines indicate *cis*- and *trans*- isomers, respectively. (Right) Time evolution of Pt-Cl bond lengths. Reproduced from Mori *et al.* (2012) by permission.

4. Prospects and conclusion

As reviewed so far, FMO-MD has been applied to various chemical phenomena in the presence of explicit solvents and has given realistic molecular pictures of the phenomena. We are planning to extend the field of FMO-MD by introduction of new capabilities, as follows.

The so-called QM/MM scheme will enhance the target size of FMO-MD. QM/MM has attracted great interest in simulating condensed-phase systems as well as proteins. In this scheme, the chemically relevant region is subjected to QM calculations while the environmental effects are incorporated through a set of MM parameters. MFMO has a conceptual similarity to QM/MM, and hence we have a plan to implement a general QM/MM ability in conjunction with MFMO.

The improvement of accuracy in FMO gradient evaluations may be a future subject. Nagata's reformulation, including the supplemental response terms of monomers (Nagata *et al.*, 2011a) as well as the BDA-related residual contributions (Nagata *et al.,* 2010), are of interest for implementation at the HF level.

Another important issue is the extraction of more information from FMO-MD trajectories. From a series of configurations, the time-dependent fluctuations in electronic densities can be derived, some of which are correlated with the creation and destruction of bonding interactions. For example, the Fourier transform-based analyses may shed light on the detailed dynamical picture of nucleophilic attack reactions.

In conclusion, FMO-MD is a highly-parallelizable *ab initio* MD method. FMO-MD has advanced rapidly by improvement of both the FMO and MD portions of the method and has been successfully applied to various chemical phenomena in solution. We are planning to extend the methodology and application of FMO-MD by incorporating several new features.

5. Acknowledgment

Thanks are due to Dr. Makoto Sato, Mr. Takayuki Fujiwara, Mr. Yuji Kato, and Professor Hiroshi Yamataka of Rikkyo University, Dr. Yoshio Okiyama of Tokyo University, Ms. Natsumi Hirayama of Ochanomizu University, Professor Takeshi Ishikawa of Gifu University, and Dr. Takatoshi Fujita and Professor Shigenori Tanaka of Kobe University for their collaboration in the FMO-MD project. The works presented in this articles have been supported by the following funds: the Core Research for Evolutional Science and Technology (CREST) project of the Japan Science and Technology Agency (JST) to YK, YM, TK, and HM; the Grant-in-Aid for Scientific Research from the Ministry of Education, Culture, Sports, Science and Technology of Japan (MEXT) to YM ("Molecular Theory for Real Systems") and to YM and YK ("Molecular-level analyses of dynamics-controlled organic reactions"); the Ocha-dai Academic Production project by JST, Funding from Sumitomo Foundation, and Advanced Scientific Computing project 2010 at the Research Institute for Information Technology of Kyushu University to HM; the Rikkyo University Special Fund for Research (SFR) to YM, YK, and HM; and the Research and Development of Innovative Simulation Software (RISS) project at the Institute of Industrial Science of the University of Tokyo to TN and YM. Some of the calculations were performed using computing resources at the Research Centre for Computational Science, Okazaki, Japan.

6. References

Aikens, C. M.; Webb, S. P.; Bell, R. L.; Fletcher, G. D.; Schmidt, M. W. & Gordon, M. S. (2003). A Derivation of the Frozen-orbital Unrestricted Open-shell and Restricted Closed-shell Second-order Perturbation Theory Analytic Gradient Expressions. *Theoretical Chemistry Accounts*, Vol. 110, No. 4, (November 2003), pp. 233-253, ISSN 1432-881X

Chiba, M.; Fedorov, D. G.; Nagata, T. & Kitaura, K. (2009). Excited state geometry optimizations by time-dependent density functional theory based on the fragment molecular orbital method. *Chemical Physics Letters*, Vol. 474, Nos. 4-6, (October 2009), pp. 227–232, ISSN 0009-2614

Fedorov, D. G.; Olson, R. M.; Kitaura, K.; Gordon, M. S. & Koseki, S. (2004a). A new hierarchical parallelization scheme: generalized distributed data interface (GDDI), and an application to the fragment molecular orbital method (FMO). *Journal of Computational Chemistry,* Vol. 25, No. 6, (April 2004), pp. 872-880, ISSN 1096-987X

Fedorov, D. G. & Kitaura, K. (2004b). Second order Moller-Plesset perturbation theory based upon the fragment molecular orbital method. *Journal of Chemical Physics*, Vol. 121, No. 6, (August 2004), pp. 2483-2490, ISSN 1089-7690

Fedorov, D. G.; Ishida, T. & Kitaura, K. (2005). Multilayer Formulation of the Fragment Molecular Orbital Method (FMO). *Journal of Physical Chemistry A*, Vol. 109, No. 11, (March 2005), pp. 2638-2646, ISSN 1089-5639

Fedorov, D. G.; Ishida, T.; Uebayasi, M. & Kitaura, K. (2007a). The Fragment Molecular Orbital Method for Geometry Optimizations of Polypeptides and Proteins. *Journal of Physical Chemistry A*, Vol.111, No. 14, (April 2007), pp. 2722-2732, ISSN 1089-5639

Fedorov, D. G. & Kitaura, K. (2007b). Extending the power of quantum chemistry to large systems with the fragment molecular orbital method. *Journal of Physical Chemistry A*, Vol.111, No. 30 (August 2007), pp. 69-4-6914, ISSN 1089-5639

Fedorov, D. G. & Kitaura, K. (2009). *The Fragment Molecular Orbital Method: Practical Applications to Large Molecular Systems,* CRC Press, ISBN 978-1420078480, London, UK

Fedorov, D. G.; Avramov, P. V.; Jensen, J. H. & Kitaura, K. (2009). Analytic gradient for the adaptive frozen orbital bond detachment in the fragment molecular orbital method. *Chemical Physics Letters*, Vol. 477, Nos. 1-3 (July 2009), pp. 169-175, ISSN 0009-2614

Fedorov, D. G.; Alexeev, Y. & Kitaura, K. (2011). Geometry Optimization of the Active Site of a Large System with the Fragment Molecular Orbital Method. *Journal of Physical Chemistry Letters*, Vol.2, No. 4 (January 2011), pp. 282-288, ISSN 1948-7185

Foreman, J. B.; Head-Gordon, M.; Pople, J. A. & Frisch, M. J. (1992). Toward a Systematic Molecular Orbital Theory for Excited States. *Journal of Chemical Physics*, Vol. 96, No. 1, (July 1992), pp. 135-149, ISSN 1089-7690

Fujita, T.; Watanabe, H. & Tanaka, S. (2009). *Ab initio* Path Integral Molecular Dynamics Based on Fragment Molecular Orbital Method. *Journal of the Physical Society of Japan,* Vol. 78, No. 10, (October 2009), 104723, ISSN 1347-4073

Fujita, T.; Nakano, T. & Tanaka, S. (2011). Fragment molecular orbital calculations under periodic boundary condition. *Chemical Physics Letters,* Vol. 506, Nos. 1-3, (April 2011), pp. 112-116, ISSN 0006-2614

Fujiwara, T.; Mori, H, Mochizuki, Y.; Tatewaki, H. & Miyoshi, E. (2010a). Theoretical study of hydration models of trivalent rare-earth ions using model core potentials. *Journal of Molecular Structure - THEOCHEM*, Vol. 949, Nos. 1-3, (June 2010), pp. 28-35, ISSN 0166-1280

Fujiwara, T.; Mochizuki, Y.; Komeiji, Y.; Okiyama, Y.; Mori, H.; Nakano, T. & Miyoshi, E. (2010b). Fragment molecular orbital-based molecular dynamics (FMO-MD) simulations on hydrated Zn(II) ion. *Chemical Physics Letters,* Vol. 490, Nos. 1-3 (April 2010), pp. 41-45, ISSN 0006-2614

Fujiwara, T.; Mori, H.; Mochizuki, Y.; Osanai, Y.; Okiyama, Y. & Miyoshi, E. (2011). 4f-in-core model core potentials for trivalent lanthanides. *Chemical Physics Letters*, Vol. 510, Nos. 4-6 (July 2011), pp. 261-266, ISSN 0006-2614

Gordon, M. S.; Fedorov, D. G.; Pruitt, S. R. & Slipchenko, L. V. (2011). Fragmentation Methods: A Route to Accurate Calculations on Large Systems. *Chemical Reviews*, in press, doi:10.1021/cr20093j, ISSN

Head-Gordon, M.; Rico, R. J.; Oumi, M. & Lee, T. J. (1994). A doubles correction to electronic excited states from configuration interaction in the space of single substitutions. *Chemical Physics Letters.* Vol. 219, Nos. 1-2, (March 1994), pp. 21-24, ISSN 0009-2614

Ishimoto, T.; Tokiwa, H.; Teramae, H. & U. Nagashima (2004). Development of an *ab initio* MO-MD program based on fragment MO method: an attempt to analyze the fluctuation of protein. *Chemical Physics Letters,* Vol. 387, Nos. 4-6 (December 2004), pp. 460-465, ISSN 0009-2614

Ishimoto, T.; Tokiwa, H.; Teramae, H. & U. Nagashima (2005). Theoretical study of intramolecular interaction energies during dynamics simulations of oligopeptides by the fragment molecular orbital-Hamiltonian algorithm method. *Journal of Chemical Physics,* Vol. 122, No. 9, (March 2005), 094905, ISSN 1089-7690

Ishikawa, T.; Mochizuki, Y. , Nakano, T.; Amari, S.; Mori, H.; Honda, H.; Fujita, T.; Tokiwa, H.; Tanaka, S.; Komeiji, Y.; Fukuzawa, K.; Tanaka, K. & Miyoshi, M. (2006). Fragment molecular orbital calculations on large scale systems containing heavy metal atom. Chemical Physics Letters, Vol. 427, Nos. 1-3, (August 2006), pp. 159-165, ISSN 0009-2614

Ishikawa, T.; Yamamoto, N. & Kuwata, K. (2010). Partial energy gradient based on the fragment molecular orbital method: application to geometry optimization. *Chemical Physics Letters,* Vol. 500, Nos. 4-6, (November 2010), pp. 149–154, ISSN 0009-2614

Kitaura, K.; Ikeo, E.; Asada, T.; Nakano, T. & Uebayasi, M. (1999). Fragment molecular orbital method: an approximate computational method for large molecules. *Chemical Physics Letters,* Vol. 313, Nos.3-4, (November 1999), pp. 701-706, ISSN 0009-2614

Kitaura, K.; Sugiki, S.; Nakano, T.; Komeiji, Y. & Uebayasi, M. (2001). Fragment molecular orbital method: analytical energy gradients. *Chemical Physics Letters,* Vol. 336, Nos. 1-2, (March 2001), pp. 163-170, ISSN 0009-2614

Komeiji, Y.; Nakano, T.; Fukuzawa, K.; Ueno, Y.; Inadomi, Y.; Nemoto, T.; Uebayasi, M.; Fedorov, D. G. & Kitaura, K. (2003). Fragment molecular orbital method: application to molecular dynamics simulation, 'ab initio FMO-MD.' *Chemical Physics Letters,* Vol. 372, Nos. 3-4, (April 2003), pp. 342-347, ISSN 0009-2614

Komeiji, Y.; Uebayasi, M.; Takata, R.; Shimizu, A.; Itsukashi, K. & Taiji, M. (1997). Fast and accurate molecular dynamics simulation of a protein using a special purpose computer. *Journal of Computational Chemistry*, Vol. 18, No. 12, (September 1997), pp. 1546-1563, ISSN 1096-987X

Komeiji, Y.; Inadomi, Y. & Nakano, T. (2004). PEACH 4 with ABINIT-MP: a general platform for classical and quantum simulations of biological molecules. *Computational Biology and Chemistry,* Vol. 28, No. 2, (April 2004), pp. 155-1621, ISSN 1476-9271

Komeiji, Y. (2007). Implementation of the blue moon ensemble method. *Chem-Bio Informatics Journal*, Vol. 7, No. 1, (January 2007), pp. 12-23, ISSN 1347-0442

Komeiji, Y.; Ishida, T.; Fedorov, D. G. & Kitaura, K. (2007). Change in a protein's electronic structure induced by an explicit solvent: an *ab initio* fragment molecular orbital study of ubiquitin. *Journal of Computational Chemistry,* Vol. 28, No. 10, (July 2007), pp. 1750-1762, ISSN 1096-987X

Komeiji, Y.; Ishikawa, T.; Mochizuki, Y.; Yamataka, H. & Nakano, T. (2009a). Fragment Molecular Orbital method-based Molecular Dynamics (FMO-MD) as a simulator for chemical reactions in explicit solvation. *Journal of Computational Chemistry,* Vol. 30, No. 1, (January 2009), pp. 140-50, ISSN 1096-987X

Komeiji, Y.; Mochizuki, Y.; Nakano, T. & Fedorov, D. G. (2009b). Fragment molecular orbital-based molecular dynamics (FMO-MD), a quantum simulation tool for large molecular systems. *Journal of Molecular Structure-THEOCHEM,* Vol. 898, Nos. 1-3, (March 2009), pp. 2-9, ISSN 0166-1280

Komeiji, Y.; Mochizuki, Y. & Nakano, T. (2010). Three-body expansion and generalized dynamic fragmentation improve the fragment molecular orbital-based molecular dynamics (FMO-MD). *Chemical Physics Letters,* Vol. 484, Nos. 4-6, (January 2010), pp. 380-386, ISSN 0009-2614

Li, H.; Fedorov, D. G.; Nagata, T.; Kitaura, K.; Jensen, J. H. & Gordon, M. S. (2010). Energy gradients in combined fragment molecular orbital and polarizable continuum model (FMO/PCM) calculation. *Journal of Computational Chemistry,* Vol. 31, No. 4, (March 2010), pp. 778-790, ISSN 1096-987X

Marx, D. & Parrinello, M. (1996). *Ab initio* path integral molecular dynamics: Basic ideas. *Journal of Chemical Physics.* Vol. 104, No. 11, (March 1996), pp. 407-412, ISSN 1089-7690

Miyoshi, E.; Mori, H.; Hirayama, R.; Osanai, T.; Noro, T.; Honda, H. & Klobukowski, M. (2005). Compact and efficient basis sets of s- and p-block elements for model core potential method. *Journal of Chemical Physics*, Vol. 122, No. 7, (February 2005), 074104, ISSN 1089-7690

Mochizuki, Y.; Koikegami, S.; Nakano, T.; Amari, S. & Kitaura, K. (2004a). Large scale MP2 calculation with fragment molecular orbital scheme. *Chemical Physics Letters,* Vol. 396, Nos. 4-6, (October 2004), pp. 473-479, ISSN 0009-2614

Mochizuki, Y.; Nakano, T.; Koikegami, S.; Tanimori, S.; Abe. Y.; Nagashima, U. & Kitaura, K. (2004b). A parallelized integral-direct second-order Moller-Plesset perturbation theory method with a fragment molecular orbital scheme. *Theoretical Chemistry Accounts*, Vol. 112, Nos. 5-6, (December 2004), pp. 442-452, ISSN 1432-881X

Mochizuki, Y.; Koikegami, S.; Amari, S.; Segawa, K.; Kitaura, K. & Nakano, T. (2005a). Configuration interaction singles method with multilayer fragment molecular orbital scheme. *Chemical Physics Letters.* Vol. 406, No. 4-6, (May 2005), pp. 283-288, ISSN 0009-2614

Mochizuki, Y.; Fukuzawa, K.; Kato, A.; Tanaka, S.; Kitaura, K. & Nakano, T. (2005b). 1A configuration analysis for fragment interaction. *Chemical Physics Letters,* Vol. 410, Nos. 4-6, (June 2005), pp. 247- 253, ISSN 0009-2614

Mochizuki, Y.; Tanaka, K.; Yamashita, K.; Ishikawa, T.; Nakano, T.; Amari, S.; Segawa, K.; Murase, M.; Tokiwa, H. & Sakurai, M. (2007a). Parallelized integral-direct CIS(D) calculations with multilayer fragment molecular orbital scheme. *Theoretical Chemistry Accounts,* Vol. 117, No. 4 (April 2007), pp. 541-553, ISSN 1432-881X

Mochizuki, Y.; Komeiji, Y.; Ishikawa, T.; Nakano, T. & Yamataka, H. (2007b). A fully quantum mechanical simulation study on the lowest nπ* state of hydrated formaldehyde. *Chemical Physics Letters,* Vol. 434, Nos.1-3, (March 2007), pp. 66-72, ISSN 0009-2614

Mochizuki, Y.; Nakano, T.; Komeiji, Y.; Yamashita, K.; Okiyama, Y.; Yoshikawa, H. & Yamataka H. (2011), Fragment molecular orbital-based molecular dynamics (FMO-MD) method with MP2 gradient. *Chemical Physics Letters,* Vol. 504, Nos. 1-3, (February 2011), pp. 95-99, ISSN 0009-2614

Mori, H.; Ueno-Noto, K.; Osanai, Y.; Noro, T.; Fujiwara, T.; Klobukowski, M. & Miyoshi, E. (2009) Revised model core potentials for third-row transition-metal atoms from Lu to Hg. *Chemical Physics Letters,* Vol. 476, No. 4-6 (June 2009), pp. 317-322, ISSN: 00092614.

Mori, H.; Hirayama, N.; Komeiji, Y. & Mochizuki, Y. (2012). Differences in hydration between cis- and trans-platin: Quantum insights by *ab initio* fragment molecular orbital-based molecular dynamics (FMO-MD). submitted

Nagata, T.; Fedorov, D. G. & Kitaura, K. (2009). Derivatives of the approximated electrostatic potentials in the fragment molecular orbital method. *Chemical Physics Letters,* Vol. 475, Nos. 1-3, (June 2009), pp. 124–131, ISSN 0009-2614

Nagata, T.; Fedorov, D. G. & Kitaura, K. (2010). Importance of the hybrid orbital operator derivative term for the energy gradient in the fragment molecular orbital method. *Chemical Physics Letters,* Vol. 492, Nos. 4-6, (June 2010), pp. 302-308, ISSN 0009-2614

Nagata, T.; Brosen, K.; Fedorov, D. G.; Kitaura, K. & Gordon, M. S. (2011a). Fully analytic energy gradient in the fragment molecular orbital method. *Journal of Chemical Physics,* Vol. 134, No. 12, (March 2011), 124115, ISSN 1089-7690

Nagata, T.; Fedorov, D. G.; Ishimura, K. & Kitaura, K. (2011b). Analytic energy gradient for second-order Moeller-Plesset perturbation theory based on the fragment molecular orbital method. *Journal of Chemical Physics,* Vol. 135, No. 4, (July 2011), 044110, ISSN 1089-7690

Nagata, T.; Fedorov, D. G. & Kitaura, K. (2011c). Analytic gradient and molecular dynamics simulations using the fragment molecular orbital method combined with effective potentials. *Theoretical Chemistry Accounts,* in press.

Nakano, T.; Kaminuma, T.; Sato, T.; Akiyama, Y.; Uebayasi, M. & Kitaura, K. (2000). Fragment molecular orbital method: application to polypeptides. *Chemical Physics Letters,* Vol. 318, No. 6, (March 2000), pp. 614-618, ISSN 0009-2614

Nakano, T.; Kaminuma, T.; Sato, T.; Fukuzawa, K.; Akiyama, Y.; Uebayasi, M. & Kitaura, K. (2002). Fragment molecular orbital method: use of approximate electrostatic potential. *Chemical Physics Letters,* Vol. 351, Nos. 5-6, (January 2002), pp. 475-480, ISSN 0009-2614

Nakano, T.; Mochizuki, Y.; Yamashita, K.; Watanabe, C.; Fukuzawa, K.; Segawa, K.; Okiyama, Y.; Tsukamoto, T. & Tanaka, S. (2011). Development of the four-body corrected fragment molecular orbital (FMO4) method. *Chemical Physics Letters*, Vol. 523, No. 1 (January 2012), pp. 128-133, ISSN 0009-2614

Osanai, Y.; Mon, M. S.; Noro, T.; Mori, H.; Nakashima, H.; Klobukowski, M. & Miyoshi, E. (2008a). Revised model core potentials for first-row transition-metal atoms from Sc to Zn. *Chemical Physics Letters,* Vol. 452, No. 1-3 (February 2008), pp. 210-214, ISSN 0009-2614

Osanai, Y.; Soejima, E.; Noro, T.; Mori, H.; Mon, M. S.; Klobukowski, M. & Miyoshi, E. (2008b). Revised model core potentials for second-row transition metal atoms from Y to Cd. *Chemical Physics Letters*, *Vol. 463*, No. 1-3 (September 2008), pp. 230-234, ISSN 0009-2614.

Sakai, Y.; Miyoshi, E.; Klobukowski, M. & Huzinaga, S. (1987). Model potentials for molecular calculations. 1. The SD-MP set for transition-metal atoms Sc through Hg. *Journal of Computational Chemistry,* Vol. 8, No. 3, (April/May 1987), pp. 226-255, ISSN 1096-987X

Sato, M.; Yamataka, H.; Komeiji, Y.; Mochizuki, Y.; Ishikawa, T. & Nakano, T. (2008). How does an S_N2 reaction take place in solution? Full *ab initio* MD simulations for the hydrolysis of the methyl diazonium ion. *Journal of the American Chemical Society,* Vol. 130, No.8, (February 2008), pp. 2396-2397, ISSN 0002-7863

Sato, M.; Yamataka, H.; Komeiji, Y.; Mochizuki, Y. & Nakano, T. (2010). Does Amination of Formaldehyde Proceed Through a Zwitterionic Intermediate in Water? Fragment Molecular Orbital Molecular Dynamics Simulations by Using Constraint Dynamics. *Chemistry-A European Journal*, Vol. 16, No. 22, (June 2010), pp. 6430-6433, ISSN 1521-3765

Sprik, M. & Ciccotti, G. (1998). Free energy from constrained molecular dynamics. *Journal of Chemical Physics*, Vol. 109, No. 18, (November 1998), pp. 7737-7744, ISSN 1089-7690

Tamura, K.; Watanabe, T.; Ishimoto, T. & Nagashima, U. (2008). *Ab Initio* MO-MD Simulation Based on the Fragment MO Method: A Case of (-)-Epicatechin Gallate with STO-3G Basis Set. *Bulletin of Chemical Society of Japan,* Vol. 81, No. 1, (January 2008), pp. 110–112, ISSN 1348-0634

2

Advanced Molecular Dynamics Simulations on the Formation of Transition Metal Nanoparticles

Lichang Wang and George A. Hudson
Southern Illinois University Carbondale
USA

1. Introduction

Metal clusters and nanoparticles have gained attention in the recent years due to their application as catalysts, antimicrobials, pigments, micro circuits, drug delivery vectors, and many other uses. Many fascinating properties exhibited by nanomaterials are highly size and structure dependent. Therefore, understanding the formation of these nanoparticles is important in order to tailor their properties. The laboratory synthesis and characterization of such clusters and nanoparticles has provided insight into characteristics such as size and shape. However, monitoring the synthesis of such a cluster (or nanoparticle) on the atomic scale is difficult and to date no experimental technique is able to accomplish this. The use of computational methods has been employed to gain insight into the movement and interactions of atoms when a metal cluster or nanoparticle is formed. The most common computational approach has been to use molecular dynamics (MD) simulation which models the movement of atoms using a potential energy surface (PES) often referred to as a force field. The PES is used to describe the interaction of atoms and can be obtained from electronic strcuture calculations, from experimental measurements, or from the combining calculations and measurements.

Molecular dynamics simulations have been used to study many phenomena associated with nanoparticles. Of particular interests are the geometric structure and energetics of nanoparticles of Au (Erkoc 2000; Shintani et al. 2004; Chui et al. 2007; Pu et al. 2010), Ag (El-Bayyari 1998; Monteil et al. 2010), Al (Yao et al. 2004), Fe (Boyukata et al. 2005), Pb (Hendy & Hall 2001), U (Erkoc et al. 1999) and of alloys such as NaMg (Dhavale et al. 1999), Pt-Ni/Co (Favry et al. 2011), Pt-Au (Mahboobi et al. 2009), Zn-Cd (Amirouche & Erkoc 2003), Cu-Ni/Pd (Kosilov et al. 2008), Co-Sb (Yang et al. 2011) as well as the behavior of nanoparticles during the melting or freezing process such as Au (Wang et al. 2005; Bas et al. 2006; Yildirim et al. 2007; Lin et al. 2010; Shibuta & Suzuki 2010), Na (Liu et al. 2009), Cu (Wang et al. 2003; Zhang et al. 2009), Al (Zhang et al. 2006), Fe (Ding et al. 2004; Shibuta & Suzuki 2008), Ni (Wen et al. 2004; Lyalin et al. 2009; Shibuta & Suzuki 2010), Pd (Miao et al. 2005), Sn (Chuang et al. 2004; Krishnamurty et al. 2006), Na-alloys (Aguado & Lopez 2005), Pt-alloys (Sankaranarayanan et al. 2005; Yang et al. 2008; Yang et al. 2009; Shi et al. 2011), Au-alloys (Yang et al. 2008; Yang et al. 2009; Gonzalez et al. 2011; Shi et al. 2011) and Ag-alloys (Kuntova et al. 2008; Kim et al. 2009). Molecular dynamics simulations have also been applied to study adsorption and desorption of nanoparticles on surfaces, such as Pd/MgO

(Long & Chen 2008) and Mn/Au (Mahboobi et al. 2010), nanoparticle aggregation such as Au (Lal et al. 2011), diffusion processes (Shimizu et al. 2001; Sawada et al. 2003; Yang et al. 2008; Alkis et al. 2009; Chen & Chang 2010), fragmentation of Au and Ag (Henriksson et al. 2005), thermal conductivity of Cu nanoparticles (Kang et al. 2011), and cluster (nanoparticle) formation of Au (Boyukata 2006; Cheng et al. 2009), Ag (Yukna & Wang 2007; Zeng et al. 2007; Hudson et al. 2010), Ir (Pawluk & Wang 2007), Co (Rives et al. 2008), and various alloys (Cheng et al. 2009; Chen & Chang 2010; Chen et al. 2010; Goniakowski & Mottet 2010; Carrillo & Dobrynin 2011).

Formation of metal clusters or nanoparticles can take place in all three phases: in liquid, gas, and on solid surfaces. Different formation mechanisms can be involved in the formation of transition metal nanoparticles. Of particular interest is coalescence, a process by which two droplets or particles collide to form a new daughter droplet or particle. Coalescence is important due to its role in nanoparticle formation and size control. Conventional MD simulations are used to describe coalescence of transition metal nanoparticles and provide information on the dynamics of nanoparticle formation, such as rate constant. However, the change of the electronic properties of the particles can only be probed by performing electronic structure calculations. Therefore, to have a complete picture of the formation of nanoparticles, the coupling of both MD and electronic structure calculations is important and forms the practice of our MD simulations. We denote it as the meta-molecular dynamics (meta-MD) method. In this chapter, we provide a description of the meta-MD method and its application in the study of Fe cluster formations. Before we present the meta-MD method and its application, we provide a general description of conventional MD simulations and the PES that is of ultimate importance in the accuracy of MD simulations.

2. Molecular Dynamics (MD) Simulations and Potential Energy Surfaces (PESs)

In a conventional molecular dynamics simulation, if the motion of atoms in the system is governed by Newton's equations of motion, we numerically solve the position of atom i with a mass of m_i in the Cartesian coordinates x_i, y_i, and z_i by

$$\frac{dx_i}{dt} = \frac{p_{x_i}}{m_i}, \tag{1a}$$

$$\frac{dy_i}{dt} = \frac{p_{y_i}}{m_i}, \tag{1b}$$

$$\frac{dz_i}{dt} = \frac{p_{z_i}}{m_i}. \tag{1c}$$

Here p_{x_i}, p_{y_i}, and p_{z_i} are the momentum of the atom i in the x, y, and z direction, respectively, and are solved by the gradient of the PES, denoted V:

$$\frac{dp_{x_i}}{dt} = -\frac{\partial V}{\partial x_i}, \tag{2a}$$

$$\frac{dp_{y_i}}{dt} = -\frac{\partial V}{\partial y_i}, \tag{2b}$$

$$\frac{dp_{z_i}}{dt} = -\frac{\partial V}{\partial z_i}. \tag{2c}$$

The accuracy of the PES determines the accuracy of the outcome of MD simulations. There are many possible force fields (a.k.a. PESs) (Mazzone 2000; Hendy et al. 2003) but two used most often are the embedded atom method (Daw & Baskes 1984; Zhao et al. 2001; Dong et al. 2004; Lummen & Kraska 2004; Lummen & Kraska 2005; Lummen & Kraska 2005a, 2005b, 2005c; Rozas & Kraska 2007) and the Sutton-Chen potential (Kim et al. 2007; Pawluk & Wang 2007; Yukna & Wang 2007; Hudson et al. 2010; Kayhani et al. 2010).

In the Sutton-Chen PES, V is expressed as

$$V = \varepsilon[\frac{1}{2}\sum_{ij} v(i,j) - c\sum_i \sqrt{\rho_i}], \tag{3}$$

where $v(i,j)$ is an interaction between atoms i and j given by,

$$v(i,j) = \left(\frac{a}{r_{ij}}\right)^n, \tag{4}$$

and ρ_i is the local electron density contribution of atom i given by,

$$\rho_i = \sum_j \left(\frac{a}{r_{ij}}\right)^m. \tag{5}$$

In the above equations of the Sutton-Chen potential, r_{ij} is the distance between atom i and atom j. The parameters; a, n, m, ε, and c depend on the element that is under study.

The N-body term, $\sum_i \sqrt{\rho_i}$, is a cohesive term that describes the tendency for the atoms to stick together. The attraction between atoms is normally described by a $1/r^6$ potential at long distances, due to van der Waals interaction, and described by an N-body form at short distances. Choosing the value of the parameter m to be 6 accomplishes these two things (Sutton & Chen 1990).

Define the lattice sum of a perfect face centered cubic (f.c.c.) crystal to be,

$$S_n^f = \sum_j \left(\frac{a^f}{r_j}\right)^n. \tag{6}$$

The sum is taken over all separations r_j from an arbitrary atom. a^f is equal to the f.c.c. lattice parameter which then defines the unit of length.

In equilibrium the total energy of the crystal does not change to first order when the lattice parameter is varied. This implies,

$$c = \frac{ns_n^f}{m\sqrt{s_m^f}}. \tag{7}$$

The cohesive energy per atom is given by,

$$E_c^f = \frac{\varepsilon s_n^f}{2m}(2n-m). \tag{8}$$

Finally the bulk modulus, B^f, is given by,

$$B^f = \frac{(2n-m)n\varepsilon s_n^f}{36\Omega^f}, \tag{9}$$

where $\Omega^f=(af)^3/4$ which is the atomic volume. Using the above equations a relation between the cohesive energy, E, and the bulk modulus, B is given by,

$$\frac{\Omega^f B^f}{E_c^f} = \frac{nm}{18}. \tag{10}$$

Using experimental measurements of the cohesive energy, E, the bulk modulus, B, and the chosen value of m=6, an integer value for n was to give the value closest in agreement with eq. (10). From the values of m and n eq. (9) can be used to obtain a value of ε and eq. (8) can be used to obtain the value for c. (Sutton & Chen 1990) The parameters ε and a are defined as units of energy and length, respectively. Thus the values of ε and a were chosen, for the different metals, to coincide with results obtained from fitting the PES with experimental or computational measurements. The parameters used in the current MD simulations of Fe cluster formations were obtained from Sutton and Chen (Sutton & Chen 1990).

3. Advanced MD simulations: Meta-MD simulations

In the meta-MD simulations, we couple the conventional MD simulation with the electronic structure calculation to study the formation of transition metal nanoparticles. Such a coupling allows us to record the electronic change of the system during the formation process in addition to the conventional properties in a MD simulation. Furthermore, we will also be able to monitor the accuracy of the PES as well as determine whether the MD simulation on a single PES is valid.

The three ingredients in a meta-MD simulation are electronic structure theory, molecular dynamics theory, and coupling method. In principle, any electronic structure theory can be chosen. Depending on the system of interest, our choice of a particular electronic structure theory is determined by the cost effectiveness and the accuracy of electronic structure calculations. For transition metal systems, the most practical choice of method is density functional theory, where a variety of functionals may be used. The molecular dynamics theory can be quantum scattering, pure classical, mixed quantum-classical, or semi-classical treatment, which also depends on the characteristics of the system to be described. For instance, our current system involves only heavy atoms, we therefore choose classical MD simulations.

Once these theories are chosen, a coupling method has to be employed so that the two types of calculations can be integrated. Appropriate techniques need to be developed in order to integrate the electronic structure calculations seamlessly to the MD simulations. There are several ways to couple MD and DFT calculations. The most straightforward way would be to perform MD simulations first and save the structural information, i.e. the Cartesian coordinates of each atom at each time step. The DFT calculations can be performed using these data. We note that the time step in a typical MD simulation is in the range of 0.01-1 fs, and the simulation can run for ~10ps or longer times. Therefore, the concern with this strategy is that far too many data have to be saved. Additionally, too much computational time is required. An alternative strategy is to carry out MD and DFT calculations simultaneously. One of the advantages of this strategy is to be able to use the electronic wavefunctions generated from the past time step as the initial electronic wavefunction in the subsequent DFT calculation. We are exploring other possibilities to save computer time. Further, the time between two DFT calculations will be set to a longer interval than a simple MD time step. A DFT calculation will be performed between the two DFT calculations only when significant changes have taken place, which will be monitored in the MD simulations. For a particular system of interest, one will need to test extensively which length of time interval will be appropriate to perform DFT calculations in order to find an optimal choice and a common ground in terms of effectiveness and accuracy. Development of the pragmatic coupling methods is in progress.

In this work, we studied the coalescence of an Fe dimer with an Fe atom and of two 15-atom Fe clusters. The numerical aspects of the MD simulations are similar to the previous MD simulations (Billing & Wang 1992a, 1992b; Ge et al. 1992; Wang & Billing 1992; Wang & Billing 1993; Wang et al. 1994a, 1994b; Wang & Clary 1996; Clary & Wang 1997; Wang & Billing 1997; Wang et al. 1999; Wang et al. 2000; McCoy et al. 2001; Wang & McCoy 2003).

The simulations for the systems were performed over a 10 ps time period with a time step of 0.01 fs. During the formation of nanoparticles, a small amount of energy was extracted at every single time step from any atom that had a kinetic energy greater than a defined minimum energy. In this work two simulations were run with a minimum of 298 K and 693 K. The subtraction of energy was done to mimic a cooling rate of 1.5625×10^{11} K/s (1.3464×10^{-8} eV/fs) and 1.5625×10^{13} K/s (1.3454×10^{-8} eV/fs). These cooling rates were used in our studies of Ag cluster formation previously (Hudson et al. 2010).

DFT calculations were performed in a similar fashion as our previous studies of transition metal clusters (Wang & Ge 2002; Cao et al. 2003; Zhang et al. 2003; Xiao & Wang 2004a, 2004b; Zhang et al. 2004a, 2004b, 2004c) Specifically, spin polarized DFT calculations were carried out via the Vienna Ab-initio Simulation Package (VASP).(Kresse & Hafner 1993; Kresse & Furthmuller 1996a, 1996b) The electron-ion interactions were described by the Projector Augmented Waves method.(Kresse & Joubert 1999) The exchange and correlation energies were calculated using the Perdew-Burke-Ernzerhof (PBE) functional.(Perdew et al. 1996) A plane wave basis set was used with a cutoff energy of 300 eV, which was shown to be sufficient from the convergence test. One k point, the Γ point, was used. In order to eliminate interactions between two neighboring images, we set the nearest distance between images no less than 1.0 nm. The simulation techniques used here are very similar to those in our previous study of Pt clusters.(Xiao & Wang 2004b) Single point calculations were performed based on the structural data from the MD simulations. The binding energy, the

energy gap between the highest occupied molecular orbital and the lowest unoccupied molecular orbital (HOMO-LUMO), and the magnetic moment of the system were obtained and discussed.

4. Formation of iron clusters

In this work, we performed MD simulations to study the formation of iron trimers and meta-MD simulations to that of 30-atom iron clusters. The results of these simulations are presented below starting from the formation of iron trimers.

4.1 Iron trimer formation

The MD results for the Fe atom collinearly colliding with an Fe dimer are summarized in Figs. 1-8.

We first examine the effects of initial kinetic energy, cooling rate, and temperature on the structure of Fe trimers. Figure 1 shows the time evolution of interatomic distances between Fe pairs. These plots show the slower cooling rate producing a faster collision and a longer lived linear trimer than the faster cooling rate, though the final products in both cooling rates are triangular trimers, which are demonstrated by the overlap of all three curves at longer times. When the minimum temperature increases from 298 K to 673 K, the linear trimers at both cooling rates last longer, as clearly shown in Fig. 2. In fact, the linear trimer exists at the end of simulation time when the cooling rate is 1.5625×10^{11} K/s. When the initial kinetic energy increases from 0.1 eV shown in Figs. 1 and 2 to 0.5 eV shown in Figs. 3 and 4, the time evolution of interatomic distances has trends similar to the lower kinetic energy cases.

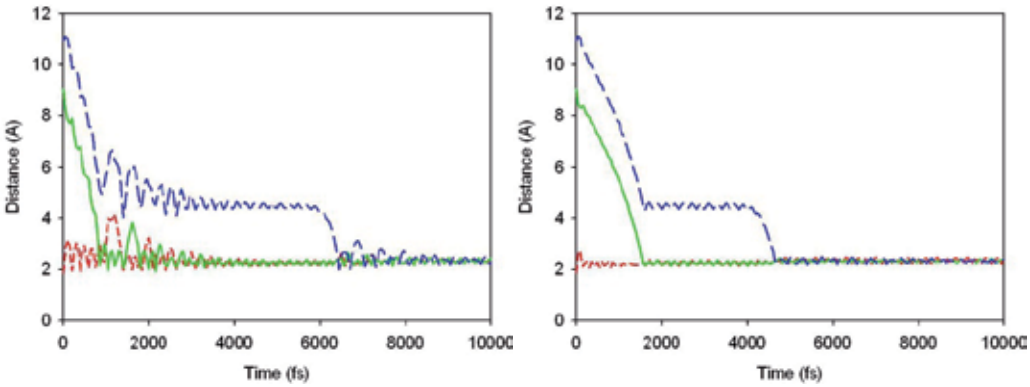

Fig. 1. The interatomic distances of a three-atom coalescence with an initial energy of 0.1 eV at a minimum temperature of 298 K and a cooling rate of 1.5625×10^{11} K/s (left) and 1.5625×10^{13} K/s (right) of atoms 1 & 2 (red/short dash), 2 & 3 (green/solid), and 1 & 3 (blue/long dash).

Among the eight collisions depicted in Figs. 1-4, the favored product was the trigonal trimer, which accounts for 6 of them. The other two were the linear trimer at the end of 10 ps. A high minimum energy and a slow cooling rate was the condition that gave the linear trimer regardless of the initial energy given to the system. The slow cooling rate resulted in a longer duration of the linear trimer configuration before the structure converted to the

trigonal structure. The slow cooling rate also shows a wild oscillation of the bond distances between atoms. This result is as expected due to the slower removal of energy from the system. It can also be noticed that the higher minimum energy resulted in a more violent oscillation of bond lengths after cluster formation (Fig. 2 vs. Fig. 1 and Fig. 4 vs. Fig. 3). This is because the greater amount of heat available is expressed as a vibration in the formed cluster. The greater initial energy of the system (0.1 eV vs. 0.5 eV) has an effect only when a slow cooling rate is employed.

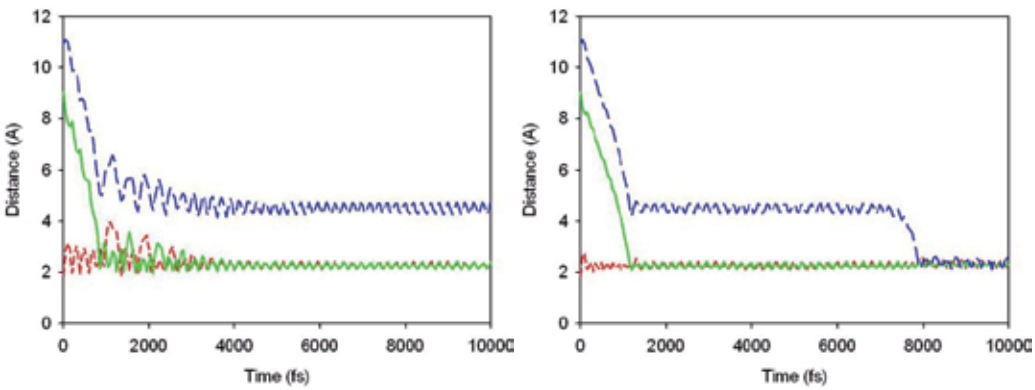

Fig. 2. The interatomic distances of a three-atom coalescence with an initial energy of 0.1 eV at a minimum temperature of 673 K and a cooling rate of 1.5625×10^{11} K/s (left) and 1.5625×10^{13} K/s (right) of atoms 1 & 2 (red/short dash), 2 & 3 (green/solid), and 1 & 3 (blue/long dash).

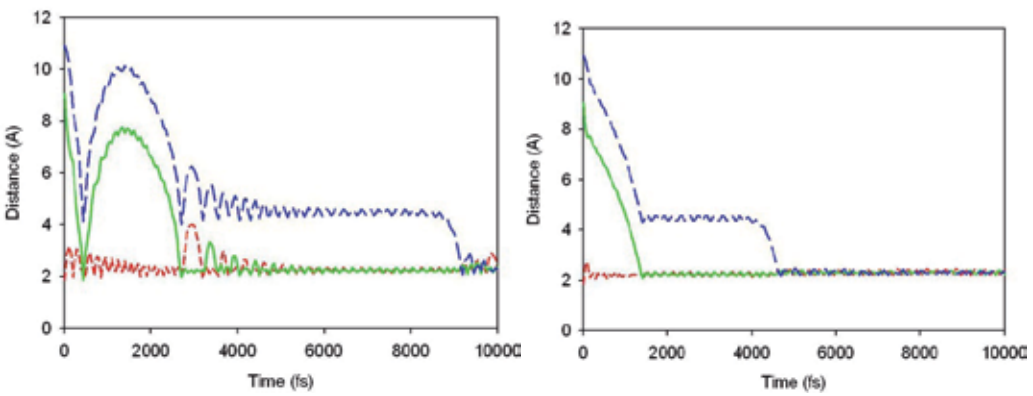

Fig. 3. The interatomic distances of a three-atom coalescence with an initial energy of 0.5 eV at a minimum temperature of 298 K and a cooling rate of 1.5625×10^{11} K/s (left) and 1.5625×10^{13} K/s (right) of atoms 1 & 2 (red/short dash), 2 & 3 (green/solid), and 1 & 3 (blue/long dash).

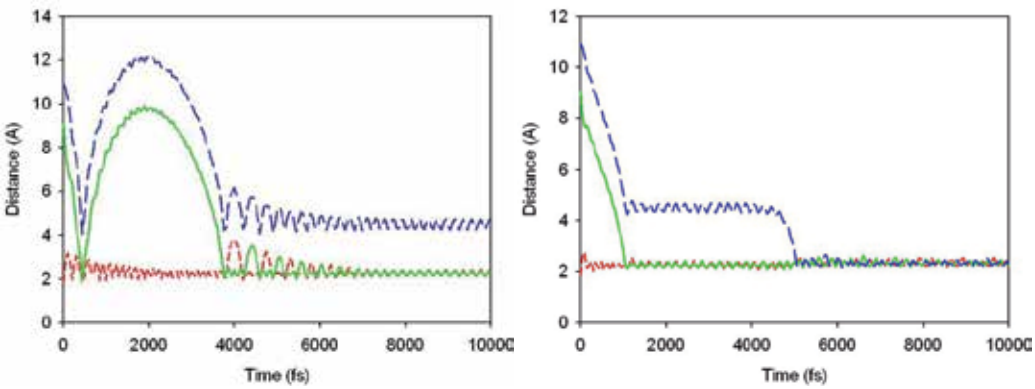

Fig. 4. The interatomic distances of a three-atom coalescence with an initial energy of 0.5 eV at a minimum temperature of 673 K and a cooling rate of 1.5625 x 10^{11} K/s (left) and 1.5625 x 10^{13} K/s (right) of atoms 1 & 2 (red/short dash), 2 & 3 (green/solid), and 1 & 3 (blue/long dash).

We now discuss the energetic aspects of the MD results. Figure 5 shows the changes of the kinetic and potential energy over time at the minimum temperature of 298 K and initial kinetic energy of 0.1 eV. The kinetic energy oscillates during the collision with the slower cooling rate (red curve of the left figure) and is essentially featureless in the case with the faster cooling rate (red curve of right figure). This is due to the slower cooling rate not being able to dissipate the kinetic energy released by the rapid decrease in potential energy.

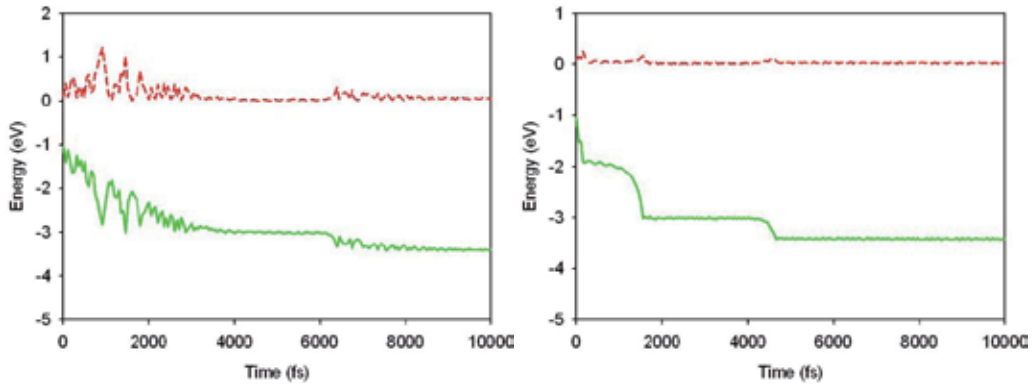

Fig. 5. The kinetic (red/dash) and potential (green/solid) energy of a three-atom coalescence with an initial energy of 0.1 eV at a minimum temperature of 298 K and a cooling rate of 1.5625 x 10^{11} K/s (left) and 1.5625 x 10^{13} K/s (right).

When the minimum energy, or similarly the reaction chamber temperature, was 673 K, similar pictures of the coalescences were obtained. The kinetic energy oscillates in a regular pattern (left of Fig. 6) for the slower cooling rate and has no feature for the faster cooling rate (right of Fig. 6). Again, this is due to the slower cooling rate not being able to remove all of the kinetic energy gained due to a rapid release of potential energy. Similar to the kinetic

energy plots, the potential energy plots show that the slower cooling rate produces a more oscillatory potential while the faster cooling rate produces a smooth curve with a sudden potential drop.

When the initial kinetic energy increases to 0.5 eV, the energy distributions at different cooling rate are similar to the case of 0.1 eV. There is a resemblance of the kinetic and potential energy plots between the two minimum temperatures, namely Fig. 7 *vs* Fig. 8. The difference between the temperature lies at the oscillatory part of the potential energy curves. In the case of the 298 K chamber, the oscillations in the potential energy curve occur at the very last of the MD simulations.

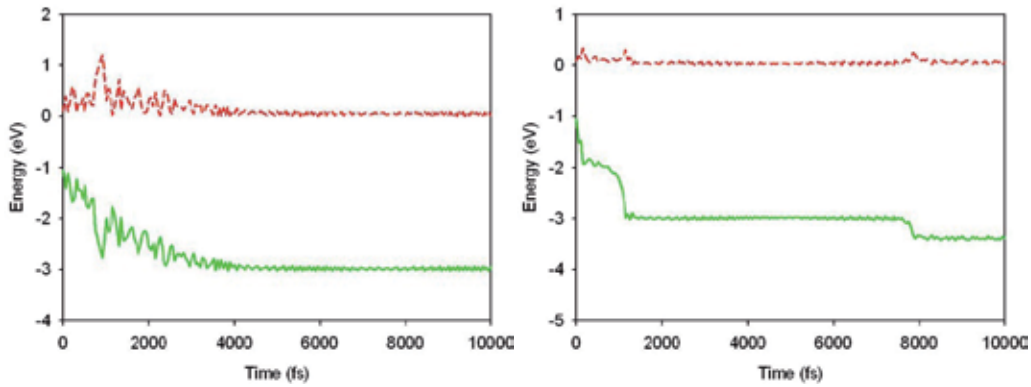

Fig. 6. The kinetic (red/dash) and potential (green/solid) energy of a three-atom coalescence with an initial energy of 0.1 eV at a minimum temperature of 673 K and a cooling rate of 1.5625×10^{11} K/s (left) and 1.5625×10^{13} K/s (right).

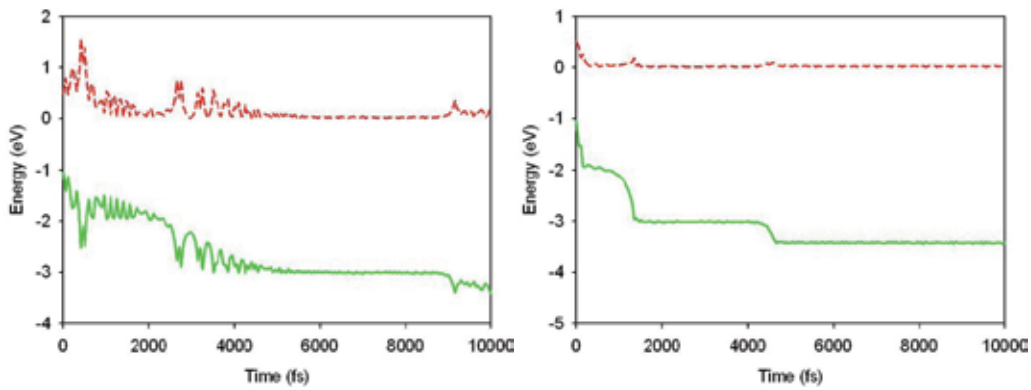

Fig. 7. The kinetic (red/dash) and potential (green/solid) energy of a three-atom coalescence with an initial energy of 0.5 eV at a minimum temperature of 298 K and a cooling rate of 1.5625×10^{11} K/s (left) and 1.5625×10^{13} K/s (right).

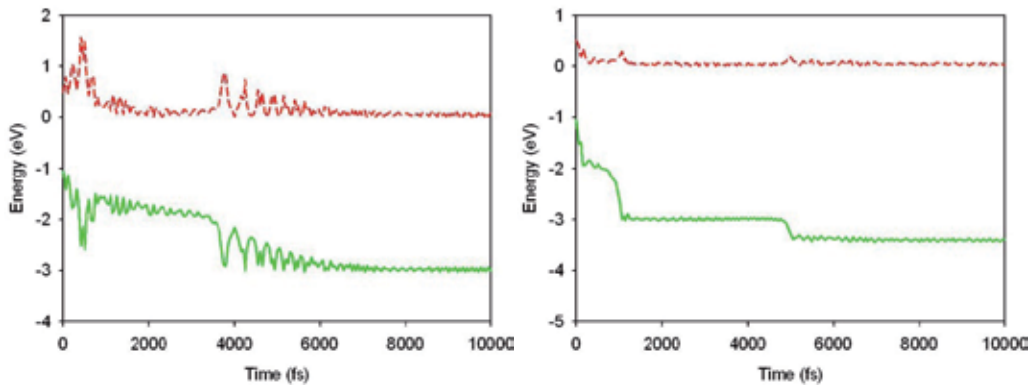

Fig. 8. The kinetic (red/dash) and potential (green/solid) energy of a three-atom coalescence with an initial energy of 0.5 eV at a minimum temperature of 673 K and a cooling rate of 1.5625×10^{11} K/s (left) and 1.5625×10^{13} K/s (right).

Figures 5-8 show that the faster cooling rate generates a smoother kinetic and potential energy plot. The minimum energy has little noticeable effect on the kinetic and potential energy plots except that the oscillations of either are more drastic with the greater minimum energy. The greater initial energy causes a spike in the kinetic energy at the beginning of the simulation which occurs later in the simulation when less initial energy is given to the system. Figures 7 and 8 both show a 'flare up' that is noticeably separate from the initial spike of kinetic energy when a slow cooling rate is used. The simulations that resulted in trigonal trimers gave an ending potential energy of around -3.5 eV while the simulations that resulted in the linear trimer (Fig. 6 left and Fig. 8 left) gave an ending potential of around -3.0 eV. This is due to the lower potential when each atom interacts with the other two atoms rather than two of the three atoms only interacting with one other atom.

4.2 Formation of 30-atom iron clusters

Four MD simulations were carried out with different minimum temperatures and cooling rates in order to investigate how these factors affect the formation process and the structure of the products.

The energy profile evolutions and the final structures of the 30-atom Fe clusters are given in Figs. 9-11.

Figure 9 shows the kinetic energy plot (left) and the potential energy plot (right) of the coalescence of two 15- atom clusters. The slow cooling rate gave a kinetic energy spike after the initial reaction (Fig. 9, left blue and red). The higher minimum temperature results in a higher kinetic energy at the end of the simulation (Fig. 9, left blue and yellow). Figure 9 also shows that the faster cooling rate negates the other parameters. The faster cooling rate plots (yellow and green) have similar kinetic energies while the slower cooling rate plots (red and blue) are very different and the difference is determined by the minimum temperature.

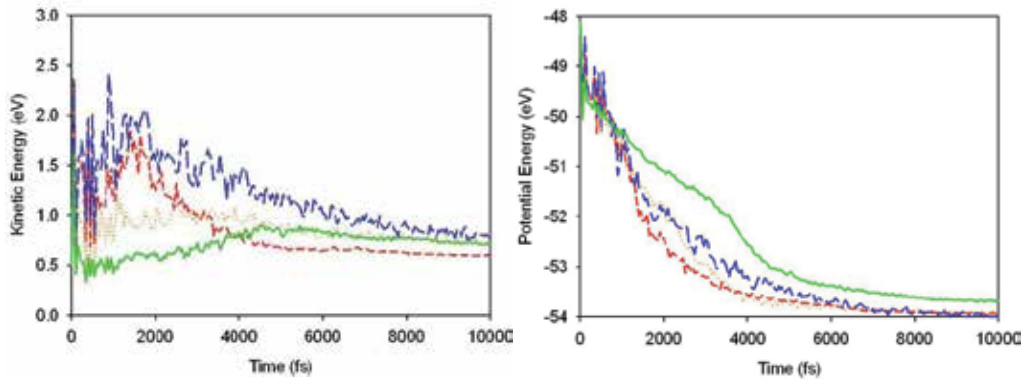

Fig. 9. Energy plots of the coalescence between two 15-atom clusters with an initial energy of 0.5 eV and a minimum temperature and cooling rate of 298 K and 1.5625 x 10^{11} K/s (red/short dash), 298 K and 1.5625 x 10^{13} K/s (green/solid), 673 K and 1.5625 x 10^{11} K/s (blue/long dash), and 673 K and 1.5625 x 10^{13} (yellow/dotted).

The potential energy plot (Fig. 9 right) shows that the slow cooling rate has a more erratic variation in potential, yet three out of the four simulation conditions gave similar potentials. The one simulation to give a higher potential than the others had a fast cooling rate and low minimum temperature. This is likely due to the cluster being stuck in a higher potential configuration and not being able to overcome an energy barrier to reach a lower energy configuration.

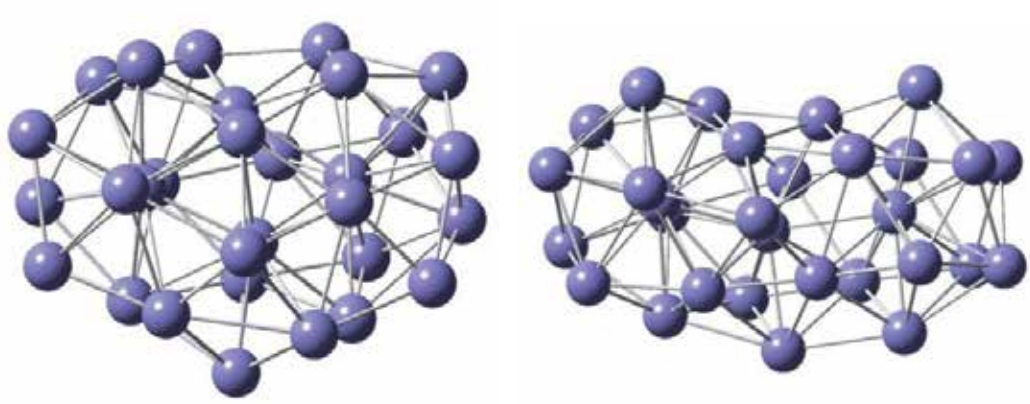

(a) **(b)**

Fig. 10. 30-atom clusters formed under 0.5 eV initial energy with 298 K minimum temperature and a cooling rate of 1.5625 x 10^{11} K/s (left, a) and 1.5625 x 10^{13} K/s (right, b).

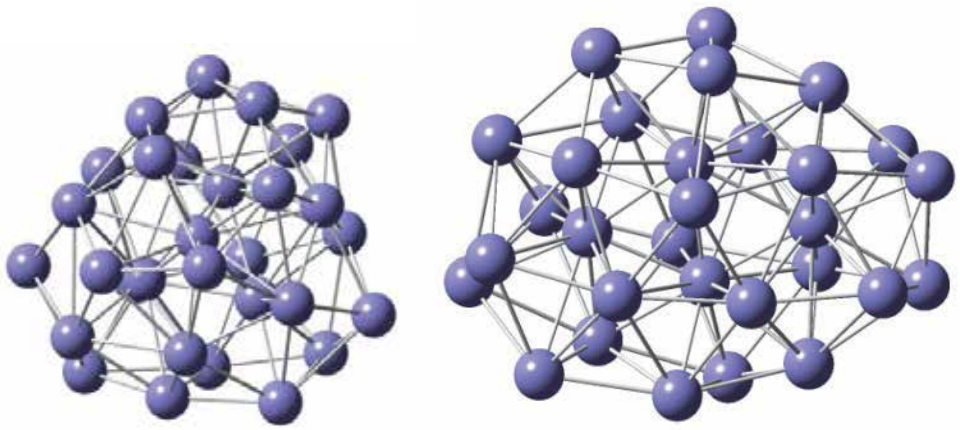

(c) **(d)**

Fig. 11. 30-atom clusters formed under 0.5 eV initial energy with 673 K minimum temperature and a cooling rate of 1.5625×10^{11} K/s (left, c) and 1.5625×10^{13} K/s (right, d).

Figures 10 and 11 show that all four simulations predict the coalescence product is a 30-atom cluster, though they are structurally different. The faster cooling rate (Fig. 10 right and Fig. 11 right) produce a cluster that is more spreading out than the clusters produced by the slower cooling rate.

DFT calculations were performed for the structures shown in Figs. 10 and 11. The results of these clusters are given in Table 1.

Structure	Energy difference	HOMO-LUMO gap	Unpaired electrons
a (Fig.10)	0.55	0.15	56
b (Fig.10)	9.69	0.13	60
c (Fig.11)	2.37	0.11	62
d (Fig. 11)	0	0.06	78

Table 1. The energy difference (eV) between cluster **d** and others, HOMO-LUMO energy gap (eV), and the number of unpaired electrons of 30-atom clusters.

The DFT results in Table 1 show that structure **b** is the least stable isomer of the 30-atom clusters, which agrees with the MD simulations as depicted in Fig. 9 (right). However, the energy differences among the other three clusters are not significant in the MD simulations but are significant in the DFT calculations. More importantly, the number of unpaired electrons of the products is very different, indicating a more complex electronic state of the final product. MD simulations based on a single PES may need to be reexamined for the accuracy of the simulations.

5. Conclusion

Meta-Molecular Dynamics (meta-MD) simulation was developed and described for studying the formation of transition metal nanoparticles. The meta-MD simulation integrates single point electronic structure calculations into the conventional molecular dynamics simulations so that instant changes of the intrinsic electromagnetic properties of the system can be monitored and obtained during the formation of nanoparticles. The results of Fe cluster formation obtained from the meta-MD simulations were presented and discussed. Additionally, the effect of cooling rates was also presented and discussed. Furthermore, using the spin-polarized DFT calculations in meta-MD simulations can also provide indications whether the electronically adiabatic treatment in the MD simulations is sufficient by monitoring the electronic state changes during the dynamic processes.

The meta-MD technique developed here should also be a good tool in studying heterogeneous catalysis by providing guidance in the design of catalysts. For instance, the detailed picture of local charge distribution may provide insight into the active site and requirement for the catalytic activity. This information will be potentially useful in the preparation of catalysts. The meta-MD simulations described here can also be employed for studying other processes where the changes of the intrinsic electromagnetic properties of the local entities of the system, i.e. subsystems, are important in order to obtain a complete picture of the dynamical processes.

6. Acknowledgement

This work is supported by the National Science Foundation (Grant CBET-0709113) and in part by Illinois Clean Coal Institute (Grant 10/ER16).

7. References

Aguado, A. & Lopez, J. M. (2005). Molecular dynamics simulations of the meltinglike transition in $Li_{13}Na_{42}$ and $Na_{13}Cs_{42}$ clusters. *Phys. Rev. B* 71: 075415.

Alkis, S., Krause, J. L., Fry, J. N., Cheng, H. P. (2009). Dynamics of Ag clusters on complex surfaces: Molecular dynamics simulations. *Phys. Rev. B* 79: 121402.

Amirouche, L. & Erkoc, S. (2003). Structural features and energetics of $Zn_{n-m}Cd_m$ (n=7,8) microclusters and Zn_{50}, Cd_{50}, and $Zn_{25}Cd_{25}$ nanoparticles: Molecular-dynamics simulations. *Phys. Rev. B* 68: 043203.

Bas, B. S. d., Ford, M. J., Cortie, M. B. (2006). Melting in small gold clusters: a density functional molecular dynamics study. *J. Phys.: Condens. Matter* 18: 55-74.

Billing, G. D. & Wang, L. (1992a). Semiclassical calculations of transport coefficients and rotational relaxation of nitrogen at high temperatures. *J. Phys. Chem.* 96: 2572257-5.

Billing, G. D. & Wang, L. (1992b). The use of stratified important sampling for calculating transport properties. *Chem. Phys. Lett.* 188: 315-9.

Boyukata, M. (2006). Molecular-dynamics study of possible packing sequence of medium size gold clusters: Au_2-Au_{43}. *Physica E* 33: 182-190.

Boyukata, M., Borges, E., Braga, J. P., Belchior, J. C. (2005). Size evolution of structures and energetics of iron clusters (Fe_n, n< 36): Molecular dynamics studies using a Lennard-Jones type potential. *J. Alloys Compounds* 403: 349-356.

Cao, Y., Ge, Q., Dyer, D. J., Wang, L. (2003). Steric effects on the adsorption of alkylthiolate self-assembled monolayers on Au(111). *J. Phys. Chem. B* 107: 3803-3807.

Carrillo, M. Y. & Dobrynin, A. V. (2011). Layer-by-Layer Assembly of Charged Nanoparticles on Porous Substrates: Molecular Dynamics Simulations. *ACS Nano* 5: 3010-3019.

Chen, C. o.-K. & Chang, S.-C. (2010). An investigation of the internal temperature dependence of Pd-Pt cluster beam deposition: A molecular dynamics study. *Appl. Surf. Sci.* 256: 2890-2897.

Chen, C. o.-K., Chang, S.-C., Chen, C.-L. (2010). Molecular dynamics simulations of the internal temperature dependent diffusing and epitaxial behaviors of Pd-Ag cluster beam deposition. *J. App. Phys.* 107: 124309.

Cheng, D., Wang, W., Cao, D., Huang, S. (2009). Simulating Synthesis of Metal Nanorods, Nanoplates, and Nanoframes by Self-Assembly of Nanoparticle Building Blocks. *J. Phys. Chem. C* 113: 3986-3997.

Chuang, F.-c., Wang, C. Z., Ogut, S., Chelikowsky, J. R., Ho, K. M. (2004). Melting of small Sn clusters by ab initio molecular dynamics simulations. *Phys. Rev. B* 69: 165408.

Chui, Y. H., Grochola, G., Snook, I. K., Russo, S. P. (2007). Molecular dynamics investigation of the structural and thermodynamic properties of gold nanoclusters of different morphologies. *Phys. Rev. B* 75: 033404.

Clary, D. C. & Wang, L. (1997). Influence of surface defects on the adsorption of HCl on ice. *J. Chem. Soc., Faraday Trans. (atmospheric chemistry special issue)* 93: 2763-2767.

Daw, M. S. & Baskes, M. I. (1984). Embedded-atom method: Derivation and application to umpurities, surfaces and other defects in metals. *Phys. Rev. B* 29: 6443-6453.

Dhavale, A., Kanhere, D. G., Majumder, C., Das, G. P. (1999). Ground-state geometries and stability of Na_nMg (n=1-12) clusters using ab initio molecular dynamics method. *Eur. Phys. J. D* 6: 495-500.

Ding, F., Rosen, A., Bolton, K. (2004). Size dependence of the coalescence and melting of iron clusters: A molecular-dynamics study. *Phys. Rev. B* 70: 075416.

Dong, H., Moon, K.-S., Wong, C. P. (2004). Molecular Dynamics Study on the Coalescence of Cu Nanoparticles and Their Deposition on the Cu Substrate. *J. Electronic Mat.* 33: 1326-1330.

El-Bayyari, Z. (1998). Molecular-Dynamics Computer Simulation of Silver Aggregates (Ag_n; n=3 to 13): Empirical Many-Body Potential Energy Function Calculation. *Phys. Stat. Sol. (B)* 208: 339.

Erkoc, S. (2000). Stability of gold clusters: molecular-dynamics simulations. *Physica E* 8: 210-218.

Erkoc, S., Bastug, T., Hirata, M., Tachimori, S. (1999). Molecular-Dynamics Simulations of Uranium Microclusters. *J. Phys. Soc. Japan* 68: 440-445.

Favry, E., Wang, D., Fantauzzi, D., Anton, J., Su, D. S., Jacob, T., Alonso-Vante, N. (2011). Synthesis, electrochemical characterization and molecular dynamics studies of surface segregation of platinum nano-alloy electrocatalysts. *Phys. Chem. Chem. Phys.* 13: 9201-9208.

Ge, Q., Wang, L., Billing, G. D. (1992). Inelastic scattering and chemisorption of CO on a Cu(111) surface. *Surf. Sci.* 277: 237-245.

Goniakowski, J. & Mottet, C. (2010). Simulation of the growth of metal nanoclusters on the MgO(100) surface. *Phys. Rev. B* 81: 155443.

Gonzalez, R. I., Garcia, G., Ramirez, R., Kiwi, M., Valdivia, J. A., Rahman, T. S. (2011). Temperature-dependent properties of 147-and 309-atom iron-gold nanoclusters. *Phys. Rev. B* 83: 155425.

Hendy, S., Brown, S. A., Hyslop, M. (2003). Coalescence of nanoscale metal clusters: Molecular-dynamics study. *Phys. Rev. B* 68: 241403.

Hendy, S. C. & Hall, B. D. (2001). Molecular-dynamics simulation of lead clusters. *Phys. Rev. B* 64: 085425.

Henriksson, K. O. E., Nordlund, K., Keinonen, J. (2005). Fragmentation of clusters sputtered from silver and gold: Molecular dynamics simulations. *Phys. Rev. B* 71: 014117.

Hudson, G. A., Li, J., Wang, L. (2010). Impact of cooling rate on the morphology of coalescence silver nanoparticles. *Chem. Phys. Lett.* 498: 151-156.

Kang, H., Zhang, Y., Yang, M. (2011). Molecular dynamics simulation of thermal conductivity of Cu-Ar nanofluid using EAM potential for Cu-Cu interactions. *Appl. Phys. A* 103: 1001-1008.

Kayhani, K., Mirabbaszadeh, K., Nayebi, P., Mohandesi, A. (2010). Surface effect on the coalscence of Pt clusters: A molecular dynamics study. *Appl. Surf. Sci.* 256: 6982-6985.

Kim, D. H., Kim, H. Y., Ryu, J. H., Lee, H. M. (2009). Phase diagram of Ag-Pd bimetallic nanoclusters by molecular dynamics simulations: solid-to-liquid transition and size-dependent behavior. *Phys. Chem. Chem. Phys.* 11: 5079-5085.

Kim, H. Y., Kim, H. G., Ryu, J. H., Lee, H. M. (2007). Preferential segregation of Pd atoms in the Ag-Pd bimetallic cluster: Density functional theory and molecular dynamics simulation. *Phys. Rev. B* 75: 212105.

Kosilov, A. T., Malivanchuk, A. A., Mikhailov, E. A. (2008). Molecular Dynamics Simulation of Cu-Ni and Cu-Pd Binary Clusters. *Phys. Sol. State* 50: 1392-1396.

Kresse, G. & Hafner, J. (1993). Ab initio Molecular-Dynamics for Liquid-Metals. *Phys. Rev. B* 47: 558-561.

Kresse, G. & Furthmuller, J. (1996a). Efficiency of ab-initio total energy calculations for metals and semiconductors using a plane-wave basis set. *Comput. Mater. Sci.* 6: 15-50.

Kresse, G. & Furthmuller, J. (1996b). Efficient iterative schemes for ab initio total-energy calculations using a plane-wave basis set. *Phys. Rev. B* 54: 11169-11186.

Kresse, G. & Joubert, J. (1999). From ultrasoft pseudopotentials to the projector augmented-wave method. *Phys. Rev. B* 59: 1758-1775.

Krishnamurty, S., Joshi, K., Kangere, D. G., Blundell, S. A. (2006). Finite-temerature behavior of small silicon and tin clusters: An ab initio molecular dynamics study. *Phys. Rev. B* 73: 045419.

Kuntova, Z., Rossi, G., Ferrando, R. (2008). Melting of core-shell Ag-Ni and Ag-Co nanoclusters studied via molecular dynamics simulations. *Phys. Rev. B* 77: 205431.

Lal, M., Plummer, M., Purton, J., Smith, W. (2011). A computer simulation study of the interaction between passivated and bare gold nanoclusters. *Proc. R. Soc. A* 467: 1986-2003.

Lin, Z., Leveugle, E., Bringa, E. M., Zhigilei, L. V. (2010). Molecular Dynamics Simulation of Laser Melting of Nanocrystalline Au. *J. Phys. Chem. C* 114: 5686-5699.

Liu, R.-s., Liu, H.-r., Dong, K.-j., Hou, Z.-y., Tian, Z.-a., Peng, P., Yu, A.-b. (2009). Simulation study of size distiributions and magic number sequences of clusters during the solidification process in liquid metal Na. *J. Non-Crystalline Solids* 355: 541-547.

Long, Y. & Chen, N. X. (2008). Molecular dynamics simulation of Pd clusters colliding onto MgO(001) surface. *Physica B* 403: 4006-4011.

Lummen, N. & Kraska, T. (2004). Investigation of the formation of iron nanoparticles from the gas phase by molecular dynamics simulation. *Nanotechnology* 15: 525-533.

Lummen, N. & Kraska, T. (2005a). Homogeneous nucleation of iron from supersaturated vapor investigated by molecular dynamics simulation. *Aerosol Science* 36: 1409-1426.

Lummen, N. & Kraska, T. (2005b). Molecular dynamics investigation of homogenous nucleation and cluster growth of platinum cluster from supersaturated vapour. *Nanotechnology* 16: 2870-2877.

Lummen, N. & Kraska, T. (2005c). Molecular dynamics investigations of the coalescence of iron clusters embedded in an inert-gas heat bath. *Phys. Rev. B* 71: 205403.

Lyalin, A., Hussien, A., Solov'yov, A. V., Greiner, W. (2009). Impurity effect on the melting of nickel clusters as seen via molecular dynamics simulations. *Phys. Rev. B* 79: 165403.

Mahboobi, S. H., Meghdari, A., Jalili, N., Amiri, F. (2009). Precise positioning and assembly of metallic nanoclusters as building blocks of nanostructures: A molecular dynamics study. *Physica E* 42: 182-195.

Mahboobi, S. H., Meghdari, A., Jalili, N., Amiri, F (2010). Molecular dynamics study of 'success evaluation' for metallic nanoparticles manupulation on gold substrate. *Micro & Nano Lett.* 5: 286-290.

Mazzone, A. M. (2000). Coalescence of metallic clusters: a study by molecular dynamics. *Philosophical Magazine B* 80: 95-111.

McCoy, A. B., Wang, L., Chen, F. (2001). Quantum/classical studies of photodissociation and reaction dynamics in clusters. *Faraday Discuss.* 118: 281-294.

Miao, L., Bhethanabotla, V. R., Joseph, B. (2005). Melting of Pd clusters and nanowires: A comparison study using molecular dynamics simulation. *Phys. Rev. B* 72: 134109.

Monteil, A., Ghemid, S., Chaussedent, S., Jouad, M. E., Santos, M. A. C. d. (2010). Molecular dynamics simulation of silver nanoparticles in a europium doped sodosilicate glass. *Chem. Phys. Lett.* 493: 118-120.

Pawluk, T. & Wang, L. (2007). Molecular dynamics simulations of the coalescence of iridium clusters. *J. Phys. Chem. C* 111: 6713-6719.

Perdew, J. P., Burk, K., Ernzerhof, M. (1996). Generalized gradient approximation made simple. *Phys. Rev. Lett.* 77: 3865.

Pu, Q., Leng, Y., Zhao, X., Cummings, P. T. (2010). Molecular Simulation Studies on the Elongation of Gold Nanowires in Benzenedithiol. *J. Phys. Chem. C* 114: 10365-10372.

Rives, S., Catherinot, A., Dumas-Bouchiat, F., Champeaux, C., Videcoq, A., Ferrando, R. (2008). Growth of Co isolated clusters in the gas phase: Experiment and molecular dynamics simulations. *Phys. Rev. B* 77: 085407.

Rozas, R. & Kraska, T. (2007). Formation of metal nano-particles on and in polymer films investigated by molecular dynamics simylation. *Nanotechnology* 18: 165706.

Sankaranarayanan, S. K. R. S., Bhethanabotla, V. R., Joseph, B. (2005). Molecular dynamics simulation study of the melting of Pd-Pt nanoclusters. *Phys. Rev. B* 71: 195415.

Sawada, S.-i., Shimizu, Y., Ikeda, K. S. (2003). Molecular-dynamics simulations of rapid alloying of microclusters using a many-body potential. *Phys. Rev. B* 67: 024204.

Shi, R., Shao, J., Zhu, X., Lu, X. (2011). On the Melting and Freezing of Au-Pt Nanoparticles Confined in Single-Walled Carbon Nanotubes. *J. Phys. Chem. C* 115: 2961-2968.

Shibuta, Y. & Suzuki, T. (2008). A molecular dynamics study of the phase transistion in bcc metal nanoparticles. *J. Chem. Phys.* 129: 144102.

Shibuta, Y. & Suzuki, T. (2010). Melting and solidification point of fcc-metal nanoparticles with respect to particle size: A molecular dynamics study. *Chem. Phys. Lett.* 498: 323-327.

Shimizu, Y., Ikeda, K. S., Sawada, S.-i. (2001). Spontaneous alloying in binary metal microclusters: A molecular dynamics study. *Phys. Rev. B* 64: 075412.

Shintani, K., Taniguchi, Y., Kameoka, S. (2004). Molecular-dynamics analysis of morphological evolution of softly deposited Au nanoclusters. *J. App. Phys.* 95: 8207-8215.

Sutton, A. P. & Chen, J. (1990). Long-range Finnis-Sinclair potentials. *Phil. Mag. Lett.* 61: 139-146.

Wang, L. & Billing, G. D. (1992). Rotational relaxation and transport coefficients for gaseous hydrogen chloride. *J. Chem. Soc., Faraday Trans.* 88: 163-166.

Wang, L. & Billing, G. D. (1993). Rotational relaxation and transport properties of oxygen by using the important sampling method. *J. Phys. Chem.* 97: 2523-2526.

Wang, L. & Billing, G. D. (1997). Molecular dynamics studies of dissociation of O_2 on Ag (111) surface. *Chem. Phys.* 224: 65-79.

Wang, L. & Clary, D. C. (1996). Time-dependent wave-packet studies on the sticking of HCl to an ice surface. *J. Chem. Phys.* 104: 5663-5673.

Wang, L. & Ge, Q. (2002). Studies of rhodium nanoparticles using the first principles density functional theory calculations. *Chem. Phys. Lett.* 366: 368-76.

Wang, L., Ge, Q., Billing, G. D. (1994a). Molecular dynamics study of H_2 diffusion on a Cu(111) surface. *Surf. Sci.* 301: 353-363.

Wang, L., Ge, Q., Billing, G. D. (1994b). Study of the surface diffusion of CO on Pt(111) by MD simulation. *Surf. Sci.* 304: L413-L419.

Wang, L., Kalyanaraman, C., McCoy, A. B. (1999). Time-dependent quantum studies of the O(^{3}P)+ HCl reaction. *J. Chem. Phys.* 110: 11221-32.

Wang, L. & A. B. McCoy (2003). "Quantum/classical studies of O (^{3}P) + Ar · HCl collision dynamics." J. Chem. Phys. 119: 1996-2003.

Wang, L., Meurer, W. J., McCoy, A. B. (2000). Multiple configuration quantum/classical treatments of reaction dynamics. *J. Chem. Phys.* 113: 10605-10614.

Wang, L., Zhang, Y., Bian, X., Chenq, Y. (2003). Melting of Cu nanoclusters by molecular dynamics simulation. *Phys. Lett. A* 310: 197-202.

Wang, Y., Teitel, S., Dellago, C. (2005). Melting of icosahedral gold nanocluster from molecular dynamics simulations. *J. Chem. Phys.* 122: 214722.

Wen, Y.-H., Zhu, Z.-Z., Zhu, R., Shao, G.-F. (2004). Size effects on the melting of nickel nanowires: a molecular dynamics study. *Physica E* 25: 47-54.

Xiao, L. & Wang, L. (2004a). From planar to three-dimensional structural transtion in gold clusters and the spin-orbit coupling effect. *Chem. Phys. Lett.* 392: 452-455.

Xiao, L. & Wang, L. (2004b). Structures of platinum clusters: planar or spherical. *J. Phys. Chem. A* 108: 8605-8614.

Yang, J., Hu, W., Tang, J., Xu, M. (2008). Long-Time Scale Molecular Dynamics Study of Diffusion Dynamics of Small Cu Clusters on Cu(111) Surface. *J. Phys. Chem. C* 112: 2074-2078.

Yang, X., Liu, L., Zhang, Q., Zhai, P. (2011). Molecular Dynamics Study of the Structural and Mechanical Properties of Skutterudite $CoSb_3$: Surface Effect. *J. Electronic Mat.* 40: 489-492.

Yang, Z., Yang, X., Xu, Z. (2008). Molecular Dynamics Simulation of the Melting Behavior of Pt-Au Nanoparticles with Core-Shell Structure. *J. Phys. Chem. C* 112: 4937-4947.

Yang, Z., Yang, X., Xu, Z., Liu, S. (2009). Structural evolution of Pt-Au nanoalloys during heating process: comparison of random and core-shell orderings. *Phys. Chem. Chem. Phys.* 11: 6249-6255.

Yao, C.-h., Song, B., Cao, P.-l. (2004). Structure of Al_{19} cluster: A full-potential LMTO molecular-dynamics study. *Phys. Rev. B* 70: 195431.

Yildirim, E. K., Atis, M., Guvenc, Z. B. (2007). Molecular dynamics simulation of melting behaviour of small gold clusters: Au_N (N=12-14). *Phys. Scr.* 75: 111-118.

Yukna, J. & Wang, L. (2007). Molecular Dynamics Studies of the Coalescence of Siliver Clusters. *J. Phys. Chem. C* 111: 13337-13347.

Zeng, Q., Jiang, X., Yu, A., Lu, G. (2007). Growth mechanisms of silver nanoparticles: a molecular dynamics study. *Nanotechnology* 18: 035708.

Zhang, L., Zhang, C.-B., Qi, Y. (2009). Molecular-dynamics investigation of structural transformations of a Cu_{201}cluster in its melting process. *Physica B* 404: 205-209.

Zhang, W., Ge, Q., Wang, L. (2003). Structure effects on the energetic, electronic, and magnetic properties of palladium nanoparticles. *J. Chem. Phys.* 118: 5793-5780.

Zhang, W., Ran, X., Zhao, H., Wang, L. (2004a). The non-metallicity of molybdenium clusters. *J. Chem. Phys.* 121: 7717-7724.

Zhang, W., Xiao, L., Hirata, Y., Pawluk, T., Wang, L. (2004b). The simple cubic structure of Ir clusters and the element effect on cluster structures. *Chem. Phys. Lett.* 383: 67-71.

Zhang, W., Zhang, F., Zhu, Z. (2006). Molecular dynamics study on the melting phase transition of aluminum clusters with around 55 atoms. *Phys. Rev. B* 74: 033412.

Zhang, W., Zhao, H., Wang, L. (2004c). The simple cubic structure of ruthenium clusters. *J. Phys. Chem. B* 108: 2140-2147.

Zhao, S. J., Wang, S. Q., Yang, Z. Q., Ye, H. Q. (2001). Coalescence of three silver nanoclusters: a molecular dynamics study. *J. Phys.: Condens. Matter* 13: 8061-8069.

3

Numerical Integration Techniques Based on a Geometric View and Application to Molecular Dynamics Simulations

Ikuo Fukuda[1] and Séverine Queyroy[2]
[1]*Computational Science Research Program, RIKEN (The Institute of Physical and Chemical Research)*
[2]*Laboratoire chimie Provence, chimie théorique, UMR 6264, Aix-Marseille Universités-CNRS*
[1]*Japan*
[2]*France*

1. Introduction

In this chapter we address numerical integration techniques of ordinary differential equation (ODE), especially that for molecular dynamics (MD) simulation. Since most of the fundamental equations of motion in MD are represented by nonlinear ODEs with many degrees of freedom, numerical integration becomes essential to solve the equations for analyzing the properties of a target physical system. To enhance the molecular simulation performance, we demonstrate two techniques for numerically integrating the ODE. The first object we present is an invariant function, viz., a conserved quantity along a solution, of a given ODE. The second one is a numerical integrator itself, which numerically solves the ODE by capturing certain geometric properties of the ODE.

In our proposed procedure (Fukuda & Nakamura, 2006), for an ODE defined on an N-dimensional phase space Ω we construct an extended phase space Ω' of $N+1$ dimension, by introducing an additional degree of freedom. Then, on Ω' we constitute a new ODE, which has an invariant but retains every solution of the original ODE, and we construct efficient integrators for the extended ODE. Advantageous features of our proposal are the simplicity and the applicability to a wide class of ODEs beyond the Hamiltonian equations. In fact, in MD methods, non-Hamiltonian equations are often used (Hoover, 1991); they have been developed (Hoover & Holian, 1996), e.g., to provide more robustness than conventional one or a rapid convergence to a targeted statistical thermodynamic ensemble, or to define a new ensemble itself. Considering such a development, new equations must be designed successively in future studies, and the simplicity and the applicability for the current techniques will be useful also in such a circumstance.

Specifically, by the first technique, the invariant can be simply constructed for any (smooth) ODE, including non-Hamiltonian equation. It can thus be easily used to examine the accuracy of numerical integration of the ODE by monitoring the invariant value, as done in

Hamiltonian system by using the Hamiltonian value. Namely, the integration accuracy check can be done in a system that does not have or may not have an invariant.

The second technique is to constitute the integrator that is widely applicable to many ODEs, including those for non-Hamiltonian systems. We require higher accuracy to avoid the accumulation of the numerical errors, as the simulation time increases. In addition, we should seriously address the issue of the computational cost: with the advancement of computational architecture, larger and larger systems can be treated and the computational cost grows consequently. In fact, the number of the interaction evaluations, which characterize the total cost in MD calculations, is considerably grown with increasing the number of degrees of freedom of the system, n; e.g. the number of the evaluation is of order of n^2 in a typical classical system. We provide a route to easily construct efficient integrators for many kinds of ODEs. Specifically, on the extended space we present integrators that are explicit, symmetric, and phase space volume-preserving.

Geometric features of integrator, including the volume preserving property (Zai-jiu, 1994; Kang & Zai-jiu, 1995, Quispel, 1995; Okunbor, 1995; Quispel & Dyt, 1998), give rise to stable simulation, as if the symplectic integrator does for Hamiltonian system (Ruth, 1983; Yoshida, 1990; McLachlan & Atela, 1992; Sanz-Serna, 1992). In fact, volume-preserving property is a generalization of the symplectic property; this corresponds to the fact that a divergence-free system, which is realized in the extended system by our protocol, is a generalization of a Hamiltonian system. For relevant geometric concepts in the analysis of molecular dynamics equations, see e.g., the work of Ezra (Ezra, 2006) and the references therein.

In section 2, we demonstrate the details of the integration method and explain the geometric view lying in our technique. To effectively present such a view in MD study, the implementation of algorithms is explicitly described in reference to the Nosé-Hoover (NH) equation (Nosé, 1984; Hoover, 1985), which is one of the representative ODEs in MD studies. In section 3 we discuss the applicability of our method and clarify the issues that should be considered for a further development of the method.

2. Geometric concept in the integration techniques

2.1 Invariant on extended space: Fiber bundle structure

Beginning with a review of our work (Fukuda & Nakamura, 2006) concerning the construction of the invariant, we give a new interpretation of this matter to clarify the geometric view under consideration. The main idea is to suitably generate a vector field in the extended dimension so that the extended ODE has an invariant.

For any ODE in phase space Ω (domain of $\mathbb{R}^N$),

$$\dot{\omega} = X(\omega), \tag{1}$$

viz., $d\omega_i/dt = X_i(\omega_1, ..., \omega_N)$ for $i = 1, ..., N$, consider an extended ODE

$$\dot{\omega}' = X'(\omega'), \tag{2}$$

which is defined, on an extended phase space $\Omega' \equiv \Omega \times \mathbb{R}_\times$, by

$$\dot{\omega} = X(\omega), \tag{3a}$$

$$\dot{v} = X_{\mathrm{e}}(\omega') \equiv -\sum_{i=1}^{N} X_i(\omega)\, D_i B(\omega)\, v, \tag{3b}$$

where a point in Ω' is expressed as $\omega' = (\omega, v)$ [$\mathbb{R}_\times$ denotes non-zero numbers; D_i the partial differentiation with respect to ω_i (all quantities are supposed to be sufficiently smooth)]. Here, B is any phase-space function. Then we can show that

$$L(\omega, v) = B(\omega) + \ln|v| \tag{4}$$

defines an invariant (dimensionless); i.e., for an arbitrary solution ϕ' of Eq. (3), the value of $L(\phi'(t))$ is constant for all time t.

The way of defining the extended equation is not unique and Eq. (3b) is constructed with the aim that we will make a volume-preserving integrator, as demonstrated in the following subsection. In fact, alternative schemes are discussed in the literature (Fukuda & Nakamura, 2006), and by applying the scheme to several MD equations the conserved quantity individually defined in each equation can be reproduced in a uniform, generalized manner. Concerning the technical issue, we assume that, for simplicity, the Liouville equation,

$$\mathrm{div}(\rho X) = 0, \tag{5}$$

holds for a certain density function ρ, and put $B \equiv -\ln\rho$ as the choice of B. Thus, it follows from Eq. (3b) that $X_\mathrm{e}(\omega') = -\mathrm{div}X(\omega)v$.

The above conception is illustrated in figure 1: A new ODE (2) in an extended phase space Ω' is defined such that (i) a projection of any solution ϕ' onto the original phase space Ω is a solution of the original ODE (1), and (ii) a function (invariant) L exists, whose value is constant along any solution (in the figure, $\omega'_t \equiv \phi'(t)$ is a point of the solution at time t with initial value ω', and the similar holds for $\omega_t \equiv \phi(t)$). The above (i) is a trivial matter, since Eq. (3a) in the extended ODE is the original ODE itself, which does not couple to the new variable v. By the suitable generation of the field (viz., X_e) in the extended dimension, the above (ii) is attained, as straightforwardly confirmed.

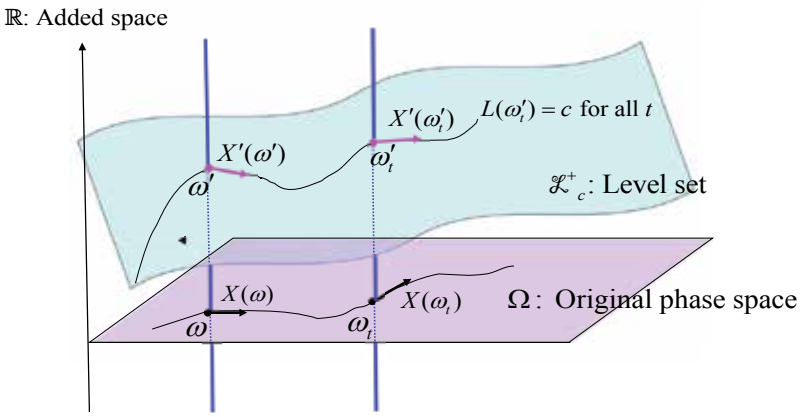

Fig. 1. A schematic figure to illustrate the basic concept for an invariant and extended phase space

As was stated, a projection of any solution with initial value (ω_0, v_0) for the extended ODE (3) onto Ω is also a solution with initial value ω_0 for the original ODE (3a). Conversely, any solution of the original ODE can be lifted to the solution of the extended ODE. However, this correspondence is not one-to-one, i.e., many lifts are possible according to the choice of

v_0. This correspondence can be naturally understood via a geometric concept, fiber bundle (e.g., Husemoller, 1966), which plays an important role in physics (see Choquet-Bruhat et al., 1982), including gauge theory, Berry's phase, and the quantum Hall effect, as well as in mathematics. In this context, our target is a product (trivial) vector bundle over Ω with fiber $\mathbb{R}$, i.e., $(E \equiv \Omega \times \mathbb{R}, \pi, \Omega)$, where we have considered that the total space is $\Omega \times \mathbb{R}$ rather than $\Omega \times \mathbb{R}_\times$. A level set (i.e., a generalization of energy surface) is represented by $\mathcal{L}_c = \mathcal{L}_c^+ \cup \mathcal{L}_c^-$, where

$$\mathcal{L}_c^\pm \equiv \left\{ \omega' \in \Omega' \mid L(\omega') = c, v \gtrless 0 \right\}. \tag{6}$$

In each piece, i.e., one component of a level set, the invariant function takes a constant value, c. It should be noted that each piece becomes a (image of) global cross section from a base space Ω, where the cross section is a map defined by

$$s_c^\pm : \Omega \to E,\ \omega \mapsto (\omega, \pm \exp(-B(\omega) + c)). \tag{7}$$

This indicates that $\mathcal{L}_c^\pm$ is equivalent, in a topological sense, to the original space Ω. This situation is different in the Hamiltonian system in which a level set $\{(x,p) \in \mathbb{R}^{2n} \mid H(x,p) = c\}$ often becomes compact and is not necessarily equivalent to $\mathbb{R}^{2n-1}$ nor $\mathbb{R}^{2n}$. The choice of v_0, under an arbitrary fixed ω_0, corresponds to the choice of the level set, i.e., the choice of the parameter c and the signature, which also characterizes the section map. The time development in the extended space is always on the (image of the) cross section.

2.2 Integrator on extended space: Volume-preserving discrete dynamical-system structure

The second technique is on the numerical integrator. We explain a general idea for constructing the current integrator through the following five procedures:

(i) Considering a solvable decomposition for the ODE originally given,

(ii) Making a solvable decomposition for the extended ODE,

(iii) Turning attention from the solutions of the (decomposed) ODE to phase-space maps in the extended space,

(iv) Combining the individual maps to get a first order integrator,

(v) Combining the maps furthermore to get a higher order integrator.

Our view is clear: the integrator Ψ_h is a (one-step) invertible map (see figure 2) parametrized by a time step h. In metaphorical terms, we have the most fundamental geometric view as

$$\text{Integration} \equiv \{\overline{T}_m \equiv \Psi_h \circ \overset{m}{\cdots} \circ \Psi_h \text{ (iteration of the map)} : \Omega' \to \Omega'\}_{m:\text{ integers}} \tag{8}$$

$$\equiv \text{Discrete dynamical system (generated by map).} \tag{9}$$

Namely, the iterations of the map Ψ_h constitute the integration [$\overline{T}_0 \equiv$identity, $\overline{T}_{-m} \equiv (\overline{T}_m)^{-1}$ can be defined]. This iteration corresponds to an approximation to

$$\text{Exact flow} \equiv \{T_t : \Omega' \to \Omega'\}_{t:\text{ real numbers}}$$

$$\equiv \text{Continuous dynamical system (generated by ODE).} \tag{10}$$

Of course, this view is applicable for a one-step map integrator and not necessarily valid for an arbitrary integrator; e.g., linear multistep methods, including the predictor-corrector

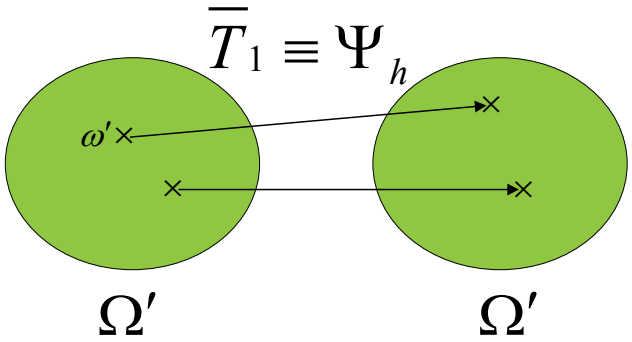

Fig. 2. A schematic picture to show that one-step map integrator is a mapping of the (extended) phase space onto itself.

method, estimate the succeeding value by using the several values previously sought with certain interpolation techniques.

To explain the procedures in a specific manner, we shall use the NH equation (Nosé, 1984; Hoover, 1985; Nosé, 1991) as an example of ODE. This is because the NH equation is frequently used in MD simulation to control the temperature, and furthermore it gives a foundation of various realizations of the Boltzmann-Gibbs dynamics (see e.g., Hoover, 1991; Nosé, 1991; Fukuda & Nakamura, 2004). The NH equation can be represented by

$$\dot{\omega} = X_{\mathrm{NH}}(\omega) \tag{11a}$$

$$\equiv \left(p \cdot \mathbf{M}^{-1},\, -\nabla U(x) - (\zeta/Q)p, 2K(p) - nk_{\mathrm{B}}T\right), \tag{11b}$$

where $\omega \equiv (x, p, \zeta)$ and $\mathbf{M} \equiv \mathrm{diag}(m_1, ..., m_n)$; $x \equiv (x_1, \ldots, x_n)$, $p \equiv (p_1, \ldots, p_n)$, $U(x)$, and $K(p) \equiv \sum_{i=1}^{n} p_i^2/2m_i$ represent the coordinates, momenta, potential energy, and kinetic energy, respectively, of a physical system; k_{B} is Boltzmann's constant, ζ a real variable to control the temperature of the physical system to targeted temperature T, and Q a positive parameter associated with ζ. The function

$$\rho(\omega) \equiv \exp\left(-[U(x) + K(p) + \zeta^2/2Q]/k_{\mathrm{B}}T\right) \tag{12}$$

is a density for the Liouville equation. Thus, extended equation (3b) becomes

$$\dot{v} = -\operatorname{div} X(\omega)v = (n\zeta/Q)v, \tag{13}$$

and invariant (4) becomes

$$L(\omega') = \left[U(x) + K(p) + \zeta^2/2Q\right]/k_{\mathrm{B}}T + \ln|v|. \tag{14}$$

Now, the five procedures are described as follows:

(i) For a given ODE (1), consider a solvable decomposition

$$X = X^{[1]} + X^{[2]} + \cdots + X^{[L]}. \tag{15}$$

That is, decompose X such that each ODE, $\dot{\omega} = X^{[j]}(\omega)$, can be solved explicitly for all time; viz., decompose the field X into "easier" field components, prior to the procedure (see (iv)) in which the individual maps generated by the individual field components are combined.

For the NH equation, a solvable decomposition is given (but not uniquely) by $X_{\mathrm{NH}} = \sum_{j=1}^{4} X^{[j]}$ defined as:

$$X^{[1]}(\omega) \equiv \left(p \cdot \mathbf{M}^{-1},\, 0, 0\right), \tag{16a}$$

$$X^{[2]}(\omega) \equiv (0,\, -\nabla U(x), 0), \tag{16b}$$

$$X^{[3]}(\omega) \equiv (0,\, 0, 2K(p) - nk_{\mathrm{B}}T), \tag{16c}$$

$$X^{[4]}(\omega) \equiv (0,\, -(\zeta/Q)p, 0). \tag{16d}$$

This is indeed the solvable decomposition as is easily seen; e.g., $\dot{\omega} = X^{[1]}(\omega)$ is

$$\dot{x} = p \cdot \mathbf{M}^{-1},\ \dot{p} = 0,\ \dot{\zeta} = 0, \tag{17}$$

so we have its solution $\phi^{[1]}$ with an initial value $\omega_0 = (x_0, p_0, \zeta_0)$ in an explicit form for all time t, as

$$\phi^{[1]}(t) = \left(tp_0 \cdot \mathbf{M}^{-1} + x_0,\ p_0, \zeta_0\right). \tag{18}$$

(ii) Consider a solvable decomposition for, in turn, the extended ODE (2), which is now represented by

$$\dot{\omega} = X(\omega), \tag{19a}$$

$$\dot{v} = -\mathrm{div}X(\omega)v. \tag{19b}$$

To obtain an extended phase-space volume-preserving integrator we should devise a decomposition $X' = \sum X'^{[j]}$ that yields, for each j, the divergence-free property,

$$\mathrm{div}X'^{[j]} = 0. \tag{20}$$

Fortunately, this can be done automatically; we have a desired decomposition:

$$X' = X'^{[1]} + X'^{[2]} + \cdots + X'^{[L]}, \tag{21}$$

$$X'^{[j]}(\omega') = (X^{[j]}(\omega), -\mathrm{div}X^{[j]}(\omega)v)\ \ (j = 1, \ldots, L). \tag{22}$$

Although, in a strict sense, regarding a solution $\Phi^{[j]}$ of

$$\dot{\omega}' = X'^{[j]}(\omega'), \tag{23}$$

its v-component is generally given via a form that is integrated with respect to time, this form can be evaluated explicitly in many cases as already discussed (Fukuda & Nakamura, 2006).

In fact, for the NH equation, according to Eqs. (16) and (22) we have

$$X'^{[1]}(\omega') = \left(p \cdot \mathbf{M}^{-1},\, 0, 0,\, 0\right), \tag{24a}$$

$$X'^{[2]}(\omega') = (0,\, -\nabla U(x), 0\,, 0), \tag{24b}$$

$$X'^{[3]}(\omega') = (0, 0, 2K(p) - nk_{\mathrm{B}}T, 0), \tag{24c}$$

$$X'^{[4]}(\omega') = \left(0, -\frac{\zeta}{Q}p, 0, \frac{n\zeta}{Q}v\right), \tag{24d}$$

where $\omega' \equiv (x, p, \zeta, v)$; and a solution with an initial value $\omega'_0 \equiv (x_0, p_0, \zeta_0, v_0)$ for ODE (23) is given, respectively, by

$$\Phi^{[1]}(t) = \left(tp_0 \cdot \mathbf{M}^{-1} + x_0,\ p_0, \zeta_0, v_0\right), \tag{25a}$$

$$\Phi^{[2]}(t) = (x_0, -t\nabla U(x_0) + p_0, \zeta_0, v_0), \tag{25b}$$

$$\Phi^{[3]}(t) = (x_0, p_0, (2K(p_0) - nk_{\mathrm{B}}T)t + \zeta_0, v_0), \tag{25c}$$

$$\Phi^{[4]}(t) = \left(x_0, \mathrm{e}^{-\frac{\zeta_0 t}{Q}} p_0, \zeta_0, \mathrm{e}^{\frac{n\zeta_0 t}{Q}} v_0\right). \tag{25d}$$

(iii) Turn attention from solutions to phase-space maps.

Consider any decomposed component j. Even when we rewrite $\Phi^{[j]}(t)$ as $\Phi^{[j]\omega'_0}(t)$ to express the initial value, $\Phi^{[j]\omega'_0}(t)$ still denotes the solution as long as we focus on the variation with respect to time t by fixing initial value ω'_0. On the other hand, if we focus on the variation with respect to initial value by fixing time, we get a phase-space map $\Phi^{[j]}_t : \Omega' \to \Omega'$ as,

$$\Phi^{[j]}_t(\omega') \equiv \Phi^{[j]\omega'}(t), \tag{26}$$

where we have dropped the suffix "0" in the initial value because we consider all the (extended) phase-space point to be impartial. Namely $\Phi^{[j]}_t$ maps every point ω' in Ω' to the point reached by the solution with initial value ω' for ODE (23) after a period t. Volume-preserving property is ensured by Eq. (20); i.e., for any area $A \subset \Omega'$, its volume and the volume of the mapped area are equal:

$$\mathrm{Vol}(\Phi^{[j]}_t(A)) = \mathrm{Vol}(A). \tag{27}$$

For the NH equation, it follows from Eq. (25) that e.g., $\Phi^{[1]}_t$ maps $\omega' = (x, p, \zeta, v)$ to $\left(tp \cdot \mathbf{M}^{-1} + x,\ p, \zeta, v\right)$; here, the variable that changes is only x, and in this way we can express the essential changes provided by each map $\Phi^{[j]}_t$ as

$$x \to tp \cdot \mathbf{M}^{-1} + x \ \text{ by } \Phi^{[1]}_t, \tag{28a}$$

$$p \to -t\nabla U(x) + p \ \text{ by } \Phi^{[2]}_t, \tag{28b}$$

$$\zeta \to (2K(p) - nk_{\mathrm{B}}T)t + \zeta \ \text{ by } \Phi^{[3]}_t, \tag{28c}$$

$$p \to \mathrm{e}^{-(\zeta/Q)t} p,\ v \to \mathrm{e}^{(n\zeta/Q)t} v \ \text{ by } \Phi^{[4]}_t. \tag{28d}$$

(iv) Combine the individual maps as

$$\Phi_t \equiv \Phi^{[1]}_t \circ \Phi^{[2]}_t \circ \cdots \circ \Phi^{[L]}_t : \Omega' \to \Omega', \tag{29}$$

giving $\Phi^{[1]}_t \left(\Phi^{[2]}_t \left(\cdots \Phi^{[L]}_t(\omega') \cdots\right)\right)$ for point ω'.

Through just this procedure we get a first-order integrator for the extended ODE (19). Here, "first-order" means that the map approximates the exact flow of the ODE locally with an order of t^1: $\Phi_t(\omega') - T_t(\omega') = O(t^2)$ as $t \to 0$. In general, map Φ_t is said to be order p if

$$\Phi_t(\omega') - T_t(\omega') = O(t^{p+1}) \text{ as } t \to 0. \tag{30}$$

(v) Combine the maps furthermore to get a higher order integrator.

The simplest manner to do this is, by using the adjoint map

$$\Phi_t^* \equiv (\Phi_{-t})^{-1} = \Phi_t^{[L]} \circ \cdots \circ \Phi_t^{[2]} \circ \Phi_t^{[1]}, \tag{31}$$

to adopt

$$\Psi_h = \Phi_{h/2} \circ \Phi_{h/2}^*, \tag{32}$$

where h stands for a time step. Equation (32) is shown to be a second order integrator, which is a generalized version of the Verlet integrator. In fact, for the NH equation, it can be easily seen from Eq. (28) that Eq. (32) gives the (position) Verlet integrator (Tuckerman et al., 1992) when one ignores the non-canonical variables ζ and v.

Reaching a construction of first order integrators (29) and (31) enables us to use several general mathematical schemes to obtain higher order integrators (Hairer et al., 2002; McLachlan, 1995). Using a number of parameters, which designate the division of time step h, a more general formula for higher order method can be

$$\Psi_h = \Phi_{\alpha_s h} \circ \Phi_{\beta_s h}^* \circ \cdots \circ \Phi_{\alpha_2 h} \circ \Phi_{\beta_2 h}^* \circ \Phi_{\alpha_1 h} \circ \Phi_{\beta_1 h}^*. \tag{33}$$

We assume the symmetric condition $\alpha_i = \beta_{s+1-i}$ to get the symmetric property:

$$(\Psi_h)^{-1} = \Psi_{-h}. \tag{34}$$

Namely, the numerical map is time-reversible as is the exact flow. Since this property is the most fundamental and universal property observed in any smooth ODE, this preservation in a numerical map is highly recommended. Volume-preserving property is achieved by the fact that each map is volume preserving due to Eq. (27):

$$\mathrm{Vol}(\Psi_h(A)) = \mathrm{Vol}(A). \tag{35}$$

Finally, we give the whole explicit algorithm for the NH equation. Equation (31) stands for the mapping from (x, p, ζ, v) to $(\overline{x}, \overline{p}, \overline{\zeta}, \overline{v})$, summarized in the following procedure:

$$\mathrm{FAIAD}(t) : \left\{ \begin{array}{ll} x \to \overline{x} \equiv tp \cdot \mathbf{M}^{-1} + x & \text{by } \Phi_t^{[1]}, \\ p \to \tilde{p} \equiv -t\nabla U(\overline{x}) + p & \text{by } \Phi_t^{[2]}, \\ \zeta \to \overline{\zeta} \equiv (2K(\tilde{p}) - nk_{\mathrm{B}}T)t + \zeta & \text{by } \Phi_t^{[3]}, \\ \tilde{p} \to \overline{p} \equiv \mathrm{e}^{-(\overline{\zeta}/Q)t}\,\tilde{p},\ v \to \overline{v} \equiv \mathrm{e}^{(n\overline{\zeta}/Q)t} v & \text{by } \Phi_t^{[4]}. \end{array} \right\} \tag{36}$$

Similarly, Eq. (29) does from $(\overline{x}, \overline{p}, \overline{\zeta}, \overline{v})$ to $(\overline{\overline{x}}, \overline{\overline{p}}, \overline{\overline{\zeta}}, \overline{\overline{v}})$, summarized in the procedure,

$$\mathrm{FAI}(t) : \left\{ \begin{array}{ll} \overline{p} \to \widetilde{\overline{p}} \equiv \mathrm{e}^{-(\overline{\zeta}/Q)t}\,\overline{p},\ \overline{v} \to \overline{\overline{v}} \equiv \mathrm{e}^{(n\overline{\zeta}/Q)t}\overline{v} & \text{by } \Phi_t^{[4]}, \\ \overline{\zeta} \to \overline{\overline{\zeta}} \equiv (2K(\widetilde{\overline{p}}) - nk_{\mathrm{B}}T)t + \overline{\zeta} & \text{by } \Phi_t^{[3]}, \\ \widetilde{\overline{p}} \to \overline{\overline{p}} \equiv -t\nabla U(\overline{x}) + \widetilde{\overline{p}} & \text{by } \Phi_t^{[2]}, \\ \overline{x} \to \overline{\overline{x}} \equiv t\overline{\overline{p}} \cdot \mathbf{M}^{-1} + \overline{x} & \text{by } \Phi_t^{[1]}. \end{array} \right\} \tag{37}$$

Therefore, the total straightforward implementation of the algorithms is described as follows:

$$\left[\begin{array}{l}\text{Do } m=1, \text{ total time step}\\ \quad \text{Do } k=1,s\\ \quad\quad t=\beta_k h\\ \quad\quad \text{call FAIAD}(t)\\ \quad\quad t=\alpha_k h\\ \quad\quad \text{call FAI}(t)\\ \quad\quad x=\overline{\overline{x}},\ p=\overline{\overline{p}},\ \zeta=\overline{\overline{\zeta}},\ v=\overline{\overline{v}}\\ \quad \text{enddo}\\ \quad x, p, \zeta, \text{ and } v \text{ are the variables at time } = mh\\ \text{enddo}\end{array}\right]. \tag{38}$$

2.3 Numerical simulation

Short (or very short) time behaviour for the numerical integration is governed by Equation (30). However, long time behaviour is beyond the reach of this equation and not so a trivial matter, especially in non-Hamiltonian systems. Since the results of the fundamental numerical investigations are already described (for the NH equation, see e.g., Queyroy et al., 2009), we here focus on the above issue. To do this, we studied the integrator for the NH equation, Eq. (11), by applying it to a one-dimensional model system, using a double-well potential. In the numerical simulation, we set $k_{\mathrm{B}}T = 1$ and $Q = 1$, with mass m_i being unity, and initial values were $x_0 = 0$, $p_0 = 1$, $\zeta_0 = 0$, $v_0 = 1$.

Figure 3 shows the trajectories (time development) of invariant (14) obtained by the integrators with time step $h = 0.01$. It exhibits the behaviours during a relatively short period. The integrators are $P2S1$ [equation (32)], its higher-order version, $P4S5$, and the local refinement second-order scheme (LR2). Local deviations of each trajectory seem to be similar in the second order schemes, but the critical difference of trajectories between them is in the behaviour of abrupt jumps. The amplitude of such a jump is highest in the $P2S1$ scheme, and the amplitude, as well as the frequency, of the jumps is smaller in the other schemes. The local refinement scheme is superior to the $P2S1$ scheme. The most accurate integrator is $P4S5$, but it needs five times more evaluations of the force function than those by the second order schemes.

Long time (10^7 time) trajectories with time step $h = 0.01$ are shown in figure 4. In the conservation behaviour of the invariant, the "jump" appearing in a certain time scale may characterize the essential "deviation" in *larger* time scale. We would like to briefly discuss this view using figures 3 and 4, where the most visible behaviours supporting this view is observed in $P2S1$. Each of the jumps in a time scale of about 10^4 observed in figure 3 appears to correspond to an "ordinary" deviation in a time scale of 10^7 in figure 4. The direction (viz., up or down) of the deviation, in general, seems to be random. However, sometimes, consecutive deviations in a same direction occur, and they eventually may form a jump. Such a relation, viz., the directed consecutive deviations form a jump and the resulting jumps characterize the deviations in a larger time scale, might continue in further larger time scale. The true origin of the jumps in the invariant is not clear, requiring further investigations for longer time simulations. However, the jump would not be directly induced by the "actual" jump of coordinate x between the two wells of the one-dimensional double-well potential, nevertheless the jump of x induces large motion in the phase space. This is because the jump of x with our schemes occurred too frequently (but plausible in the sense of producing the Boltzmann-Gibbs distribution), compared with the invariant jump.

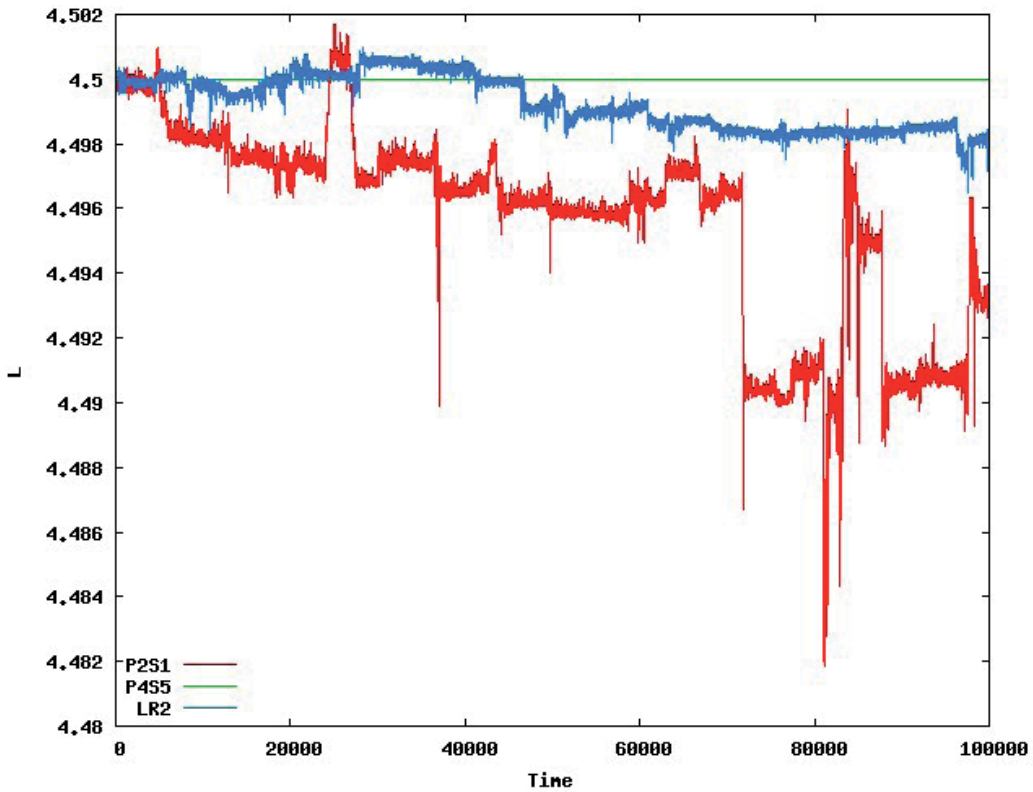

Fig. 3. Trajectories of the invariant using the current integration scheme, applied to the NH equation of the one dimensional system.

3. Discussions

We have utilized the NH equation to explain the integration techniques. The NH equation is a representative of the Boltzmann-Gibbs dynamics, i.e., an ODE that can directly generate the Boltzmann-Gibbs distribution or NTV ensemble (Hoover & Holian, 1996). For such a dynamics, the Nosé-Hoover chain (NHC) equation (Martyna et al. 1992), the Kusnezov, Bulgac, and Bauer equation (Kusnezov et al. 1990), and the generalized Gaussian moment thermostat equation (Liu & Tuckerman, 2000) have been developed, along the line of the generalization of the NH method. Martyna et al. (Martyna et al. 1996) have developed the numerical algorithms to integrate the NHC equations and generalized the scheme to NTP ensemble. The current method described so far is also applicable to NTV equations other than the NH equation and different ensembles, e.g., NTP protocol, including the non-Hamiltonian method derived by Melchionna et al. (Melchionna et al., 1993), and the generalized ensemble (Fukuda & Nakamura, 2002) for the Tsallis statistics (Tsallis, 1988). These targets are well suited to our method, since we have assumed the Liouville equation with $B \equiv -\ln \rho$ and since they have densities satisfying the Liouville equation.

The Liouville equation is valid in many MD equations. As well as the Liouvillian case, our scheme is applicable to the locally Liouvillian case such as the Gaussian isokinetic equation (Hoover et al., 1982; Evans, 1983; Evans et al., 1983; Evans & Morris, 1983). However,

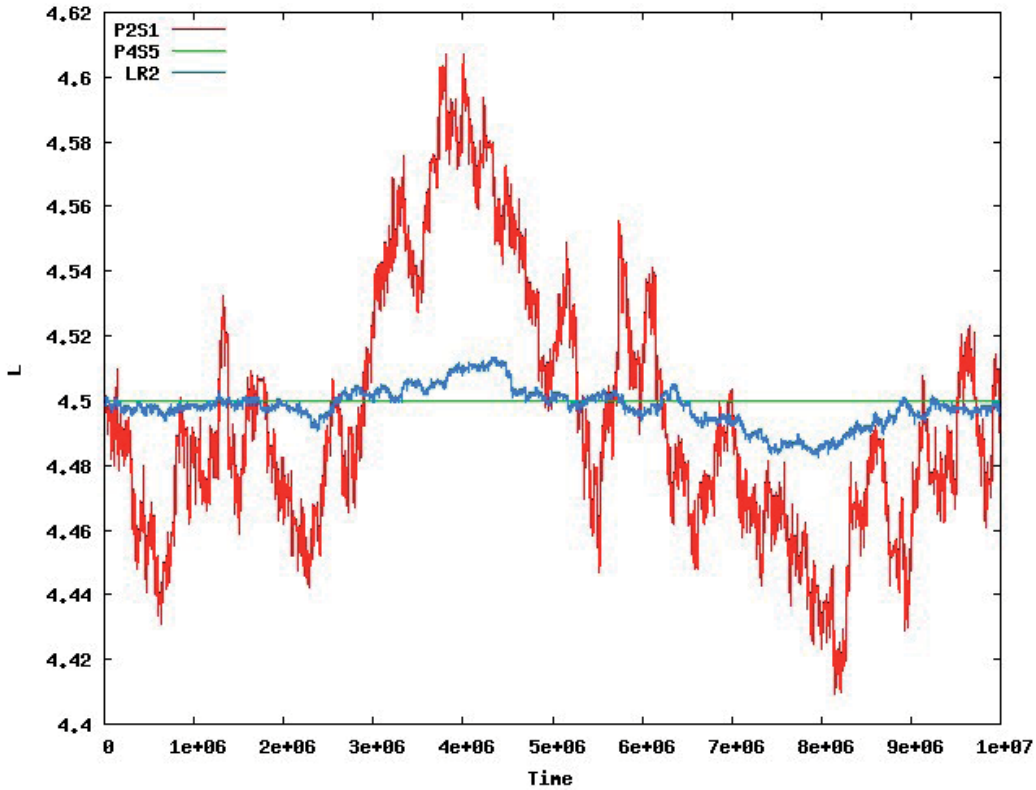

Fig. 4. Long time behaviours of the invariant shown in Figure 3.

the assumption itself for the validness of the Liouville equation in our method can actually be removed if we employ the twisting technique (Fukuda & Nakamura, 2006). Using this technique or its variant, we can apply our method to the system that is not Liouvillian. For example, non-equilibrium problems, including the heat flow problem, are important targets. As an alternative method to control the temperature, the equation developed by Berendsen et al. (Berendsen et al., 1984), which is not Liouvillian to the best of our knowledge, is also a target of our method. Berendsen's method is simple, stable, and has been employed by many researchers to perform e.g., biomolecular simulations. Our protocol is expected to introduce a systematic efficient scheme also in such a situation.

Note that our protocol is also applicable when the force function defined in the equations of motion does not correspond to an explicit potential function, such as in the case where a tabulated force is used (Queyroy et al., 2004). Then, the numerical integration error check using the ordinary MD protocol (NVE, NTV, etc.) is not sufficient, since the invariants always use the potential function. However, even in such a situation, our protocol offers a solution for the consistent numerical integration error check. This is because the function B (in the definition of the invariant; see Eq. (4)) is an arbitrary function in general and so does not necessarily require the potential function.

Regarding the technical issues, we note two points. The first point is the multiple extended-variable formalism developed by Queyroy et al. (Queyroy et al., 2009). Extended

phase-space volume-preserving integrator should keep the volume of the extended space spanned by the original variables $\omega_1, ..., \omega_N$ and the extended variable v. Sometimes, the subspace volume change derived by the former variables is very large, which is emphasized as the system size n is large. In such a case, to compensate the large change, the single extended variable v takes a very large or very small absolute value, as seen in the mapping $v \rightarrow \mathrm{e}^{(n\zeta/Q)t}v$ by $\Phi_t^{[4]}$ n the NH equation. This situation can be avoided by the multiple extended-variable formalism, where $v_1, ..., v_M$ are used instead of v (practically $M = n$).

The second point is the order of appearance of each map for constructing the basic first order integrator. The first order integrator, Eq. (29), has an arbitrariness for the permutation of $\Phi_t^{[1]}, \Phi_t^{[2]}, \cdots, \Phi_t^{[L]}$, since the decomposition (15) is independent of the order of appearance of each vector field. Regarding the local accuracy, any permutation gives the same order of accuracy in a mathematical sense. However, other properties may be distinguishable in general (e.g., historically, the difference between the velocity Verlet and the position Verlet was discussed). For instance, the long-time behaviour and the robustness would be changed by the permutation. Further, they also depend on the physical system (particle interaction, the number of degrees of freedom, etc.) and the equations of motion (ensembles, system parameters including temperature and pressure, etc.). Thus we require more studies to clarify these issues. The cost of the force evaluation is critical in MD, and the number of force evaluations during a unit period should be small. This number depends on the permutation, in general (but the maps (25) in the NH equation is not the case, and the number is always once in the unit map $\Phi_{h_1} \circ \Phi_{h_2}^*$ in Eq. (33)). Thus the permutation yielding a small number is preferable.

So far, we have considered the volume-preserving property of the integrator in the extended phase space. Considering further the measure-preserving property in the original phase space will be of great value to the improvement of the integration. Moreover, the difficulty we should surmount is the resonance phenomena (see e.g., Schlick, 2006), which disturbs the use of larger unit time step.

4. Acknowledgments

This research was supported by Research and Development of the Next-Generation Integrated Simulation of Living Matter, a part of the Development and Use of the Next-Generation Supercomputer Project of the Ministry of Education, Culture, Sports, Science and Technology of Japan.

5. References

[1] H. J. C. Berendsen, J. P. M. Postma, W. F. van Gunsteren, A. DiNola, & J. R. Haak (1984). Molecular-dynamics with coupling to an external bath, *J. Chem. Phys.* 81: 3684-3690.

[2] Y. Choquet-Bruhat, C. Dewitt-Morette, & M. Dillard-Bleick (1982). *Analysis, Manifolds and Physics, Part I, Rev. ed.*, North-Holland, Amsterdam.

[3] D. J. Evans (1983). Computer "experiment" for nonlinear thermodynamics of Couette flow, *J. Chem. Phys.* 78: 3297-3302.

[4] D. J. Evans, W. G. Hoover, B. H. Failor, B. Moran, & A.J. C. Ladd (1983). Nonequilibrium molecular dynamics via Gauss's principle of least constraint, *Phys. Rev. A* 28: 1016-1021.

[5] D. J. Evans & G. P. Morris (1983). *Phys. Lett.* 98A: 433.

[6] G. S. Ezra (2006). Reversible measure-preserving integrators for non-Hamiltonian systems, *J. Chem. Phys*. 125: 034104.
[7] I. Fukuda & H. Nakamura (2002). Tsallis dynamics using the Nosé-Hoover approach, *Phys. Rev. E* 65: 026105.
[8] I. Fukuda & H. Nakamura (2004). Efficiency in the generation of the Boltzmann-Gibbs distribution by the Tsallis dynamics reweighting method, *J. Phys. Chem. B* 108: 4162-4170.
[9] I. Fukuda & H. Nakamura (2006). Construction of an extended invariant for an arbitrary ordinary differential equation with its development in a numerical integration algorithm, *Phys. Rev. E* 73: 026703.
[10] E. Hairer, C. Lubich, & G. Wanner (2002). *Geometric Numerical Integration*, Springer-Verlag, Berlin.
[11] W. G. Hoover, A. J. C. Ladd, & B. Moran (1982). High-strain-rate plastic flow studied via nonequilibrium molecular dynamics, *Phys. Rev. Lett.* 48: 1818-1820.
[12] W. G. Hoover (1985). Canonical dynamics: Equilibrium phase-space distributions, *Phys. Rev. A* 31: 1695-1697.
[13] Wm. G. Hoover (1991). *Computational Statistical Mechanics,* Elsevier, N.Y.
[14] W. G. Hoover & B. L. Holian (1996). Kinetic moments method for the canonical ensemble distribution, *Phys. Lett. A* 211: 253-257.
[15] D. Husemoller (1966). *Fibre Bundles, second edition*, Springer, N.Y.
[16] F. Kang & S. Zai-jiu (1995). Volume-preserving algorithms for source-free dynamical systems, *Numer. Math.* 71: 451-463.
[17] D. Kusnezov, A. Bulgac, & W. Bauer (1990). Canonical ensembles from chaos, *Ann. Phys. (N.Y.)* 204: 155-185.
[18] Y. Liu & M. E. Tuckerman (2000). Generalized Gaussian moment thermostatting: A new continuous dynamical approach to the canonical ensemble, *J. Chem. Phys.* 112: 1685-1700.
[19] G. J. Martyna, M. L. Klein, & M. Tuckerman (1992). Nosé-Hoover chains: The canonical ensemble via continuous dynamics, *J. Chem. Phys.* 97: 2635.
[20] G. J. Martyna, M. E. Tuckerman, D. J. Tobias, & M. L. Klein (1996). Explicit reversible integrators for extended systems dynamics, *Mol. Phys*. 87: 1117-1157.
[21] R. I. McLachlan & P. Atela (1992). The accuracy of symplectic integrators, *Nonlinearity* 5: 541-562.
[22] R. I. McLachlan (1995). On the numerical integration of ordinary differential equations by symmetric composition methods, *SIAM J. Sci. Comput*. 16: 151-168.
[23] S. Melchionna, G. Ciccotti, & B. L. Holian (1993). Hoover NPT dynamics for systems varying in shape and size, *Mol. Phys.* 78: 533-544.
[24] S. Nosé (1984). A unified formulation of the constant temperature molecular dynamics methods, *J. Chem. Phys.* 81: 511-519.
[25] S. Nosé (1991). Constant temperature molecular dynamics methods, *Prog. Theor. Phys. Suppl.* 103: 1-46.
[26] D. I. Okunbor (1995). Energy conserving, Liouville, and symplectic integrators, *J. Comp. Phys.* 120: 375-378.
[27] S. Queyroy, S. Neyertz, D. Brown, & F. Müller-Plathe (2004). Preparing relaxed systems of amorphous polymers by multiscale simulation: Application to cellulose, *Macromolecules* 37: 7338-7350.
[28] S. Queyroy, H. Nakamura & I. Fukuda (2009). Numerical examination of the extended phase-space volume-preserving integrator by the Nosé-Hoover molecular dynamics equations, *J. Comput. Chem*. 30: 1799-1815.

[29] G. R. W. Quispel (1995). Volume-preserving integrators, *Phys. Lett. A* 206: 26-30.
[30] G. R. W. Quispel & C. P. Dyt (1998). Volume-preserving integrators have linear error growth, *Phys. Lett.* A 242: 25-30.
[31] R. D. Ruth (1983). A canonical integration technique, *IEEE Trans. Nucl. Sci.* NS-30: 2669-2671.
[32] J. M. Sanz-Serna (1992). Symplectic integrators for Hamiltonian problems: an overview, *Acta Numerica* 1: 243-286.
[33] T. Schlick (2006). *Molecular Modeling and Simulation*, Springer-Verlag, Berlin.
[34] C. Tsallis (1988). Possible generalization of Boltzmann-Gibbs statistics, *J. Stat. Phys.* 52: 479-487.
[35] M. Tuckerman, B. J. Berne, & G. J. Martyna (1992). Reversible multiple time scale molecular-dynamics, *J. Chem. Phys.* 97: 1990-2001.
[36] H. Yoshida (1990). Construction of higher order symplectic integrators, *Phys. Lett.* A 150: 262-268.
[37] S. Zai-jiu (1994). Construction of volume-preserving difference-schemes for source-free systems via generating-functions, *J. Comp. Math.* 12: 265-272.

4

Application of Molecular Dynamics Simulation to Small Systems

Víctor M. Rosas-García and Isabel Sáenz-Tavera
Facultad de Ciencias Químicas, Universidad Autónoma de Nuevo León,
San Nicolás de los Garza, N. L.
México

1. Introduction

The study of chemical behavior includes answering questions as 'which isomer is the most stable?', 'which relative orientation is the most favorable for such-and-such interaction?', 'which conformer is the global minimum?', 'what are the lowest energy configurations and their relative energies?'. The answer to these questions–and many others–depends on the ability to find and study a variety of configurations of the system of interest. Recently, (Atilgan, 2007) briefly reviewed the use of molecular dynamics simulation for conformational search in the process of drug design, concluding that its use could reduce the errors in estimating binding affinities and finding more viable conformations. In addition, (Corbeil, 2009) considered the need to include ring flexibility in the conformational searches used in flexible docking. Most of the flexible docking algorithms skip searching for conformations in rings, even though a protein may stabilize a conformation other than the most stable one.

The need for a tool to examine the diverse configurations of the constituent particles of a system becomes obvious even as we consider relatively small systems (10-100 atoms). Finding by hand all the conformers of cyclohexane is feasible and maybe even instructive; this is somewhat more complex when doing morpholine and even something as small as an eight-membered heterocycle can be prohibitively complex to analyze by manipulating molecular models by hand. One of the methods available to the researcher to tackle this kind of problem is Molecular Dynamics (MD) simulation. MD allows an exploration of the configurational space of a system, respecting chemical constraints. Chemical constraints–such as atomic connectivities–are needed in cases such as conformations of molecular rings and configurations of molecular clusters, e.g., solvation shells. In both cases, atomic connectivities must be kept intact, otherwise we risk breaking up the ring or the molecular constituents of the cluster. In our research group we routinely employ MD simulation, sometimes in its semiempirical variety, to study small systems (systems with fewer than 100 atoms) whether they be solvation shells, inorganic clusters or heterocycles.

This review is narrowly focused on current software and methods appropriate for doing MD simulations of small heterocycles and clusters composed of 10-100 molecules. In particular, we try to systematize the tools available to tackle the problem of searching for minima in heterocycles and in molecular clusters. We want to use MD simulations as a tool to explore the energy landscape of a small system, so we can locate the global minimum. We do not include the vast literature simulating water solvation by MD. Even though the aggregates of water

molecules around a solute can be considered clusters, we focus our attention on non-water clusters and we only borrow some tools for our purposes.

When MD is based on molecular mechanics force-fields, it cannot model bond breaking-forming processes. For these cases, there are mixed methods such as Quantum Mechanics/Molecular Mechanics (QM/MM), where the bond breaking and formation is taken care of by the quantum mechanical part, while everything else is handled by the molecular mechanics/dynamics part. Another method that considers bond breaking-formation is Car-Parrinello Molecular Dynamics, where the electrons are also considered particles in the dynamics. Such methods are beyond the scope of this chapter.

2. Basic concepts of molecular dynamics simulation

Let us imagine a container (an imaginary box) with a finite number of particles. These particles move about the box at varying velocities (both speed and direction can vary), continuously colliding and bouncing off each other. The trajectories of the particles, taken as a set, contain valuable physical information. For example, if the particles interact with each other, making the particles move more slowly (equivalent to lowering the temperature) the interaction may allow the particles to associate and form a liquid. In a condensed phase, collisions happen more often, and the distance a particle can travel before colliding is much shorter than in the gas phase. It follows that, the movements of the particles correspond to the state of the system. It is by analyzing trajectories that we can compute properties. One can also hope that the results of such analysis will yield *physical insight* about the behavior of a system. For a full introduction to MD simulation see the book by Haile(Haile, 1992). It is of the foremost importance to have a correct description of the interactions between the particles.

2.1 Is MD ready for general consumption?

For a long time, MD simulation has been the province of specialists, and the literature is still packed with obscure vocabulary and long descriptions of complicated algorithms. All these are necessary when the purpose is the calculation of dynamical macroscopic properties of the system, such as viscosities, surface tensions or rheological properties. Unfortunately, finding such a scenario can put off the non-specialist that does not want to become an expert in the theory of molecular dynamics before attempting some configurational search.

When narrowly restricted to the task of configurational search, we can prescind with many of the details like periodic boundary conditions, equilibration, thermostats and the like. In addition, the field has produced software packages increasingly friendly to the user so, doing a MD simulation becomes just a little harder than using a molecular visualization program.

2.2 Description of the interactions

Every MD simulation depends on specifying an interaction model, that is, some analytical function that calculates the energy of interaction between the particles of a system (a potential). The Lennard-Jones (L-J) potential is probably the most popular potential in MD studies, (eq 1)

$$V_{LJ}(r) = 4\varepsilon \left(\frac{\sigma}{r^{12}} \right) - \left(\frac{\sigma}{r^{6}} \right) \tag{1}$$

where σ is the particle diameter, ε is the depth of the energy well and r is the distance between the centers of the particles. σ and ε are determined empirically, to fit observed properties of the

system of interest, such as boiling point or density, to name a few. The L-J potential illustrates one of the main stumbling blocks faced by the simulator, that is, the need to determine values of empirical parameters, so the simulation has physical meaning.

The L-J potential as such is of little use in chemical systems because it does not consider chemically important bonds, such as covalent or hydrogen bonds. To take into account the *intra*molecular interactions, as well as the *inter*molecular interactions, the potential has to be defined in terms of the bond lengths, bond angles and torsions present in the molecule (its internal coordinates). When the potential energy functions are defined in terms of the molecular internal coordinates, the potential function is called a 'force-field'(Engler, 1973). There are many force-fields available for simulation of chemical systems: AMBER(Case, 2005; 2010; Pearlman, 1995), CHARMM(Brooks, 2009), MM3(Allinger, 1989), OPLS(Jorgensen, 1988) and TRIPOS(Clark, 1989), among others. In a MD simulation we use the force-field together with the equations of motion to obtain the dynamic behavior of the system (the trajectories of the particles).

2.3 Description of the trajectories

The MD algorithm is a way to compute such trajectories and analyze them to extract physical information about a system. How do we describe the particle trajectories? At any given moment, each particle can be described in tridimensional space by 3 numbers, the x-coordinate, the y-coordinate, the z-coordinate. Since we are interested in the trajectories, we need to know the location of a particle and where it is headed at each point in time. So, we also need the momenta along each axis: p_x, p_y and p_z. The first three numbers (XYZ coordinates) are known as *configuration space*; while the three momenta define the *momentum space*. Taken together they form the *phase space*. In the same way that a set of values for XYZ coordinates defines a point in configuration space, any set of values for these 6 coordinates (three XYZ and three momenta) defines a point in phase space. Inasmuch as both the positions and momenta depend on the time, as time changes the phase space coordinates also change, thus defining a trajectory in phase space. So a MD simulation is about computing the trajectories of particles in phase space.

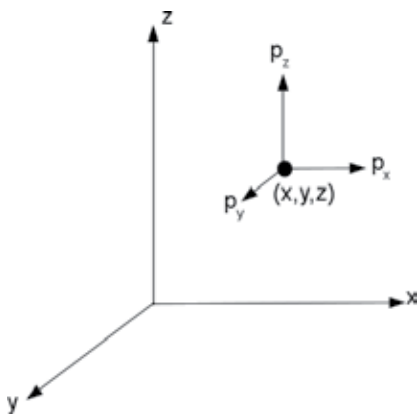

Fig. 1. Phase space coordinates of a particle with position in x,y,z and momenta p_x, p_y, p_z

2.4 Calculation of the trajectories

The forces acting on that particle dictate where a particle is located in space and its direction of movement at each point in time. The classical way to deal with forces uses Newton's laws of motion. The first law states that "every object persists in its state of rest or uniform motion in a straight line unless it is compelled to change that state by forces impressed on it". So, if $\mathbf{r}$ is a vector that contains the particle coordinates at a given moment, and its first derivative with respect to time (its velocity) is symbolized by $\dot{\mathbf{r}}$, then the first law of motion can be mathematically expressed as

$$\dot{\mathbf{r}} = constant \tag{2}$$

keeping in mind that quantities written in bold are vectors.

The second law of motion states that "force is equal to the change in momentum (mV) per change in time. For a constant mass, force equals mass times acceleration". If $\mathbf{F}$ is the force, m is the particle mass, and $\ddot{\mathbf{r}}$ indicates a second derivative of position with respect to time (or the first derivative of velocity with respect to time), then $\ddot{\mathbf{r}}$ corresponds to an acceleration. The second law can be mathematically expressed as follows,

$$\mathbf{F} = m\ddot{\mathbf{r}} \tag{3}$$

The third law states that "For every action, there is an equal and opposite re-action". Assuming an isolated system of identical particles, where the total net force, $\mathbf{F}_{total}$, is zero, $\mathbf{F}_{total} = 0$, then any force exerted by particle 1 on particle 2, $\mathbf{F}_1$, is compensated by an equal and opposite force, $\mathbf{F}_2$, exerted by particle 2 on particle 1. Using the same notation, this law can be expressed as,

$$\mathbf{F}_1 = -\mathbf{F}_2 \tag{4}$$

To calculate the trajectory in phase space, a MD simulation relies on solving Newton's equations of motion. We just need to use a slightly modified notation. Since we need to keep track of each particle, we use subindices, just as we did for the two particles used in the third law

$$\mathbf{F}_i = m_i\ddot{\mathbf{r}}_i \tag{5}$$

We now turn our attention to an interesting fact: the trajectories depend on time, but the mathematical form of the second law (see equation 3 is time-independent, that is, at any moment the relationship between forces, masses and accelerations is expressed by the same formula. So we expect to find a quantity that remains constant with time for the whole system of particles. In an isolated system, the total energy is constant with time, so this means that the sum of kinetic and potential energies for all the particles in the system is constant. This invariant quantity is also known as the Hamiltonian. The kinetic energy for each particle can be expressed by

$$E_{ki} = \frac{1}{2} m_i \dot{\mathbf{r}}_i \tag{6}$$

while the potential energy is calculated according the the model for description of the interactions, such as the Lennard-Jones potential (see equation 1), although it could be any of the force-fields available in the literature. So the form of the equation for the total energy might be

$$E_{total} = E_{ki} + E_{poti} = \Sigma_i \frac{1}{2} m_i \dot{\mathbf{r}}_i + \Sigma_i \Sigma_j 4\varepsilon \left(\frac{\sigma}{r_{ij}^{12}} \right) - \left(\frac{\sigma}{r_{ij}^{6}} \right) \tag{7}$$

where the new variable r_{ij} denotes the center-to-center distance between each pair of particles. This formidable-looking equation tells us that the total energy is calculated by adding the contribution of each particle and of each pair of particles to the kinetic and potential energy, respectively.

Once an initial configuration of atoms is specified and values for location and momenta have been assigned to each atom in the system, the system is allowed to evolve as time progresses. This evolution causes a redistribution of energy, and allows the formation of an energy distribution characteristic of the temperature. This step is known as equilibration. The key step in the calculation of an equilibrated distribution is the determination of the time between collisions and the pairs of colliding particles, because the collisions are the ones responsible for the energy redistribution. After the system has achieved equilibration, we can register the trajectories of the particles. This is the simulation step, and it is the only stage when the trajectories have physical meaning. Once the trajectories have been calculated, properties can be estimated, as long as they can be formulated as averages over time. In dealing with small systems, let us say, macrocycles, we do not expect ever to achieve equilibration, because all the atoms that form the system have restrictions on them that preclude an accurate calculation of the parameters that indicate equilibrium.

All the calculations are performed using finite-difference methods, of which Runge-Kutta is probably the best known, although the Runge-Kutta family of methods finds little use in MD simulations because of the large computational demands. One of the most widely used finite-difference methods is Verlet's algorithm, a third-order Störmer algorithm. It is not as stable as a Runge-Kutta, but its computational demands are much lower.

2.5 Keeping the system in one piece

Each atom has its own velocity, which could take it in a direction very different from that of the other atoms so, what happens when a particle, atom or molecule, moves far away from the others? The usual way to deal with this problem is to employ *periodic boundary conditions* (PBC). In PBC we formally consider the system as made up by multiple copies of itself along all three X, Y, and Z axes. With this setup, if a particle wanders far enough from the others in one direction as to be located outside the box that contains the particles, another, identical, particle comes into the system from the opposite direction, bearing the same velocity. In general, when dealing with a single molecule–within the molecular mechanics formalism–we do not have to worry about losing atoms, because all the atoms are connected by chemical bonds, and molecular mechanics does not allow for bond breaking. In the case of clusters, it is conceivable that a single group (either a neutral molecule or an ion) might wander off the box limits, but that could give us information about the intensity of the interaction and about the optimum equilibrium geometry.

2.6 Simulated annealing

Simulated annealing is a technique able to locate the global minimum of a system of particles. The concept is obtained by analogy with the process of annealing a metal, where the metal is heated to high temperature and then suddenly cooled down by submersion in water. By raising the temperature of the system, it leaves the local minimum where we happened to find it (or build it), and is able to sample the configuration space so it can find another energy minimum when lowering the temperature. Hopefully the new energetic minimum will be

lower in energy than the previous one. In a MD simulation, we can maintain the system at high temperature (even unrealistically high temperatures, like 2000 K) and then the system temperature is reduced. This adds a cooling step to the simulation.

3. Software that implements molecular dynamics simulation

AMBER(Case, 2005; 2010; Pearlman, 1995) designates two different things: a force-field and a package for MD simulation. AMBER the package uses AMBER the force-field for its calculations, but it is entirely possible to use AMBER the force-field in a non-AMBER package, such as GROMACS or CHARMM. Beware, though, that using the same force-field in two different packages will not necessarily get identical results. AMBER the package is currently in version 11. Its learning curve is steep. It is possible to simulate small species, with at least one tutorial showing how to do it.

CHARMMBrooks (2009) also shares the situation of AMBER, in that the name designates both a force-field and a computational engine for MD simulation. It is also possible to use CHARMM the force-field in a non-CHARMM engine. Similar caveats apply, although these authors could not find any information on using CHARMM for small molecules.

Gabedit(Allouche, 2011) makes quantum chemistry software accessible to the novice modeller. It presents to the user a rather limited array of options, making for a less confusing experience. On the other hand, this means that to take full advantage of the capabilities of the quantum chemistry software, the user needs to be well versed in the respective manuals. Gabedit can perform MD simulations by itself, using the AMBER99 force-field. It can also setup MD simulations using semiempirical quantum mechanical energy evaluations, and submit them to a variety of computational engies, such as MOPAC2009(Stewart, 2009), ORCA(Radoul, 2010) or FireFly(Granovsky, 2011). When using quantum-mechanical energy evaluations, the user should keep in mind that these methods allow for bond breaking and formation, so it is entirely possible to end up with an isomerized structure.

Ghemical(Hassinen, 2001) can perform MD simulations, and defines a graphical user interface for this. It has a convenient facility to generate water solvation boxes. The user has to make sure that the force-field contains appropriate parameters. New parameters can be added by editing some configuration files. Its graphical user interface makes Ghemical very accessible to the beginning modeller.

GROMACS(Berendsen, 1995; Hess, 2008; Lindahl, 2001; van der Spoel, 2005) is a molecular dynamics software tailored to simulations with hundreds of millions of particles. It is certainly not made with the novice user in mind, and its learning curve is steep. However, it is an extremely fast computational engine. It is not recommended for dynamics of small species because then the advantages of the fast computation are lost, and because it is command-line based. Building the required topology before running the simulation can be daunting to a novice.

AMBER, CHARMM and GROMACS are tailored towards simulation of bio-macromolecules, and the force-fields included reflect this. They contain force-fields highly optimized for aminoacids or nucleotides or carbohydrates.

HyperChem(Hyperchem, 2011) is a commercial software product has a module for MD simulation, in addition to ab initio, density functional and semiempirical capabilities. It can

simulate chemical reactions by molecular dynamics, because it is not limited to molecular mechanics parameters.

MacroModel(Mohamadi, 1990) is a well-developed molecular dynamics package for biomolecules, and it includes a polished interface known as Maestro.

TINKER(Ponder, 2011) is a molecular dynamics package created and maintained by the group of Jay W. Ponder. It employs molecular mechanics and currently lacks a graphical user interface. Its learning curve is somewhat steep.

VASP(Kresse, 1993; 1994; 1996a;b) seems to be very popular in the metal clusters community. It can do MD simulations using density functional theory (considered as part of Ab Initio Molecular Dynamics) and its use does require the skills of an expert computational chemist.

4. Conformational analysis of heterocycles

It is well known that MD is a very inefficient way to search for minima in large rings(Saunders, 1990). However, it should not be underestimated for searches in medium and small rings (rings < 10 atoms). The use of MD simulations for conformational search is in large part favored by convenience, given that many different software programs include it.

Isayev et al.(Isayev, 2007) claim that the pyrimidine ring in nucleic acid bases has a range of effective non-planar conformations under ambient conditions. Saiz et al.(Saiz, 1996) demonstrated that MD simulation with the Tripos force-field was good at reproducing the conformational behavior of a dioxo ring in aqueous solution. Rosas-García et al.(Rosas-Garcia, 2010) studied conformations of fosforinanes using MD simulations in Ghemical, although some parameters had to be determined at the Hartree-Fock level (basis set 6-31G*). An extensive search by MD found all the conformers for two diastereomers, and a comparison of the global minima allowed to explain why the axial preference of the phenyl ring was linked to the relative configuration of the stereocenters in the molecule.

Sometimes a side chain can modify the conformational behavior of small rings, like the case of Tosco et al. (Tosco, 2008) who used MD simulations in CHARMM to do conformational search on a series of cyclic oxadiazolol, and thiadiazolol isosteres of carboxylate, where most of the conformational freedom came from the side chain attached to the ring. A similar case is that of Bombasaro et al.(Bombasaro, 2008) who used GROMACS in combination with a systematic grid conformational search to study bullacin. Bullacin contains three five-membered rings, with one 11-carbon side chain, and two rings joined by a 12-carbon chain (see Figure 2).

Regarding structures with fused rings, Aleksandrov and Simonson(Aleksandrov, 2006; 2009) reported development of CHARMM22 parameters (employing the TIP3P(Jorgensen, 1983) model for water) for several tetracycline derivatives and a tetracycline/Mg^{2+} complex (see the structure in Figure 2). Tetracyclines exist in two conformations, twisted and extended. In this case the interest was not so much the conformational variety but the possibility of several protonation sites, and the uncertainty of the binding sites for metals such as Mg^{2+}. They employed TINKER and the MM3 force-field for MD/simulated annealing. On the other hand, Kiliç et al.(Kiliç, 2000) found out by simulations using quantum MD that cubane and their group 14 analogs can convert to eight-membered rings at high temperature.

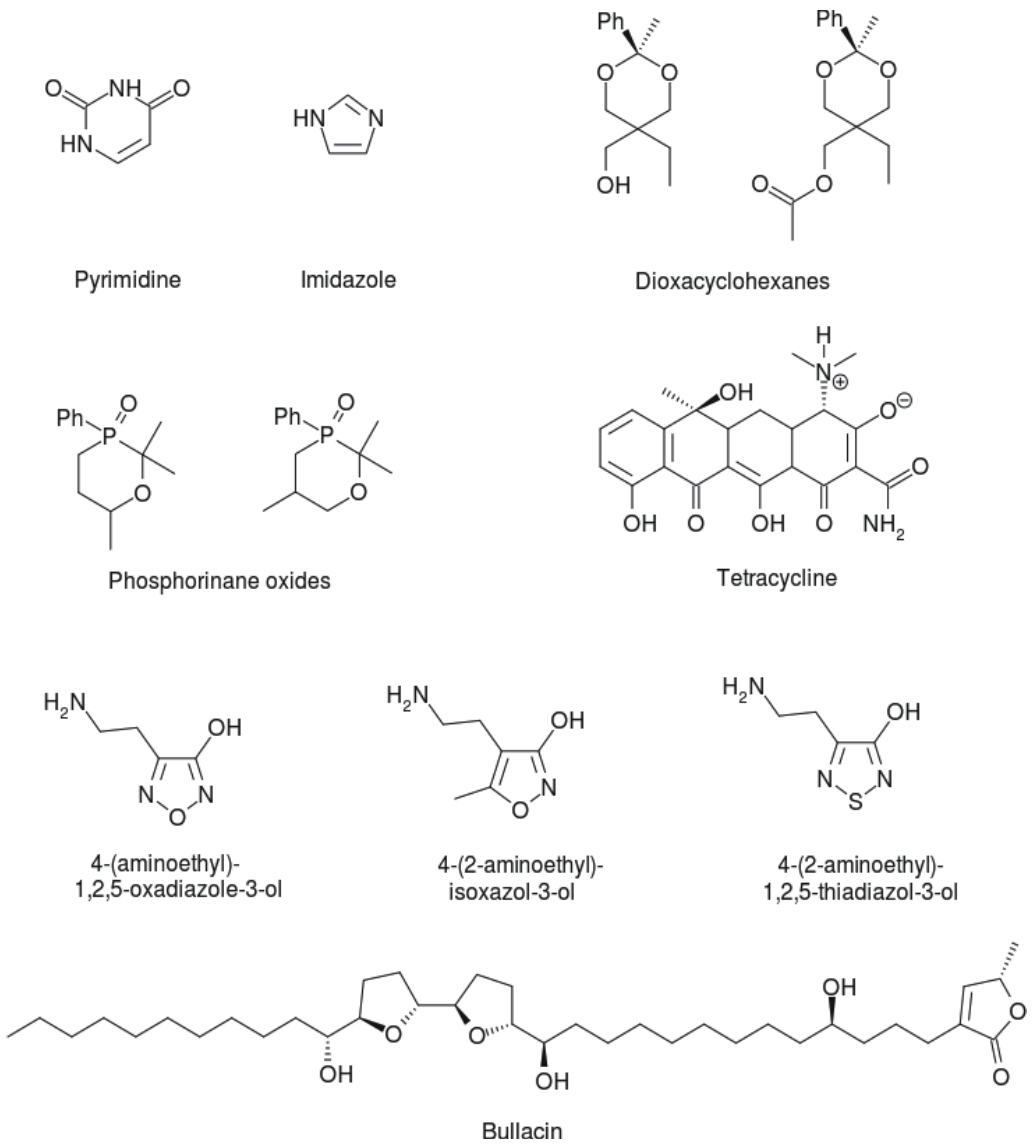

Fig. 2. Some heterocycles and fused cycles studied by molecular dynamics simulations.

5. Configurational search of clusters by molecular dynamics simulation

A lot of work on clusters is based on atomic clusters. In this case it may suffice to develop a random-placement algorithm to generate structural variety. Many researchers have taken this route. Chen et al.(Chen, 2011) employed VASP to study clusters of metal carbides. They first generated a variety of Ca_8 clusters and used step-wise addition of carbon atoms and geometry optimization after each step. MD simulations were used to evaluate the thermodynamic stability of several cage structures. The presence of only small distortions in the cage structures at 400 K was taken as evidence of their thermodynamic stability. Fujima and Oda employed VASP to study titanium clusters adsorbed on a single wall nano-capsule. There is no description of the parameters used in the MD calculations (temperature, time step, total simulation time or any others). The only configurational searching took place by putting Ti atoms on different adsorption sites on the carbon wall and doing geometry optimization. Given that they attempted to maximize the contact area between the cluster and the nano-wall, such approach seems justified(Fujima, 2009). Jian-Song and Li(Jiang-Song, 2010) did a configurational search for Ga_7As_7 clusters by randomly choosing points in space from a tridimensional box, cage or sphere, applying distance constraints to keep the atoms at chemically reasonable distances. This is not MD, and they had to generate thousands of structures, although the original paper is sketchy on the details of how many structures were generated. It could well be that the imposed distance constraints biased the resulting structures. This method does have the advantage of not requiring force-field parameters for generating the structures. Jiménez-Sáez(Jiménez-Sáez, 2006) studied the equilibrium structures of copper clusters as a function of the kinetic energy of deposition on a gold surface. For the starting geometries, no configurational search was done. The configurations of the deposited clusters were analyzed in terms of the deformation produced as the kinetic energy of deposition varied. Kuzmin et al.(Kuzmin, 2008) used software developed in-house to study configurations of silver clusters using MD simulations with the embedded atom model on clusters between 13 and 2057 atoms. They used temperatures between 0 and 1300 K. Li et al.(Li, 2007) used full-potential linear-muffin-tin-orbital MD (FP-LMTO-MD) calculations to study the effect of Al impurities on Si clusters. The method is suitable for semiconductor and metal clusters. As for the generation of the initial structures, the authors took the reported ground states of the silicon clusters and added or substituted Al atoms in all possible positions of each cluster. Yang and Xiong(Yang, 2008) used a similar method to generate the initial geometries for FeB_n clusters. So there appears to be a need for more systematically searching the configurational space of clusters.

In our literature review, we found only one recent example of a configurational search on a cluster using MD simulations, that of Chandrachud et al.(Chandrachud, 2009). These researchers employed VASP to study gold cages using Born-Oppenheimer MD to generate initial configurations. They did MD runs at four different constant temperatures, for 60 ps each, obtaining 600 structures (150 for each constant temperature run). Geometry optimization of these structures yielded 50 distinct isomeric clusters.

Clusters are not limited to groups of separate individual particles like in the case of metal clusters. When we have polyatomic species involved in cluster formation, it becomes important to maintain chemical bonds intact. Shiroishi et al.(Shiroishi, 2005) used Car-Parrinello Molecular Dynamics to study iron oxide clusters. Doll et al.(Doll, 2010) used Ab Initio Molecular Dynamics calculations to study clusters of lithium fluoride. They used a two-part protocol: first generation of candidate structures by means of simulated annealing at

a low level of theory (Hartree-Fock) and, second, optimization of the obtained structures using the Local Density Approximation. Takayanagi(Takayanagi, 2008) studied clusters of solvated glycine using the PM6 Hamiltonian. Their semiempirical MD simulations were performed at 300 K, and the initial geometries were taken from previously reported higher-level results and reoptimized using PM6. They observed dissociation of the proton from a carboxylate group, although could not observe formation of the zwitterion. In our group we have studied calcium carbonate clusters(Rosas-Garcia, 2011), and we have explored the configurational space by means of semiempirical MD simulations, using the PM6 Hamiltonian in MOPAC2009. Pang et al.(Pang, 1994) studied inclusion compounds in cycloalkanes by simulated annealing using HyperChem using the MM+ force-field (a variant of MM2. We cannot recommend the use of MM+ due to the lack of a published description of the modifications) and varying the temperature from 300 to 1000 K in 100 K increments. The dynamics revealed that there was orientational flexibility within the cycle and that the interconversion barriers were as low as 1 kcal/mole.

6. How to run a basic simulation

Setting up the run is probably the part of the MD simulation that a novice finds most intimidating. This requires several steps: creation of an initial configuration for the system, choice of physical conditions as defined by an ensemble and a temperature for the run; and some numerical parameters necessary for the integration of the equations: time-step, simulation time, integrator and thermostat.

6.1 Creation of the initial geometry

We have to create an initial geometry for the system, that is, to position the atoms and molecules in three dimensions so the calculation can proceed. A simple random placement is not useful, because we must be careful to avoid placing two atoms at the same coordinates, or closer than the sum of their atomic radii. This situations, known as bad contacts, tend to destabilize the numerical algorithms used in the determination of the trajectory (the integration step). Most MD packages, such as GROMACS or AMBER, provide their own utilities for building starting configurations.

For the creation of a starting configuration, we can use programs such as Ghemical, Avogadro(Avogadro, 2011) or Gabedit. Both Avogadro and Ghemical have polished graphic interfaces, and they are very easy to use for building single molecules. Gabedit is still somewhat lacking in this regard, as its interface is harder to use than that of Ghemical or Avogadro. For building clusters, use of a graphical interface quickly becomes tedious and prone to errors. PACKMOL(Martínez, 2009) seems particularly convenient for building any kind of cluster due to its ability to add a given number copies of a molecule, water or any other at the user's choice. For the specific case of water solvation, Ghemical provides a function to build a water box or a water sphere around any compound previously loaded in Ghemical's memory, although the number of water molecules added is less intuitive, because it depends on both the dimensions of the box and of the molecule to be solvated.

Our preferred tools for building systems are packages with graphical user interface, like Ghemical, Avogadro or Gabedit. For running MD simulations we have used, with varying degrees of success Ghemical, MOPAC2009 and Gabedit. PACKMOL is very well suited for the construction of clusters because it lets the user specify the structures of the molecules

of interest and how many of them are to be added. Ghemical is less flexible in this regard, because it has tools only for building solvation shells, and the number of water molecules added is not specified directly by the user, but by the volume specified for the water box. Adding a precise number of water molecules in Ghemical can be a hit-and-miss experience.

6.2 Choice of physical conditions

The set of 'physical' information contains: temperature, pressure, relaxation times, compresibilities, whether the simulation will be at constant temperature or constant pressure and–probably most important of all–the force-field used to evaluate the interactions within a molecule and between molecules. Given that the trajectories should have physical meaning, how do we know what kind of experimental conditions are we simulating? This corresponds to the choice of the ensemble. We should be familiar with three ensembles: the microcanonical ensemble, the canonical ensemble and the isothermal-isobaric ensemble.

The microcanonical ensemble maintains constant number of particles (N), constant volume (V) and constant total energy (E), so it is also known as the NVE ensemble. The canonical ensemble keeps a constant number of particles, constant volume and constant temperature (T), so it is also called the NVT ensemble.

The isothermal-isobaric ensemble keeps constant number of particles, constant pressure and constant temperature, so it is also known as the NPT ensemble. Physically, the NPT ensemble is the most important in chemistry, because many chemical processes are performed under constant pressure and temperature.

For our particular situation, when we deal with so few molecules that even the concepts of pressure and temperature are not well defined, it suffices to say that these ensembles are different ways to give energy to the system and any one of them can accomplish the task of taking the system out of an energy well and into another one.

In our group we typically choose the program defaults, as we are not interested in the physical meaning of the trajectories, but only in the energetic minima resulting from the dynamic search.

6.3 Choice of force-field

Choosing a force-field can be daunting to a novice, because of all the options available. In terms of the specific strengths and weaknesses of each force-field, the reader is referred to the literature. However, the main roadblock in using molecular mechanics force-fields is that, sooner or later, one wants to study a molecule lacking adequate parameters in any force-field. Here, the user of MD software needs to know that some software packages, particularly the most friendly to the user, sometimes allow a dynamics calculation to run substituting default values for the missing parameters. Such calculations have practically no value at all. Ghemical uses the TRIPOS force-field, but the user should be aware of the error messages because usually many parameters are missing, and Ghemical will substitute default values. Gabedit will not run a dynamics unless all the parameters are defined or one decides to use semiempirical methods. The lack of adequate parameters usually requires doing ab initio calculations on a model compound, so the parameters can be generated. This route is reasonable when the molecules of interest are large compared to the model molecule, but what are we supposed to do if the molecule and the model compound are the same?

Inasmuch as a MD simulation will evaluate thousands of structures, it may still be worth doing the work of generating molecular mechanics parameters, although this may need a collaboration with a computational chemist. Another option would be to use dynamics not based on molecular mechanics. As previously mentioned, Ab Initio Molecular Dynamics, such as Car-Parrinello, is a specialist technique well beyond the scope of this review but there is a middle ground, in terms of complexity and computational requirements: semiempirical MD simulations. Computational packages exist that are able to use semiempirical methods, such as AM1(Dewar, 1985), PM3(Stewart, 1989) or PM6(Stewart, 2007), for energy evaluation without the need to determine molecular parameters. The user must exercise due care when using semiempirical methods because, at temperatures high enough, the molecules can break apart. This is because semiempirical methods calculate the electronic structure so, even the strongest covalent bonds can break if the temperature is high enough. In our studies of ionic clusters, it was all too easy to destroy the species by giving too much kinetic energy to the system.

6.4 Computational parameters for the run

The set of computational information, includes how long the simulation is supposed to run in picoseconds (the simulation time), the length of simulation time elapsed between energy evaluations in femtoseconds (the time-step), the algorithm for integration, from a variety such as Verlet, Leapfrog-Verlet and Beeman, among others (the integrator) and the thermostat, which is the algorithm that enforces the constancy of temperature.

The duration of the simulation is usually split in three steps: heating, equilibration and cooling of the system. For the purposes of conformational searching, it is advisable to take a simulation length longer than the program default, probably two times or three times the default value, depending on the complexity of the system.

6.5 Choice of software

For the MD-based conformational search, both Gabedit and Ghemical can do it, but Gabedit has a more automated implementation. Gabedit automatically saves a user-defined number of geometries from the trajectory and minimizes their energies, either with molecular mechanics or with a semiempirical method.

7. Further efforts

We hope that this brief introduction to molecular dynamics will pique the interest of other researchers in exploring mechanical or semiempirical molecular dynamics as a useful tool for the study of small chemical systems. Recent progress on inclusion of dispersion and H-bonding interactions in semiempirical Hamiltonians, such as the corrections to the PM6 Hamiltonian by Řezáč(Řezáč, 2009) and Korth(Korth, 2010), should prove valuable in this regard. As we have focused on small molecules, the ability to run calculations in parallel over several computers seems unnecessary.

Work remaining to be done includes some benchmarking/callibration of semiempirical MD simulations against higher-level QM/MM simulations or pure ab initio calculations to find out its realm of applicability, and perhaps some further improvement of the semiempirical Hamiltonians to this end. It is also necessary to ascertain the adequacy of including solvation

models, whether continuum or explicit, in these calculations. After all, a global minimum obtained in the gas phase may or may not resemble the global minimum under the influence of aqueous solvation. In addition, the general performance of semiempirical MD simulations to study the behavior of solvated ions is still unknown. We caution the reader against an uncritical application of this technique for conformational, configurational searches or otherwise, e.g., the ability of semiempirical Hamiltonians to model transition structures has been questioned(Schenker, 2011), so modeling the dynamics of chemical reactions by semiempirical means may be dangerous, at best.

8. References

Aleksandrov, A.; Simonson, T. (2006). The tetracycline: Mg^{2+} complex: A molecular mechanics force field. *Journal of Computational Chemistry* Vol. 27, No. 13, (October 2006), 1517–1533

Aleksandrov, A.; Simonson, T. (2009). Molecular mechanics models for tetracycline analogs. *Journal of Computational Chemistry*, Vol. 30, No. 2, (January 2009) 243–255

Allinger, N. L. (1977) Conformational analysis. 130. MM2. A hydrocarbon force field utilizing V1 and V2 torsional terms. *Journal of the American Chemical Society* Vol. 99, No. 25, (December 1977) 8127–8134.

Allinger, N. L.; Yuh, Y. H.; Lii, J. H. (1989). Molecular mechanics. The MM3 force field for hydrocarbons. 1. *Journal of the American Chemical Society* Vol. 111, No. 23, (November 1989) 8551–8566.

Allouche, A.-R. (2011). Gabedit-A graphical user interface for computational chemistry softwares. *Journal of Computational Chemistry* Vol. 32, No. 1, (January 2011) 174–182

Atilgan, C.; Aviyente, V. (2007). Hybrid Usage of Computational Tools in Drug Synthesis. *Current Computer-Aided Drug Design* Vol. 3, No. 2, (June 2007) 149–159

Avogadro: an open-source molecular builder and visualization tool. Version 1.0.0 URL: http://avogadro.openmolecules.net/

Berendsen, H. J. C.; van der Spoel, D.; van Drunen, R. (1995). GROMACS: A message-passing parallel molecular dynamics implementation *Computer Physics Communications* Vol. 91, No. 1-3, (September 1995) 43–56

Bombasaro, J. A.; Masman, M. F.; Santágata, L. N.; Freile, M. L.; Rodríguez, A. M.; Enriz, R. D. (2008) A Comprehensive Conformational Analysis of Bullacin B, a Potent Inhibitor of Complex I. Molecular Dynamics Simulations and Ab Initio Calculations. *Journal of Physical Chemistry A* Vol. 112, No. 32, (July 2008) 7426–7438.

Brooks, B. R.; Brooks III, C. L.; Mackerell, A. D.; Nilsson, L.; Petrella, R. J.; Roux, B.; Won, Y.; Archontis, G.; Bartels, C.; Boresch, S.; Caflisch, A.; Caves, L.; Cui, Q.; Dinner, A. R.; Feig, M.; Fischer, S.; Gao, J.; Hodoscek, M.; Im, W.; Kuczera, K.; Lazaridis, T.; Ma, J.; Ovchinnikov, V.; Paci, E.; Pastor, R. W.; Post, C. B.; Pu, J. Z.; Schaefer, M.; Tidor, B.; Venable, R. M.; Woodcock, H. L.; Wu, X.; Yang, W.; York, D. M.; Karplus, M. (2009). CHARMM: The Biomolecular simulation Program, *Journal of Computational Chemistry*, Vol. 30, No. 10, (July 2009) 1545–1615

Case, D. A.; Cheatham, T.; Darden, T.; Gohlke, H.; Luo, R.; Merz Jr., K. M.; Onufriev, A.; Simmerling, C.; Wang, B.; Woods, R. (2005). The Amber biomolecular simulation programs. *Journal of Computational Chemistry*, Vol. 26, No. 16, (December 2005) 1668–1688

Case, D. A.; Darden, T. A.; Cheatham III, T. E.; Simmerling, C. L.; Wang, J.; Duke, R. E.; Luo, R.; Walker, R. C.; Zhang, W.; Merz, K. M.; Roberts, B.; Wang, B.; Hayik, S.; Roitberg, A.;

Seabra, G.; Kolossváry, I.; Wong, K. F.; Paesani, F.; Vanicek, J.; Liu, J.; Wu, X.; Brozell, S. R.; Steinbrecher, T.; Gohlke, H.; Cai, Q.; Ye, X.; Wang, J.; Hsieh, M.-J.; Cui, G.; Roe, D. R.; Mathews, D. H.; Seetin, M. G.; Sagui, C.; Babin, V.; Luchko, T.; Gusarov, S.; Kovalenko, A.; Kollman P. A. (2010). AMBER 11. University of California, San Francisco.

Chandrachud, P.; Joshi, K.; Krishnamurty, S.; Kanhere, D. G. (2009) Stability of gold cages (Au_16 and Au_17) at finite temperature. *Pramana* Vol. 72, No. 5, (August 2009) 845–855

Chen, G.; Peng, Q.; Kawazoe, Y. (2011). First-principles study on Ca_8C_n ($n \leq 12$) and $CamC1_2$ ($m \leq 8$) metal carbides. *Physics Letters A* Vol. 375, No. 6, (February 2011) 994–999

Clark, M.; Cramer III, R. D.; van Opdenhosch, N. (1989). Validation of the General Purpose Tripos 5.2 Force Field, *Journal of Computational Chemistry* Vol. 10, No. 8, (December 1989) 982–1012

Corbeil, C. R.; Therrien, E.; Moitessier, N. (2009). Modeling Reality for Optimal Docking of Small Molecules to Biological Targets. *Current Computer-Aided Drug Design* Vol. 5, No. 4, (December 2009) 241–263

Dewar, M. J. S.; Zoebisch, E. G.; Healy, E. F.; Stewart, J. J. P. (1985). Development and use of quantum mechanical molecular models. 76. AM1: a new general purpose quantum mechanical molecular model. *Journal of the American Chemical Society* Vol. 107, No. 13, (June 1985) 3902–3909

Doll, K.; Schön, J.C; Jansen, M. (2010). Ab initio energy landscape of LiF clusters. *Journal of Chemical Physics* Vol. 133, No. 2, (July 2010) 024107-8

Engler, E. M.; Andose, J. D.; Schleyer, P. V. R. (2011). Critical evaluation of molecular mechanics. *Journal of the American Chemical Society* Vol. 95, No. 24, (October 2011) 8005–8025

Fujima, N.; Oda, T. (2009). Bonding properties and structures of titanium clusters on (10,0) single wall carbon nano capsule. *European Physical Journal D* Vol. 52, No. 1-3, (March 2009) 87–90

Granovsky, A. A.; Firefly version 7.1.G, URL: http://classic.chem.msu.su/gran/firefly/index.html

Haile, J. M. (1992) *Molecular Dynamics Simulation. Elementary Methods*, John Wiley & Sons, Inc. Wiley-Interscience, New York

Hassinen, T.; Peräkylä, M. (2001). New energy terms for reduced protein models implemented in an off-lattice force field. *Journal of Computational Chemistry*, Vol. 22, No. 12, (September 2001) 1229–1242

Hess, B.; Kutzner, C.; van der Spoel, D.; Lindahl, E. (2008). GROMACS 4: Algorithms for Highly Efficient, Load-Balanced, and Scalable Molecular Simulation. *Journal of Chemical Theory and Computation* Vol. 4, No. 3, (February 2008) 435–447

HyperChem(TM) Professional 7.51, Hypercube, Inc., 1115 NW 4th Street, Gainesville, Florida 32601, USA

Isayev, O.; Furmanchuk, A.; Shishkin, O. V.; Gorb, L.; Leszczynski, J. (2007). Are Isolated Nucleic Acid Bases Really Planar? A Car-Parrinello Molecular Dynamics Study. *Journal of Physical Chemistry B* Vol. 111, No. 13, (April 2007) 3476–3480

Jian-Song, Y.; Li, B.-X. (2010). First-principles study of Ga_7As_7 ionic cluster and influence of multi-charge on its structure. *Chinese Physics B* Vol. 19, No. 9, (September 2010) 097103

Jimenez-Saez, J.; Perez-Martin, A.; Jimenez-Rodriguez, J. (2006). A molecular dynamics study of atomic rearrangements in Cu clusters softly deposited on an Au(001) surface.

Nuclear Instruments and Methods in Physics Research Section B: Beam Interactions with Materials and Atoms Vol. 249, No. 1-2, (August 2006) 816–819

Jorgensen, W. L.; Chandrasekhar, J.; Madura, J. D.; Impey, R. W.; Klein, M. L. (1983). Comparison of simple potential functions for simulating liquid water. *Journal of Chemical Physics* Vol. 79, No. 2, (July 1983) 926–935

Jorgensen, W. L.; Tirado-Rives, J. (1988). The OPLS [optimized potentials for liquid simulations] potential functions for proteins, energy minimizations for crystals of cyclic peptides and crambin. *Journal of the American Chemical Society* Vol. 110, No. 6, (March 1988) 1657–1666.

Kiliç, Ç.; Yildirim, T.; Mehrez, H.; Ciraci, S. (2000). A First-Principles Study of the Structure and Dynamics of C_8H_8, Si_8H_8, and Ge_8H_8 Molecules. *Journal of Physical Chemistry A* Vol. 104, No. 12, (March 2000) 2724–2728

Korth, M.; Pitoňák, M.; Řezáč, J.; Hobza, P. (2010) *Journal of Chemical Theory and Computation* Vol. 6, No. 1, (January 2010) 344–352

Kresse, G.; Hafner, J. (1993). Ab initio molecular dynamics for liquid metals. *Physical Reviews B* Vol. 47, No. 1, (January 1993) 558–561

Kresse, G.; Hafner, J. (1994). Ab initio molecular-dynamics simulation of the liquid-metal-amorphous-semiconductor transition in germanium. *Physical Reviews B* Vol. 49, No. 20, (May 1994) 14251–14269

Kresse, G.; Furthmüller, J. (1996). Efficiency of ab-initio total energy calculations for metals and semiconductors using a plane-wave basis set. *Computational Materials Science* Vol. 6, No. 1, (July 1996) 15–50

Kresse, G.; Furthmüller, J. (1996). Efficient iterative schemes for ab initio total-energy calculations using a plane-wave basis set. *Physical Reviews B* Vol. 54, No. 16, (October 1996) 11169–11186

Kuzmin, V. I.; Tytik, D. L.; Belashchenko, D. K.; Sirenko, A. N. (2008). Structure of silver clusters with magic numbers of atoms by data of molecular dynamics. *Colloid Journal* Vol. 70, No. 3, (June 2008) 284–296

Li, B.-X.; Wang, G.-Y.; Ye, M.-Y.; Yang, G.; Yao, C.-H. (2007). Geometric and energetic properties of Al-doped Si_n (n=2-21) clusters: FP-LMTO-MD calculations. *Journal of Molecular Structure: THEOCHEM* Vol. 820, No. 1-3, (October 2007) 128–140

Lindahl, E.; Hess, B.; van der Spoel, D. (2001) GROMACS 3.0: a package for molecular simulation and trajectory analysis . *Journal of Molecular Modelling*, Vol. 7, No. 8, (August 2001) 306–317

Martínez, L.; Andrade, R.; Birgin, E. G.; Martínez, J. M. (2009). Packmol: A package for building initial configurations for molecular dynamics simulations. *Journal of Computational Chemistry* Vol. 30, No. 13, (October 2009) 2157-2164

Mohamadi, F.; Richard, N. G. J.; Guida, W. C.; Liskamp R.; Lipton, M.; Caufield, C.; Chang, G.; Hendrickson, T.; Still, W. C. (1990). MacroModel - an Integrated Software System for Modeling Organic and Bioorganic Molecules Using Molecular Mechanics, *Journal of Computational Chemistry* Vol. 11, No. 4, (May 1990) 440–467

Pang, L.; Brisse, F. (1994) Structural and conformational analysis of six-, seven-, and eight-membered cycloalkanes in tris(5-acetyl-3-thieny1)methane inclusion compounds. *Canadian Journal of Chemistry* Vol. 72, No. 11, (November 1994) 2318–2325

Pearlman, D.A.; Case, D.A.; Caldwell, J.W.; Ross, W.S.; Cheatham III, T.E.; DeBolt, S.; Ferguson, D.; Seibel, G.; Kollman, P.A. (1995). AMBER, a package of computer programs for applying molecular mechanics, normal mode analysis, molecular

dynamics and free energy calculations to simulate the structural and energetic properties of molecules. *Comp. Phys. Commun.* Vol. 91, No. 1-3, (September 1995) 1–41

Ponder, J. (2011). *TINKER* URL: http://dasher.wustl.edu/tinker/

Radoul, M.; Sundararajan, M.; Potapov, A.; Riplinger, C.; Neese, F.; Goldfarb, D. (2010). Revisiting the nitrosyl complex of myoglobin by high-field pulse EPR spectroscopy and quantum mechanical calculations. *Physical Chemistry Chemical Physics*, Vol. 12, No. 26, (May 2010) 7276–7289

Řezáč, J.; Fanfrlík, J.; Salahub, D.; Hobza, P. (2009) *Journal of Chemical Theory and Computation* Vol. 5, No. 7, (July 2009) 1749–1760

Rosas-Garcia, V. M.; Lopez-Cortina, S. T.; Chavarria-Resendez, A. *Journal of Molecular Structure: THEOCHEM* Vol. 958, No. 1-3, (October 2010) 133–136

Rosas-Garcia, V. M.; Saenz-Tavera, I.; Cantu-Morales, D. accepted manuscript, DOI:10.1007/s10876-011-0420-4

Saiz, E.; Guzmán, J.; Iglesias, M. T.; Riande, E. (1996). Dynamics and Polarity of Substituted 1,3-Dioxacyclohexanes. *Journal of Physical Chemistry* Vol. 100, No. 47, (January 1996) 18345–18350

Saunders, M.; Houk, K. N.; Wu, Y. D.; Still, W. C.; Lipton, M.; Chang, G.; Guida, W. C. (1990). Conformations of cycloheptadecane. A comparison of methods for conformational searching. *Journal of the American Chemical Society* Vol. 112, No. 4, (February 1990) 1419–1427

Schenker, S.; Schneider, C.; Tsogoeva, S. B.; Clark, T. (2011) *Journal of Chemical Theory and Computation* Vol. 7, No. 11, (October 2011) 3586–3595

Shiroishi, H.; Oda, T.; Hamada, I.; Fujima, N. (2005). Structure and magnetism of anion iron oxide clusters, Fe_nO_m-(n=3,4). *Polyhedron* Vol. 24, No. 16-17, (November 2005) 2472–2476

Stewart, J. J. P. (1989). Optimization of parameters for semiempirical methods I. Method. *Journal of Computational Chemistry* Vol. 10, No. 2, (March 1989) 209–220

Stewart, J. J. P. (2007). Optimization of parameters for semiempirical methods V: Modification of NDDO approximations and application to 70 elements. *Journal of Molecular Modeling* Vol. 13, (September 9) 1173–1213

Stewart, J. J. P. 2008. MOPAC2009. Colorado Springs, CO, USA: Stewart Computational Chemistry. URL: http://OpenMOPAC.net

Takayanagi, T.; Yoshikawa, T.; Kakizaki, A.; Shiga, M.; Tachikawa, M. (2008). Molecular dynamics simulations of small glycine-$(H_2O)_n$ (n = 2-7) clusters on semiempirical PM6 potential energy surfaces. *Journal of Molecular Structure: THEOCHEM* Vol. 869, No. 1-3, (November 2008) 29–36

Tosco, P.; Lolli, M. L. (2008). Hydroxy-1,2,5-oxadiazolyl moiety as bioisoster of the carboxy function. A computational study on γ-aminobutyric acid (GABA) related compounds. *Journal of Molecular Modeling* Vol. 14, No. 4, February 2008, 279–291.

Van Der Spoel, D.; Lindahl, E.; Hess, B.; Groenhof, G.; Mark, A. E.; Berendsen, H. J. C. (2005). GROMACS: Fast, flexible, and free. *Journal of Computational Chemistry*, Vol. 26, No. 16, (December 2005) 1701–1718

Yang, Z.; Xiong, S.-J. (2008). Structures and electronic properties of small FeB_n (n = 1-10) clusters. *Journal of Chemical Physics* Vol. 128, No. 18, (May 2008) 184310-8

5

Molecular Dynamics Simulations and Thermal Transport at the Nano-Scale

Konstantinos Termentzidis[1,2] and Samy Merabia[3]
[1]*CETHIL-UMR5008, INSA de Lyon, CNRS, Université Lyon 1,*
[2]*EM2C-UPR288, Ecole Centrale Paris, CNRS,*
[3]*LPMCN-UMR5586, Université Lyon 1,*
France

1. Introduction

This chapter presents an overview of the Molecular Dynamics (MD) simulation technique to predict thermal transport properties of nanostructured materials. This covers systems having characteristic lengths of the order of a few nanometers like carbon nanotubes, nanowires and also superlattices, i.e. composite materials made of submicronic thickness of solid layers. The common features of these systems is the small ratio between their characteristic system size and the phonon mean free path, which leads to ballistic heat transport and deviations from the classical Fourier law. Also when the density of interfaces gets large, the energy transport properties of the materials can not longer be described solely by the thermal conductivities of the constituents of the material, but depend also on the thermal boundary resistance which measures the transmission of phonons across an interface. In this context, molecular dynamics was proven to be a very useful technique to study heat transport in nanostructured materials. The main reasons are; the length scale probed by the method is in the nanometer range, and it does not make any assumption on the phonons dynamics except their classical nature.

In this contribution, we present two MD methods, the equilibrium and the non-equilibrium method, which are now commonly used to determine both the thermal conductivity and the thermal boundary resistance of nanostructured materials. We focus on superlattices and discuss how the structural features of the interfaces like height, shape, inter-diffusion phenomena and the layer thickness affect the thermal conductivity of the superlattice. We show how these complex phenomena can be predicted by simple models of Lennard-Jones crystals with a mass ratio corresponding to the acoustic impedance ratio of Si/Ge and GaAs/AlAs superlattices.

2. Molecular dynamics

The development of molecular simulations began in the early fifties after the considerable development of computer facilities in the United States during World War II. A few years after the first Monte-Carlo simulation, Alder and Wainwright, first introduced in the late 50's the Molecular Dynamics (MD) method (Alder & Wainwright, 1957, 1959). The aim of

the first simulations both Monte-Carlo or MD was to probe the different phases of model hard spheres. The necessity to model liquids motivated the development of realistic potentials. Rahman was the first to model Argon using Lennard-Jones potential , which is still considered as a standard potential for MD (Rahman, 1964). This opened the way to consider a broad range of condensed matter systems, ranging from liquid water first modelled by Rahman and Stillinger to silicon (Rahman & Stillinger, 1974). The efforts towards realistic modelling have permitted to applicate MD to characterize the collective excitations in solids (Hensen 1976). The last step came with the implementation of MD thermostats opening the way to probe the phonon dynamics in rare-gas solids (Ladd 1986). More recently, there has been an increasing number of MD studies on nano-scale heat transport motivated by fine measurements of energy transport in nano-materials (Volz 1999). We refer the reader to the classical textbooks on MD (Allain & Tildesley 1987 and Frenkel & Smit 1996) for a thorough introduction.

MD is a simulation method based on the numerical integration of Newton's equation of motion:

$$m\frac{d^2\vec{r}_i}{dt^2} = -\frac{\partial V}{\partial \vec{r}_i} \tag{1}$$

where: m, $\vec{r}_i$ and V denote respectively the mass of the particle i, its position vector and the inter-atomic potential. The integration scheme commonly used is the Verlet algorithm (Verlet 1967a, 1967b) which predicts the positions at time $t+dt$ given the positions at the earlier times t and $t-dt$:

$$\vec{r}_i(t+dt) = 2\vec{r}_i(t) - \vec{r}_i(t-dt) + \frac{d^2\vec{r}_i}{dt^2}dt^2 + O\left(dt^4\right) \tag{2}$$

where the acceleration is calculated using the inter-atomic forces. The velocities can be computed using

$$\vec{v}_i(t) = \frac{\vec{r}_i(t+dt) - \vec{r}_i(t-dt)}{2dt} + O\left(dt^2\right) \tag{3}$$

and the error is larger than the error on the positions, but as soon as the velocities are only used to compute the instantaneous kinetic energy the consequences are minor. Of course there are other integration schemes, but the Verlet algorithm has the advantage to be simple, easy to implement, stable and time-reversible. The typical time step used in the integration algorithms is a fraction of the characteristic atomic period

$$\tau = \sqrt{\frac{m\sigma^2}{k_B T}} \approx 1ps \tag{4}$$

where m is the mass of the particles and σ denotes a typical atomic diameter.

Given the power of modern computers, it takes a few hours on a mono-processor machine to follow the trajectory of a set of 10000 particles over a time comparable to 1 ns. Using parallel MD codes or GPUs (graphics processing units) opens the way to model larger

systems or reach orders of magnitude longer times . The system represented in a MD simulation has microscopic dimensions, and usually one is not so much interested in simulating a nano system with free surfaces, but rather a part of a bulk system. To embed the small system simulated in a bulk-like system, one can use *periodic boundary conditions*. These conditions assume that the system is repeated periodically in all space directions and thus any particle close to the boundaries of the simulation box interacts with an image particle, and when a particle crosses one of the face of the central simulation box, one of its images will enter the central box through the opposite face. One of the consequences of the use of periodic boundary conditions is the cut-off of long wavelengths fluctuations, i.e. those having a wavelength larger than the simulation box length. In the context of heat transport simulations this will imply that phonons with long wavelengths are not present.

The strength of MD lies on the versatility and the flexibility in the choie of the atomic potential (eq.1). Generally speaking, the total potential can be decomposed in the sum

$$V(\vec{r}_i) = \sum_i V_1(\vec{r}_i) + \sum_{i<j} V_2(\vec{r}_i, \vec{r}_j) + \sum_{i<j<k} V_3(\vec{r}_i, \vec{r}_j, \vec{r}_k) + \ldots \tag{5}$$

where the first term represents the one body contribution to the potential and is often associated to an external field like e.g. an electric field. The second and third terms represent respectively two-body and three-body potentials of the inter-atomic interaction. The choice of the inter-atomic potential depends on the problem at hand (type of atomic structure and on the properties to be studied), and on the necessity to model a real system or an experiment. One of the simplest potential used in condensed matter physics is the Lennard-Jones (LJ) potential, where the total potential decomposes in a sum of pair potentials:

$$V = \sum_{i<j} V_2(r_{ij}) \tag{6}$$

with

$$V_2(\vec{r}_{ij}) = 4\varepsilon\left(\left(\sigma / r_{ij}\right)^{12} - \left(\sigma / r_{ij}\right)^{6}\right) \tag{7}$$

This is the LJ pair potential, which depends only on the distance between neighbouring particles $r_{ij} = \vec{r}_{ij}$. The interaction energy ε identifies with the depth well of the potential, and σ is the atomic diameter. Although very simple, the LJ potential is often thought to be a good potential to model rare gas and in particular Argon, using the following parameters: $\varepsilon = 1{,}67 \times 10^{-21} J$ and $\sigma = 3{,}40 \times 10^{-10} m$. Due to the algebraic decay of the LJ potential, all the atoms of the simulation box interact. From a practical point of view however, it would be computationally costly to estimate $N^2/2$ inter-atomic forces at each time step, with $N \approx 10000$. To bring back the computational cost of the force calculation to $O(N)$, the inter-atomic pair potential is often truncated at a cut-off radius, usually $r_c = 2{,}5\sigma$, which represents typically a neighbourhood of 50 atoms per particle. It should be mentioned at this point, that even if the potential at the radius of truncation is small compared to the well depth: $V(r_c) \approx 0{,}016 \cdot \varepsilon$, truncating the potential may have a non negligible effect on the thermodynamics of the system modelled. As an example, let us estimate the effect of truncating the inter-atomic potential respectively on the internal energy per particle and on the pressure. The respective errors are given by:

$$\Delta U = \rho \int_{r_c}^{+\infty} 4\pi r^2 V_2(r) dr \approx 1{,}07 \rho \sigma^3 \varepsilon \tag{8}$$

and

$$\Delta P = \frac{-\rho^2}{6} \int_{r_c}^{+\infty} r \frac{\partial V_2}{\partial r} 4\pi r^2 dr \approx -1.07 \rho^2 \sigma^3 \varepsilon \tag{9}$$

where we have used the previous value of the cut-off radius and we have assumed that beyond r_c, the medium is structureless, i.e. the pair correlation function may be considered close to unity. The previous errors are found to be typically 10% the values of the internal energy and pressure for a condensed phase. This is not worrying since the calculation of thermodynamic quantities can be corrected using the previous estimations, but this has to be kept in mind when calculating a phase diagram for instance.

Although the LJ potential is quite simple, some situations require to use more sophisticated semi-empirical potentials whose parameters are chosen to reproduce either microscopic or macroscopic properties of a model system. These semi-empirical potentials are usually no longer pair potentials like the LJ potential but many-body, where the many-body terms describes how does the potential energy of an atom depends on its coordination.

As an illustration, let us mention the embedded atom model (EAM) used in the context of metals (Daw & Baskes 1984), where the potential

$$\sum_{i<j} \phi\left(r_{ij}\right) + \sum_i u\left(\rho\left(r_i\right)\right) \tag{10}$$

consists of a pair term $\phi(r)$ accounting for repulsion at short distances and a many body term $u\left(\rho(r)\right)$ which accounts for the cohesion of the metallic bond and which depends on the local density measured using the positions of neighbouring particles $\rho\left(r_i\right) = \sum_j w\left(r_{ij}\right)$. The choice of the functional $u(\rho)$ and the weight function $w(r)$ depends on the microscopic and macroscopic properties to be reproduced, usually the lattice constant, the elastic constants and the sublimation energy of the metal (Daw & Baskes 1984).

Another limitation of LJ potentials is the description of solids crystalizing in non-compact structures. Indeed, Lennard Jones atoms form close-packed structures at low temperatures (usually fcc at low pressure), and thus LJ potentials are also not adapted to model materials which crystallize in opened structures such as diamond. Semi-conductors like silicon or germanium are usually modelled using many-body semi-empirical potentials, in which the many body terms account for the local preferential bond ordering of the semi-conductor. Among the most famous potentials for silicon, let us quote the Tersoff potential (Tersoff 1986, 1988a, 1988b) and the Stillinger-Weber potential (Stillinger & Weber 1985). The parameters of the former are chosen so as to reproduce the elastic properties of bulk silicon, while the latter describes satisfactorily the structural properties of liquid silicon. Of course the list of potentials is non exhaustive and there exists plethora of empirical potentials to model as disparate systems as charged systems, liquid crystals, polymers, surfactants, granular media,... and mixtures of them!

As we have already briefly mentioned, the output of MD simulations can be compared to experiments if we know how to relate the microscopic state of the material under study to the macroscopic observables typically measured in an experiment. Generally speaking, one can distinguish three classes of information that can be extracted from MD. On the one hand, MD allows to compute global quantities which correspond usually to the thermodynamics of the system modelled. For instance, the internal energy can be expressed as:

$$U = \left\langle \sum_i V(r_i) \right\rangle + KE \tag{11}$$

and the total kinetic energy:

$$KE = \left\langle \sum_i \frac{1}{2} m \vec{v}_i^2 \right\rangle \tag{12}$$

where the brackets denote an ensemble average. If sufficient time has been left to the system to reach equilibrium, the ensemble average may be performed by averaging over a sufficient long time thanks to ergodicity. On the other hand, in non-equilibrium situations, different initial conditions (usually the positions and the velocities of the atoms) may be used to generate independent trajectories in phase space. The latter definition of the kinetic energy is intimately related to the definition of the local temperature :

$$T(\vec{r}) = \left\langle \sum_{i \in V(\vec{r})} \frac{m \vec{v}_i^2}{3n(\vec{r}) k_B} \right\rangle \tag{13}$$

where the sum runs over particles i in a small volume V(r) centred around r and which contains n(r) particles. Another important quantity in heat transport simulations is the energy flux, defined as

$$\vec{J} = \frac{d}{dt} \left(\sum_i E_i \vec{r}_i \right) \tag{14}$$

where E_i is the total energy of particle i, yielding for pair potentials:

$$\vec{J} = \sum_i E_i \vec{v}_i + \frac{1}{2} \sum_{i<j} \vec{F}_{ij} \cdot \left(\vec{v}_i + \vec{v}_j \right) \vec{r}_{ij} \tag{15}$$

For simulations in crystals at low temperatures, the previous energy flux displays large oscillations due to optical phonons which carry a negligible amount of heat, and sometimes it can be more suited to work with the equivalent definition of the flux:

$$\vec{J} = \frac{1}{2} \sum_{i<j} \vec{F}_{ij} \cdot \left(\vec{v}_i + \vec{v}_j \right) \vec{r}_{ij}^{\,0} \tag{16}$$

where the superscript "0" denotes the equilibrium positions of the atoms. From the knowledge of the local temperature and the energy flux, it is possible to measure thermal conductivity and we would come back to the measurement of transport coefficients in MD in the next section, with a particular emphasis on heat transport.

The other type of information that one can extract from MD is structural. Since the output of a MD simulation is the set of positions $\vec{r}_{ij}$, it is possible to compute the pair distribution function

$$\rho g(\vec{r}) = \left\langle \frac{1}{N} \sum_{i \neq j} \delta\left(\vec{r} - \vec{r}_{ij}\right) \right\rangle \tag{17}$$

where ρ is the mean number density of the system. Physically, g(r) represents the probability to find two particles separated by a distance r, and $4\pi r^2 \rho g(r) dr$ is the average number of particles located at a distance between r and r+dr from a given particle. Note that sometimes, it may be more useful to compute the structure factor:

$$S(\vec{q}) = \left\langle \frac{1}{N} \sum_{i,j} \exp\left(i\vec{q} \cdot \left(\vec{r}_i - \vec{r}_j\right)\right) \right\rangle \tag{18}$$

which is simply related to the pair distribution function through a Fourier transform:

$$S(\vec{q}) = 1 + \rho \int g(\vec{r}) \exp\left(-i\vec{q} \cdot \vec{r}\right) d\vec{r} \tag{19}$$

Finally, MD may be used to compute the vibrational properties of a model system. In particular, the vibrational density of states (DOS)

$$g(\omega) = \frac{1}{V} \sum_k \delta(\omega - \omega_k) \tag{20}$$

where the sum runs over the eigenmodes of the system can be estimated using the Fourier transform of the velocity autocorrelation function:

$$g(\omega) = \int_0^\infty \langle \vec{v}(t) \cdot \vec{v}(0) \rangle exp(-i\omega t) dt \tag{21}$$

where here $\vec{v}(t)$ is the velocity of an atom. One has to keep in mind that the previous equation is only approximate, as it assumes small deviations from harmonicity, and thus is only valid strictly speaking at low temperatures. Note also that the resulting DOS mixes information about the different polarizations of the atomic vibrations, e.g. transversal or longitudinal, and to determine the DOS relative to a particular polarization, a more refined analysis of the atomic displacement should be undertaken. Apart from the DOS, MD is a common technique to characterise the propagation of phonons in a crystal.

The vibrations of a crystal containing N atoms may be decomposed in normal modes:

$$S_{\vec{k},\nu}(t) = N^{-1/2} \sum_i m_i^{1/2} exp\left(-i\vec{k} \cdot \vec{r}_i^{\,0}\right) \vec{e}\left(\vec{k},\nu\right) \cdot \vec{u}_i \tag{22}$$

where $\vec{u}_i(t)$ denotes the displacement of atom i in the crystal vibrating around the equilibrium position $\vec{r}_i^{\,0}$, ν is an index designating the polarization of the vibration, e.g. longitudinal or transversal and $\vec{e}\left(\vec{k},\nu\right)$ is the corresponding polarization vector. From the normal mode amplitude, one can compute the dispersion relation and the phonon lifetime as follows. First consider the autocorrelation of the atomic displacement:

$$\langle \tilde{u}S_{\vec{k},\nu}(t)\overline{S}_{\vec{k},\nu}(0)\tilde{u} \rangle \tag{23}$$

It is a straightforward exercize to show that

$$\langle \tilde{u}S_{\vec{k},\nu}(t=0)\tilde{u}^2 \rangle = k_B T / w_{\vec{k}}^2 \tag{24}$$

Hence, from the previous autocorrelation function, one can determine the dispersion relation $\omega = \omega(\vec{k})$ for the two polarizations. From the dispersion relation, the phonon phase $v_\phi(\vec{k}) = \omega / (\vec{k})$ and group velocities $\vec{v}_g(\vec{k}) = \partial\omega/\partial\vec{k}$ may be predicted.

Secondlv, from the time decay of $\left\langle \left(S_{\vec{k},\nu}(t)\overline{S}_{\vec{k},\nu}(0) \right) \right\rangle$, one can compute the lifetime of the mode $\vec{k},\nu$ (Ladd 1986):

$$\tau_{\vec{k},\nu} = \frac{\int \langle S_{\vec{k},\nu}(t)\overline{S}_{\vec{k},\nu}(0) \rangle dt}{\langle \tilde{u}S_{\vec{k},\nu}(t=0)\tilde{u}^2 \rangle} \tag{25}$$

The wavelength dependance of the phonon lifetime may then be compared to the theoretical predictions, given either by Callaway 1959 or Holland 1963, see e.g. (McGaughey 2004).

As we have already mentioned, the conversion of the microscopic information given by a MD simulation to macroscopic observables requires to evaluate averages over phase space. The phase space is a multidimensional space generated by the positions and the momenta of a classical system, and has dimension of 6N for a system of N particles. A molecular dynamics simulation generates a sequence of points in phase space as a function of time, whose points belong to the same thermodynamic ensemble. The first MD simulations were performed in the micro-canonical ensemble or NVE ensemble, which corresponds to a fixed number of atoms N, a fixed volume V, and a fixed energy E. Although these simulations are very easy to implement, they do not represent a realistic system as the set of molecules studied is completely isolated. The need to model real situations led to the development of thermostats for MD, which allow to simulate the dynamics of a system in the canonical or the grand-canonical ensemble for instance (Frenkel & Smit, 1996).

Although MD can be used to calculate the thermodynamics, structural and vibrational properties of systems at equilibrium, it is more designed to study the non-equilibrium situations where the system under study is driven by an external force; the latter can be of thermodynamic nature. In the language of out of equilibrium statistical physics, MD can help in determining the relation between the forces and the fluxes. Statistical physics predicts that there is proportionality between the forces and the fluxes if the system under study is driven weakly out of equilibrium. The coefficients of proportionality are called transport coefficients and measure the susceptibility of the system to respond to a given thermodynamic force. For instance, the thermal conductivity quantifies the amount of energy flowing in a material submitted to a temperature gradient. MD is a very powerful tool to calculate the transport coefficients of a model system. To this end, two routes can be traditionally followed: either the model system is submitted to an external force or the thermally induced fluctuations of an internal variable are probed at equilibrium. Statistical physics states indeed that the typical time decay of the spontaneous thermal fluctuations is

proportional to the appropriate transport coefficient. This will be illustrated in the context of the heat transfer in the next sextion. Before focusing on energy transfer applications of MD, let us mention that MD can be used also beyond the linear response domain of out of equilibrium systems. This includes situations of large external forcing such as e.g. polymer melts flowing at large shear rates (Vladkov 2006b). But this includes also systems for which intrinsically the linear relationship between forces and fluxes is violated. As an example consider a nano-structured system at low temperatures for which the phonon mean free path is comparable with the characteristic system size. Heat transfer in such systems is no longer described by Fourier law, but is rather described by an effective conductivity which depends on the strength of the thermal flux flowing across the system. Molecular dynamics has been shown to predict the effective conductivity under conditions where the heat carriers travel ballistically in the system and being scattered only by the boundaries of the nanostructure.

2.1 Limitations of molecular dynamics

As any simulation technique, molecular dynamics suffers from some intrinsic limitations. The most obvious is the limitation in system size. This may be critical in the modeling of real scale devices with disparate length scales ranging from 1nm to microns. To address such situations, MD should be coupled with a more mesoscopic method, such as the Boltzmann Transport Equations, where the microscopic information on the phonon lifetime is used as input in a Boltzmann equation.

We have also mentioned that a finite system size cuts the long wavelength phonon modes. As we will see, this affects only mildly the measurement of the thermal conductivity unless we couple the system with heat reservoirs.

The second limitation of MD is its classical nature. Each phonon mode is equally populated, and the heat capacity is given to a good approximation by the Dulong-Petit law. This is a good approximation if one ever considers solids above or just below their Debye temperature. However, many materials do not obey this condition at ambient temperature. Quantum effects in MD may be accounted for in different ways. The phonon lifetimes computed from MD may be used in a Boltzmann transport equation which includes quantum statistics in the phonon occupation number (McGaughey 2004). Quantum effects may be also directly incorporated in the course of a MD simulation, using a Langevin thermostat with a colored noise consistent with a Bose-Einstein distribution for the phonon modes (Dammak2009).

Finally, the electronic degrees of freedom are not explicitly simulated in MD. Hence, it is not possible to probe thermal transport in electrical conductors, and in its basic version the contribution of electron-phonon scattering to the transport in semi-conductors is not accounted for.

3. Predicting thermal conductivity with EMD and NEMD

In general the heat energy is transmitted through a solid by electrons (mainly in metals) or phonons (mainly in insulators) or other excitations as spin waves. In this paragraph, we focus on the lattice thermal conductivity, which is the dominant mechanism in

semiconductors (Yang, 2004). There are three principal techniques used to evaluate the thermal conductivity with molecular dynamic simulations (Allen & Tildesley 1987, Chantrenne, 2007); a. the equilibrium approach based on the Green-Kubo formulae (Frenkel & Smit, 1996), b. the non-equilibrium MD, also called the direct method, which uses a heat source and a heat sink, or the so-called direct method, based on the creation of a temperature gradient, and c. the homogeneous non-equilibrium MD, where a heat flux is induced (Evans, 1982, 1986). The comparison between the two methods has been undertaken by many researchers, who have concluded that the two methods give consistent results (Shelling et al, 2002; Mahajan et al, 2007; Termentzidis et al, 2011b).

3.1 Non-equilibrium molecular dynamics method (NEMD)

Kotake and Wakuri proposed the direct method (Kotake & Wakuri, 1994), which is similar to the hot-plate experiment setup. A temperature gradient is imposed across the structure under study by allowing thermal power exchange between the heat source and sink and measure the resulting heat flux (Chantrenne & Barrat, 2004a, 2004b, Termentzidis et al, 2009). The thermal conductivity is then obtained as the ratio of the heat flux and the temperature gradient. An alternative, but equivalent way consists in inducing a heat flux and to measure the resulting temperature gradient (Muller-Plathe, 1997). In both cases the system is first allowed to reach a steady state, after which prolong simulations are conducted allowing to obtain correct statistical measurements (Stevens et al, 2007). The NEMD method is often the method of choice for studies of nanomaterials (Poetzsch & Botter, 1994) while for bulk thermal conductivity, particularly of high-conductivity materials, equilibrium method is typically preferred due to less severe size effects. The size effects in the determination of the thermal conductivity using NEMD can be understood using the following simple line of thought (Schelling & al 2002). Imagine a phonon travelling in the crystal between the two heat reservoirs. This phonon can experience at least two kinds of scattering events: either it can be scattered by other phonons travelling in the material, or it can be scattered by the reservoirs which are seen by the considered phonon as a different material with an almost infinite thermal conductivity. The mean free path associated with this former mechanism can be roughly approximated by $\Lambda_{reservoir} = L/2$, where L is the distance between the reservoirs, because on average a phonon will travel ballistically a distance L/2 before being scattered by the heat source/sink. Now invoking Mathiessen rule to predict the effect of reservoir scattering on the overall thermal conductivity, the effective mean free path is given by:

$$1/\Lambda(L) = 2/L + 1/\Lambda(L \to \infty) \tag{26}$$

where the last term $\Lambda(L \to \infty)$ describes the phonon-phonon interaction in a bulk-like medium. The length dependence of the thermal conductivity can now be estimated using kinetic theory of gas: $\lambda(L) = cv\Lambda(L)/3$ where c is the heat capacity per unit volume, v is the mean group velocity. Of course, this analysis is simplified because we have assumed that the effect of phonon-phonon scattering can be described in terms of a

single mean free path, and we should have rather done the analysis mode by mode (Sellan et al 2010).

However, the previous simple kinetic model predicts:

$$1/\lambda(L) = 1/\lambda(L \to \infty) + 6/(cvL) \tag{27}$$

and the size dependence is found to be consistent with MD NEMD simulations (Schelling et al 2002, Termentzidis et al 2009). Because of the algebraic decay, size effects in NEMD are severe, and sometimes it is faster to run equilibirum simulations to determine the thermal conductivity.

We now illustrate the determination of the thermal conductivity using the direct method with the exemple of superlattices composed of a regular alternative arrangement of solid layers, having different physical properties. Thermal transport in superlattices is characterized by the cross-plane and the in-plane conductivities, which correspond respectively to heat flowing in the direction perpendicular or parallel to the interfaces.

The geometry used for the determination of the cross-plane and in-plane thermal conductivities using NEMD is given in figure 3.1.1. Periodic boundary conditions are used in all directions, while in all cases the heat flux is imposed in z-direction. The interatomic interactions are described with Lennard-Jones (LJ) potentials, with energy unit ε_{ij}=1.0 and length unit σ_{ij}=1.0. The use of LJ potential is justified by the interest in focusing on the main phenomena introduced by the interface roughness of the super-lattices (for all the following results). The two types of materials A and B may represent respectively the Si and Ge, if one considers Si/Ge-type superlattice (paragraph 5) or the GaAs and AlAs in case of GaAs/AlAs-type superlattice (paragraph 6). The two solids have the same lattice constants and they differ only by the mass ratio of the atoms constituting the superlattices layers. For the Si/Ge-type superlattices the mass ratio is taken to be 2.0, while for GaAs/AlAs this ratio is equal to 1.5. This mass ratio is consistent with the acoustic impedance ratio in the case of Si/Ge (1.78) and in the case of GaAs/AlAs (1.2), as the ratio of acoustic impedances is equal to the square root of the ratio of masses (Swartz & Pohl, 1989).

In this chapter the equilibrium (EMD) and the non-equilibrium (NEMD) methods are presented and the results of the thermal conductivity are reported. For both methods the molecular dynamics code LAMMPS is used (Plimpton, 1995, 1997).

In the NEMD method or direct method, a temperature gradient is imposed across the structure under study. Depending on the boundary conditions the geometry of the thermostats can change. For periodic boundary conditions there is one thermostat (cold or hot) at the middle of the slab and a second thermostat (hot or cold) is divided in two parts, which are positioned at the two edges of the slab (fig. 1). This configuration gives the opportunity to increase the statistics (double the results). The thermal conductivity is then calculated using the Fourier's law monitoring the thermal power exchange and the temperature profile of the system (fig. 2). The infinitive system size thermal conductivity then can be extrapolated by plotting the inverse of the thermal conductivity as a function of the inverse of the system size (Schelling et al, 2002).

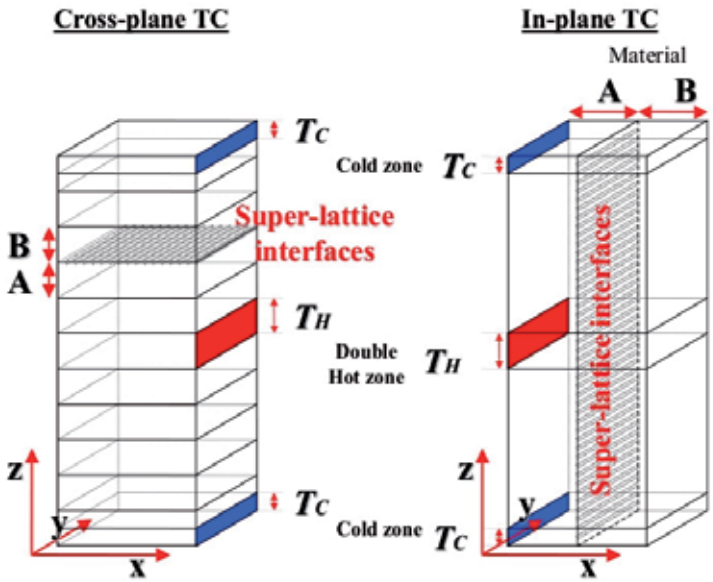

Fig. 1. Geometric configuration for the determination of the cross-plane (left) and in-plane (right) thermal conductivity simulations with NEMD and periodic boundary conditions are used in all directions.

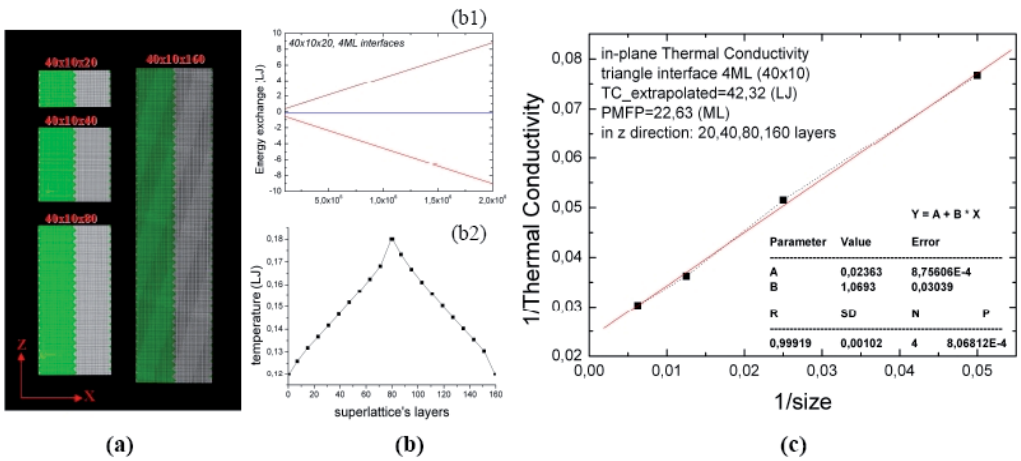

Fig. 2. To calculate the thermal conductivity (in the example the in-plane TC) of the superlattices the energy exchange (b1) and the temperature profile (b2) is extracted for each of the structures (at least 4 structures with increasing length see (a)). Then the inverse thermal conductivity is plotted as a function of the inverse of the size of slab (c). The last diagram helps in calculating the thermal conductivity of an infinitive size superlattice.

3.2 Equilibrium molecular dynamics method (EMD)

Alternately, the thermal conductivity of a model system can be determined using equilibrium simulations (Shelling et al, 2002). The principle relies on the fact that the regression of the thermal fluctuations of an internal variable, in our case the thermal flux, obeys macroscopic laws. Hence, the time decay of the fluctuations of the flux is proportional to the thermal conductivity. This is mathematically expressed by the Green-Kubo formulae which state that the time integral of the heat flux autocorrelation function is proportional to the thermal conductivity tensor (Evans & Morris, 1990):

$$\lambda_{\alpha,\beta} = \frac{1}{Vk_B T^2} \int_0^{+\infty} \left\langle J_\alpha(t) J_\beta(0) \right\rangle dt \tag{28}$$

where V is the volume of the system, and J_α denotes the component of the heat flux vector along the direction α. The equilibrium method consists then in computing the corresponding autocorrelation, which requires following the dynamics of a system over time scales a few times larger than the longest relaxation time present in the system. In the case of heat transfer in solid materials, the longest relaxation times correspond to long wavelengths phonons (a few nm) with a lifetime on the order of 100 picoseconds.

The advantage of the equilibrium method is that it allows to compute the full conductivity tensor from one simulation, which may be appreciated in superlattice simulations for instance, which display large thermal anisotropies. Another advantage of the equilibrium method is that it does not suffer from severe finite size effects as NEMD, mainly because in EMD the phonons are not strongly scattered by the boundaries of the simulation box. We can estimate the finite size effects in EMD using the following assumptions: the thermal conductivity measured in a MD simulation is given by:

$$\lambda = \int_{\omega_c(L)}^{\omega_D} g(\omega) c(\omega) v^2(\omega) \tau(\omega) d\omega \tag{29}$$

where

$$\omega_c(L) = \omega(k = \pi / L) \tag{30}$$

is the low pulsation cut-off introduced by the periodic boundary conditions, and the upper bound is

$$\omega_D = \omega(k = \pi / a) \tag{31}$$

where a is the interatomic step, since high frequency phonons are supposed to contribute weakly to the overall thermal conductivity. In the latter expression of the thermal conductivity, $c(\omega) = k_B$ is the heat capacity which obeys Dulong and Petit law, $v(\omega)$ is the phonon group velocity, and $\tau(\omega)$ is the relaxation time of phonon having a pulsation ω. In the following, we have ignored the possible different polarization states of the phonons to simplify the discussion. The error in the determination of the thermal conductivity is thus:

$$\delta\lambda = \int_0^{\omega_c(L)} g(\omega)c(\omega)v^2(\omega)\tau(\omega)d\omega \tag{32}$$

and if we assume that for sufficient low wavevectors that the medium behaves like a Debye solid, $g(\omega) \sim \omega^2$, the group velocity is constant and the phonon relaxation time is supposed to obey Callaway model: $\tau(\omega) \sim \omega^{-2}$, then the error in the conductivity scales as $\delta\lambda \sim \omega_c(L) \sim a / L$ and thus decreases faster as the error in NEMD $\delta\lambda_{NEMD} \sim \Lambda(L \to \infty) / L$.

This allows obtaining good estimates of the thermal conductivity with rather small systems. The main drawback is intrinsic to the method, as we need to probe small thermal fluctuations around equilibrium over long time scales, which requires also performing several statistical averages over different initial conditions.

3.3 Thermal boundary resistance

Apart from the thermal conductivity, both NEMD and EMD simulation techniques may be used to calculate the thermal boundary resistance characterizing heat transport across the interface between two media (Barrat, 2003). The thermal boundary resistance (TBR), also known as the Kapitza resistance is defined as the ratio of the temperature jump at the interface ΔT over the heat flux J crossing the interface:

$$R_K = \frac{\Delta T}{J} \tag{33}$$

The Kapitza resistance is thus a measure of the ability of phonons to be transmitted by the interface, with common values falling in the range between $0{,}01$ and $0{,}1 MW^{-1} \cdot m \cdot K$ (Cahill et al 2003) depending on the dissimilarity between the two media. There have been several models to predict the TBR between two solids (Swartz & Pohl 1987, 1989). Among the most popular, let us mention the acoustic mismatch model (AMM) (Khalatnikov 1952) in which the transmission of phonons is assumed to be specular and depends only the acoustic impedance mismatch between the two media, in a way similar to Snell Descartes's law ruling the transmission of an electromagnetic wave across the interface between two dielectrics with different optical indexes. The other popular model is the so-called diffuse mismatch model (DMM) (Swartz & Pohl 1989), in which it is assumed that the phonons are diffusively scattered by the interface, and the transmission coefficient depends in this limit in the mismatch of the density of states characterizing the two media. Generally speaking, both models fail to predict the thermal boundary resistance of real interfaces (Cahill et al 2003), and a deep physical understanding of interfacial heat transport between two solids is still missing. In this context, MD may be a convenient tool to probe the transmission of phonons across ideal surfaces, and also has the flexibility to introduce defects at the interface and study their effect on interfacial heat transport. Again, two routes may be followed to calculate the interfacial resistance: in NEMD simulations, the interface to be charaterized is placed between two heat reservoirs fixed at a distance a few atomic layers away from the interface. A net heat flux in the direction perpendicular to the interface is created, and the resulting temperature jump at the interface is measured, allowing to derive the interfacial resistance. With NEMD method only the TBR of smooth interfaces can be

calculated, as for rough interfaces there are geometrical issues about the cross-section/effective surface of the interfaces.

Equilibrium simulations rely again on the Green-Kubo formula for the interfacial conductance G=1/R (Puech 1986):

$$G = \frac{1}{Ak_B T^2} \int_0^{+\infty} \langle q(t) q(0) \rangle dt \tag{34}$$

where A is the interfacial area and q(t) is the instantaneous value of the flux flowing across the interface.

The latter quantity may be computed in a MD simulation using the power of interfacial forces (Barrat 2003):

$$q(t) = \sum_{i \in 1, j \in 2} \vec{F}_{ij} \cdot \vec{v}_i \tag{35}$$

where the indexes 1 and 2 denote the two media separating the interface to be studied, and we have assumed pair potentials to simplify. Equilibrium simulations have been performed for interface between simple Lennard Jones solids, where the dissimilarity between the two solids is introduced by changing the acoustic impedance ratio between the two solids. The results were found to disagree with NEMD determinations of the Kapitza conductance (McGaughey 2006), especially for solids with a weak acoustic mismatch. These discrepancies are not surprising and can be traced back to the formulation of the equations themselves (Pettersson 1990), as the Green-Kubo formula above predicts a finite conductance for the interface between two identical media, while of course in NEMD one measures an infinite conductance in this situation. Maybe for this reason, most of the MD works on Kapitza resistance have considered the direct method.

Among significant work, let us mention Stevens et al. 2007, who showed that the DMM and AMM models underpredicts the thermal boundary conductance obtained by NEMD, which is found to increase with the temperature, in contrast with the theoretical models predicting a constant value, at least above the Debye temperature of the softer solid. The authors showed also that the existence of a large lattice mismatch induces interfacial stress, which deteriorates thermal transport significantly. The existence of grain boundaries has been shown also to increase the interfacial resistance (Schelling 2004).

Further work is needed, in particular using equilibrium molecular dynamics to compare MD with the available theoretical models.

4. Heat transport in nanostructured materials

Thermal transport in nanostructured materials has attracted an increasing international interest in the last decades. From a theoretical point of view, nanostructured materials are platforms for testing novel phonon and electron transport theories. From the research and development point of view, nanomaterials are promising candidates for nanoscale on chip coolers (Zhang & Li, 2010). A high density of interfaces, which is the source of phonon scattering, appeared in advanced technological devices affecting their reliability and performance. Phonon interactions are modified significantly in nanostructures due to the

dimensional confinement of the phonon modes. This effect shares some similarities with the electron confinement in a quantum well (Stroscio & Dutta 2001). Phonon engineering in nanostructures can be succeeded in tailoring the phonon modes through the designing of the dimensions and the roughness of nanostructured materials.

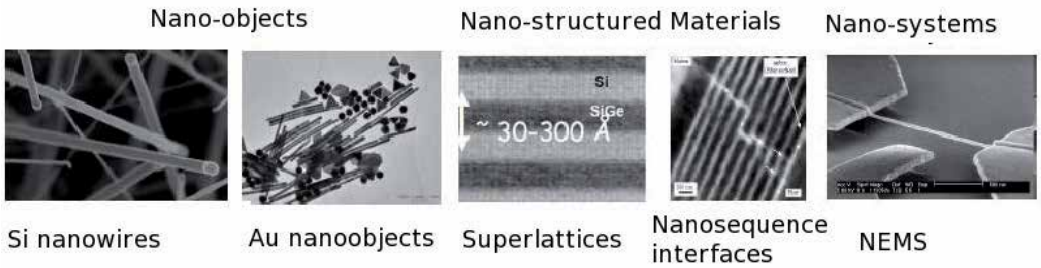

Fig. 3. Several types of nanostructured materials, including nano-wires, nano-objects, superlattices etc.

Nanomaterials are composite materials with at least one characteristic dimension smaller than 0.5μm. Super-lattices, nanofilms, nanowires, nanotubes and nanoparticles are typical examples of such materials (fig. 3). Nanomaterials exhibit transport properties different from their constituents and a fundamental understanding of heat conduction at the nanoscale is absolutely necessary to tailor their properties. Heat conduction on nanoscale differs significantly from heat transfer laws describing macroscopic transport. Among others, nanoscale energy transport can be controlled by phonon confinement (Montroll, 1950), the modification of the density of states induced by the confinement and also the ballistic behaviour of phonons. At low temperatures, phonons may travel ballistically in the bulk of the nanostructured material being scattered only by the interfaces, the latter mechanism providing the scattering mechanism which controls the thermal conductivity of the material. The crucial parameter describing ballistic transport is the ratio of the phonon mean free path (MFP) over the characteristic lengths of the nanostructure (eg. for 3D-structures: period and roughness of the interfaces of superlattices, for 2D: interfacial roughness in case of thin films or 1D: length of nanowires). Three different regimes may be distinguished, depending on the ratio of the characteristic length of the nanostructures, over the mean free path of the energy carriers. When the characteristic length is larger than the MFP of carriers the transport is diffusive and can be described by Fourier law, while when it is smaller, the heat carriers feel the nanostructured material as a homogeneous medium with a low thermal conductivity. There is an intermediate regime, where the transport becomes ballistic and diffusion scattering becomes predominant. As we will see, this third regime offers the possibility to tailor the thermal properties of nanostructures.

Nanoscale heat transfer has indeed an old history, which can be traced back to the Fermi-Pasta-Ulam study of heat transport in a 1D anharmonic chain (Dhar 2008). It is theoretically predicted that the thermal conductivity of model 1D chain assumptotically increases with the chain length L $\lambda \propto L^{\alpha}$, at least as soon as phonon scattering is ensured by momentum conserving process (Dhar 2008). The possibility of a diverging conductivity together with thte fantastic developement of nanotechnologies in the nineties motivated experimental investigation of energy transfer in 1D systems. There has been however considerably fewer

thermal measurement in low dimensional systems compared to electrical measurements for instance, because of the difficulty to measure directly the thermal current. Carbon nanotubes is a good paradigm of 1D objects, because all the heat carriers travel in the axial direction. The first experiments probing energy transfer in isolated multi-wall carbon nanotubes (Kim 2001) reported values of the thermal conductivity $\lambda \approx 3000 W/mK$ even larger than the conductivity of diamond at room temperature. These large values have been confirmed by other experiments on isolated single wall (Yu 2005, Pop 2006).

This experimental effort has been accompanied by several molecular dynamics works (Berber 2000, Maruyama 2002, Zhang 2005, Yao 2005, Donadio 2007), which have concluded that the phonon mean free path may be μm and that the thermal conductivity converges for very long nanotubes (Mingo 2005, Donadio 2007). We note besides that Green-Kubo equilibrium simulations are preferred because in the direct method, it is hard to compute an effective conductivity in a material where heat is transported ballistically. Also the coupling between the nanotube and heat reservoirs in NEMD would certainly affect the conductivity measurement.

Thermal transport in nanowires has been also extensively studied during the last decade. The motivations of the first experimental works was to measure the quantum of conductance (Schwab 2000):

$$g_0 = \pi^2 k_B^2 T / (3\mathrm{h}) \tag{36}$$

at very low temperatures. During the years 2000, the thermal conductivity of Si nanowires at room temperatures has been measured (Li 2003) reporting values two orders of magnitude smaller than bulk Si. These low values of the thermal conductivity may be understood because in a nanowire the free surfaces induce diffuse scattering of the phonons, contrary to carbon nanotubes where phonons can only travel in the axial direction. As a consequence, the transport properties of semi-conductor nanowires depend on the state of the nanowire surface, and in particular its roughness, opening the way to achieve materials combining low thermal conductivity but electrical transport properties comparable to bulk semi-conductor, with promising applications in thermoelectric conversion (Hochbaum 2008).

On the computational side, the first MD simulation of heat transport in a nanowire has been performed by Volz and Chen (Volz 1999), who already measured a two orders of magnitude reduction of the conductivity compared to the bulk. Recent simulations have confirmed the reduction, but yielding contradicting results for very small nanowires diameters (Ponomareva 2007, Donadio 2009, Abs-Da-Cruz 2011). Molecular simulations have been also pointed out the role of surface disorder on the conductivity reduction (Donadio 2009). Comparatively, there has been fewer studies on heat transport in molecular junctions, probably because of the difficulty to measure a thermal current flowing across a molecule. Molecular junctions have been however proposed to be good candidates for thermal rectifiers (Chang 2006, Casati 2007). Whang et al. recently used ultrafast thermal to probe ballistic heat transport in alkane-thiol chains supported on a gold substrate (Whang 2007). This opens the way to measure the conductance of a molecular chain as a function of its length. Theoretical studies have first considered simple one-dimensional chains (Dhar 2008, Segal 2003). Realistic models of molecular junctions have been studied recently (Mingo 2006) using Green function technique. There is relatively few molecular dynamics studies in the

field, with the exception of the modeling of self-assembled monolayers (Luo 2010), Henry and Chen used equilibrium simulations to show that the conductivity of polyethylene chains may be orders of magnitude larger than bulk polyethylene (Henry 2008). A recent study concluded that the conductance of molecular chain is also strongly affected by its environment (Merabia 2011), with a transition between ballistic and Fourier regime.

Finally, heat transfer in the vicinity of nano-particles has also shown an increasing interest during the last years. This interest has been motivated first by the early measurements of large thermal conductivity in the so-called nanofluids, i.e. suspensions of nano-particles in a liquid solvent (Keblinski 2008). Molecular simulations have helped in solving the controversy and showed that for well dispersed nano-particles, no enhancement is expected with respect to the effective medium theory (Vladkov 2006a). These simulations have also helped in determining the interfacial thermal resistance characterising the nanoparticle/liquid interface (Vladkov 2006a). Heat transfer around strongly heated nanoparticles has also attracted attention after the development of ultrafast optical techniques which allow to selectively heat nanoparticles in suspension (Plech 2004). When the metallic particles are excited at wavelengths close to the maximum of their optical extinction, their temperature can be raised by hundreds of Kelvin, while the liquid environment in the immediate vicinity may remain at ambient temperature, thus creating very large temperature gradients and energy fluxes flowing from the nanoparticles. This raises interesting new questions regarding nanoscale heat transfer, e.g. regarding the validity of Fourier law at very large temperature gradients (Merabia 2009b), and the competition between heat transfer and boiling of the fluid surrounding the nanoparticles (Merabia 2009b). Apart from the academic interest, these questions have important bio-medical applications in hyperthermia, as the appearance of vapor bubbles with submicronic radius would concentrate large thermomechanical stresses which may destroy tumors for instance. Further work is needed to understand the conditions of formation of these "nanobubbles". Let us conclude saying that nanoparticles may also served as thermal contacts to measure the conductance of molecular chains as demonstrated using MD (Merabia2011).

5. Thermal conductivity predictions for Si/Ge superlattices, impact of rough interfaces

Heat transport in superlattices, which are materials composed of a periodic or a random arrangement of different alternating materials with a submicronic thickness, has attracted a large scientific interest, as they exhibit low thermal conductivity (Cahill et al, 2003), at least in one direction, usually the direction normal to the interfaces. This makes superlattices promising materials for applications in MEMS and NEMS devices such as semiconductor lasers (Sale, 1995), optical data-storage media (Kim et al, 2000), thermoelectric (Hicks et al, 1993; Lin-Chung & Reinecke, 1993) and thermomechanic devices (Ezzahri et al, 2008). For the latter two categories the thermal-conductivity characteristics are very important to ensure the correct function of the device(Daly et al, 2002). Depending on the use, the highest possible thermal conductivity is required for example to remove the Joule heat in electronic devices, or very low thermal conductivity for thermoelectric applications (Mahan 2004). With a clever tailoring of the properties of superlattice, one can succeed in both directions.

The phonon thermal conductivity of superlattices has been started to be in the center of scientific interest quite early as superlattice are promising structures for new electronic devices (Ren & Dow 1982). It has been reported that the thermal conductivity of

superlattices may be dramatically smaller than the corresponding values of the constituent materials in their bulk form. This decrease has been related to the folding of the Brillouin zone and the related mini-umklapp three-phonon scattering process. Tamura & al 1999 analysed the effect on the phonon spectra in superlattices by three major reasons: a. folding of the phonon branches caused by the periodicity of the superlattices, b. the formation of the mini-band and c. the confinement of the acoustic phonons in the different layers due to the mismatch of the spectra. These three reasons impose reduction of the group velocity in the cross-plane direction, leading to the decrease of the cross-plane thermal conductivity. Chen & Yang 2005a claimed that the group velocity reduction is not sufficient to explain the dramatic decrease of the thermal conductivity, and they argued that one should add the diffusive scattering at the interfaces and treat phonons as incoherent particles. Chen & Neagu 1997 solving the Boltzmann Transport Equation for specular and diffuse interfaces showed that depending on the superlattice period, the thermal conductivity might be influenced either by the diffuse interface scattering or by the scattering induced by the dislocations. The literature is rich in this subject and a series of articles appeared with a lot of experimental (Capinski et al 1999, Huxtable et al 2002, Lee et al 1997) or theoretical results using lattice dynamics method or Equilibrium (Volz 2000, Landry 2008, Termentzidis 2011b, Termentzidis 2011c) and Non-Equilibrium Molecular Dynamics method (Liang & Shi 2000, Chen 2004, Termentzidis 2009, Termentzidis 2010).

One very interesting property of superlattices is their thermal anisotropy. In the paragraphs below the distinction between the in-plane (parallel to the interfaces) and cross-plane (perpendicular to the interfaces) thermal conductivity has been underlined. In general one expects a value of the in-plane thermal conductivity close to the bulk conductivity especially for superlattices with smooth interfaces, where phonons are expected to specularly reflect from the interfaces, and in which each layer behaves like a phonon waveguide. For the cross-plane direction the picture is totally different, with thermal conductivity even smaller than a random alloy of the same material (Mahan 2004). A key point for the physical explanation of the phenomena related to the superlattice thermal conductivity is the thermal boundary resistance or the Kapitza resistance, which has been discussed before.

Molecular dynamics simulations have been performed recently to understand the physical mechanisms ruling the transport properties of superlattices (Landry et al, 2008, 2009, Termentzidis et al, 2009,2010,2011a,2011b,2011c). In this contribution, we will discuss the influence of the interface roughness and of the superlattice period on the in-plane and the cross-plane thermal conductivities of Si/Ge superlattices using both the EMD and NEMD methods. This study proves that heat transport in superlattices is controlled by the interfaces. An atomic knowledge (or description) of the interfaces is necessary for the correct prediction of the thermal conductivity. In turn, understanding the link between the interfacial structure and the thermal conductivity will certainly help in tailoring and controlling the phonon behaviour in nanostructures. This can lead to the augmentation of the lifetime and to optimize the working of several nano-devices. The state of the interfaces is crucial for the determination of the behavior of phonons within the nanostructures. When the layer thickness of the superlattice is comparable with the MFP, the thermal conductivity is controlled by the transmission of phonons across the interfaces of the superlattice. In particular, the thermal boundary resistance or the Kapitza resistance, which has been discussed before, will play a key role in the thermal transport in superlattices with thin layers.

5.1 Modelling Si/Ge superlattices with rough interfaces

In this subsection, we study the effect of the superlattice period and the structure of the interface on both the in-plane and the cross-plane superlattice thermal conductivities. Simulations have been held for two periods of superlattices 20 and $40\alpha_0$, which are comparable to the phonon meat free path at the temperature we are working at. To understand the role of the interfacial structure, we have considered two types of interfaces: smooth interfaces on the one hand, and rough interfaces with a right-isoscele-triangles shape, as shown in fig. 4. In the case of rough interfaces, the height of the interfaces has been varied between 1 monolayer (ML) which is half of a lattice constant for a fcc crystal, up to $12\alpha_0$, which is more than the half of the superlattice period for superlattices with period of $20\alpha_0$ and from 1ML up to $24\alpha_0$ for superlattices with period of $40\alpha_0$ (see fig. 4). The maximal interface height is thus more than half the superlattice's period.

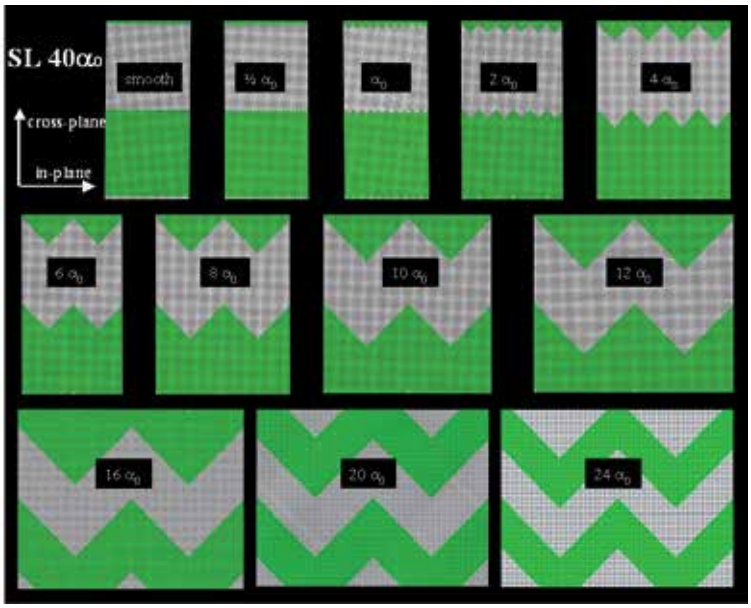

Fig. 4. Several triangular shaped interfaces with varing height, for superlattice period of $40\alpha_0$.

We examined also the effect of the shape of the interface on the cross-plane and the in-plane thermal conductivities. In this case, the superlattice period is kept constant and equal to $20\alpha_0$ and we considered only one height of interfaces, the $6\alpha_0$ or 12MLs. Fig. 5 shows the smooth interfaces, the periodic triangular isosceles interfaces and the additional 4 other shapes. The structure shown in 5.iii is obtained by superposing the periodic isosceles of small lengths with the periodic triangular interfaces shown in 5.ii. Cosine like, random like and square like interfaces are also examined.

5.2 Thermal conductivity of Si/Ge like superlattices with rough interfaces

The in-plane and cross-plane thermal conductivities have been calculated using the EMD and the NEMD methods. The results are displayed in figure 6 as a function of the interface

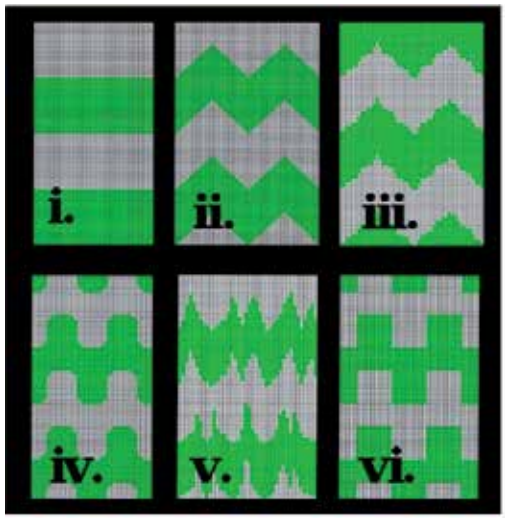

Fig. 5. Shapes of different superlattice interfaces i) smooth interfaces, ii) periodic isosceles triangles, iii) superposition of small triangles over the interfaces of the type ii, iv) cosine like v) random like, vi) periodic square like interfaces. In all cases, the height of the rough interfaces is kept constant equal to 12ML (taken from Termentzidis et al 2011b).

roughness. Again, two superlattice periods have been considered $20\alpha_0$ (left) and $40\alpha_0$ (right). The figures show also some points named "intra-plane" thermal conductivity, which is defined as the thermal conductivity in the direction of 45° both of the in-plane or cross-plane directions. For the case of infinite roughness (with isosceles periodic triangles) the thermal conductivity in both the in-plane and the cross-plane directions is expected to be equal to this of the intra-plane conductivity, which is verified in our simulations.

For smooth interfaces, it is expected that the transmission of phonons across the interface is specular and depends only on the acoustic impedance mismatch between the bulk materials of the superlattice (Swartz and Pohl, 1987, 1989). This is actually not the case since it is observed that the thermal conductivity of the layer decreases when the film thickness decreases (at least enough to be of the same order of magnitude as the phonon mean-free path). For rough surfaces with small roughness the transmission of phonons becomes more diffusive and the transmitted phonons are distributed over a wide range of angles, which induces an additional resistance to in-plane transport. This is consistent with the MD results which conclude to a decrease of the in-plane conductivity with the interfacial roughness. For rough surfaces with large roughness there is a combination of specular and diffusive transmission. This last case shows some similarities with the smooth surface case but now specular reflection is accompanied by back scattering.

This back-scattering explains the existence of a minimum in the thermal conductivity observed for free surfaces, as well as for the in-plane conductivity of superlattices. A further increase in the surface roughness leads to higher thermal conductivity. This further increase in the thermal conductivity is related to the fact that on average, phonons experience less reflections on the asperities of the superlattice, and the mean free path length between scattering events increases, leading to an enhanced in plane transport. For the randomlike roughness, the monotonous decrease in the thermal conductivity in

increasing the roughness's height can be interpreted if we assume that the phonon scattering at the interface remains diffusive, phenomena of back scattering and specular reflection, playing a secondary role here. Hence, we conclude that the variation in the ratio of interface roughness to the superlattice period can tailor the thermal properties of superlattices.

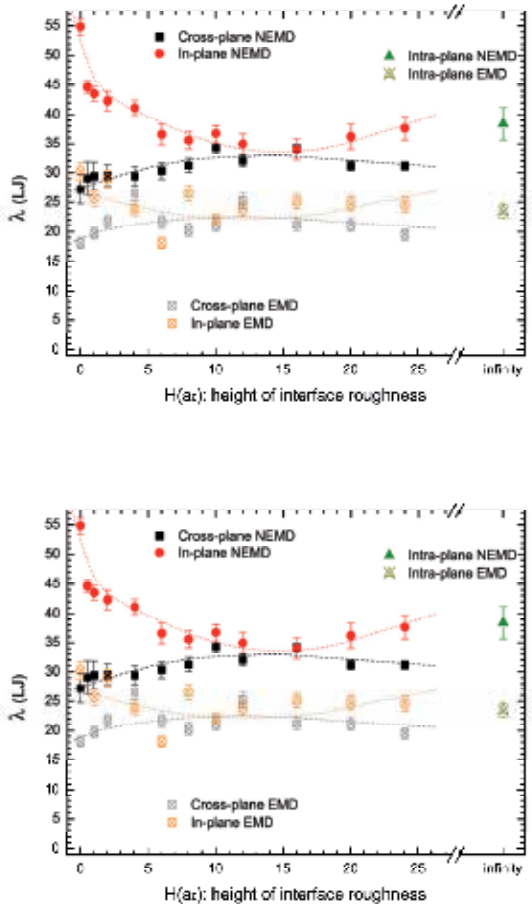

Fig. 6. In-plane and cross-plane thermal conductivity as a function of the interface roughness obtained by EMD and NEMD for superlattice with period 20 α_0 (top) and with $40\alpha_0$ (bottom).

The cross-plane and in-plane thermal conductivities obtained by NEMD and EMD for superlattices with various shapes of interfaces are plotted in figure 7. Further details about the modelling of these interfaces and the physical explanation of the results are given in Termentzidis et al, 2011b. It is striking to note that for rough interfaces, the anisotropy of the thermal conductivity is drastically reduced. Regarding the anisotropy between the in-plane and cross-plane directions, we can categorize the interfaces in three different groups, first

the smooth interfaces which displays the maximum anisotropy, with the in-plane thermal conductivity being more than twice larger than the cross-plane thermal conductivity; A second group contains totally random interfaces for which the two thermal conductivities exhibit their minimum values and a third group with periodic rough interfaces of a specific shape (triangular, square or cosine) where the thermal anisotropy is negligible compared to the uncertainties of the methods.

6. Thermal conductivity predictions for GaAs/AlAs superlattices, impact of rough interfaces

The GaAs/AlAs superlattices are important materials mainly for their optical properties. Simulations of the thermal conductivity of superlattices as a function of their period exhibit a minimum for period around 8 to 10 monolayers (Daly et al 2002, Imamura et al 2003, Chen 2005b), but this minimum is not observed in experimental measurements (Capinski et al 1999). The quality of the interfaces might be the reason to explain this discrepancy. For perfectly smooth interfaces the minimum exists, while for rough interfaces with a height as small as one monolayer the minimum disappears and the thermal conductivity increases with the periodicity of the superlattice. The works of Daly et al 2002 and Imamura and al 2003 are based on rough interfaces of one atomic layer and with a stochastic distribution of the two types of atoms that compose the superlattice.

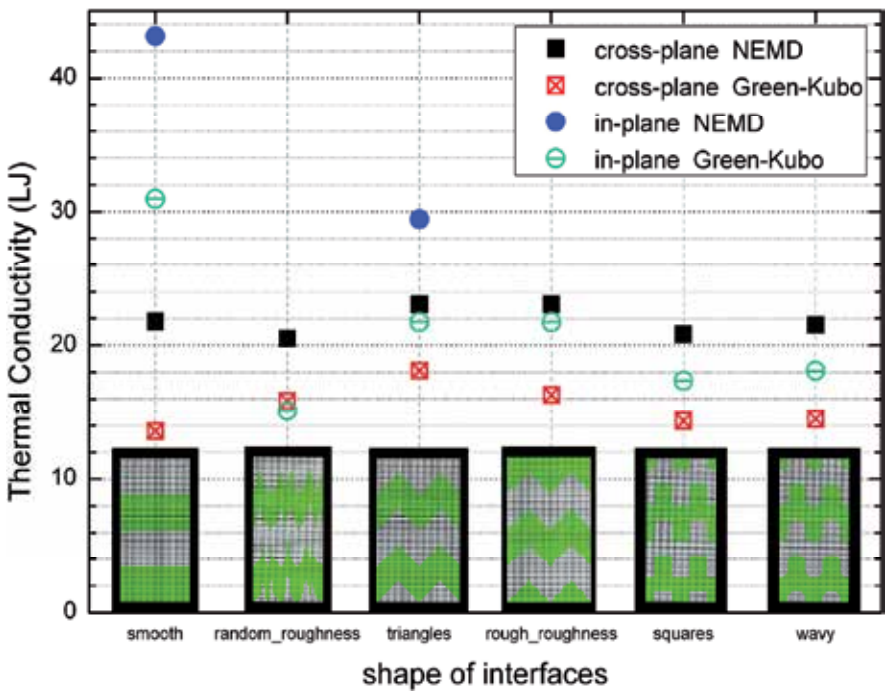

Fig. 7. In-plane and cross-plane thermal conductivities for several shapes of the interfaces obtained by EMD and NEMD for superlattices with period $20a_0$ and with constant height of interfaces $6a_0$.

6.1 Modelling rough interfaces for the GaAs/AlAs superlattices

A new modeling of realistic interfaces is considered with the present study (Termentzidis et al 2010, 2011a). Interfaces with square formed islands of one monolayers and pyramide like islands of two monolayers are modelled. Furthermore there are two characteristic lengths of square islands depending if GaAs or AlAs is on top. It has been proven that large scale islands are formed when an AlAs layer grows on a GaAs layer while small scale islands are formed when a GaAs layer grows on an AlAs layer (Tanaka & Sakaki 1987, Jusserand et al 1990). Furthermore interfaces with interdiffusion parts are also considered. Figure 8 depicts the two kind of interfaces with interface height of one monolayer and in figure 9 with two monolayers (these figures are taken from Termentzidis et al 2010)

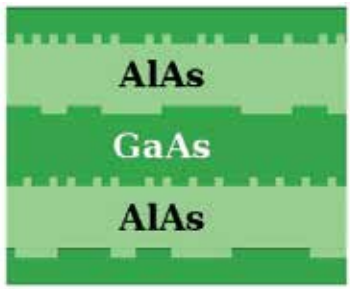

Fig. 8. Schematic representation of the two different scale interfaces between the GaAs/AlAs and the AlAs/GaAs, for height of interfaces of one monolayer – square like interfaces.

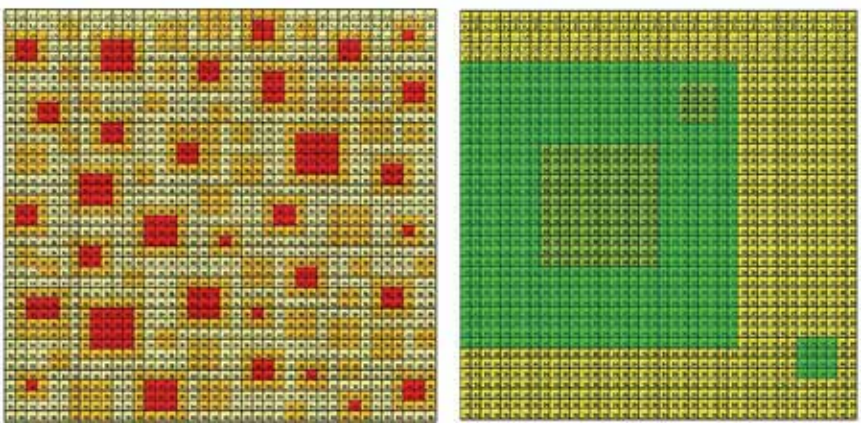

Fig. 9. Schematic representation of the two different scale interfaces between the GaAs/AlAs and the AlAs/GaAs, for height of interfaces of two monolayers – pyramoidal like interfaces (taken from Termentzidis et al 2010).

6.2 Thermal conductivity of GaAs/AlAs like superlattices with rough interfaces

Figure 10 shows the predicted cross-plane thermal conductivity as a function of the superlattice period, for a variety of interface configurations. In figure 10 at left the thermal conductivity is plotted for smooth interfaces, for rough interfaces with height of one monolayer and three coverage factors (1%, 10% and 50%) and finally for interfaces with

height of 2 monolayers. The coverage factor of 1% exhibits the minimum in thermal conductivity as the smooth interfaces. For coverage factor of 10% and 50% the minimum dissapears and the results confirm previous theoretical observations (Daly et al 2002, Imamura et al 2003), while the two defect concentrations do not influence the thermal conductivity. For height of roughness of 2MLs, the thermal conductivity is higher than for smooth interfaces and exhibits a maximum for a $8\alpha_0$. In the same figure at the right the influence of interdiffusion of the two species is shown, with similar behavior as the interfaces of height of two MLs. These unexpected results are related with the fact that inelastic scattering could enhance the thermal conductivity through interfaces (Lepi et al 2003). The study shows that the thermal conductivity depends strongly on the detailed description of the interfaces, including height, shape of roughness, interdiffusion of species etc. Changing the structure of the interface can favor or deteriorate the thermal transport through interfaces, and we showed that the interface structure is a relevant parameter which controls the thermal properties of superlattices.

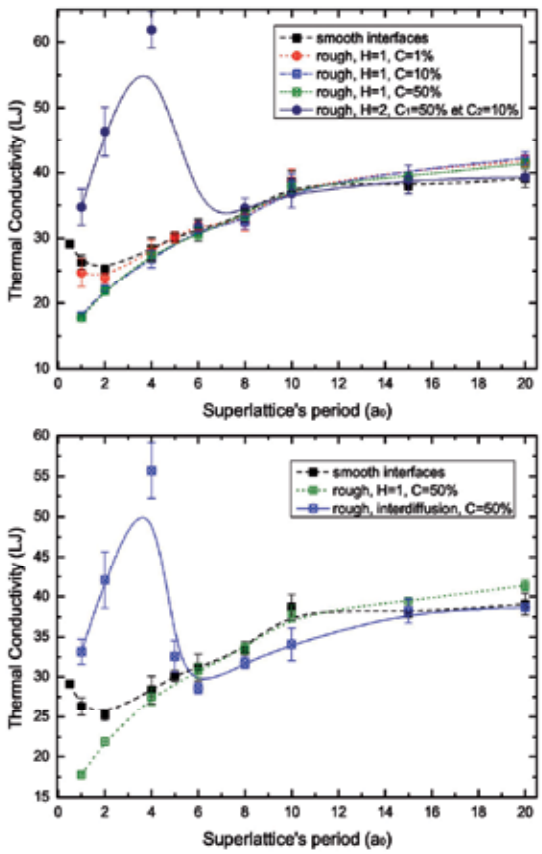

Fig. 10. Cross-plane thermal conductivity as a function of the superlattice period with NEMD for GaAs/AlAs systems. Left: smooth interfaces, rough interfaces of height of 1ML with three different concentrations and rough interfaces of height of 2ML are presented. Right: rough interfaces with interdiffusion. The smooth and rough interfaces with a concentration of 50% are also shown for comparison.

7. Conclusion

We hope we have helped in showing the possibilities of the molecular dynamics technique to probe heat transport in solids, and in particular nanomaterials. Molecular dynamics is a relatively simple and flexible method to be used especially today when stable optimized open source codes have become avalaible: LAMMPS, DLPOLY, GROMACS to name a few. The ever increasing number of publications has helped in resolving controversies regarding heat transfer at the nanoscale, and also getting physical insights in classical problems. A physical understanding of energy transport across two solids-a very simple question-still poses a challenge ! MD simulations may help in observing the scattering of phonons at interfaces, which certainly complements experimental investigations. In the context of nanomaterials, MD is well adapted to characterize ballistic heat transport in nano-objects, although care should be taken not to introduce spurious sources of scattering ! Let us hope that further experimental measurements may improve the modeling of the nanomaterials that we have considered.

8. References

Abs-Da-Cruz, C. Termentzidis, K. Chantrenne, P. & Kleber, X. (2011). Molecular Dynamics simulations for the prediction of thermal conductivity of bulk silicon and silicon nanowires: Influence of interatimic potentials and boundary condictions. Journal of Applied Physics, Vol 110, No. 3, (August 2011), pp 034309, doi:10.1063/1.3615826

Alder, BJ and Wainwright, TE. (1957). Phase Transition for Hard Sphere System. Journal of Chemical Physics, Vol 27, No. 5, (August 1957), pp 1208-1209, doi:10.1063/1.1743957

Alder, BJ and Wainwright, TE. (1959). Studies in Molecular Dynamics. I. General Method. Journal of Chemical Physics, Vol 31, No. 2, (Februaury 1959), pp 459-466, doi:10.1063/1.1730376

Allain MP. & Tildesley DJ. (1987). *Computer Similution of Liquids*. Oxford University Press, ISBN: 0-19 855645 4 (Pbk), New York, USA

Barrat, JL. & Chiaruttini, F. (2003). Kapitza resistance at the liquid-solid interface. Molecular Physics, Vol 101, No. 11, pp 1605-1610, doi:10.1080/0026897031000068578

Berber, S. Kwon, YK. & Tomanek, D. (2000). Unusual High Thermal Conductivity of Carbon Nanotubes. Physical Review Letters, Vol. 84, pp 4613-4617, DOI:10.1103/PhysRevLett.84.4613

Cahill, DG. et al. (2003). Nanoscale thermal transport. J. Applied Physics, Vol 93, No. 2 (August 2002), pp 793-818, DOI:10.1063/1.1524305

Callaway J. (1959) Model for Lattice Thermal Conductivity at Low Temperatures, Physical Review, Vol 113, pp 1046-1051, DOI:10.1103/PhysRev.113.1046

Capinski, W. Maris, H. Ruf, T. Cardona, M. Ploog, K. and Katzer D. (1999). Thermal-conductivity measurements of GaAs/AlAs superlattices using a picosecond optical pump-and-probe technique. Phys. Rev. B, Vol 59, No. 12 (March 1999), pp 8105-8113, DOI:10.1103/PhysRevB.59.8105

Casati, G. (2007), Device Physics: The Heat on is off. Nature Nanotechnology, Vol 2, pp 23-24, DOI: 10.1038/nnano.2006.191

Chang, CW. Okawa, D. Majumdar, A. and Zettl, A. (2006). Solid-state Thermal Rectifier. Science. Vol 314, pp 1121 -1124, DOI: 10.1126/science.1132898

Chantrenne, P & Barrat, LJ. (2004a). Analytical model for the thermal conductivity of nanostructures. Superlatt. Microstruct. , Vol 35, pp 173-186

Chantrenne, P & Barrat, LJ. (2004b). Finite size effects in determination of thermal conductivities: comparing molecular dynamics results with simple models. J. Heat Transfer, Vol 126, pp 577-585

Chantrenne, P. (2007). *Molecular Dynamics, In: Microscale and Nanoscale Heat Transfer*, Sebastian Volz, pp. (155-179), Springer-Verlag Berlin and Heidelberg GmbH & Co.K, ISBN-10: 3540360565, Berlin, Germany

Chen, G. & Neagu, M. (1997). Thermal Conductivity and Heat Transfer in Superlattices. Applied Physics Letters, Vol 71, pp 2761-2763, DOI:10.1063/1.120126

Chen, G. & Yang, RG. (2005a). Nanostructured Thermoelectric Materials : from Superlattices to Nanocomposites. Material Integration, special issue, Vol 18

Chen, Y. Li, D. Lukes, JR. Ni Z. & Chen, M. (2005b). Minimum superlattice thermal conductivity from molecular dynamics. Physical Review B, Vol. 72 (Novembre 2005), pp 174302, DOI:10.1103/PhysRevB.72.174302

Chen, Y. Li, D. Yang, J. Wu, Y. Lukes, JR. & Majumdar, A. (2004). Molecular Dynamics study of the lattice thermal conductivity of Kr/Ar superlattice nanowires. Physica B : Condensed Matter, Vol 349, No. 1-4 (June 2004), pp 270-280, DOI:10.1016/j.physb.2004.03.247

Daly, BC. Maris, HJ. Imamura, K. & Tamura, S. (2002). Molecular Dynamics calculation of the thermal conductivity of superlattices. Physical Review B, Vol 66, No. 2 (June 2002), pp 024301, DOI:10.1103/PhysRevB.66.024301

Dammak H., Chalopin Y., Laroche M., Hayoun M. And Greffet J-J. (2009) Quantum Thermal Bath for Molecular Dynamics Simulation, Physical Review Letters, Vol. 103, pp 190601 - 190604 DOI:10.1103/PhysRevLett.103.190601

Daw, MS and Baskes MI (1984) Embedded-atom method: derivation and application to impurities, surfaces and other defects in metals, Phys. Rev. B, Vol 29, 6443-6453 DOI 10,1103/PhysRevB,29,6443

Dhar, A. (2008). Heat Transport in Low-dimensional systems. Advances in Physics, Vol 75, No. 5, (Dec 2008), pp 457-537

Donadio, D. & Galli, G. (2007). Thermal Conductivity of Isolated and Interacting Carbon Nanotubes : Comparing Results from Molecular Dynamics and the Boltzmann Transport Equation. Physical Review Letters, Vol. 99, pp 255502, DOI:10.1103/PhysRevLett.99.255502

Donadio, D. & Galli, G. (2009). Atomistic Simulations of Heat Transport in Silicon Nanowires. Physical Review Letters, Vol. 102, pp 195901, DOI: 10.1103/PhysRevLett.102.195901

Dove M.T. (2005) *Introduction to Lattice Dynamics*, Cambridge University Press , ISBN 0521398940, Cambridge United Kingdom

Evans, DJ. (1982). Homogeneous NEMD algorithm for thermal conductivity-Application of non-canonical linear response theory. Physics Letters A, Vol 91, No. 9, (October 1982), pp 457-460, doi:10.1016/0375-9601(82)90748-4

Evans, DJ. (1986). Thermal Conductivity of the Lennrd-Jones fluid. Physical Review A, Vol 34, No. 2, (August 1986), pp 1449-1453, doi:10.1103/PhysRevA.34.1449

Evans, DJ. & Morris, GP. (1990). *Statistical Mechanics of nonequilibrium liquids*, Cambridge University Press, ISBN-13 978-0-521-85731-8, New York

Ezzahri, Y. Zeng, G. Fukutani, K. Bian, Z. & Reinecke, TL. (2008). A comparison of thin film microfrigerators based on Si/SiGe superlattice and bulk SiGe. Microelectronics J., Vol 39, (August 2007), pp 981-991, DOI:10.1016/j.mejo.2007.06.007

Frenkel, D & Smit, B. (1996). *Understanding Molecular Simulation: From Algorithms to Applications*, Academic Press, ISBN: 0-12-267351-4, San Diego

Hansen, JP. & Klein, ML. (1976). Dynamical Structure Factor of Rare-Gas Solids. Physical Review B. Vol 13, pp 878-887, DOI: 10.1103/PhysRevB.13.878

Henry, A. & Chen, G. (2008). High Thermal Conductivity of Single Polyethylene Chains Using Molecular Dynamics Simulations. Physical Review Letters, Vol. 101, pp 235502, DOI: 10.1103/PhysRevLett.101.235502

Hicks, LD. Harman, TC. & Dresselhaus, MS. (1993). Use of quantum-well superlattices to obtain a high figure of merit from nonconventional thermoelectric materials. Applied Physics Letters, Vol 63, No. 23 (October 1993), pp 3230-3232, DOI:10.1063/1.110207

Hochbaum, AI. Chen, RK. Delgado, RD. Liang, WJ. Garnett, EC. Najarian, M. Majumdar, A. and Yang, PD. (2008). Nature, Vol. 451, pp 163-U5, DOI: 10.1038/nature06381

Holland, MG. (1963) Analysis of Lattice Thermal Conductivity, Physical Review 132, pp 2461-2471, DOI: 10.1103/PhysRev.132.2461

Huxtable, S. et al (2002). Thermal conductivity of Si/SiGe and SiGe/SiGe superlattices. Applied Physics Letters, Vol 80, No. 10 (March 2002), pp 1737-1739, DOI:10.1063/1.1455693

Imamura, K. Tanaka, Y. Nishiguchi, S. Tamura, S. and Maris, HJ. (2003). Lattice thermal conductivity in superlattices: molecular dynamics calculations with a heat reservoir method. J. Physics: Condensed Matter, Vol 15, No. 50 (December 2003), pp 8679-8690, DOI:10.1088/0953-8984/15/50/002

Jusserand, B. Mollot, F. Moisson, JM. And Le-Roux, G. (1990). Atomistic-scale roughness of GaAs/AlAs interfaces: A Raman scattering study of asymmetrical short-period superlattices. Applied Physics Letters, Vol 57, No. 6 (May 1990), pp 560-562, DOI:10.1063/1.103646

Keblinski, P. Prasher, R. & Eapen, J. (2008). Thermal Conductance of Nanofluids: Is the Controversy Over? J. Nanoparticle Res., Vol. 10, p 1089-1097

Khalatnikov, IM. (1952). Zh. Eksp. Teor. Fiz. 22, pp 687.

Kim, E. et al. (2000). Thermal boundary resistance at Ge2Sb2Te5/ZnS:SiO2 interface. Applied Physics Letters, Vol 76, No. 26 (April 2000), pp 3864-3866, DOI:10.1063/1.126852

Kim, P. Shi, L. Amjumdar, A. & McEuen, PL. (2001) Thermal Transport Measurements of Individual Multiwall Nanotubes. Physical Review Letters. Vol. 87, pp 215502-215505, DOI:10.1103/PhysRevLett.87.215502

Kotake, S & Wakuri S. (1994). Molecular dynamics study of heat conduction in solid materials. JSME International Journal, Series B: Fluids and Thermal Engineering, Vol 37, No. 1, (Febrouary 1994), pp 103-108, ISSN:09148817

Ladd, AJC., Moran, B. and Hoover, WG. (1986), Lattice thermal conductivity: a comparison of molecular dynamics and anharmonic lattice dynamics. Physical Review B, Vol 34, No. 8, pp 5058-5064, DOI:10.1103/PhysRevB.34.5058

Landry, ES. Hussein, MI. & McGaughey, AJH. (2008). Complex superlattice unit cell designs for reduced thermal conductivity. Physical Review B, Vol 77, No. 18, pp 18184302, doi:10.1103/PhysRevB.77.184302

Landry, ES. & McGaughey, AJH. (2009). Thermal boundary resistance predictions from molecular dynamics simulations and theoretical calculations. Physical Review B, Vol 80, No. 16, pp 16165304, doi:10.1103/PhysRevB.80.165304

Lee, SM. Cahill, DG. & Venkatasubramanian, R. (1997). Thermal conductivity of Si-Ge superlattices. Applied Physics Letters, Vol 70, (June 1997), pp 2957-2959, DOI:10.1063/1.118755

Lepri, S. Livi, R. & Politi, A. (2003). Thermal conduction in classical low-dimensional lattices. Physics Reports, Vol 377, (October 2002), pp 1-80, DOI:10.1016/S0370-1573(02)00558-6

Li, D. Wu, YY. Kim, P. Shi, L. Yang, PD. & Majumdar, A. (2003). Thermal Conductivity of Individual Silicon Nanowires. Applied Physics Letters. Vol. 83, pp 2934-2936. DOI: 10.1063/1.1616981

Liang, XG. & Shi, B. (2000). Two-dimensional molecular dynamics simulation of the thermal conductance of superlaticces. Materials Science and Engineering: A, Vol 292, (Novembre 2002), pp 198-202, DOI:10.1016/S0921.5093(00)01012-1

Lin-Chung, PJ. & Reinecke, TL. (1995). Thermoelectric figure of merit of composite superlattice systems. Physical Review B, Vol 51, No. 19 (May 1995), pp 13244-13248, DOI:10.1103/PhysRevB.51.13244

Luo, T. & Lloyd, JR. (2010). International J. Heat Mass Transfer, Vol. 53, pp 1-11, DOI: 10.1016/j.ijheatmasstransfer.2009.10.033

Mahajan, S, Subbarayan, G & Sammakia, BG. (2007). Estimating thermal conductivity of amorphous silica nanoparticles and nanowires using molecular dynamics simulations. Physical Review E, Vol 76, No. 5, (Novembre 2007), pp 056701, DOI:10.1103/PhysRevE.76.056701

Mahan, GD. (2004). *Thermal Conductivity of Superlattices, In: Thermal Conductivity: Theory, Properties and Applications*. Terry T. Tritt, pp. (153-165), Klumer Academic/Plenum Publishers, ISBN: 0-306-48327-0, New York, USA

Maruyama, S. (2002). A Molecular Dynamics Simulation of Heat Conduction in Finite Length SWNTs. Physica B, Vol. 323, pp 193-195, DOI 10.1016/S0921-4526(02) 00898-0

McGaughey, AJH. & Kaviany, M. (2004) Quantitative validation of the Boltzmann transport equation phonon thermal conductivity model under the signle-mode relaxation time approximation. Physical Review B. Vol. 69, pp 094303-1, 094303-12, DOI:10.1103/PhysRevB.69.094303

Mcgaughey, AJH. & Li, J. (2006) Molecular Dynamics Prediction of the Thermal Resistance of Solid-Solid Interfaces in Superlattices, Proceedings of IMECE 2006, ASME International Mechanical Engineering Conference and Exhibition, November 5-10, 2006, Chicago USA

Merabia, S. Shenogin, S. Joly, L. Keblinski, P. & Barrat, JL. (2009a). Proc. Nat. Ac. Sci., Vol. 106, pp 15113-15118, DOI: 10.1073/pnas.0901372106

Merabia, S. Keblinski, P. Joly, L. Lewis, LJ. & Barrat, JL. (2009b). Critical Heat Flux Around Strongly Heated Nanoparticles. Physical Review E, Vol. 79, pp 021404, DOI: 10.1103/PhysRevE.79.021404

Merabia, S. Barrat, JL. & Lewis, L. (2011). Heat Conduction across Molecular Junctions Between Nanoparticles. J. Chemical Physics. Vol. 134. pp 234707, DOI: 10.1063/1.3600667

Mingo, N. & Broido, DA. (2005). Carbon Nanotube Ballistic Thermal Conductance and Its Limits. Physical Review Letters. Vol. 95, pp 096105, DOI: 10.1103/PhysRevLett.95.096105

Mingo, N. (2006). Anharmonic phonon flow through molecular-sized junctions. Physical Review B. Vol. 74, pp 125402, DOI: 10.1103/PhysRevB.74.125402

Montroll, E. (1950). Size Effect in Low Temperature Heat Capacities. J. Chemical Physics, Vol 18, No. 2, (August 1949), pp 183-185, DOI:10.1063/1.1747584

Mûller-Plathe, F. (1997). A simple nonequilibrium molecular dynamics method for calculating the thermal conductivity. J. Chemical Physics, Vol 106, No. 14, (January 1997), pp 6082-6085, DOI:10.1063/1.473271

Pettersson, S. & Mahan, GD. (1990) Theory of the Thermal Boundary Resistance between dissimilar lattices, Physical Review B, Vol. 42, No. 12, pp 7386-7390, DOI:10.1103/PhysRevB.42.7386

Plech, A. Kotaidis, V. Grésillon, S. Dahmen, C. & Von-Plessen, G. (2004) Laser-induced heating and melting of gold nanoparticles studied by time-resolved X-ray scattering. Physical Review B. Vol. 70, pp 195423

Plimpton, S. (1995). Fast Parallel Algorithms for Short-Range Molecular Dynamics. J. Computational Physics, Vol 117, (Mars 1995), pp 1-19.

Plimpton, S. Pollock, R. and Stevens, M. (1997). Particle-Mesh Ewald and rRESPA for Parallel Molecular Dynamics Simulations. In Proceedings of the Eigth SIAM Conference on Parallel Processing for Scientific Computing, Minneapolis, MN, March 1997

Poetzsch, RH & Bôttger, H. (1994). Interplay of disorder and anharmonicity in heat conduction: Molecular dynamics study. Physical Review B, Vol 50, No. 21, (December 1994), pp 15757-15763, DOI:10.1103/Phys.RevB.50.15757

Ponomareva, I. Srivastava, D. & Menon, M. (2007). Thermal Conductivity in thin Silicon Nanowires: Phonon Confinement Effect. NanoLetters. Vol. 7. pp 1155-1159

Pop, E. Mann, D. Wang, Q. Goodson, K. & Dai, H. (2006). Thermal Conductance of an Individual Single-wall carbon nanotube above room Temperature. NanoLetters. Vol 6, pp 96-100, DOI: 10.1021/nl052145f

Puech, L. Bonfait, G. and Castaing, B. (1986) Mobility of the He-3 Solid Liquid Interface-Experience and Theory Journal of Low Temperature Physics, Vol 62, pp 315-327, DOI: 10.1007/BF00683467

Rahman, A. (1964). Correlations in the Motion of Atoms in Liquid Argon. Physical Review, Vol 136, No. 2A, (May 1964), pp A405-A411, doi:10.1103/Phys.Rev.136.A405

Rahman, A and Stillinger, F. (1974). Propagation of sound in water. A molecular-dynamics study. Physical Review A, Vol 10, No. 1, (March 1974), pp 368-378, doi:10.1103/Phys.RevA.10.368

Ren, SY. & Dow, J. (1982). Thermal Conductivity of Superlattices. Physical Review B, Vol 25, (March 1982), pp 3750-3755, DOI:10.1103/Phys.RevB.25.3750

Sale, TE. (1995). Cavity and Reflector Design for Vertical Cavity Surface Emitting Lasers, Proceedings of SIOE'94, SCardiff, UK, March 1994

Schelling, PK. Phillpot, SR. & Keblinski, P. (2002). Comparison of atomic-level simulation methods for computing thermal conductivity. Physical Review B, Vol 65, No. 14, (April 2002), pp 144306, DOI:10.1103/PhysRevB.65.144306

Schelling, PK. Phillpot, SR. and Keblinski, P, (2004) Kapitza conductance and phonon scattering at grain boundaries by simulation, J. Applied Physics, Vol. 95, No 11, pp 6082-6090

Schwab, K. Henriksen, EA. Worlock, JM. & Roukes, ML. (2000). Measurement of the Quantum of Thermal Conductance, Nature, Vol. 404, pp 974-977, ISSN: 0028-0836

Segal, D. Nitzan, A. Hanggi, P. (2003). Thermal Conductance through Molecular Wires, J. Chemical Physics. Vol. 119, pp 6840-6855, DOI: 10.1063/1.1603211

Stevens, RJ, Zhigilei, LV & Norris, PM. (2007). Effects of temperature and disorder on thermal boundary conductance at solid-solid interfaces: Nonequilibrium molecular dynamics simulations. International J. Heat and Mass Transfer, Vol 50, No. 19-20, (September 2007), pp 3977-3989, DOI:10.1016/j.ijheatmasstransfer.2007.01.040

Stillinger F.H. and Weber T.A. (1985) Computer simulations in condensed phases of silicon. Physical Review B. Vol 31, pp 5262-5271 DOI 10,1103/PhysRevB,31,5262

Stroscio, M. & Dutta, M. (2011). *Phonons in nanostructures*, Cambridge University Press, ISBN-0-521-79279-7, Cambridg, United Kingdom

Swartz, ET. & Pohl, RO. (1987). Thermal resistance at interfaces. Applied Physics Letters, Vol 51, No. 26 (October 1987), pp 2200-2202, DOI:10.1063/1.988939

Swartz, ET. & Pohl, RO. (1989). Thermal boundary resistance. Review Modern Physics, Vol 61, No. 3, pp 605-668, DOI:10.1103/RevModPhys.61.605

Tamura, S. Tanaka, Y. & Maris, HJ. (1999). Phonon group velocity and thermal conduction in superlattices. Physical Review B, Vol 60, (July 1999), pp 2627-2630, DOI:10.1103/Phys.RevB.60.2627

Tanaka, M. & Sakaki, H. (1987). Atomistic models of interface structures of GaAs-AlxGa1-xAs (x=0.2-1) quantum wells grown by interrupted MBE. Journal of Crystal Growth, Vol 81, No. 1-4, pp 153-158, DOI:10.1016/0022-0248(87)90383-6

Termentzidis, K, Chantrenne, P & Keblinski, P. (2009). Nonequilibrium molecular dynamics simulations of the in-plane thermal conductivity of superlattices with rough interfaces. Physical Review B, Vol 79, No. 21, (June 2009), pp 214307, DOI:10.1103/PhysRevB.79.214307

Termentzidis, K. Chantrenne, P. Duquense, JY. & Saci, A. (2010). Thermal conductivity of GaAs/AlAs superlattices and the puzzle of interfaces. J. Physics: Condensed Matter, Vol 22, No. 47, (November 2010), pp 475001, DOI:10.1088/0953-8984/22/47/475001

Termentzidis, K. Chantrenne, P. Duquense, JY. & Saci, A. (2011a). Molecular dynamics calculations of the cross-plane thermal conductivity of GaAs/AlAs superlattices with rough interfaces. Chinese J. Physics, Vol 49, No. 1, (February 2011), pp 443-447.

Termentzidis, K. Merabia, S. Chantrenne, P. & Keblinski, P. (2011b). Cross-plane thermal conductivity of superlattices with rough interfaces using equilibrium and non-equilibrium molecular dynamics. International J. Heat and Mass Transfer, Vol 54, No. 9, (April 2011), pp 2014-2020, ISSN:0017-9310

Termentzidis, K. Parasuraman, J. Abs Da Cruz, C. Merabia, S. Angelescu, D. Marty, F. Bourouina, T. Kleber, X. Chantrenne, P. and Basset (2011c). Thermal conductivity and thermal boundary resistance of nanostructures. Nanoscale Research Letters, Vol 6, No. 1, (April 2011), pp 288, DOI:10.1186/1556-276X-6-288.

Tersoff, J. (1986) New empirical model for the structural properties of silicon, Physical Review Letters, Vol 56, pp 632-635, DOI:10.1103/PhysRevLett.56.632

Tersoff, J. (1988a) New empirical approach for the structure and energy of covalent systems, Physical Review B, Vol 37, pp 6991-7000, DOI:10,1103/PhysRevB.37,6991

Tersoff, J. (1988b) Empirical interatomic potential for silicon with improved elastic properties, Physical Review B, Vol. 38, pp 9902- 9905, DOI:10.1103/PhysRevB.38.9902

Verlet, L. (1967) Computer "Experiments" on Classical Fluids. I. Thermodynamical Properties of Lennard-Jones Moleculaes. Physical Review, Vol 159, (July 1967), pp 98-103, DOI:10,1103/PhysRev.159.98

Verlet, L. (1968) Computer "Experiments" on Classical Fluids. II. Equilibrium Correlation Functions. Physical Review, Vol 165, (January 1968), pp 201-214, DOI:10,1103/PhysRev.165.201

Vladkov, M. & Barrat, JL. (2006a). Modeling Transient Absorption and Thermal Conductivity in a simple Nanofluid, NanoLetters, Vol. 6, pp 1224-1228, DOI: 10.1021/nl060670o

Vladkov, M. & Barrat, JL. (2006b). Linear and nonlinear viscoelasticity of a model unentangled polymer melt: Molecular dynamics and Rouse mode analysis. Macromolecular Theory and Simulations. Vol. 15. pp 252-262, DOI: 10.1002/mats.200500079

Volz, S. & Chen, G. (1999). Molecular dynamics simulation of thermal conductivity of silicon nanowires. Applied Physics Letters, Vol 75, No. 14, (October 1999), pp 2056-2058, DOI:10.1063/1.124914

Volz, S. Saulnier, JB. Chen, G. & Beauchamp, P. (2000). Computation of thermal conductivity of Si/Ge superllatices by molecular dynamics techniques. Microelectronics J., Vol 31, No. 9-10, (October 2000), pp 815-919, DOI:10.1016/S0026-2692(00) 00064-1

Wang, Z. Carter, JA. Lagutchev, A. Koh, YK. Seong, NH. Cahill, DG. & Dlott, DD. (2007) Ultrafast Flash Thermal Conductance of Molecular Chains Science. Vol. 317. pp 787-790, DOI: 10.1126/science.1145220

Yang, J. (2004). *Theory of Thermal Conductivity, In: Thermal Conductivity, Theory, Properties, and Applications*. Terry M.Trutt, pp. (1-17), Kluwer Academic/Plenum Publishers, ISBN 0-306-48327-0, New York

Yao, Z. Wang, JS. Li, B. & Liu, GR. (2005). Thermal Conduction of Carbon Nanotubes Using Molecular Dynamics. Physical Review B. Vol. 71, pp 085417, DOI:10.1103/PhysRevB.71.085417

Yu, C. Shi, L. Yao, Z. Li, D. & Majumdar, A. (2005). Thermal Conductance and thermopower of an individual single-wall carbon nanotube. NanoLetters, Vol 5, pp 1842-1846, DOI: 10.1021/nl051044e

Zhang, G. & Li, B. (2005). Thermal Conductivity of Nanotubes Revisited: Effects of Chirality, Isotope Impurity, Tube Length, and Temperature. J. Chemical Physics, Vol. 123, pp 114714, DOI: 10.1063/1.2036967

Zhang, G & Li, B. (2010). Impacts of doping on thermal and thermoelectric properties of nanomaterials. Nanoscale, Vol 2, (May 2010), pp 1058-1068, DOI:10.1039/c0nr00095g

Part 2

Molecular Dynamics Theory Beyond Classical Treatment

6

Developing a Systematic Approach for *Ab Initio* Path-Integral Simulations

Kin-Yiu Wong
BioMaPS Institute for Quantitative Biology
Rutgers, The State University of New Jersey
USA

1. Introduction

An ultimate level of theory in molecular simulations [e.g., molecular dynamics (MD) and Monte Carlo (MC) simulations], which can accurately reproduce or even predict many experimental values, should be *ab initio* path integral. In *ab initio* path-integral simulations, both electrons and nuclei are treated quantum mechanically and adiabatically. No empirical parameter is involved, other than those fundamental physical constants (e.g., electronic mass and Planck's constant). The only *inherent* approximations are the Born-Oppenheimer approximation (to decouple internuclear dynamics from electronic motions) and the ergodicity in MD simulations or the importance samplings in MC simulations (to partly integrate the entire phase space). Consequently, correlation energy among electrons, anharmonic zero-point motions and tunnelling effects in nuclei, and isotope effects can all be incorporated in the simulations. Proper consideration of the electronic and internuclear quantum effects, even just partially, can be critical to compare computed values with state-of-the-art experiments, e.g., (I) hydrogen adsorption in carbon nanotechnology (Tanaka, Kanoh et al. 2005; Kowalczyk, Gauden et al. 2007; Kowalczyk, Gauden et al. 2008); (II) electronic redistributions and isotope effects (Wong and Gao 2007; Wong and Gao 2008; Wong, Richard et al. 2009; Gao and Wong 2008) on biochemical reactions in protein (Wong and Gao 2007; Wong and Gao 2011; Wu and Wong 2009; Warshel, Olsson et al. 2006; Gao, Major et al. 2008; Major, Heroux et al. 2009) and RNA enzymes (Wong, Lee et al. 2011; Wong, Gu et al. 2012).

However, owing to the extraordinarily high computational cost, *ab initio* path-integral simulations are thus far not practical even for modest size molecules, and are limited to only some relatively simpler or smaller molecular systems, e.g., thirty-two water molecules, and malonaldehyde [$CH_2(CHO)_2$]. Nevertheless, the unique information and invaluable insight for a molecular system, which can be provided perhaps only from *ab initio* path-integral simulations, have already been recognized in a number of pure computational publications in some high-profile journals, e.g., *Nature*, *Science*, and *Physical Review Letters*, etc (Marx and Parrinello 1995; Tuckerman, Marx et al. 1997; Marx, Tuckerman et al. 1999; Tuckerman and Marx 2001; Tuckerman, Marx et al. 2002; Ohta, Ohta et al. 2004; Hayashi, Shiga et al. 2006; Paesani, Iuchi et al. 2007).

In this chapter, after quickly going over the fundamental physical laws tailoring MD simulations, we (wongky@biomaps.rutgers.edu; kiniu@alumni.cuhk.net) discuss a new

theoretical method that combines our novel systematic free-energy expansion approach, based on Zwanzig's free-energy perturbation theory, with our recently developed automated integration-free path-integral method, based on Kleinert's variational perturbation theory, (Wong and Gao 2007; Wong and Gao 2008; Wong, Richard et al. 2009; Wong, Gu et al. 2012) to perform *ab initio* path-integral simulations for realistic macromolecules at an affordable computational cost. Since in this new method, we can progressively choose computationally affordable levels of theory, now important physical quantities, e.g., free-energy barrier, change of binding energy, pK_a value, and isotope effect, can all be computed at an *ab initio* path-integral level. Therefore, we anticipate this new systematic approach will become an essential computational tool to catch up with or even predict experimental results for breaking down subtle mechanisms underlying a variety of molecular systems in Life and Materials Sciences.

2. Fundamental physical laws governing molecular dynamics simulations

In this section, we lay the theoretical foundation for molecular dynamics (MD) simulations.

2.1 Molecular Schrödinger equation

Ever since quantum mechanics was constructed in the 1920s, solving the non-relativistic time-independent Schrödinger equation for a system of nuclei and electrons has become an essential step to understand *every single* detail of atomic or molecular properties (Kleppner and Jackiw 2000). The non-relativistic time-independent Schrödinger equation for a molecular system (the molecular Schrödinger equation) is:

$$\hat{H}_{mole}\Psi_n = E_n\Psi_n, \tag{1}$$

where $\hat{H}_{mole}$ is the complete (non-relativistic) molecular Hamiltonian, Ψ_n and E_n are an energy eigenfunction (or wave function) and an energy eigenvalue at an eigenstate n, respectively. In contrast to the (intra)nuclear or nucleon Hamiltonian (Dean 2007), the complete molecular Hamiltonian (Hehre, Radom et al. 1986; Szabo and Ostlund 1996; Kohn 1999; Pople 1999; Helgaker, Jørgensen et al. 2000; Springborg 2000) for N_n nuclei and N_e electrons can fortunately be written in an analytic closed form (thanks to the inverse square-distance proportionality in Coulomb's electrostatic force law):

$$\hat{H}_{mole} = \sum_{j}^{N_n} -\frac{1}{2M_j}\nabla_j^2 + \sum_{j<j'}^{N_n}\frac{Z_{j'}Z_j}{x_{jj'}} - \frac{1}{2}\sum_{i}^{N_e}\nabla_i^2 - \sum_{j}^{N_n}\sum_{i}^{N_e}\frac{Z_j}{r_{ij}} + \sum_{i<i'}^{N_e}\frac{1}{r_{ii'}}. \tag{2}$$

In Eq. (2), the units are atomic units, M_j is the mass ratio of nucleus j to electron, and Z_j is the atomic number of nucleus j. The Laplacian operators ∇_j^2 and ∇_i^2 denote the second order differentiation with respect to the coordinates of the jth nucleus and the ith electron, respectively. The first term in Eq. (2) represents the kinetic energy operator for nuclei; the second term is the Coulomb repulsion between nuclei; the third term is the operator for the kinetic energy of electrons; the fourth and fifth terms indicate the Coulomb attraction between electrons and nuclei, and the repulsion between electrons, respectively. The distance between the jth and the j'th nuclei is $x_{jj'}$; the separation between the ith and the i'th electrons is $r_{ii'}$; the distance between the jth nucleus and the ith electrons is r_{ij}.

2.2 Central quantity in quantum thermodynamics: Quantum partition function

Once the energy eigenvalues or the quantized energy spectrum in Eq. (1) are calculated, it is straightforward to obtain a central physical quantity in thermodynamics, i.e., the quantum canonical partition function Q_{qm} (McQuarrie 2000), by the following summation of the Boltzmann energy distribution:

$$Q_{qm} = \sum_n \exp(-\beta E_n), \tag{3}$$

where $\beta = 1/k_B T$, k_B is Boltzmann's constant, and T is temperature. All standard thermodynamic quantities for a system of nuclei and electrons, e.g., free energy, internal energy, entropy, pressure, etc., can be derived from it. In Eq. (3), the lowest energy level E_0, which is often called the ground state energy or zero-point energy (ZPE), is usually the dominant energy level contributing to the partition function. Further, by virtue of Heisenberg's uncertainty principle, the ZPE is always larger than the minimum value of potential energy because a particle can never be at rest anywhere in a given potential or a particle with a particular momentum can be everywhere in a given potential.

2.3 Origin of potential energy surface: Born-Oppenheimer approximation

Unfortunately, even though *all* physics and chemistry of a (time-independent) molecular system is essentially in the molecular Schrödinger equation [Eq. (1)], it can be exactly solved only for simplest one-electron atoms or ions. For other systems, approximations must be introduced to calculate numerical solutions with the aid of computers. The most common and perhaps the mildest approximation is the Born-Oppenheimer approximation (Born and Oppenheimer 1927; Hirschfelder and Meath 1967; Kolos 1970; Ballhausen and Hansen 1972; Hehre, Radom et al. 1986; Szabo and Ostlund 1996; Helgaker, Jørgensen et al. 2000; Springborg 2000; Mielke, Peterson et al. 2003). It decouples internuclear motions from electrons so that nuclei effectively move on a potential energy surface (PES) obtained by solving the electronic part of Schrödinger equation.

This approximation is based on the fact that an electron is much lighter than any nucleus (e.g., a proton, the lightest nucleus, is about 1840 times heavier than an electron). Nuclei move, consequently, much slowlier. As a result, from the electronic perspective, for a given set of nuclear positions, electrons adjust their positions 'instantly' before nuclei have a chance to move. On the other hand, from the standpoint of nuclei, electrons are moving so fast that their effects on nuclei are averaged out over the electronic wave functions. Mathematically, to simplify the molecular Hamiltonian, we first solve the electronic part of the Schrödinger equation for a particular set of nuclear configurations $\{x_j\}$. The electronic part of the complete molecular Hamiltonian [Eq. (2)] is called electronic Hamiltonian:

$$\hat{H}_{elec} = -\frac{1}{2}\sum_i^{N_e} \nabla_i^2 - \sum_j^{N_n}\sum_i^{N_e} \frac{Z_j}{r_{ij}} + \sum_{i<i'}^{N_e} \frac{1}{r_{ii'}}. \tag{4}$$

With this electronic Hamiltonian, we can obtain the electronic energy E_{elec} from the corresponding electronic Schrödinger equation:

$$\hat{H}_{elec}\psi_{elec} = E_{elec}\left(\left\{x_j\right\}\right)\psi_{elec}, \tag{5}$$

where ψ_{elec} is the electronic wave function. Note that the electronic energy $E_{elec}\left(\left\{x_j\right\}\right)$ depends parametrically on the nuclear positions $\left\{x_j\right\}$. With this electronic energy, the molecular Hamiltonian in Eq. (2) can be simplified as follows:

$$\begin{aligned}\hat{H}_{mole} &\approx \sum_{j}^{N_n} -\frac{1}{2M_j}\nabla_j^2 + \sum_{j<j'}^{N_n}\frac{Z_{j'}Z_j}{x_{jj'}} + \left\langle -\frac{1}{2}\sum_{i}^{N_e}\nabla_i^2 - \sum_{j}^{N_n}\sum_{i}^{N_e}\frac{Z_j}{r_{ij}} + \sum_{i<i'}^{N_e}\frac{1}{r_{ii'}}\right\rangle \\ &= \sum_{j}^{N_n} -\frac{1}{2M_j}\nabla_j^2 + \left[\sum_{j<j'}^{N_n}\frac{Z_{j'}Z_j}{x_{jj'}} + E_{elec}\left(\left\{x_j\right\}\right)\right] \\ &= \sum_{j}^{N_n} -\frac{1}{2M_j}\nabla_j^2 + V\left(\left\{x_j\right\}\right),\end{aligned} \tag{6}$$

where $\langle\cdots\rangle$ signifies the average over electronic wave functions or the expectation value. In Eq. (6), V is defined as the sum of the nuclear repulsion energy and electronic energy, which effectively turns out to be the internuclear potential energy function as a consequence of the Born-Oppenheimer approximation:

$$V\left(\left\{x_j\right\}\right) \equiv \sum_{j<j'}^{N_n}\frac{Z_{j'}Z_j}{x_{jj'}} + E_{elec}\left(\left\{x_j\right\}\right). \tag{7}$$

There are many systematic and rigorous theories in electronic structure calculations to derive the internuclear potential energy from first principles (i.e., besides the universal fundamental constants in physics, there is no other empirical parameter involved in the calculations), e.g., Hartree-Fock theory, configuration interaction method, Møller-Plesset perturbation theory, coupled cluster approach, and Kohn-Sham density functional theory. All these quantum mechanical (QM) approaches for electronic structure calculations are often known as *ab initio* methods (Hehre, Radom et al. 1986; Szabo and Ostlund 1996; Kohn 1999; Pople 1999; Helgaker, Jørgensen et al. 2000; Springborg 2000).

In contrast, a complete empirical method to determine an internuclear potential energy surface is to parameterize the potential energy as an analytic function without treating electronic degrees of freedom. This type of approach is referred to as molecular mechanical (MM) method and the empirical potential energy is called force-field energy. Comparing to *ab initio* approach, MM methods are computationally much less expensive and can be applied to describe equilibrium properties in macromolecular systems involving over tens of thousands of heavy atoms (Hagler, Huler et al. 1974; Brooks, Bruccoleri et al. 1983; Weiner, Kollman et al. 1984; Jorgensen and Tirado-Rives 1988; Mayo, Olafson et al. 1990). But for the process involving electronic redistributions (e.g., electronic transfer, chemical bond breaking or forming, etc.), MM force field is often unable to describe it. Later, a hybrid approach called combined QM/MM method has emerged to synthesize the efficiency of MM force field with the accuracy of QM calculations (Field, Bash et al. 1990; Gao and Truhlar 2002). For the rest of this chapter, discussions are limited to the Born-Oppenheimer approximation, which adiabatically decouples nuclear and electronic degrees of freedom.

2.4 Classical free-energy profile vs classical potential of mean force

In practice, quantum effects on internuclear motions are much smaller than those on the electronic part. In many applications, the internuclear quantum effects are insignificant and could even be neglected. Thus, the eigenenergy spectrum E_n in Eq. (1) would become continuous. Given an internuclear potential V, the quantum canonical partition function in Eq. (3) consequently reduces to the classical canonical partition function as:

$$Q_{cl} = \int_{-\infty}^{\infty}\int_{-\infty}^{\infty} \frac{dx^{3N_n} dp^{3N_n}}{h^{3N_n}} \exp\left\{-\beta\left[\left(\sum_j^{3N_n} \frac{p_j^2}{2M_j}\right) + V\left(\{x_j\}\right)\right]\right\}, \tag{8}$$

where h is Planck's constant and p is the momenta associated with the nuclear coordinates x. Subsequently, the classical free energy G_{cl} of a molecular system can be expressed in terms of the classical partition function Q_{cl} as follows:

$$G_{cl} = -k_B T \ln Q_{cl} = -k_B T \ln \int_{-\infty}^{\infty}\int_{-\infty}^{\infty} \frac{dx^{3N_n} dp^{3N_n}}{h^{3N_n}} \exp\left\{-\beta\left[\left(\sum_j^{3N_n} \frac{p_j^2}{2M_j}\right) + V\left(\{x_j\}\right)\right]\right\}. \tag{9}$$

Note that the partition function and the free energy defined above are 'state' functions, which is independent of any nuclear coordinate and momentum (as we integrate out the entire phase space). Given a particular $3N_n$-degree-of-freedom molecular system described by a particular potential energy function V at particular temperature, the partition function and the free energy are *constants*.

On the other hand, of significant interest in simulating a many-body biochemical or physical event is to examine how the free energy of a molecular system *varies* during the event. Conventionally, we first predetermine a coordinate which should be able to describe the event of interest from the start to the end. Next, we generate a free energy profile, which is an energy function of that predetermined coordinate, to investigate how the profile changes during the event. In fact, such a kind of free-energy profile can also be termed as potential energy of ensemble-average or mean force (Kirkwood 1935). Reasons are given below.

The free energy profile of a molecular system as a function of a predetermined coordinate of interest z can be written as follows:

$$\begin{aligned} G_z(z) &= -k_B T \ln\left[\int_{-\infty}^{\infty}\int_{-\infty}^{\infty} \frac{dx^{3N_n} dp^{3N_n}}{h^{3N_n}} \lambda_z \delta(x_z - z) \exp\left\{-\beta\left[\left(\sum_j^{3N_n} \frac{p_j^2}{2M_j}\right) + V\left(\{x_j\}\right)\right]\right\}\right] \\ &= -k_B T \ln\left[\int_{-\infty}^{\infty} dx^{3N_n - 1} \exp\left\{-\beta\left[V\left(\{x_j\}, x_z = z\right)\right]\right\}\right] + C, \end{aligned} \tag{10}$$

where δ is Dirac delta function, λ_z is the thermal de Broglie wavelength for the degree of freedom along z-direction, and C is a normalization factor dependent on the inverse of the thermal de Broglie wavelengths for all degrees of freedom (the wavelength is a function of the nuclear mass M_j, and temperature T). C should be a constant during the biochemical or physical event of our interest. The integrand in the final configurational integral of Eq. (10)

is basically the probability density of the molecular system as a function of z. In practice, it is rare to determine the value of C because what we often care about is the free-energy difference at various values of z.

Notably, by taking the negative derivative of $G_z(z)$, i.e., $-dG_z(z)/dz$, we obtain the average force over all ensembles or over all degrees of freedom, which is called the mean force (Kirkwood 1935), based on the ensemble average definition in Eq. (16):

$$\begin{aligned}
&\langle \mathbf{F}(z) \rangle \\
&= \frac{\int_{-\infty}^{\infty}\int_{-\infty}^{\infty} \frac{dx^{3N_n}dp^{3N_n}}{h^{3N_n}} \lambda_z \delta(x_z - z)\left[-\bar{\nabla}_{x_z} V(\{x_j\})\right]\Big|_{x_z=z} \exp\left\{-\beta\left[\left(\sum_j^{3N_n} \frac{p_j^2}{2M_j}\right) + V(\{x_j\})\right]\right\}}{\int_{-\infty}^{\infty}\int_{-\infty}^{\infty} \frac{dx^{3N_n}dp^{3N_n}}{h^{3N_n}} \lambda_z \delta(x_z - z) \exp\left\{-\beta\left[\left(\sum_j^{3N_n} \frac{p_j^2}{2M_j}\right) + V(\{x_j\})\right]\right\}} \\
&= \frac{\int_{-\infty}^{\infty} dx^{3N_n-1}\left[-\bar{\nabla}_z V(\{x_j\}, x_z = z)\right] \exp\left\{-\beta\left[V(\{x_j\}, x_z = z)\right]\right\}}{\int_{-\infty}^{\infty} dx^{3N_n-1} \exp\left\{-\beta\left[V(\{x_j\}, x_z = z)\right]\right\}} = \frac{-dG_z(z)}{dz}\hat{z}.
\end{aligned} \tag{11}$$

Thus $G_z(z)$, the free energy profile as a function of a predetermined coordinate, is also called the potential of mean force (PMF) (Kirkwood 1935).

However, please note that if the predetermined coordinate of interest is *not* a linear combination of rectilinear coordinates, or in other words, if it is a curvilinear coordinate, then PMF is oftentimes *not* exactly equal to free-energy profile. Not only the Jacobian-determinant contribution makes their difference (Ruiz-Montero, Frenkel et al. 1997; Hénin, Fiorin et al. 2010), but also in a forthcoming paper, we will show that actually change of domains with respect to the coordinate of interest can also contribute to the free-energy profile, i.e., the Leibnizian contribution (Flanders 1973).

In addition, we will also show that according to differential geometry and general relativity, once we realize the equivalence between orthogonal covariant and contravariant vectors (Arfken and Weber 2001), then the Jacobian scale factor for a predetermined curvilinear coordinate of interest, q_ξ, can be proved to be (in contravariant space):

$$h_{q_\xi} = \left|\bar{\nabla} q_\xi\right|^{-1} \tag{12}$$

and the unit vector for q_ξ can be proved as (in contravariant space):

$$\hat{q}_\xi = \bar{\nabla} q_\xi \Big/ \left|\bar{\nabla} q_\xi\right| \tag{13}$$

In Eq. (12) and (13), q_ξ must belong to at least one *complete* set of curvilinear coordinates, hypothetically. In general, unless we explicitly define the rest of the *complete* curvilinear coordinates, the sole definition of q_ξ is *not* sufficient to make the PMF be unique. But, we will show the free-energy profile does *not* suffer from this uniqueness problem. In fact, if we restrict ourselves to a *complete* set of curvilinear coordinates in which q_ξ is orthogonal to the

rest of coordinates, then the PMF will be unique and its relation with the free-energy profile can be proved as follows (den Otter 2000), after using Eq. (12) and Eq. (13):

$$\frac{dG_\xi(\xi_0)}{d\xi_0} = \left\langle \bar{\nabla} V \cdot \left(\frac{\bar{\nabla} q_\xi}{\left| \bar{\nabla} q_\xi \right|^2} \right) \right\rangle_{q_\xi = \xi_0} - k_B T \left\langle \bar{\nabla} \cdot \left(\frac{\bar{\nabla} q_\xi}{\left| \bar{\nabla} q_\xi \right|^2} \right) \right\rangle_{q_\xi = \xi_0} \tag{14}$$

In Eq. (14), the Leibnizian contribution is nil, the first term on RHS is the mean force for q_ξ, the second term is the Jacobian contribution, and $\langle \cdots \rangle_{q_\xi = \xi_0}$ is the ensemble average over all configurations with $q_\xi = \xi_0$.

Finally, the Fixman potential (Fixman 1974), which corrects the velocity-bias in constrained MD, will also be presented with correct dependence on mass in our forthcoming paper.

2.5 Simulating classical thermodynamics: Molecular dynamics simulations

By assuming the molecular system of our interest is ergodic, molecular dynamics (MD) simulation techniques can be employed to compute the ensemble average of a physical quantity. In essence, MD simulations is numerically solving, integrating or propagating the Newtonian equations of motion, one-time-step by one-time-step. Given an internuclear potential V (regardless of using QM, MM, or hybrid QM/MM to construct), the motion or trajectory of a nucleus j as a function of time t is governed by Newton's second law:

$$-\bar{\nabla}_j V\left(\{x_j(t)\}\right) + (\textbf{Extended Forces}) = M_j \frac{d^2 \bar{x}_j}{dt^2}. \tag{15}$$

Note the extended forces in Eq. (15) are *essential* for having *canonical* ensemble (constant temperature) instead of *microcanonical* ensemble (constant energy) in MD simulations (Hünenberger 2005). In the ergodic hypothesis (Lebowitz and Penrose 1973; Cogswell 1999) [the dynamical version of ergodic theory was first proposed by Birkhoff (Birkhoff 1931), in which Liouville's theorem was applied to ensure the ensemble distribution in phase-space is invariant with time], if the simulation time for propagating the trajectory $x_j(t)$ of the nucleus j is *infinitely long*, the ensemble average of a physical quantity $\mathbf{f}(\{x\},\{p\})$ (which can be either a scalar or a vector) over the *entire* phase space, i.e.,

$$\langle \mathbf{f} \rangle = \frac{1}{Q_{cl}} \int_{-\infty}^{\infty} \int_{-\infty}^{\infty} \frac{dx^{3N_n} dp^{3N_n}}{h^{3N_n}} \mathbf{f}(\{x\},\{p\}) \exp\left\{ -\beta \left[\left(\sum_j^{3N_n} \frac{p_j^2}{2M_j} \right) + V\left(\{x_j\}\right) \right] \right\}, \tag{16}$$

is equal to the time average in MD simulations:

$$\langle \mathbf{f} \rangle = \lim_{t_f \to \infty} \frac{1}{t_f} \int_0^{t_f} \mathbf{f}(\{x(t)\},\{p(t)\}) dt. \tag{17}$$

In other words, longer MD simulation time allows us to sample more phase space for computing the corresponding ensemble average, which in turn could be in higher accuracy.

3. Zwanzig's free-energy perturbation theory

Owing to the Boltzmann exponential energy distribution, one of the major difficulties in computing a converged free-energy profile or potential of mean force [Eq. (10)] via MD and MC sampling techniques is that it takes longer simulation time or runs more MC steps to have enough higher-energy samples. Yet, many interesting biochemical or physical molecular properties could be in higher-energy regions, e.g., the transition state during protein folding or biochemical reaction.

In practice, in order for having effective samplings on both the lower-energy (e.g., reactant state) and higher-energy regions (e.g., transition state), Zwanzig's free-energy perturbation (Zwanzig 1954) [which is also referred to as statistical-mechanical perturbation theory (McQuarrie 2000)] has been extensively applied. The feature of the perturbation is relating the change of free energy between *two* systems (both have the same number of degrees of freedom) by an ensemble average taken in only *one* of the two systems. This can be illustrated by first writing the classical free energy G_{cl} corresponding to the partition function in Eq. (8) as follows:

$$G_{cl} = -k_B T \ln Q_{cl} = \int_{-\infty}^{\infty}\int_{-\infty}^{\infty} \frac{dx^{3N_n} dp^{3N_n}}{h^{3N_n}} \exp(-\beta E), \tag{18}$$

where E is the energy at a point $\left(\{p_j\},\{x_j\}\right)$ in the phase space, i.e.,

$$E = E\left(\{p_j\},\{x_j\}\right) = \left(\sum_j^{3N_n} \frac{p_j^2}{2M_j}\right) + V\left(\{x_j\}\right). \tag{19}$$

Next, we rewrite Eq. (18) as:

$$\begin{aligned} G_{cl} &= -k_B T \ln \left[\frac{\int_{-\infty}^{\infty}\int_{-\infty}^{\infty} \frac{dx^{3N_n} dp^{3N_n}}{h^{3N_n}} \exp\left[-\beta\left(E - E_0\right)\right] e^{-\beta E_0}}{\int_{-\infty}^{\infty}\int_{-\infty}^{\infty} \frac{dx^{3N_n} dp^{3N_n}}{h^{3N_n}} e^{-\beta E_0}} \right] - k_B T \ln \int_{-\infty}^{\infty}\int_{-\infty}^{\infty} \frac{dx^{3N_n} dp^{3N_n}}{h^{3N_n}} e^{-\beta E_0} \\ &= -k_B T \ln \left\langle \exp\left[-\beta\left(E - E_0\right)\right] \right\rangle_0 + G_0, \end{aligned} \tag{20}$$

where G_0 is the free energy of the reference system, E_0 is the energy at a point in the phase space of the reference system, and $\langle \cdots \rangle_0$ is an ensemble average for the reference system. From Eq. (20), we obtain Zwanzig's free-energy perturbation (Zwanzig 1954):

$$G - G_0 = -k_B T \ln \left\langle \exp\left[-\beta\left(E - E_0\right)\right] \right\rangle_0. \tag{21}$$

As a result, by taking the advantage of the perturbation [Eq. (21)], we can readily have enough samples in higher-energy regions in a reference frame where their original high potential energy values intentionally get lowered. Afterwards, the corrected free energy can straightforwardly be recovered by taking the average of the exponential factor $\exp\left[-\beta\left(E - E_0\right)\right]$ over the ensembles sampled in the reference system. This is exactly the idea behind many enhanced sampling methods, such as the umbrella sampling technique.

4. Systematic *ab initio* molecular dynamics approach: Free-energy expansion method as a series of covariance tensors

A fundamental key to have successful molecular simulations is the accuracy of internuclear potential for describing atomic motions during biochemical or physical events. By exploiting Zwanzig's free-energy perturbation (FEP) theory, we are developing a new rigorous method to systematically obtain accurate free-energy profiles, in which the internuclear potential energy is effectively computed at a high-level *ab initio* theory. Our new method is a systematic free-energy expansion (FEE) in terms of a series of covariance tensors. The new expansion will enable us to have a free-energy profile at a level as high as the coupled cluster theory at an affordable computational cost, which is currently known as the gold standard but unreachable level of theory for free-energy simulations. The focus of our FEE method will be on the difference of free energy calculated by two different internuclear potential. Furthermore, in contrast to Car-Parrinello MD (CPMD) which is limited to potential energy derived from DFT (Car and Parrinello 1985), our method is independent of how the potential energy functions being constructed. Therefore, by combining it with our novel automated integration-free path-integral (AIF-PI) method together (See Section 5; Wong and Gao 2007; Wong and Gao 2008; Wong, Richard et al. 2009; Wong, Gu et al. 2012), we will also be able to compute free-energy barriers, changes of binding energy, pK_a values, and isotope effects at an *ab initio* path integral level (see Section 6).

Let's begin with the FEP theory. From Eq. (21), the free energy difference between using lower-level (LL) and higher-level (HL) *ab initio* methods can be expressed as:

$$G_{HL} - G_{LL} = \Delta G = -k_B T \ln\left\langle \exp\left[-\beta\left(E_{HL} - E_{LL}\right)\right]\right\rangle_{LL}. \tag{22}$$

Next we expand the ensemble average in Eq. (22) and sum up the prefactors into a series of cumulants:

$$G_{HL} - G_{LL} = \Delta G = -\frac{1}{\beta}\ln\left\langle \exp\left[-\beta\,\Delta E\right]\right\rangle_{LL} = -\frac{1}{\beta}\ln\left\{\exp\left[\sum_{n=1}^{\infty}\left\langle\left(-\beta\,\Delta E\right)^n\right\rangle_{LL,c}\right]\right\}, \tag{23}$$

where

$$\Delta E = E_{HL} - E_{LL}, \tag{24}$$

$\langle\cdots\rangle_{LL,c}$ is a cumulant, and n is the order of a cumulant. In his original 1954 paper (Zwanzig 1954), Zwanzig showed that the cumulant expansion is fast converging when the change of energy ΔE in the ensemble is reasonably small relative to the inverse of β. However, in terms of computational cost, this cumulant expansion does not provide an advantage for correcting lower-level free energy. This is because the time required for calculating the cumulant average $\langle\cdots\rangle_{LL,c}$ with computer is basically as much as the time needed to directly compute the higher-level free energy G_{HL}, regardless of whether the perturbation ΔE is big.

In order to ease up this situation, in a forthcoming paper we will prove that each cumulant can be further expanded as a Taylor series expansion fluctuating about the ensemble average position $\bar{\mathbf{x}}_{LL}$ in the form:

$$\left\langle \left(-\beta\ \Delta E\right)^n \right\rangle_{LL} = \left\langle f_n(\mathbf{x}) \right\rangle_{LL} = f_n(\bar{\mathbf{x}}_{LL}) + \frac{1}{2!}\left[\hat{\mathbf{D}}^2 f_n(\bar{\mathbf{x}}_{LL})\right]\mathrm{cov}\left(\mathbf{x}^{T_p}, \mathbf{x}\right) + \cdots \tag{25}$$

where T_p is transpose, $f_n(\mathbf{x}) = \left(-\beta\ \Delta E\right)^n$, $\mathbf{x}$ is a position vector of $3N$ Cartesian coordinates of the system, $\hat{\mathbf{D}}^n$ is the nth-order tensor operator for differentiation with respect to the $3N$ coordinates (e.g., $\hat{\mathbf{D}} f_n(\bar{\mathbf{x}}_{LL})$ is the gradient and $\hat{\mathbf{D}}^2 f_n(\bar{\mathbf{x}}_{LL})$ is the Hessian matrix), and $\mathrm{cov}\left(\mathbf{x}^{T_p}, \mathbf{x}\right)$ is the covariance matrix. The higher order terms in Eq. (25) involve higher order covariance tensors. Note that the term associated with the gradient is not shown in Eq. (25) because the first order central moment, i.e., $\left\langle \mathbf{x} - \bar{\mathbf{x}}_{LL} \right\rangle_{LL}$, is always zero by definition.

By combining Eq. (25) with Eq. (23), we have enough equations to systematically approach the exact value of high-level free energy at a reduced computational cost. The number of calculations involving E_{HL} is now considerably decreased to only a single-point energy calculation at $\bar{\mathbf{x}}_{LL}$ for the zeroth order correction, and merely a normal-mode frequency analysis at $\bar{\mathbf{x}}_{LL}$ for the second order correction.

To increase the converging property for the expansion in Eq. (25) as well as to overcome the problem of multi-model probability distribution, we can further generalize the FEE method by considering a decomposition of the ensemble average into subgroups by clustering methods. The clustering scheme will be determined in a way such that the FEE expansion is converged up to the second order correction in each group or each cluster. Please note that, in the limit that the number of clusters becomes as many as the number of ensembles, the formalism reduces back to the original ensemble average, and inclusion of only the zeroth order term in Eq. (25) is able to return us back the exact result of Eq. (23).

Cumulant	Tensor	ΔG (kcal/mol)	Error
1st	0th	−170.601	0.316
	1st	−170.601	0.316
	2nd	−170.680	0.237
	3rd	−170.680	0.237
	∞	−170.680	0.237
2nd	0th	−170.601	0.316
	1st	−170.601	0.316
	2nd	−170.875	0.042
	3rd	−170.877	0.040
	∞	−170.883	0.034
6th	∞	−170.917	0.000

Table 1. Free-Energy correction ΔG for H_2O from HF/6-31G(d) to MP2/6-311G(d,p).

Since single-point energy calculations and a normal-mode frequency analysis at high-level electronic structure calculations are actually very common in literature (which are often used for minimized structures, though), we anticipate this new free-energy expansion method would be particularly useful for coupling accurate results from high-level *ab initio* theory with computational efficiency of lower-level samplings in free-energy calculations.

The preliminary results using this new systematic FEE method, i.e., Eq. (23), are very encouraging. Table 1 shows the free energy correction ΔG for a single water molecule from HF/6-31G(d) to MP2/6-311G(d,p). Even just up to the first cumulant at the zeroth order correction, the computed error is in the order of magnitude ~0.1 kcal/mol. The first cumulant is basically converged as soon as the second order correction is included.

5. Simulating quantum thermodynamics: Feynman's path integral

All the above discussions on simulating internuclear thermodynamics are limited to classical mechanics (regardless of using QM, MM, hybrid QM/MM to construct potential energy). However, the real world is described by quantum mechanics, including nuclei. In some important applications of Life and Materials Sciences, such as hydrogen adsorption in carbon nanotechnology, the transport mechanism of hydrated hydroxide ions in aqueous solution, and kinetic isotope effects on a proton-transfer reaction, actually internuclear quantum-statistical effects (e.g., quantization of vibration and quantum tunneling) are not negligible. A popular choice for incorporating such internuclear quantum-statistical effects in the conventional molecular dynamics (MD) or Monte Carlo (MC) simulations (Tanaka, Kanoh et al. 2005; Warshel, Olsson et al. 2006; Kowalczyk, Gauden et al. 2007; Gao, Major et al. 2008; Kowalczyk, Gauden et al. 2008; Major, Heroux et al. 2009; Wong, Gu et al. 2012) is using Feynman's path integral (Feynman 1948; Feynman 1966; Kleinert 2004; Brown 2005; Feynman, Hibbs et al. 2005).

The essence of Feynman's path integral is to transform the Schrödinger *differential* equation to become an *integral* equation. As a result, the many-body path integrations can be carried out by the conventional MD or MC sampling techniques. In addition, the quantum canonical partition function can be directly obtained with no need to compute individual energy eigenvalues.

5.1 Kleinert's variational perturbation theory for centroid density of path integrals

Kleinert's variational perturbation (KP) theory (Kleinert 2004) for the centroid density (Gillan 1987; Gillan 1987; Voth 1996; Ramírez, López-Ciudad et al. 1998; Ramírez and López-Ciudad 1999; Feynman, Hibbs et al. 2005) of Feynman path integrals (Feynman 1948; Feynman 1966; Kleinert 2004; Brown 2005; Feynman, Hibbs et al. 2005) provides a complete theoretical foundation for developing non-stochastic methods to systematically incorporate internuclear quantum-statistical effects in condensed phase systems. Similar to the complementary interplay between the rapidly growing quantum Monte Carlo simulations (Anderson 1975; Grossman and Mitas 2005; Lester and Salomon-Ferrer 2006; Wagner, Bajdich et al. 2009) and the well-established *ab initio* or density-functional theories (DFT) for electronic structure calculations (Hehre, Radom et al. 1986; Szabo and Ostlund 1996; Kohn 1999; Pople 1999; Helgaker, Jørgensen et al. 2000; Springborg 2000), non-stochastic path-integral methods can complement the conventional Fourier or discretized path-integral Monte-Carlo (PIMC) (MacKeown 1985; Coalson 1986; Ceperley 1995; Mielke and Truhlar 2001; Sauer 2001) and molecular dynamics (PIMD) (Cao and Voth 1994; Voth 1996) simulations which have been widely used in condensed phases.

To simplify the illustration of the essence of Kleinert's variational perturbation theory, we now consider a one-particle one-dimensional system. For a one-particle one-dimensional system, the classical canonical partition function in Eq. (8) reduces to become:

$$Q_{cl} = \sqrt{\frac{Mk_BT}{2\pi\hbar^2}} \int_{-\infty}^{\infty} e^{-\beta V(x_0)} dx_0. \tag{26}$$

The traditional way to obtain the quantum canonical partition function, i.e., Eq. (3), is to solve the internuclear Schrödinger equation to get the individual energy eigenvalues. But in the path-integral (PI) formulation, we do not know the individual energy eigenvalues for obtaining the quantum partition function. This is because the PI representation of the quantum partition function can be written in terms of the centroid effective potential W as a classical configuration integral (Gillan 1987; Gillan 1987; Voth 1996; Ramírez, López-Ciudad et al. 1998; Ramírez and López-Ciudad 1999; Kleinert 2004; Feynman, Hibbs et al. 2005):

$$Q_{qm} = \sum_n \exp(-\beta E_n) = \sqrt{\frac{Mk_BT}{2\pi\hbar^2}} \int_{-\infty}^{\infty} e^{-\beta W(x_0)} dx_0. \tag{27}$$

Given the centroid potential $W(x_0)$, thermodynamic and quantum dynamic quantities can be accurately determined, including molecular spectroscopy of quantum fluids and the rate constant of chemical and enzymatic reactions. The mass-dependent nature of $W(x_0)$ is also of particular interest because isotope effects can be obtained, and it has been applied to carbon nanotubes (Tanaka, Kanoh et al. 2005; Kowalczyk, Gauden et al. 2007; Kowalczyk, Gauden et al. 2008), and biochemical reactions in protein (Warshel, Olsson et al. 2006; Gao, Major et al. 2008; Major, Heroux et al. 2009) and RNA enzymes (Wong, Gu et al. 2012).

The centroid potential $W(x_0)$ in Eq. (27) is defined as follows (Gillan 1987; Gillan 1987; Voth 1996; Ramírez, López-Ciudad et al. 1998; Ramírez and López-Ciudad 1999; Kleinert 2004; Feynman, Hibbs et al. 2005):

$$W(x_0) = -k_BT \ln\left[\sqrt{\frac{2\pi\hbar^2}{Mk_BT}} \oint \mathrm{D}[x(\tau)]\,\delta(\bar{x} - x_0) \exp\{-\mathcal{A}[x(\tau)]/\hbar\}\right], \tag{28}$$

where τ is a real number and represents the component for pure imaginary time in path integral, $x(\tau)$ describes a path in space-time, $\oint \mathrm{D}x(\tau)\delta(\bar{x} - x_0)$ denotes a summation over *all* possible closed paths in which $\bar{x}$ is equal to x_0 (i.e., a functional integration), and $\bar{x}$ is the time-average position, called 'centroid'

$$\bar{x} \equiv \frac{1}{\beta\hbar} \int_0^{\beta\hbar} x(\tau) d\tau \,. \tag{29}$$

In Eq. (28), $\mathcal{A}$ is the quantum-statistical action:

$$\mathcal{A}[x(\tau)] = \int_0^{\beta\hbar} d\tau \left\{\frac{M}{2}\dot{x}(\tau)^2 + V[x(\tau)]\right\}, \tag{30}$$

where $V(x)$ is the original potential energy of the system. Generalization of Eq. (28) to a multi-dimensional system is straightforward (Kleinert 2004; Feynman, Hibbs et al. 2005).

A number of non-stochastic approaches have been developed to approximately estimate the centroid potential. For example, Feynman and Hibbs described a first-order cumulant expansion by introducing a Gaussian smearing function in a free-particle reference frame to yield an upper bound on the centroid potential (Feynman, Hibbs et al. 2005). This was subsequently modified by Doll and Myers (DM) by using a Gaussian width associated with the angular frequency at the minimum of the original potential (Doll and Myers 1979). Mielke and Truhlar employed a free-particle reference state and approximated the sum over paths by a minimal set of paths constrained for a harmonic oscillator. The action integral is obtained by using the three-point trapezoidal rule for the potential to yield the displaced-point path integral (DPPI) centroid potential (Mielke and Truhlar 2001).

A closely related theoretical approach to the KP theory is the variational method independently introduced by Giachetti and Tognetti (Giachetti and Tognetti 1985), and by Feynman and Kleinert (hereafter labeled as GTFK) (Feynman and Kleinert 1986), which formally corresponds to the first order approximation in the KP theory, i.e., KP1. The GTFK approach is a variational method that adopts a harmonic reference state by variationally optimizing the angular frequency. This variational method has been applied to a variety of systems, including quantum dynamic processes in condensed phases (e.g., water and helium). Although the original GTFK approach is among the most accurate approximate methods for estimating the path-integral centroid potential in many applications (Mielke and Truhlar 2001), significant errors can exist in situations in which quantum effects are dominant, especially at low temperatures. Higher order perturbations of KP theory can significantly and systematically improve computational accuracy over the KP1 results.(Kleinert 2004; Wong and Gao 2007; Wong and Gao 2008; Wong, Richard et al. 2009; Wong, Gu et al. 2012)

In essence, what Kleinert's variational perturbation (KP) theory does is to systematically builds up anharmonic corrections to the harmonic centroid potential calculated in a harmonic reference state characterized by a trial angular frequency Ω (Kleinert 2004). Given the reference, or trial harmonic action:

$$\mathcal{A}_{\Omega}^{x_0} = \int_0^{\beta\hbar} d\tau \left\{ \frac{M}{2}\dot{x}(\tau)^2 + \frac{1}{2}M\Omega^2\left[x(\tau) - x_0\right]^2 \right\}. \tag{31}$$

the centroid potential $W(x_0)$ in Eq. (28) can be expressed as a path integral of the harmonic action which is perturbed by the anharmonicity of the original potential:

$$e^{-\beta W(x_0)} = \sqrt{\frac{2\pi\hbar^2}{Mk_BT}} \oint \mathrm{D}x(\tau)\,\delta(\bar{x} - x_0)\, e^{-\mathcal{A}_{\Omega}^{x_0}/\hbar} e^{-\left(\mathcal{A} - \mathcal{A}_{\Omega}^{x_0}\right)/\hbar} = Q_{\Omega}^{x_0} \left\langle e^{-\left(\mathcal{A} - \mathcal{A}_{\Omega}^{x_0}\right)/\hbar} \right\rangle_{\Omega}^{x_0}, \tag{32}$$

where $Q_{\Omega}^{x_0}$ is the local harmonic partition function given as follows:

$$Q_{\Omega}^{x_0} = \sqrt{\frac{2\pi\hbar^2}{Mk_BT}} \oint \mathrm{D}x(\tau)\,\delta(\bar{x} - x_0)\, e^{-\mathcal{A}_{\Omega}^{x_0}/\hbar} = \frac{\beta\hbar\Omega/2}{\sinh\left(\beta\hbar\Omega/2\right)}, \tag{33}$$

and $\langle\cdots\rangle_{\Omega}^{x_0}$ is the expectation value over all closed paths of the action in Eq. (31):

$$\left\langle e^{-F[x(\tau)]/\hbar}\right\rangle_{\Omega}^{x_0}=\frac{1}{Q_{\Omega}^{x_0}}\sqrt{\frac{2\pi\hbar^2}{Mk_BT}}\oint \mathrm{D}x(\tau)\,\delta(\bar{x}-x_0)\,e^{-F[x(\tau)]/\hbar}e^{-A_{\Omega}^{x_0}/\hbar}, \tag{34}$$

In Eq. (34), $F[x(\tau)]$ denotes an arbitrary functional. It is of interest to note that Eq. (32) is similar to the starting point of Zwanzig's free-energy perturbation (Section 3), which has been extensively used in free-energy calculations through Monte Carlo and molecular dynamics simulations. Their difference is one is for ordinary ensemble average, while another one is for closed-path average, i.e., *functional* average.

If we expand the exponential functional in Eq. (32) and sum up the prefactors into an exponential series of cumulants, then the *n*th-order approximation, $W_n^{\Omega}(x_0)$, to the centroid potential $W(x_0)$ can be written as follows (Kleinert 2004):

$$\begin{aligned} e^{-\beta W_n^{\Omega}(x_0)}=Q_{\Omega}^{x_0}\exp\Bigg\{&-\frac{1}{\hbar}\int_0^{\beta\hbar}d\tau\left\langle A_{\mathrm{int}}^{x_0}\right\rangle_{\Omega,c}^{x_0}+\frac{1}{2!\hbar^2}\int_0^{\beta\hbar}d\tau_1\int_0^{\beta\hbar}d\tau_2\left\langle A_{\mathrm{int}}^{x_0}[x(\tau_1)]A_{\mathrm{int}}^{x_0}[x(\tau_2)]\right\rangle_{\Omega,c}^{x_0}\\ &+\cdots+\left\{\prod_{j=1}^{n}\int_0^{\beta\hbar}d\tau_j\right\}\frac{(-1)^n}{n!\hbar^n}\left\langle\prod_{k=1}^{n}A_{\mathrm{int}}^{x_0}[x(\tau_k)]\right\rangle_{\Omega,c}^{x_0}\Bigg\}, \end{aligned} \tag{35}$$

where $A_{\mathrm{int}}^{x_0}=A-A_{\Omega}^{x_0}$ is the so-called inter-*action*, representing the perturbation to the harmonic reference state, $\langle\cdots\rangle_{\Omega,c}^{x_0}$ is a cumulant which can be written in terms of expectation values $\langle\cdots\rangle_{\Omega}^{x_0}$ by the cumulant expansion (Zwanzig 1954; Kubo 1962; Kleinert 2004), e.g.,

$$\left\langle A_{\mathrm{int}}^{x_0}[x(\tau)]\right\rangle_{\Omega,c}^{x_0}\equiv\left\langle A_{\mathrm{int}}^{x_0}[x(\tau)]\right\rangle_{\Omega}^{x_0}, \tag{36}$$

$$\left\langle A_{\mathrm{int}}^{x_0}[x(\tau_1)]A_{\mathrm{int}}^{x_0}[x(\tau_2)]\right\rangle_{\Omega,c}^{x_0}\equiv\left\langle A_{\mathrm{int}}^{x_0}[x(\tau_1)]A_{\mathrm{int}}^{x_0}[x(\tau_2)]\right\rangle_{\Omega}^{x_0}-\left\{\left\langle A_{\mathrm{int}}^{x_0}[x(\tau)]\right\rangle_{\Omega}^{x_0}\right\}^2, \tag{37}$$

$$\begin{aligned} \left\langle A_{\mathrm{int}}^{x_0}[x(\tau_1)]A_{\mathrm{int}}^{x_0}[x(\tau_2)]A_{\mathrm{int}}^{x_0}[x(\tau_3)]\right\rangle_{\Omega,c}^{x_0}\equiv&\left\langle A_{\mathrm{int}}^{x_0}[x(\tau_1)]A_{\mathrm{int}}^{x_0}[x(\tau_2)]A_{\mathrm{int}}^{x_0}[x(\tau_3)]\right\rangle_{\Omega}^{x_0}\\ &-3\left\langle A_{\mathrm{int}}^{x_0}[x(\tau_1)]A_{\mathrm{int}}^{x_0}[x(\tau_2)]\right\rangle_{\Omega}^{x_0}\left\langle A_{\mathrm{int}}^{x_0}[x(\tau)]\right\rangle_{\Omega}^{x_0}+2\left\{\left\langle A_{\mathrm{int}}^{x_0}[x(\tau)]\right\rangle_{\Omega}^{x_0}\right\}^3 \end{aligned} \tag{38}$$

More importantly, Kleinert and co-workers derived a math equation for expressing the expectation value $\left\{\prod_{j=1}^{n}\int_0^{\beta\hbar}d\tau_j\right\}\left\langle\prod_{k=1}^{n}F_k[x(\tau_k)]\right\rangle_{\Omega}^{x_0}$ from the *functional-integral* form to be in terms of Gaussian smearing convolution integrals (*ordinary* integrals) (Kleinert 2004):

$$\begin{aligned} \left\{\prod_{j=1}^{n}\int_0^{\beta\hbar}d\tau_j\right\}\left\langle\prod_{k=1}^{n}F_k[x(\tau_k)]\right\rangle_{\Omega}^{x_0}=&\left\{\prod_{j=1}^{n}\int_0^{\beta\hbar}d\tau_j\right\}\left\{\prod_{k=1}^{n}\int_{-\infty}^{\infty}dx_kF_k(x_k)\right\}\\ &\times\frac{1}{\sqrt{(2\pi)^n\,\mathbf{Det}\left[a_{\tau_k\tau_{k'}}^2(\Omega)\right]}}\exp\left\{-\frac{1}{2}\sum_{\substack{k=1\\k'=1}}^{n}(x_k-x_0)\,a_{\tau_k\tau_{k'}}^{-2}(\Omega)(x_{k'}-x_0)\right\}, \end{aligned} \tag{39}$$

where $\mathbf{Det}\left[a^2_{\tau_k\tau_{k'}}(\Omega)\right]$ is the determinant of the $n\times n$**-matrix** consisting of the Gaussian width $a^2_{\tau_k\tau_{k'}}(\Omega)$, $a^{-2}_{\tau_k\tau_{k'}}(\Omega)$ is an element of the inverse matrix of $a^2_{\tau_k\tau_{k'}}(\Omega)$, and the Gaussian width is a function of the trial frequency Ω:

$$a^2_{\tau\tau'}(\Omega)=\frac{1}{\beta M\Omega^2}\left\{\frac{\beta\hbar\Omega}{2}\frac{\cosh\left[\left(|\tau-\tau'|-\beta\hbar/2\right)\Omega\right]}{\sinh\left(\beta\hbar\Omega/2\right)}-1\right\}. \tag{40}$$

After using these smearing potentials given in Eq. (39), the *n*th-order Kleinert variational perturbation (KP*n*) approximation, $W^{\Omega}_n(x_0)$, shown in Eq. (35) as *functional* integrals, can now be written in terms of *ordinary* integrals as follows (Kleinert 2004):

$$\begin{aligned}&W^{\Omega}_n(x_0)\\&=-k_BT\ln Q^{x_0}_{\Omega}+\frac{k_BT}{\hbar}\int_0^{\beta\hbar}d\tau\left\langle V^{x_0}_{\rm int}\left[x(\tau_1)\right]\right\rangle^{x_0}_{\Omega}-\frac{k_BT}{2!\hbar^2}\int_0^{\beta\hbar}d\tau_1\int_0^{\beta\hbar}d\tau_2\left\langle V^{x_0}_{\rm int}\left[x(\tau_1)\right]V^{x_0}_{\rm int}\left[x(\tau_2)\right]\right\rangle^{x_0}_{\Omega,c}\\&\quad+\cdots+k_BT\frac{(-1)^{n+1}}{n!\hbar^n}\left\{\prod_{j=1}^{n}\int_0^{\beta\hbar}d\tau_j\right\}\left\langle\prod_{k=1}^{n}V^{x_0}_{\rm int}\left[x(\tau_k)\right]\right\rangle^{x_0}_{\Omega,c},\end{aligned} \tag{41}$$

where $V^{x_0}_{\rm int}\left[x(\tau)\right]=V\left[x(\tau)\right]-\frac{1}{2}M\Omega^2\left[x(\tau)-x_0\right]^2$ (the kinetic energy terms in Eq. (30) and Eq. (31) cancel each other out).

As *n* tends to infinity, $W^{\Omega}_n(x_0)$ approaches the exact value of the centroid potential $W(x_0)$ in Eq. (28), which is independent of the trial Ω. But the truncated sum in Eq. (41) does depend on Ω, and the optimal choice of this trial frequency at a given order of KP expansion and at a particular centroid position x_0 is determined by the least-dependence of $W^{x_0}_n(\Omega)$ on Ω itself. This is the so-called frequency of least dependence, which provides a variational approach to determine the optimal value of Ω, $\Omega_{\mathbf{opt},n}(x_0)$ (Kleinert 2004).

Of particular interest is the special case when $n=1$, which turns out to be identical to the original GTFK variational approach. An important property of KP1 or the GTFK variational approach is that there is a definite upper bound for the computed $W^{\Omega}_1(x_0)$ by virtue of the Jensen-Peierls inequality, i.e., from Eq. (32) and (35):

$$e^{-\beta W(x_0)}=Q^{x_0}_{\Omega}\left\langle\exp\left(-\frac{A-A^{x_0}_{\Omega}}{\hbar}\right)\right\rangle^{x_0}_{\Omega}\geq Q^{x_0}_{\Omega}\exp\left\langle-\frac{A-A^{x_0}_{\Omega}}{\hbar}\right\rangle^{x_0}_{\Omega}=e^{-\beta W^{\Omega}_1(x_0)}. \tag{42}$$

Note that by choosing $\Omega=0$ (i.e., the reference state is for a free particle), KP1 or GTFK (Giachetti and Tognetti 1985; Feynman and Kleinert 1986) reduces to the Feynman-Hibbs approach (Feynman, Hibbs et al. 2005). For higher orders of *n*, unfortunately, it is not guaranteed that a minimum of $W^{x_0}_n(\Omega)$ actually exists as a function of Ω. In this case, the least dependent Ω is obtained from the condition that the next derivative of $W^{x_0}_n(\Omega)$ with respect to Ω is set to zero. Consequently, Ω is considered as a variational parameter in the Kleinert perturbation theory such that $W^{x_0}_n\left[\Omega_{\mathbf{opt},n}(x_0)\right]$ is least-dependent on Ω.

This variational criterion relies on the uniformly and exponentially convergent property demonstrated from the KP theory. Kleinert and coworkers proved that his theory exhibits this property in several strong anharmonic-coupling systems. More importantly, this remarkably fast convergent property can also be observed even for computing the *electronic* ground state energy of a hydrogen atom (3 degrees of freedom). The ground state energy was determined by calculating the electronic centroid potential at the zero-temperature limit. The accuracies of the first three orders of the KP theory for a hydrogen atom are 85%, 95%, and 98%, respectively (Kleinert 2004).

In practice, for odd n, there is typically a minimum point in Ω, but due to the alternating sign of the cumulants in Eq. (41), there is usually *no* minimum in Ω for even n. Nevertheless, the frequency of least-dependence for an even order perturbation in n can be determined by locating the inflexion point, i.e., the zero-value of the second derivative of $W_n^{x_0}(\Omega)$ with respect to Ω. Since the KP expansion is uniformly and exponentially converged, Kleinert has demonstrated that the least-dependent plateau in $W_n^{x_0}(\Omega)$, which is characterized by a minimum point for odd n or by an inflexion point for even n, grows larger and larger with increasing orders of n (Kleinert 2004).

5.2 Automated integration-free path-integral method

An especially attractive feature of Eq. (41) is that the if the real system potential is expressed as a series of polynomials or Gaussians, then analytic expressions of Eq. (41) can be obtained, making the computation extremely efficient because the time-demanding Monte Carlo samplings for multi-dimensional numerical integrations could be avoided. Hereafter, the level of calculations up to nth order KP expansion for an mth-order-polynomial potential is denoted as KPn/Pm. For other potentials, KPn theory still involves elaborate n-dimensional space-time ($2n$ degrees of freedom) smearing integrals in Eq. (39). The intricacy of the smearing integrals increases tremendously for multidimensional potentials, where Ω becomes a $3N \times 3N$ matrix Ω_{ij} for N nuclei. This complexity is a major factor limiting applications of the KP theory beyond KP1, the original FK approach.

To render the KP theory feasible for many-body systems with N particles, we decouple the instantaneous normal mode (INM) coordinates $\left\{q^{x_0}\right\}^{3N}$ for a given configuration $\{x_0\}^{3N}$ (Wong and Gao 2007; Wong 2008; Wong and Gao 2008; Wong, Richard et al. 2009; Wong, Gu et al. 2012). Hence the multidimensional V effectively reduces to $3N$ one-dimensional potentials along each normal mode coordinate. Note that INM are naturally decoupled through the second order Taylor expansion of V. The approximation of decoupling the INM coordinates has also been used elsewhere (Stratt 1995; Deng, Ladanyi et al. 2002). This approximation is particularly suited for the KP theory because of the exponential decaying property of the Gaussian convolution integrals in Eq. (39). In the decoupling INM approximation, the total effective centroid potential for N nuclei can be simplified as:

$$W_n^{\Omega}\left(\{x_0\}^{3N}\right) \approx V\left(\{x_0\}^{3N}\right) + \sum_{i=1}^{3N} w_{i,n}^{\Omega}\left(q_i^{x_0}\right), \tag{43}$$

where $w_{i,n}^{\Omega}\left(q_i^{x_0}\right)$ is the centroid potential for normal mode i. Although the INM approximation sacrifices some accuracy, in exchange, it allows analyses of quantum mechanical vibration and tunneling, and their separate contributions to the W. Positive and negative values of w_i raise (vibration) and lower (tunneling) the original potential, respectively. In practice, real frequencies from the INM analysis often yields positive w_i's in Eq. (43) with dominant contributions from zero-point-energy effects. For imaginary frequencies in the INM, the values of w_i are often negative, due to tunneling contributions.

To obtain analytical expressions for the expectation values in Eq. (41), we use an mth order polynomial (Pm) to approximate or interpolate the potential along q_i. Hereafter, an mth order polynomial representation of the original potential energy function obtained with an interpolating step size q Å both in the forward and backward directions along the normal mode coordinate at x_0 is denoted as Pm-qA. Note that analytical results for P4 have been used by Kleinert for a quadratic-quartic anharmonic potential and a double-well potential (Kleinert 2004); however, higher order polynomials are needed to achieve the desired accuracy in real systems. We have thus derived the analytical closed forms of Eq. (41) up to P20 (Wong and Gao 2007; Wong 2008; Wong and Gao 2008; Wong, Richard et al. 2009; Wong, Gu et al. 2012). Consequently, the W as a function of an arbitrary Ω can be promptly obtained. This provides a convenient way to determine the least dependent Ω value without computing the complicated smearing integrals [Eq. (39)] iteratively for different trial values of Ω by Monte Carlo multi-dimensional numerical integrations. In fact, after the interpolating potential along each instantaneous normal-mode coordinate is determined, there is little computational cost for obtaining the W. Thereby, high level *ab initio* or density-functional (DFT) methods can be used to evaluate the potential energy function for *ab initio* path-integral calculations (Wong, Richard et al. 2009; Wong, Gu et al. 2012).

The computational procedure for obtaining the first and second order KP approximations to the centroid potential using our automated integration-free path-integral (AIF-PI) method is summarized below (Wong and Gao 2007; Wong 2008; Wong and Gao 2008; Wong, Richard et al. 2009; Wong, Gu et al. 2012):

1. For each $\{x_0\}^{3N}$, the mass-scaled Hessian matrix is diagonalized to obtain $\left\{q^{x_0}\right\}^{3N}$.
2. The original potential V is scanned from the configuration $\{x_0\}^{3N}$ along each $q_i^{x_0}$ for 10 points both in the forward and backward directions to interpolate V as P20-0.1A. A step size of 0.1 Å should be a reasonable choice to yield W in a few per cent of the exact.
3. After the P20-0.1A interpolations, each $w_{i,n}^{\Omega}(q_i^{x_0})$ as a function of Ω is readily obtained using the analytical expressions of KP1/P20 or KP2/P20. Note that the path integrals for these polynomials have been analytically integrated.
4. The values of $w_{i,n}^{\Omega}(q_i^{x_0})$ are determined by numerically locating the least dependence of $w_{i,n}^{\Omega}(q_i^{x_0})$ on Ω, i.e., zeroing the lowest order derivative of $w_{i,n}^{\Omega}(q_i^{x_0})$ w.r.t. Ω (first derivative for KP1 and usually second derivative for KP2).

The procedure presented above is integration-free and essentially automated (Wong and Gao 2007; Wong 2008; Wong and Gao 2008; Wong, Richard et al. 2009; Wong, Gu et al. 2012). We hope it could be used by non-path-integral experts or experimentalists as a "black-box" for any given system. We are currently developing a formalism to systematically couple instantaneous normal-mode coordinates.

Due to the integration-free feature, our AIF-PI method is computationally efficient such that the potential energy can be evaluated using *ab initio* or density-functional theory (DFT) for performing the so-called *ab initio* path-integral calculations. Consequently, we used DFT to construct the internuclear potential energy function for computing kinetic isotope effects (KIE) on several series of proton transfer reactions in water with the AIF-PI method. These reactions are relevant to biosynthesis of cholesterol. The computed KIE results at the KP2 level are in good agreement with experiment (Wong, Richard et al. 2009). Recently, we also employed the same computational technique to perform *ab initio* path-integral calculations of KIE on some RNA model reactions. Again, as shown in Table 2, the calculated values are in good agreement with experiments (Wong, Gu et al. 2012).

Reaction	KP2		Expt	
	$^{18}k_{Nu}$	$^{18,34}k_{Lg}$	$^{18}k_{Nu}$	$^{18,34}k_{Lg}$
Native	0.968	1.059	0.981(3)	1.034(4)
S3′	1.043	1.008	1.119(6)	1.0118(3)
S5′	1.042	1.002	1.025(5)	1.0009(1)

Table 2. Calculated primary kinetic isotope effects (KIEs) on 2′ nucleophile ($^{18}k_{Nu}$) and 5′ leaving ($^{18}k_{Lg}$ or $^{34}k_{Lg}$) oxygens for RNA-model reactions using our AIF-PI method based on second order of Kleinert's variational perturbation theory (KP2), along with the most relevant available experimental (Expt) results for comparison. Experimental errors in the last decimal place are given in parenthesis.

Another compelling feature of the AIF-PI method is that it does not suffer the convergence difficulties of PIMC or PIMD simulations at the zero-temperature limit, i.e., absolute zero temperature. At the zero-temperature limit (T = 0 K), in principle, minimizing the centroid effective potential with respect to the nuclear positions can give us two important physical quantities: the exact value of the eigenenergy for zero-point motion (i.e., the zero-point energy ZPE or the ground state energy) and the exact expectation values of the nuclear positions at the ground state (Ramírez, López-Ciudad et al. 1998; Ramírez and López-Ciudad 1999), i.e.,

$$\lim_{T\to 0} W_{\min}(x_{\min}) = E_0, \tag{44}$$

and

$$x_{\min} = \langle \psi_0 | x | \psi_0 \rangle, \tag{45}$$

where x is the position operator, and $x_{\min}$ and $W_{\min}(x_{\min})$ are, respectively, the coordinate and value at the (global) minimum of the centroid potential. In Eq. (44) and (45), ψ_0 is the nuclear ground state wave function and E_0 is the lowest eigenvalue of the Hamiltonian, i.e., the zero-point energy. In a forthcoming paper, we will have a rigorous proof showing that in fact at absolute zero temperature, there is *only one* stationary and minimum point in centroid potential, which is true even for any many-body systems. Hence, our recently derived analytical zero-temperature-limit results provide a convenient way to compute these two important physical quantities without solving the Schrödinger

equation (Wong 2008; Wong and Gao 2008), e.g., see Table 3. Together with the accurate low-lying excitation energies (Ramírez and López-Ciudad 2001) which could be obtained by the frequency analysis of the Hessian matrix at the sole minimum point at absolute zero temperature (including tunneling splitting), potentially one day our AIF-PI method could replace MC or MD *simulations* to have highly *reproducible* and *precise* free-energy *calculations* for many-body systems.

Molecule	Quantum	Harmonic	KP1	KP2
HCl	4.231	4.274	4.253	4.234
HF	5.732	5.793	5.762	5.736
H_2	6.193	6.284	6.238	6.202

Table 3. Ground state energy values (kcal/mol) for hydrogen chloride, hydrogen fluoride, and hydrogen molecules from the Morse potential using the harmonic-oscillator approximation, and our AIF-PI method based on first and second orders of the Kleinert's variational perturbation theory (KP1 and KP2).

Born-Oppenheimer Approximation	
Electronic Schrödinger equation *Ab initio* molecular orbital theory	**Internuclear** Schrödinger equation Systematic internuclear thermodynamics theory
Most molecular properties of interest are at **low lying electronic energy states**	All thermodynamic properties virtually can be derived from **quantum partition functions**
Hartree-Fock (HF) theory	**Kleinert's variational perturbation theory** for centroid effective potential
Independent electron (single-electron) approximation	**Decoupled instantaneous normal coordinate** approximation (DINCA)
Roothaan and Hall expressed the Fock operator in terms of **basis functions** for solving HF equations in matrix algebra self-consistently (SCF)	We propose interpolating potential energy functions to *m*th order **polynomials** in which analytic results of path-integration can be derived
Explain chemical properties in terms of **frontier occupied** and **unoccupied** molecular orbitals	Quantum effects from **vibration** and **tunneling** are separated and quantified in one mathematical framework
Post Hartree-Fock method to include **correlation energy by systematically couple single-electron orbitals**	Work out a formalism to **systematically couple instantaneous normal coordinates**

Table 4. Comparison (1) between Kleinert's variational perturbation (KP) theory and Hartree-Fock (HF) theory, (2) between our decoupled instantaneous normal coordinate approximation and independent electron approximation, and (3) between our integration-free path-integral results for polynomials in the KP theory and Roothann-Hall basis function approach for HF theory.

Finally, we make a quite interesting table (Table 4) to compare the traditional *ab initio* molecular orbital theory for electronic structure calculations with our systematic approach for computing internuclear quantum effects. In short, the rigor and the spirit of both types of methods is the same. We first breakdown or dissect a complicated many-body problem into many one-body problems. Then we identify which one bodies are more important. Next we couple back those important one bodies to systematically approach the exact.

6. Systematic *ab initio* path-integral free-energy expansion approach

In order to systematically refine a classical free-energy profile to become ultimate quantum free-energy profile, in which both electrons and nuclei are treated quantum mechanically and adiabatically, we are developing a systematic *ab initio* path-integral free-energy expansion (SAI-PI-FEE; $\psi\pi\phi$) approach. In this $\psi\pi\phi$ approach, we combine our novel free-energy expansion (FEE) method (Section 4) with our automated integration-free path-integral (AIF-PI) method (Section 5.2) such that we can perform *ab initio* path-integral simulations for realistic molecular systems. The key of this combination is that first we realize the quantum partition function can be computed as a classical configuration shown in Eq. (27), then now in Eq. (23), we treat the ΔE as:

$$\Delta E = W - V, \tag{46}$$

where V is the original internuclear potential and W is the centroid potential. So once we get the accurate value of W using our AIF-PI method, we can go ahead using our FEE method to systematically upgrade the level of our classical free-energy profile to an *ab initio* path-integral level, in which zero-point energy and tunnelling effects in nuclei, and isotope effects could all be incorporated.

In order to rigorously validate our $\psi\pi\phi$ method in a more effective way, the free-energy perturbation (FEP) in the Hamiltonian space will be performed, using the recently derived "universal" probability density function (UPDF), which is defined as follows:

$$P(\Delta E) = K \exp\left\{a\left[b(\Delta E - s) - e^{b(\Delta E - s)}\right]\right\}. \tag{47}$$

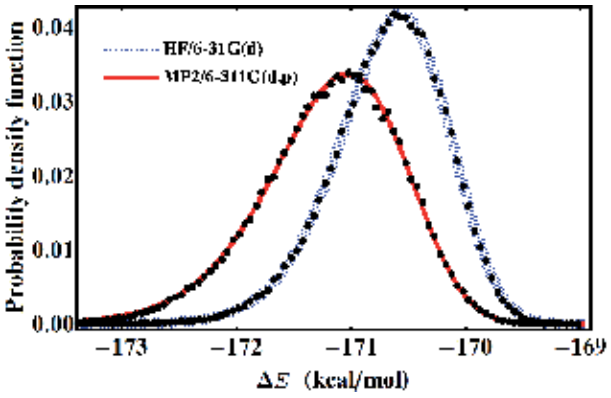

Fig. 1. Free energy perturbation for a water molecule in the Hamiltonian space using the universal probability density function (UPDF).

This UPDF can be used to determine the change of free energy ΔG in Eq. (23), by simply locating the intersection point of two probability density functions (Nanda, Lu et al. 2005; Chipot and Pohorille 2007). In Eq. (47), ΔE is a variable for the difference of the Hamiltonian or energy between two levels of theory, while K, a, b, and s are the fitting parameters. In Figure 1, we demonstrate the simultaneous fitting to the UPDF to determine the change of free-energy for a water molecule from HF/6-31G(d) to MP2/6-311G(d,p). The intersection point of the two probability functions at −170.917 kcal/mol is the best estimate value for the ΔG in Table 1 above.

7. Conclusion and outlook

In this chapter, we (wongky@biomaps.rutgers.edu; kiniu@alumni.cuhk.net) discuss developing the $\psi\pi\phi$ method to systematically generate quantum free-energy profiles at an *ab initio* path-integral level in molecular simulations. Since quantum free energy or partition function is a universal central quantity in thermodynamics of biology, chemistry, and physics, we anticipate our $\psi\pi\phi$ method would be very crucial in both Life and Materials Sciences and wish that it could be used by non-specialists as a black box one day.

8. References

Anderson, J. B. (1975). Random-walk simulation of the Schroedinger equation. Hydrogen ion (H_3^+). *Journal of Chemical Physics*, Vol. 63, No. 4, pp. 1499-1503.

Arfken, G. B. and H.-J. Weber (2001). *Mathematical methods for physicists*. San Diego, Academic Press. See exercise 2.2.3 for the fundamental definition of an orthogonal unit vector; See section 2.10 for the discussion of the covariant and contravariant vectors.

Ballhausen, C. J. and A. E. Hansen (1972). Electronic spectra. *Annual Review of Physical Chemistry*, Vol. 23, pp. 15-38.

Birkhoff, G. D. (1931). Proof of the Ergodic Theorem. *Proceedings of the National Academy of Sciences of the United States of America*, Vol. 17, No. 12, pp. 656-660.

Born, M. and J. R. Oppenheimer (1927). Zur Quantentheorie der Molekeln (On the Quantum Theory of Molecules). *Annalen der Physik*. 84,pp. 457-484. English translation: *Quantum chemistry : classic scientific papers,* Hettema, H., Ed.; World Scientific: Singapore; London, 2000, pp 1-24.

Brooks, B. R., R. E. Bruccoleri, et al. (1983). CHARMM: a program for macromolecular energy, minimization, and dynamics calculations. *Journal of Computational Chemistry*, Vol. 4, No. 2, pp. 187-217.

Brown, L. M. (2005). *Feynman's thesis : a new approach to quantum theory*. Singapore ; Hackensack, NJ, World Scientific.

Cao, J. and G. A. Voth (1994). The formulation of quantum statistical mechanics based on the Feynman path centroid density. IV. Algorithms for centroid molecular dynamics. *Journal of Chemical Physics*, Vol. 101, No. 7, pp. 6168-6183.

Car, R. and M. Parrinello (1985). Unified approach for molecular dynamics and density-functional theory. *Physical Review Letters*, Vol. 55, No. 22, pp. 2471-2474.

Ceperley, D. M. (1995). Path integrals in the theory of condensed helium. *Reviews of Modern Physics*, Vol. 67, No. 2, pp. 279-355.

Chipot, C. and A. Pohorille (2007). Calculating free energy differences using perturbation theory. *Springer Series in Chemical Physics.*, Vol. 86, Free Energy Calculations, pp. 33-75.

Coalson, R. D. (1986). On the connection between Fourier coefficient and Discretized Cartesian path integration. *Journal of Chemical Physics*, Vol. 85, No. 2, pp. 926-936.

Cogswell, K. (1999). Computers and Advanced Mathematics in the Calculus Classroom. *The College Mathematics Journal*, Vol. 30, No. 3, pp. 213-216.

Dean, D. J. (2007). Beyond the nuclear shell model. *Physics Today*, Vol. 60, No. 11, pp. 48-53.

den Otter, W. K. (2000). Thermodynamic integration of the free energy along a reaction coordinate in Cartesian coordinates. *Journal of Chemical Physics*, Vol. 112, No. 17, pp. 7283-7292.

Deng, Y., B. M. Ladanyi, et al. (2002). High-frequency vibrational energy relaxation in liquids: the foundations of instantaneous-pair theory and some generalizations. *Journal of Chemical Physics*, Vol. 117, No. 23, pp. 10752-10767.

Doll, J. D. and L. E. Myers (1979). Semiclassical Monte Carlo methods. *Journal of Chemical Physics*, Vol. 71, No. 7, pp. 2880-2883.

Feynman, R. P. (1948). Space-Time Approach to Non-Relativistic Quantum Mechanics. *Reviews of Modern Physics*, Vol. 20, No. 2, pp. 367-387.

Feynman, R. P. (1966). The development of the space-time view of quantum electrodynamics. *Science*, Vol. 153, No. 3737, pp. 699-708.

Feynman, R. P., A. R. Hibbs, et al. (2005). *Quantum mechanics and path integrals*. Mineola, N.Y., Dover Publications.

Feynman, R. P. and H. Kleinert (1986). Effective classical partition functions. *Physical Review A*, Vol. 34, No. 6, pp. 5080-5084.

Field, M. J., P. A. Bash, et al. (1990). A combined quantum mechanical and molecular mechanical potential for molecular dynamics simulations. *Journal of Computational Chemistry*, Vol. 11, No. 6, pp. 700-733.

Fixman, M. (1974). Classical statistical mechanics of constraints: a theorem and application to polymers. *Proceedings of the National Academy of Sciences of the United States of America,* Vol. 71, No. 8, pp. 3050-3053.

Flanders, H. (1973). Differentiation Under the Integral Sign. *The American Mathematical Monthly,* Vol. 80, No. 6, pp. 615-627.

Gao, J., K.-Y. Wong, et al. (2008). Combined QM/MM and path integral simulations of kinetic isotope effects in the proton transfer reaction between nitroethane and acetate ion in water. *Journal of Computational Chemistry,* Vol. 29, No. 4, pp. 514-522.

Gao, J., D. T. Major, et al. (2008). Hybrid quantum and classical methods for computing kinetic isotope effects of chemical reactions in solutions and in enzymes. *Molecular Modeling of Proteins*. A. Kukol, Humana Press: 37-62.

Gao, J. and D. G. Truhlar (2002). Quantum mechanical methods for enzyme kinetics. *Annual Review of Physical Chemistry*, Vol. 53, pp. 467-505.

Giachetti, R. and V. Tognetti (1985). Variational approach to quantum statistical mechanics of nonlinear systems with application to sine-Gordon chains. *Physical Review Letters*, Vol. 55, No. 9, pp. 912-915.

Gillan, M. J. (1987). Quantum-classical crossover of the transition rate in the damped double well. *Journal of Physics C: Solid State Physics*, Vol. 20, No. 24, pp. 3621-3641.

Gillan, M. J. (1987). Quantum simulation of hydrogen in metals. *Physical Review Letters*, Vol. 58, No. 6, pp. 563-566.

Grossman, J. C. and L. Mitas (2005). Efficient Quantum Monte Carlo Energies for Molecular Dynamics Simulations. *Physical Review Letters*, Vol. 94, No. 5, pp. 056403/056401-056403/056404.

Hagler, A. T., E. Huler, et al. (1974). Energy functions for peptides and proteins. I. Derivation of a consistent force field including the hydrogen bond from amide crystals. *Journal of the American Chemical Society*, Vol. 96, No. 17, pp. 5319-5327.

Hayashi, A., M. Shiga, et al. (2006). H/D isotope effect on the dihydrogen bond of $NH4^{+}$.BeH2 by ab initio path integral molecular dynamics simulation. *Journal of Chemical Physics*, Vol. 125, No. 20, pp. 204310.

Hehre, W. J., L. Radom, et al. (1986). *Ab initio molecular orbital theory*. New York, Wiley.

Helgaker, T., P. Jørgensen, et al. (2000). *Molecular electronic-structure theory*. Chichester ; New York, Wiley.

Hénin, J. r., G. Fiorin, et al. (2010). Exploring Multidimensional Free Energy Landscapes Using Time-Dependent Biases on Collective Variables. *Journal of Chemical Theory and Computation*, Vol. 6, No. 1, pp. 35-47.

Hirschfelder, J. O. and W. J. Meath (1967). Nature of intermolecular forces. *Advances in Chemical Physics*, Vol. 12, pp. 3-106.

Hünenberger, P. H. (2005). Thermostat Algorithms for Molecular Dynamics Simulations. *Advances in Polymer Science*, Vol. 173, pp. 105-149.

Jorgensen, W. L. and J. Tirado-Rives (1988). The OPLS [optimized potentials for liquid simulations] potential functions for proteins, energy minimizations for crystals of cyclic peptides and crambin. *Journal of the American Chemical Society*, Vol. 110, No. 6, pp. 1657-1666.

Kirkwood, J. G. (1935). Statistical mechanics of fluid mixtures. *Journal of Chemical Physics*, Vol. 3, No. 5, pp. 300-313.

Kleinert, H. (2004). *Path integrals in quantum mechanics, statistics, polymer physics, and financial markets*. Singapore; River Edge, NJ, World Scientific. For the quantum mechanical integral equation, see Section 1.9; For the variational perturbation theory, see Chapters 3 and 5.

Kleppner, D. and R. Jackiw (2000). Pathways of discovery: One hundred years of quantum physics. *Science*, Vol. 289, No. 5481, pp. 893-898.

Kohn, W. (1999). Nobel lecture: electronic structure of matter-wave functions and density functionals. *Reviews of Modern Physics*, Vol. 71, No. 5, pp. 1253-1266.

Kolos, W. (1970). Adiabatic approximation and its accuracy. *Advances in Quantum Chemistry*, Vol. 5, pp. 99-133.

Kowalczyk, P., P. A. Gauden, et al. (2008). Cryogenic Separation of Hydrogen Isotopes in Single-Walled Carbon and Boron-Nitride Nanotubes: Insight into the Mechanism of Equilibrium Quantum Sieving in Quasi-One-Dimensional Pores. *Journal of Physical Chemistry B*, Vol. 112, No. 28, pp. 8275-8284.

Kowalczyk, P., P. A. Gauden, et al. (2007). Thermodynamics of Hydrogen Adsorption in Slit-like Carbon Nanopores at 77 K. Classical versus Path-Integral Monte Carlo Simulations. *Langmuir*, Vol. 23, No. 7, pp. 3666-3672.

Kubo, R. (1962). Generalized Cumulant Expansion Method. *Journal of the Physical Society of Japan*, Vol. 17, No. 7, pp. 1100-1120.

Lebowitz, J. L. and O. Penrose (1973). Modern Ergodic Theory. *Physics Today*, Vol. 26, No. 2, pp. 23-29.

Lester, W. A. and R. Salomon-Ferrer (2006). Some recent developments in quantum Monte Carlo for electronic structure: Methods and application to a bio system. *Theochem*, Vol. 771, No. 1-3, pp. 51-54.

MacKeown, P. K. (1985). Evaluation of Feynman path integrals by Monte Carlo methods. *American Journal of Physics*, Vol. 53, No. 9, pp. 880-885.

Major, D. T., A. Heroux, et al. (2009). Differential quantum tunneling contributions in nitroalkane oxidase catalyzed and the uncatalyzed proton transfer reaction. *Proceedings of the National Academy of Sciences of the United States of America*, Vol. 106, No. 49, pp. 20734-20739.

Marx, D. and M. Parrinello (1995). Structural quantum effects and three-center two-electron bonding in $CH5^+$. *Nature (London)*, Vol. 375, No. 6528, pp. 216-218.

Marx, D., M. E. Tuckerman, et al. (1999). Quantum dynamics via adiabatic ab initio centroid molecular dynamics. *Computer Physics Communications*, Vol. 118, No. 2-3, pp. 166-184.

Mayo, S. L., B. D. Olafson, et al. (1990). DREIDING: a generic force field for molecular simulations. *Journal of Physical Chemistry*, Vol. 94, No. 26, pp. 8897-8909.

McQuarrie, D. A. (2000). *Statistical mechanics*. Sausalito, Calif., University Science Books

Mielke, S. L., K. A. Peterson, et al. (2003). $H+H_2$ Thermal Reaction: A Convergence of Theory and Experiment. *Physical Review Letters*, Vol. 91, No. 6, pp. 063201.

Mielke, S. L. and D. G. Truhlar (2001). Displaced-points path integral method for including quantum effects in the Monte Carlo evaluation of free energies. *Journal of Chemical Physics*, Vol. 115, No. 2, pp. 652-662.

Mielke, S. L. and D. G. Truhlar (2001). A new Fourier path integral method, a more general scheme for extrapolation, and comparison of eight path integral methods for the quantum mechanical calculation of free energies. *Journal of Chemical Physics*, Vol. 114, No. 2, pp. 621-630.

Nanda, H., N. Lu, et al. (2005). Using non-Gaussian density functional fits to improve relative free energy calculations. *Journal of Chemical Physics*, Vol. 122, No. 13, pp. 134110/134111-134110/134118.

Ohta, Y., K. Ohta, et al. (2004). Ab initio centroid path integral molecular dynamics: Application to vibrational dynamics of diatomic molecular systems. *Journal of Chemical Physics*, Vol. 120, No. 1, pp. 312-320.

Paesani, F., S. Iuchi, et al. (2007). Quantum effects in liquid water from an ab initio-based polarizable force field. *Journal of Chemical Physics*, Vol. 127, No. 7, pp. 074506.

Pople, J. A. (1999). Nobel lecture: Quantum chemical models. *Reviews of Modern Physics*, Vol. 71, No. 5, pp. 1267-1274.

Ramírez, R. and T. López-Ciudad (1999). The Schroedinger formulation of the Feynman path centroid density. *Journal of Chemical Physics*, Vol. 111, No. 8, pp. 3339-3348.

Ramírez, R., T. López-Ciudad, et al. (1998). Feynman Effective Classical Potential in the Schrödinger Formulation. *Physical Review Letters*. 81,pp. 3303-3306. Comment: Andronico, G.; Branchina, V.; Zappala, D. *Phys. Rev. Lett.* 2002, *88,* 178901; Reply to comment: Ramirez, R.; López-Ciudad, T. *Phys. Rev. Lett.* 2002, *88,* 178902.

Ramírez, R., T. López-Ciudad, et al. (2001). Low lying vibrational excitation energies from equilibrium path integral simulations. *Journal of Chemical Physics,* Vol. 115, No. 1, pp. 103-114.

Ruiz-Montero, M. J., D. Frenkel, et al. (1997). Efficient schemes to compute diffusive barrier crossing rates. *Molecular Physics*, Vol. 90, No. 6, pp. 925-942.

Sauer, T. (2001). The Feynman path goes Monte Carlo. *Fluctuating paths and fields : festschrift dedicated to Hagen Kleinert on the occasion of his 60th birthday*. W. Janke, A. Pelster, H.-J. Schmidt and M. Bachmann. River Edge, NJ, World Scientific,pp. 29-42. And in Los Alamos National Laboratory, Preprint Archive, Physics arXiv:physics/0107010v1 [physics.hist-ph], 1 (2001).

Springborg, M. (2000). *Methods of electronic-structure calculations : from molecules to solids*. Chichester ; New York, Wiley.

Stratt, R. M. (1995). The Instantaneous Normal Modes of Liquids. *Accounts of Chemical Research*, Vol. 28, No. 5, pp. 201-207.

Szabo, A. and N. S. Ostlund (1996). *Modern quantum chemistry : introduction to advanced electronic structure theory*. Mineola, N.Y., Dover Publications

Tanaka, H., H. Kanoh, et al. (2005). Quantum Effects on Hydrogen Isotope Adsorption on Single-Wall Carbon Nanohorns. *Journal of the American Chemical Society*, Vol. 127, No. 20, pp. 7511-7516.

Tuckerman, M. E. and D. Marx (2001). Heavy-Atom Skeleton Quantization and Proton Tunneling in "Intermediate-Barrier" Hydrogen Bonds. *Physical Review Letters*, Vol. 86, No. 21, pp. 4946-4949.

Tuckerman, M. E., D. Marx, et al. (1997). On the quantum nature of the shared proton in hydrogen bonds. *Science*, Vol. 275, No. 5301, pp. 817-820.

Tuckerman, M. E., D. Marx, et al. (2002). The nature and transport mechanism of hydrated hydroxide ions in aqueous solution. *Nature*, Vol. 417, No. 6892, pp. 925-929.

Voth, G. A. (1996). Path-integral centroid methods in quantum statistical mechanics and dynamics. *Advances in Chemical Physics*, Vol. 93, New Methods in Computational Quantum Mechanics, pp. 135-218.

Wagner, L. K., M. Bajdich, et al. (2009). QWalk: A quantum Monte Carlo program for electronic structure. *Journal of Computational Physics*, Vol. 228, No. 9, pp. 3390-3404.

Warshel, A., M. H. M. Olsson, et al. (2006). Computer simulations of isotope effects in enzyme catalysis. *Isotope Effects in Chemistry and Biology*. A. Kohen and H.-H. Limbach. Boca Raton, Taylor & Francis: 621-644.

Weiner, S. J., P. A. Kollman, et al. (1984). A new force field for molecular mechanical simulation of nucleic acids and proteins. *Journal of the American Chemical Society*, Vol. 106, No. 3, pp. 765-784.

Wong, K.-Y. (2008). Simulating biochemical physics with computers: 1. Enzyme catalysis by phosphotriesterase and phosphodiesterase; 2. Integration-free path-integral

method for quantum-statistical calculations. Ph.D. thesis, Minneapolis, University of Minnesota (USA), pp. 342.

Wong, K.-Y. and J. Gao (2007). The Reaction Mechanism of Paraoxon Hydrolysis by Phosphotriesterase from Combined QM/MM Simulations. *Biochemistry,* Vol. 46, No. 46, pp. 13352-13369.

Wong, K.-Y., T.-S. Lee, et al. (2011). Active Participation of the Mg^{2+} Ion in the Reaction Coordinate of RNA Self-Cleavage Catalyzed by the Hammerhead Ribozyme. *Journal of Chemical Theory and Computation.* Vol. 7, No. 1, pp. 1-3.

Wong, K.-Y. and J. Gao (2011). Insight into the phosphodiesterase mechanism from combined QM/MM free energy simulations. *FEBS Journal,* Vol. 278, No. 14, pp. 2579-2595.

Wong, K.-Y. and J. Gao (2007). An automated integration-free path-integral method based on Kleinert's variational perturbation theory. *Journal of Chemical Physics*, Vol. 127, No. 21, pp. 211103.

Wong, K.-Y. and J. Gao (2008). Systematic Approach for Computing Zero-Point Energy, Quantum Partition Function, and Tunneling Effect Based on Kleinert's Variational Perturbation Theory. *Journal of Chemical Theory and Computation*, Vol. 4, No. 9, pp. 1409-1422.

Wong, K.-Y., J. P. Richard, et al. (2009). Theoretical Analysis of Kinetic Isotope Effects on Proton Transfer Reactions between Substituted alpha -Methoxystyrenes and Substituted Acetic Acids. *Journal of the American Chemical Society*, Vol. 131, No. 39, pp. 13963-13971.

Wong, K.-Y., H. Gu, et al. (2012). Characterization of the Reaction Path and Transition States for RNA Transphosphorylation Models from Theory and Experiment. *Angewandte Chemie, International Edition*, Vol. 51, No.3, pp. 647-651.

Wu, E. L., K.-Y. Wong, et al. (2009). Determination of the Structure Form of the Fourth Ligand of Zinc in Acutolysin A Using Combined Quantum Mechanical and Molecular Mechanical Simulation. *Journal of Physical Chemistry B,* Vol. 113, No.8, pp. 2477-2485.

Zwanzig, R. W. (1954). High-temperature equation of state by a perturbation method. I. Nonpolar gases. *Journal of Chemical Physics*, Vol. 22, No. 8, pp. 1420-1426.

7

Antisymmetrized Molecular Dynamics and Nuclear Structure

Gaotsiwe J. Rampho and Sofianos A. Sofianos
Department of Physics, University of South Africa
South Africa

1. Introduction

One of the aims of nuclear physics studies is to establish a complete theoretical description of the structure of nuclear systems. The correct theoretical description of nuclear structure is expected to help explain and accurately predict different properties of and process in nuclei (Donnelly & Raskin, 1986). Fundamental to a complete description of nuclear structure are the wave function describing nuclear systems, the Hamiltonian describing interactions in the nucleus and electromagnetic form factors describing charge and currents distributions in the nucleus. None of these components is completely understood and, therefore, none can be completely determined for a given nuclear system, yet. As a result, theoretical models of these components, based on different approximations that are guided by experimental observations, are usually employed in the description of nuclear systems. The quality of such models is often judged by their ability to explain existing experimental observations. Parallel to the theoretical developments, the developments in experimental technologies has led not only to the availability of more precise experimental data, but also to data in kinematical regions previously not accessible. The availability of precise experimental data in a wide kinematical region allow for more accurate quantitative testing and, therefore, development of realistic theoretical models that, in turn, generate more accurate predictions of experimental outcomes (Golak et al., 2005).

Besides the understanding of static and dynamical properties of nuclear matter, studies in nuclear physics are aimed at constructing a comprehensive description of properties of nucleon-nucleon interactions. Few-nucleon systems provide unique favourable environment for such investigations (Rampho, 2010). In theoretical investigations, the interaction models in few-nucleon systems can be treated realistically and the resulting dynamical equations can be solved directly. The formulation and solution of dynamical equations for many-body systems is, on the other hand, quite challenging. Progress towards a better understanding of the nuclear force has been made over the years. Based on the accumulated experimental nucleon-nucleon scattering data different phenomenological nucleon-nucleon interaction models have been suggested. The models are constructed by fitting the models to existing nucleon-nucleon scattering data as well as some properties of the ^{2}H nucleus (Cottingham et al., 1973; Lagaris & Pandharipande, 1981; Machleidt et al., 1987; Nagels et al., 1978; Wiringa et al., 1984). These interaction models are known as modern or realistic nucleon-nucleon potentials and are able to explain most of the static properties of light nuclei. Since the exact form of the short-range behavior of the nucleon-nucleon interaction is not completely determined, yet, the short-range part of many of these potential models is

often musked by introducing short-distance cut-off factors. Knowledge of the short-range behavior of the nucleon-nucleon force may reveal some information about the limits and boundaries between hadronic degrees of freedom and quark degrees of freedom. The suggestion that the short-range behavior of the strong nuclear interaction could manifest itself through short-range nucleon-nucleon correlations and momentum distributions in a nucleus (Schroeder et al., 1979) refocused the need for a better understanding of, and therefore more intensive investigations into, these concepts. Hence, there are continued experimental (Egiyan et al., 2007; 2006; Jones et al., 2000; Ulmer et al., 2002) and theoretical (Alvioli et al., 2008; Frankfurt et al., 1993; Piasetzky et al., 2006) investigations of these concepts.

Over the years a variety of methods have been developed and refined in the study of properties of nuclei. Very accurate wave functions for bound and scattering states in few-nucleon systems can now be constructed using realistic Hamiltonian for the systems. A demonstration of the level of accuracy that can now be achieved in describing ground state properties of the four-nucleon system using seven different state-of-the-art methods is given in reference (Kamada et al., 2001). The use of some of these methods in the study of properties of few-nucleon systems is shown in references (Carlson & Schiavilla, 1998; Golak et al., 2005). The application of these methods to systems consisting of more than four particles is still a challenge. For investigations of light to medium nuclei microscopic models have been employed in the study of static and dynamical properties of nuclei (Aichelin, 1991; Boffi et al., 1968; Kanada-En'yo et al., 2003; Neff et al., 2005; Ono & Horiuchi, 2004). These methods are continuously developing. Following the Time-Dependent Cluster Model (Caurier et al., 1982), microscopic simulation models were developed (Feldmeier, 1990; Horiuchi, 1991) for the study of fermionic systems. These models combine Fermi-Dirac statistics with elementary quantum mechanics to treat the motion of particles in a system (Feldmeier, 1990). However, the models are not fully quantum mechanical and do not assume a shell structure for the system. In this work the antisymmetrized molecular dynamics (AMD) approach is employed. The AMD total wave function is constructed as Slater determinant of single particle shifted Gaussian wave functions. The shift parameters of the Gaussian functions are complex variational parameters which are treated as generalised coordinates of the system. The width parameters are taken as free real parameters and are chosen to be the same for all the Gaussian. The equations of motion for the variational parameters are determined from the time-dependent variational principle. The equations are then solved by using the frictional cooling technique (Ono et al., 1992) to determine the variational parameters.

In the past, the AMD approach was employed in the study of dynamics of heavy-ion collisions (Ono et al., 1992) and elastic proton-nucleus scattering (Engel et al., 1995; Tanaka et al., 1995). Clustering in nuclei as well as angular distributions of scattered protons in proton-nucleus scattering can be well explained with the AMD model (Tanaka et al., 1995). Some properties and/or processes in physical systems are governed by conservation laws related to parity and total angular momentum of the system. Such systems are best described in terms of wave functions that have definite parity and angular momentum. The AMD wave function does not have definite parity nor does it possess definite total angular momentum. As a result, for applications in realistic investigations of properties of physical systems the AMD wave function requires some improvement. A number of modifications have since been introduced in the AMD formalism. In reference (Kanada-En'yo et al., 1995) numerical technique are used to project the AMD wave function onto the eigenstates of parity and total angular momentum. The resulting wave functions have definite parity and total angular momentum. In addition, a number of different techniques were considered for constructing a more flexible total wave function. One way was to use linear combinations

of variational spatial, spin and isospin functions to represent single-particle wave functions (Doté & Horiuchi, 2000; Doté et al., 2006). The resulting wave functions are suitable for investigating systems with tensor forces. The other approach is to use a linear combination of several Slater determinants (Kanada-En'yo et al., 1995; 2003; Kimura, 2004) to represent the total wave function of the system. In the approach of reference (Doté et al., 1997) orthogonal single-particle wave functions characteristic of the Hartree-Fock orbitals are constructed from the AMD wave function. The AMD+Hartree-Fock wave function is also more flexible than the original AMD wave function. These modifications to the AMD wave function introduced significant improvements in the description of ground-state properties, mean-field and cluster structure of nuclear systems. It should be noted that most of the studies indicated employed phenomenological nucleon-nucleon potentials of Gaussian radial form. The main reason for this is that the expectation values of this type of potentials can be evaluated analytically.

To extend the application of the AMD approach to realistic potentials further proposals were made. In Refs. (Togashi & Kat$\bar{o}$, 2007; Togashi et al., 2009) the *G*-matrix approach was used to incorporate two-body correlations in the wave function. The resulting Bruckner-AMD wave function can be constructed with realistic nuclear potentials. In Ref. (Watanabe et al., 2009; Watanabe & Oryu, 2006) Jacobi coordinates are employed to construct the wave function. Many-body correlations are included, more variational parameters are considered and the effects of the center-of-mass are completely and explicitly removed. Most realistic potentials are of non-Gaussian form and are, in many cases, expanded as the sum-of-Gaussian for application in the AMD approach. In Ref. (Rampho, 2011) a numerical technique of evaluating expectation values of non-Gaussian potentials is introduced. The technique approximates the expectation value of the potential operator with a rapidly converging series of Talmi integrals. This technique is further elaborated on in this work. Ground-state properties of selected few-nucleon systems are determined using the Argonne V4′ nucleon-nucleon potential.

In section 2 the construction of the AMD wave function is outlined while the variational technique used to determine the variational parameters is briefly discussed in section 3. Application of AMD to selected light nuclei is presented in section 4 while section 5 is devoted to the charge form factors of ground state in three- and four-nucleon systems. Conclusions are given in section 6.

2. The AMD wave function

Consider a nuclear system consisting of A nucleons. The wave function Ψ describing the system depends on the position $\vec{r}_i$, spin $\vec{\sigma}_i$ and isospin $\vec{\tau}_i$ $(i = 1, 2, 3, \ldots, A)$, vectors of the nucleons. In what follows the collective vector, $\vec{v}_i$, is used to represent the set $\{\, \vec{s}_i\, \vec{r}_i\, \vec{\sigma}_i\, \vec{\tau}_i \,\}$ where $\vec{s}_i$ is a complex variational parameter. For a systems of fermions, like nuclei, the total wave function is required to be antisymmetric with respect to the interchange of any two particles in the system. One way of constructing such a wave function is by the use of Slater determinants of single-particle wave functions $\psi_i(\vec{v}_j)$ as

$$\Psi_t(\vec{v}_1, \vec{v}_2, \vec{v}_3, \ldots, \vec{v}_A) = \frac{1}{\sqrt{A!}} \begin{vmatrix} \psi_1(\vec{v}_1) & \psi_2(\vec{v}_1) & \psi_3(\vec{v}_1) & \cdots & \psi_A(\vec{v}_1) \\ \psi_1(\vec{v}_2) & \psi_2(\vec{v}_2) & \psi_3(\vec{v}_2) & \cdots & \psi_A(\vec{v}_2) \\ \psi_1(\vec{v}_3) & \psi_2(\vec{v}_3) & \psi_3(\vec{v}_3) & \cdots & \psi_A(\vec{v}_3) \\ \vdots & \vdots & \vdots & \ddots & \vdots \\ \psi_1(\vec{v}_A) & \psi_2(\vec{v}_A) & \psi_3(\vec{v}_A) & \cdots & \psi_A(\vec{v}_A) \end{vmatrix} . \quad (1)$$

The functions $\psi_i(\vec{v}_j)$ do not form an orthogonal basis. However, an orthonormal basis can be constructed from these functions (Doté et al., 1997; Togashi & Katō, 2007; Togashi et al., 2009). The ground state wave function of the system is represented by $\Psi_t(\vec{\mathrm{S}})$ where $\vec{\mathrm{S}} \equiv \{\vec{s}_1, \vec{s}_2, \vec{s}_3, \ldots, \vec{s}_A\}$.

The single-particle wave function $\psi(\vec{v})$ is assumed to be separable in the form

$$\psi(\vec{v}) \;=\; \phi(\vec{s},\vec{r})\,\chi(\vec{\sigma})\,\xi(\vec{\tau}) \tag{2}$$

where $\phi(\vec{s},\vec{r})$, $\chi(\vec{\sigma})$, and $\xi(\vec{\tau})$ are the spatial, spin and isospin wave functions, respectively. The intrinsic spin state $\chi(\vec{\sigma})$ of a fermion, with spin s and third component of the spin m_s, is denoted by

$$\chi(\vec{\sigma}) \;=\; |\, s\,,\, m_s \,\rangle = \begin{cases} \left|\, \tfrac{1}{2}\,,\, +\tfrac{1}{2} \,\right\rangle = |\uparrow\rangle \\ \left|\, \tfrac{1}{2}\,,\, -\tfrac{1}{2} \,\right\rangle = |\downarrow\rangle \end{cases} \tag{3}$$

where $|\uparrow\rangle$ represents the *spin-up* and $|\downarrow\rangle$ the *spin-down* state. These two spin states are orthogonal to each other. To improve the quality of the wave function the spins of the fermions may be allowed to vary. This is done by representing the fermion spin as a general spinor. Such a spinor is expressed as a linear combination of the spin-up and spin-down states using complex variational parameters (Kanada-En'yo et al., 2003). The isospin state, $\xi(\vec{\tau})$, in the case of a nucleon, with isospin t and third component of the isospin m_t, is given by

$$\xi(\vec{\tau}) \;=\; |\, t\,,\, m_t \,\rangle = \begin{cases} \left|\, \tfrac{1}{2}\,,\, +\tfrac{1}{2} \,\right\rangle = |\, p \,\rangle \\ \left|\, \tfrac{1}{2}\,,\, -\tfrac{1}{2} \,\right\rangle = |\, n \,\rangle \end{cases} \tag{4}$$

where $|\, p \,\rangle$ refers to a proton while $|\, n \,\rangle$ refers to a neutron state. These states are time-independent also.

All the constituent particles are described by the same form of the spatial wave function. The spatial component, $\phi(\vec{s},\vec{r})$, is parametrized as a normalized Gaussian wave packet (Ono et al., 1992)

$$\phi(\vec{s},\vec{r}) = \left(\frac{2\alpha}{\pi}\right)^{3/4} \exp\left[-\alpha\left(\vec{r} - \frac{\vec{s}}{\sqrt{\alpha}}\right)^2 + \frac{\vec{s}^{\,2}}{2}\right] . \tag{5}$$

The phase $\vec{s}^{\,2}/2$ is included mainly to simplify the structure of the elements of the resulting overlap matrix, $\langle\, \phi_i \,|\, \phi_j \,\rangle$. The width parameter α is treated as a real constant and assumed to be the same for both protons and neutrons in the nucleus. It can be argued that the assumption is still valid if the masses of the constituents are not significantly different, like in nuclear systems. When the momentum operator of a fermion is denoted by $\vec{p}$, then the real component $\mathrm{Re}[\vec{s}]$ and the imaginary component $\mathrm{Im}[\vec{s}]$ of the parameter $\vec{s}$ are given by

$$\mathrm{Re}[\vec{s}] \;=\; \sqrt{\alpha}\,\frac{\langle\, \phi(\vec{r}) \,|\, \vec{r}\,|\, \phi(\vec{r}) \,\rangle}{\langle\, \phi(\vec{r}) \,|\, \phi(\vec{r}) \,\rangle} \qquad \text{and} \qquad \mathrm{Im}[\vec{s}] \;=\; \frac{1}{2\hbar\,\sqrt{\alpha}}\,\frac{\langle\, \phi(\vec{r}) \,|\, \vec{p}\,|\, \phi(\vec{r}) \,\rangle}{\langle\, \phi(\vec{r}) \,|\, \phi(\vec{r}) \,\rangle} \;. \tag{6}$$

The single-particle wave function in Eq. (5) satisfies the minimum uncertainty $\Delta\vec{r}\,\Delta\vec{p} = \hbar/2$ (Ono & Horiuchi, 2004) which helps in the choice of the value for the width parameter α. Following Ref. (Ono et al., 1992), the value of α is chosen so as to generate reasonable description of the ground state properties of light nuclei. The expectation values of relevant operators calculated with this form of the wave function can be determined in analytical form.

A more realistic wave function is constructed from the AMD wave function (1) by projecting on to states with definite parity π and total angular momentum J. The parity projected wave function has the form

$$\Psi^{\pi} = \frac{1}{2}\left[1 \pm P^{\pi}\right]\Psi(\vec{S}) \tag{7}$$

where P^{π} is the parity projection operator. A wave function with a definite parity π, total angular momentum J, and angular momentum projections MK, is constructed from the AMD wave function as

$$\Psi^{J\pi}_{MK} = \frac{1}{2}\, P^{J}_{MK}(\Omega)\, \left[1 \pm P^{\pi}\right]\, \Psi_{AMD} \tag{8}$$

where $P^{J}_{MK}(\Omega)$ is the angular momentum projection operator, P^{π} the parity projection operator. The angular momentum projection operator is defined by (Peierls & Yoccoz, 1957)

$$P^{J}_{MK}(\Omega) = \frac{2J+1}{8\,\pi^2} \int \mathrm{d}\Omega\, D^{J*}_{MK}(\Omega)\, \hat{R}(\Omega) \tag{9}$$

where $D^{J}_{MK}(\Omega)$ is the Wigner D-function and $\hat{R}(\Omega)$ the rotation operator with $\Omega \equiv \{\alpha, \beta, \gamma\}$ representing Euler rotation angles.

3. Equations of motion

The wave function of the system $\Psi(\vec{S})$ depends on the set of complex variational parameters $\vec{S}$. To establish the time evolution of such a wave function, the form of the time dependence of the variational parameters, and therefore the equations of motion, is determined. The equations of motion of the parameters are derived from the time-dependent variational principle (Kramer & Saraceno, 1981)

$$\delta \int_{t_1}^{t_2} \left[\frac{\mathrm{i}\hbar}{2} \frac{\langle \Psi\, |\dot{\Psi}\rangle - \langle \dot{\Psi}|\, \Psi\rangle}{\langle \Psi|\Psi\rangle} - \frac{\langle \Psi\, |H|\, \Psi\rangle}{\langle \Psi|\Psi\rangle} \right] \mathrm{d}t = 0 \tag{10}$$

with the constraints

$$\delta\Psi(t_1) = \delta\Psi(t_2) = \delta\Psi^*(t_1) = \delta\Psi^*(t_2) = 0 \tag{11}$$

where $\dot{\Psi} = \mathrm{d}\Psi/\mathrm{d}t$ and Ψ^* the complex conjugate of the wave function. In this definition of the variational principle the wave function Ψ is not normalized. Therefore the equations of motion for the variational parameters will not depend on either the normalization or the phase of the wave function. The variation of the wave function in Eq. (10) with respect to time can be cast in the form

$$\frac{\mathrm{d}\,\Psi}{\mathrm{d}\,t} = \sum_i \left[\frac{\mathrm{d}\,\tilde{\mathrm{s}}_{\mathrm{i}}}{\mathrm{d}t}\, \frac{\partial\,\Psi}{\partial\,\vec{s}_i} + \frac{\mathrm{d}\,\tilde{\mathrm{s}}^*_{\mathrm{i}}}{\mathrm{d}t}\, \frac{\partial\,\Psi}{\partial\,\vec{s}^*_i} \right]. \tag{12}$$

The equations of motion of the variational parameters can then be obtained by expressing Eq. (10) in terms of the parameters as

$$\delta \int_{t_1}^{t_2} \left[\frac{\mathrm{i}\,\hbar}{2} \sum_j \left(\frac{\mathrm{d}\,\tilde{\mathrm{s}}_{\mathrm{j}}}{\mathrm{d}t}\, \frac{\partial}{\partial\,\vec{s}_j} - \frac{\mathrm{d}\,\tilde{\mathrm{s}}^*_{\mathrm{j}}}{\mathrm{d}t}\, \frac{\partial}{\partial\,\vec{s}^*_j} \right) \ln\langle\Psi|\Psi\rangle - E \right] \mathrm{d}t = 0 \tag{13}$$

with the constraints

$$\delta\vec{s}(t_1) = \delta\vec{s}(t_2) = \delta\vec{s}^*(t_1) = \delta\vec{s}^*(t_2) = 0 \tag{14}$$

where

$$E(\vec{S},\vec{S}^*) = \frac{\langle\Psi(\vec{S})|\,H\,|\Psi(\vec{S})\rangle}{\langle\Psi(\vec{S})|\Psi(\vec{S})\rangle} \tag{15}$$

is the energy functional of the system. Minimizing the action in Eq. (13) with the constraints (14) results in the equations

$$\frac{\mathrm{i}\hbar}{2}\sum_i\left(\frac{\partial^2\ln\langle\Psi|\Psi\rangle}{\partial\vec{s}_i\,\partial\vec{s}_j^*}\right)\frac{\mathrm{d}\,\tilde{\mathrm{s}}_\mathrm{i}}{\mathrm{d}t} = \frac{\partial E}{\partial\vec{s}_j^*} \qquad \text{and} \qquad -\frac{\mathrm{i}\hbar}{2}\sum_j\left(\frac{\partial^2\ln\langle\Psi|\Psi\rangle}{\partial\vec{s}_i\,\partial\vec{s}_j^*}\right)\frac{\mathrm{d}\,\tilde{\mathrm{s}}_\mathrm{j}^*}{\mathrm{d}t} = \frac{\partial E}{\partial\vec{s}_i} \tag{16}$$

of the variational parameters. Defining a Hermitian and positive definite matrix $\mathcal{C}$ with elements

$$\mathcal{C}_{ij} = \frac{\partial^2\ln\langle\Psi|\Psi\rangle}{\partial\vec{s}_i\,\partial\vec{s}_j^*}, \tag{17}$$

the equations of motion can be compactly expressed in the form (Kramer & Saraceno, 1981)

$$\frac{\mathrm{i}\hbar}{2}\begin{bmatrix} 0 & \mathcal{C} \\ -\mathcal{C}^* & 0 \end{bmatrix}\begin{bmatrix} \dfrac{\mathrm{d}\,\vec{s}^*}{\mathrm{d}\,t} \\ \dfrac{\mathrm{d}\,\vec{s}}{\mathrm{d}\,t} \end{bmatrix} = \begin{bmatrix} \dfrac{\partial\,E}{\partial\,\vec{s}^*} \\ \dfrac{\partial\,E}{\partial\,\vec{s}} \end{bmatrix} . \tag{18}$$

The solution to these equations provide the time evolution of the variational parameters and therefore of the wave function of the system.

To determine the parameters $\vec{s}_i$ and the variational energy E of the system Eq. (18) are modified by multiplying the right-hand-side by a complex constant $\mu = a + \mathrm{i}b$ where a and b are arbitrary real numbers. The coefficient μ introduce friction in the equations. The resulting equations can be solved numerically. To show that solving the modified equation of motion minimizes the energy the matrix $\mathcal{C}$ is replaced by a simpler positive definite matrix, the unit matrix I (Ono & Horiuchi, 2004). Then the equations of motion for the variational parameters takes the form

$$\frac{\mathrm{d}\vec{s}_i}{\mathrm{d}\,t} = \frac{2\mu}{\mathrm{i}\hbar}\frac{\partial\,E}{\partial\,\vec{s}_i^*} \qquad \text{and} \qquad \frac{\mathrm{d}\,\vec{s}^*}{\mathrm{d}\,t} = -\frac{2\mu^*}{\mathrm{i}\hbar}\frac{\partial\,E}{\partial\,\vec{s}_i} . \tag{19}$$

These equations have a form similar to that of Hamilton's classical equations of motion for canonically conjugate variables. The variation of the energy functional with time leads to

$$\frac{\mathrm{d}\,\mathrm{E}}{\mathrm{d}\,t} = \sum_i\left[\frac{\partial\,E}{\partial\,\vec{s}_i}\frac{\mathrm{d}\,\tilde{\mathrm{s}}_\mathrm{i}}{\mathrm{d}\,t} + \frac{\partial\,E}{\partial\,\vec{s}_i^*}\frac{\mathrm{d}\,\tilde{\mathrm{s}}_\mathrm{i}^*}{\mathrm{d}\,t}\right] = \frac{4b}{\hbar}\sum_i\frac{\partial\,E}{\partial\,\vec{s}_i}\frac{\partial\,E}{\partial\,\vec{s}_i^*}. \tag{20}$$

The same result can be obtained using the positive definite matrix $\mathcal{C}$ (Ono & Horiuchi, 2004). Since the two terms in Eq. (20) are positive at all times, it is evident that

$$\frac{\mathrm{d}\,\mathrm{E}}{\mathrm{d}\,t} < 0 \quad \text{when} \quad b < 0\,, \tag{21}$$

so that choosing $b < 0$ results in the energy functional decreasing with time during the variation of the parameters. Hence the parameter μ is referred to as the coefficient of friction and this technique of lowering the energy of a system is called *frictional cooling*. The equations

are solved with the constraint $\sum_i \vec{s}_i = 0$. The zero-point oscillation of the center-of-mass need be subtracted from the expectation value of the Hamiltonian of the system.

4. Nuclear ground state properties

To evaluate the variational energy functional and solve for the variation parameters, the Hamiltonian H of the nucleus is required as input. Considering only two-body interactions in the nucleus the nuclear Hamiltonian has the form

$$H = -\sum_i \frac{\hbar^2}{2\,m_i}\,\nabla_i^2 + \frac{1}{2}\sum_{i\neq j}\Big[\,V_{NN}(\vec{r}_{ij}) + V_C(\vec{r}_{ij})\,\Big] \tag{22}$$

where m_i is the mass of nucleon i, $V_{NN}(\vec{r})$ the nucleon-nucleon NN potential, $V_C(\vec{r})$ the Coulomb potential and $\vec{r}$ the relative position vector of the interacting nucleons. In this work the AV4′ NN potential with the $V_{C1}(\vec{r})$ Coulomb component is used (Wiringa & Pieper, 2002). In operator form the general Argonne nucleon-nucleon potential can be written in the form

$$V(\vec{r}_{ij}) = \sum_m v_m(r_{ij})\,\mathcal{O}_{ij}^m \tag{23}$$

where $v_m(r_{ij})$ are radial form factors and $\mathcal{O}_{ij}^m$ two-body nucleon operators. The Argonne V4′ potential employed in this work consists of the first four operators

$$\mathcal{O}_{ij}^{1\to 4} \;\equiv\; \{\,1\,,\,\vec{\sigma}_i\cdot\vec{\sigma}_j\,\}\otimes\{\,1\,,\,\vec{\tau}_i\cdot\vec{\tau}_j\,\}\,. \tag{24}$$

The V4 potential model can also be cast in the form

$$V(\vec{r}_{ij}) = \sum_{T=0}^{1}\sum_{S=0}^{1} V_{ST}^c(r_{ij})\,\Omega_{ij}^{(S)}\,\Omega_{ij}^{(T)} \tag{25}$$

where the subscripts S (T) indicate the coupled spin (isospin) of the interacting nucleon pair. Using the transformations

$$\Omega_{ij}^{(S)} = \frac{1}{2}\Big[\,1+(-1)^{S+1}\,P_{ij}^{\sigma}\,\Big] \qquad \text{and} \qquad \Omega_{ij}^{(T)} = \frac{1}{2}\Big[\,1+(-1)^{T+1}\,P_{ij}^{\tau}\,\Big] \tag{26}$$

of the spin and isospin projection operators, respectively, where P_{ij}^{σ} (P_{ij}^{τ}) is the spin (isospin) exchange operator, one obtains

$$V(\vec{r}_{ij}) \;=\; V_c(r_{ij}) + V_\sigma(r_{ij})\,P_{ij}^{\tau} - V_\tau(r_{ij})\,P_{ij}^{\sigma} - V_{\sigma\tau}(r_{ij})\,P_{ij}^{\sigma}\,P_{ij}^{\tau}\;\;. \tag{27}$$

The relation between the form factors in equations (23) and (27) are

$$V_c \;=\; v_c - v_\tau - v_\sigma + v_{\sigma\tau} \tag{28}$$

$$V_\tau \;=\; 2\,\big[\,v_\tau - v_{\sigma\tau}\,\big] \tag{29}$$

$$V_\sigma \;=\; 2\,\big[\,v_\sigma - v_{\sigma\tau}\,\big] \tag{30}$$

$$V_{\sigma\tau} \;=\; 4\,v_{\sigma\tau} \tag{31}$$

where the dependence on r is understood. These radial form factors are very difficult to approximate satisfactorily with less than twenty Gaussian functions.

The variational energy E_0, root-mean-square (rms) radius $\sqrt{\langle r^2 \rangle}$ and magnetic moment μ of the nuclei are calculated using the parity projected AMD wave function, Ψ^π. These three quantities are given by

$$E_0 = \frac{\langle \Psi^\pi | \, H \, | \Psi^\pi \rangle}{\langle \Psi^\pi | \Psi^\pi \rangle} \tag{32}$$

$$\langle r^2 \rangle = \frac{1}{A} \frac{\langle \Psi^\pi | \sum_{i=1}^{A} \left[\vec{r}_i - \vec{R} \right]^2 | \Psi^\pi \rangle}{\langle \Psi^\pi | \Psi^\pi \rangle} \tag{33}$$

$$\vec{\mu} = \frac{\langle \Psi^\pi | \sum_{i=1}^{A} \left[g_\ell \vec{\ell}_i + g_s \vec{s}_i \right] | \Psi^\pi \rangle}{\langle \Psi^\pi | \Psi^\pi \rangle} \tag{34}$$

where $\vec{R}$ is the center-of-mass of the nucleus, $\vec{\ell}_i$ ($\vec{s}_i$) the orbital (spin) angular momentum and g_ℓ (g_s) the corresponding g-factor of a nucleon. The g-factors are constants with values (Wong, 1998)

$$g_\ell = \begin{cases} 1 \text{ for proton} \\ 0 \text{ for neutron} \end{cases} \quad : \quad g_s = \begin{cases} 5.585695 \text{ for proton} \\ -3.826085 \text{ for neutron} \end{cases} \tag{35}$$

The integrals in equations (32), (33) and (34) can be analytically evaluated (Rampho, 2010). As an illustration the evaluation of the variational energy is summarized. The variational energy is evaluated as

$$E_0 = \sum_{ik} \mathcal{T}_{ik} \, B^{-1}_{ik} + \sum_{ijkl} \mathcal{V}_{ijkl} \, B_{li} \, B_{kj} \left[\mathcal{P}^{\rm d}_{ij} \, B^{-1}_{il} B^{-1}_{jk} - \mathcal{P}^{\rm e}_{ij} \, B^{-1}_{ik} B^{-1}_{jl} \right] \tag{36}$$

where the first sum generate the total kinetic energy while the second generate the total potential energy of the system. In this energy functional $\mathcal{T}_{ik}$ and $\mathcal{V}_{ijkl}$ represent the integrals involving the kinetic operator and potential functions, respectively, with $B_{ij} = \langle \psi_i | \psi_j \rangle$ and $\mathcal{P}^{\rm d}_{ij}$ ($\mathcal{P}^{\rm e}_{ij}$) resulting from direct (exchange) interactions. The evaluation of the expectation values of the potential can be evaluated analytically when the these radial components are given in terms of Gaussian functions (Tohsaki, 1992). Instead of expanding the potential in terms of Gaussians the corresponding expectation value is approximated by the series (Rampho, 2011)

$$\mathcal{V}_{ijkl} = \exp\left(-\frac{\eta_2^2}{4} \right) \sum_{m=0}^{\infty} \left(\frac{\eta_2^2}{4} \right)^m I_\alpha(m) \tag{37}$$

where $\vec{\eta}_2 = \vec{s}_l - \vec{s}_k + \vec{s}_i - \vec{s}_j$ and

$$I_\alpha(m) = \frac{2 \, \alpha^{m+3/2}}{\Gamma(m+1)\Gamma(m+\frac{3}{2})} \int_0^\infty r^{2\,m+2} V(r) \mathrm{e}^{-\alpha \, r^2} \, \mathrm{d}r \tag{38}$$

the Talmi integral involving the gamma function $\Gamma(x)$. If the range of the potential is not greater than $1/\sqrt{2\,\alpha}$ then the series in Eq. (37) converges quite fast for any value of $\vec{\eta}_2$ (Brink, 1965). Therefore, only the first few terms in the series tend to be significant. The Coulomb potential is treated with a Gaussian integral transform. In solving the cooling equations a random number generator is used to set up the initial values of the variational parameters. The required wave function is obtained when the energy functional for the system is independent of the variations of the parameters of the wave function. The parity projection of the wave functions is done before the variation of the parameters. Only the first five terms

of the series in (37) were considered. The integral in $I_\alpha(m)$ is evaluated numerically using a Gaussian quadrature. The value of α was chosen to satisfactorily reproduce the experimental binding energy of the three-nucleon systems. The variational energies are corrected by subtracting contributions from spurious center-of-mass. The results are presented along with corresponding experimental data in Table 1. As can be observed from this table the theoretical prediction of the experimental binding energies of the three-nucleon systems is satisfactory, as expected. However, the experimental binding energy of the ^{2}H nucleus is overestimated by about 60 %. The binding energy of the ^{4}He nucleus is underestimated by 10 % whereas that of the ^{6}Li and ^{8}Be nuclei are underestimated by 14 %. The ^{8}Be nucleus is very unstable (Audi et al., 2003) and, therefore, very challenging to study experimentally.

The AMD generates reasonable predictions of the experimental values for the rms radii of the nuclei. The deviation of the predicted values from the experimental values for the nuclei range from 0 %, for the ^{3}He nucleus, to 11 %, for the ^{6}Li nucleus. The theoretical radii of the ^{6}Li and the ^{8}Be nuclei are almost the same. In general the theoretical results overestimate the experimental values of the rms radii for all the nuclei. The calculated magnetic moments of the three-nucleon systems are different from the experimental values by 6 % and 10 %. For the three-nucleon systems the theoretical moments equal the magnetic moment of the unlike nucleon in the system. This reason also explains why the calculated magnetic moments of the ^{2}H and ^{6}Li nuclei, which overestimate the respective experimental values by 3 % and 7 %, are equal. The calculated magnetic moments of the ^{4}He and ^{8}Be nuclei are both equal to zero. These results are consistent with the theoretical expectation when only the dominant spherical ground state wave function of the system is used in the calculations (Phillips, 1977). The results for the parity and angular momentum projected wave function are given in Table 2 for the three-nucleon and the four-nucleon systems. The parity projection is done before the variation of the parameters and the angular momentum projection is done after the optimisation of the parameters. The rotation increases the theoretical energies of the three-nucleon systems by 10 % and decreases that of the four-nucleon system by 10 %, relative to the un-rotated wave function. Since the nuclear systems are described with spherical wave functions, spatial rotations are not expected to introduce significant modifications to the results presented in Table 1. The binding energy found for the ^{3}H system overestimates

	E_0 (MeV)		$\sqrt{\langle r^2 \rangle}$ (fm)		μ (μ_N)	
^{A}X$^\pi$	AMD	EXP	AMD	EXP	AMD	EXP
^{2}H$^+$	-3.53	-2.23	2.16	1.96	0.880	0.857
^{3}H$^+$	-8.12	-8.48	1.76	1.60	2.793	2.979
^{3}He$^+$	-7.78	-7.72	1.76	1.77	-1.913	-2.128
^{4}He$^+$	-25.50	-28.3	1.53	1.47	0.000	
^{6}Li$^+$	-27.54	-31.99	2.70	2.4	0.880	0.822
^{8}Be$^+$	-49.38	-55.99	2.75		0.000	

Table 1. The ground state energies, rms radii and magnetic moments of selected light nuclei. The experimental data are taken from reference (Suzuki et al., 2008).

	E_0 (MeV)		$\sqrt{\langle r^2 \rangle}$ (fm)		μ (μ_N)	
${}^A\mathrm{X}(J^\pi)$	AMD	EXP	AMD	EXP	AMD	EXP
${}^3\mathrm{H}\ (\frac{1}{2}^+)$	-8.95	-8.48	1.33	1.60	2.769	2.979
${}^3\mathrm{He}(\frac{1}{2}^+)$	-8.61	-7.72	1.33	1.77	-1.847	-2.128
${}^4\mathrm{He}(0^+)$	-23.04	-28.30	1.16	1.47	0.000	

Table 2. The ground state energies, rms radii and magnetic moments of the three- and four-nucleon systems. The experimental values are taken from reference (Suzuki et al., 2008).

the experimental energy by 5 % and for the ^{3}He system by 12 %. In contrast, the ^{4}He results are lower than the experimental value by $\sim$ 19 %, a result which is in line with other calculations in the field using the same rank in the potential. The rms radii obtained for the ^{3}H and ^{3}He systems are lower than the experimental values by $\sim$ 16 % and $\sim$ 22 % less, respectively. Similar results are obtained for the ^{4}He system where the calculated rms radius is underestimated by $\sim$ 21 %. In general, the AMD approach reproduces the experimental values for the magnetic moment of the nuclei quite satisfactorily.

Intrinsic density distribution in a nucleus is determined by rotating the arbitrary space-fixed coordinate axes on to the body-fixed principal axes of the nucleus. The rotation is generated by diagonalising the moment-of-inertia tensor of the nucleus which is defined by elements

$$I_{\mu\nu} = \frac{\left\langle \Psi^\pi \right| \sum_{i=1}^{A} \left[\vec{r}_i - \vec{R}\right]_\mu \left[\vec{r}_i - \vec{R}\right]_\nu \left| \Psi^\pi \right\rangle}{\left\langle \Psi^\pi | \Psi^\pi \right\rangle} \tag{39}$$

where $\{\mu, \nu\} \equiv \{x, y, z\}$. The calculated intrinsic density using the parity projected wave function, in the body-fixed coordinate axes, are shown in Figure 1 for the ^{4}He nucleus and in Figure 2 for the ^{6}Li and ^{8}Be nuclei. The ^{4}He nuclei displays a spherical density distribution whereas the ^{6}Li and ^{8}Be nuclei display distinct cluster structures.

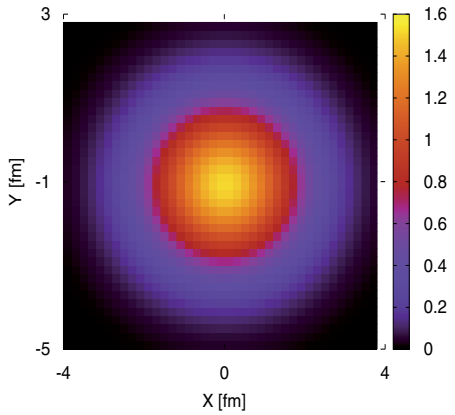

Fig. 1. Density distribution of the ^{4}He nucleus.

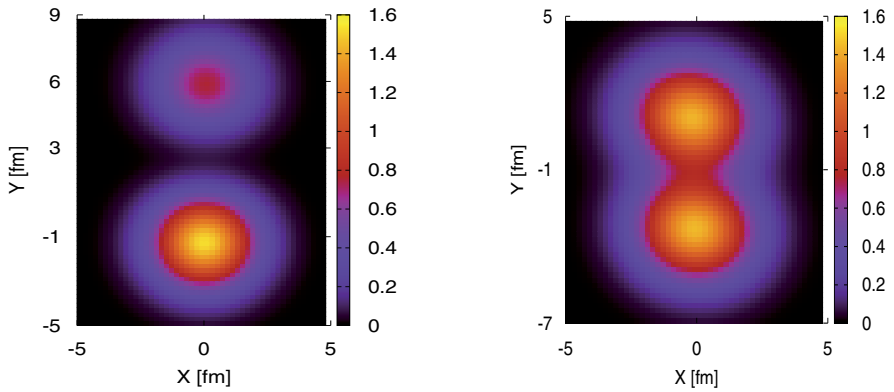

Fig. 2. Density distributions of the ^{6}Li nucleus (left) and the ^{8}Be nucleus (right).

5. Charge form factors

Most of the information accumulated about nuclear structure is derived from electron-nucleus scattering. In electron-nucleus scattering the electron transfers momentum $\vec{q}$ and energy ω to the target nucleus and the nucleus undergoes some transitions that are governed by selection rules related angular momentum and parity. For elastic scattering the initial and final states of the nucleus have the same angular momentum (de Forest Jr. & Walecka, 1966). This type of electron scattering is used to probe ground state charge and magnetisation distributions in nuclei. The ground state of the ^{3}He nucleus has total angular momentum and parity $J^\pi = \frac{1}{2}^+$ whereas the ^{4}He system has $J^\pi = 0^+$. Theoretical predictions of electromagnetic provide a good test of the quality of the wave function describing the system. In this section the charge form factors of ^{3}He and ^{4}He nuclei are calculated in the plane wave impulse approximation (PWIA) (Chew & Wick, 1952). In this approximation the nucleons inside the target nucleus are assumed non-interacting with one another during the interaction with the electron. This means that the electron interacts with independent nucleons inside the nucleus. Since the transitions are between states of definite angular momentum, the parity and angular momentum projected wave functions are employed.

The charge distribution in the nucleus is inferred from the electric transitions in the nucleus due elastic electron-nucleus scattering. The charge form factor is the expectation value of the nuclear charge operator. For a nucleus in an initial state $\left|\Psi^{J\pi}_{MK}\right\rangle$ the charge form factor is given by

$$F_{\rm ch}(\vec{q}) = \frac{1}{Z}\frac{\left\langle\Psi^{J\pi}_{MK}\right|\rho(\vec{q})\left|\Psi^{J\pi}_{MK}\right\rangle}{\left\langle\Psi^{J\pi}_{MK}\right|\left.\Psi^{J\pi}_{MK}\right\rangle} \tag{40}$$

where Ze is the total charge on and $\rho(\vec{q})$ the charge operator of the nucleus with $\vec{q}$ being the momentum transferred to the nucleus by the electron. In the PWIA the nuclear charge operator is formed by the superposition of the individual nucleon charge operators and is given by (Rampho, 2010)

$$\rho(\vec{q}) = \sum_{k=1}^{A}\left[\frac{q}{Q}\,G^N_{Ek}(Q^2) - \frac{2\,G^N_{Mk}(Q^2) - G^N_{Ek}(Q^2)}{4\,m_N^2\,\sqrt{1+\tau}}\,\mathrm{i}\vec{\sigma}_k\cdot\vec{q}\times\vec{p}_k\right]\exp\left(\mathrm{i}\,\vec{q}\cdot\vec{r}_k\right) \tag{41}$$

where $\tau = Q^2/4\,m_N^2$, $Q^2 = q^2 - \omega^2$, $\omega = \sqrt{q^2 + m_N^2} - m_N$ and G_E^N (G_M^N) the nucleon Sachs electric (magnetic) form factor. For the Sachs form factors the phenomenological parametrization derived in Ref. (Friedrich & Walcher, 2003) is adopted. The general multipole analysis of nuclear charge form factors is given by (Uberall, 1971)

$$F_{\rm ch}(\vec{q}) = \sqrt{4\,\pi} \sum_{L=0}^{\leq 2J} \langle JJL0|JJ\rangle\, F_L^{\rho}(q)\, Y_{L0}^*(\hat{\mathbf{q}}) \tag{42}$$

where $Y_{LM}^*(\hat{\mathbf{q}})$ are the spherical harmonics, L the nuclear orbital angular momentum and $\langle JJL0|JJ\rangle$ the Clebsch-Gordan coefficients and $\hat{\mathbf{q}} = \vec{q}/|\vec{q}|$. The summation is over even values of L only. The intrinsic charge form factor is corrected by dividing the calculated charge form factor by the contributions of the center-of-mass (Rampho, 2010). The integrals in Eq. (42) can be analytically evaluated.

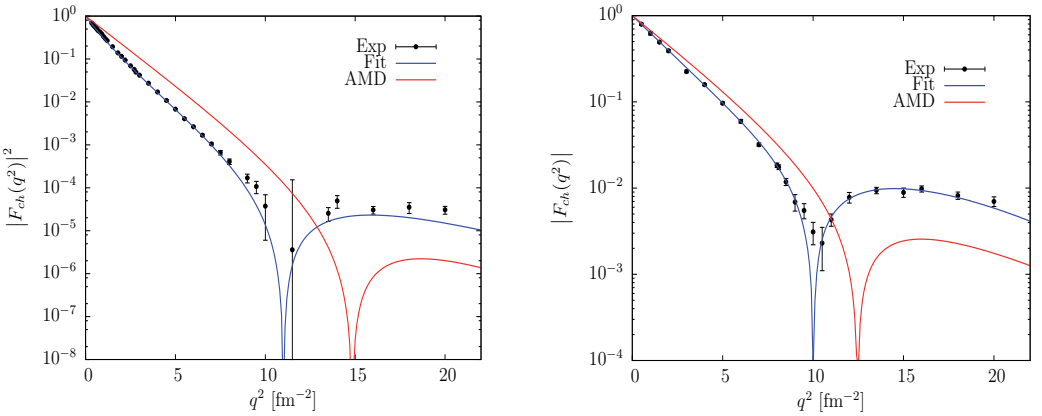

Fig. 3. The charge form factor of ^{3}He (left) and ^{4}He (right) compared with the experimental data of (McCarthy et al., 1977) and the theoretical fit to the data (Amroun et al., 1994).

The results of the calculated ground-state charge form factors of the ^{3}He and ^{4}He nuclei are presented in Figure 3. In these figures the theoretical charge form factors are compared with experimental data from (Frosch et al., 1967; McCarthy et al., 1977). In the comparison phenomenological parametrization (Amroun et al., 1994) that fit experimental universal data of the form factors for electron-nucleus scattering are also shown. The charge form factors are normalized such that $F_{\rm ch}(0) = 1$. As can be seen in these figures, for low momentum transfers, up to the first diffraction minimum, the AMD gives a reasonable description, albeit it slightly overestimates the experimental data. Beyond the first diffraction minimum the results are lower than the data. The first diffraction minimum for the nuclei are consistent with, but not better than, the predictions of other theoretical models obtained with various nucleon-nucleon potentials in the PWIA (Kloet & Tjon, 1974). It should be noted that the overestimation of the position of the diffraction minimum indicates an underestimation of the nuclear charge radius.

6. Conclusions

To test the applicability of the AMD model in nuclear structure studies, the angular momentum and parity projected AMD wave function were used to calculate binding energies,

rms radii, and the magnetic moments for selected few-nucleon systems. The nuclear Hamiltonian was constructed from the Argonne AV4′ NN potential that includes also the Coulomb interaction. Comparison with the experimental data revealed that the reproduction of the ground state properties of light nuclei is quite satisfactory. The discrepancies observed can be attributed to reasons not entirely related to the AMD. These include i) the omission of mixed-symmetric states (for three-body) ii) the use of a limited rank for the Argonne AV18 potential, and iii) the omission of three-nucleon forces. As far as the magnetic moment is concerned, the inclusion of relativistic corrections to the magnetic moment operator, are also expected to contribute to the reduction of the discrepancy between theory and experiment. The technique used in the approximation of the variational energy can be easily extended to the three-body interactions. The implementation of this technique in nuclear three-body interactions will be considered future projects.

The angular momentum and parity projected AMD was used to calculate the ground state charge form factors for the ^{3}He and ^{4}He nuclei. In overall, the results obtained, within the AMD and PWIA approximation, reproduce the general behavior of the experimental form factors. For momentum transfer below the first diffraction minimum the reproduction of experimental form factors is fairly good. However, beyond the first diffraction minimum the results are lower than the data. The deviations of the theoretical results from experimental data can be minimize by employing improved wave functions. The wave functions can be constructed by using a more complete realistic Hamiltonian, three-body forces, and relativistic corrections in the electromagnetic operators. It should be noted that these results are consistent with other results obtained by competing theoretical models. In conclusion, the results indicate that the AMD method is a very promising method in calculating electromagnetic form factors of the general A-body nuclear system.

Work is underway to construct wave functions for scattering processes applicable in nuclear breakup reactions (Rampho, 2010). In these constructs the AMD is combined with the Glauber multiple scattering to account for final state interactions. Wave functions for two-body and three-body scattering reactions can be treated accurately in the Faddeev formalism (Golak et al., 2005; Merkuriev et al., 1976). In the hyperspherical harmonics approach some progress in being made towards the construction of accurate wave functions for two-body scattering processes (Kievsky et al., 2008). However, these methods become involved for systems consisting of more than four constituent particles.

7. References

Aichelin, J. (1991). "Quantum" molecular dynamics - a dynamical microscopic n-body approach to investigate fragment formation and the nuclear equation of state in heavy ion collisions, *Phys. Rep.* 202(5): 233–360.

Alvioli, M., Ciofi degli Atti, C. & Morita, H. (2008). Proton-neutron and proton-proton correlations in medium-weight nuclei and the role of the tensor force, *Phys. Rev. Lett.* 100(16): 162503.

Amroun, A., Breton, V., Cavedon, J. M., Frois, B., Goutte, D., Juster, F. P., Leconte, P., Martino, J., Mizuno, Y., Phan, X. H., Platchkov, S. K., Sick, I. & Williamson, S. (1994). ^{3}H and ^{3}He electromagnetic form factors, *Nucl. Phys.* A 579(3-4): 596–626.

Audi, G., Bersillon, O., Blachot, J. & Wapstra, A. (2003). The NUBASE evaluation of nuclear and decay properties, *Nucl. Phys.* A 729(1): 3–128.

Boffi, S., Bouten, M., Ciofi degli Atti, C. & Sawicki, J. (1968). Elastic and quasi-free electron scattering from ^{12}C and projected hartree-fock wave functions, *Nucl. Phys.* A 120(1): 135–144.

Brink, D. (1965). The alpha-particle model of light nuclei, *in* C. Bloch (ed.), *Proceedings of the International School of Physics "Enrico Fermi"*, Vol. 36, Academic Press, New York, pp. 247–276.

Carlson, J. & Schiavilla, R. (1998). Structure and dynamics of few-nucleon systems, *Rev. Mod. Phys* 70(3): 743–841.

Caurier, E., Grammaticos, B. & Sami, T. (1982). The time dependent cluster model, *Phys. Lett.* B 109(3): 150–154.

Chew, G. F. & Wick, G. C. (1952). The impulse approximation, *Phys. Rev.* 85(4): 636–642.

Cottingham, W. N., Lacombe, M., Loiseau, B., Richard, J. M. & Mau, R. V. (1973). Nucleon-nucleon interaction from pion-nucleon phase-shift analysis, *Phys. Rev.* D 8(3): 800–819.

de Forest Jr., T. & Walecka, J. D. (1966). Electron scattering and nuclear structure, *Adv. Phys.* 15(57): 1–109.

Donnelly, T. W. & Raskin, A. S. (1986). Considerations of polarization in inclusive electron scattering from nuclei, *Ann. Phys.* 169(2): 247–351.

Doté, A. & Horiuchi, H. (2000). Study of he isotopes with amd+hartree-fock, *Prog. Theor. Phys.* 103(2): 261–283.

Doté, A., Horiuchi, H. & Kanada-En'yo, Y. (1997). Antisymmetrized molecular dynamics plus hartree-fock model and its application to be isotopes, *Phys. Rev.* C 56(4): 1844–1854.

Doté, A., Kanada-En'yo, Y., Horiuchi, H., Akaishi, Y. & Ikeda, K. (2006). Explicit treatment of the tensor force with the method of antisymmetrized molecular dynamics, *Prog. Theor. Phys.* 115(6): 1069–1092.

Egiyan, K. S., Asryan, G., Gevorgyan, N., Griffioen, K. A. & et al. (2007). Experimental study of exclusive ^{2}H$(e,e'p)n$ reaction mechanisms at high Q^2, *Phys. Rev. Lett.* 98(26): 262502.

Egiyan, K. S., Dashyan, N. B., Sargsian, M. M., Strikman, M. I. & et al. (2006). Measurement of two- and three-nucleon short-range correlation probabilities in nuclei, *Phys. Rev. Lett.* 96(8): 082501.

Engel, A., Tanaka, E. I., Maruyama, T., Ono, A. & Horiuchi, H. (1995). Δ degrees of freedom in antisymmetrized molecular dynamics and (p,p') reactions in the Δ region, *Phys. Rev.* C 52(6): 3231–3248.

Feldmeier, H. (1990). Fermionic molecular dynamics, *Nucl. Phys.* A 515(1): 147–172.

Frankfurt, L. L., Strikman, M. I., Day, D. B. & Sargsian, M. (1993). Evidence for short-range correlations from high q^2 (e,e') reactions, *Phys. Rev.* C 48(5): 2451–2461.

Friedrich, J. & Walcher, T. (2003). A coherent interpretation of the form factors of the nucleon in terms of a pion cloud and constituent quarks, *Eur. Phys. J.* A 17(4): 607–623.

Frosch, R. F., McCarthy, J. S., Rand, R. E. & Yearian, M. R. (1967). Structure of the ^{4}He nucleus from elastic electron scattering, *Phys. Rev.* 160(4): 874–879.

Golak, J., Skibiński, R., Witala, H., Glöckle, W., Nogga, A. & Kamada, H. (2005). Electron and photon scattering on three-nucleon bound states, *Phys. Rep.* 415(2): 89–205.

Horiuchi, H. (1991). Microscopic study of clustering phenomena in nucle, *Nucl. Phys.* A 522(1): 257–274.

Jones, M. K., Aniol, K. A., Baker, F. T., Berthot, J. & et al. (2000). G_{E_p}/G_{M_p} ratio by polarization transfer in $\vec{e}p \to e\vec{p}$, *Phys. Rev. Lett.* 84(7): 1398–1402.

Kamada, H., Nogga, A., Glöckle, W., Hiyama, E., Kamimura, M., Varga, K., Suzuki, Y., Viviani, M., Kievsky, A., Rosati, S., Carlson, J., Pieper, S. C., Wiringa, R. B., Navrátil, P., Barrett,

B. R., Barnea, N., Leidemann, W. & Orlandini, G. (2001). Benchmark test calculation of a four-nucleon bound state, *Phys. Rev.* C 64(4): 044001.

Kanada-En'yo, Y., Horiuchi, H. & Ono, A. (1995). Structure of li and be isotopes studied with antisymmetrized molecular dynamics, *Phys. Rev.* C 52(2): 628–646.

Kanada-En'yo, Y., Kimura, M. & Horiuchi, H. (2003). Antisymmetrized molecular dynamics: a new insight into the structure of nuclei, *C. R. Physique* 4(4): 497–520.

Kievsky, A., Rosati, S., Viviani, M., Marcucci, L. E. & Girlanda, L. (2008). A high-precision variational approach to three- and four-nucleon bound and zero-energy scattering states, *J. Phys. G: Nucl. Part. Phys.* 35(6): 063101.

Kimura, M. (2004). Deformed-basis antisymmetrized molecular dynamics and its application to ^{20}Ne, *Phys. Rev.* C 69(4): 044319.

Kloet, W. M. & Tjon, J. A. (1974). Meson exchange effects on the charge form factors of the tri-nucleon system, *Phys. Lett.* B 49(5): 419–422.

Kramer, P. & Saraceno, M. (1981). *Geometry of the Time-Dependent Variational Principle in Quantum Mechanics*, Vol. 140, Springer-Verlag, Berlin, Germany.

Lagaris, I. E. & Pandharipande, V. R. (1981). Phenomenological two-nucleon interaction operator, *Nucl. Phys.* A 359(2): 331–348.

Machleidt, R., Holinde, K. & Elster, C. (1987). The bonn meson-exchange model for the nucleon-nucleon interaction, *Phys. Rep.* 149: 1–89.

McCarthy, J. S., Sick, I. & Whitney, R. R. (1977). Electromagnetic structure of the helium isotopes, *Phys. Rev.* C 15(4): 1396–1414.

Merkuriev, S. P., Gignoux, C. & Laverne, A. (1976). Three-body scattering in configuration space, *Ann. Phys.* 99(1): 30–71.

Nagels, M. M., Rijken, T. A. & de Swart, J. J. (1978). Low-energy nucleon-nucleon potential from regge-pole theory, *Phys. Rev.* D 17(3): 768–776.

Neff, T., Feldmeier, H. & Roth, R. (2005). Structure of light nuclei in fermionic molecular dynamics, *Nucl. Phys.* A 752: 321–324.

Ono, A. & Horiuchi, H. (2004). Antisymmetrized molecular dynamics for heavy ion collisions, *Prog. Part. Nucl. Phys.* 53(2): 501–581.

Ono, A., Horiuchi, H., Maruyama, T. & Ohnishi, A. (1992). Antisymmetrized version of molecular dynamics with two-nucleon collisions and its application to heavy ion reactions, *Prog. Theor. Phys.* 87(5): 1185–1206.

Peierls, R. E. & Yoccoz, J. (1957). The collective model of nuclear motion, *Proc. Phys. Soc.* A 70(5): 381–387.

Phillips, A. C. (1977). Three-body systems in nuclear physics, *Rep. Prog. Phys.* 40(8): 905–961.

Piasetzky, E., Sargsian, M., Frankfurt, L., Strikman, M. & Watson, J. W. (2006). Evidence for strong dominance of proton-neutron correlations in nuclei, *Phys. Rev. Lett.* 97(16): 162504.

Rampho, G. J. (2010). *Electromagnetic Processes in Few-Body Systems*, PhD thesis, Physics, University of South Africa.

Rampho, G. J. (2011). Antisymmetrised molecular dynamics with realistic nucleon-nucleon potentials, *Few-Body Syst.* 50(1): 467–469.

Schroeder, L. S., Chessin, S. A., Geaga, J. V., Grossiord, J. Y., Harris, J. W., Hendrie, D. L., Treuhaft, R. & Bibber, K. V. (1979). Energy dependence of charged pions produced at 180° in 0.8-4.89-gev proton-nucleus collisions, *Phys. Rev. Lett.* 43(24): 1787–1791.

Suzuki, Y., Horiuchi, W., Orabi, M. & Arai, K. (2008). Global-vector representation of the angular motion of few-particle systems II, *Few-Body Syst.* 42(1): 33–72.

Tanaka, E. I., Ono, A., Horiuchi, H., Maruyama, T. & Engel, A. (1995). Proton inelastic scattering to continuum studied with antisymmetrized molecular dynamics, *Phys. Rev.* C 52(1): 316–325.

Togashi, T. & Kat$\overline{o}$, K. (2007). Brueckner-amd method and its applications to light nuclei, *Prog. Theor. Phys.* 117(1): 189–194.

Togashi, T., Murakami, T. & Kat$\overline{o}$, K. (2009). Description of nuclear structures with brueckner-amd plus J^{π} projection, *Prog. Theor. Phys.* 121(2): 299–317.

Tohsaki, A. (1992). Microscopic representation of α-cluster matter. I, *Prog. Theor. Phys.* 88(6): 1119–1129.

Uberall, H. (1971). *Electron Scattering from Complex Nuclei: Part A*, Academic Press, New York.

Ulmer, P. E., Aniol, K. A., Arenhövel, H. & et al. (2002). $^2\mathrm{H}(e,e'p)n$ reaction at high recoil momenta, *Phys. Rev. Lett.* 89(6): 062301.

Watanabe, T., Oosawa, M., Saito, K. & Oryu, S. (2009). A new molecular dynamics calculation and its application to the spectra of light and strange baryons, *J. Phys. G: Nucl. Part. Phys.* 36(1): 015001.

Watanabe, T. & Oryu, S. (2006). A new antisymmetrized molecular dynamics approach to few-nucleon systems, *Prog. Theor. Phys.* 116(2): 429–434.

Wiringa, R. B. & Pieper, S. C. (2002). Evolution of nuclear spectra with nuclear forces, *Phys. Rev. Lett.* 89(18): 182501.

Wiringa, R. B., Smith, R. A. & Ainsworth, T. L. (1984). Nucleon-nucleon potentials with and without $\Delta(1232)$ degrees of freedom, *Phys. Rev.* C 29(4): 1207–1221.

Wong, S. S. M. (1998). *Introductory Nuclear Physics*, 2 edn, John Wiley and Sons Inc., New York.

8

Antisymmetrized Molecular Dynamics with Bare Nuclear Interactions: Brueckner-AMD, and Its Applications to Light Nuclei

Tomoaki Togashi[1] and Kiyoshi Katō[2]
[1]*Faculty of Advanced Life Science, Hokkaido University*
[2]*Division of Physics, Graduate School of Science, Hokkaido University*
Japan

1. Introduction

Ab initio calculation starting from the bare nuclear interactions is one of recent major theoretical subjects in nuclear physics. One hopes to understand the property of nuclei based on the nuclear forces against the background of the progress of the fundamental understanding of bare nuclear interactions and the study of unstable nuclei far from the beta stable line, which are expected to have structures different from stable nuclei. Nowadays, one can obtain the three-, four-, or few-body wave functions starting from the bare Hamiltonian by applying many kinds of few-body exact methods (Kamada et al., 2001). It is difficult to apply such methods directly to heavier nuclei in viewpoint of computational costs at this stage, therefore, in many of *ab initio* approaches, the effective interaction is constructed based on the bare interaction by applying, for example, the unitary correlated operator method (UCOM) (Neff & Feldmeier, 2004) and so on. As one of remarkable achievements in *ab initio* approaches, the quantum Monte Carlo method (Wiringa et al., 2000) has presented the appearance of the two-alpha (^{4}He) cluster structure in ^{8}Be starting from the bare interactions. That suggests that one has the ability to discuss cluster structures based on the bare nuclear forces.

The existence of cluster states appearing around thresholds, which are weakly bound systems of subunits consisting of several nucleons to be strongly correlated each other, is predicted by the Ikeda diagram and the cluster models (Ikeda et al., 1972). The cluster states in some excited states of a light nucleus can be described as the states different from the mean-field-like structures. Cluster models in nuclear physics are able to describe these states successfully. In unstable nuclei, it is expected that mean-field-like and cluster-like structures coexist because their ground states often exist around the thresholds of decaying particles. The antisymmetrized molecular dynamics (AMD) (Kanada-En'yo et al., 1995) to be one of the recent developments of the cluster model has succeeded in understanding and predicting many properties of unstable nuclei. AMD can describe the nuclear structures without any assumption of configurations as the results of the energy variation in quantum mechanics. However, it is difficult for the bare nuclear interactions to be applied straightforwardly to the AMD framework because of the singularity and complexity in the interactions. Hence, AMD calculations have been performed with phenomenological interactions represented by

the simple forms and adjusted parameters to be suitable for the wave functions of AMD so far.

For the purpose of the fundamental understanding of nuclear structures, we have recently developed a new AMD framework, "Brueckner-AMD" (Togashi & Katō, 2007; Togashi et al., 2009), which makes AMD available to us with bare nuclear interactions. It is the basic idea of Brueckner-AMD that the effective interaction with no singularity to be applicable to the AMD wave functions is constructed starting from the bare interaction. Instead of the unitary transformation of the bare Hamiltonian, we introduce the effective interaction, *G*-matrix, based on the Brueckner theory to be combined with the single-particle orbits and energies solved by the AMD+Hartree-Fock (AMD-HF) method (Doté et al., 1997). In this framework, the *G*-matrix and single-particle states of AMD can be solved self-consistently so as to reflect structural changes of nucleus to the effective interactions. In that sense, Brueckner-AMD is a kind of *ab initio* calculations.

The appearance of alpha clusters has been studied in many light nuclei for many years. It is well known that the alpha particle, ^{4}He, which is the unit of alpha clusters, has the strong stability as its threshold energy for a nucleon is about 20 MeV, while normal nuclei have about 8 MeV. Theoretical few-body studies (Kamada et al., 2001) have proven that the tensor force in the bare nuclear interaction, which has the operator: $S_{12} = 3(\sigma_1 \cdot \hat{\mathbf{r}})(\sigma_2 \cdot \hat{\mathbf{r}}) - \sigma_1 \cdot \sigma_2$ where $\sigma_{1,2}$ represent the Pauli matrices, contributes more than half of the binding potential energy of the alpha particle, and the correlations induced by the tensor force play an important role in the structure of ^{4}He (Myo et al., 2009). Therefore, it is considered that the peculiar stability of the alpha particle supported by the tensor force contributions induces the strong correlations to realize the alpha clusters. However, the reason for the stability of alpha clusters in a nucleus has not yet been clarified, and it is still one of the central problems in nuclear theories at present. Although the recent *ab initio* approach (Wiringa et al., 2000) has provided the result of the alpha-alpha cluster structure in ^{8}Be as previous mentioned, it has been difficult to explain the reason why the alpha-alpha cluster in ^{8}Be appears for the complicated wave function solved from the bare Hamiltonian. Therefore, as our works, we present the prescription to simulate and visualize the development of alpha-alpha clustering in ^{8}Be, and elucidate its mechanism of the clustering as the result of effects of nuclear interactions in the Brueckner-AMD framework.

In this chapter, we plan to introduce the formulation and applications of Brueckner-AMD. In the second section, we present the formulation of Brueckner-AMD and focus on the details of the way how to solve the *G*-matrix in this framework. In the third section, we show the applications to several light nuclei and the study of alpha-alpha clustering in ^{8}Be in Brueckner-AMD. Finally, in the forth section, we conclude our works in this chapter.

2. Formulation

In this section, we explain the formulation of Brueckner-AMD. In the first subsection 2.1, we explain the concept of Brueckner-AMD, in which the *G*-matrix within the AMD framework can be calculated straightforwardly. In the second subsection 2.2, the detail of the way how to solve the *G*-matrix in Brueckner-AMD and its explicit examples are presented, and then the energy variation method in Brueckner-AMD is explained in the third subsection 2.3.

2.1 G-matrix in Brueckner-AMD

In this framework, we use the A-nucleons wave function of AMD, which represents the Slater determinant of Gaussian wave packets to be satisfied with the Fermi statistics in quantum mechanics as

$$|\Phi\rangle = \frac{1}{\sqrt{A!}} \det\left\{|\vec{Z}_i\rangle \cdot |\chi_i\rangle\right\}, \quad \langle \vec{r}\,|\vec{Z}_i\rangle = \left(\frac{2\nu}{\pi}\right)^{3/4} \exp\left[-\nu\left(\vec{r} - \frac{\vec{Z}_i}{\sqrt{\nu}}\right)^2 + \frac{\vec{Z}_i^2}{2}\right], \quad (1)$$

where $|\vec{Z}_i\rangle$ and $|\chi_i\rangle$ represent the spatial and spin-isospin parts of a nucleon, respectively. The spin-isospin functions $|\chi_i\rangle$ are given by spin-up (or spin-down) protons (or neutrons) in this work. The complex vector $\vec{Z}_i$ represents the position of a nucleon in the phase space.

The bare nuclear interactions have the high repulsive potential at a short distance and the non-central potentials to induce the admixture of high orbital angular moments (Wiringa et al., 1995). Every pair wave function in AMD is too simple to describe their induced nucleon-nucleon correlations. Therefore, we construct the effective interactions to be applicable to AMD, G-matrix ($\hat{G}$), starting from bare interactions as

$$\hat{G} = \hat{v} + \hat{v}\frac{Q}{\varepsilon_\alpha + \varepsilon_\beta - (\hat{t}_1 + \hat{t}_2)}\hat{G}, \quad (2)$$

where $\hat{v}$, Q, ε_i and $\hat{t}_i$ represent the bare interaction, the Pauli projection operator, the single-particle energy and kinetic operator, respectively. The above equation called "Bethe-Goldstone equation" denotes an infinite sum of scattering processes of two nucleons in the medium. In this equation, several methods of choosing the energy denominator of the propagator have been proposed. Here, we adopt the "QTQ(gap) choice" (Baldo et al., 2001) where only kinetic energy appears and there is no single-particle potential in intermediate states, as seen in Eq. (2). In the nuclear matter theory, it is known that the convergence of the hole-line expansion in the QTQ choice is inferior to that in the "continuous choice" (Baldo et al., 2001). However, at this stage, we check the adequacy of the QTQ choice in finite nuclei.

In the Brueckner theory, single-particle orbits and energies are needed to determine the G-matrix self-consistently. The single-particle orbits and energies in AMD can be defined by the AMD+Hartree-Fock (AMD-HF) method (Doté et al., 1997). Following AMD-HF, we construct an orthonormal basis $\{\tilde{f}_p\}$ for single-particle orbits by diagonalizing the overlap matrix B_{ij} expressed as

$$B_{ij} = \langle\, \vec{Z}_i \,|\, \vec{Z}_j \,\rangle \cdot \langle\, \chi_i \,|\, \chi_j \,\rangle, \quad (3)$$

and then we have

$$\sum_j B_{ij} \cdot \tilde{C}_{jp} = \mu_p \cdot \tilde{C}_{ip}, \quad \sum_j \tilde{C}^*_{jp}\,\tilde{C}_{jq} = \delta_{p,q}, \quad (4)$$

$$|\,\tilde{f}_p\,\rangle = \frac{1}{\sqrt{\mu_p}} \sum_j \tilde{C}_{jp}\,|\,\vec{Z}_i\,\rangle \cdot |\,\chi_i\,\rangle, \quad \langle\,\tilde{f}_p\,|\,\tilde{f}_q\,\rangle = \delta_{p,q}. \quad (5)$$

The Hartree-Fock Hamiltonian matrix can be written with $\{\tilde{f}_p\}$:

$$h_{pq} = \langle\,\tilde{f}_p\,|\,\hat{t}\,|\,\tilde{f}_q\,\rangle + \sum_r \langle\,\tilde{f}_p\,\tilde{f}_r|\,\hat{G}\,|\,\tilde{f}_q\,\tilde{f}_r - \tilde{f}_r\,\tilde{f}_q\,\rangle. \quad (6)$$

Then we obtain the single-particle orbit as the solution $\{f_\alpha\}$ for the following equations:

$$\sum_q h_{pq} \cdot g_{q\alpha} = \varepsilon_\alpha \cdot g_{p\alpha}, \quad \sum_q g^*_{q\alpha}\, g_{q\beta} = \delta_{\alpha,\beta}\,, \tag{7}$$

$$|\, f_\alpha \,\rangle = \sum_q g_{q\alpha}\, |\, \tilde{f}_q \,\rangle = \sum_j \left(\sum_q \frac{\tilde{C}_{jq}}{\sqrt{\mu_q}} \cdot g_{q\alpha} \right) |\, \vec{Z}_j \,\rangle \cdot |\, \chi_j \,\rangle = \sum_j C_{j\alpha}\, |\, \vec{Z}_j \,\rangle \cdot |\, \chi_j \,\rangle,$$
$$\langle\, f_\alpha \,|\, f_\beta \,\rangle = \delta_{\alpha,\beta}. \tag{8}$$

And then the single-particle energy is solved as

$$\varepsilon_\alpha = \langle\, f_\alpha \,|\, \hat{t} \,|\, f_\alpha \,\rangle + \sum_\gamma \langle\, f_\alpha\, f_\gamma \,|\, \hat{G} \,|\, f_\alpha\, f_\gamma \,-\, f_\gamma\, f_\alpha \,\rangle. \tag{9}$$

In Brueckner-AMD, both the single-particle energies (ε_α) of the wave function and the G-matrix ($\hat{G}$) are determined self-consistently. That means that the G-matrix within the AMD framework can be determined theoretically without any corrections.

2.2 Details of the G-matrix calculation

2.2.1 How to treat the Pauli projection operator

The Pauli projection operator Q in the Bethe-Goldstone equation, Eq. (2), is introduced in order to take account of the Pauli principle in the scattering processes in the medium. In this framework, the Pauli projection operator Q is represented as

$$Q = 1 - P = 1 - \sum_{\alpha<\beta} |\, f_\alpha\, f_\beta \,\rangle\langle\, f_\alpha\, f_\beta \,|\,, \tag{10}$$

where P is the projection operator for occupied states. In the nuclear matter, the occupied states are represented as the Fermi gas states below the Fermi momentum k_F and the operator Q can be defined in terms of k_F. In Brueckner-AMD, the occupied states are composed of single-particle orbits with AMD single-particle wave functions, and so it is hard to solve the Bethe-Goldstone equation directly because of treating the Q-operator. Therefore, following the prescription formulated by Bandō et al. (Bandō et al., 1970), which presents an appropriate means of treating Eq. (2) in the finite nuclear systems, we calculate the G-matrix in the following two steps: First, ignoring the Q-operator ($Q \to 1$), we solve the equation for G^0:

$$\hat{G}^0 = \hat{v} + \hat{v} \frac{1}{\varepsilon_\alpha + \varepsilon_\beta - (\hat{t}_1 + \hat{t}_2)} \hat{G}^0. \tag{11}$$

Second, we solve the following equation to take into account the Q-operator:

$$\hat{G} = \hat{G}^0 + \hat{G}^0 \frac{Q-1}{\varepsilon_\alpha + \varepsilon_\beta - (\hat{t}_1 + \hat{t}_2)} \hat{G}. \tag{12}$$

The explicit form of Eq. (12) becomes the algebraic equations as

$$\sum_{\alpha<\beta} \left\{ \delta_{\gamma_1,\alpha}\, \delta_{\delta_1,\beta} + \frac{\langle\, f_{\gamma_1}\, f_{\delta_1} \,|\, \hat{G}^0 \,|\, f_\alpha\, f_\beta - f_\beta\, f_\alpha \,\rangle}{e(\gamma_0\delta_0, \alpha\beta)} \right\} \langle\, f_\alpha\, f_\beta \,|\, \hat{G} \,|\, f_{\gamma_0}\, f_{\delta_0} - f_{\delta_0}\, f_{\gamma_0} \,\rangle$$
$$= \langle\, f_{\gamma_1}\, f_{\delta_1} \,|\, \hat{G}^0 \,|\, f_{\gamma_0}\, f_{\delta_0} - f_{\delta_0}\, f_{\gamma_0} \,\rangle, \tag{13}$$

$$e(\gamma_0\delta_0, \alpha\beta) = \varepsilon_{\gamma_0} + \varepsilon_{\delta_0} - \langle\, f_\alpha \,|\, \hat{t} \,|\, f_\alpha \,\rangle - \langle\, f_\beta \,|\, \hat{t} \,|\, f_\beta \,\rangle. \tag{14}$$

2.2.2 How to solve the Bethe-Boldstone equation

In order to see the way how to solve Eq.(11), we use another expression of the Bethe-Goldstone equation with wave functions as

$$\begin{aligned}\psi_{kl} &= \varphi_{kl} + \frac{Q}{\varepsilon_\alpha + \varepsilon_\beta - (\hat{t}_1 + \hat{t}_2)}\,\hat{G}\cdot\varphi_{kl} \\ &= \varphi_{kl} + \frac{Q}{\varepsilon_\alpha + \varepsilon_\beta - (\hat{t}_1 + \hat{t}_2)}\,\hat{v}\cdot\psi_{kl}\,,\end{aligned} \tag{15}$$

where the following relationship is used:

$$\langle\,\varphi_{ij}\,|\,\hat{G}\,|\,\varphi_{kl}\,\rangle = \langle\,\varphi_{ij}\,|\,\hat{v}\,|\,\psi_{kl}\,\rangle\,. \tag{16}$$

In the above equations, ψ_{kl} and φ_{kl} represent the solution of the Bethe-Goldstone equation and the two-body part of the AMD wave function, respectively. As any analogy of Eq. (15), the equation for G^0, Eq. (11), becomes

$$\psi^0_{kl} = \varphi_{kl} + \frac{1}{\varepsilon_\alpha + \varepsilon_\beta - (\hat{t}_1 + \hat{t}_2)}\,\hat{v}\cdot\psi^0_{kl}\,, \tag{17}$$

where ψ^0_{kl} represents the solution of Eq. (11) and it has

$$\langle\,\varphi_{ij}\,|\,\hat{G}^0\,|\,\varphi_{kl}\,\rangle = \langle\,\varphi_{ij}\,|\,\hat{v}\,|\,\psi^0_{kl}\,\rangle\,. \tag{18}$$

Then, Eq. (17) can be solved as the differential equation for every pair (kl) of particles:

$$[\,\hat{T}_{rel} - \omega\,]\,\left\{\,\delta_{l',l_0}\cdot\varphi_{l_0m}\left(r\,;\,\vec{Z}^{rel}_{kl}\right) - \psi^{0\,JS}_{l'l_0m}(r)\,\right\} = \sum_{l''} V^{JS}_{l'l''}(r)\,\psi^{0\,JS}_{l''l_0m}(r)\,, \tag{19}$$

where $\hat{T}_{rel}$ represents the relative kinetic energy operator and $\omega = \varepsilon_\alpha + \varepsilon_\beta - T_{cm}\,(ij:kl)$. In this case, $\hat{T}_{rel}$ can be expressed as

$$\hat{T}_{rel} = -\frac{\hbar^2}{M}\frac{1}{r}\frac{d^2}{dr^2}r + \frac{\hbar^2}{M}\frac{l'(l'+1)}{r^2}\,, \tag{20}$$

and $T_{cm}\,(ij:kl)$ is the expectation value of the two-body center-of-mass kinetic energy:

$$T_{cm}(ij:kl) = \frac{\langle\,\vec{Z}^{cm}_{ij}\,|\,\hat{T}_{cm}\,|\,\vec{Z}^{cm}_{kl}\,\rangle}{\langle\,\vec{Z}^{cm}_{ij}\,|\,\vec{Z}^{cm}_{kl}\,\rangle}\,, \tag{21}$$

where $\hat{T}_{cm}$ represents the two-body center-of-mass kinetic energy operator and $|\,\vec{Z}^{cm}_{kl}\,\rangle$ is the two-body AMD wave function of the center-of-mass part: $\vec{Z}^{cm}_{kl} = (\vec{Z}_k + \vec{Z}_l)/\sqrt{2}$. Note that the two-body AMD wave function is decomposed into the center-of-mass and relative parts and its relative one can be applied directly to Eq. (17). In Eq. (19), $\varphi_{l_0m}\left(r\,;\,\vec{Z}^{rel}_{kl}\right)$ represent the two-body AMD wave function of the relative part $|\,\vec{Z}^{rel}_{kl}\,\rangle$: $\vec{Z}^{rel}_{kl} = (\vec{Z}_k - \vec{Z}_l)/\sqrt{2}$ for the partial wave having the orbital angular momentum l_0 and its z component m as

$$\langle\,\vec{r}\,|\,\vec{Z}^{rel}_{kl}\,\rangle = \left(\frac{2\nu_{rel}}{\pi}\right)^{3/4}\exp\left[-\nu_{rel}\left(\vec{r} - \frac{\vec{Z}^{rel}_{kl}}{\sqrt{\nu_{rel}}}\right)^2 + \frac{\vec{Z}^{rel\,2}_{kl}}{2}\right] = \sum_{l_0,\,m}\varphi_{l_0m}\left(r\,;\,\vec{Z}^{rel}_{kl}\right)\,|\,l_0m\,\rangle\,, \tag{22}$$

where $\nu_{rel} = \nu/2$ and the explicit expression of $\varphi_{l_0 m}\left(r\,;\,\vec{Z}_{kl}^{rel}\right)$ is given later. $\psi^{0\,JS}_{l'l_0m}(r)$ is the solution of Eq. (19) which has the dependence on (i,j,k,l,α,β) due to ω and $\varphi_{l_0 m}\left(r\,;\,\vec{Z}_{kl}^{rel}\right)$, and $V^{JS}_{l\,l'}(r)$ is the potential for the two-body channel of total angular momentum J and total spin S with the transition between the angular momenta l and l' in the bare interaction $\hat{v}$,

$$V^{JS}_{l\,l'}(r) = \int_{spin} \int d\Omega_{\vec{r}}\, y^{M\,*}_{lSJ}\left(\Omega_{\vec{r}}\right) \hat{v}\, y^{M}_{l'SJ}\left(\Omega_{\vec{r}}\right), \tag{23}$$

where $y^{M}_{lSJ}\left(\Omega_{\vec{r}}\right)$ represents the eigenfunction of two-body total angular momentum.

Here, we present explicit expressions of Eq.(19). In the nucleon-nucleon interaction, two-body total angular momentum J, total spin S, total isospin T, and parity are conserved. However, due to the Fermi statistics of two nucleons, two-body states are restricted to the four states under conditions of $S + T + l = odd$ where l is the two-body angular moment: in the case of even parity $(l = 0, 2, 4, \cdots)$, the spin-triplet $S = 1$ state called "triplet-even (3E)" with the isospin-singlet $T = 0$ and the spin-singlet $S = 0$ state called "singlet-even (1E)" with the isospin-triplet $T = 1$; in the case of odd parity $(l = 1, 3, 5, \cdots)$, the spin-triplet $S = 1$ state called "triplet-odd (3O)" with the isospin-triplet $T = 1$ and the spin-singlet $S = 0$ state called "singlet-odd (1O)" with the isospin-singlet $T = 0$. Hence, the expressions of Eq. (19) for the above four two-body channels with the lowest allowed angular momentum are presented in the following.

At this stage, one has no unique nucleon-nucleon interaction and many varieties. However, at least, nucleon-nucleon interactions have central ($\hat{v}_c$), spin-orbit ($\hat{v}_{ls}$), and tensor ($\hat{v}_t$) forces. Here, we consider only the case of the interaction with the above three forces. For spin-singlet states, the interaction has only the central force, and then, Eq. (19) for the singlet-even (1E) with $l = 0$ becomes

$$\left[-\frac{\hbar^2}{M}\frac{1}{r}\frac{d^2}{dr^2}r - \omega\right]\left\{\varphi_{0m}\left(r\,;\,\vec{Z}_{kl}^{rel}\right) - \psi^{0\,J=0\,S=0}_{00m}(r)\right\} = v_c^{(1E)}(r)\,\psi^{0\,J=0\,S=0}_{00m}(r), \tag{24}$$

and that for the singlet-odd (1O) with $l = 1$ becomes

$$\left[-\frac{\hbar^2}{M}\frac{1}{r}\frac{d^2}{dr^2}r + \frac{\hbar^2}{M}\frac{2}{r^2} - \omega\right]\left\{\varphi_{1m}\left(r\,;\,\vec{Z}_{kl}^{rel}\right) - \psi^{0\,J=1\,S=0}_{11m}(r)\right\} = v_c^{(1O)}(r)\,\psi^{0\,J=1\,S=0}_{11m}(r). \tag{25}$$

For spin-triplet states, nucleon-nucleon interactions include central, spin-orbit, and tensor forces. Note that the orbital angular momentum l state may be admixed with higher angular momentum l' state by the tensor force. Hence, Eq. (19) for the triplet-even (3E) with $l = 0$ becomes the coupled equation to $l' = 2$ as

$$\begin{aligned}
&\left[-\frac{\hbar^2}{M}\frac{1}{r}\frac{d^2}{dr^2}r - \omega\right]\left\{\varphi_{0m}\left(r\,;\,\vec{Z}_{kl}^{rel}\right) - \psi^{0\,J=1\,S=1}_{00m}(r)\right\} = 2\sqrt{2}\,v_t^{(3E)}(r)\,\psi^{0\,J=1\,S=1}_{20m}(r) \\
&+v_c^{(3E)}(r)\,\psi^{0\,J=1\,S=1}_{00m}(r), \\
-&\left[-\frac{\hbar^2}{M}\frac{1}{r}\frac{d^2}{dr^2}r + \frac{\hbar^2}{M}\frac{6}{r^2} - \omega\right]\psi^{0\,J=1\,S=1}_{20m}(r) = 2\sqrt{2}\,v_t^{(3E)}(r)\,\psi^{0\,J=1\,S=1}_{00m}(r) \\
&+\left[\,v_c^{(3E)}(r) - 3v_{ls}^{(3E)}(r) - 2v_t^{(3E)}(r)\,\right]\psi^{0\,J=1\,S=1}_{20m}(r).
\end{aligned} \tag{26}$$

For the the triplet-odd (3O) with $l = 1$, the cases of $J = 0, 1$, and 2 are considered. And then, Eq. (19) for the 3O with $J = 0$ and $l = 1$ becomes

$$\begin{aligned}&[-\frac{\hbar^2}{M}\frac{1}{r}\frac{d^2}{dr^2}r+\frac{\hbar^2}{M}\frac{2}{r^2}-\omega\,]\,\left\{\,\varphi_{1m}\left(r\,;\,\vec{Z}_{kl}^{\,rel}\right)-\psi_{11m}^{0\;J=0\;S=1}(r)\,\right\}\\&=[\,v_c^{(3O)}(r)-2v_{ls}^{(3O)}(r)-4v_t^{(3O)}(r)\,]\,\psi_{11m}^{0\;J=0\;S=1}(r)\,,\end{aligned}\tag{27}$$

that for the 3O with $J = 1$ and $l = 1$ becomes

$$\begin{aligned}&[-\frac{\hbar^2}{M}\frac{1}{r}\frac{d^2}{dr^2}r+\frac{\hbar^2}{M}\frac{2}{r^2}-\omega\,]\,\left\{\,\varphi_{1m}\left(r\,;\,\vec{Z}_{kl}^{\,rel}\right)-\psi_{11m}^{0\;J=1\;S=1}(r)\,\right\}\\&=[\,v_c^{(3O)}(r)-v_{ls}^{(3O)}(r)+2v_t^{(3O)}(r)\,]\,\psi_{11m}^{0\;J=1\;S=1}(r)\,,\end{aligned}\tag{28}$$

and that for the 3O with $J = 2$ and $l = 1$ becomes the coupled equation to $l' = 3$ as

$$\begin{aligned}&[-\frac{\hbar^2}{M}\frac{1}{r}\frac{d^2}{dr^2}r+\frac{\hbar^2}{M}\frac{2}{r^2}-\omega\,]\,\left\{\,\varphi_{1m}\left(r\,;\,\vec{Z}_{kl}^{\,rel}\right)-\psi_{11m}^{0\;J=2\;S=1}(r)\,\right\}=\frac{6\sqrt{6}}{5}\,v_t^{(3O)}(r)\,\psi_{31m}^{0\;J=2\;S=1}(r)\\&+[\,v_c^{(3O)}(r)+v_{ls}^{(3O)}(r)-\frac{2}{5}v_t^{(3O)}(r)\,]\,\psi_{11m}^{0\;J=2\;S=1}(r)\,,\\-\,&[-\frac{\hbar^2}{M}\frac{1}{r}\frac{d^2}{dr^2}r+\frac{\hbar^2}{M}\frac{12}{r^2}-\omega\,]\,\psi_{31m}^{0\;J=2\;S=1}(r)=\frac{6\sqrt{6}}{5}\,v_t^{(3O)}(r)\,\psi_{11m}^{0\;J=2\;S=1}(r)\\&+[\,v_c^{(3O)}(r)-4v_{ls}^{(3O)}(r)-\frac{8}{5}v_t^{(3O)}(r)\,]\,\psi_{31m}^{0\;J=2\;S=1}(r).\end{aligned}\tag{29}$$

In the following, we explain the partial-wave expansion of the two-body AMD wave function of the relative part in Eq. (22). It becomes

$$\langle\,\vec{r}\,|\,\vec{Z}_{kl}^{\,rel}\,\rangle=\left(\frac{2\nu_{rel}}{\pi}\right)^{3/4}\exp\left[-\nu_{rel}\,\vec{r}^{\,2}-\frac{\vec{Z}_{kl}^{\,rel\,2}}{2}\right]\cdot\exp\left[\,2\sqrt{\nu_{rel}}\,\vec{Z}_{kl}^{\,rel}\cdot\vec{r}\,\right]\,,\tag{30}$$

where the complex vector $\vec{Z}_{kl}^{\,rel} = \vec{Z}_R + i\vec{Z}_I$. Here, the term "$\exp\left[\,2\sqrt{\nu_{rel}}\,\vec{Z}_{kl}^{\,rel}\cdot\vec{r}\,\right]$" can be expanded as multipole:

$$\begin{aligned}\exp\left[\,2\sqrt{\nu_{rel}}\,\vec{Z}_{kl}^{\,rel}\cdot\vec{r}\,\right]=(4\pi)^2\sum_{l_1,\,l_2,\,m_1,\,m_2}&J_{l_1}\,(2\sqrt{\nu_{rel}}Z_R r)\cdot i^{l_2}\,j_{l_2}\,(2\sqrt{\nu_{rel}}Z_I r)\,\times\\&Y_{l_1m_1}^*(\hat{\boldsymbol{Z}}_R)\,Y_{l_2m_2}^*(\hat{\boldsymbol{Z}}_I)\,Y_{l_1m_1}(\hat{\boldsymbol{r}})\,Y_{l_2m_2}(\hat{\boldsymbol{r}})\,,\end{aligned}\tag{31}$$

where $Z_{R,\,I} = |\vec{Z}_{R,\,I}|$ and $\hat{\boldsymbol{Z}}_{R,\,I} = \vec{Z}_{R,\,I}/|\vec{Z}_{R,\,I}|$. In Eq. (31), we use the formulas

$$\begin{aligned}\exp[\,i\vec{k}\cdot\vec{r}\,]&=4\pi\sum_{l,\,m}i^l\,j_l(kr)\,Y_{lm}^*(\hat{\boldsymbol{k}})\,Y_{lm}(\hat{\boldsymbol{r}})\,,\\\exp[\,\vec{k}\cdot\vec{r}\,]&=4\pi\sum_{l,\,m}J_l(kr)\,Y_{lm}^*(\hat{\boldsymbol{k}})\,Y_{lm}(\hat{\boldsymbol{r}})\,,\end{aligned}\tag{32}$$

where $J_l(r) \equiv (-i)^l\,j_l(ir)$. We use the following formula for the product of two spherical harmonics with 3-j symbols:

$$Y_{l_1m_1}(\hat{\boldsymbol{r}})\,Y_{l_2m_2}(\hat{\boldsymbol{r}})=\sum_{l,\,m}\sqrt{\frac{(2l_1+1)(2l_2+1)(2l+1)}{4\pi}}\begin{pmatrix}l_1 & l_2 & l\\ m_1 & m_2 & m\end{pmatrix}\begin{pmatrix}l_1 & l_2 & l\\ 0 & 0 & 0\end{pmatrix}Y_{lm}^*(\hat{\boldsymbol{r}}).\tag{33}$$

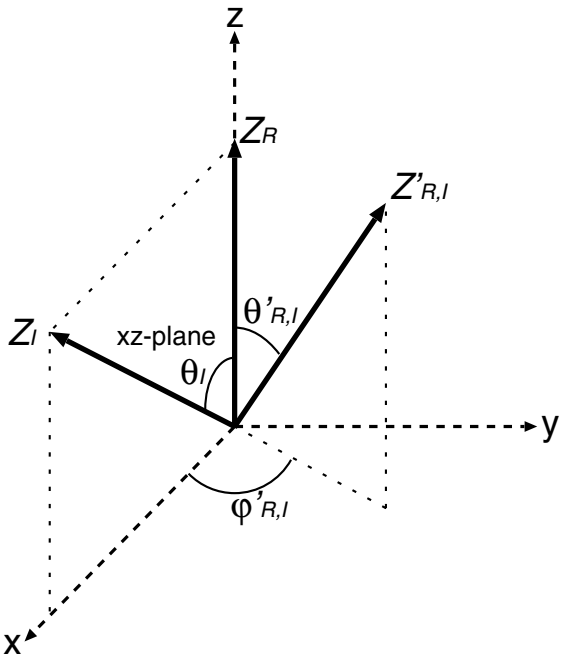

Fig. 1. The vectors $\vec{Z}_{kl}^{rel} = \vec{Z}_R + i\vec{Z}_I$ and $\vec{Z}_{ij}^{rel} = \vec{Z}'_R + i\vec{Z}'_I$ in the body-fixed frame we adopt in this framework are schematically shown.

Thus, in the calculations of $\langle \vec{Z}_{ij}^{rel} \,|\, \hat{O} \,|\, \vec{Z}_{kl}^{rel} \rangle$, the state of $|\, \vec{Z}_{kl}^{rel} \rangle$ can be expressed as the expansion of angular momental states $|\, lm \rangle$:

$$\begin{aligned} \langle \vec{r} \,|\, \vec{Z}_{kl}^{rel} \rangle &= \sum_{l,m} \varphi_{lm}\left(r\,;\, \vec{Z}_{kl}^{rel}\right) |\, lm \rangle \\ &= \left(\frac{2\nu_{rel}}{\pi}\right)^{3/4} \exp\left[-\nu_{rel}\vec{r}^{\,2} - \frac{\vec{Z}_{kl}^{rel\,2}}{2}\right] \sum_{l,m} z_{lm}\left(2\sqrt{\nu_{rel}}\, r\,;\, \vec{Z}_{kl}^{rel}\right) |\, lm \rangle\,, \end{aligned} \tag{34}$$

where

$$\begin{aligned} z_{lm}\left(r\,;\, \vec{Z}_{kl}^{rel}\right) \equiv (4\pi)^{3/2} \sum_{l_1,l_2,m_1,m_2} &\sqrt{(2l_1+1)(2l_2+1)}\, J_{l_1}(Z_R r)\cdot i^{l_2}\, j_{l_2}(Z_I r) \times \\ &Y^*_{l_1 m_1}(\hat{\mathbf{Z}}_R)\, Y^*_{l_2 m_2}(\hat{\mathbf{Z}}_I)\sqrt{2l+1} \begin{pmatrix} l_1 & l_2 & l \\ m_1 & m_2 & m \end{pmatrix} \begin{pmatrix} l_1 & l_2 & l \\ 0 & 0 & 0 \end{pmatrix}. \end{aligned} \tag{35}$$

In the case of the rotational-invariant operator, for example, nucleon-nucleon interaction, its expectation value may be calculated in the arbitrary body-fixed frame because $\langle \vec{Z}_{ij}^{rel} \,|\, \hat{O} \,|\, \vec{Z}_{kl}^{rel} \rangle = \langle \vec{Z}_{ij}^{rel} \,|\, \hat{R}^\dagger(\Omega)\hat{O}\hat{R}(\Omega) \,|\, \vec{Z}_{kl}^{rel} \rangle$ where $\hat{R}(\Omega)$ is the operator of rotation by the arbitrary Euler angle Ω. Here, we adopt the body-fixed frame shown in Fig. 1 where $\vec{Z}_R$ is fixed along the z-axis with the angle $\hat{\mathbf{Z}}_R = (\theta_R = 0, \varphi_R = 0)$ and $\vec{Z}_I$ is in the xz-plane with the angle $\hat{\mathbf{Z}}_I = (\theta_I, \varphi_I = 0)$.

2.2.3 G-matrix calculations with correlation functions

In order to explain the way how to calculate the G-matrix element, we provide another viewpoint of Eq. (15):

$$\psi_{kl} = \varphi_{kl} + \frac{Q}{\varepsilon_\alpha + \varepsilon_\beta - (\hat{t}_1 + \hat{t}_2)} \hat{G} \cdot \varphi_{kl} \equiv \hat{F}_{kl} \cdot \varphi_{kl} \,, \tag{36}$$

where we call $\hat{F}_{kl}$ the "correlation function" defined schematically as $\hat{F}_{kl} = \psi_{kl}/\varphi_{kl}$ which represents nucleon-nucleon correlations induced by the interaction. From Eqs. (16) and (36), one can obtain the G-matrix element as

$$\langle\, \varphi_{ij} \,|\, \hat{G} \,|\, \varphi_{kl} \,\rangle = \langle\, \varphi_{ij} \,|\, \hat{v} \cdot \hat{F}_{kl} \,|\, \varphi_{kl} \,\rangle \,. \tag{37}$$

The equation for $\hat{G}^0$ has the analogy to Eq. (37):

$$\langle\, \varphi_{ij} \,|\, \hat{G}^0 \,|\, \varphi_{kl} \,\rangle = \langle\, \varphi_{ij} \,|\, \hat{v} \cdot \hat{F}^0_{kl} \,|\, \varphi_{kl} \,\rangle \,, \tag{38}$$

where the correlation function $\hat{F}^0_{kl}$ is defined as $\hat{F}^0_{kl} = \psi^0_{kl}/\varphi_{kl}$ by using the solution ψ^0_{kl} of Eq. (17). Hence, $\hat{G}^0$ for each J and S channel becomes

$$G^{0\,JS}_{\;l_0 l'}(r) = \sum_{l''} V^{JS}_{l' l''}(r)\, F^0_{kl}\, [\,{}^{JS}_{l'' l_0}\,](\omega, r) \,, \tag{39}$$

where the correlation function is given by $\psi^{0\,JS}_{l' l_0 m}(r)$ and $\varphi_{l_0 m}\left(r\,;\, \vec{Z}^{rel}_{kl}\right)$ in Eq. (19) as

$$F^0_{kl}\, [\,{}^{JS}_{l' l_0}\,](\omega, r) = \psi^{0\,JS}_{l' l_0 m}(r) \,/\, \varphi_{l_0 m}\left(r\,;\, \vec{Z}^{rel}_{kl}\right) . \tag{40}$$

Note that the above correlation function has the dependence on $(i, j, k, l, \alpha, \beta)$ through $\varphi_{l_0 m}\left(r\,;\, \vec{Z}^{rel}_{kl}\right)$ and $\omega = \varepsilon_\alpha + \varepsilon_\beta - T_{cm}(ij : kl)$ of Eq. (19). The correlation function of Eq. (40) is approximated as $m = 0$ in $\psi^{0\,JS}_{l' l_0 m}(r)$ and $\varphi_{l_0 m}\left(r\,;\, \vec{Z}^{rel}_{kl}\right)$ because we find that it has little dependence on m. In order to carry the practical calculations, we determine $\hat{G}^0$ with explicit operators as follows:

$$\hat{G}^{0\,S}_{\;l_0 l'} = \sum_{\lambda=0}^{2} G^{0\,S}_{\;l_0 l',\lambda}(r)(\boldsymbol{R}_\lambda \cdot \boldsymbol{S}_\lambda) \,, \tag{41}$$

where $(\boldsymbol{R}_\lambda \cdot \boldsymbol{S}_\lambda)$ is a scalar product of an orbital tensor $\boldsymbol{R}_\lambda$ and a spin tensor $\boldsymbol{S}_\lambda$ of rank λ. The components of $\lambda = 0, 1$, and 2 correspond to the central, spin-orbit, and tensor forces in a potential, respectively. And then, one can utilize the following equation

$$G^{0\,S}_{\;l_0 l',\lambda}(r) = \frac{(2\lambda+1)}{\langle\, l_0 \,||\, \boldsymbol{R}_\lambda \,||\, l' \,\rangle\, \langle\, S \,||\, \boldsymbol{S}_\lambda \,||\, S \,\rangle} \sum_J (-1)^{J-l_0-S}(2J+1)\, W(l_0 l' SS; \lambda J)\, G^{0\,JS}_{\;l_0 l'}(r) \,, \tag{42}$$

where the expressions with double bars such as $\langle\, l_0 \,||\, \boldsymbol{R}_\lambda \,||\, l' \,\rangle$ represent the reduced matrix elements and $W(l_0 l' SS; \lambda J)$ is the Racah coefficient. In this calculation, the angular momenta l_0 and l' in Eq. (42) are taken as the allowed lowest values for each two-body channel: $l_0 = l' = 0$ in the 1E and 3E central force, $l_0 = l' = 1$ in all forces of the 1O and 3O channels, $l_0 = l' = 2$ in the 3E spin-orbit force, and $l_0 = 0$, $l' = 2$ in the 3E tensor force. As a result, $\hat{G}^0$ becomes

$$\hat{G}^0 = G^0_{\lambda=0}(r) + G^0_{\lambda=1}(r)\vec{L} \cdot \vec{S} + G^0_{\lambda=2}(r) S_{12}. \tag{43}$$

Note that $\hat{G}^0$ has the dependence on (i,j,k,l,α,β) drived from the correlation function of Eq. (40). By using the matrix element for $\hat{G}^0$, $\langle f_\gamma f_\delta \,|\, \hat{G}^0 \,|\, f_\alpha f_\beta - f_\beta f_\alpha \rangle$, one can obtain the G-matrix element $\langle f_\gamma f_\delta \,|\, \hat{G} \,|\, f_\alpha f_\beta - f_\beta f_\alpha \rangle$ from Eq. (13).

The G-matrix has the dependence on the bra state (i,j) and difficulty to treat the case of superpostion of wave functions. In addition, the G-matrix is given by the matrix element not to be easy to analyze its properties. Hence, in the following, we present the practical alternative. In Eq. (19), we use $T_{cm}(kl)$ instead of $T_{cm}(ij:kl)$ in ω as

$$T_{cm}(kl) = \frac{\langle \vec{Z}^{cm}_{kl} \,|\, \hat{T}_{cm} \,|\, \vec{Z}^{cm}_{kl} \rangle}{\langle \vec{Z}^{cm}_{kl} \,|\, \vec{Z}^{cm}_{kl} \rangle}, \tag{44}$$

which reprents the expectation value of the two-body center-of-mass kinetic energy for only the ket state. We solve Eq. (19) using $\omega_0 = \varepsilon_\alpha + \varepsilon_\beta - T_{cm}(kl)$ instead of ω, and then, by using its solution, we determine the correlation function $F^0_{kl}\,[\,{}^{JS}_{l'l_0}\,](\omega_0, r)$ with no dependence on the bra state (i,j). One can obtain the alternative of the G^0-matrix, $\langle f_\gamma f_\delta \,|\, \hat{G}'^0 \,|\, f_\alpha f_\beta - f_\beta f_\alpha \rangle$, by applying Eqs. (39) and (42) with the correlation function $F^0_{kl}\,[\,{}^{JS}_{l'l_0}\,](\omega_0, r)$. Here, we consider the ratio of the G-matrix element solved by $\langle f_\alpha f_\beta \,|\, \hat{G}^0 \,|\, f_\alpha f_\beta - f_\beta f_\alpha \rangle$ with $F^0_{kl}\,[\,{}^{JS}_{l'l_0}\,](\omega, r)$ from Eq. (13), $\langle f_\alpha f_\beta \,|\, \hat{G} \,|\, f_\alpha f_\beta - f_\beta f_\alpha \rangle$, to the matrix element $\langle f_\alpha f_\beta \,|\, \hat{G}'^0 \,|\, f_\alpha f_\beta - f_\beta f_\alpha \rangle$:

$$C^{\alpha\beta}_Q = \frac{\langle f_\alpha f_\beta \,|\, \hat{G} \,|\, f_\alpha f_\beta - f_\beta f_\alpha \rangle}{\langle f_\alpha f_\beta \,|\, \hat{G}'^0 \,|\, f_\alpha f_\beta - f_\beta f_\alpha \rangle}, \tag{45}$$

which represents the effects of the operator Q and $T_{cm}(ij:kl)$. By using the above value $C^{\alpha\beta}_Q$, one can present the explicit form of the correlation function $\hat{F}_{kl}$ in Eq. (36) as

$$F_{kl}\,[\,{}^{JS}_{l'l_0}\,](\omega_0, r) = C^{\alpha\beta}_Q \cdot F^0_{kl}\,[\,{}^{JS}_{l'l_0}\,](\omega_0, r). \tag{46}$$

Hence, the G-matrix for each J and S channel becomes

$$G^{JS}_{l_0 l'}(r) = \sum_{l''} V^{JS}_{l'l''}(r)\, F_{kl}\,[\,{}^{JS}_{l''l_0}\,](\omega_0, r). \tag{47}$$

Applying Eq. (42) with $G^{JS}_{l_0 l'}(r)$ instead of $G^{0\,JS}_{\quad l_0 l'}(r)$, the G-matrix can be determined as

$$\hat{G} = G_{\lambda=0}(r) + G_{\lambda=1}(r)\vec{L}\cdot\vec{S} + G_{\lambda=2}(r) S_{12}. \tag{48}$$

Note that the expectation value for the potential of Eq. (48) reproduces the G-matrix element. As seen in the above discussion, one can obtain the G-matrix as the effective interaction with the explicit form by using the correlation function of Eq. (46).

2.2.4 Explicit examples of G-matrix

In order to see the properties of G-matrix in Brueckner-AMD, we present the G-matrix in the specific case. As the bare nucleon-nucleon interaction, we adopt the Argonne $v8'$ (AV8′) (Wiringa & Pieper, 2002). AV8′ is constructed by renormalizing the $\vec{L}^2$ and $(\vec{L}\cdot\vec{S})^2$ terms in the Argonne $v18$ (AV18) (Wiringa et al., 1995), which is the high accurate bare nucleon-nucleon

interaction, into the central, spin-orbit, and tensor forces. And the iso-spin symmetry and independence breaking included in AV18 are ignored in the case of AV8′. In the following, we switch off the electromagnetic interactions.

As a preparation, several explicit terms of the G-matrix in Eq. (48) are shown. For the spin-singlet states, the G-matrix has only the central force given by the simple product of the bare interaction multiplied by the correlation function. For example, the singlet-even (1E) central force of the G-matrix becomes

$$G_c^{(1E)}(r) = v_c^{(1E)}(r) \cdot F_{kl}\,[\,{}^{J=0\,S=0}_{l'=0\,l_0=0}\,](\omega_0, r). \tag{49}$$

The singlet-odd (1O) central G-matrix is given as the same way as the above equation. On the other hand, for the spin-triplet states, the non-central forces in the bare interaction are renormalized into the central G-matrix through the correlation functions. Hence, the triplet-even (3E) central G-matrix becomes

$$G_c^{(3E)}(r) = v_c^{(3E)} \cdot F_{kl}\,[\,{}^{J=1\,S=1}_{l'=0\,l_0=0}\,] + 2\sqrt{2}\,v_t^{(3E)} \cdot F_{kl}\,[\,{}^{J=1\,S=1}_{l'=2\,l_0=0}\,], \tag{50}$$

and the triplet-odd (3O) central becomes

$$\begin{aligned} G_c^{(3O)}(r) = \frac{1}{9}\ \{\ & (v_c^{(3O)} - 2v_{ls}^{(3O)} - 4v_t^{(3O)}) \cdot F_{kl}\,[\,{}^{J=0\,S=1}_{l'=1\,l_0=1}\,] \\ & + 3(v_c^{(3O)} - v_{ls}^{(3O)} + 2v_t^{(3O)}) \cdot F_{kl}\,[\,{}^{J=1\,S=1}_{l'=1\,l_0=1}\,] \\ & + 5(v_c^{(3O)} + v_{ls}^{(3O)} - \frac{2}{5}v_t^{(3O)}) \cdot F_{kl}\,[\,{}^{J=2\,S=1}_{l'=1\,l_0=1}\,] + 6\sqrt{6}\,v_t^{(3O)} \cdot F_{kl}\,[\,{}^{J=2\,S=1}_{l'=3\,l_0=1}\,]\ \}, \end{aligned} \tag{51}$$

where the (ω_0, r) dependence in the above right hands is omitted for simplicity. In addition, as examples, for the 3E tensor and 3O spin-orbit G-matrices, their expressions where the (ω_0, r) dependence is omitted as the aboves are given:

$$G_t^{(3E)}(r) = v_t^{(3E)} \cdot F_{kl}\,[\,{}^{J=1\,S=1}_{l'=0\,l_0=0}\,] + \frac{1}{2\sqrt{2}}(v_c^{(3E)} - 3v_{ls}^{(3E)} - 2v_t^{(3E)}) \cdot F_{kl}\,[\,{}^{J=1\,S=1}_{l'=2\,l_0=0}\,], \tag{52}$$

$$\begin{aligned} G_{ls}^{(3O)}(r) = -\frac{1}{12}\ \{\ & 2(v_c^{(3O)} - 2v_{ls}^{(3O)} - 4v_t^{(3O)}) \cdot F_{kl}\,[\,{}^{J=0\,S=1}_{l'=1\,l_0=1}\,] \\ & + 3(v_c^{(3O)} - v_{ls}^{(3O)} + 2v_t^{(3O)}) \cdot F_{kl}\,[\,{}^{J=1\,S=1}_{l'=1\,l_0=1}\,] \\ & - 5(v_c^{(3O)} + v_{ls}^{(3O)} - \frac{2}{5}v_t^{(3O)}) \cdot F_{kl}\,[\,{}^{J=2\,S=1}_{l'=1\,l_0=1}\,] - 6\sqrt{6}\,v_t^{(3O)} \cdot F_{kl}\,[\,{}^{J=2\,S=1}_{l'=3\,l_0=1}\,]\ \}. \end{aligned} \tag{53}$$

In Brueckner-AMD, the G-matrix for each pair have dependence on not only the paricle pair (k, l) but also the single-particle orbits (α, β) due to the dependence on $\omega_0 = \varepsilon_\alpha + \varepsilon_\alpha - T_{cm}(kl)$ in the correlation function. Therefore, in general, one cannot abstract the explicit form as the interaction between particles (k, l). However, as the special case, in the system of ^{4}He consisting of the spin-up proton, spin-up neutron, spin-down proton, and spin-down neutron, the G-matrix is given as the interaction between particles (k, l) because the single-particle orbits $|\, f_{\alpha,\beta}\,\rangle$ are equal to the one-particle wave funcions, which means $(\alpha, \beta) = (k, l)$, on condition that the overlap matrix B_{ij} in Eq. (3) becomes a diagonal matrix such as this system. Here, we consider the G-matrix between particles in the 3N-N cluster system of ^{4}He where

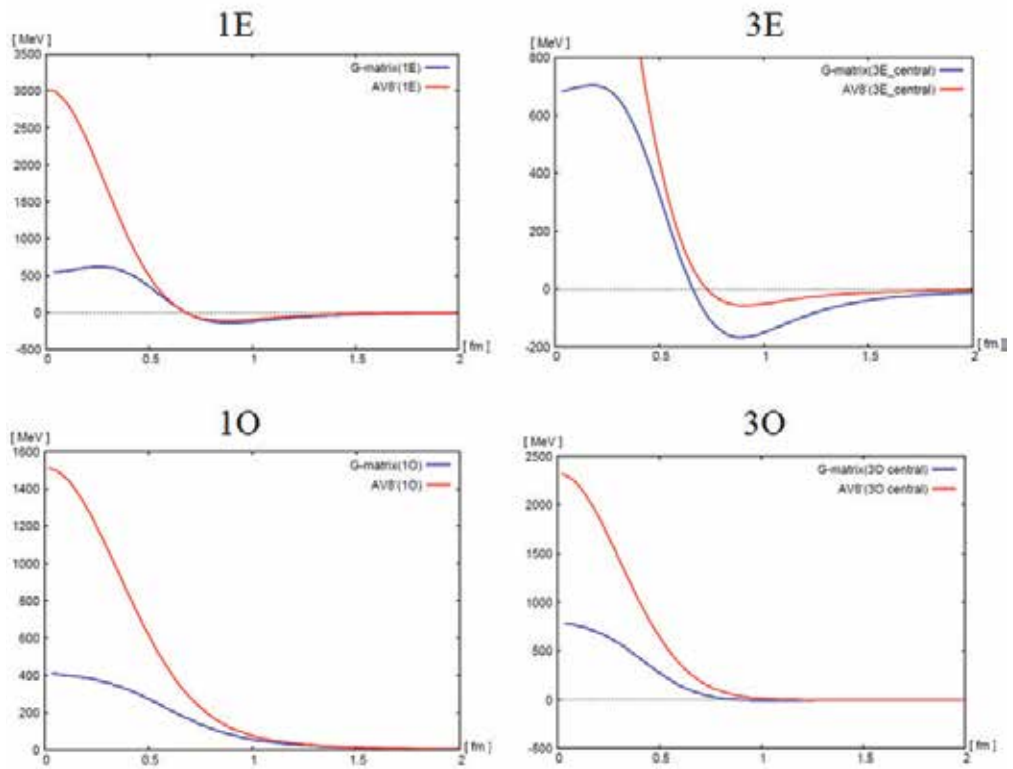

Fig. 2. The comparison of the G-matrix with the bare interaction AV8′ for the central components of two-body four channels. In these graphs, the x- and y-axes represent the distances between nucleons (fm) and the potential energies (MeV), respectively. The blue and red lines represent the G-matrix and AV8′, respectively. The explanation of the G-matrix is in text in detail. In the 3E channel, the attractive part is enlarged.

three nucleons (3N) located at the same positon are separated from one nucleon (N). We assume that three nucleons consist of the spin-up proton, spin-up neutron, and spin-down proton and one nucleon to be sperated is the spin-down neutron, and the distance between three nucleons and one nucleon is 1.0 fm. The AMD wave funciton of Eq. (1) with $\nu = 0.238$ (fm^{-2}) is used in this calculation. In Figs. 2 and 3, we present all forces of the G-matrix between the spin-up proton in three nucleons and the spin-down neutron to be one nucleon sperated from three nucleons at a distance of 1.0 fm and compare them with those of the bare interaction AV8′. As seen in Fig. 2, the central forces of the bare interaction AV8′ have huge repulsive parts at a short distance, while, in the central G-matrices, the short range repulsion is reduced to be applicable to the AMD wave function. At a long distance, each force of the G-matrix except the 3E state agrees with the behaviour of the bare interaction. For the 3E G-matrices, the renormalization of the strong 3E tensor force with a long range tail in the bare interaction acts as the long range correlation to be large contributions. Especially, in the 3E central G-matrix, the renormalization of tensor force by the correlation for the admixture of $l' = 2$, $F_{kl}\left[\begin{smallmatrix} J=1\, S=1 \\ l'=2\, l_0=0 \end{smallmatrix}\right]$ in Eq. (50), induces the more attractive part than that of the bare interaction and contributes largely to the binding energy of a nucleus.

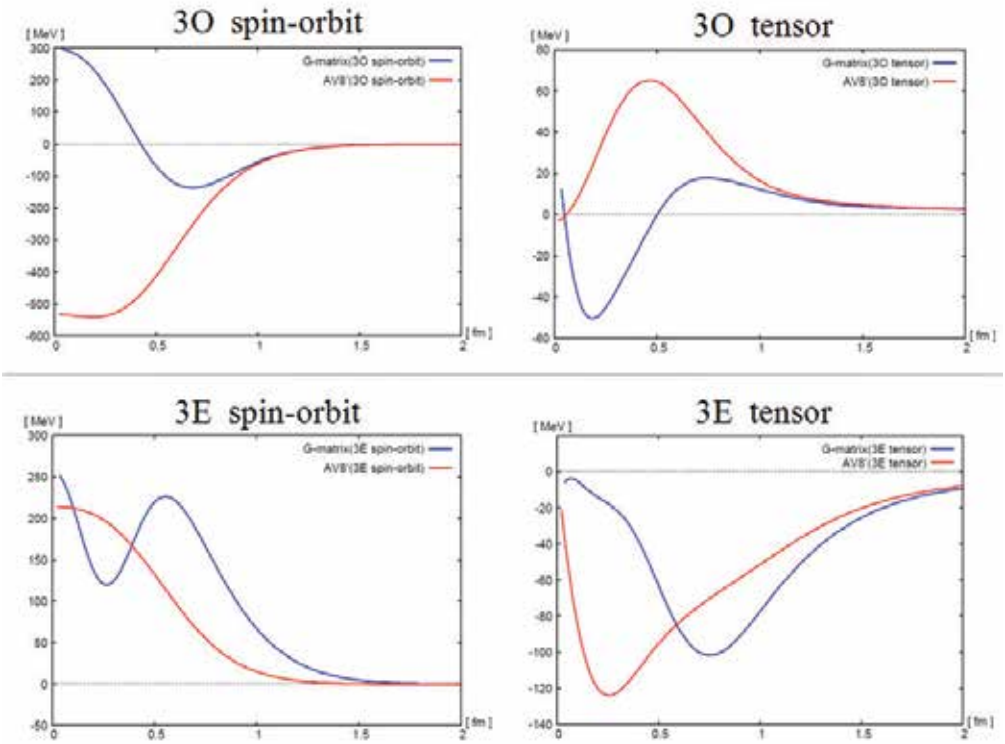

Fig. 3. The comparison of the G-matrix with the bare interaction AV8′ for the non-central components of 3O and 3E channels in the upper and lower panels, respectively. In these graphs, the meanings of the axes and lines are the same as Fig. 2.

2.3 Energy variation in Brueckner-AMD

In the AMD method, the wave-packet positions $\vec{Z}_i$ in Eq. (1) are complex variational parameters in the A-nucleons wave function. In this method, one usually sets the initial configuration of the wave-packet positions $\{\vec{Z}_i\}$ randomly and obtains the optimized solution automatically with no assumption by using the frictional cooling method of molecular dynamics (Kanada-En'yo et al., 1995) to determine $\vec{Z}_i$. The brief expression of frictional cooling equation is given by

$$\frac{d\vec{Z}_i}{dt} = -\frac{\partial\langle H\rangle}{\partial\vec{Z}_i^*}, \quad \frac{d\vec{Z}_i^*}{dt} = -\frac{\partial\langle H\rangle}{\partial\vec{Z}_i}, \tag{54}$$

where $\langle H\rangle$ is the expectation value of Hamiltonian. In Brueckner-AMD, the expectation value of Hamiltonian is expressed as $\langle H\rangle = \langle T\rangle - \langle T_{CM}\rangle + \langle G\rangle$ where $\langle T\rangle$, $\langle T_{CM}\rangle$, and $\langle G\rangle$ represent the expectation values of the A-body summation of the one-body kinetic energy operator $\hat{t}_i$ as $\hat{T} = \sum_i^A \hat{t}_i$, the center-of-mass kinetic energy of the system, and the G-matrix as two-body interactions, respectively. In Eq. (54), the next positions of $\vec{Z}_i$ in the time evolution are decided as

$$\vec{Z}_i(t+\Delta t) = \vec{Z}_i(t) - \Delta t \cdot \frac{\partial\langle H\rangle}{\partial\vec{Z}_i^*}. \tag{55}$$

If $\langle H \rangle$ converges in this time evolution, we consider that the optimized energy and state are attained. In Brueckner-AMD, the derivative of $\vec{Z}_i$ in $\langle H \rangle$ cannot be calculated analytically because the G-matrix depends on the change of the single-particle orbits and the Pauli projection operator derived from the configuration of the wave-packet positions $\{\vec{Z}_i\}$. Therefore, we determine the G-matrix self-consistently for each small displaced configuration of $\{\vec{Z}_i + \Delta\vec{Z}_i\}$ and calculate this derivative as the difference in $\vec{Z}_i$.

3. Applications

We apply Brueckner-AMD to various light nuclei and present the applicability of this method. In the subsection 3.1, we present the results of light nuclei with the mass number $A < 10$ to describe cluster structures and reproduce the energy level schemes in Brueckner-AMD. Furthermore, we discuss the mechanism of clustering in ^{8}Be which has the alpha-alpha cluster structure in the subsection 3.2. In these calculations, we adopt the bare nuclear interaction of the Argonne $v8'$ (AV8$'$) (Wiringa & Pieper, 2002) explained in the previous section and switch off the electromagnetic interactions.

3.1 Description of the structures and energy-level schemes of light nuclei

In Brueckner-AMD, the bound states of nucleus can be obtained as the solution of energy variation starting from the bare nuclear interactions without any assumption of configurations. However, in general, since the AMD wave functions are not good quantum states of the spin and parity (J^π), one cannot calculate the energy-level scheme by a single AMD wave function and must project out the AMD wave functions onto the spin and parity eigenstates, which means the superposition of space-reflected and rotated Slater determinants (Kanada-En'yo et al., 1995). The parity projection means a linear combination of two Slater determinants:

$$|\,\Phi^\pm\,\rangle = \frac{1}{\sqrt{2}}\left(1 \pm \hat{P}\right)|\,\Phi\,\rangle, \tag{56}$$

where $\hat{P}$ is the space-reflection operator that operates at the spatial coordinate $\vec{Z}_i$ of each nucleon. In projecting out the wave functions onto each spin-parity $J^\pm$ state, the spin- and parity-projected state $|\,\Phi^{J\pm}_{MK}\,\rangle$ is expressed as

$$|\,\Phi^{J\pm}_{MK}\,\rangle = \frac{2J+1}{8\pi^2}\int d\Omega\, D^{J\,*}_{MK}(\Omega)\,\hat{R}(\Omega)\,|\,\Phi^\pm\,\rangle, \tag{57}$$

where $D^J_{MK}(\Omega)$ is the Wigner D-function and $\hat{R}(\Omega)$ is the rotational operator that makes the spatial and spin coordinates rotated by the Euler angle Ω. In the above equation, the integration means a linear combination of differential rotated Slater determinants. The energy expectation value of $|\,\Phi^{J\pm}_{MK}\,\rangle$ is given by

$$\langle\,\hat{H}^{J\pm}_{K'K}\,\rangle \equiv \frac{\langle\,\Phi^{J\pm}_{MK'}\,|\,\hat{H}\,|\,\Phi^{J\pm}_{MK}\,\rangle}{\langle\,\Phi^{J\pm}_{MK'}\,|\,\Phi^{J\pm}_{MK}\,\rangle} = \frac{\int d\Omega\, D^{J\,*}_{K'K}(\Omega)\left\{\langle\,\Phi\,|\,\hat{R}(\Omega)\cdot\hat{H}\,|\,\Phi\,\rangle \pm \langle\,\Phi\,|\,\hat{P}\hat{R}(\Omega)\cdot\hat{H}\,|\,\Phi\,\rangle\right\}}{\int d\Omega\, D^{J\,*}_{K'K}(\Omega)\left\{\langle\,\Phi\,|\,\hat{R}(\Omega)\,|\,\Phi\,\rangle \pm \langle\,\Phi\,|\,\hat{P}\hat{R}(\Omega)\,|\,\Phi\,\rangle\right\}}. \tag{58}$$

In order to calculate the energy expectation value of the $J^\pm$ state correctly, we perform the K-mixing by diagonalizing the Hamiltonian matrix $\langle\,\Phi^{J\pm}_{MK'}\,|\,\hat{H}\,|\,\Phi^{J\pm}_{MK}\,\rangle$ and norm matrix $\langle\,\Phi^{J\pm}_{MK'}\,|\,\Phi^{J\pm}_{MK}\,\rangle$ simultaneously for the quantum numbers of K and K'.

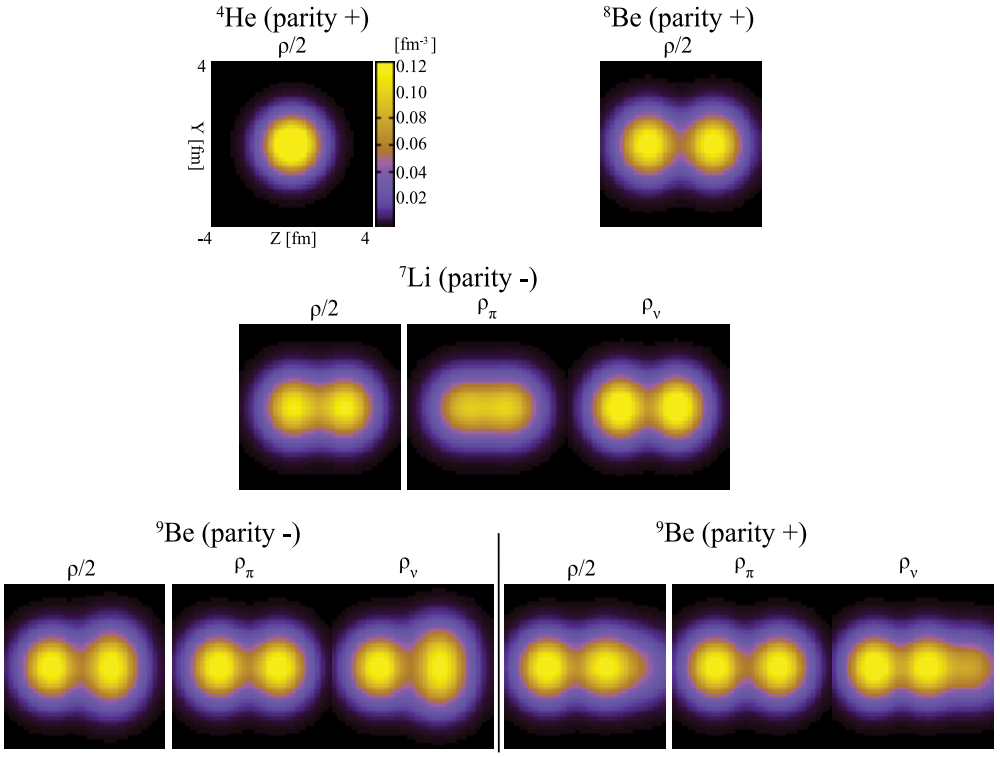

Fig. 4. Intrinsic matter ρ densities as a half value, the proton ρ_π and neutron ρ_ν ones of the lowest-energy parity solutions in ^{4}He, ^{7}Li, ^{8}Be, and ^{9}Be. The size of these squares is shown in the panel of ^{4}He.

In these calculations, we determine the wave functions $|\Phi\rangle$ by performing the energy variation for the parity-projected states $|\Phi^\pm\rangle$. Therefore, we can obtain not only the lowest-energy parity solution corresponding to the ground state but also the excited parity solution, whose parity is opposite to that of the lowest-energy state. Projecting out the solutions of the energy variation, $|\Phi^\pm\rangle$, onto each J state, we calculate the energy levels. In the following, we present the results of ^{4}He, ^{7}Li, ^{8}Be, and ^{9}Be using the above procedure. As the Gaussian width parameter ν for every wave packet in Eq. (1), we adopt $\nu = 0.222$ (fm^{-2}) for ^{4}He and $\nu = 0.208$ (fm^{-2}) for other nuclei. Fig. 4 shows the intrinsic densities obtained from the wave functions $|\Phi\rangle$. For ^{9}Be, both the lowest-energy negative-parity solution and the excited positive-parity one are shown. In these figures, the X-, Y-, and Z-axes in the body-fixed frame are chosen so as to be $\langle\sum_i z_i^2\rangle \geq \langle\sum_i y_i^2\rangle \geq \langle\sum_i x_i^2\rangle$, and each density distribution in the Z-Y plane is displayed. As seen in Fig. 4, the alpha particle (^{4}He) is compactly spherical and ^{8}Be consists of two-alpha cluster. In this result, the density of ^{7}Li does not present the explicit cluster structure as seen in an almost symmetric distribution. In the densities of ^{9}Be, the structures of two-alpha cluster plus a valence neutron can be seen. In the negative-parity state of ^{9}Be, the density distribution of the valence neutron corresponds to a π-molecular orbit; on the other hand, that of the positive-parity state corresponds to a σ-molecular orbit.

In Table 1, the calculated binding energy of the ground state for each nucleus is listed to be compared with the experimental one. Although the calculated ground states are underbinding for the experimental ones, it is known that bare three nucleons interactions are needed to reproduce the experimental binding energies from accurate few-body calculations (Wiringa et al., 2000). However, in this work, there seems to be room for improvement to develop these calculations to the superposition with the wave functions having different configurations $\{\vec{Z}_i\}$ or Gaussian width parameters ν. The calculated energy-level schemes of ^{7}Li, ^{8}Be, and ^{9}Be are shown in Fig. 5. These energy levels are reproduced well. In the result of ^{9}Be, the energy levels including the first excited states, $3/2^-_2$, $5/2^-_2$, and $7/2^-_2$, which can be described by the K-mixing, are also reproduced well. In these calculations, in the negative-parity states of ^{9}Be, the group of the dominant $K = 3/2$ i.e. $K^\pi = 3/2^-$ band contains $3/2^-_1$, $5/2^-_1$, and $7/2^-_1$ states, while the $1/2^-_1$, $3/2^-_2$, $5/2^-_2$, and $7/2^-_2$ states belong to the $K^\pi = 1/2^-$ band. The predicted $9/2^-_1$ state is described coherently by the $K = 1/2$ and $K = 3/2$ states, which has almost equal weights to the $K = 1/2$ and $K = 3/2$. The positive-parity states of ^{9}Be are described as the $K^\pi = 1/2^+$ band.

nucleus	J^π	B-AMD (MeV)	EXP (MeV)
^{4}He	0^+	-24.6	-28.3
^{7}Li	$3/2^-$	-29.6	-39.2
^{8}Be	0^+	-44.0	-56.5
^{9}Be	$3/2^-$	-41.9	-58.2

Table 1. Total binding energies of the ground states for ^{4}He, ^{7}Li, ^{8}Be, and ^{9}Be. The column labeled "J^π" lists the spin and parity of the ground state for each nucleus, and the columns labeled "B-AMD" and "EXP" list the calculated binding energies and the experimental ones, respectively.

3.2 Investigation of the mechanism of alpha-alpha clustering

In the following, we simulate the development of the alpha-alpha cluster in ^{8}Be and investigate its mechanism by using the bare nuclear interaction AV8′ in the Brueckner-AMD framework. In this work, we construct the states that have the definite distance between two quasi-clusters consisting of four nucleons of the spin-up proton, spin-up neutron, spin-down proton, and spin-down neutron by using the constraint cooling method (Yamamoto et al., 2010). The definition of the distance between quasi-clusters in this case is represented as

$$\langle d^2 \rangle^{1/2} = |\vec{R}_1 - \vec{R}_2|, \quad \vec{R}_1(\vec{R}_2) = \frac{1}{4} \sum_{i \in C_1(C_2)} \frac{\mathrm{Re}\vec{Z}_i}{\sqrt{\nu}}, \tag{59}$$

where the $\vec{R}_1(\vec{R}_2)$ represents the center of mass of the quasi-cluster $C_1(C_2)$ consisting of four nucleons. We take the z-axis as an inertia axis and the center of mass of quasi-clusters on the z-axis. We define a quasi-cluster as an initial set of nucleons that are chosen arbitrarily and determine a configuration of eight nucleons for ^{8}Be by solving the following equation of the constraint cooling method as an energy variation:

$$\frac{d\vec{Z}_i}{dt} = -\frac{\partial \langle H \rangle}{\partial \vec{Z}_i^*} - \frac{\partial C}{\partial \vec{Z}_i^*}, \quad C = C_0 \cdot \left(\langle d^2 \rangle^{1/2} - d \right)^2, \tag{60}$$

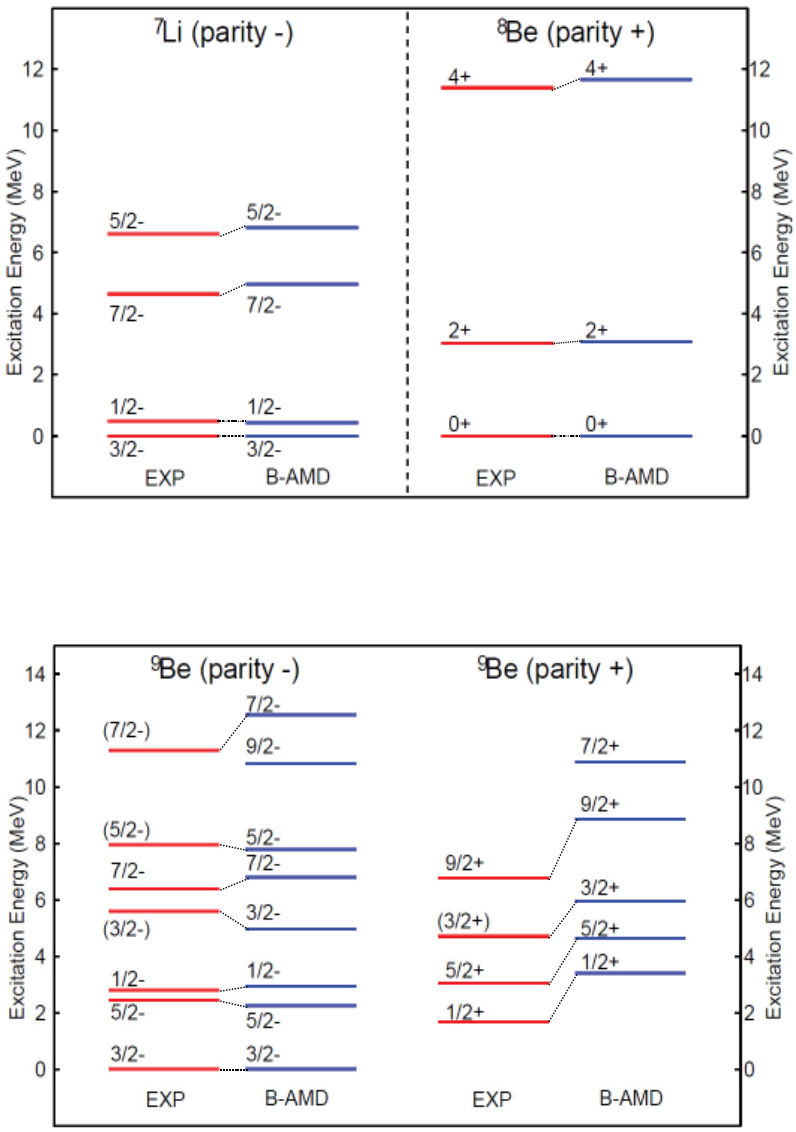

Fig. 5. Low-lying energy-level schemes of the experiments and Brueckner-AMD calculations labeled "EXP" and "B-AMD", respectively. The groud states are normalized to zero energy in these figures. Each energy level is represented as the line labeled its spin and parity.

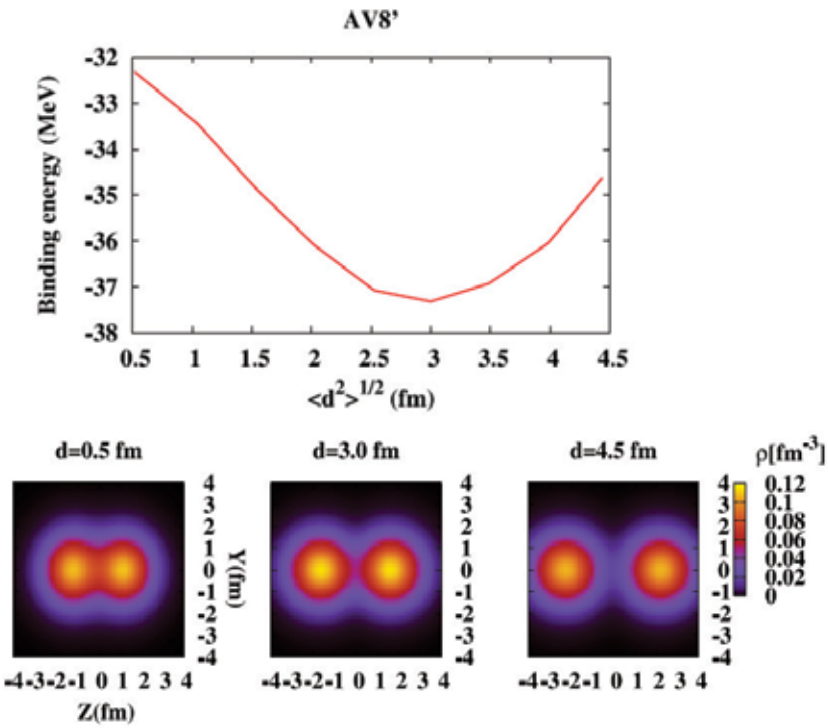

Fig. 6. Upper panel: Total binding energies of ^{8}Be are shown as a function of the distance of quasi-clusters. Lower panels: Density distributions of ^{8}Be at $d = 0.5, 3.0, 4.5$ fm.

where C_0 is the positive constant and d is the constraint parameter; in this work, d is the distance of quasi-clusters. The above equation makes it possible to obtain the solution of the energy variation under the constraint of a distance between two quasi-clusters. Note that the set of nucleons is not assumed to be localized spatially in this case. As a parameter of the wave function, we use the optimized Gaussian width for every wave packet in Eq. (1); $\nu = 0.195$ (fm^{-2}). We perform the energy variation and calculate the total binding energy for the parity-projected states corresponding to the lowest-energy parity solutions $|\,\Phi^+\,\rangle$ in Eq. (56). In Fig. 6, the energy curve of calculated total binding energies are shown as a function of the distance between two quasi-clusters in the upper panel, and we show the intrinsic density distribution of wave functions obtained at different d-values ($d = 0.5, 3.0$, and 4.5 fm) in the lower panels. As seen in Fig. 6, one can see that the optimum distances are around 3.0 fm, where the alpha-alpha structure is realized starting from the bare nuclear interaction AV8′, and the situation that the localized clusters are more developed at larger distances is reproduced as the results of the energy variation. In Fig. 7, we present single-particle energies and orbits at different distances d. Single-particle energies of eight nucleons are degenerated approximately into two types of energy ε_1 and ε_2 as seen in the upper panel of Fig. 7. The two energy orbits correspond to gerade and ungerade orbits in the molecular orbital method (Bandō et al., 1970). However, in the present approach without the molecular-orbit assumption, the single-particle orbits describe not only molecular orbits but also atomic orbits of a mean field. At the small distance $d = 0.5$ fm, $\varepsilon_2 - \varepsilon_1 = 15$ MeV are obtained in this calculation. That energy difference between the lowest (ε_1) and the excited (ε_2) single-particle

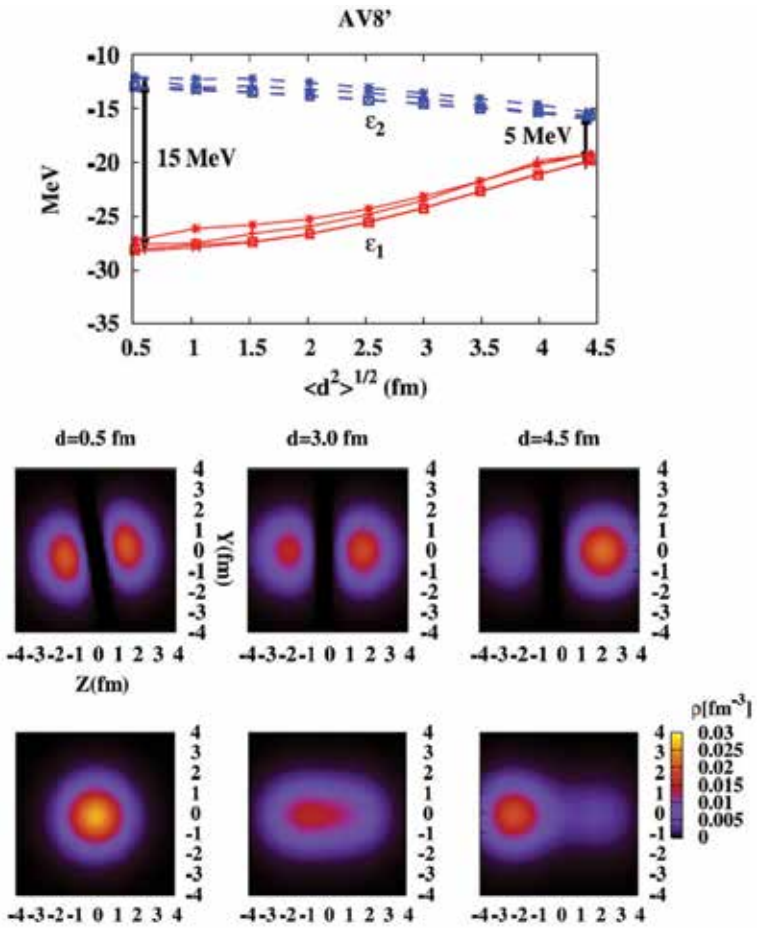

Fig. 7. Upper panel: Single-particle energies of ^{8}Be are shown. Lower panels: The density distributions of single-particle orbits for the two spin-up protons at $d = 0.5, 3.0, 4.5$ fm. The other single-particle orbits also have similar behavior. The upper and lower density distributions represent the higher-energy (ε_2) and lower-energy (ε_1) states, respectively.

orbits are consistent with $\hbar\omega$ of a shell model in nuclear systems. At the large distance $d = 4.5$ fm, ε_1 and ε_2 degenerate within 5 MeV. This result suggests that the single-particle orbits for ε_1 and ε_2 have configurations similar to each other. As shown in the lower panels of Fig. 7, at the small distance region of $d = 0.5$ fm, the two types of single-particle energy ε_1 and ε_2 are understood as those of s-wave and p-wave orbits, respectively. The four nucleons of the p-wave orbit (ε_2), which has a node at the origin, occupy around the z-direction in the intrinsic framework. This is the cause of the dumbbell shape of the density distribution at the small distance. On the other hand, at the large distance region far from $d = 4.5$ fm, these single-particle energies are expected to degenerate because all eight nucleons occupy the same type of single-particle orbit around different alpha clusters. At the intermediate distance region of $d = 3.0$ fm, they are interpreted to form gerade and ungerade orbits in the molecular orbital picture. In this work, we discuss the mechanism to cause this energy curve focusing on the state (d) dependence of the G-matrix. For this purpose, we decompose the G-matrix

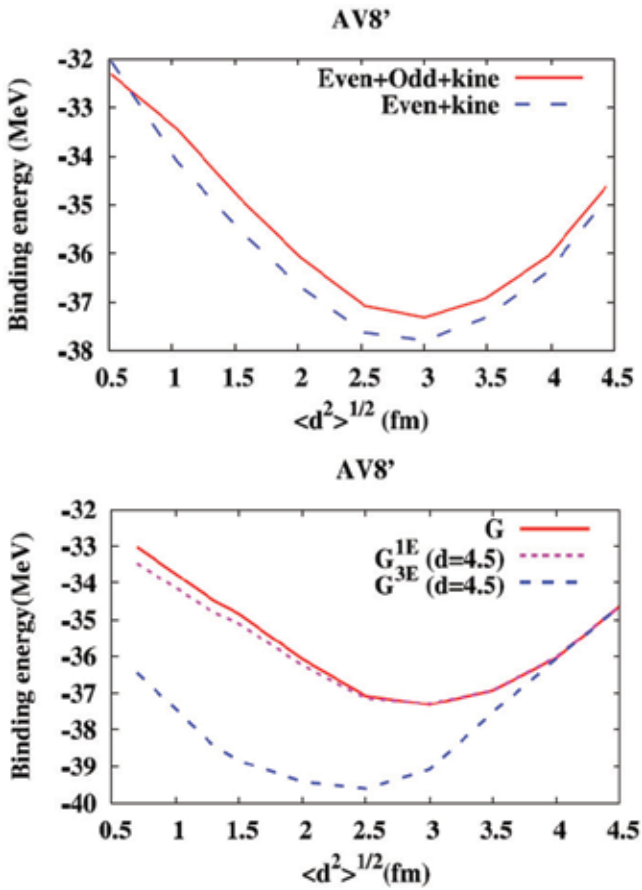

Fig. 8. Upper panel: Energy curves with and without odd-force contributions. The solid line, "Even+Odd+kine", and the dashed line, "Even+kine", represent the energy curves with and without the odd-force, respectively. Lower panel: the solid line, "G", is the energy curve for the distance of quasi clusters, which is identical with the curve in the upper panel of Fig. 6, and the dotted line, "G^{1E} (d=4.5)", and dashed line, "G^{3E} (d=4.5)", are the energy curves calculated using the fixed G-matrices at $d = 4.5$ fm for 1E and 3E channels, respectively.

into the two-body spin-parity channels and recalculate the energy curve fixing the G-matrix calculated at the largest $d = 4.5$ (fm) for each two-body spin-parity channel. The upper panel of Fig. 8 indicates that the energy surface does not change even if the odd-force contributions of the triplet-odd (3O) and singlet-odd (1O) channels are taken off, and therefore, in the lower panel of Fig. 8, we focus on only the even-force contributions of the triplet-even (3E) and singlet-even (1E) channels. As seen in the lower panel of Fig. 8, the energy curve using the fixed G-matrix for the 1E channel has no difference from the original energy curve; the energy curve using the fixed G-matrix for the 3E channel is shifted largely from the original one. That means the 1E G-matrix has no state dependence but the 3E one is responsible for the state dependence of the G-matrix to cause the development of clusters in ^{8}Be. This large state dependence is caused by the contributions of the tensor force of the bare nuclear interaction renormalized mainly by the correlation function $F_{kl}\left[\begin{smallmatrix} J=1\,S=1 \\ l'=2\,l_0=0 \end{smallmatrix}\right]$ in Eq. (50). If the G-matrix had

no state dependence, the energy curve would be deeper at a small distance, in other words, the actual energy curve becomes shallow due to the suppression of contributions at a small distance as the state dependence of the G-matrix and induces the separated clusters.

4. Conclusion

We develop a new *ab initio* framework, Brueckner-AMD, to makes AMD available with bare nuclear interactions. In this theory, we focus on the fact that one can apply the Brueckner theory straightforwardly to the AMD framework by using AMD-HF and the correlation functions constructed by the solutions of the Bethe-Goldstone equation make it possible to calculate the G-matrix in the AMD calculation. In these applications of Brueckner-AMD, we show that one can describe various states of nucleus starting from bare nuclear interactions with no assumption of a configuration. Furthermore, we simulate the development of alpha-alpha cluster in ^{8}Be and elucidate the origins of its formation in the Brueckner-AMD framework. The alpha-alpha clustering of ^{8}Be is induced by the contributions of the interaction for the triplet-even (3E) channel, where the 3E G-matrix has large state dependence caused by the correlations derived from the tensor force of the bare nuclear interaction.

5. Acknowledgments

We would like to express our gratitude to Professor K. Ikeda and Professor H. Horiuchi for their encouragements and useful comments. We also thank our collaborators, Mr. T. Murakami, Mr. Y. Yamamoto, Mr. T. Morimoto, and Professor M. Kimura in the Nuclear Theory Laboratory at Hokkaido University. This work is supported by the Grant-in-Aid for Exploratory Research.

6. References

Kamada, H., Nogga, A., Glöckle, W., Hiyama, E., Kamimura, M., Varga, K., Suzuki, Y., Viviani, M., Kievsky, A., Rosati, S., Carlson, J., Pieper, S. C., Wiringa, R. B., Navrátil, P., Barrett, B. R., Barnea, N., Leidemann, W., & Orlandini, G. (2001). Benchmark test calculation of a four-nucleon bound state. *Physical Review C*, Vol.64, (August 2001), pp.044001, ISSN 0556-2813

Neff, T. & Feldmeier, H. (2004). Cluster structures within Fermionic Molecular Dynamics. *Nuclear Physics A*, Vol.738, (June 2004), pp.357-361, ISSN 0375-9474

Wiringa, R. B.; Stoks, V. G. J. & Schiavilla, R. (1995). Accurate nucleon-nucleon potential with charge-independence breaking. *Physical Review C*, Vol.51, No.1 (January 1995), pp.38-51, ISSN 0556-2813

Wiringa, R. B., Pieper, S. C., Carlson, J., & Pandharipande, V. R. (2000). Quantum Monte Carlo calculations of $A = 8$ nuclei. *Physical Review C*, Vol.62, (June 2000), pp.014001, ISSN 0556-2813

Wiringa, R. B.& Pieper, S. C. (2002). Evolution of Nuclear Spectra with Nuclear Forces. *Physical Review Letters*, Vol.89, No.18, (October 2002), pp.182501, ISSN 0031-9007

Ikeda, K., Marumori, T., Tamagaki, R., & Tanaka, H. (1972). Formation of the Viewpoint, Alpha-Like Four-Boby Correlations and Molecular Aspects in Nuclei. *Progress Theoretical Physics Supplement*, No.52, (December 1972), pp.1-24, ISSN 1347-0481

Kanada-En'yo, Y.; Horiuchi, H. & Ono, A. (1995). Structure of Li and Be isotopes studied with antisymmetrized molecular dynamics. *Physical Review C*, Vol.52, No.2, (August 1995), pp.628-646, ISSN 0556-2813

Togashi, T. & Katō, K. (2007). Brueckner-AMD Method and Its Applications to Light Nuclei. *Progress Theoretical Physics*, Vol.117, No.1, (January 2007), pp.189-194, ISSN 1347-0481

Togashi, T.; Murakami, T. & Katō, K. (2009). Description of Nuclear Structures with Brueckner-AMD plus J^{π} Projection. *Progress Theoretical Physics*, Vol.121, No.2, (February 2009), pp.299-317, ISSN 1347-0481

Doté, A.; Horiuchi , H. & Kanada-En'yo, Y. (1997). Antisymmetrized molecular dynamics plus Hartree-Fock model and its application to Be isotopes. *Physical Review C*, Vol.56, No.4, (October 1997), pp.1844-1854, ISSN 0556-2813

Myo, T.; Toki, H. & Ikeda, K. (2009). Tensor-Optimized Shell Model with Bare Nucleon-Nucleon Interaction for ^{4}He. *Progress Theoretical Physics*, Vol.121, No.3, (March 2009), pp.511-531, ISSN 1347-0481

Baldo, M., Fiasconaro, A., Song, H. Q., Giansiracusa, G., & Lombardo, U. (2001). High density symmetric nuclear matter in the Bethe-Brueckner-Goldstone approach. *Physical Review C*, Vol.65, (December 2001), pp.017303, ISSN 0556-2813

Bandō, H.; Nagata, S. & Yamamoto, Y. (1970). Reaction Matrix Theory for Cluster States in Light Nuclei. I -Be^{8}-. *Progress Theoretical Physics*, Vol.44, No.3, (September 1970), pp.646-662, ISSN 1347-0481

Yamamoto, Y.; Togashi, T. & Katō, K. (2010). Tensor Force Effects on α-α Clustering of ^{8}Be. *Progress Theoretical Physics*, Vol.124, No.2, (August 2010), pp.315-330, ISSN 1347-0481

Part 3

Formation and Dynamics of Nanoparticles

9

Formation and Evolution Characteristics of Nano-Clusters (For Large-Scale Systems of 10^6 Liquid Metal Atoms)

Rang-su Liu*, Hai-rong Liu, Ze-an Tian,
Li-li Zhou and Qun-yi Zhou
Hunan University
China

1. Introduction

It is well known that the formation and evolution characteristics of clusters and nano-clusters have been studied, both experimentally and theoretically over the years. Many experimental works were carried out by using physical or chemical methods, such as ionic spray, thermal evaporation, chemical action deposition, and so on, to obtain some nice particles or clusters consisted of dozens to hundreds of atoms in special configurations (Echt et al, 1981; Knight et al, 1984; Harris et al, 1984; Schriver et al, 1990; Robles et al, 2002; Magudoapathy et al, 2001; Spiridis et al, 2001; Liu X H et al, 1998; Yamamoto et al, 2001; Bruhl R et al, 2004; Kostko et al, 2007; Alexander & Moshe, 2001) . The theoretical works were mainly carried out on diversified individual clusters configured by accumulating atoms according to some fixed pattern (Liu C. S. et al, 2001; Solov'yov et al, 2003; Doye & Meyer, 2005; Li H. & Pederiva, 2003; Ikeshoji et al, 1996; Wang L et al, 2002; Haberland et al., 2005; Joshi et al., 2006; Noya et al., 2007; Cabarcos et al., 1999; Orlando & James, 1999; Alfe, 2003). However, it is interesting that the similar clusters or aggregations have been found in some liquid metals during rapid solidification processes in our MD simulations (Liu R. S. et al., 1992a, 1992b, 1995, 2002, 2005a, 2005b, 2007a, 2007b, 2007c, 2009; Dong K. J. et al., 2003; Liu F. X. et al., 2009; Hou Z. Y. et al., 2009, 2010a, 2010b) and that it is also important for understanding in depth the solidification processes from liquid state to solid state. Furthermore, the formation and evolution characteristics of cluster configurations, especially the nano-cluster configurations, formed during solidification processes of liquid metals are still not well known up to now.

In this chapter, the main purpose is to further extended our previous MD simulation method (Liu R. S. et al., 2007a, 2007b, 2007c, 2009; Tian et al., 2008, 2009; Zhou et al., 2011) to study the large-sized systems consisting of 10^6 atoms of liquid metal Al and Na. Using the center-atom method, bond-type index method, and cluster-type index method (we proposed), the results have been analyzed and demonstrated that the larger simulation system can lead to a better understanding of the formation and evolution characteristics of the cluster configurations, especially the nano-clusters during solidification processes.

* Corresponding Author

2. Simulation conditions and methods

The molecular dynamics (MD) technique used here is based on canonical MD, and the simulation conditions are as follows: 10^6 atoms of metal Al, and the same for Na, are placed in a cubic box, respectively, and the systems run under periodic boundary conditions. The cubic box sizes are determined by both the number of atoms in each system and the mean volume of each atom at each given temperature, for these simulations the mean volumes are taken from the Ω-T curve as shown in Fig.5 of Ref (Qi D. W. & Wang S, 1991a) thus the box sizes would be changed with temperature. The motion equations are solved using leap-frog algorithm. The interacting inter-atomic potentials adopted here are the effective pair potential function of the generalized energy independent non-local model-pseudo-potential theory developed by Wang et al (Wang S. & Lai S. K., 1980; Li D. H., Li X. R. & Wang S., 1986). The effective pair potential function is

$$V(r) = \left(Z_{eff}^2 / r\right)\left[1 - \left(\frac{2}{\pi}\right)\int_o^\infty dqF(q)\sin(rq)/q\right] \tag{1}$$

where Z_{eff} and $F(q)$ are, respectively, the effective ionic valence and the normalized energy wave number characteristics, which were defined in detail in Refs. (Wang S. & Lai S. K., 1980; Li D. H., Li X. R. & Wang S., 1986). These pair potentials are cut off at 20 a.u (atom unit). The time step of simulation is chosen as 10^{-15}s.

The simulating calculations are performed for different metals respectively. For example, the simulation starts at 943K (the melting point (T_m) of Al is 933K), (for other metals at different temperatures). First of all, let the system run at the same temperature so as to reach an equilibrium liquid state determined by the energy change of system. Thereafter, the damped force method (Hoover et al., 1982; Evans, 1983) is employed to decrease the temperature of the system with the cooling rate of 1.00×10^{13} K/s to some given temperatures: 883, 833, 780, 730, 675, 625, 550, 500, 450, 400 and 350K. At each given temperature, the instantaneous spatial coordinates of each atom are recorded for analysis below. The bond-type index method of Honeycutt-Andersen (HA) (Honeycutt & Andersen, 1987), the center-atom method (Liu R. S., Li J. Y. & Zhou Q. Y., 1995) and the cluster-type index method (Dong et al., 2003; Liu R. S., et al., 2005a) are used to detect and analyze the bond-types and cluster-types of the related atoms in the system, and we go further to investigate the formation mechanisms and magic number characteristics of various clusters configurations formed during solidification processes at atomic level as follows.

3. Microstructure analysis

3.1 Pair distribution function

The pair distribution function $g(r)$ can be obtained by Fourier transformation of X-ray scattering structure factors $S_{\alpha\beta}(Q)$, and has been widely used to describe the structure characterization for liquid and amorphous metals. The validity of the simulation results can be verified by comparing the calculated pair distribution function $g(r)$ with the experimental results.

In this chapter, we inspect the g(r) curves of the system of Al at 943K and of the system of Na at 573K, 473K and 373K obtained from simulations and compare them with the experimental results obtained by Waseda (Waseda, 1980), as shown in corresponding

Figures 1 and 2 for Al and Na, respectively. From these Figures, it can be clearly seen that the simulation results are in good agreement with the experimental results. This means that the effective pair-potentials adopted here have successfully described the objective physical nature of these systems.

3.2 Bond-type index analysis

For deep understanding the formation and evolution mechanism of clusters in liquid metals, it is very important for us to know the concrete relationship of an atom with its near neighbors. Recently, the pair analysis technique has become an important method to describe and discern the concrete relationship of an atom with the near neighbors in liquid and amorphous systems. For a long time, the pair analysis technique, especially, the Honeycutt-Andersen (HA) bond-type indexes (Honeycutt & Andersen, 1987) have been successfully applied to describe and analyze the microstructure transitions in simulation systems, the details was shown in Refs (Liu R. S., et al., 2002; Dong K. J., et al., 2003). In this chapter, for the systems consisting of 10^6 atoms for Al and Na, various bond-types are also described by HA indexes, as shown in Table 1 and 2, respectively.

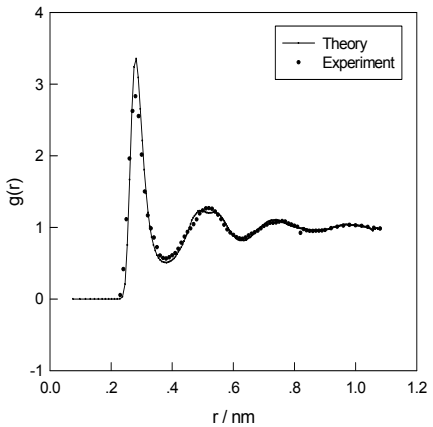

Fig. 1. Pair distribution function of liquid Al at 943K

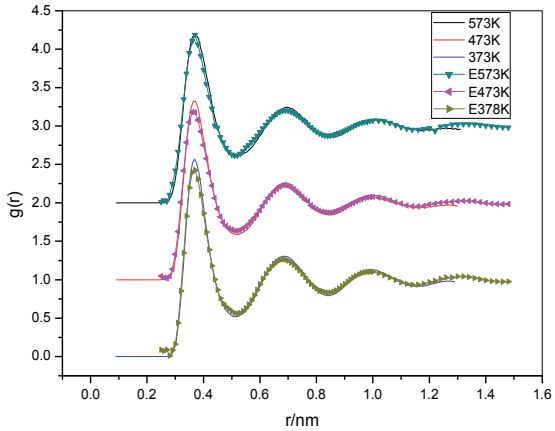

Fig. 2. Pair distribution function of liquid Na at 573K, 473K and 373K

From Table 1 and 2, it can be clearly seen that:

Firstly, the relative numbers of 1551 and 1541 bond-types, related to the icosahedral configurations and amorphous structures, play an important role: (1) For Al, they represent 14.3% and 13.2% at 943K, respectively, and the two bond-types represent 27.5% of the total bond-types. It is worth noting that these percentages change with the system temperature. At 350K, the proportion of 1551 bond-type increases remarkably with decreasing temperature, reaching 29.4% of the total, whilst the 1541 bond-type only increase slightly to 14.6% of the total; the sum of the 1551 and 1541 bond-types makes up 44.0% of all bond-types, indicating an increase of 16.5% from the corresponding proportion at 943K. (2) For Na, they represent 6.0% and 9.0% of all bond-types at 973K, respectively. While the sum of the 1551 and 1541 bond-types represents 45.8% of all bond-types, being increased about 30.8%. Highly interesting is that the relative numbers of 1551 bond-type is also increased remarkably with decreasing temperature, reaching 31.2% at 223K. From these results, it can be obviously seen that for the two systems, the 1551 bond-type plays a decisive role in the whole evolution process of microstructures.

For the relative numbers of the 1441, 1431, 1421 and 1422 bond-types related to the tetrahedral structures, the 1331, 1321, 1311 and 1301 bond-types related to the rhombohedral structures, and the 1661 bond-type related to hcp and bcc structures, are also similar to those obtained from previous works as above-mentioned.

Highly interesting is the 1771 bond-type, according to the definition of Honeycutt-Andersen bond-type indexes, it should possess seven-fold symmetry. It is well known that the seven-fold symmetry cannot exist in crystal solid state. However, in the Al system, although the relative number of 1771 bond-type is less than 0.1%, it still only exists in liquid and supercooled liquid states above 500K, and disappears in the solid state below 500K. This result just proves that the seven-fold symmetry cannot exist in crystal solid state, and further proves that the seven-fold symmetry also cannot exist in amorphous solid state. But for Na system, at 123K, it is still in the suppercooled liquid, so the 1771 bond-type can exist in it.

Temp (K)	Bond types and corresponding relative numbers (%)													
	1201	1211	1301	1311	1321	1331	1421	1422	1431	1441	1541	1551	1661	1771
943	1.6	1.5	1.0	7.2	7.2	0.7	3.3	7.1	21.2	4.4	13.2	14.3	4.5	0.1
883	1.5	1.4	0.9	6.9	7.0	0.6	3.2	6.9	21.3	4.5	13.5	15.2	4.7	0.1
833	1.3	1.3	0.9	6.5	6.7	0.6	3.1	6.8	21.3	4.5	13.7	16.3	4.9	0.1
780	1.2	1.2	0.8	6.1	6.4	0.5	3.0	6.5	21.3	4.6	13.9	17.7	5.1	0.1
730	1.1	1.1	0.7	5.7	6.1	0.5	2.9	6.3	21.2	4.6	14.1	19.1	5.4	0.1
675	0.9	0.9	0.7	5.2	5.7	0.5	2.8	6.0	21.1	4.6	14.3	20.9	5.6	0.1
625	0.9	0.9	0.6	5.1	5.6	0.4	2.7	5.9	21.1	4.5	14.5	22.0	5.7	0.1
550	0.9	0.9	0.6	4.8	5.4	0.4	2.6	5.7	21.0	4.3	14.6	24.0	5.7	0.1
500	0.8	0.9	0.6	4.7	5.4	0.3	2.5	5.6	21.1	4.1	14.6	25.3	5.6	0.1
450	0.8	0.9	0.5	4.5	5.3	0.3	2.4	5.4	21.0	3.9	14.6	26.8	5.6	0.0
400	0.7	0.9	0.5	4.3	5.2	0.3	2.3	5.3	20.9	3.8	14.6	28.2	5.6	0.0
350	0.7	0.9	0.5	4.2	5.2	0.3	2.2	5.1	20.8	3.6	14.6	29.4	5.5	0.0

Table 1. Relations of the number of various bond types (%)of Al with temperature (K).

	1201	1211	1301	1311	1321	1331	1421	1422	1431	1441	1541	1551	1661	1771
973	2.9	3.0	1.4	9.2	9.1	1.8	3.4	7.1	16.7	4.0	9.0	6.0	2.4	0.2
923	2.8	2.8	1.4	9.2	8.9	1.7	3.4	7.3	17.1	4.1	9.4	6.3	2.5	0.2
873	1.5	1.8	0.8	6.3	7.3	1.9	2.7	5.8	16.3	5.1	9.8	8.1	3.5	0.3
823	2.4	2.3	1.4	9.0	8.5	1.4	3.6	7.6	18.1	4.2	10.3	7.2	2.9	0.2
773	2.3	2.1	1.4	8.8	8.2	1.2	3.7	7.8	18.5	4.3	10.8	7.8	3.1	0.2
723	1.1	1.3	0.8	5.7	6.5	1.4	2.8	6.0	17.4	5.6	11.3	10.2	4.4	0.3
673	1.3	1.4	0.9	6.3	6.8	1.4	3.0	6.4	17.9	5.3	11.4	9.8	4.1	0.3
623	0.9	0.9	0.7	5.1	5.7	1.2	2.8	5.9	17.8	6.0	12.4	12.3	5.2	0.3
573	0.7	0.7	0.7	4.8	5.3	1.0	2.8	5.9	18.2	6.2	13.1	13.4	5.7	0.3
523	0.6	0.6	0.6	4.4	4.8	0.9	2.8	5.9	18.5	6.3	13.8	14.7	6.2	0.3
473	0.5	0.4	0.6	3.9	4.3	0.8	2.8	5.8	18.4	6.6	14.4	16.3	6.8	0.3
423	0.3	0.3	0.5	3.4	3.7	0.6	2.8	5.7	18.5	6.8	15.3	18.2	7.4	0.3
373	0.2	0.2	0.4	2.9	3.1	0.5	2.7	5.5	18.3	7.0	16.0	20.3	8.2	0.2
323	0.1	0.1	0.4	2.4	2.5	0.4	2.6	5.3	18.0	7.3	16.7	22.8	9.0	0.2
273	0.1	0.1	0.3	1.8	1.9	0.3	2.6	5.1	17.4	7.6	17.4	25.2	9.9	0.2
223	0.0	0.0	0.1	0.6	0.9	0.3	1.3	2.5	12.5	10.0	14.6	31.2	14.2	0.2
173	0.0	0.1	0.0	0.3	0.6	0.2	1.2	2.1	11.0	11.7	14.1	33.1	16.2	0.2
123	0.0	0.0	0.0	0.1	0.3	0.2	0.6	0.9	7.4	13.2	10.3	35.7	19.8	0.2

Table 2. Relations of the number of various bond types (%) of Na with temperature (K).

On the whole, these simulation results are rather close to those obtained in our previous works on different-sized liquid metal systems (Liu R. S., et al., 1998, 1999, 2005a, 2005b; Dong K. J., et al., 2003) ; that is to say, for different-sized liquid metal systems, the simulation results of relative numbers of corresponding bond-types are similar to each other, there being only a minor difference during solidification processes.

3.3 Cluster-type index analysis

As is well known that different combinations of bond-types can form different cluster configurations, however, the HA bond-type indices cannot be used to describe and discern different basic clusters formed by an atom with its nearest neighbors, especially, the different nano-clusters formed by some different basic clusters.

In order to differentiate the basic cluster and the polyhedron, we define the “basic cluster“ as the smallest cluster composed of a core atom and its surrounding neighbor atoms. A larger cluster can be formed by continuous expansion, with a basic cluster as the core, according to a certain rule, or by combining several basic clusters together. A polyhedron is generally a hollow structure with no central atom as the core. This is the essential distinction of a polyhedron from a “basic cluster“, such as the Bernal polyhedron. However, if a basic cluster is shaped as a certain polyhedron, for simplicity, we also call it a polyhedron cluster, such as icosahedral cluster, Bernal polyhedron cluster, and so on.

It is clear that the bond-types formed by each atom with its neighbor atoms in the system are different; the cluster configurations formed by these bond-types are also different. Even if some cluster configurations are formed by the same number of bond-types, their structures may still be completely different from each other, owing to a slight difference in bond-length or bond-angle. On this point, at present it is hard to use the bond-type index method

to describe clearly the cluster configurations of different types. In order to deal with this difficult matter, a cluster-type index method (CTIM) has been proposed (Liu R. S., et al., 1998, 1999, 2005a, 2005b; Dong K. J., et al., 2003) based on the HA indexes (Honeycutt & Andersen, 1987) and the work of Qi and Wang (Qi. & Wang, S., 1991b). According to the definition of basic cluster, four integers (N, n1441,n1551,n1661) also adopted to describe the basic clusters. The meaning of the four integers used in CTIM are as follows: the first integer represents the number of surrounding atoms which form a basic cluster with the central atom, i. e. the coordination number Z of the central atom; the second, third and fourth integers respectively represent the numbers of 1441, 1551 and 1661 bond-types, by which the surrounding atoms are connected with the central atom of the basic cluster. For example, (12 0 12 0) stands for an icosahedral cluster that is composed of 13 atoms: the central atom is connected to the surrounding atoms through twelve 1551 bond-types (i. e. the coordination number of the central atom Z=12); (13 1 10 2) stands for the defective polyhedron cluster composed of 14 atoms, the core atom is connected to the surrounding atoms with one 1441, ten 1551 and two 1661 bond-types (the coordination number Z=13). For ease of representation, some main basic clusters have been chosen from the simulation system of liquid metal Al as shown in Fig. 3.

By using the CTIM, the statistical numbers of various cluster-types at each given temperature have been obtained. For liquid metal Al, during the whole solidification process, there are 53 different basic cluster-types in the system, only 34 of them appearing more than 5 times at some temperatures are listed in Table 3. For liquid metal Na, there are 63 different basic cluster-types, of which only 34 main types are listed in Table 4 (only 17 types appearing more than 1000 times play a critical role).

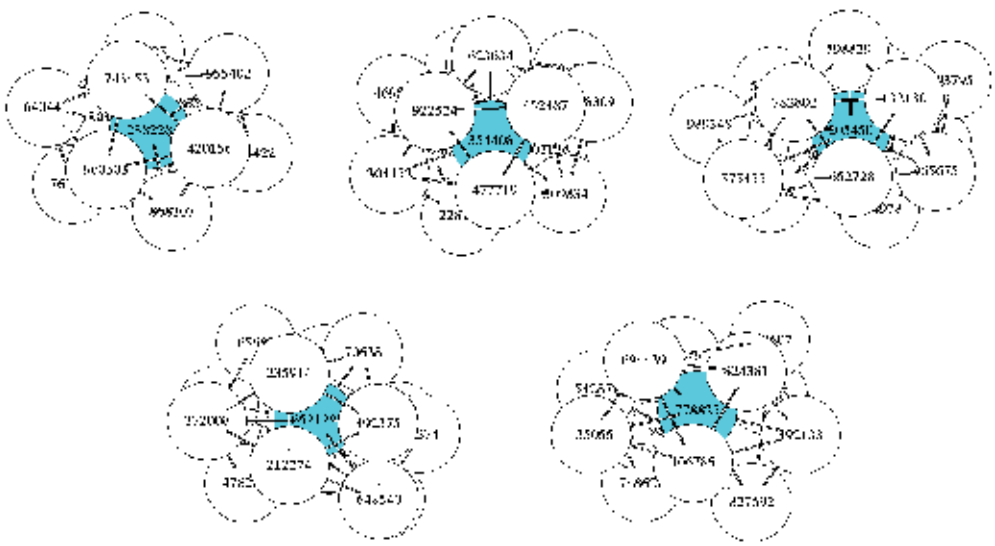

Fig. 3. Schematics of five main basic clusters at 350K: (a) icosahedral cluster（12 0 12 0） with central atom of 238228; (b) basic cluster（13 1 10 2）with central atom of 354408; (c) basic cluster（14 2 8 4）with central atom of 205450; (d) basic cluster（14 1 10 3）with central atom of 652129; (e) basic cluster（12 2 8 2）with central atom of 778825.

Types of Cluster	Temperature (K) and the number of various cluster types											
	943	883	833	780	730	675	625	550	500	450	400	350
(12 0 12 0)	2106	2819	3671	4867	6389	8698	10833	14857	18328	22216	26207	30153
(14 0 12 2)	183	210	253	368	447	564	751	881	1007	1189	1203	1360
(15 0 12 3)	78	68	103	126	165	208	262	358	410	391	478	472
(16 0 12 4)	8	19	17	27	31	40	34	46	55	63	74	83
(13 1 10 2)	1544	1919	2341	3078	3750	4870	5357	6522	7244	8125	8974	9417
(14 1 10 3)	427	536	684	894	1113	1366	1585	1881	2136	2382	2638	2892
(15 1 10 4)	172	213	285	366	452	568	647	845	899	1026	1092	1117
(16 1 10 5)	29	37	42	67	76	95	104	111	127	136	163	175
(17 1 10 6)	2	6	2	4	4	3	6	9	5	7	4	5
(10 2 8 0)	13	7	16	13	15	11	12	3	5	2	2	0
(11 2 8 1)	231	243	260	269	273	274	250	215	188	173	148	110
(12 2 8 2)	969	1066	1208	1440	1624	1865	1974	2117	2037	2067	2051	1956
(13 2 8 3)	396	452	548	585	740	882	933	960	1051	1029	999	1035
(14 2 8 4)	735	865	1014	1291	1632	1992	2194	2635	2758	2985	3286	3363
(15 2 8 5)	188	224	288	346	415	573	619	750	810	791	939	1023
(16 2 8 6)	23	26	52	59	56	75	86	94	77	102	110	122
(17 2 8 7)	0	3	2	6	5	5	7	8	4	0	2	3
(10 3 6 1)	3	6	5	2	1	5	4	3	1	1	1	0
(11 3 6 2)	41	36	38	33	29	23	19	19	20	13	5	8
(12 3 6 3)	288	260	301	359	375	345	322	253	276	199	174	140
(13 3 6 4)	914	1016	1191	1412	1651	1810	1951	1936	1884	1857	1782	1689
(14 3 6 5)	318	400	527	570	669	739	800	845	884	834	853	868
(15 3 6 6)	103	106	149	182	227	224	295	267	358	330	364	371
(16 3 6 7)	11	9	13	12	14	28	25	28	29	30	25	27
(11 4 4 3)	19	16	21	13	21	16	15	11	6	5	2	2
(12 4 4 4)	102	106	83	80	95	88	89	63	47	55	33	33
(13 4 4 5)	131	112	124	151	133	192	149	131	102	107	85	65
(14 4 4 6)	175	225	226	261	266	332	354	336	311	258	268	269
(15 4 4 7)	42	56	59	58	62	76	105	101	88	84	113	83
(16 4 4 8)	5	5	3	6	3	7	10	10	9	6	5	13
(12 5 2 5)	7	9	17	10	11	3	8	5	4	2	1	2
(13 5 2 6)	27	30	33	30	40	30	30	39	15	18	23	17
(15 5 2 8)	1	4	1	7	5	6	5	7	12	2	5	4
(14 6 0 8)	4	2	6	8	3	8	9	9	5	4	1	3
Total number of all clusters	9300	11117	13589	17006	20796	26029	29854	3 6365	41203	46498	52122	56885
Icosahedra expressed by (12 0 12 0) to total number (%)	22.65	25.36	27.01	28.62	30.72	33.42	36.29	40.85	44.48	47.78	50.28	53.01

Table 3**.** Variation of the number of clusters with temperature (K) for liquid metal Al.

Types of clusters	Temperatures (K) and the numbers of various cluster-types											
	973	873	773	673	573	523	473	423	373	323	273	223
(12 0 12 0)	16	39	58	92	320	536	749	1275	1888	2911	4475	7536
(14 0 12 2)	5	16	10	22	121	174	223	379	624	1000	1519	2879
(15 0 12 3)	1	6	11	14	54	68	118	185	284	431	673	1330
(16 0 12 4)	1	1	1	3	7	14	30	34	46	93	111	248
(13 1 10 2)	44	99	126	216	749	1089	1624	2357	3511	5270	7112	15029
(14 1 10 3)	10	28	39	109	289	414	662	923	1401	2076	2761	6360
(15 1 10 4)	7	19	7	52	181	241	373	533	812	1223	1760	4011
(16 1 10 5)	1	4	4	11	43	43	68	118	147	241	294	751
(10 2 8 0)	12	9	17	21	24	23	24	22	21	28	19	7
(11 2 8 1)	37	79	87	139	242	272	320	364	417	466	400	510
(12 2 8 2)	60	134	142	269	633	800	1073	1402	1946	2529	3031	5331
(13 2 8 3)	24	65	70	135	351	434	641	836	1098	1465	1792	4185
(14 2 8 4)	27	79	75	178	643	895	1355	1893	2805	4261	5808	14582
(15 2 8 5)	4	21	36	65	233	273	452	584	928	1310	1887	4979
(16 2 8 6)	3	4	2	16	36	60	86	83	145	207	217	662
(17 2 8 7)	0	1	0	1	4	2	6	9	14	5	16	34
(10 3 6 1)	11	16	11	18	23	31	19	19	15	11	13	5
(11 3 6 2)	16	42	41	53	73	49	82	66	89	62	69	57
(12 3 6 3)	44	127	119	184	408	525	649	743	793	946	1019	1653
(13 3 6 4)	76	163	184	365	1007	1350	1895	2538	3597	5027	6777	16150
(14 3 6 5)	13	62	71	159	420	510	816	1004	1565	2279	3050	8760
(15 3 6 6)	3	17	14	36	136	187	282	366	545	786	1055	3248
(16 3 6 7)	1	2	1	3	19	20	23	30	49	61	74	288
(11 4 4 3)	27	29	13	39	45	72	72	60	57	47	35	33
(12 4 4 4)	20	67	49	104	189	211	248	332	313	361	367	691
(13 4 4 5)	14	54	47	80	246	295	367	490	592	786	908	2240
(14 4 4 6)	11	36	43	78	289	420	575	781	1174	1751	2613	8125
(15 4 4 7)	2	8	5	19	61	75	114	157	240	347	511	1992
(16 4 4 8)	0	2	0	2	3	7	13	11	14	17	27	121
(12 5 2 5)	2	6	10	19	31	34	38	43	33	53	50	87
(13 5 2 6)	2	2	17	16	43	62	101	113	173	202	349	856
(15 5 2 8)	0	0	1	4	2	11	8	19	27	44	71	319
(16 5 2 9)	0	0	0	1	0	1	0	2	4	1	5	27
(14 6 0 8)	0	1	0	3	11	9	17	30	47	102	173	731
Total numbers of all clusters	494	1238	1311	2527	6936	9207	13123	17801	25414	36399	49041	113817
Icosahedrons expressed by (12 0 12 0) to total numbers(%)	3.23	3.15	4.42	3.64	4.61	5.82	5.71	7.16	7.43	7.99	9.13	6.6

Table 4. Variation of the number of clusters with temperatures (K) for liquid metal Na.

For liquid metal Al, from Table 3, however, it can be clearly seen that only 18 cluster-types appearing more than 100 times play a critical role in the solidification process. For convenience of discussion, we only show the variations of ten significant basic clusters with temperature in Figure 4(a) and (b). From Figure 4 (a), it is clear that among the most significant five basic clusters, the highest one is the icosahedral basic cluster expressed by (12 0 12 0), which increases rapidly as the temperature comes down. The number of basic cluster (12 0 12 0) climbs above 30,000 at 350K, and this cluster-type plays the most important role in the microstructure transitions during rapid solidification process. The second one is the basic cluster expressed by (13 1 10 2) and its number over 9400 at 350K. The number of the fifth cluster type expressed by (12 2 8 2) is over 1956 at 350K and still plays a certain role.

Figure 4 (b) presents that the numbers of basic clusters (14 0 12 2), (15 1 10 4), (13 2 8 3) and (15 2 8 5) all changed at about the same rate, except the basic cluster (13 3 6 4), and their numbers are in the range of 1023 - 1360 at 350K. Therefore, these clusters play only a secondary role.

However, as we go further to observe the Figures 4 (a), (b) and Table 3 carefully, it can be seen that the basic clusters (12 0 12 0) and (13 3 6 4) have almost a same turning point T_t in the range of 550-625K; in particular for cluster (13 3 6 4), T_t is a peak value point, it means that the cluster (13 3 6 4) plays an opposite role to the cluster (12 0 12 0) in the solidification process. Maybe just these cluster-types play a particular role, this turning point T_t is in agreement with the glass transition temperature T_g obtained by Liu et al (Liu R. S., Qi & Wang S., 1992; Wendt & Abraham, 1978; Zheng *et al.*, 2002). On the other hand, this confirms that the glass transition temperature T_g can also be found by the turning point T_t in the relations of the numbers of main basic clusters with temperature. Therefore, it is possible to find a new method to determine the glass transition temperature T_g.

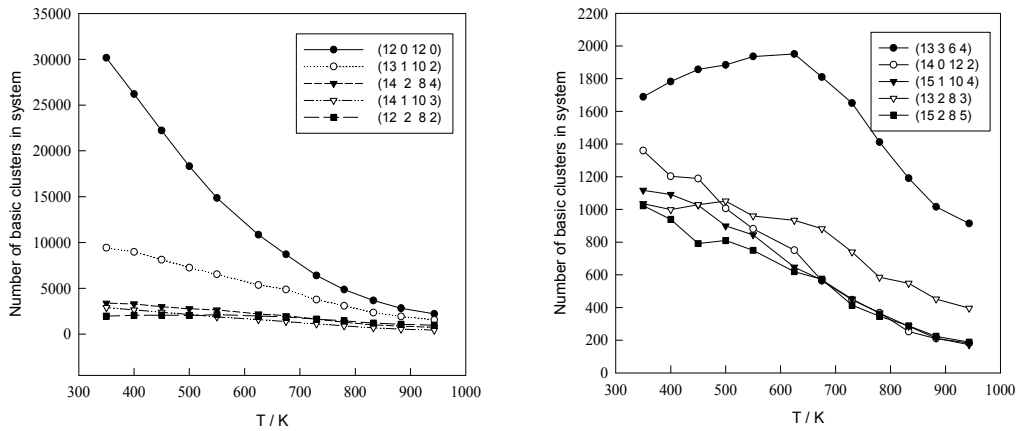

(a) (b)

Fig. 4. Variation of the numbers of the ten main basic clusters with temperatures for Al.

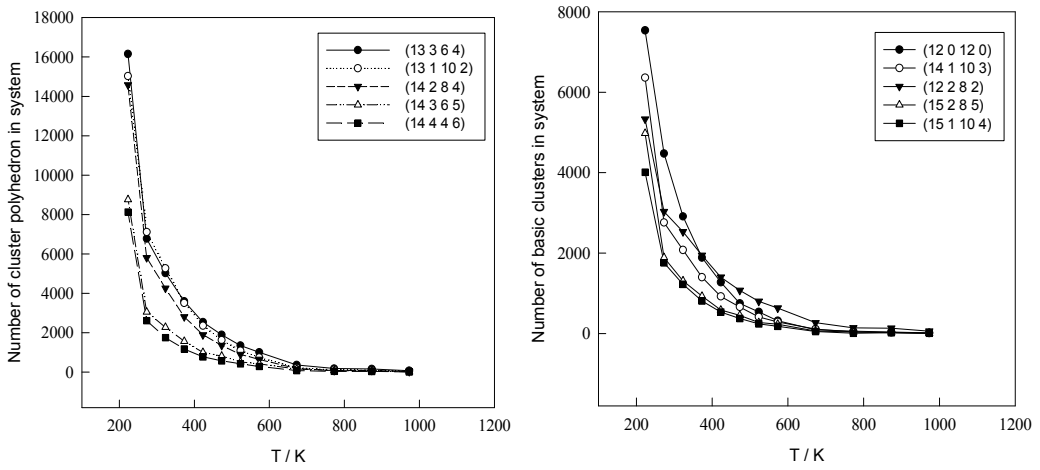

(a) (b)

Fig. 5. Relations of the numbers of 10 main basic clusters with temperature for Na.

It is worth noting that, from Table 3, it can be clearly seen that even at 943K, there are still a certain number of various basic clusters in the liquid state. That is to say, the liquid state discussed here is not an ideal liquid, as usually imagined, in which no cluster exist and each atom is free to diffuse. Furthermore, from our previous works for a small system consisting of 500 Al atoms, as shown in Fig.3 of Ref (Liu R. S., et al, 1999), it can be seen that even the temperature is increased up to 1800K ($\approx 2T_m$), the number of 1551 bond-type (which plays a leading role in microstructure transition of liquid metal Al) is still occupied 7.3 % of the total bond-types (and 16.5 % at 943K); thus some basic clusters formed mainly by 1551 bond-type would still be in the liquid system. If we want to get an ideal liquid state, the temperature should be increased higher and higher. In general, from the view point of microscopic structure, it is hard to completely reach the ideal case.

For liquid metal Na, for convenience of discussion, only the relations of the former 10 main basic clusters with temperature are shown in Fig.5. From Fig.5 (a), it can be clearly seen that the first 3 basic clusters (13 3 6 4), (13 1 10 2) and (14 2 8 4) are increased rapidly with decreasing temperature, and play almost the same important role in the microstructure transitions of liquid metal Na. While the basic cluster (12 0 12 0) has been ranked as the sixth one and only plays a secondary role; however, in the liquid metal Al, it is the first one and plays the most important role in the microstructure transitions (Liu R. S. et al., 2005a).

4. Formation and evolution of nano-clusters

4.1 Formation and description of nana-clusters

In this section, some nano-clusters have been described. They are composed of various kinds of smaller clusters, and their sizes and amounts are increased with temperature decreasing. Their configurations are very complex.

As above mentioned, we have defined the basic cluster as the smallest cluster composed of a core atom and its surrounding neighbor atoms. A larger cluster can be formed by

continuous expansion, with a basic cluster as the core, according to a certain rule, or by combining several basic clusters together.

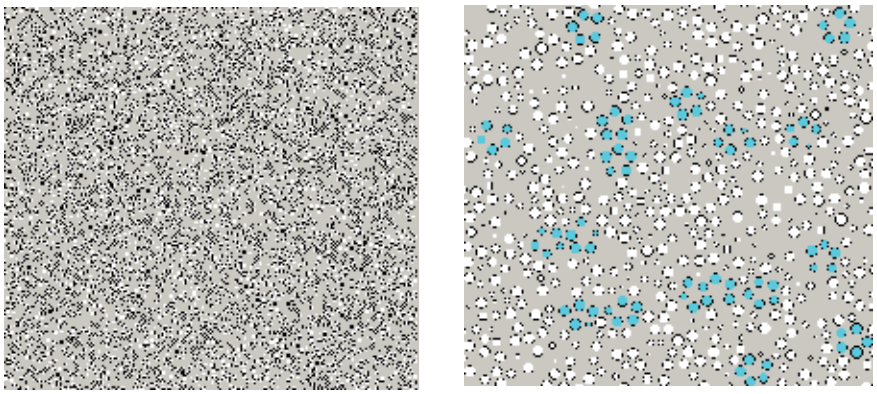

(a) (b)

Fig. 6. The 2D schematic of the whole system consisting of 1,000,000 atoms at 350K: (a) a part of (111) cross section×2 times ; (b) a part of (111) cross section ×5 times.

First of all, we display the whole schematic diagram of the 2D (111) cross section of the 1000000 atoms system of Al at 350 K, as shown in Fig.6(a) and (b), a part of (111) cross section × 2 times and a part of (111) cross section × 5 times, respectively. Fig.6(a), (b) show that the system has become amorphous state and formed two types of region: the dense region and the loose region. In the dense regions, some regular or distorted five-lateral patterns appear in Fig.6(b), which are just the cross sections of some icosahedron and their combining configurations. The loose regions are also of different sizes and shapes without apparent regulation and the atoms are randomly distributed there. The dense regions and the loose regions are also distributed randomly in the system; the inhomogeneous solid seems to be rather sponge-like with cavities (also commonly called "free volume") in different sizes and shapes.

It is clear that the microstructure of this system is hard to be described by the well-known model of "random hard sphere packing", since that model is too simple for describing amorphous metals. Figure 6, however, shows a typical amorphous picture, thus it is necessary to establish a new model to describe the complex structures of amorphous metals in the near future.

In these simulations, some larger clusters have been found. They are composed of various kinds of basic clusters and their sizes and numbers increase with temperature decreasing. Their configurations are very complex. For example, a larger cluster consisting of 68 atoms is composed of 10 basic clusters with central atoms (represented by gray circle) in Al system as shown in figure 7(a) , (b), displaying the whole atoms and the central atoms, respectively. From figures 7(a) and (b), it can be clearly seen that the larger cluster is formed by combining different medium-sized clusters, and each medium-sized cluster is also composed of some basic clusters that can be described by a set of indexes in the CTIM as shown in the caption. Interestingly, the larger clusters formed during rapid solidification processes of liquid metals Al and Na do not consist of multi-shell configurations

accumulated by atoms as obtained by gaseous deposition or ionic spray methods. However, the cluster configurations of Al formed by gaseous deposition have been verified by mass-spectrometer to be crystals or similar structures formed in octahedral shell structures (Martin, et al., 1992). Therefore, it can be concluded that different methods of preparing metallic materials would produce different cluster configurations. Figure 7 shows that the atoms contained in the larger clusters are labeled randomly, that is to say, the atoms in the system have been distributed homogeneously.

4.2 Evolution of nana-clusters

In order to display clearly the evolution characteristics of nano-clusters, it is necessary to trace the evolution processes of nano-clusters during rapid solidification processes. Adopting an inverse-evolving method, some tracking studies for the structural configurations of the nano-clusters have been performed. The evolution processes of the nano-clusters, at different temperatures, have been shown in Figures. It can be clearly seen that the central atoms of basic clusters of the nano-clusters are bonded with each other, some central atoms are multi-bonded, and others single-bonded.

In this simulation, some nano-clusters have been found. They are composed of various kinds of smaller clusters, and their size and amount are increased with temperature decreasing. Their configurations are very complex. For example, a nano-cluster consisting of 126 atoms are composed of 24 basic clusters with center atoms (represented by gray circle), as shown in Fig.8 (a), (b). It can be seen that the nano-cluster is produced by combining three different middle clusters, and each middle cluster composed of some basic clusters, and each basic cluster described by a set of indexes in CTIM.

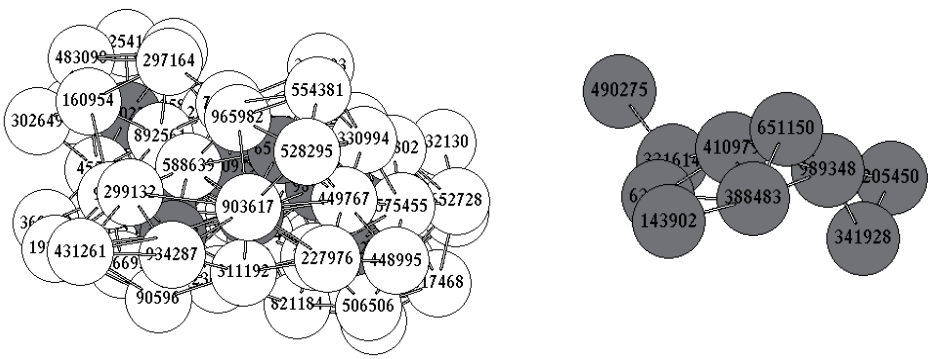

Fig. 7. Schematic diagram of a larger cluster consisting of 68 atoms within ten basic clusters with connecting bonds at 350 K (the gray spheres are the center atoms of basic clusters). The cluster is composed of 1 icosahedron (12 0 12 0), and basic clusters of 1 (16 0 12 4), 5 (13 1 10 2), 1 (14 1 10 3), 1 (14 2 8 4) and 1 (14 3 6 5). (a) displays all the atoms; (b) displays only the central atoms.

In order to display clearly the evolution characteristics of nano-clusters, it is necessary to trace the evolution processes of nano-clusters during rapid solidification processes. From our previous simulation results (Liu R S, et al., 1995, 2002), we have known that once an atom became the center of a cluster, it would possess certainly relative stability and

continuity (namely heredity). According to this feature, we can adopt the label of the central atom of a basic cluster to simplify the description of the nano-clusters, thus we can understand the whole evolution process of them more clearly. Adopting an inverse-evolving method, a tracking study for the structural configurations of this nano-cluster has been made.The evolution process of the nano-cluster, at different temperatures (for simplicity, we only select 2 different temperatures), has been shown in Fig.8(c),(d). It can be clearly seen that when the temperature is below 350K, the central atoms of 24 basic clusters of the nano-cluster are bonded with each other, some central atoms are multi-bonded, and others single-bonded. However, this is a very important characteristic for simplifying the research on the evolution processes and mechanisms of nano-clusters. With the increase of temperature, the maximal size of the original middle and small clusters decreases continuously. From the macro-viewpoint, such a degree of order is rather consistent with the statistical rules of thermodynamics. It can be clearly seen that this nano-cluster is also formed by connecting various middle and small clusters with different cluster-types or sizes, and different from that obtained by gaseous deposition, ionic spray and so on. It is well known that the latter is proved by mass-spectrometric analysis to be the nano-level crystal clusters formed by octahedron-shells configuration accumulated with an atom as the center (Joshi et al., 2006).

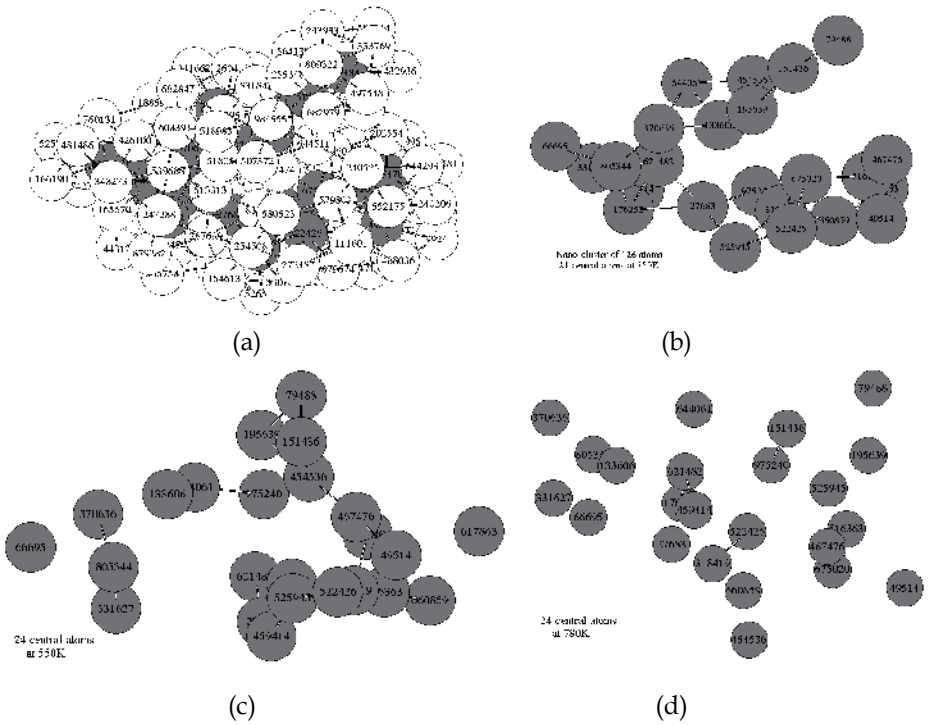

Fig. 8. Schematic figures of a nano-clusters consisting of 126 atoms within 24 basic clusters with connecting bonds at 350 K(the gray spheres are the center atoms of basic clusters). The cluster is composed of 7 icosahedron (12 0 12 0), and basic clusters of 1 (14 0 12 2), 5 (13 1 10 2), 3 (14 1 10 3), 3 (15 1 10 4), 1 (12 2 8 2), 2 (14 2 8 4), 1 (15 2 8 5) and 1 (15 3 6 6). (a) the whole atoms; (b) at 350K; (c) at 550K; (d) at 780K.

4.3 Size distribution and magic number sequence of nana-clusters

In order to investigate the size distribution characteristics of various clusters in the system, the relationship between the numbers of various clusters and their sizes (the numbers of atoms contained in each cluster) should be displayed clearly according to some statistical method. For convenience of discussion, we propose a new statistical method as follows.

Since a larger cluster can be described clearly by different basic clusters in the CTIM, all the clusters (from basic cluster to larger cluster) in the system can be classified according to the numbers of basic clusters contained in the larger cluster under consideration. Then, the clusters containing the same numbers of basic clusters can be further classified as a group. However, the clusters within a same group may not have the same number of atoms because the different basic clusters they contained would have different number of atoms. Thus there is a certain range of the numbers of atoms for a group of clusters, this can be clearly seen below.

Cluster consisting of 1 basic clusters		Cluster consisting of 2 basic clusters		Cluster consisting of 3 basic clusters		Cluster consisting of 4 basic clusters		Cluster consisting of 5 basic clusters	
Cluster size	Cluster number	Cluster size	Cluster number	Cluster size	Cluster number	Cluster size	Cluster number	Cluster size	Cluster number
Number of atom	943K 350K	Number of atom	943K350K	Number of atom	943K350K	Number of atom	943K350K	Number of atom	943K350K
11	13 0	17	1 0	23	9 210	26	0 7	30	0 2
12	245 55	18	6 4	24	19 204	27	0 27	31	0 6
13	**2254 10606**	**19**	167 **2761**	**25**	28 **647**	28	2 47	32	0 9
14	1912 3159	**20**	**269** 1432	26	53 551	29	4 130	33	1 23
15	998 1611	21	311 1370	**27**	**62 588**	30	10 128	34	3 46
16	300 433	22	202 730	28	43 451	31	8 212	35	0 69
17	39 37	23	86 273	29	32 202	32	9 210	36	4 69
18	0 1	24	46 56	30	21 106	**33**	10 **225**	37	1 105
		25	13 15	31	3 38	34	7 194	**38**	**7 118**
		26	2 1	32	4 15	**35**	**15** 126	39	6 106
				33	1 3	36	3 83	40	0 110
						37	4 27	41	2 69
						38	1 17	42	1 46
						39	1 7	43	1 27
						40	0 1	44	1 15
						41	0 1	45	0 7
						42	0 2	46	0 5
								47	0 2

(continued)

Cluster consisting of 6 basic clusters		Cluster consisting of 7 basic clusters		Cluster consisting of 8 basic clusters		Cluster consisting of 9 basic clusters		Cluster consisting of 10 basicclusters	
Cluster size	Cluster number	Cluster size	Cluster number	Cluster size	Cluster number	Cluster size	Cluster number	Cluster size	Cluster number
Number of atom	943K 350K	Number of atom	943K350K	Number of atom	943K350K	Number of atom	943K350K	Number of atom	943K350K
35	0 2	37	0 1	44	0 1	46	0 1	56	0 2
36	0 3	38	0 0	45	0 0	47	0 0	57	0 1
37	0 7	39	0 0	46	0 1	48	0 0	58	0 1
38	1 7	40	0 0	47	0 2	49	0 2	59	0 1
39	2 16	41	0 4	48	0 4	50	0 0	60	0 2
40	0 34	42	1 3	49	0 3	51	0 0	61	0 1
41	1 36	43	1 8	50	1 8	52	0 3	**62**	0 **7**
42	2 **54**	44	0 13	51	0 12	53	0 0	63	0 5
43	0 51	45	0 12	52	0 11	54	0 4	64	0 4
44	2 33	46	0 19	53	0 13	55	0 6	65	0 3
45	0 51	47	0 23	54	0 16	56	0 3	66	0 4
46	0 45	**48**	2 **33**	55	0 17	57	0 7	**67**	0 **9**
47	0 21	49	1 17	56	0 16	58	0 5	68	0 6
48	0 27	50	0 27	57	0 10	59	0 5	69	0 6
49	0 12	51	0 29	58	0 13	60	0 7	70	0 2
50	0 9	52	0 20	**59**	0 **22**	61	0 9	71	0 0
51	0 8	53	0 18	60	0 11	62	0 3	72	0 1
52	0 1	54	0 12	61	0 6	63	0 7	73	0 1
53	0 1	55	0 6	62	0 3	64	0 2	74	0 2
		56	1 4	63	0 0	**65**	0 **14**	75	0 1
		57	0 4	64	0 1	66	0 4	76	0 0
		58	0 3	65	0 1	67	0 1	77	0 0
		59	0 1	66	0 1	68	0 6	78	0 1
						69	0 1		
						70	0 2		

Table 5. Relations of the number of clusters consisting of 1-10 basic clusters with the cluster size (number of atoms included) for liquid metal Al.

4.3.1 Magic number sequence of nana-clusters for liquid metal Al

For liquid metal Al, for simplicity, we only analyze ten groups in the system in turn by the numbers of basic clusters contained in each group for two cases of liquid state at 943K and solid state at 350K, as shown in Table 5. From Table 5, it can be clearly seen that there is a peak value (maximum) of the numbers of clusters for each group and this is shown with a short underline in the table. As we compare this peak value with the abundance usually used in the research of cluster configurations, it is found that the two concepts are

completely consistent with each other. As we display the relations of the numbers of clusters formed in system with the size (the number of atoms contained in them) of these clusters, it is further found that the positions of the peak value points of the numbers of clusters also correspond to the magic number points. It is also clearly seen that the numbers of clusters at 943K are much less than those for the same group level at 350K for the former five group levels and there are few or almost none for the latter five group levels; and the front five peak value positions of clusters at 943K are not all consistent with those at 350K, for convenience of discussion for magic numbers, we only show the simulation results at 350K in figure 9.

It is clear from figure 9 that the quantity of various clusters is sensitive to the size of a cluster, and the magic numbers do exist. In the solid state at 350K, the total magic number sequence of all groups are in turn as 13, 19, 25, 27, 31, 33, 38, 40, 42, 45, 48, 51, 59, 65, 67…. However, when the number of atoms contained in a cluster is more than 70, the position of its magic number would be ambiguous.

In order to further reveal the magic number characteristics of the above-mentioned groups, we show the variation of the numbers of clusters in the system with the numbers of atoms contained in the clusters for ten groups in Figure 10, respectively.

It is observed in Fig.10 that although the ranges of neighboring groups have overlapped each other, one or two partial magic numbers still can be obviously distinguished for each group, and all the partial magic numbers for the ten groups rather correspond to the total magic number sequence for the whole system as shown in Figure 10. Going further, the total magic number sequence can be classified again according to the order of the ten groups of clusters in the following sequence: 13 (first magic number), 19 (second), 25-27(third), 31-33(fourth), 38-40(fifth), 42-45(sixth), 48-51(seventh), 55-59(eighth), 61-65(ninth) and 67(tenth). The ninth and tenth magic numbers are not so obvious in figure 10 because the numbers of clusters containing 9 and 10 basic clusters are insufficient, however, they stand out in figure 10 (c). For simplicity, the magic number sequence corresponding to the order of the ten groups of clusters can be listed again as 13, 19, 25(27), 31(33), 38(40), 42(45), 48(51), 55(59), 61(65) and 67, where the numbers in bracket are the secondary magic numbers of the corresponding groups of clusters. We think the above-mentioned analysis is very important for searching the origin of the magic number of clusters formed in the system.

We compare the total magic number sequence mentioned above to the experimental results of the photo-ionization mass spectra of clusters, formed through supersonic deposition from supersaturated gaseous phase Al, obtained by Schriver et al as shown in Fig.3 of Ref. (Schriver et al., 1990), it can be clearly seen that the magic numbers reported (14, 17, 23, 29, 37, 43, 47, 55, 67…), and those not reported (19, 21, 25, 33, and 39) (they can be clearly seen in the same Fig.3, maybe the authors thought those numbers were not consistent with the magic number rule at that time), are almost all consistent with our magic number sequence (in the error range of ±1). Thus, it can be said that the magic number sequence from our simulation is supported by the experimental results, but their clusters are produced by both different formation processes even though they are of the same element, Al.

In particular, as we further compare the magic number sequence from our simulation to the experimental results of inert gas clusters, it can be also clearly seen that the magic number sequence obtained from the mass spectra of Ar clusters formed in a supersaturated ionic

phase given by Harris et al is 13, 19, 23, 26, 29, 32, 34, 43, 46, 49, 55, 61, 64, 66... (see Fig.1 in Ref. (Harris, Kidwell & Northby, 1984), and the sequence obtained from the mass spectra of Xe clusters formed in a supersaturated vapor phase given by Echt et al (Echt, Sattler & Recknagle, 1981) is 13, 19, 23, 25, 29, 55, 71... (see Fig.1 in this Ref.), these results are also in good agreement with our sequence in the same error range. That is to say that the this simulation result from metal Al is similar to those from inert gases Ar and Xe, and this similarity should reflect in certain degree some essential relations between different elements, especially in different states.

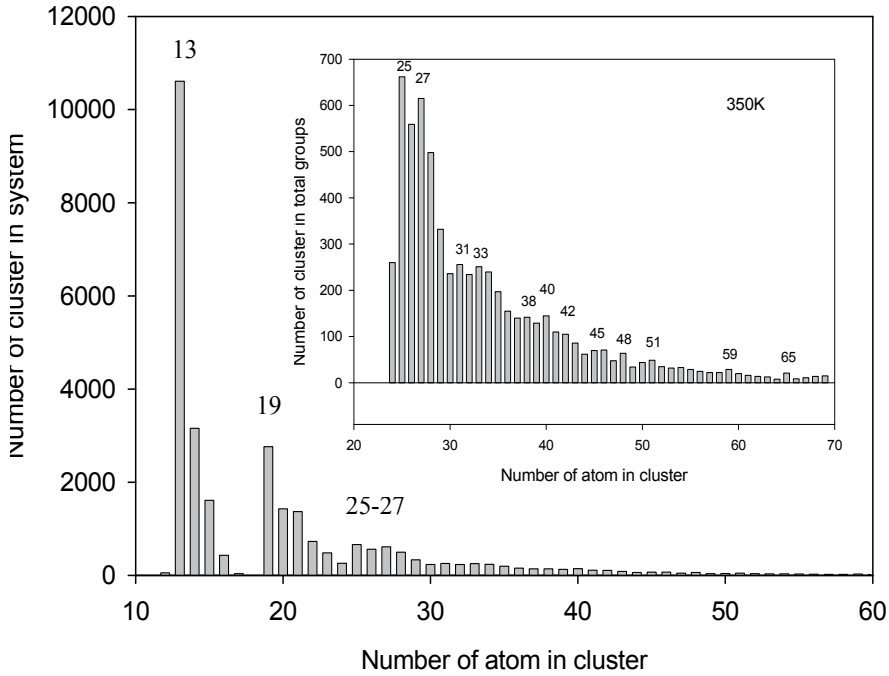

Fig. 9. Variation of the number of clusters in system of Al with sizes of clusters (i. e. the number of atoms contained in the cluster) at 350K.

It is highly interesting that this magic number sequence is also in good agreement with the results, obtained by using MD simulation and other model potentials from Solov'yov's and Doye's works, such as 13, 19, 23, 26, 29, 32, 34, 43, 46, 49, 55, 61, 64, 71, … (see Fig.1 and 2 in Ref. (Solov'yov I A, Solov'yov A V & Greiner, 2003)), and 13, 19, 23, 26, 29, 34, 45, 51, 55,… (see Fig.1 and 2 in Ref. (Doye & Meyer, 2005)) , respectively. From these, it can be explained that as long as the methods used to solve the similar problem are reasonable, the results should also be similar.

4.3.2 Magic number sequence of nana-clusters for liquid metal Na

For liquid metal Na, for deep understanding the size distribution of the clusters mentioned above, we also only analyze ten group levels in the system in turn by the numbers of basic clusters contained in each group level for two cases of liquid state at 573 K and solid state at

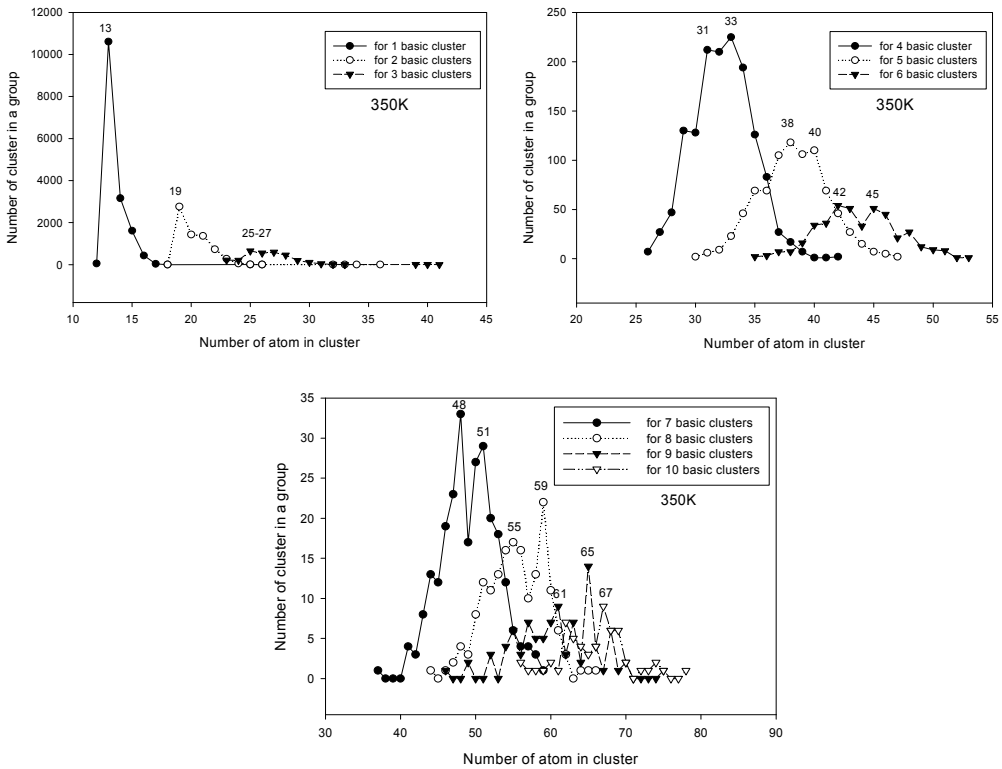

Fig. 10. Relationship of the numbers of basic clusters in a group with the size of cluster (number of atoms contained in a cluster) at 350K in system of Al. (a) for 1 ~ 3 group; (b) for 4 ~ 6 group; (c) for 7 ~ 10 group.

223 K, as shown in Table 6. From Table 6, it can be clearly seen that there is a peak value (maximum) of the numbers of clusters for each group, and this is shown with a short underline in the table. It is also found that the positions of the peak value points of the numbers of clusters are corresponded to the magic number points. In liquid state, the magic numbers are in the order of 14, 21, 28, 34…, and it is not clear for the clusters contained more than five basic clusters. In solid state, the magic numbers are in the order of 14, 22, 28, 34, 41(43), 46(48), 52(54), 57(59), 61(66), 70(74), which are corresponding to the first, second, third, …. and tenth group levels, respectively, the numbers in the brackets are the second magic numbers corresponding to the same group level. The first four magic numbers are almost the same as in liquid state; thereafter, it is also not clear for the clusters contained more than ten basic clusters.

On the other hand, for further understanding the magic number characteristics of the group level of clusters, the relations of the number of clusters in each group level with the number of atoms contained in each cluster for twelve groups, and the total number of clusters in all the group levels enclosed at 223K are shown in Fig 11 (a), (b), (c) and (d).

Cluster consisting of 1 basic clusters		Cluster consisting of 2 basic clusters		Cluster consisting of 3 basic clusters		Cluster consisting of 4 basic clusters		Cluster consisting of 5 basic clusters	
Cluster size	Cluster number	Cluster size	Cluster number	Cluster size	Cluster number	Cluster size	Cluster number	Cluster size	Cluster number
Number of atom	573K 223K	Number of atom	573K223K	Number of atom	573K223K	Number of atom	573K223K	Number of atom	573K223K
10	2 0	17	3 0	23	0 5	28	0 7	32	0 1
11	43 4	18	9 8	24	2 28	29	0 21	33	0 6
12	297 149	19	46 227	25	15 108	30	2 54	34	0 17
13	1180 2771	20	133 788	26	18 369	31	4 131	35	2 26
14	**1650** **5962**	**21**	**213** 1736	27	26 620	32	1 193	36	0 66
15	1119 4992	**22**	182 **1883**	**28**	**36 708**	33	4 271	37	1 92
16	412 1404	23	102 1167	29	25 638	**34**	**6 334**	38	1 120
17	59 151	24	46 507	30	19 503	35	4 322	39	0 156
18	6 0	25	9 134	31	12 305	36	5 284	40	1 162
		26	2 22	32	4 138	37	3 239	**41**	**0 179**
		27	0 3	33	2 47	38	1 153	42	0 164
				34	0 11	39	1 84	43	0 154
						40	0 36	44	1 105
						41	0 17	45	1 68
						42	0 1	46	0 51
						43	0 1	47	0 24
								48	0 10
								49	0 4
								50	0 1

(continued)

Cluster consisting of 6 basic clusters		Cluster consisting of 7 basic clusters		Cluster consisting of 8 basic clusters		Cluster consisting of 9 basic clusters		Cluster consisting of 10 basicclusters	
Cluster size	Cluster number	Cluster size	Cluster number	Cluster size	Cluster number	Cluster size	Cluster number	Cluster size	Cluster number
Number of atom	573K 223K	Number of atom	573K223K	Number of atom	573K223K	Number of atom	573K223K	Number of atom	573K223K
38	0 6	41	0 1	44	0 1	51	0 3	53	0 1
39	0 19	42	0 3	45	0 0	52	0 2	54	0 0
40	0 24	43	0 4	46	0 3	53	0 4	55	0 2
41	0 29	44	0 2	47	0 4	54	0 7	56	0 2
42	1 59	45	1 16	48	0 8	55	0 15	57	0 5
43	2 79	46	0 38	49	0 6	56	0 11	58	0 5
44	0 96	47	0 40	50	1 21	57	0 15	59	0 5
45	0 **114**	48	0 60	51	0 17	58	0 27	60	0 10
46	1 **114**	49	0 54	52	0 30	**59**	1 **34**	61	0 14
47	0 97	50	0 50	53	0 38	60	0 31	62	0 7
48	0 **107**	**51**	0 **65**	**54**	0 **54**	**61**	0 **34**	63	0 14
49	1 98	**52**	0 **66**	55	0 36	62	0 34	64	0 17
50	1 73	53	0 56	56	0 41	63	0 32	65	0 20
51	0 44	54	0 63	**57**	0 **50**	64	0 20	**66**	**0 23**
52	0 33	**55**	0 **65**	58	0 45	65	0 32	67	0 18
53	0 23	56	0 42	**59**	0 **50**	**66**	0 **39**	68	0 25
54	0 20	57	0 42	60	0 41	67	0 26	69	0 23
55	0 10	58	0 36	61	0 42	68	0 23	**70**	**0 26**
56	0 2	59	0 26	62	0 39	69	0 17	71	0 21
57	0 1	60	0 18	63	0 25	**70**	0 22	72	0 19
		61	0 11	64	0 19	71	0 15	73	0 21
		62	0 11	65	0 17	72	0 14	**74**	**0 22**
		63	0 1	66	0 10	73	0 12	75	0 21
		64	0 1	67	0 4	74	0 6	76	0 8
				68	0 1	75	0 1	77	0 8
				69	0 5	76	0 1	78	0 8
				70	0 2	77	0 2	79	0 5
								80	0 8
								81	0 5

Table 6. Relations of the number of clusters consisting of 1-10 basic clusters with the cluster size (number of atoms included) for liquid metal Na.

Highly interesting is that though the ranges of neighboring group levels are overlapped each other as shown in Fig 11, the magic number of each group level is still clearly corresponded to the magic number of the total magic number sequence for all the group

levels at the same group level. For this point, as we consider the magic number of each group level as the corresponding partial magic number, the total magic number sequence of all the group levels can be considered as the superposition of all the partial magic numbers.

Therefore, the total magic number sequence can be analyzed according to the corresponding group level in the order of 14(the first magic number), 22(second), 28(third), 34(fourth), 41-43(fifth), 46-48(sixth), 52-54 (seventh), 57-59(eighth), 61-66(ninth) and 70-74(tenth). However, the last three magic numbers also cannot be clearly distinguished in the Fig.11 (d), since the numbers of the larger clusters containing more basic clusters are not enough.

Going further, it can be seen that not only have the experimental results reported by Schriver and Harris et al (Schriver et al., 1990; Harris, Kidwell & Northby, 1984) provided a vital experimental certification to our simulation results, but also our simulation results could provide a reasonable model explanation to those experimental results. As regards the magic numbers obtained from experimental researches, some of them can be explained as usual with the viewpoint of geometric shell structure of cluster configurations being closed regularly (for neutral clusters and charged clusters) (Knight et.al., 1984; Harris et al., 1984; Echt, Sattler & Recknagle, 1981; Schriver et al., 1990; Robles, Longo & Vega, 2002), and the others cannot be explained with the same viewpoint because they are corresponding to the geometric non-shell structure of cluster configurations. However, from our simulation, it can be clearly seen that during the forming process of larger clusters, only a few clusters accumulate and extend continuously with a basic cluster as the core according to a certain rule; most of them are formed with combining different numbers and different types of basic clusters. So, it is the normal case and can be explained to find more clusters with geometric non-shell structure in their magic number sequence as above-noted.

So far, the critical question is why the magic number sequence of clusters formed by solidification of liquid metal Al from our simulation is so similar to those magic number sequences of clusters formed by ionic spray and gaseous deposition of metal Al, inert gases Ar and Xe from experimental studies? We think the main reason is that the solidification process of liquid metal is essentially similar to the formation process of clusters in the above-mentioned experimental studies. We consider that in the solidification process of liquid metals, various cluster configurations could be formed by the rapid agglomerating of a large number of atoms as the system spreads over a large space for a short time, while in the formation process of clusters in the experiments, various cluster configurations could be formed by slow gathering of a few atoms as the system spreads over a small space for a long time, and both their final results could be similar each other on the whole (even though they are not be similar completely). On the other hand, at present, the essential differences between different elements, especially different states, are still not be distinguished in detail, it is necessary to analyze and compare in detail various similar and dissimilar magic numbers of these sequences in the future.

Therefore, it may be feasible to adopt magic numbers, especially the partial magic numbers of the group levels, obtained during the rapid solidification process of liquid metals to understand the magic number characteristics obtained with experimental methods.

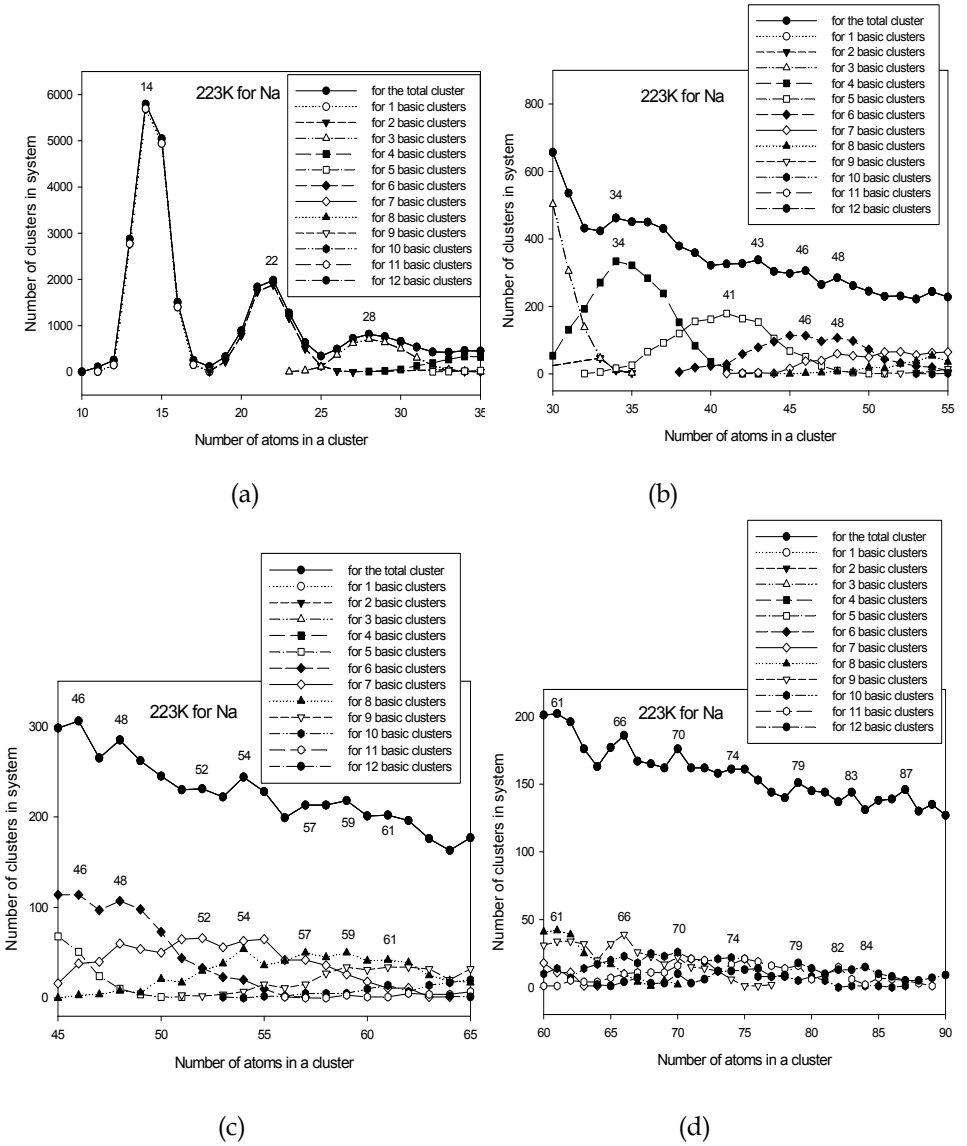

Fig. 11. Relations of the number of cluster in a group with the size of cluster (i. e. atoms included in cluster) at 223K .(a) for 1 ~ 3 groups; (b) for 4 ~ 6 groups; (c) for 7 ~ 9 groups; (d) for 10 ~ 12 group levels of clusters .

4.3.3 Stability of nana-clusters

From the above mentioned, it can be clearly seen that the larger clusters within a same group level should have not the same number of atoms because they contained different basic clusters containing different number of atoms. Therefore, these larger clusters would have different number of atoms. It can be clearly seen that those larger clusters containing

minority of atoms in which the central atoms of basic clusters are connected tightly each other with multi-bonded, would be more stable than others and they would possess better stability and higher heredity, and so on.

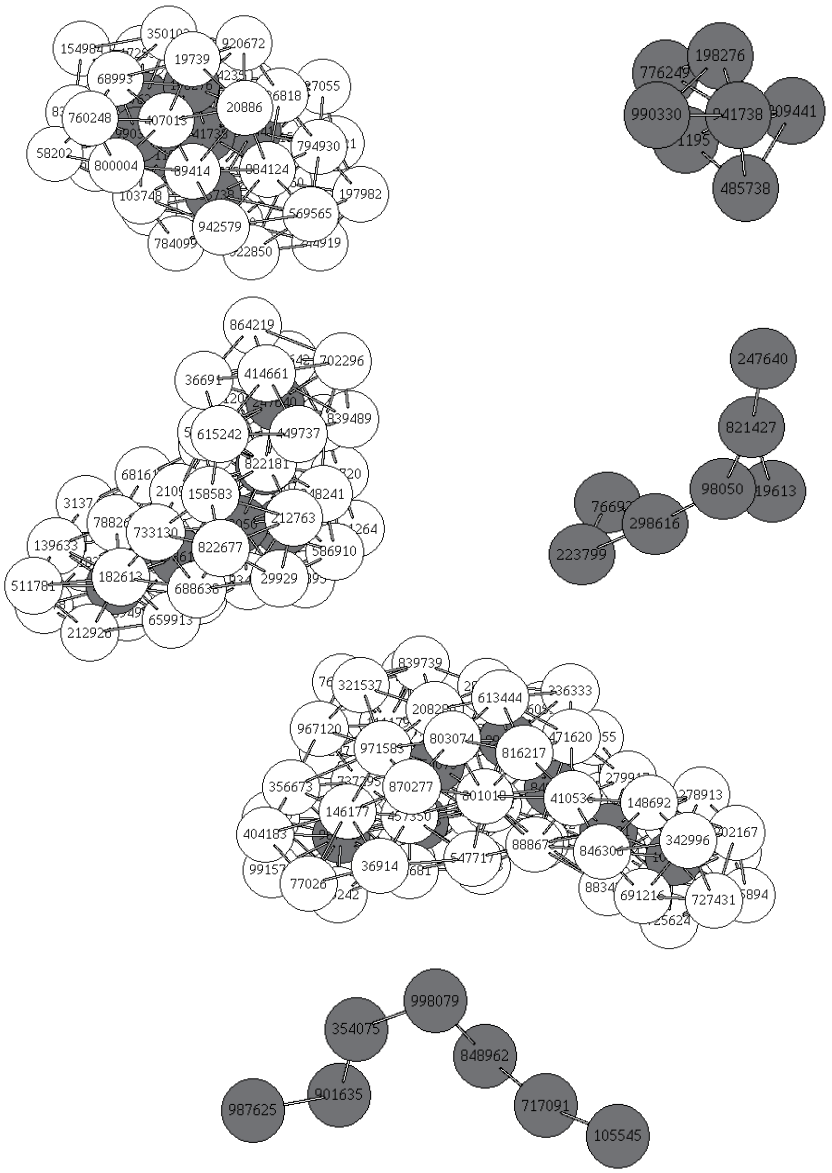

Fig. 12. Schematic diagram of three larger clusters consisting of 43, 53 and 69 atoms within 7 basic clusters with connecting bonds, respectively, at 223K (the gray spheres are the center atoms of basic clusters).

These features can be shown in Fig.12. It is the schematic diagram of three larger clusters consisting of 43, 53 and 69 atoms within the same group level of 7 basic clusters, with

connecting bonds, respectively, at 223K (the gray spheres are the center atoms of basic clusters). From the diagrams of their center atoms with multi-bonded or single-bonded each other, it can be clearly seen that the cluster consisting of 43 atoms has a dense connecting of all atoms and would possess better stability and higher heredity than other two clusters consisting of 53 and 69 atoms, respectively, in turn.

5. Conclusions

In this chapter, for deeply understanding the formation and evolution characteristics of various clusters, especial of nano-clusters formed during solidification processes, molecular dynamic simulation studies have been performed for a large-sized system consisting of 10^6 liquid metal for Al and Na atoms, respectively. Several microstructure analysis methods, especial the cluster-type index method (CTIM) have been adopted to describe various types of cluster, especial of nano-cluster by basic clusters. It is demonstrated that the icosahedral cluster (12 0 12 0) is the most important basic cluster, and plays a critical role in the microstructure transition. The nano-clusters are formed by connecting various middle and small clusters with different cluster-types or sizes, and their structures are different from those obtained by gaseous deposition, ionic spray and so on.

For the evolution processes of the nano-clusters, at different temperatures, it is demanstrated clearly that the central atoms of basic clusters in the nano-clusters are bonded each other with different ways, some central atoms are multi-bonded, and others single-bonded. A new statistical method has been proposed to classify the clusters (from basic cluster to nano-cluster) formed in the system by the number of basic cluster contained in them, and the clusters consisting of the same number of basic cluster but not the same number of atoms can be classified as a group level of clusters. It can be clearly seen that the size distribution characteristics of various clusters in the system is related to the magic number of each group level of clusters. The total magic number sequence of the system can be obtained for metal Al as 13, 19, 25(27), 31(33), 38(40), 42(45), 48(51), 55(59), 61(65) , 67, ... the numbers in the brackets are the second magic numbers corresponding to the same group level of clusters. This magic number sequence is in good agreement with the experimental results obtained by Schriver and Harris et al (for Al). For metal Na, the magic number sequence are in the order of 14, 22, 28, 34, 41(43), 46(48), 52(54), 57(59), 61(66), 70(74), …This magic number sequence is in good agreement with the experimental results obtained by Knight et al and the calculating results obtained by Noya et al (containing the primary and secondary magic numbers) (for Na). Highly interesting, these simulation results can be used to provide a reasonable explanation for those experimental results.

6. Acknowledgment

This work was supported by the National Natural Science foundation of China (Grant No 50831003, 50571037)

7. References

Alexander, V. M. & Moshe, B. Z., (2001). Temporal evolution of an argon cluster during the process of its evaporation, *Chemical Physics*, Vol. 264: 135−143.

Alfe, D. (2003). First-principles simulations of direct coexistence of solid and liquid aluminum, *Phys. Rev. B* , Vol. 68: 064423.

Bruhl, R., Guardiola, R., Kalinin, A., et al., (2004) Diffraction of Neutral Helium Clusters: Evidence for "Magic Numbers", *Phys. Rev. Lett.* , Vol.92: 185301.

Cabarcos, O. M. & Lisy, J. M. (1999). Molecular dynamics simulation of gas phase ion cluster formation, *International Journal of Mass Spectrometry,* Vol. 185/186/187: 883-903.

Dong, K. J., Liu, R. S., Yu, A. B., et al., (2003). Simulation study of the evolution mechanisms of clusters in a large-scale liquid Al system during rapid cooling processes, *J. Phys. : Condens. Matter,* Vol. 15: 743-753.

Doye, J. P. K. & Meyer, L. (2005). Mapping the Magic Numbers in Binary Lennard-Jones Clusters，*Phys. Rev. Lett.*, Vol. 95: 063401.

Echt, O., Sattler, K. & Recknagle, E. (1981). Magic numbers for sphere packings: Experimental verification in free xe-non clusters，*Phys. Rev. Lett.,* Vol.47: 1121-1124.

Evans, D. J. (1983). Computer ''experiment'' for nonlinear thermodynamics of Couette flow, *J. Chem. Phys.,* Vol. 78: 3297-3302.

Kostko, O., Huber, B., Moseler, M., et al., (2007). Structure determination of medium-sized sodium clusters, *Phys. Rev. Lett.,* Vol. 98: 043401.

Knight, W. D., Clemenger, K., de Heer, W. A., et al., (1984). Electronic shell structure and abundances of sodium clusters, *Phys. Rev. Lett.,* Vol. 52: 2141-2143.

Harris, I. A., Kidwell, R. S. & Northby, J. A. (1984). Structure of charged argon clusters formed in a jet expansion, *Phys. Rev. Lett.,* Vol.53: 2390－2393.

Haberland, H., Hippler, T., Donges, J., et al., (2005). Melting of sodium clusters: where do the magic numbers come from?, *Phys. Rev. Lett.,* Vol. 94: 035701

Honeycutt, J. D. & Andersen, H. C. (1987). Molecular-dynamics study of melting and freezing of small Lennard-Jones, *J. Phys Chem.,* Vol. 91: 4950-4963.

Hoover, W. G., Ladd, A. J. C. & Moran, B. (1982). High-strain-rate plastic flow studied via nonequilibrium molecular dynamics, *Phys. Rev. Lett.,* Vol. 48: 1818.-1820

Hou, Z. Y., Liu, L. X., Liu, R. S., et al., (2009). Simulation study on the evolution of thermodynamic, structural and dynamic properties during the crystallization process of liquid Na, *Modelling Simul. Mater. Sci. Eng*, Vol. 17 : 035001.

Hou, Z. Y., Liu, L. X., Liu, R. S., et al., (2010a) Short-range and medium-range order in Ca7Mg3 metallic glass, *J Appl. Phys.*, Vol. 107: 083511

Hou, Z. Y., Liu, L. X., Liu, R. S., et al., (2010b). Kinetic details of nucleation in supercooled liquid Na: A simulation tracing study, *Chemical Physics Letters*, Vol. 491: 172-176

Ikeshoji, T., Hafskjold, B., Hashi, Y., et al., (1996). Molecular Dynamics Simulation for the Formation of Magic-Number Clusters with a Lennard-Jones Potential，*Phys. Rev. Lett.* , Vol. 76: 1792-1795.

Joshi, K., Krishnamurty, S. & Kanhere, D. G.,(2006), "Magic melters" have geometrical origin, *Phys. Rev. Lett.,* Vol. 96 : 135703

Kostko, O., Huber, B., Moseler, M., et al., (2007). Structure determination of medium-sized sodium clusters, *Phys. Rev. Lett.,* Vol. 98: 043401.

Li, D. H., Li, X. R. & Wang, S. (1986). Variational calculation of helmholtz free energies with applications to the sp-type liquid metals, *J. Phys F,* Vol. 16: 309-321.

Li, H. & Pederiva, F. (2003). Anomalies in liquid structure of Ni_3Al alloys during a rapid cooling process, *Phys. Rev. B*, Vol. 68: 054210

Liu, C. S., Zhu, Z. G., Xia, J. C., et al., (2001). Cooling rate dependence of structural properties of aluminium during rapid solidification, *J. Phys.:Condens. Matter,* Vol. 13 : 1873-1890.

Liu, F. X., Liu, R. S., Hou, Z. Y., et al., (2009). Formation mechanism of atomic cluster structures in Al-Mg alloy during rapid solidification processes, *Annals of Physics*，Vol. 324 : 332–342.

Liu, R. S., Qi, D. W. & Wang, S. (1992a). Subpeaks of structure factors for rapidly quenched metals, *Phys. Rev. B,* Vol. 45: 451-453.

Liu, R. S. & Wang S. (1992b). Anomalies in the structure factor for some rapidly quenched metals, *Phys. Rev. B*, Vol. 46:12001-12003.

Liu, R. S., Li, J. Y. & Zhou, Q. Y. (1995). A simulation study on the transition feature of the microstructure in the forming process of amorphous metals, *Chinese Science Bulletin*, Vol. 40: 1429-1433.

Liu, R. S., Li, J. Y., *et al.*, (1998). The stability of microstructures during rapid cooling processes of Al liquid metal, *Trans. Nonferrous Met. Soc. China,* Vol. 8: 533－538.

Liu, R. S., Li, J. Y., Zhou, Z., et al., (1999) The high-temperature properties of the micro-structure transition in liquid metals, *Mater. Sci. Eng. B,* Vol. 57: 214-217.

Liu, R. S., Li, J. Y., Dong, K. J., et al., (2002). Formation and evolution properties of clusters in a large liquid metal system during rapid cooling processes, *Mater. Sci. Eng. B,* Vol. 94:141-148.

Liu, R. S., Dong, K. J., Li, J. Y.,et al., (2005a). Formation and description of nano-clusters formed during rapid solidification processes in liquid metals , *J. Non-Cryst. Solids,* Vol. 351: 612-617.

Liu, R. S., Dong, K. J., Liu, F. X., et al., (2005b). Formation and evolution mechanisms of large-clusters during rapid solidification process of liquid metal A1, *Science in China (Series G),* Vol. 48: 101-112.

Liu, R. S., Liu, F. X., Zhou, Q. Y., (2007a). Formation and magic number characteristics of cluster configurations during rapid cooling processes of liquid metals, in Editor(s): Bai, C., et al,. *Nanoscience and Technology, Pts 1 and 2* of Book Series: *Solid State Phenomena,* Vol. 121-123 pp: 1139-1142.

Liu, R. S., Tian, Z. A., Yi, X. H., et al., (2007b). Evolution mechanisms of nano-clusters in a large-scale system of 10(6) liquid metal atoms during rapid cooling processes, in Editor(s): Bai, C., et al,. *Nanoscience and Technology, Pts 1 and 2* of Book Series: *Solid State Phenomena,* Vol. 121-123 pp: 1049-1052.

Liu, R. S., Dong, K. J., Tian, Z. A., et al., (2007c). Formation and magic number characteristics of clusters formed during solidification processes, *J. Phys.:Condens. Matter*, Vol.19: 196103.

Liu, R. S., Liu, H. R., Dong, K. J., et al., (2009). Simulation study of size distributions and magic number sequences of clusters during the solidification process in liquid metal Na, *J. Non-Cryst. Solids*，Vol. 355: 541-547.

Liu, X. H., Zhang, X. G., Li, Y. *et al.*, (1998). Cluster formation by direct laser vaporization: Evidence for the twofold mechanism, *Chem. Phys. Lett.*, Vol. 288: 804—808.

Magudoapathy, P., Gangopadhyay, P., Panigrahi, B. K., et al., (2001). Electrical transport of Ag nanoclusters embedded in glass matrix, *Physica B,* Vol.299: 142-146.

Martin, T. P., Naher, U. & Schaber, H. (1992). Evidence for octahedral shell structure in aluminum clusters, *Chem. Phys. Lett.,* Vol. 199: 470-474.

Noya, E.G., Doye, J.P.K., Wales, D.J., et al., (2007). Geometric magic numbers of sodium clusters: Interpretation of the melting behaviour, *Eur. Phys. J. D*, Vol. 43: 57-60.

Orlando, M. C. & James, M. L., (1999). Molecular dynamics simulation of gas phase ion cluster formation, *International Journal of Mass Spectrometry*, Vol. 185/186/187: 883 - 903.

Qi, D. W. & Wang, S. (1991a). Thermodynamic calculations for glasses: thermodynamic properties of the metallic glass transition, *J. Non-Cryst. Solids,* Vol. 135: 73-78.

Qi, D. W. & Wang, S. (1991b). Icosahedral order and defects in metallic liquids and glasses, *Phys Rev. B,* Vol. 44 : 884-887.

Robles, R., Longo, R. C. & Vega, A. (2002). Magnetic magic numbers are nt magic for clusters embedded in noble metals, *Phys. Rev. B,* Vol. 66: 064410.

Schriver, K. E., Person, J. L., Honea, E. C., et al., (1990). Electronic shell structure of group-IIIA metal atom clusters, *Phys. Rev. Lett.* , Vol. 64: 2539-2542.

Solov'yov, I. A., Solov'yov, A. V. & Greiner, W. (2003). Cluster growing process and a sequence of magic numbers, *Phys. Rev. Lett.* , Vol. 90: 053401.

Spiridis, N., Haber, J. & Korecki, J. (2001). STM studies of Au nano-clusters on TiO_2(1 1 0) , *Vacuum,* Vol. 63: 99-105.

Tian, Z. A., Liu, R. S., Zheng, C. X., et al., (2008). Formation and Evolution of Metastable bcc Phase during Solidification of Liquid Ag: A Molecular Dynamics Simulation Study, J. Phys. Chem. A, Vol. 112 : 12326.

Tian, Z. A., Liu, R. S., Peng, P., et al., (2009). Freezing structures of free silver nanodrplets: A moleculart dynamics simulation study, *Phys. Lett. A,* Vol. 373: 1667-1671.

Wang, L., Bian, X. F. & Zhang, J. X. (2002). Structural simulation of clusters in liquid Ni50Al50 alloys, *Modelling Simul. Mater. Sci. Eng.* ,Vol. 10: 331-339

Wang, S. & Lai, S. K. (1980). Structure and electrical resistivities of liquid binary alloys, *J. Phys F,* Vol. 10: 2717-2737.

Waseda, Y. (1980). *The structure of Non-crystalline Materials* (New York: McGraw-Hill), p. 270.

Wendt, H. R. & Abraham, F. F. (1978). Empirical criterion for the glass transition region based on Monte Carlo simula-tions, *Phys. Rev. Lett.,* Vol. 41: 1244-1246.

Yamamoto, H. & Asaoka, H. (2001). Formation of binary clusters by molecular ion irradiation, *Appl. Surf. Sci.,* Vol.169-170: 305-309.

Zheng, C. X., Liu, R. S., *et al.*,(2002). Simulation study on the formation and transition properties of cluster structures in liquid metals during rapid cooling processes, *Science in China, Series A,* Vol. 45(2): 233—240.

Zhou, L. L., Liu, R. S., Tian, Z. A., et al.,(2011). Formation and evolution characteristics of bcc phase during isothermal relaxation processes of supercooled liquid and amorphous metal Pb, *Trans. Nonferrous Met. Soc. China,* Vol. 21: 588-597.

10

A Molecular Dynamics Study on Au

Yasemin Öztekin Çiftci[1], Kemal Çolakoğlu[1] and Soner Özgen[2]
[1]*Gazi University; Science Faculty, Physics Department, Ankara*
[2]*Firat University; Faculty of Art and Science, Physics Department, Elaziğ*
Turkey

1. Introduction

Theoretical and computational modeling is becoming increasingly important in the devolopment of advanced high performance materials for industrial applications.[1] Computer simulations on various metallic systems usually use simple pairwise potentials. However, the interactions in real metallic materials can not be represented by simple pairwise interactions only. A pure pairwise potential model gives the Cauchy relation, C_{12}=$C_{44,}$ between the elastic constants, which is not the case in real metals. Therefore, many-body interactions should be taken into account in any studies of metals and metal alloys.

It is very important to calculate the phase diagrams of metallic systems and their alloys in order to achieve technological improvements. The phase diagrams are still obtained by using experimental techniques because there are no available methods for entirely theoretical predictions of all of the phase diagrams of any pure metal. Therefore, in the calculations of the phase diagrams some expressions have been formed by using theoretical or semi-empirical approach and their validity have been investigated in a selected portion of the phase diagrams. The expressions suggested in semi-empirical approaches generally contain some factors depending on temperature and pressure. Therefore, the calculated phase region is restricted by experimental limits. Today, the free energy concepts, such as Gibbs and Helmholtz, on the other hand, have been widely used to calculate the macroscopic phase diagrams [2, 3] in which thermodynamics parameters are dominant. In microscopic scale, their calculations require some vibrational properties which can be derived from elastic constants of the material. So, the correct calculations of the elastic constants are important as well as the calculations of phase diagrams.

MD simulations can be utilized to compute the thermodynamic parameters and the results of the external effects, such as temperature and pressure or stress acted on a physical system [4, 5]. In the MD simulations, the interatomic interactions are modeled with a suitable mathematical function, and its gradient gives the forces between atoms. Hence, Newton's equations of motion of the system are solved numerically and the system is forced to be in a state of minimum energy, an equilibrium point of its phase space. Although many properties of the system, such as enthalpy, cohesive energy and internal pressure, have been directly calculated in the MD simulations, the entropy which is required for the free energy calculations has not been directly obtained and it is possible to obtain it by some approaches involved harmonic and anhormonic assumptions. There are some investigations related to

these approaches: the calculation of the free energy between FCC and HCP structures [6, 7], the investigation of first order phase transition [8], the dependence of the phase diagram on the range of attractive intermolecular forces [9], the investigation of harmonic lattice dynamics and entropy calculations in metal and alloys [10], the calculation of the *P-T* diagram of hafnium [11], etc. Recently, the *P-T* diagrams for Ni and Al have been calculated by Gurler and Ozgen [12] by using the MD simulations based on the EAM technique [13].

The reliability of the results obtained from MD simulations depends on the suitable modeling of the interatomic interactions. Interatomic interactions are usually results of fits to various experimental data. However, it is not clear whether simulations performed at other temperatures still reproduce the experimental data accurately. Comparing theoretical and experimental elastic constants and other properties at various temperatures can serve as a measure of reliability and usefulness of potential models [14, 15]. In fact, there are several potential energy functions that can be used for the metallic systems. However, the EAM, originally developed by Daw and Baskes [16, 17] to model the interatomic interactions of face-centered cubic (FCC) metals, has been successfully used to compute the properties of metallic systems such as bulk, surface and interface problems. The reliability of the EAM in the bulk and its simple form for use in computer simulations make it attractive.

When a liquid metal is quenched through the super-cooled region, a phase transition from liquid to glass takes place. Several techniques have been proposed to obtain a disordered state [18-20]. Among them the rapid solidification method is widely used for the amorphous phase. However, due to the demand of a high cooling rate this method is restiricted in most experimental cases. Thus, the computer simulation of molecular dynamics is applied.

In this study, in order to model Au metallic systems we have used the EAM functions modified by us (Ciftci and Colakoğlu [21]), developed firstly by Cai [22]. In this work, we have carried out MD simulations to obtain the *P-V* diagrams at 300 K and the *P-T* diagrams of the systems for an ideal FCC lattice with 1372 atoms, by using an anisotropic MD scheme. In addition, the bulk modulus and specific heat of the system in solid phase are determined and results-driven simulations are interpreted by comparing with the values in literature. We have also calculated the pressure derivatives of elastic constants and bulk moduli for Au. The obtained results are compared with the values in the literature. The another purpose of this work is to explore the glass transition and crystallization of Au using EAM .

2. Potential energy function

According to the embedded atom method, the cohesive energy of an assembly of N atoms is given by [16, 17]

$$E_{tot} = \sum_i F_i(\rho_i) + \sum_{i>j} \phi(r_{ij}) \tag{1}$$

$$\rho_i = \sum_{j(\neq i)} f(r_{ij}) , \tag{2}$$

where E_{tot} is the total cohesive energy, ρ_i is the host electron density at the location of atom i due to all other atoms, $f(r_{ij})$ is the electronic density function of an atom, r_{ij} is the distance

between i and j atoms, $F_i(\rho_i)$ is the embedding energy to embed atom i in an electron density ρ_i, and $\phi(r_{ij})$ is the pairwise potential energy function between atoms i and j.

In this work, we used a modified pairwise potential function in the framework of the Cai version [22] of the EAM. Recently, this potential function has been used by us for predicting several physical properties of some transitional metals [21,23-25]. The present form of the potential makes it more flexible owing to the constants, m and n in the multiplier forms. Such a factor included in the classical Morse function is treated by Verma and Rathore [26] to compute the phonon frequencies of Th, based on the central pair potential model. The modified parts of the potential and the other terms are as follows:

$$f(r) = f_e e^{-\alpha(r-r_e)}, \tag{3}$$

$$F(\rho) = -F_0[1 - \ln\left(\frac{\rho}{\rho_e}\right)^n]\left(\frac{\rho}{\rho_e}\right)^n + D_2\left(\frac{\rho}{\rho_e}\right), \tag{4}$$

$$\phi(r) = \frac{D_1}{(m-1)}\left[\frac{e^{-m\beta(\frac{r}{r_e}-1)}}{(\beta\frac{r}{r_e})^n} - (\beta\frac{r}{r_e})^n e^{-\beta(\frac{r}{r_e}-1)}\right], \tag{5}$$

where a, β, D_1 and D_2 are fitting parameters that are determined by the lattice parameter a_0, the cohesive energy E_c, the vacancy formation energy E_v^f, the elastic constants C_{ij}. Here ρ_e is the host electron density at equilibrium state, r_e is the nearest neighbor equilibrium distance, and $F_0=E_c-E_v^f$. In this potential model, there are four parameters: β and D_1 are from two-body term, m and n are adjustable selected constants. The fitting parameters are determined by minimizing the value of $W = \sum [(X^{cal} - X^{\exp}) / X^{\exp}]^2$. Here X represents the calculated and experimental values of the quantities taken into account in the fitting process. Hence, the potential functions can be fitted very well to the experimental properties of the matter, such as the vacancy formation energy (E_v), cohesive energy (E_c), elastic constants (C_{ij}), and lattice constants (a_0) in an equilibrium state. In the fitting process here, the cutoff distance is taken to be $r_{cut}=1.65a_0$. In the Eq. (3), the f_e parameter is selected as unity for mono atomic systems because it is used for alloy modeling as an adjustable parameter to constitute suitable electron density. For the selected values of the constants m and n, the computed potential parameters and experimental input data for Au are given in Table 1.

The cohesive energy changes with the variation of lattice constants of Au calculated from Eq. (1) and from the general expression of the cohesive energy of metals proposed by Rose et al. [32] are compared in Fig.1. The Rose energy is also called as the generalized equation of state of metals and written as

$$E_R(a^*) = -E_0(1 + a^*)e^{-a^*} \tag{6}$$

$$a^* = \left(\frac{a}{a_0} - 1\right) / \left(\frac{E_C}{9B_m\Omega}\right)^{1/2} \tag{7}$$

where E_0 is a constant to be taken as an equilibrium cohesive energy of solid, B_m is the bulk modulus, and Ω is the atomic volume in equilibrium. It has been determined that the cohesive energy calculated from Eq. (1) with the parameter given in Table1 for Au is in good agreement with Rose energies in equilibrium.

	a_0 (Å)	r_0 (Å)	E_c (eV)	E_v^f (eV)	B_m (GPa)	C_{11} (GPa)	C_{12} (Gpa)	C_{44} (GPa)	T_m (K)	C_p (K/mol.K)
Au	4.079	2.8842	3.81	0.93	180.32	201.63	169.67	45.44	1337	25.42

	m	n	α (Å^{-1})	β	D_1 (eV)	D_2 (eV)
Au	7	0.5	4.3482	3.5361	0.0685	0.3097

Table 1. The experimental properties and potential parameters of Au. The experimental lattice parameters (a_0) at room temperature are from ref. [27]. Bulk modulus (B_m) and elastic constants (C_{ij}) given at zero temperature are from [28], vacancy formation energy (E_v^f) is from ref. [29], melting temperature (T_m), the coefficient of linear thermal expansion a are from [30], and specific heat C_p is from [31].

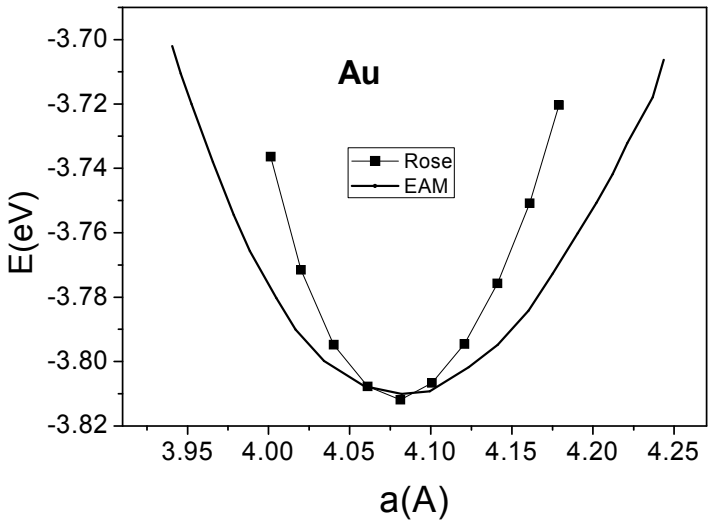

Fig. 1. Rose and EAM energies versus lattice constant for Au.

3. Molecular dynamics simulation

The Lagrange function, written for an anisotropic box, i.e. MD cell, containing N particles by Parrinello and Rahman, is given by [33, 34]

$$L_{PR} = \frac{1}{2}\sum_{i=1}^{N} m_i(\dot{\mathbf{s}}_i^t \mathbf{G}\dot{\mathbf{s}}_i) - E_{tot} + \frac{1}{2}M\mathrm{Tr}(\dot{\mathbf{h}}^t\dot{\mathbf{h}}) - P_{\mathrm{ext}}V \ , \tag{8}$$

where m_i is mass of particle i, $\mathbf{s}_i$ is the scaled coordinate of atom i and is represented by a column vector whose elements are between zero and unity, **h**=(**a**, **b**, **c**); **a**, **b** and **c** vectors are MD cell axes, the metric tensor **G** is given by matrix product $\mathbf{h}^t\mathbf{h}$, M is an arbitrary constant which represents mass of the computational box, P_{ext} is external pressure applied on the cell, V is the volume of the MD cell and is obtained from det(**h**). Thus, square of distance between particles i and j is described by $r_{ij}^2 = s_{ij}^t G s_{ij}$. The classical equations of motion of the system obtained from Eq. (1) become

$$\ddot{\mathbf{s}}_i = -\frac{1}{m_i}\mathbf{F}_i = \mathbf{G}^{-1}\dot{\mathbf{G}}\dot{\mathbf{s}}_i \tag{9}$$

$$\ddot{\mathbf{h}} = M^{-1}(\mathbf{\Pi} - \mathbf{I}P_{ext})\boldsymbol{\sigma} \ , \tag{10}$$

where $\boldsymbol{\sigma} = (\mathbf{b}\mathrm{x}\mathbf{c}, \mathbf{c}\mathrm{x}\mathbf{a}, \mathbf{a}\mathrm{x}\mathbf{b}) = V(\mathbf{h}^t)^{-1}$ and microscopic stress tensor, Π, is a dyadic given as follows;

$$\mathbf{\Pi} = V^{-1}\left[\sum_{i=1}^{N} m_i \mathbf{v}_i.\mathbf{v}_i - \sum_{i=1}^{N}\sum_{j>i}^{N} \frac{F_{ij}}{r_{ij}}\mathbf{r}_i.\mathbf{r}_i\right]. \tag{11}$$

Also the force on an atom i in the system is calculated from the following equation,

$$\mathbf{F}_i = -\mathbf{\Delta}_s E_i = -\sum_{\substack{j=1 \\ j\neq i}}^{N}\left[F_i'\rho_j' + F_j'\rho_i' + \phi_{ij}'\right]\frac{\hat{\mathbf{s}}_{ij}}{r_{ij}} \ , \tag{12}$$

where the primes denote the first derivatives of the functions with respect to their arguments.

In all of the simulation studies, the equation of motion given in Eqs. (9) and (10) were numerically solved by using the velocity version of the Verlet algorithm [35]. The size of integration step was chosen to be $7.87\text{x}10^{-15}$s for Au. Initial structures of the systems were constructed on a lattice with 1372 atoms and an FCC unit cell. It has been observed that, with these initial conditions, the systems were equilibrated in 5000 integration steps. Time averages of the thermodynamic properties of the system in each simulation run were determined by using 30,000 integration steps following the equilibration of the system. The structures of the system in solid phase were examined by using the radial distribution function. Melting temperatures were determined from the plots of the cohesive energy versus temperature. It is possible to classify our simulation runs in two groups as thermal and pressure applications. In the thermal applications, the temperature of the system under zero pressure is raised from 100K to 2400K for Au with an increment of 100K in each run of 35,000 integration step; but near the melting temperatures, the increment is reduced to 20K. The pressure applications are also implemented by repeating the thermal applications under pressure values of 0.5, 1.0, 1.5, 2.5, 5.0, 7.5, 10.0, 15.0 and 20.0 GPa. The simulation is restarted with different pressure in each run, to avoid algorithmic errors.

The temperature dependency of the elastic constants and the bulk moduli are calculated by following the procedure given by Karimi et al [14].

For the calculation of glass formation and crystallization, firstly, we run 20 000 time steps to make the system into equilibrium state, then the liquid phase is cooled to 100K at the rate of 1.5833×10^{13} K/s and 1.5833×10^{12} K/s , respectively to examine the formation process of amorphization and crystallization.

4. Results and discussion

4.1 Thermal and mechanical properties

We can classify our results on thermal and mechanical properties of Au in to seven different categaries (i) the *P-V* diagram has been analyzed to determine the bulk modulus under zero pressure, (ii) the specific heat has been determined by using the changes of the enthalpy with temperature, (iii) the radial distribution function has been obtained in solid and liquid phases for the estimation of structural properties, (iv) the *P-T* graph, which is plotted by using the variation in melting temperatures with increasing pressure acted on the system, have been examined. (v) the pressure dependence of V/V_o has been obtained, (vi) elastic constants and pressure derivatives of elastic constants and bulk modulus has been investigated.

The change on the atomic volume with the gradually increasing pressure, which acts on the system at 300K temperature, is given in Fig.2 for Au. The bulk modulus calculated from the *P-V* diagram shown in Fig.2 is obtained as *B*=174.3 GPa for Au. The calculated bulk modulus is in good agreement with their experimental values (see Table 1) within an error of ~3.4% for Au.

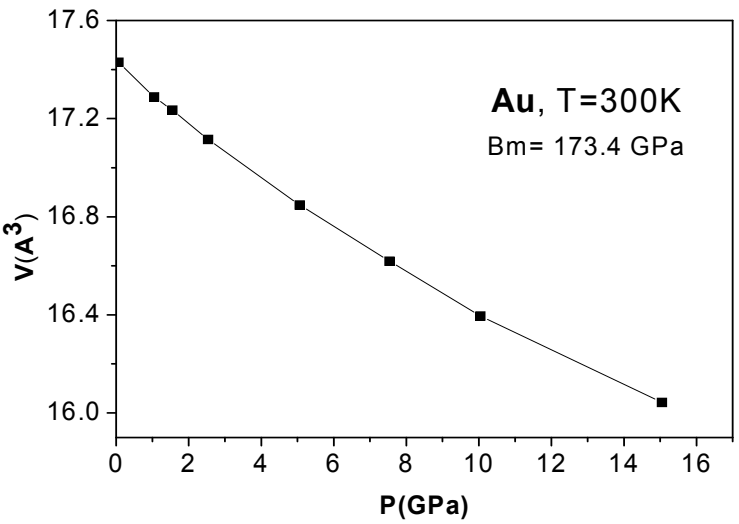

Fig. 2. P-V diagrams for Au.

The variations of enthalpy with temperatures under zero pressure for solid Au is given in Fig.3, and this graph is used to compute specific heats under the constant pressure. The calculated values of specific heats over 0-300K are found to be C_p= 28.2 J/molK for Au.

Considering the experimental data in Table 1, it can be seen that the specific heat is calculated with an error of 9.8 % for Au.

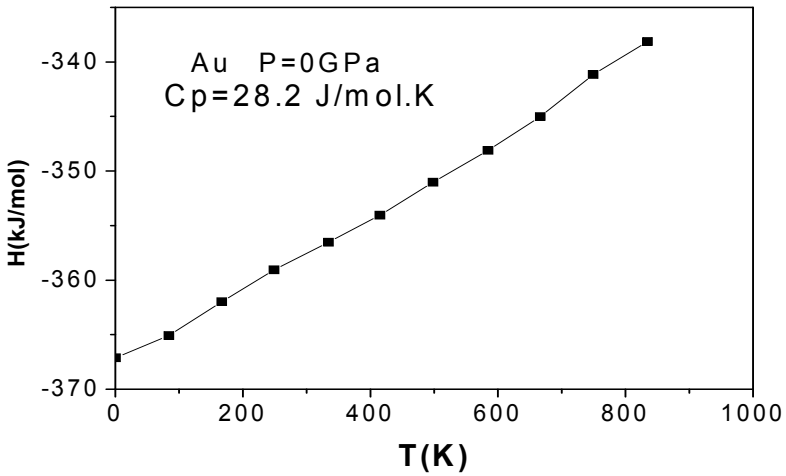

Fig. 3. Variation of the enthalpy with temperature for Au.

There are several methods for determining the melting temperature of a crystal. MD simulations are performed on system at various temperatures, and the cohesive energy is plotted as a function of temperature in one of these methods, as we did here. At the melting point, a discontinuity occurs in the cohesive energy. The other way of determining the melting temperature is to plot caloric curve which is the change of the total energy of crystal versus kinetic energy [36]. Indeed, the melting temperature of metal is obtained as the temperature at which the Gibbs free energy of the solid and liquid phases become equal. The entropy is required to compute the free energy, but it can not be directly calculated from MD simulations. For this reason, some other approaches are required [3]. Another way of determining the melting temperature is to simulate the solid-liquid interface [14]. In this way, the temperature for which the interface velocity goes to zero is determined as the melting temperature and it is reproduced more correctly than the way of caloric curve. Karimi et al [14] estimated the melting temperature for Ni as 1630±50K within an error of -5.6%, using the solid-liquid interface technique.

In the present work, the variations of cohesive energy with temperature for different pressures acted on the system are given in Fig. 4 for Au. We have computed the melting temperatures under zero pressure as 1100±20K for Au. When these values are compared with the experimental ones of 1337K given in Table 1, the error for Au becomes 21%.

The radial distribution function (RDF) is used to investigate the structural properties of the solid and liquid phases. The plot of radial distribution functions acquired in solid and liquid phases for Au is given in Fig. 5. First peak location of radial distribution curves represents the distance of the nearest neighbor atoms, r_0. The second peak location denotes the distances of next nearest neighbors, a_0. These distances are found to be 2.907Å and 4.144Å, respectively for Au. By comparing with experimental data given in Table1, the calculated

error on a_0 and r_0 are 0.8% and 1.5% for Au. So, the present errors can be omitted since the parameters of the potential energy function were fitted to the crystal properties in static case. Since the peak locations shown in Fig. 5 satisfy the certain peak locations at $\sqrt{2}$, $\sqrt{3}$, $\sqrt{4}$, $\sqrt{5}$, etc. times r_0 in an ideal FCC unit cell, the metal of Au has an FCC unit cell under zero pressure.

The *P-T* diagrams plotted by using the melting temperatures under different pressures are given in Fig. 6 for Au. The binding energies of the metals can be reduced by increasing temperature. At high temperatures near the melting point, it is generally expected that the Gibbs free energy is lowered by phase transition like martensitic types from one structure to another one which has lower energy at higher temperatures, like a BCC lattice.

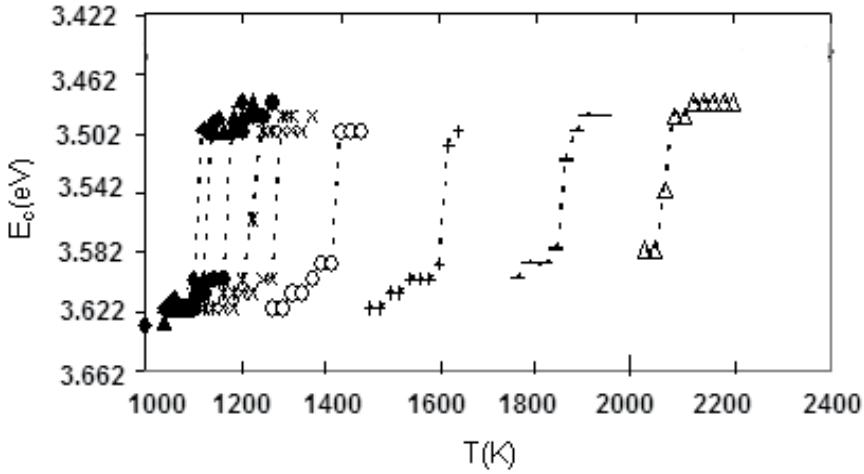

Fig. 4. The cohesive energy as a function of temperature at different pressure for Au. The symbols ◆,▲,●,×,✳,○, + reppresents the pressure values of 0.0, 0.5, 1.0, 1.5, 2.5, 5.0, 7.5 GPa, respectively.

We calculated V/V_o as a function of pressure (0-45 kbar) for Au and added experimental points [37] for comparing with MD results. The plot of V/V_o versus pressure for Au is given in Fig. 7. Here V_o is the volume under the zero pressure. MD results are in very good agreement with the experimental data at pressures below 25GPa.

We also calculated elastic constans and pressure derivatives of the elastic constants and bulk modulus at 0 K and in P=0 GPa pressure. The results are summarized in Table 2. Obtained results are in good agreement with available other theoretical results.

	C_{11} (GPa)	C_{12} (GPa)	C_{44} (GPa)	$(\partial C_{11}/\partial P)_T$	$(\partial C_{12}/\partial P)_T$	$(\partial C_{44}/\partial P)_T$	$(\partial B/\partial P)_T$
This study	195.43	163.67	44.56	6.99	3.98	2.01	4.02
[38]	192.9	162.8	41.5	5.72	4.96	1.52	4.66
[39]	192.2	162.8	42.0	7.01	6.14	1.79	6.43

Table 2. Second order elastic constants and pressure derivatives of elastic constants and bulk modulus (P=0 GPa).

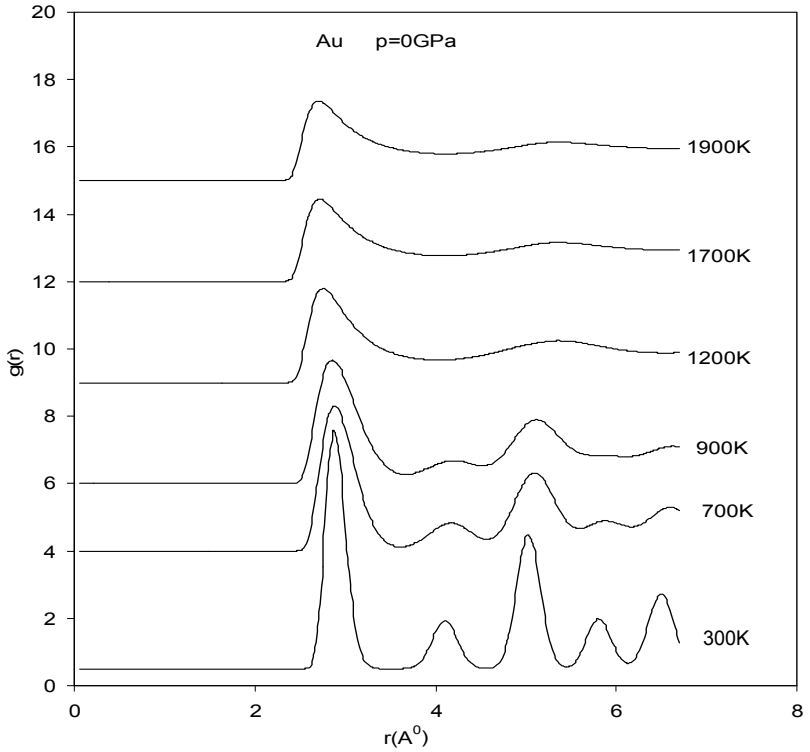

Fig. 5. The radial distribution curves in solid and liquid phases forAu.

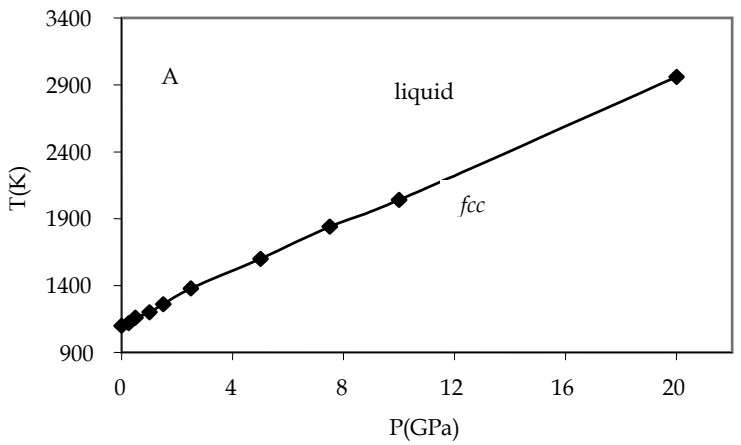

Fig. 6. P-T diagrams for Au.

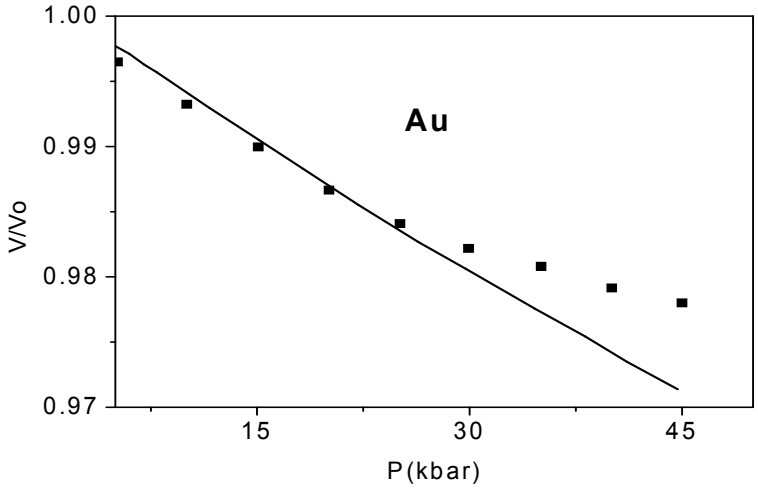

Fig. 7. Variation of pressure as a function of V/Vo for Au. Experimental points are taken from Ref.[37].

4.2 Glass formation and crystallization

Traditionally,the heating and cooling processes are applied to examine the formation process of amorphization and crystallization. The Fig.8(a) and (b) show the variation of volume at the rate of 1.5833×10^{13} K/s and 1.5833×10^{12} K/s, respectively. The sudden jump in volume in the temperature range of 1000 to 1100K for the heating process is due to the melting of the Au. In contrast to heating, cooling curves show a continuous change in volume.

The slope of the volume versus temperature curve in Fig.8(a) at the rate of 1.5833×10^{13} K/s decreases below 500K. This is a sign of glass formation. Since the glass is a frozen liquid, the change in configurational entropy vanishes. Thus, the derivative of entropy with respect to pressure is the derivative of volume with respect to temperature[40]. The Fig. 8(b) at rate of 1.5833×10^{12} K/s shows a sharp change in the volume as the temperature is lowered below 300K. At 350 K system shows that the cooled Au has crystallized.

Different methods are suggested to determine the glass transition temperature (T_g) which is observed widely in amorphous materials. According to one of these definitions, which is known as Wendt-Abraham ratio [41], to determine T_g in MD simulations, the g_{min}/g_{max} ratios of RDF curves at different temperatures are calculated [39]. Here, g_{min} is the first minimum value and g_{max} is first maximum value of RDF curve. In such a plot, two lines in different slopes occur, and glass transition temperature is taken as intersection point of these lines. The graph of g_{min}/g_{max} ratios versus temperature obtained in this study is given in Fig. 9. The T_g is obtained from this figure to be 500K.

The RDF curves of the model structure during the heating and cooling processes at different temperature are given in Fig10. The RDF shows an fcc crystal structure as the sample is heated from 0 to 500 K. But, at 1200 K (above the melting temperature) the emergence of

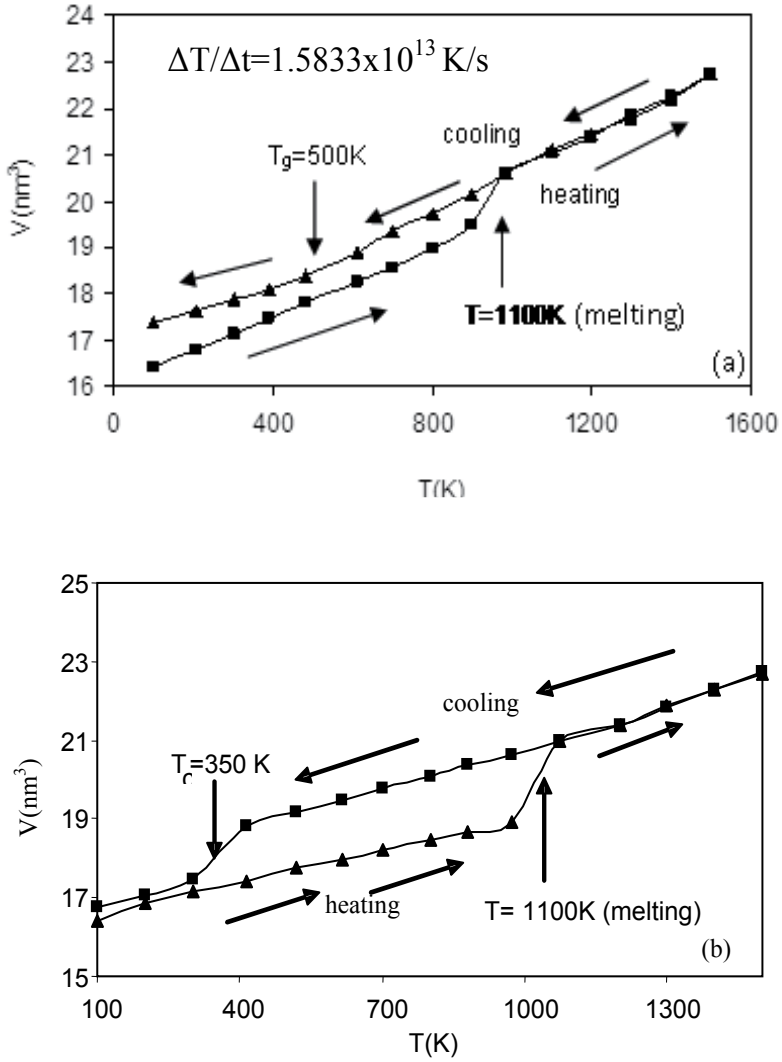

Fig. 8. Average volume of Au during heating and cooling at a rate of (a) 1.5833×10^{13} K/s and (b) 1.5833×10^{12} K/s.

broad peaks shows that the structure has melted. The sample was heated to 1500K and then cooled back to 1200 K, leading to the same structure as for heating, indicating a stable liquid state. Cooling to 500K, from RDF we still see the structure of a liquid, in fact a supercooled liquid. However, after cooling to 300K, we see that the second peak of RDF is split. This splitting of the second peak is a well-known characteristic feature in the RDF of a metallic glass.

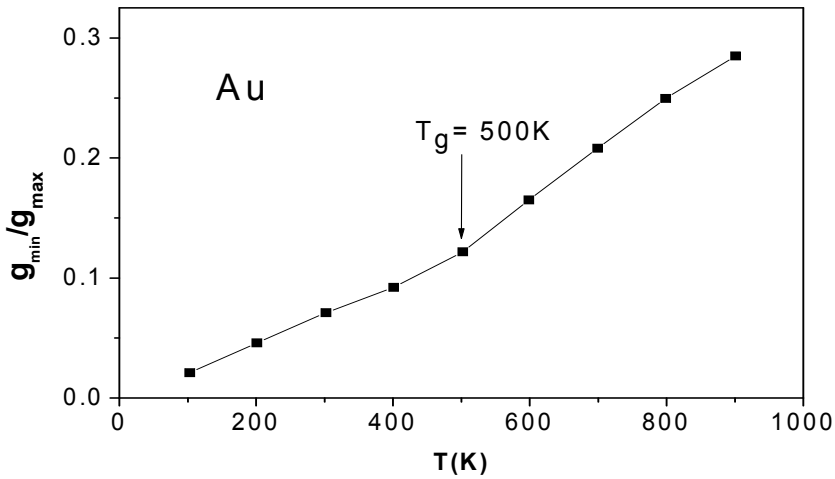

Fig. 9. Determination of glassy transition temperature.

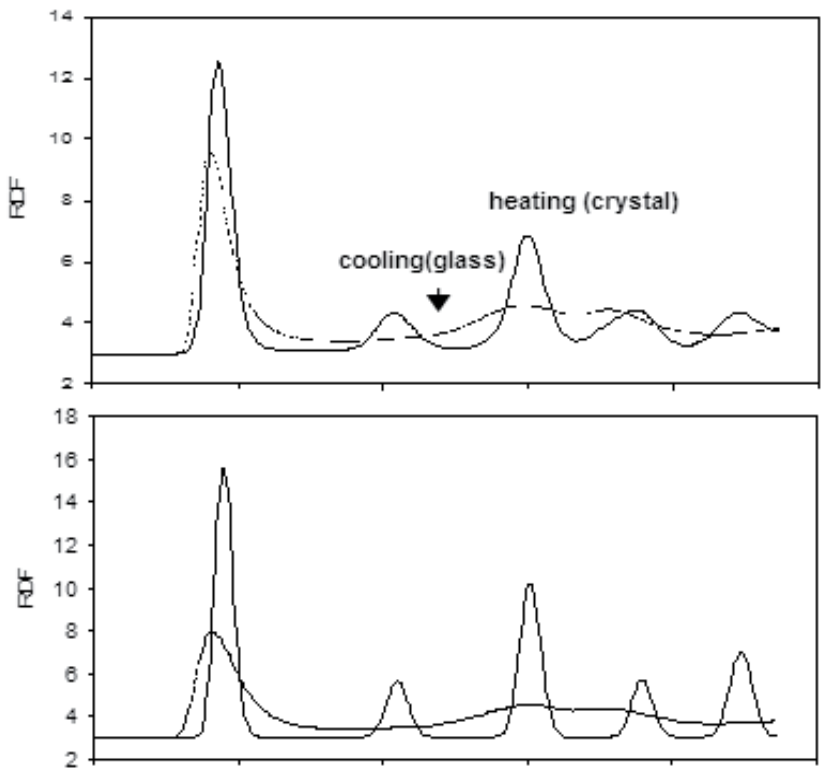

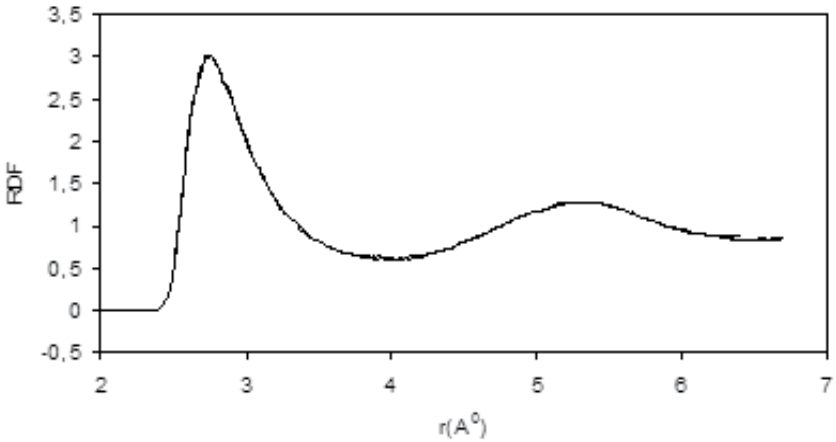

Fig. 10. Radial distribution function (RDF) of Au during the heating and cooling processes at rate of 1.5833×10^{13} K/s (a) at 0K (b)at 500 K , and (c) at 1200K.

5. Conclusion

It has been found that the present version of EAM with a recently developed potential function, which makes it more flexible owing to the parameter *n*, represents quite well the interactions between the atoms to simulate the studied mono atomic systems. Since the parameterization technique of our potential is based on the bulk properties of metals at 0K, it can describe the temperature-dependent behaviors of our crystals particularly, qualitatively. As a whole, present model well describes the many physical properties ,and our results are in reasonable agreement with the corresponding experimental findings, and provide another measure of the quantitative limitations of the EAM for bulk metals.

6. References

[1] T. Çağın, G. Dereli, M. Uludoğan, and M. Tomak, Phys. Rev. B, 59,5, (1999)3468.
[2] P. Haasen, Physical Metallurgy, 2 nd ed., Cambridge Univ. Press., UK, 1992.
[3] D. A. Porter, K.E. Easterling, Phase Transformation in Metals and Alloys, 1, 2nd ed., Chapman& Hall, T. J. Press (Padstow), UK, 1992.
[4] J.M. Haile, Molecular Dynamics Simulation, Elementary Methods, Wiley, Canada, 1992.
[5] C.R.A Catlow., in: C.R.A Catlow. et al. (Eds.), Computer Modelling of Fluids Polymers and Solids, Kluwer Academic Publishing, USA, 1990, pp. 1-28.
[6] M.C. Moody, J.R. Ray, J. Chem. Phys. 84 (3) (1986) 1795.
[7] J. Ihm, Rep. Prog. Phys. 51 (1988) 105.
[8] W.C. Kerr, A.M. Hawthorne, R.J Gooding, A.R Bishop., J. A Krumhansl, Phys. Rev. B 45 (13) (1992) 7036.
[9] M. Hasegawa, K. Ohno, J. Phys. Condens. Matter, 9 (1997) 3361.
[10] G.D. Barrera, R.H. Tendler, Comput. Phys. Commun.,105 (1997) 159.
[11] S.A. Ostanin, V.Y. Trubitsin, Comput. Mater. Sci., 17 (2000) 174.

[12] Y.Gurler, S. Ozgen, Matt. Lett. 57 (2003) 4336.
[13] M. W. Finnis, J.E. Sinclair, Philos. Mag., A. 50 (1) (1984) 45.
[14] M. Karimi, G. Stapay, T. Kaplan and M. Mostoller, Modelling Simul. Mater. Sci. Eng., 5 (1997) 337.
[15] S. Erkoc, Phys. Rep. 278 (1997) 79.
[16] M.S. Daw, M.I. Baskes, Phys. Rev. Lett., 50 (17) (1983) 1285.
[17] M.S. Daw, M.I. Baskes, Phys. Rev. B, 29(12) (1984) 6443.
[18] C. Massobric, V. Pontikis, G. Martin, Phys. Rev. B, 41(15)(1990)10486.
[19] F. Cardellini, V. Contini, G.Mazzone, Scripta Metall Mater, 4(1995) 641.
[20] J.S.C. Jang, C.C. Koch, J. Mater Res., 5(3)(1990) 498.
[21] Y.O Ciftci. and K.Colakoğlu, Acta Physica Polanica A, (100)4 (2001) 539.
[22] J. Cai and Y.Y. Ye, Phys. Rev.B 54 (12) (1996) 8398.
[23] S. Kazanc, Y.O. Ciftci, K.Colakoglu, and S.Ozgen,Physica B, 381(2006)96.
[24] Y.O. Ciftci, K.Colakoglu, S.Ozgen and S.Kazanc, Cent. Eur. J.Phys. 4(2006)472.
[25] Y.O. Ciftci, K.Colakoglu, S.Ozgen and S.Kazanc, J. Phys: Condens. Matter 19 (2007) 326204.
[26] M.L. Verma, R.P.S. Rathore, Phys. Stat. Sol. b, 185 (1994) 93.
[27] W. B.Pearson, Handbook of lattice Spacing and structure of Metals and Alloys ,Pergamon, Oxford,1967.
[28] R. O. Simmons and H. Wang, Single Crystal Elastic Constants and Calculated Aggregate Properties,A Handbook, MIT Press, Cambridge, 1991
[29] Londolt –Bornstein New Series, vols. III-11 and III-18 ,Springer –Verlag, Berlin,1991
[30] C. Kittel, Introduction to solid state physics, Wiley, New York,1986.
[31] Y. S. Touloukian and E.H. Buyco, Specific Heat: Metallic Elements and Alloys (New York: IFI/ Plenum, 1970)
[32] J. H. Rose, J.R Smith., F Guinea., J. Ferrante, Phys. Rev. B. 29(6) (1984) 2963.
[33] M. Parrinello, A. Rahman, Phys. Rev. Lett. 45(11) (1980) 1196.
[34] M. Parrinello, A. Rahman, J. App. Phys. 52 (12) (1981) 7182.
[35] L. Verlet, Phys. Rev. 159 (1967) 98.
[36] S.K. Nayak, S.N. Khanna, B.K. Rao, P. Jena, J. Phys. Cond. Mat., 10 (1988) 10853.
[37] M.H. Rice, R.G. McQueen , J.H. Walsh, Solid State Physics, 6 (1958) 1.
[38] Y. Hiki, A.Granato, Phys. Rev. B, 144 (1966) 411.
[39] W.B. Daniels, C.S. Smith, Phys. Rev. B, 111 (1958) 713.
[40] Y. Qi, T. Çağın, Y. Kimura, and W.A. Goddard, Phys. Rev. B, 59(5) (1999)3527.
[41] L.Wang, X.B. Fang, H. Li, Mater. Lett. 51(2001) 7.

11

Gelation of Magnetic Nanoparticles

Eldin Wee Chuan Lim
National University of Singapore
Singapore

1. Introduction

The study of magnetic nanoparticles and ferrofluids has gained considerable interests among research workers in recent years. The potential range of application that these novel magnetic nanomaterials can offer is gradually being recognized and continues to be explored. As described in a recent review article (Pamme, 2006), magnetic particles have already been used for such diverse applications as the fabrication of ferrofluidic pumps, solid supports for bioassays, fast DNA hybridization, giant magnetoresistive sensors and superconducting quantum interference devices (SQUID). At a more fundamental level, one of the most important and widely investigated aspects of magnetic nanoparticles and ferrofluids is the formation of self-organized microstructures under the influence of an externally applied magnetic field. A suspension of magnetic nanoparticles in a fluid medium can generally be considered as a single magnetic domain with macroscopic properties that are dependent on the properties of individual nanoparticles as well as the interactions between them (Rosensweig, 1985). In the presence of an external magnetic field, the magnetic domain will be oriented in the direction of the field and may approach saturation magnetization. When the external magnetic field is removed, the domain will revert to a randomly oriented state which exhibits no macroscale magnetism. Although it is well-established that the magnetization of a magnetic fluid or ferrofluid is related to the arrangement of the suspended magnetic nanoparticles, which in turn arises due to the effects of interactions between various types of forces present such as Brownian and dipole-dipole interactions for example, current understanding of the kinetics, dynamics and resulting microstructure of the nanoparticle aggregation process is far from complete.

In the research literature, a variety of experimental, theoretical and computational approaches have been applied towards studies of the aggregation and microstructure formation process of magnetic nanoparticles and ferrofluids. In particular, the computational techniques that have been used for such investigations include Monte Carlo simulations (Davis et al., 1999; Richardi et al., 2008), Brownian dynamics (Meriguet et al., 2004, 2005; Yamada and Enomoto, 2008), lattice-Boltzmann method (Xuan et al., 2005), molecular dynamics simulations (Huang et al., 2005), combination of analytical density functional theory and molecular dynamics (Kantorovich et al., 2008), stochastic dynamics (Duncan and Camp, 2006) and analytical methods (Furlani, 2006; Furlani and Ng, 2008; Nandy et al., 2008). Further, several recent studies have also reported comparisons between experimental and theoretical or computational results. For example, the chain formation process of magnetic particles in an external magnetic field and under

the effects of shear in microchannels was analyzed and the chain growth rate predicted by the Smoluchowski model was observed to be consistent with experimental observations (Brunet et al., 2005). The transport of an isolated magnetic microsphere or of very dilute suspensions where dipole-dipole interactions are negligible through a microchannel have also been investigated both experimentally and numerically (Sinha et al., 2007). The controlled aggregation of Janus magnetic nanoparticles was studied using dynamic light scattering and cryo-TEM imaging techniques and the main features of the aggregation behavior were consistent with predictions provided by a modified version of the classic Monte Carlo simulation algorithm (Lattuada and Hatton, 2007). Brownian dynamics has also been applied towards the study of motion of magnetic particles in a magnetic field gradient and shown to be in agreement with experimental measurements based on an optical detection method (Schaller et al., 2008).

While most of the investigations of magnetic nanoparticles dispersions have targeted colloidally stable systems, a few studies have also focused on suspensions undergoing aggregation. Colloidal systems undergoing aggregation exhibit complex behaviors due to several factors such as particle-particle interactions, fractal structure of individual clusters and the aggregation mechanism and kinetics. Several modeling approaches have been proposed in the literature to simulate the aggregation kinetics of colloidal systems, either based on Monte-Carlo simulations, or on population balance equations, or on a combination of the cluster mass distribution computed based on the population balance equations with the structure properties of individual clusters determined by Monte-Carlo simulations (Lattuada et al., 2004a). It was found that the average sizes and structure properties predicted in both the diffusion-limited and reaction-limited aggregation regimes were in good agreement with light scattering measurements (Lattuada et al., 2004b). In the case of magnetic nanoparticles aggregation, both experimental and computational studies have underlined substantial differences between diffusion limited aggregation in the absence and in the presence of an applied magnetic field (Tsouris and Scott, 1995; Promislow et al., 1995; Miyazima et al., 1987). In the presence of magnetic fields, clusters grow as chains aligned in the direction of the applied magnetic field. The kinetics of chain growth has been modeled using Monte-Carlo methods (Miyazima et al., 1987), Brownian Dynamics simulations (Dominguez-Garcia et al., 2007), and population balance equations (Martinez-Pedrero et al., 2008). All of these studies have demonstrated how the average size of chains grows as a power law of time, with an exponent that depends upon the particle volume fraction and the strength of the dipolar interactions (Climent et al., 2004). However, no studies to the best of our knowledge have focused on gelation and percolation of magnetic dispersions at high particles volume fractions.

In this work, we report the first application of a modified version of the Discrete Element Method (DEM) towards the simulation of magnetic nanoparticle aggregation with and without an external magnetic field. The various types of interparticle forces that are important in the dynamics of the aggregation process, such as dipole-dipole interactions, van der Waals forces, electrostatic forces and Brownian effects, are taken into account through the incorporation of the respective force models into the classical DEM model. The effects of overall solid fraction and the presence or absence of an external magnetic field on the propensity of such magnetic nanoparticles to aggregate and the microstructure of the resulting clusters or chain-like assemblies formed are investigated computationally.

2. Computational model

2.1 Discrete element method

The molecular dynamics approach to modeling of particulate systems, otherwise known as the Discrete Element Method (DEM), has been applied extensively for studies of flow behaviors in various types of granular and multiphase systems (Lim et al., 2006a, 2006b; Lim and Wang, 2006; Lim et al., 2007; Lim, 2007, 2008, 2009, 2010a, 2010b; Lim et al., 2011). For a comprehensive review, the interested reader is referred to a recent review article by Zhu et al. (2008). The methodology of DEM and its corresponding governing equations have also been presented numerous times in the research literature and only a brief description will be presented here for sake of completeness.

The translational and rotational motions of individual solid particles are governed by Newton's laws of motion:

$$m_i \frac{dv_i}{dt} = \sum_{j=1}^{N} \left(f_{c,ij} + f_{d,ij} \right) + f_{f,i} + f_{dd,ij} + f_{vdw,ij} + f_{e,ij} + f_{B,i} + f_{\mathrm{lub},ij} \tag{1}$$

$$I_i \frac{d\omega_i}{dt} = \sum_{j=1}^{N} T_{ij} \tag{2}$$

where m_i and v_i are the mass and velocity of the i^{th} particle respectively, N is the number of particles in contact with the i^{th} particle, $f_{c,ij}$ and $f_{d,ij}$ are the contact and viscous contact damping forces respectively, $f_{f,i}$ is the fluid drag force that is governed by Stokes' Law, $f_{dd,ij}$ is the dipole-dipole interaction between particles i and j in the presence of an applied magnetic field, $f_{vdw,ij}$ and $f_{e,ij}$ are the van der Waals interaction and electrostatic repulsion between particles i and j respectively, $f_{B,i}$ is the random force arising due to Brownian effects, $f_{lub,ij}$ is the lubrication force due to hydrodynamic effects, I_i is the moment of inertia of the i^{th} particle, ω_i is its angular velocity and T_{ij} is the torque arising from contact forces which causes the particle to rotate. The effect of gravity is neglected in the present study.

Contact and damping forces have to be calculated using force-displacement models that relate such forces to the relative positions, velocities and angular velocities of the colliding particles. A linear spring-and-dashpot model is implemented for the calculation of these collision forces. With such a closure, interparticle collisions are modeled as compressions of a perfectly elastic spring while the inelasticities associated with such collisions are modeled by the damping of energy in the dashpot component of the model. The normal ($f_{cn,ij}$, $f_{dn,ij}$) and tangential ($f_{ct,ij}$, $f_{dt,ij}$) components of the contact and damping forces are calculated according to the following equations:

$$f_{cn,ij} = -\left(\kappa_{n,i} \delta_{n,ij} \right) n_i \tag{3}$$

$$f_{ct,ij} = -\left(\kappa_{t,i} \delta_{t,ij} \right) t_i \tag{4}$$

$$f_{dn,ij} = -\eta_{n,i} \left(v_r \cdot n_i \right) n_i \tag{5}$$

$$f_{dt,ij} = -\eta_{t,i}\left\{\left(v_r \cdot t_i\right)t_i + \left(\omega_i \times R_i - \omega_j \times R_j\right)\right\} \tag{6}$$

where $\kappa_{n,i}$, $\delta_{n,ij}$, n_i, $\eta_{n,i}$ and $\kappa_{t,i}$, $\delta_{t,ij}$, t_i, $\eta_{t,i}$ are the spring constants, displacements between particles, unit vectors and viscous contact damping coefficients in the normal and tangential directions respectively, v_r is the relative velocity between particles and R_i and R_j are the radii of particles i and j respectively. If $\left|f_{ct,ij}\right| > \left|f_{cn,ij}\right|\tan\phi$, then 'slippage' between two contacting surfaces is simulated based on Coulomb-type friction law, i.e. $\left|f_{ct,ij}\right| = \left|f_{cn,ij}\right|\tan\phi$, where tan ϕ is analogous to the coefficient of friction.

2.2 Long range interactions

In the presence of an externally applied magnetic field, paramagnetic nanoparticles can be considered as magnetic single-domains with a permanent magnetic moment, μ_i proportional to their volume, $\mu_i = \frac{\pi d_i^3}{6} M_i$, where M_i is the intensity of magnetization. By the superparamagnetic magnetization law for a monodisperse, colloidal ferrofluid (Rosensweig, 1985),

$$\frac{M_i}{\phi_s M_d} = \coth\alpha_i - \frac{1}{\alpha_i} \tag{7}$$

where $\alpha_i = \frac{\pi}{6}\frac{\mu_o M_d H d_i^3}{kT}$, μ_o is the magnetic permeability of free space, M_d is the saturation magnetization of the bulk magnetic solid, H is the magnetic field strength, k is the Boltzmann's constant, T is thermodynamic temperature and ϕ_s is the volume fraction of solid present. The anisotropic dipole-dipole interaction energy $E_{dd,ij}$ is then given by (Rosensweig, 1985)

$$E_{dd,ij} = \frac{1}{4\pi\mu_o}\left[\frac{\mu_i \cdot \mu_j}{r_{ij}^3} - \frac{3}{r_{ij}^5}\left(\mu_i \cdot r_{ij}\right)\left(\mu_j \cdot r_{ij}\right)\right] \tag{8}$$

where μ_i and μ_j are the magnetic moments of particles i and j respectively and r_{ij} is the displacement vector between the two particles. The dipole-dipole force of interaction acting on particle i is then derived from $f_{dd,ij} = -\nabla E_{dd,ij}$.

The van der Waals forces of interaction and electrostatic repulsion between particles are calculated as follows (Russel et al., 1989):

$$f_{vdw,ij} = \frac{H_a}{6}\frac{d_i^6}{\left(h_{ij}^2 + 2d_i h_{ij}\right)^2\left(h_{ij} + d_i\right)^3} n_i \tag{9}$$

where H_a is the Hamaker constant and h_{ij} is the surface-to-surface separation distance along the line of centers of particles i and j. When the actual surface-to-surface separation distance between two particles is less than 1 nm, h_{ij} is fixed at 1 nm to avoid the singularity in the above equation.

The electrostatic repulsion between particles due to the so called double layer forces is described by the DLVO theory (Russel et al., 1989):

$$f_{e,ij} = 2\pi\varepsilon\varepsilon_o\left(\frac{kT}{ze}\right)^2 \kappa R_i q^2 \frac{\exp\left(-\kappa h_{ij}\right)}{1-\exp\left(-\kappa h_{ij}\right)} \tag{10}$$

where ε is relative permittivity, ε_o is the absolute permittivity of free space, z is the valency of ions, q is the surface charge, e is the fundamental electronic charge, κ^{-1} is the Debye decay length given by $\kappa^{-1} = \left(\frac{\varepsilon\varepsilon_o kT}{2e^2 z^2 n_b}\right)^{1/2}$, n_b is the concentration of ions.

For the size of nanoparticles simulated, it is also pertinent to consider the random forces arising due to Brownian effects. The algorithm for simulating Brownian forces is similar to that for generating a Gaussian white noise process (Russel et al., 1989):

$$f_{B,i} = \sqrt{12\pi\mu_f\left(\frac{d_i}{2}\right)kT\Delta t}\; n_i' \tag{11}$$

where Δt is the time step used in the simulation and n_i' is a unit vector with a random direction. It is well-established that Brownian effects become less significant at small separation distances between particles due to the presence of hydrodynamic lubrication effects. As such, Brownian forces were set to zero for surface-to-surface distances less than 1 nm in all simulations.

2.3 Hydrodynamic interactions

Hydrodynamic interactions due to lubrication effects become important at small surface-to-surface separation distances between particles. The lubrication force between two spheres is described by the lubrication theory and may be calculated as follows (Russel et al., 1989):

$$f_{\text{lub},ij} = \frac{6\pi\mu\left(v_r \cdot n_i\right)}{h_{ij}}\frac{d_i^2}{16}n_i \tag{12}$$

Here, as with the calculation of van der Waals forces described earlier, when the surface-to-surface separation distance between two particles is less than 1 nm, h_{ij} is fixed at 1 nm to avoid the singularity in the above equation.

3. Simulation conditions

The simulation conditions applied were based as much as possible on the materials and methods used for experimental studies reported in the literature so that a meaningful comparison between the simulations and experiments can be made. Spherical nanoparticles of diameter 70 nm and density 1000 kg m^{-3} were simulated within a pseudo-three-dimensional computational domain. The dimensions of the computational domain were 5 μm × 5 μm with thickness in the spanwise direction equivalent to one particle diameter. The

numbers of nanoparticles simulated were 485, 975, 1460 and 1950 which correspond to solid volume fractions of 0.05, 0.10, 0.15 and 0.20 respectively. Here, solid volume fraction is defined to be the ratio of the total volume of all nanoparticles present to the volume of the pseudo-three-dimensional domain. To ensure numerical stability and accuracy, a relatively small time step of 10 ps was applied for all simulations carried out in this study. Table 1 summarizes the values of pertinent material properties and system parameters applied in the simulations. At the start of each simulation, the positions of all nanoparticles were assigned randomly within the computational domain such that no overlap between any two nanoparticles occurred. Periodic boundary conditions were applied on all four sides of the computational domain so as to eliminate any possible effects that may arise due to the presence of boundaries. The application of such boundary conditions also allowed the possibility of simulating a large system using a significantly smaller computational domain which leads to more efficient utilization of computing resources.

Shape of particles	Spherical
Number of particles, N	485, 975, 1460, 1950
Solid volume fraction	0.05, 0.10, 0.15, 0.20
Particle diameter, d	70 nm
Particle density, ρ_p	1000 kg m^{-3}
Spring constant in force model, κ	1.0×10^{-3} N m^{-1}
Viscous contact damping coefficient, η	1.0×10^{-12}
Coefficient of restitution	0.99
Coefficient of friction	0.5
Saturation magnetization, M_d	1.0×10^{5} A m^{-1}
Hamaker constant, H_a	1.0×10^{-19} J
Surface charge, q	1.6×10^{-15} C
Ion concentration, n_b	1.0 M
Temperature, T	298 K
Domain size	5 μm × 5 μm × 70 nm
Simulation time step, Δt	10 ps

Table 1. Material properties and system parameters for DEM simulations

4. Results and discussion

Fig. 1 shows the aggregation patterns of magnetic nanoparticles formed in the absence of an external magnetic field obtained from computer simulations with the modified DEM methodology. It may be seen that small isolated aggregates of nanoparticles are observed at low solid volume fractions while at high solid volume fractions, an extended network of nanoparticles usually referred to as a percolated network is observed to form spontaneously. The former is typically associated with gelation experiments carried out at insufficient concentrations of nanoparticles resulting in simple destabilisation of the suspension and formation of a collapsed structure.

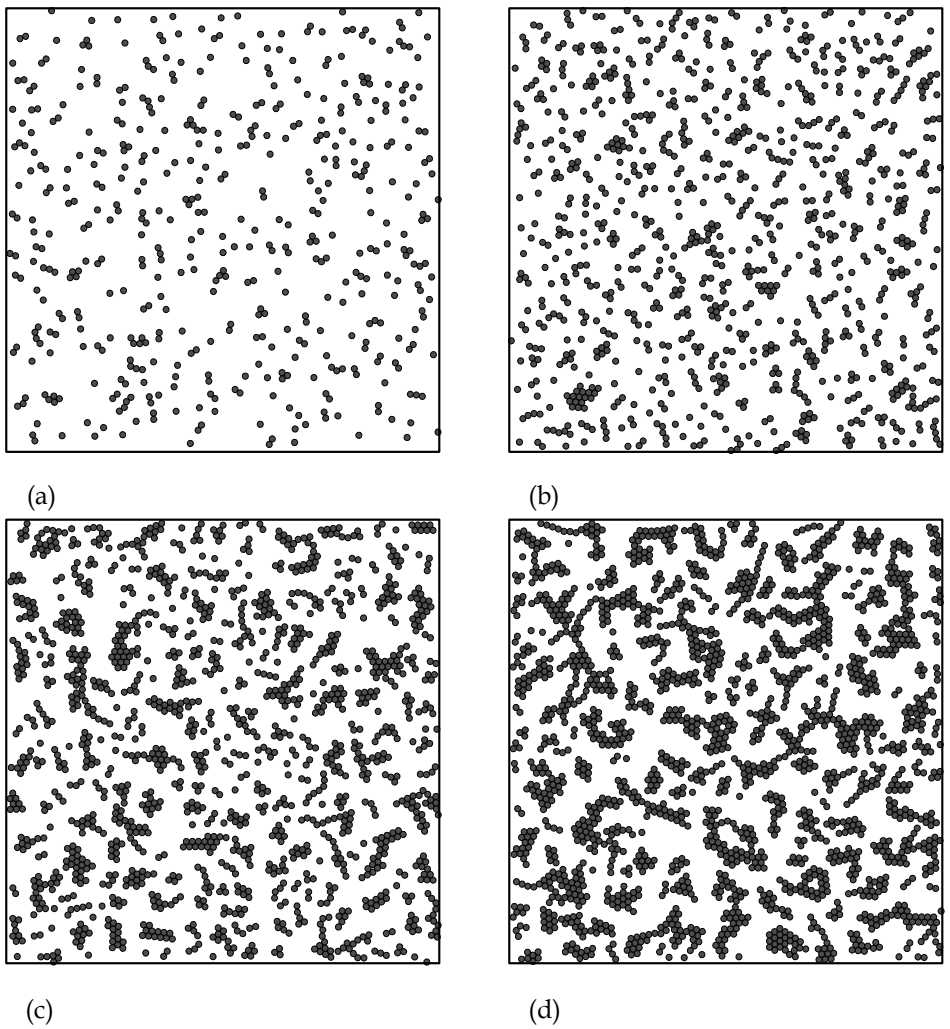

Fig. 1. Aggregation patterns of magnetic nanoparticles in the absence of an external magnetic field at 10^{-3} s physical time obtained from the modified DEM simulations. The solid volume fractions applied were (a) 0.05, (b) 0.10, (c) 0.15 and (d) 0.20.

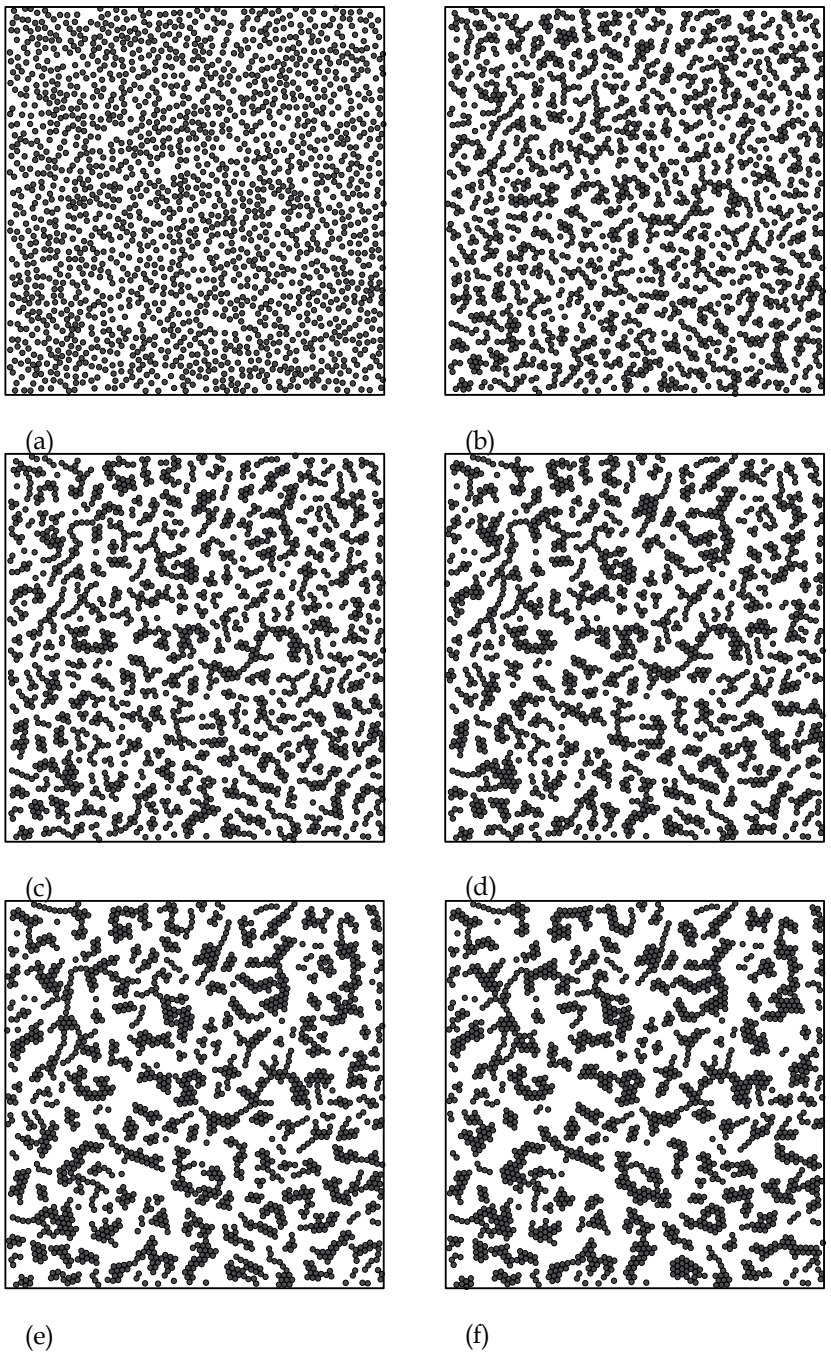

Fig. 2. Aggregation process of magnetic nanoparticles of solid volume fraction 0.20 in the absence of an external magnetic field. The states of aggregation correspond to (a) 0.0 s, (b) 2.0×10^{-4} s, (c) 4.0×10^{-4} s, (d) 6.0×10^{-4} s, (e) 8.0×10^{-4} s and (f) 10^{-3} s.

To observe gelation of nanoparticle suspensions, the present simulations have shown that solid concentrations must be sufficiently high and beyond the percolation threshold in order for a stable network structure to form. Although the simulations presented here are computationally expensive and so have been carried out at smaller length and time scales than those associated with experiments, it may be seen that the main qualitative features of the type of gel networks formed in the absence of an external magnetic field have been reproduced computationally. In particular, Fig. 2 shows that the gelation process takes place with the initial formation of small random aggregates throughout the domain which then join to form a fairly open network with no specific orientation of the various branches.

The intermediate states of the gel during its formation process that are unobservable experimentally with present day technology are readily available from DEM simulations. With the advent of computing power, this computational technique is expected to become more important in this research field as such information will be necessary for more fundamental and mechanistic understanding of nanoparticle gelation processes. Fig. 3 shows that in the presence of an external magnetic field, the aggregates of nanoparticles are aligned along the direction of the magnetic field due to the anisotropic nature of the magnetic forces exerted on each nanoparticle and aggregate. At low solid volume fractions, individual elongated strands of aggregates are formed while at high solid volume fractions, such aggregates are capable of joining together due to smaller distances between aggregates. In comparison with the previous case where an external magnetic field was absent, the branches of the network that is beginning to form here are composed of more particles and are thus longer. This can be understood from inspection of the intermediate states of aggregation obtained from the simulations.

Fig. 4 shows that the aggregation process in the presence of an external magnetic field starts, as in the previous case, with the formation of random aggregates throughout the domain. However, due to the anisotropic magnetic forces, aggregates formed are rotated to align along the direction of the magnetic field. Elongation of aggregates occurs as the growth of these aggregates also occurs along the direction of the magnetic field imposed. The final network structure consisting of long, parallel chains of nanoparticles is also in good agreement with structures of gels obtained experimentally with an applied magnetic field.

Fig. 5 shows quantitatively the time evolution of the average sizes of clusters formed by the magnetic nanoparticles both in the absence and presence of an external magnetic field. Here, average cluster size is defined as the average number of nanoparticles forming a cluster or aggregate. It may be observed that average cluster sizes increase with increasing total number of nanoparticles present within the domain or, equivalently, the overall solid volume fraction. Interestingly, the average size of clusters formed at each solid volume fraction evolves in a similar fashion with respect to time regardless of the presence or absence of an external magnetic field. This is despite the fact that the morphologies of the clusters or aggregates formed are significantly different as seen earlier. At the end of 1 ms, the average cluster sizes for N = 485 and N = 975 both in the absence and presence of an external magnetic field have reached more or less steady values. In contrast, the clusters formed for N = 1460 and N = 1950 are still growing in size, indicating that the percolation process is not completed yet at the end of 1 ms.

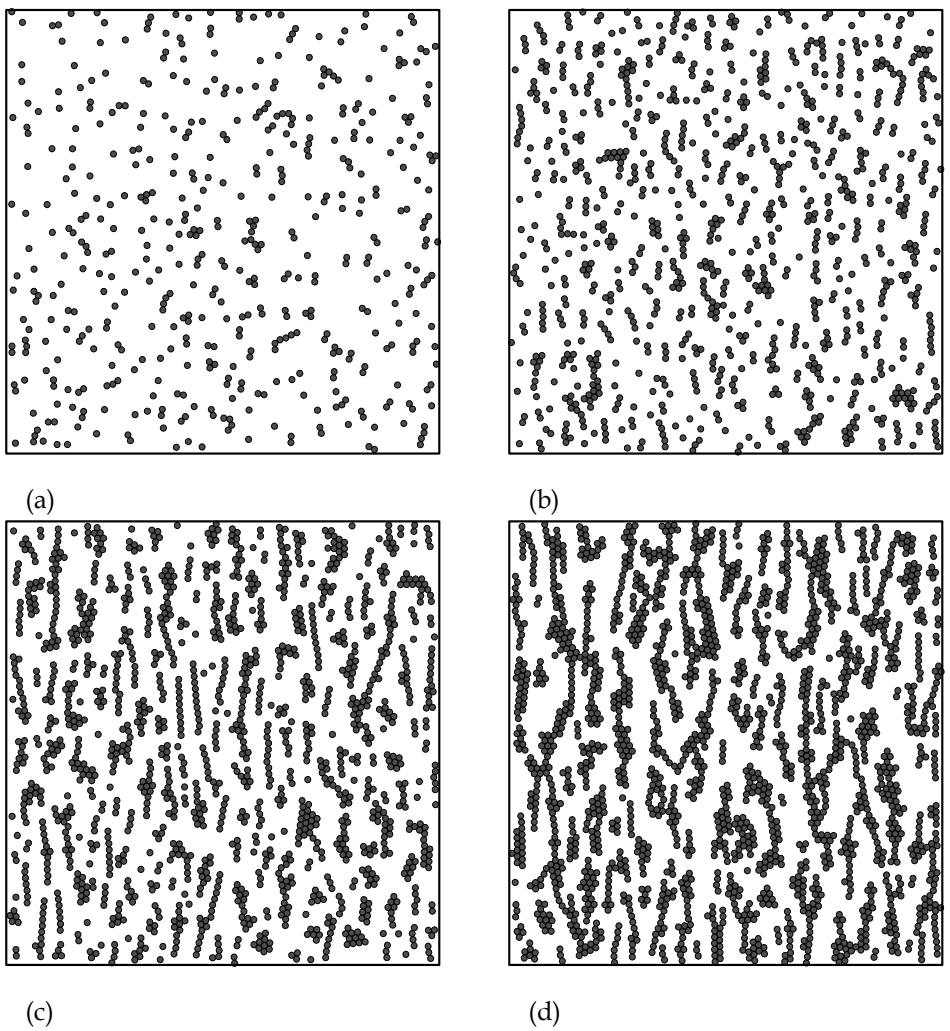

Fig. 3. Aggregation patterns of magnetic nanoparticles in the presence of an external magnetic field at 10^{-3} s physical time obtained from the modified DEM simulations. The orientation of the simulated magnetic field was in the vertical direction. The solid volume fractions applied were (a) 0.05, (b) 0.10, (c) 0.15 and (d) 0.20.

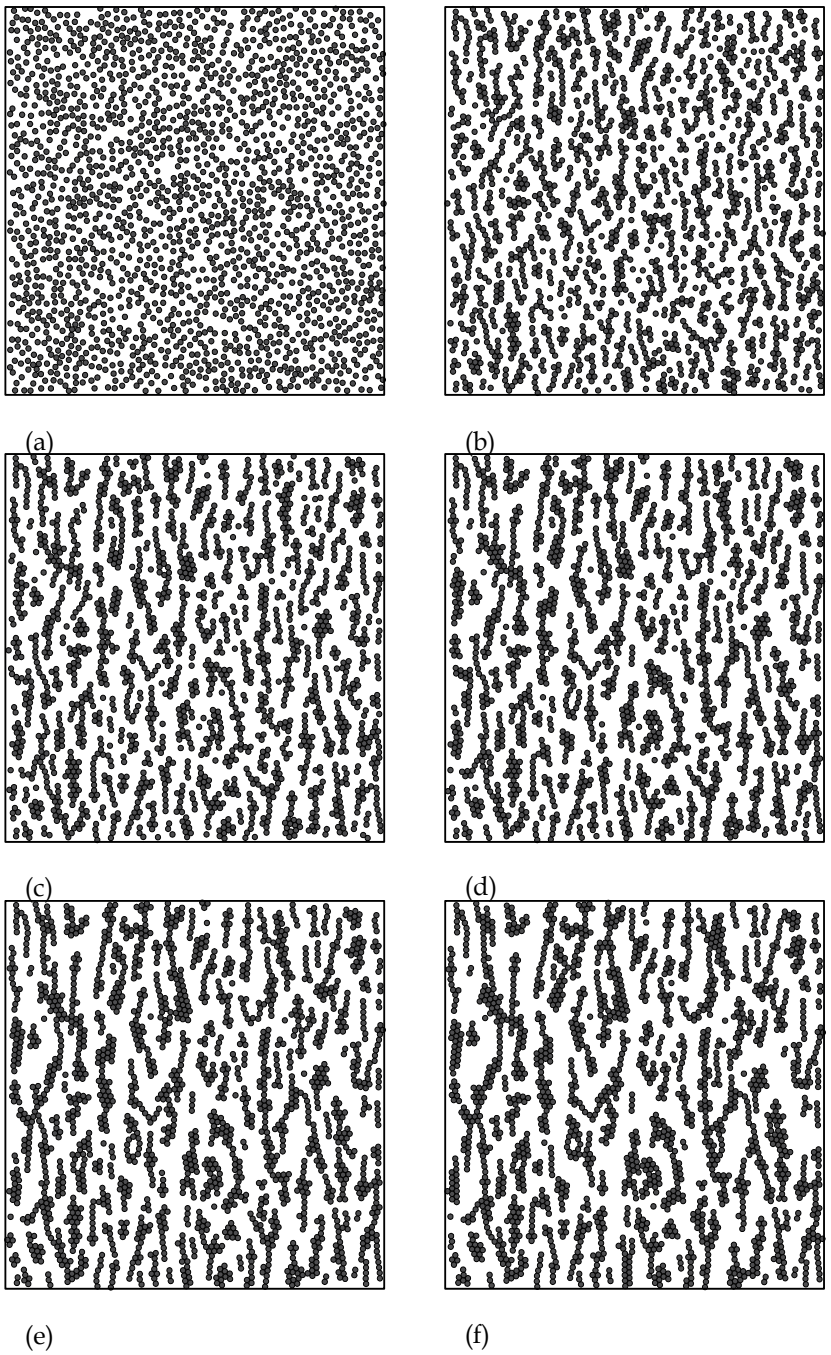

Fig. 4. Aggregation process of magnetic nanoparticles of solid volume fraction 0.20 in the presence of an external magnetic field. The states of aggregation correspond to (a) 0.0 s, (b) 2.0×10^{-4} s, (c) 4.0×10^{-4} s, (d) 6.0×10^{-4} s, (e) 8.0×10^{-4} s and (f) 10^{-3} s.

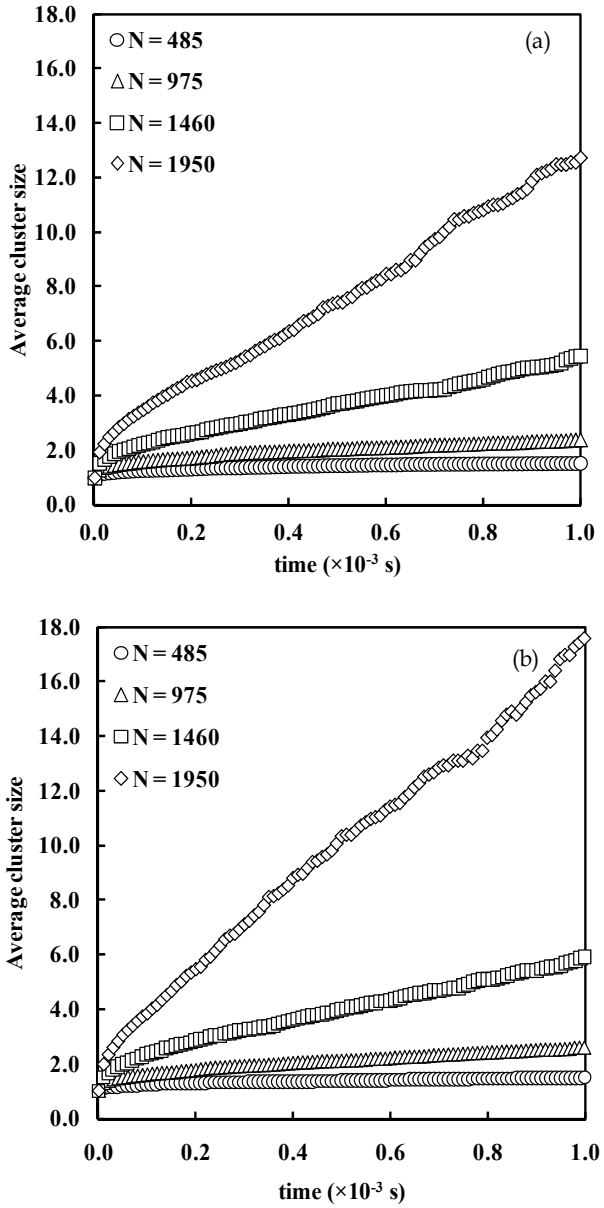

Fig. 5. Time evolution of average size of clusters formed by magnetic nanoparticles (a) in the absence of an external magnetic field and (b) in the presence of an external magnetic field.

5. Conclusions

The process of gelation with and without the application of an external magnetic field giving rise to the different internal pore structures could be understood mechanistically by results of

the simulations performed using a modified Discrete Element Method. Gelation occurred by the formation of random aggregates of nanoparticles within the domain which then joined with one another to form a network. However, in the presence of anisotropic magnetic forces, these aggregates were rotated to align along the direction of the magnetic field. Elongation of aggregates occurred and the final network formed consisted largely of such elongated branches of magnetic nanoparticles arranged more or less parallel to one another.

6. Acknowledgment

This study has been supported by the National University of Singapore under Grant Number R-279-000-275-112.

7. References

Brunet, E.; Degre, G.; Okkels, F.; Tabeling, P. (2005). Aggregation of Paramagnetic Particles in the Presence of a Hydrodynamic Shear. *J. Colloid Interface Sci.*, Vol. 282, pp. 58–68

Climent, E.; Maxey, M. R.; Karniadakis, G. E. (2004). Dynamics of Self-Assembled Chaining in Magnetorheological Fluids. *Langmuir*, Vol. 20, pp. 507–513

Davis, S. W.; McCausland, W.; McGahagan, H. C.; Tanaka, C. T.; Widom, M. (1999). Cluster-based Monte Carlo Simulation of Ferrofluids. *Phys. Rev. E*, Vol. 59, pp. 2424–2428

Dominguez-Garcia, P.; Melle, S.; Pastor, J. M.; Rubio, M. A. (2007). Scaling in the Aggregation Dynamics of a Magnetorheological Fluid. *Phys. Rev. E*, Vol. 76, pp. 051403

Duncan, P. D.; Camp, P. J. (2006). Aggregation Kinetics and the Nature of Phase Separation in Two-Dimensional Dipolar Fluids. *Phys. Rev. Lett.*, Vol. 97, pp. 107202

Furlani, E. P. (2006). Analysis of Particle Transport in a Magnetophoretic Microsystem. *J. Appl. Phys.*, Vol. 99, pp. 024912

Furlani, E. P.; Ng, K. C. (2008). Nanoscale Magnetic Biotransport with Application to Magnetofection. *Phys. Rev. E*, Vol. 77, pp. 061914

Huang, J. P.; Wang, Z. W.; Holm, C. (2005). Computer Simulations of the Structure of Colloidal Ferrofluids. *Phys. Rev. E*, Vol. 71, pp. 061203

Kantorovich, S.; Cerda, J. J.; Holm, C. (2008). Microstructure Analysis of Monodisperse Ferrofluid Monolayers: Theory and Simulation. *Phys. Chem. Chem. Phys.*, Vol. 10, pp. 1883–1895

Lattuada, M.; Alan Hatton, T. (2007). Preparation and Controlled Self-Assembly of Janus Magnetic Nanoparticles. *J. Am. Chem. Soc.*, Vol. 129, pp. 12878–12889

Lattuada, M.; Wu, H.; Sandkuhler, P.; Sefcik, J.; Morbidelli, M. (2004a). Modelling of Aggregation Kinetics of Colloidal Systems and its Validation by Light Scattering Measurements. *Chem. Eng. Sci.*, Vol. 59, pp. 1783–1798

Lattuada, M.; Wu, H.; Morbidelli, M. (2004b). Experimental Investigation of Colloidal Gel Structures. *Langmuir*, Vol. 20, pp. 4355–4362

Lim, E. W. C.; Wang, C. H., Yu, A. B. (2006a). Discrete Element Simulation for Pneumatic Conveying of Granular Material. *AIChE J.*, Vol. 52, pp. 496–509

Lim, E. W. C.; Zhang, Y.; Wang, C. H. (2006b). Effects of an Electrostatic Field in Pneumatic Conveying of Granular Materials through Inclined and Vertical Pipes. *Chem. Eng. Sci.*, Vol. 61, pp. 7889–7908

Lim, E. W. C.; Wang, C. H. (2006). Diffusion Modeling of Bulk Granular Attrition. *Ind. Eng. Chem. Res.*, Vol. 45, pp. 2077–2083

Lim, E. W. C.; Wong, Y. S.; Wang, C. H. (2007). Particle Image Velocimetry Experiment and Discrete-Element Simulation of Voidage Wave Instability in a Vibrated Liquid-Fluidized Bed. *Ind. Eng. Chem. Res.*, Vol. 46, pp. 1375–1389

Lim, E. W. C. (2007). Voidage Waves in Hydraulic Conveying through Narrow Pipes. *Chem. Eng. Sci.*, Vol. 62, pp. 4529–4543

Lim, E. W. C. (2008). Master Curve for the Discrete-Element Method. *Ind. Eng. Chem. Res.*, Vol. 47, pp. 481–485

Lim, E. W. C. (2009). Vibrated Granular Bed on a Bumpy Surface. *Phys. Rev. E*, Vol. 79, pp. 041302

Lim, E. W. C. (2010a). Density Segregation in Vibrated Granular Beds with Bumpy Surfaces. *AIChE J.*, Vol. 56, pp. 2588–2597

Lim, E. W. C. (2010b). Granular Leidenfrost Effect in Vibrated Beds with Bumpy Surfaces. *Eur. Phys. J. E*, Vol. 32, pp. 365–375

Lim, E. W. C.; Yao, J.; Zhao, Y. (2011). Pneumatic Transport of Granular Materials with Electrostatic Effects. *AIChE J.*, Article in Press, DOI 10.1002/aic.12638

Martinez-Pedrero, F.; El-Harrak, A.; Fernandez-Toledano, J. C.; Tirado-Miranda, M.; Baudry, J.; Schmitt, A.; Bibette, J.; Callejas-Fernandez, J. (2008). Kinetic Study of Coupled Field-Induced Aggregation and Sedimenation Processes Arising in Magnetic Fluids. *Phys. Rev. E*, Vol. 78, pp. 011403

Meriguet, G.; Jardat, M.; Turq, P. (2004). Structural Properties of Charge-Stabilized Ferrofluids under a Magnetic Field: A Brownian Dynamics Study. *J. Chem. Phys.*, Vol. 121, pp. 6078–6085

Meriguet, G.; Jardat, M.; Turq, P. (2005). Brownian Dynamics Investigation of Magnetization and Birefringence Relaxations in Ferrofluids. *J. Chem. Phys.*, Vol. 123, pp. 144915

Miyazima, S.; Meakin, P.; Family, F. (1987). Aggregation of Oriented Anisotropic Particles. *Phys. Rev. A*, Vol. 36, pp. 1421–1427

Nandy, K.; Chaudhuri, S.; Ganguly, R.; Puri, I. K. (2008). Analytical Model for the Magnetophoretic Capture of Magnetic Microspheres in Microfluidic Devices. *J. Magn. Magn. Mater.*, Vol. 320, pp. 1398–1405

Pamme, N. (2006). Magnetism and Microfluidics. *Lab Chip*, Vol. 6, pp. 24–38

Promislow, J. H. E.; Gast, A. P.; Fermigier, M. (1995). Aggregation Kinetics of Paramagnetic Colloidal Particles. *J. Chem. Phys.*, Vol. 102, pp. 5492–5498

Richardi, J.; Pileni, M. P.; Weis, J.-J. (2008). Self-organization of Magnetic Nanoparticles: A Monte Carlo Study. *Phys. Rev. E*, Vol. 77, pp. 061510

Rosensweig, R. E. (1985). *Ferrohydrodynamics*, Cambridge University Press

Russel, W. B.; Saville, D. A.; Schowalter, W. R. (1989). *Colloidal Dispersions*, Cambridge University Press

Schaller, V.; Kraling, U.; Rusu, C.; Petersson, K.; Wipenmyr, J.; Krozer, A.; Wahnstrom, G.; Sanz-Velasco, A.; Enoksson, P.; Johansson, C. (2008). Motion of Nanometer Sized Magnetic Particles in a Magnetic Field Gradient. *J. Appl. Phys.*, Vol. 104, pp. 093918

Sinha, A.; Ganguly, R.; De, A. K.; Puri, I. K. (2007). Single Magnetic Particle Dynamics in a Microchannel. *Phys. Fluids*, Vol. 19, pp. 117102

Tsouris, C.; Scott, T. C. (1995). Flocculation of Paramagnetic Particles in a Magnetic Field. *J. Colloid Interface Sci.*, Vol. 171, pp. 319–330

Xuan, Y.; Ye, M.; Li, Q. (2005). Mesoscale Simulation of Ferrofluid Structure. *Int. J. Heat Mass Trans.*, Vol. 48, pp. 2443–2451

Yamada, Y.; Enomoto, Y. (2008). Effects of Oscillatory Shear Flow on Chain-like Cluster Dynamics in Ferrofluids without Magnetic Fields. *Physica A*, Vol. 387, pp. 1–11

Zhu, H. P.; Zhou, Z. Y.; Yang, R. Y.; Yu, A. B. (2008). Discrete Particle Simulation of Particulate Systems: A Review of Major Applications and Findings. *Chem. Eng. Sci.*, Vol. 63, pp. 5728–5770

12

Inelastic Collisions and Hypervelocity Impacts at Nanoscopic Level: A Molecular Dynamics Study

G. Gutiérrez, S. Davis, C. Loyola, J. Peralta, F. González,
Y. Navarrete and F. González-Wasaff
Group of NanoMaterials, Departamento de Física, Facultad de Ciencias,*
Universidad de Chile
Chile

1. Introduction

In this chapter we present an atomic level study of nano-particle impact using molecular dynamics simulation. Two cases have been considered. First, we simulate the bouncing of a ball over a surface due to a constant force (which mimic the gravity force), modeling the inter-atomic interaction by a modified Lennard-Jones potential, where the ball-surface atom interaction is represented by a purely repulsive term. The analysis of the results makes it possible, among other aspects, to determine the restitution coefficient in each bounce as well as to understand the processes of energy loss in inelastic collisions, which are actually not a loss, but a transfer to thermal and vibrational energy. The second simulation describes the impact mechanisms of a solid projectile hitting a target at high velocity. Both the projectile and the target are made of copper, which is modeled by a realistic many-body tight-binding potential. The projectile velocity is kept constant during all the simulation, representing an extreme condition, where the momentum and hardness of the projectile is much higher than the momentum and hardness of the target. In this regime, we identify two different behavior in dependence of the projectile velocity: at low velocities (less than 4 km/s) the target basically recover its structure after the passage of the projectile, but at higher velocities, the projectile left a permanent hole in the target.

Both problems, inelastic collisions and hypervelocity impacts, are non-equilibrium related phenomena which are important from a basic and applied point of view, in several areas of science: physics, materials science, aeronautics, mechanics, among others. From a theoretical point of view, they have been extensively treated in the macroscopic level, by using continuum hydrodynamic simulation, and only recently researchers are using molecular dynamic simulation, intended to an understanding of these phenomena at the scale of inter-atomic interactions. Besides the calculation of equilibrium properties and their associated fluctuations, molecular dynamics allows for a wider range of problems to be tackled: given that we have access to the atomic trajectories we can study the transit to equilibrium, as well as purely non-equilibrium phenomena (where we are interested not in the final state but in the process itself), for instance, shock-induced plasticity and fracture of materials. In this regard, Non-Equilibrium Molecular Dynamics (NEMD) has emerged recently as a branch dealing with, and promising to shed light on, the mechanism behind these (and other similar) irreversible processes.

*www.gnm.cl

2. Molecular dynamics in non-equilibrium conditions

The framework to tackle the problems out of equilibrium is Non-equilibrium Statistical Mechanics. Its concerns the extension of the usual formalism of Statistical Mechanics (microcanonical, canonical and other extended ensembles, partition functions) to systems either approaching thermodynamic equilibrium after a perturbation, or definitely far away from it. So far there is no unified theory we can appropriately call non-equilibrium statistical mechanics [1], only a number of results applicable to processes in the linear response regime (thermodynamic fluxes proportional to the thermodynamic forces), such as the celebrated Onsager regression hypothesis (Callen, 1985) that relates the decay of macroscopic variables in a non-equilibrium setting to the regression of fluctuations in equilibrium. Prigogine's minimum entropy production (Prigogine, 1968) principle, also restricted to the linear response regime, is a possible explanation for the emergence of order in dissipative systems. The fluctuation-dissipation theorem and the Green-Kubo formulas (Zwanzig, 2001) determine transport coefficients from equilibrium measurements. There are also a few results valid arbitrarily far away from equilibrium, such as the family of fluctuation theorems (Evans & Searles, 2002) quantifying the likelihood of instantaneous violations of the Second Law of thermodynamics.

Non-equilibrium Molecular Dynamics (NEMD) is then the natural extension of molecular dynamics techniques to study non-equilibrium problems, and attempts to fill the void left by a missing theoretical framework.

Stationary (or *steady-state*) processes like deformation under shear stress, or a sample submitted under a temperature gradient, among others, require the implementation of NEMD under temperature control. In this case the use of thermostat algorithms is necessary to maintain the steady-state regime, extracting the excess heat generated by the process. However this has the drawback of modifying the equations of motion, introducing friction and noise forces which perturb the original dynamics (energy is not conserved), and affecting the performance of the usual numerical integration methods.

A comprehensive review of thermostat methods and their implementation in the context of NEMD is given by Hoover (Hoover & Hoover, 2007). Briefly, the standard implementation of the thermostat is the Nosé-Hoover equation of motion,

$$\frac{d\vec{p}_i}{dt} = \vec{F}_i - \zeta \vec{p}_i, \tag{1}$$

where ζ is a friction coefficient governed by

$$\frac{d\zeta}{dt} = \frac{1}{N\tau^2} \sum_{i=1}^{N} \left(p_i^2 / m k_B T_0 - 1 \right), \tag{2}$$

T_0 the imposed temperature and τ is a relaxation time, controlling the degree of coupling of the "thermal bath" with the system.

It is possible, however, to perform NEMD in a completely microcanonical way (i.e. without modifying Newton's equations) for systems outside the steady-state regime (for instance in

[1] The maximum caliber formalism (Jaynes, 1980; Stock et al., 2008), based on information-theoretic ideas, together with the maximum entropy production principle derived from it seem to show promising early results as such a unifying basis (Dewar, 2005; 2003; Kleidon et al., 2005).

the case of shockwave propagation (Holian, 1995), collisions, fast fracture, detonations) where it is not necessary to remove the excess heat. Here energy is conserved, being converted from kinetic or elastic into thermal, vibrational and other forms, the heat eventually produced in the process remains inside the system, causing an increase in temperature and eventually being able to induce local melting. This kind of NEMD simulations are justified because we are implicitly solving the Liouville equation,

$$\frac{\partial P(\mathbf{p},\mathbf{q})}{\partial t} = -\{P,\mathcal{H}\}, \tag{3}$$

which describes the evolution of the phase space distribution function $P(\mathbf{p},\mathbf{q})$ of a system of particles obeying Newton's equations, and this is valid arbitrarily away from equilibrium.

It is important to consider that, away from the linear response regime, there is no unique definition of thermodynamic intensive variables such as temperature, pressure or chemical potential if those variables are not fixed (Casas-Vásquez & Jou, 2003). However, the usual practice is to take the instantaneous kinetic energy of the system (or even of a region of the system) to evaluate an instantaneous "kinetic" temperature,

$$T_K(t) = \frac{m}{3k_B}\sum_{i=1}^{N} v_i^2. \tag{4}$$

When using the instantaneous kinetic energy to evaluate a local instantaneous temperature, it might be required to remove the translational part of the velocities for the atoms in the region, if they happen to have non-zero linear momentum. For instance, a projectile approaching a target cannot be assigned a higher temperature by virtue of its translational speed.

It is also possible to evaluate an instantaneous "configurational" temperature (Baranyai, 2000),

$$T_C(t) = \frac{1}{k_B}\frac{|\nabla\Phi(t)|^2}{\nabla^2\Phi(t)}, \tag{5}$$

where Φ is the potential energy function, which depends on t only through the atomic positions. Away from equilibrium both definitions (kinetic and configurational) do not necessarily coincide, because an object immersed in the non-equilibrium system and used as a thermometer could equilibrate in different time scales to the configurational and kinetic degrees of freedom and therefore measure different temperatures. In fact "operational" definitions of non-temperature exist that measure the kinetic energy of a tracer (probably heavier) particle placed inside the system, and assumed to be in thermal equilibrium with it.

In the following, we briefly describe the molecular dynamic method and its implementation our in-house code *Las Palmeras Molecular Dynamics*. Next, the inelastic collisions and hypervelocity impacts simulations are presented, as examples of the potential of an atomic-level description. Finally, general conclusions are drawn.

3. Las Palmeras Molecular Dynamics

Although there are many general purpose MD codes, they are usually subjected to design limitations arising mostly due to efficiency considerations. A given code is usually optimized to perform extremely well for one kind of system (for instance bulk systems) but because of

said optimization it performs poorly on a different kind of system. This, in practice, only allows the study of certain systems and conditions.

Most codes cannot handle in an easy way the requirements of some setups, such as non-periodic boundary conditions, non-negligible variations of density inside a sample, or initial states prepared far from equilibrium. It might be possible to modify these codes to lift some of the limitations, but it could be cumbersome and error-prone. For these cases, a more flexible MD code is needed, even though some performance could be sacrificed.

We could say that the early way of doing MD was to implement a tailor-made computer program with precisely the chosen algorithms for numerical integration of the equations of motion and computation of the interatomic potentials and forces. Thus, one different computer code for each system to be simulated.

The next stage in MD computer codes is the ability to choose the interatomic potential at runtime (i.e., every time the program is executed, without the need to recompile for every change) along with all the other options such as the time step used for integration, total simulation time, initial conditions of pressure and temperature and so on. This has led to general purpose MD codes such as Moldy (Refson, 2000) and DL_POLY (Smith & Forester, 1996) among many others. While the ability to choose the potential function is commonplace nowadays, very few computer codes offer the choice of changing the integration algorithm at runtime, although several have the choice at compile-time (i.e., during the compilation stage).

From a general point of view, the MD procedure consist of four main stages, namely: (a) the initialization of the sample, (b) the calculation of interatomic forces, (c) the integration of the equations of motion, and (d), collecting statistics and the computation of properties. It work quite well in several different cases, like equilibrium conditions or even for metastable system, like glasses (see, for example (Gutiérrez et al., 2010)). But also MD procedure can be applied to more extreme conditions.

When the MD simulation that we intend to perform is not standard, for example in the case of simulations far away from thermodynamic equilibrium (shockwaves (Loyola et al., 2010), high velocity impacts,) or non-standard potential functions and forces (for example friction forces or external fields) one can clearly see the need for an hybrid approach between the tailor-made MD code (containing exactly the algorithms we need for a given simulation) and the general purpose MD code (with several choices available at run-time and compile-time). We would want to replace pieces of the program at will, including (but not limited to) integration methods, potential functions and other algorithms, such as the one responsible for computing interatomic distances or the thermostat algorithms used to control the applied temperature or pressure in an isothermal-isobaric (NPT) MD simulation. Here the general purpose approach is not general enough, only allowing some limited choices.

Our motivation for writing yet another MD code, *Las Palmeras Molecular Dynamics* (LPMD) (Davis et al., 2010) is to fill this practical void. LPMD is designed as a completely modular MD code, consisting of a set of interchangeable pieces or *plug-ins* which can be linked together in different ways to accommodate the needs of a non-standard MD simulation. Beyond that, the user can also perform post-simulation analysis, convert between input/output formats, prepare samples with ease and visualize simulations in real time. LPMD's modular design also improves efficiency in some cases. It also allows the user to add new pieces (integration methods, interatomic potentials, properties, file formats, and many others) without the need for learning the complete code architecture. LPMD is open source software written in standard C++ language, and released under the General Public License

(GPL) version 3. Figure 1 displays an example of the control file. For more information, visit `www.lpmd.cl`.

```
#This is a comment. Comments are used usually as a title:
########################################
# System file of Au crystal using LPMD  #
########################################
cell cubic 28.56
input module=lpmd file=300K-Gold.lpmd level=1
output module=lpmd file=au.lpmd each=15 level=1
periodic false true true
steps 5000

#Integrator
use velocityverlet as vv
    dt 1.0
enduse

#CellManager

use linkedcell
     mode auto
     cutoff 7.5
enduse

# Sutton-Chen Potential (parameters for gold)
use suttonchen as sc
    e 0.013
    n 10
    a 4.08
    m 8
    c 34.408
    cutoff 7.5
enduse

#- Applying Plugins -#
integrator vv
cellmanager linkedcell
potential sc Au Au
```

Fig. 1. Example of an LPMD control file. The components are loaded (`use...enduse`) and then applied.

3.1 Structural properties with LPMD

We will denote by structural property, any quantity A_S which depends on the instant t only through the atomic coordinates,

$$A_S(t) = A_S(\vec{r}_1(t), \ldots, \vec{r}_N(t)), \tag{6}$$

with N the number of particles.

LPMD allows the calculation of several structural properties (either as instantaneous values or as averages), including the radial distribution function $g(r)$ (using the `gdr` plug-in) and common neighbor analysis (through the `cna` plug-in), both of which can be used to measure a degree of deviation from an ideal crystal structure.

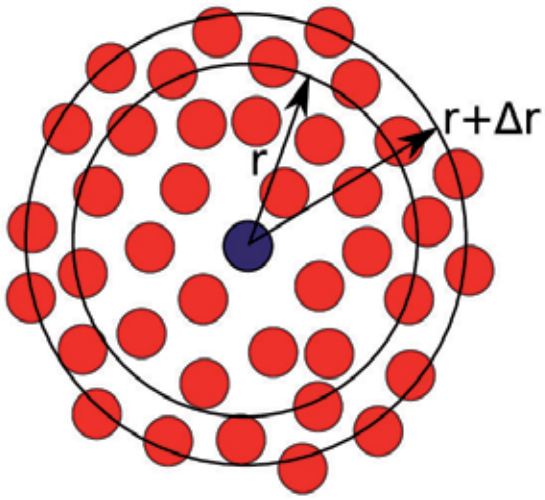

Fig. 2. Schematic representation of the computation of the radial distribution function $g(r)$.

The radial distribution function $g(r)$ represents the probability density for finding a neighboring atom at a distance r, normalized to the same probability density in a perfectly uniform distribution of atoms. This ensures that $g(r)$ goes to unity for large enough r, independently of the system. It is formally defined as

$$g(r) = \frac{V}{N^2} \left\langle \sum_i \sum_{j \neq i} \delta(\vec{r} - \vec{r_{ij}}) \right\rangle . \tag{7}$$

where N is the total number of atoms in the system and V is the total volume. However, in practice, it is computed from an histogram of the neighbor distribution,

$$g(r) = \frac{V}{N} \frac{n(r)}{\frac{4}{3}\pi((r+\Delta r)^3 - r^3)} \approx \frac{V}{N} \frac{n(r)}{4\pi r^2 \Delta r} \tag{8}$$

where $n(r)$ is the number of atoms in the spherical shell between r and $r + \Delta r$ (see figure 2).

The Common Neighbor Analysis (CNA) (Honeycutt & Andersen, 1987) is a technique used in atomistic simulations to determine the local ordering in a given structure. CNA gives more detailed information than the radial distribution function $g(r)$, as it considers not only the number of neighbors at a given distance but also their location with respect to other common neighboring atoms. In the CNA method (see figure 3), every pair of atoms is labeled according to four indices (i, j, k, l): the first index, i, is 1 for nearest neighbor pairs, 2 for next-nearest neighbors, and so on. The second index, j, corresponds to the number of *common neighbors* shared by the atoms in the pair. The third index, k, corresponds to the number of *bonds* that can be "drawn" between the j common neighbors (taking the bond length as the nearest neighbor distance). Finally, the fourth index, l, corresponds to the length of the longest chain that connects all the k bonds. The different structures have the following distribution of pairs: FCC has only **1-4-2-1** pairs, in hcp the pairs are distributed equally between **1-4-2-1** and **1-4-2-2**, and in bcc there are **1-4-4-4** and **1-6-6-6** present in ratios $3/7$ and $4/7$, respectively.

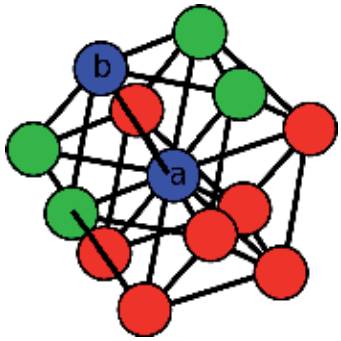

Fig. 3. Four common neighbors (green atoms) of the pair *a-b* (in blue) in a face-centered cubic structure. The pair depicted as *a-b* has indices 1-4-2-1 in CNA notation, and is the only kind of pair appearing in the FCC structure.

4. Bouncing of a ball over a surface: atomic level study

A typical problem in classical mechanics is the bouncing of a bead in free fall over a surface, due to the action of the force of gravity (Alonso & Finn, 1992; Eisberg & Lerner, 1981). After each bouncing, the body reaches different heights, each one of them less or equal than the previous one. The most common explanation for this phenomenon is the viscoelastic dissipation, which results in an energy loss due to the inelastic collision (Aguirregabiria et al., 2008; Falcon et al., 1998).

Although there have been many works dealing with the dynamics of inelastic collisions (Goldsmith, 2001; Johnson, 1987; Zukas et al., 1982) and many measurements of the energy loss in such collisions (Bridges et al., 1984; Goldsmith, 2001; Hatzes et al., 1988; Lifshitz & Kolsky, 1964; Lun & Savage, 1986; Raman., 1918; Reed, 1985; Supulver et al., 1995; Tabor, 1948; Tillett, 1954; Tsai & Kolsky, 1967; Zener, 1941), there is a considerable scatter in existing data, and the mechanisms of dissipation and the behavior of the restitution coefficient with the impact velocity are still open problems (Falcon et al., 1998). At high impact velocities, i.e., when fully plastic deformations occur, this behavior is well known both experimentally (Goldsmith, 2001; Raman., 1918; Reed, 1985; Tabor, 1948; Tillett, 1954; Zener, 1941) and theoretically (Goldsmith, 2001; Johnson, 1987; Tabor, 1948), but the mechanisms of energy loss during a collision are hard to track at a macroscopic level.

Molecular dynamics allows us to keep track of the position and velocity of every particle in the system at any instant of time. Using statistical mechanics, the calculation of energy, temperature and other thermodynamic properties is straightforward. Moreover, if the target (surface) is considered as being a part of the system, the total energy remains constant, and the "energy loss" that the bead experiments is just a transfer of translational kinetic energy to internal potential and thermal energy, which can be identified with mechanisms of energy loss, such as plastic deformation, vibrational energy and others.

To show how this phenomenon occurs, molecular dynamics simulations were performed using the LPMD program(Davis et al., 2010) (see section 3). A bead is dropped from rest at different heights in a constant force field over a surface. The resulting collisions show two main types of deformation: slight deformation, where the bead remains vibrating after the collision, and substantial deformation, where the bead changes its shape. Then, the evolution of the different energies in time is computed in order to show in detail the energy transfer.

4.1 Simulation details

The system consist of a solid ball that interacts repulsively with a solid surface, both made of argon in the solid state (see figure 4). The interaction between atoms separated by a distance

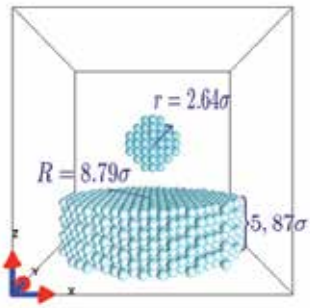

Fig. 4. Argon ball over a solid argon surface, immersed in a constant force field. Image generated by the LPVisual plugin of the LPMD program.

r is modeled using a modified form of the Lennard-Jones potential (Barrat & Bocquet, 1999):

$$V(r) = \begin{cases} 4\varepsilon \left[\left(\frac{\sigma}{r}\right)^{12} - c \left(\frac{\sigma}{r}\right)^{6} \right] & r < r_c = 2.5\sigma \\ 0 & r \geqslant r_c \ , \end{cases} \tag{9}$$

where r_c is a cut-off chosen here to be 2.5σ (σ is the Lennard-Jones diameter and ε is the depth of the potential well). For our system, the parameters $\varepsilon/k_B = 119.8$ K and $\sigma = 3.40$ Å are the same for all atoms and correspond to the values for argon (Kittel, 2005), whose atomic mass is $M = 39.948$ amu. In the rest of this section, all quantities are expressed in LJ reduced units, using σ, ε and M as length, energy and mass scales, respectively [2].

The interaction between atoms in the ball and atoms in the surface is given by the equation (9) with $c = 0$ (i.e., purely repulsive), while the interactions between any pair of atoms in the ball is given by the usual Lennard-Jones potential (eq. (9) with $c = 1$). The last also holds for every pair of atoms inside the surface. The Newton equations of motion are integrated using the Beeman algorithm, with a time step $\Delta t = 4.651 \times 10^{-4} \tau$.

The solid ball and the surface slab were equilibrated at zero temperature for 5×10^3 time steps to allow them to adopt relaxed configurations.

The ball, composed of less than 100 atoms, was immersed in a constant force field in the direction of the negative $z-$axis, whose magnitude was $0.026\, F_0$, and it was dropped from different heights over the surface, composed of about 1500 atoms. This force produces a constant acceleration of the center of mass of the ball of $0.026\, a_0$, which means that it travels $0.49\, \sigma$ after a time τ of being dropped. Each simulation took about 3×10^4 time steps ($\sim$14 τ).

Different types of collisions were observed. The most representatives are shown in figures 5 and 6. Figure 5 shows one of the simulations where the ball is falling over the surface. In

[2] Time: $\tau \equiv \sigma\sqrt{M/\varepsilon} = 2.15$ ps.
Velocity: $v_0 \equiv \sqrt{\varepsilon/M} = 157.91$ m/s.
Acceleration: $a_0 = \varepsilon/M\sigma = 0.73$ Å/ps^2.
Force: $F_0 \equiv \varepsilon/\sigma = 3.04 \times 10^{-3}$ eV/Å.

this case, the ball was dropped from $z = 11.03\,\sigma$. While the ball is hitting the surface, it gets compressed, and then leaves the ground, oscillating harmonically (figures 5(c) and 5(d)).

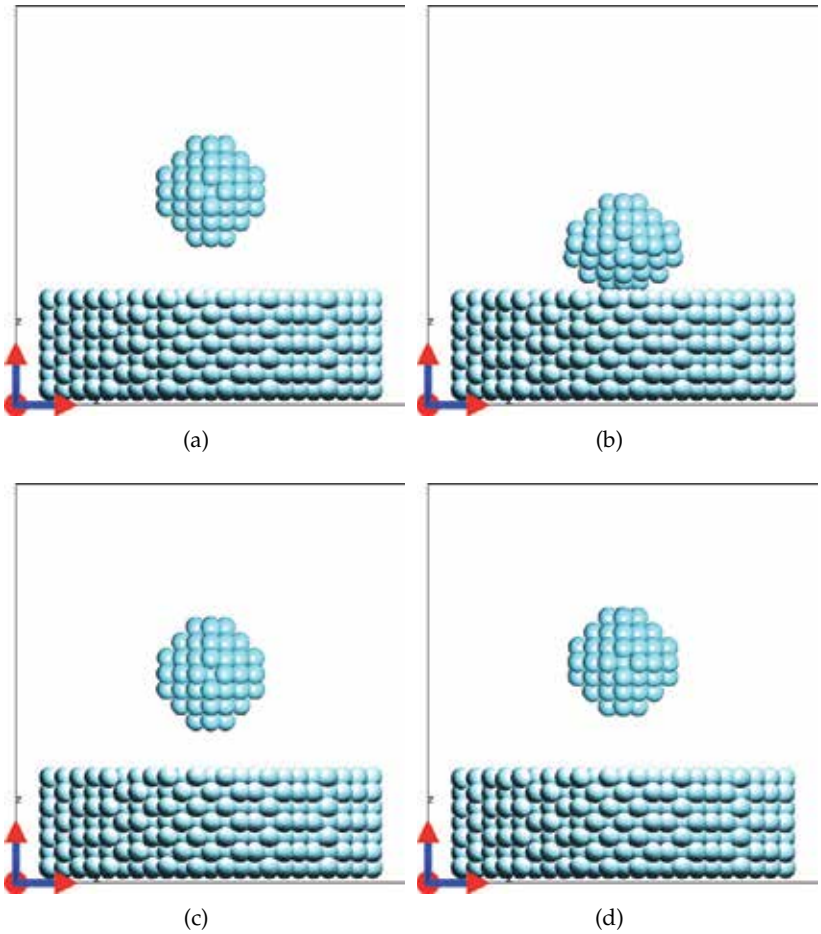

Fig. 5. Ball dropped from $z = 11.03\,\sigma$. (a) The ball is falling towards the surface. (b) The ball hits the surface and gets compressed, inducing an oscillatory movement on it. (c) The ball leaves the surface vibrating. A maximum amplitude is reached. (d) A minimum amplitude is reached due to the induced oscillatory movement. The maximum amplitude is slightly greater than the minimum, so the difference between the size of the ball in 5(c) and its size in 5(d) is not clearly appreciated. You can see the simulations at `www.lpmd.cl` in the examples section, where these oscillations can be clearly appreciated in the videos.

Figure 6 shows another simulation, where the ball was dropped from $z = 28.15\,\sigma$. After the collision, the ball acquires a new shape.

4.2 Results

In this section we present the results of several simulated collisions. The ball was dropped from heights h_0 between $11.03\,\sigma$ and $79.53\,\sigma$. We begin by describing the dynamics of the ball and discuss about the height reached after each bounce. Then, we analyze the deformation

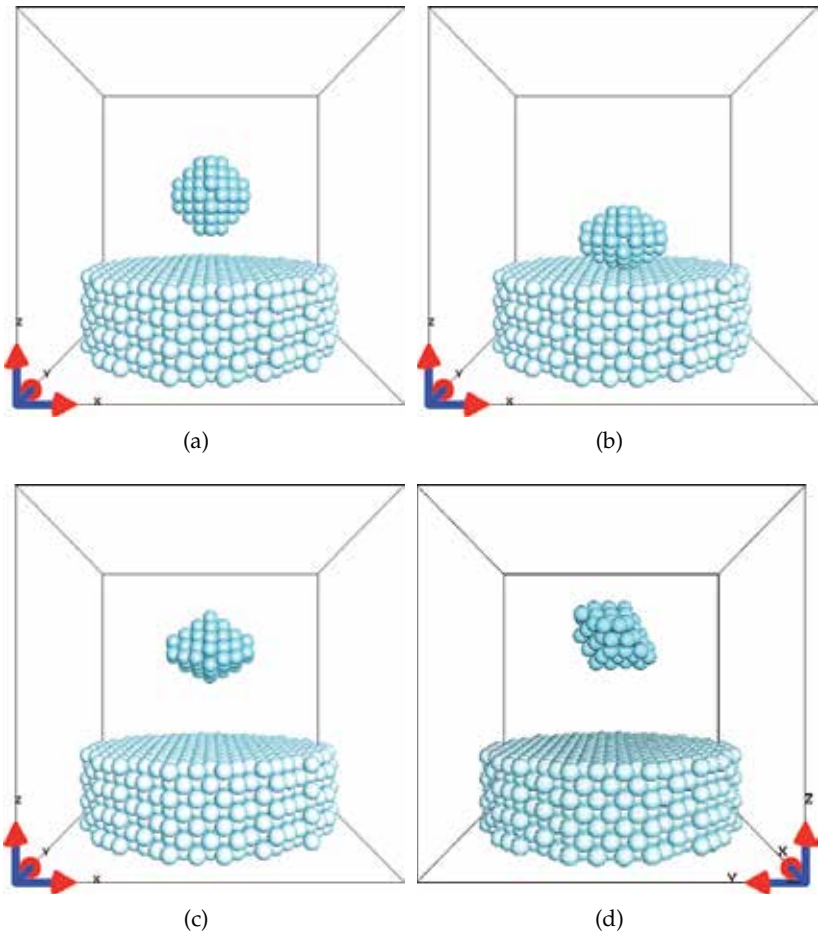

Fig. 6. Ball dropped from $z = 28.15\,\sigma$. (a) The ball is falling towards the surface. (b) The ball hits the surface and gets compressed. (c) The ball lifts the surface acquiring a new shape, with almost none internal vibrations. (d) The ball keeps its new shape after the collision.

of the ball by evaluating the pair-distribution function $g(r)$. Finally, we classify kinetic and potential energies in different types and then examine how these energies are transferred from one to another to keep the total energy constant.

4.2.1 Heights reached

Fig. 7 shows the heights reached by the center of mass of the ball after each bounce. The zeroth bounce represents the initial height h_0. The case in which the ball is dropped from a height of $11.03\,\sigma$ corresponds to a quasi-elastic bounce because the height of bounces are almost the same. When $h_0 = 18.64\,\sigma$, the height reached by the ball after the first bounce is smaller than the initial height from where it was dropped, and something similar happens with the other bounces: the maximum heights reached decrease until the ball remains static over the target. For $h_0 = 41.47\,\sigma$, the maximum height reached after the first bounce is considerably smaller than h_0. Big differences of height are observed also for $h_0 = 58.6\,\sigma$, where a notorious

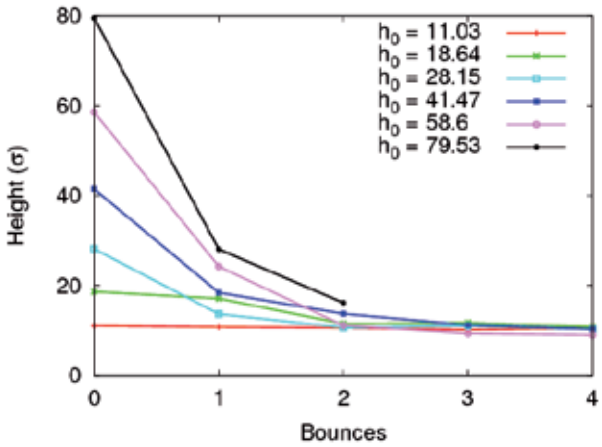

Fig. 7. (Color online) Maximum heights reached after each bounce, by the center of mass of the ball.

decrease is appreciated in the first bounce as well as in the second. For $h_0 = 79.53\,\sigma$ only two bounces are observed because, after the first bounce, the ball gets deformed and loses its solid structure, which does not allow it to keep bouncing. Nevertheless, a common behavior is observed for all cases: after the third bounce, the height reached is almost the same. At this point, the ball remains over the surface.

4.2.2 Deformation of the ball

We analyze in detail the structure of the ball evaluating the pair-distribution function $g(r)$ for the atoms that constitute the ball for different time steps (Fig. 8) in different simulations.

Before the first impact, i.e., when the ball is falling, it has a FCC structure (for any h_0), because the first neighbors are clearly appreciated at $1.09\,\sigma$ for all cases (Fig. 8), which is the known value for first neighbors in argon lattice structure (Kittel, 2005). In Fig. 8(a) it can be seen that for times between $t = 0$ and $t = 5.581\tau$ the initial FCC structure is conserved, despite of the effects of the impacts with the surface, which took place at $t = 0.71\,\tau$, $t = 2.07\,\tau$, $t = 3.38\,\tau$, $t = 4.52\,\tau$ and $t = 5.83\,\tau$. The peaks also have similar widths, which means that there are small temperature effects. If h_0 is increased, the peaks become wider and smaller (Fig. 8(b) to 8(c)) but still distinguishables, which implies a rising of the temperature inside the ball without melting. We will analyze this subject deeper in the next section (4.2.3). In the latter case (Fig. 8(c)), the ball acquires a new solid structure (Fig. 6), that seems to be, just looking at the $g(r)$ function, still FCC type. For $h_0 > 41.47\,\sigma$ (Fig. 8(d) to 8(f)) just one peak is distinguishable as long as the distance r to an atom increases, which means that an atom has, in average, a neighbor at $1.09\,\sigma$ and no well defined second neighbors or further. This can be interpreted as the melting of the ball.

4.2.3 Energy

In an inelastic collision, the dissipation of energy of a body is given by the energy transfer from mechanical energy to internal energies, such as thermal energies and vibrational energies, being the last one the responsible of plastic deformations of the body. Since our simulations consider the surface as part of the system, no dissipation is observed, because the total energy

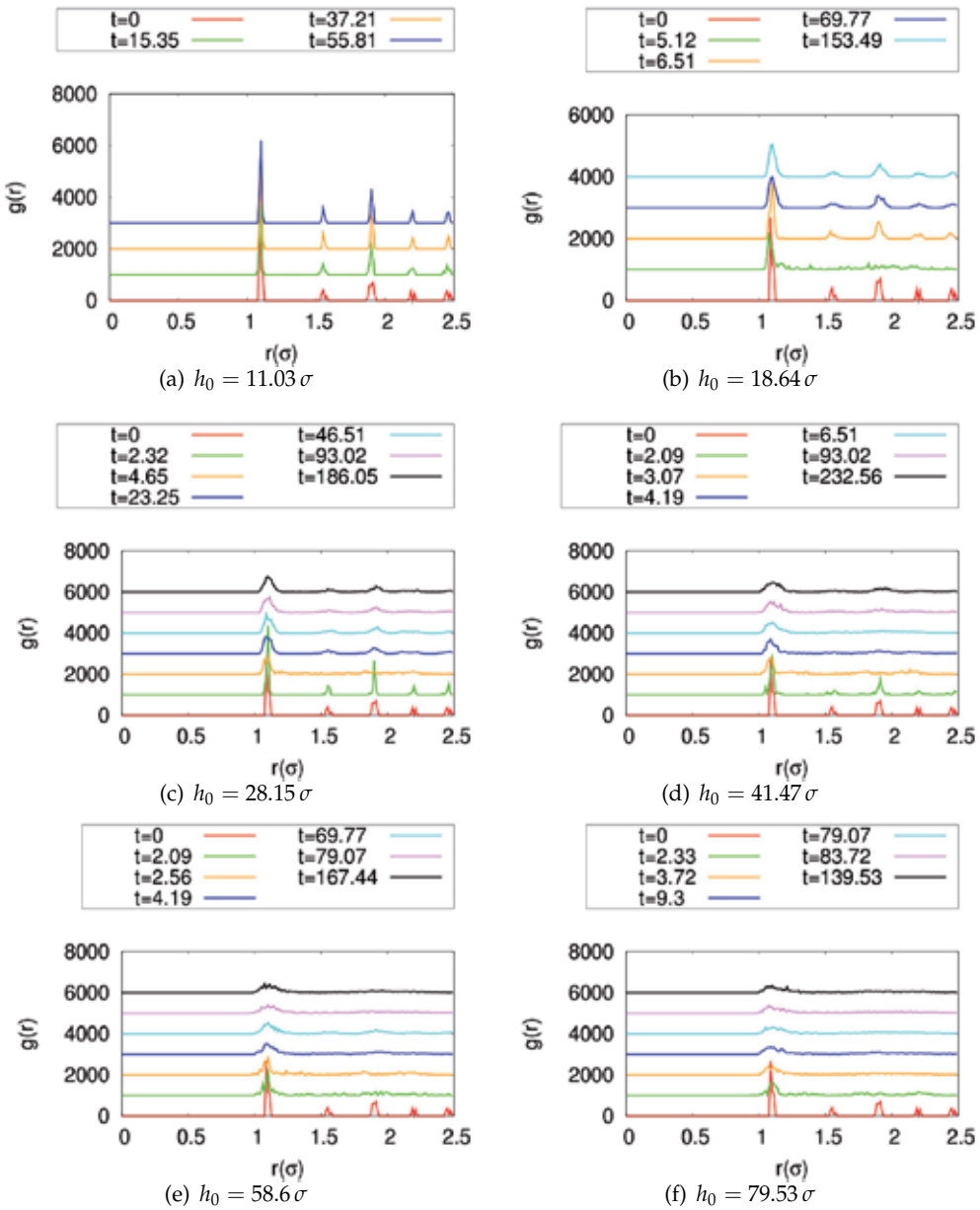

(a) $h_0 = 11.03\,\sigma$ (b) $h_0 = 18.64\,\sigma$

(c) $h_0 = 28.15\,\sigma$ (d) $h_0 = 41.47\,\sigma$

(e) $h_0 = 58.6\,\sigma$ (f) $h_0 = 79.53\,\sigma$

Fig. 8. (Color online) Pair-distribution functions calculated for the atoms in the ball, for different times (see inset in $\tau/10$). Each graph corresponds to different initial heights h_0. The pair distribution function for each t at h_0, has been shifted upwards for clarity.

remains constant. The internal energies of the ball change in each bounce, and the mechanism of loss and gain of energy are explained by considering the following classification of energies:

The velocity of the center of mass of the ball ${\mathbf{V}_{\mathrm{CM}}}^B$ is calculated for each time-step to compute the **translational kinetic energy of the ball**, defined by

$$K_B = \frac{1}{2} M_B \|{\mathbf{V}_{\mathrm{CM}}}^B\|^2, \tag{10}$$

where $M_B = 79\,M$ is the mass of the ball. The velocity of the center of mass of the surface ${\mathbf{V}_{\mathrm{CM}}}^S$ is calculated for each time-step to compute the **translational kinetic energy of the surface**, defined by

$$K_S = \frac{1}{2} M_S \|{\mathbf{V}_{\mathrm{CM}}}^S\|^2, \tag{11}$$

where $M_S = 1444\,M$ is the mass of the surface. For a given time step, the difference between the velocity of the center of mass ${\mathbf{V}_{\mathrm{CM}}}^B$ and the velocity of the atom i, $\mathbf{v}_i$, defines $\bar{\mathbf{v}}_i = \mathbf{v}_i - {\mathbf{V}_{\mathrm{CM}}}^B$, the velocity of the atom i relative to the center of mass of the ball, which is used to define the kinetic energy of the ball relative to its center of mass, what we call **thermal energy of the ball**, by

$$T_B = \sum_{\substack{\text{all ball}\\ \text{atoms}}} \frac{1}{2} m_i \|\bar{\mathbf{v}}_i\|^2, \tag{12}$$

where $m_i = M$ is the mass of the atom i. In the same way, we define the **thermal energy of the surface** by

$$T_S = \sum_{\substack{\text{all surface}\\ \text{atoms}}} \frac{1}{2} m_i \|\bar{\mathbf{v}}_i\|^2, \tag{13}$$

where, in this case, $\bar{\mathbf{v}}_i = \mathbf{v}_i - {\mathbf{V}_{\mathrm{CM}}}^S$. Now, since the interaction between any pair of atoms is given by equation (9), the total potential energy U is given by the sum over all pairs of atoms plus the energy given by the force field, $U_F = M_B\, a\, z_{\mathrm{CM}}$, where $a = 0.026\, a_0$ and z_{CM} is the $z-$axis coordinate of the center of mass of the ball. We divide the sum in four terms as follows:

$$U = V_B + V_S + U_c + U_F. \tag{14}$$

The first term corresponds to the potential energy of the ball, which keeps together all the pairs that belong to the ball, and we can associate it to a **vibrational energy of the ball**:

$$V_B = \sum_{\substack{\text{all ball}\\ \text{atoms}}} V(r). \tag{15}$$

The second term corresponds to the potential energy of the surface, which keeps together all the pairs that belong to the surface, and we can associate it to a **vibrational energy of the surface**:

$$V_S = \sum_{\substack{\text{all surface}\\ \text{atoms}}} V(r). \tag{16}$$

The third term corresponds to the potential energy generated by the interaction of an atom of the ball with an atom of the surface, i.e., between atoms of different types. We will refer to this term as collisional energy:

$$U_c = \sum_{\substack{\text{all}\\ \text{ball-surface}\\ \text{atom pairs}}} V(r). \tag{17}$$

The last term U_F was already explained and corresponds to the potential that generates the force field.

Fig. 9 shows the evolution of all these energies in time, except for V_S, which is a negative term that remains almost constant and does not add additional information to the phenomenon. The energies are expressed in the Lennard-Jones energy unit, ε. The energy U_F has been shifted $2\,\varepsilon$ downwards and V_B, $400\,\varepsilon$ upwards to keep all energies in the same range, since what matters is the changes in energy rather than their absolute values. Other cases, where the ball was dropped at different h_0, are quite similar in shape, but some peaks are bigger than others.

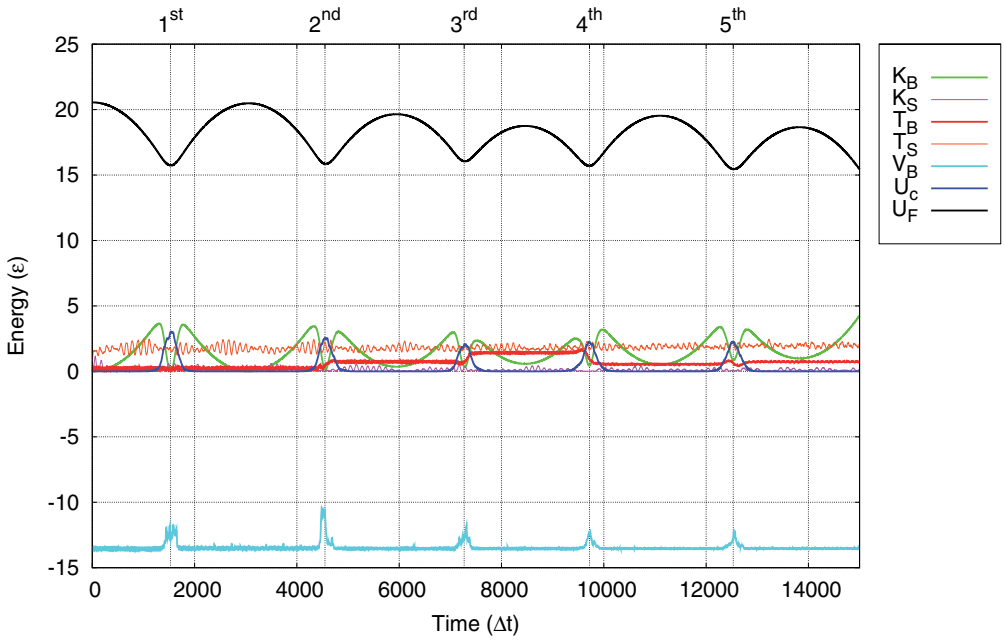

Fig. 9. (Color online) Evolution of the different energies in time for the simulation where the ball was dropped from $h_0 = 11.03\,\sigma$.

In the Fig. 9 it can be observed that the translational energy of the ball has several local minima, located between two maxima placed symmetrically around each of them. These minima represent the instant in which the kinetic translational energy K_B vanishes, i.e., when the ball is completely stopped over the surface during a bounce. The maximum at the left hand of each minimum shows the instant in which the velocity of the center of mass of the ball acquires its maximum value before it begins to stop. The repulsive potential of the surface is equivalent to a force exerted upwards, but this force does not reduce velocity of the ball immediately, in fact, the velocity keeps growing with time before reaching the maximum, but its rate of change, that is, its acceleration, is reduced. Considering just the z coordinate of the velocity of the center of mass, the first derivative of K_B is given by

$$\frac{dK_B}{dt} = M_B V^B_{\mathrm{CM}} \dot{V}^B_{\mathrm{CM}} = M_B V^B_{\mathrm{CM}} A^B_{\mathrm{CM}},$$

where A^B_{CM} is the acceleration of the center of mass of the ball. This derivative vanishes whether the velocity or the acceleration is zero, this is, when the net force exerted over the

ball is zero. This happens at the minima and maxima of K_B, so the maxima show where the force exerted by the surface equals the force $F = M_B\, a = \|\nabla U_F\|$.

When the ball has reached the point of maximum velocity, that is, the impact velocity, the velocity begins to decrease, because now the acceleration (and so the net force) is directed upwards. The ball reaches the point of null velocity (the minima) and then keeps accelerating until a maximum velocity that, for the first bounce, is the same as the impact velocity. In this interval of time, the energy U_c becomes greater while the energy K_B and T_S decreases, which means that most of the energy was stored in the collision energy and a little bit in the vibrational energy of the surface, with almost no energy transferred to the thermal energy of the ball (T_B). In the second bounce (see labels above Fig. 9), much of the energy is transferred to the collision energy U_c, but now a little bit of energy is now transferred to the thermal energy of the ball T_B, so the ball lose translational energy and the maximum velocity after the collision (the departure velocity) is smaller than the impact velocity, so it is not able to reach the same height than before the collision. In the third bounce, the thermal energy of the ball is transferred back to kinetic translational energy, and the ball can reach a departure velocity greater than the impact velocity. Something similar happens with the fourth bounce, and what all bounces has in common is that the fluctuations of the thermal energy of the ball T_B are comparable to the fluctuations of its vibrational energy V_B and the thermal energy of the surface T_S.

Finally, we want to mention that, since U_c is non-zero only when atoms of the ball are close to atoms of the surface, this energy gives a reasonable definition of the collision time as the width of the peak generated by this energy in each bounce.

In conclusion, a molecular dynamics study of the behavior of a ball bouncing repeatedly off a surface, considered as part of the system, has been done. We have observed that a study of the different types of energies of the system clearly shows what may be considered as the duration of a collision which, in contrast with typical macroscopic classical mechanics considerations, is not instantaneous, but a non negligible time interval. We have also shown that, despite of the fact that the collision is actually a continuous process that does not allow us to determine the "instant just before the collision" and the "instant just after the collision", which are always mentioned in macroscopic problems of momentum conservation, the impact velocity (maximum velocity reached before the ball stops) and the departure velocity (maximum velocity reached after the ball stops) can be determined precisely. This makes possible to determine the restitution coefficient in each bounce, a well studied property of bouncing systems, as the usual quotient of these velocities. The study of these energies have also helped to understand the processes of energy loss in inelastic collisions, which are actually not a loss, but a transfer to thermal and vibrational energy, within others. We could conclude that the force exerted by the surface acts as a break for the ball, and this force is the responsible for the decrease of the acceleration of the ball to zero (where the net force is null). So the impact velocity (maximum velocity reached before hitting the surface) is reached after the ball begins its collision with the floor, which can be considered as the moment in which the energy U_c becomes relevant. It is clear that $K_T + U_F$ is constant when the collision is not taking place, but when it happens, in all bounces, despite of the fact that the collision energy U_c behaved similar in every bounce, it was the most important among the energies in the collision, since it stores most of the "dissipated" energy by the ball, more than the vibrational energy transferred to the surface. The other energies, in spite of their changes, do not contribute significantly to the energy transfer.

5. Hypervelocity impact of projectiles

Hypervelocity impact of projectiles is of great interest in basic and applied research, and it is present in areas such as engineering and physics of materials, including civilian and military applications, among others. For example, since the development in the 1980's of cluster beam technology, the quality of the beams and the number of applications continues to grow (Jacquet & Beyec, 2002; Kirkpatrick, 2003; Popok & Campbell, 2006), as is the case of the materials which are bombarded with cluster beams in order to clean or smooth their surface or to analyze their composition, as well as to consolidate clusters. In several cases the effect of the cluster beams result from the combined effects of a single impact, which occurs separately and independently (Hsieh et al., 1992). Therefore it is important to understand the dynamics of such a single impact. In the field of space applications, hypervelocity impacts are being studied to see the damage they produce on ceramic tiles when nano and micrometeorites hit satellites, spacecraft and space stations. Because the experimental study at such high velocities (ranging from 3 km/s to 15 km/s approximately) is extremely difficult, computer simulation is an ideal tool to deal with them.

In the following we will study, by classical molecular dynamics simulations, the impact of a cluster composed of 47 atoms of copper (Cu) on a solid target of approximately 50 000 atoms of copper. The main goal is to depict the structural response of the target with respect to three different velocities of impact, 1.5 km/s, 3.0 km/s and 5.0 km/s. There will be a detailed description of the different processes, emphasizing the structural changes suffered by the target.

5.1 Computational procedure

The impact simulations were performed at high speeds with classical molecular dynamics, using the computer program *LPMD* (Davis et al., 2010). To simulate the impact of a projectile on a target, we initially built a cubic box of edge 86.64 Å containing 55,296 copper atoms in a FCC structure, which is used as target. This target was thermalized to 300 K through rescaling of velocities, for 15,000 time steps with $1\Delta t = 1$ fs. Then it was allowed to evolve without temperature control for another 15,000 time steps. The projectile is spherical in shape with a diameter of approximately 8 Å (one tenth the length of the edge of the target). Both projectile and target were placed in a tetragonal simulation cell length $x = y = 198.55$ Å and $z = 249.09$ Å, centered at x and y, and separated by a distance 11 Å in z, as is shown in Figure 10.

The atomic interaction is represented by the empirical many-body Sutton-Chen potential,

$$\phi = \varepsilon \left\{ \sum_{i=1} \sum_{j=i+1} \left(\frac{a}{r_{ij}} \right)^n - c \sum_{i=1} \left[\sum_{j=1, j\neq i} \left(\frac{a}{r_{ij}} \right)^m \right]^{1/2} \right\}, \tag{18}$$

where $\varepsilon = 0.0124$ eV, $a = 3.61$ Å (Cu lattice parameter), and $c = 39.432$, $n = 9$, $m = 6$ are adimensional parameters.

The simulations we perform used three different velocities for the projectile: 1.5 km/s, 3.0 km/s and 5.0 km/s, while the target is at rest. The projectile velocity is kept constant during all the simulation, irrespective of the friction or the force exerted by the target. Although this is not a real situation, it represent an extreme condition, where the momentum and hardness of the projectile is much higher than the momentum and hardness of the target.

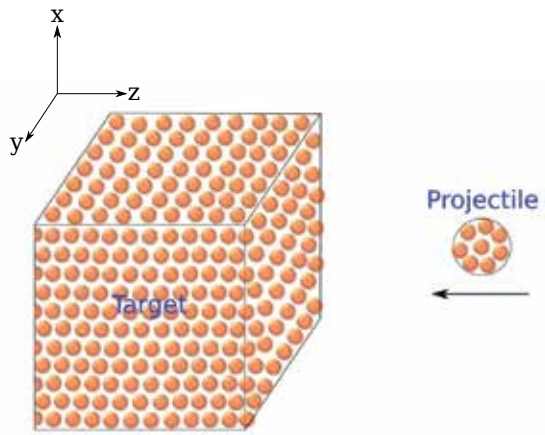

Fig. 10. Cu spherical projectile with velocity $-v_z$. Both are sitting in the xy plane of the simulation box

In the following we present a detailed description of the different processes, emphasizing the structural changes suffered by the target. To perform the analysis of the target in a better way, atoms belonging to the projectile were removed and the target was divided into two radial sections.

5.2 Results

In Figure 11 is shown a general view of the passage of the projectile, in this case corresponding to 1.5 km/s. As can be seen, it melts the sample locally when it is going through. After the passage of the projectile, there are two regimes on the behavior of the target: 1) to certain speeds, including 1.5 and 3.0 km/s, the sample returns to its initial fcc structure, but with at higher temperature and with dislocations of planes, and 2) for speeds equal to or greater than 5.0 km/s, the projectile left a hole in the target and even though the atoms regroup in the same way, the target as a whole can not return its initial fcc structure, resulting a large percentage in the amorphous state.

Here we will analyze in details only the case at lower velocity, 1.5 km/s. From the snapshots showed in Figure 11, we can see that at 1.2 ps the projectile hits the target producing an increase in temperature at the impact zone. Then the projectile continues to move through the target producing, in addition to local temperature increases (in the vicinity of the projectile trajectory), a wake of disturbed material, which is perceived as temperature fluctuations. At 4.8 ps dislocations appeared. When the projectile begins to leave the target, at 8.4 ps, some target atoms are ejected. At this same time, the area where the bullet impacts begins to become disordered. After a longer time, at 15 ps, the area where the projectile leaves the target (back side) is disordered. Finally, at 28.2 ps, we observe that the whole area which had been disturbed by the projectile is re-ordered, resembling its original structure, but with dislocations. In general, it appears that the projectile disturbs the zone which corresponds to its trajectory and its neighborhood, but it does not causes great impact beyond that (Loyola, 2010).

In order to quantify the just described picture, we analyze the change of local temperature, and the atomic order, by means of $g(r)$ and by the CNA. Temperature profiles are shown in Figs. 12, 13, which correspond to a radial zone close and far to bullet trajectory, respectively. In

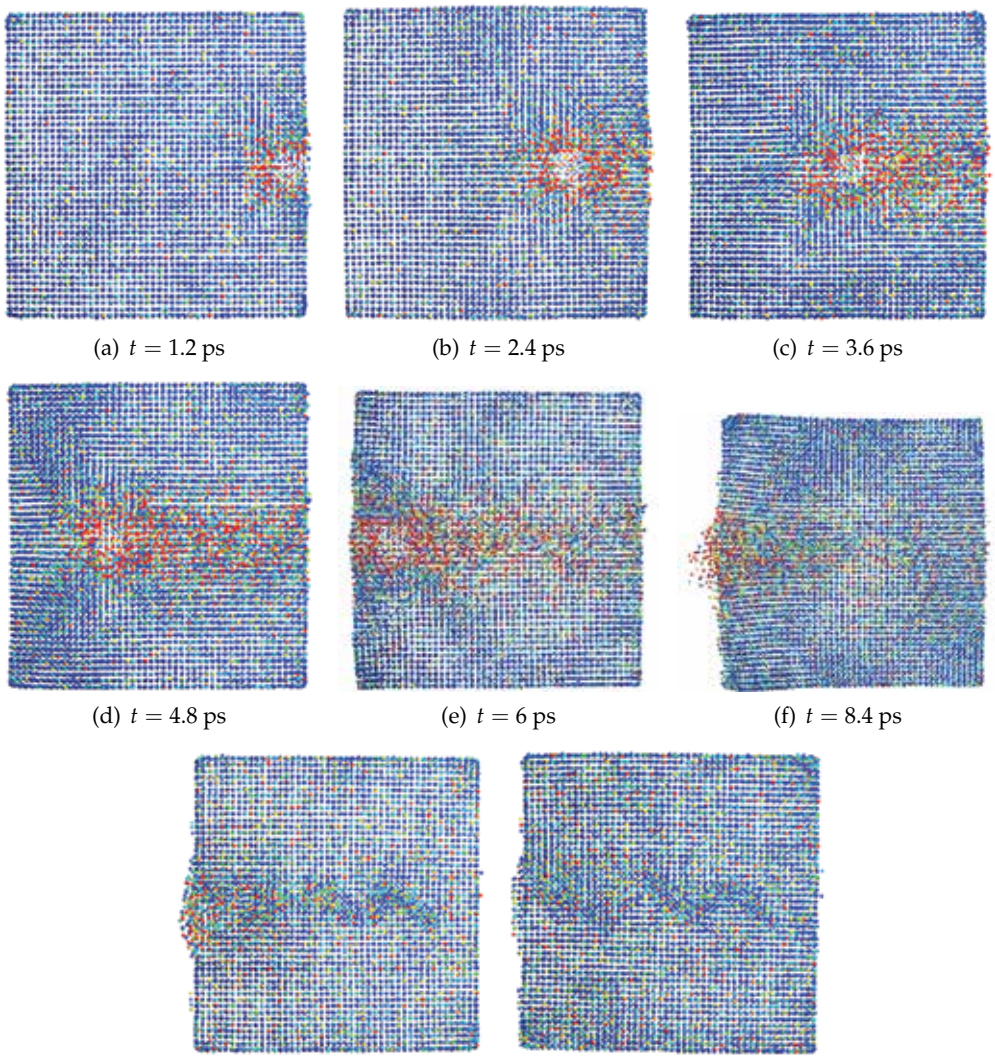

(a) $t = 1.2$ ps (b) $t = 2.4$ ps (c) $t = 3.6$ ps

(d) $t = 4.8$ ps (e) $t = 6$ ps (f) $t = 8.4$ ps

(g) $t = 15$ ps (h) $t = 28.2$ ps

Fig. 11. Snapshots of the impact of the projectile traveling at 1.5 km/s over a copper target at different times. The colors are assigned according to the atom's temperature, from low temperature (blue) to high temperature (red) (Loyola, 2010).

general, we can observe a temperature front that is moving in the same direction as the bullet. In Fig. 12 can be seen a temperature maxima of 1760 K at 3.6 ps. After that, at 28.2 ps, this part of the sample is thermalized at 450 K. The temperature, of course, propagates in radial direction from the center outward of the sample. Figure 13 displays the temperature profile beyond the central zone. Although there are not prominent peaks, the information about the passage of the projectile is shown in the 1.2 ps panel as a small peak at 65 Å , indicating that the temperature perturbation propagates at higher velocity than the projectile, ruling out the occurrence of a shock wave.

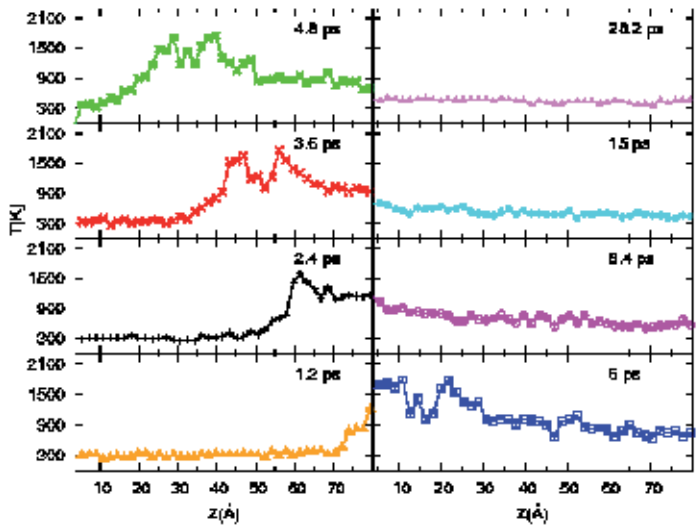

Fig. 12. Local temperature along the $z-$direction for different times, in the zone close to the center of the target, as the 1.5 km/s projectile is moving.

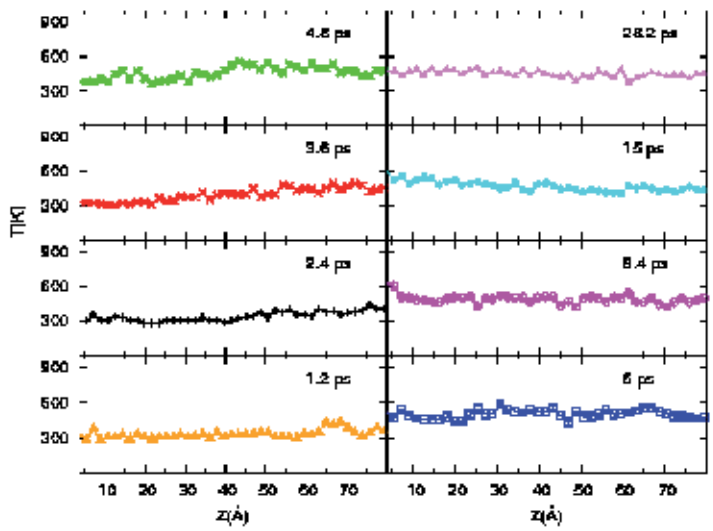

Fig. 13. Local temperature along the $z-$direction for different times, in the zone far the center of the target, as the 1.5 km/s projectile is moving.

The structural analysis of the sample was made by the pair distribution function, $g(r)$ for three different region in the z direction: region A, where the bullet hit the sample (Fig. 14 a), region B, in the middle (Fig. 14 b), and region C, at the end of the sample (Fig. 14 c), where the bullet

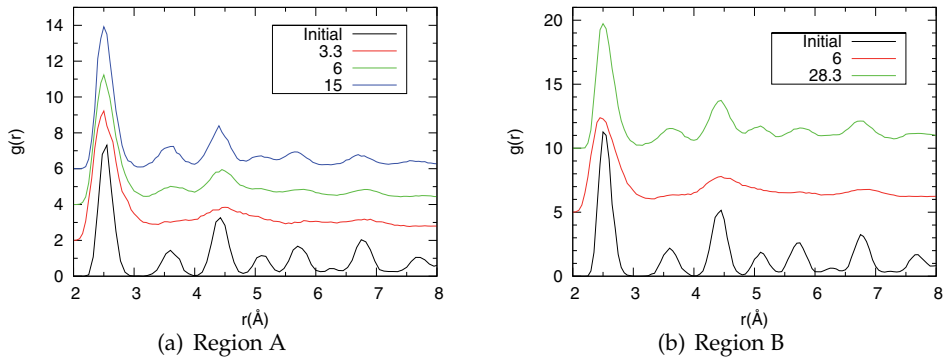

(a) Region A (b) Region B

(c) Region C (d) Region A, but far from the center

Fig. 14. Pair distribution function for different region of the sample. The curves have been shifted for clarity

go out. Figures 14 a, and 14 b show the same phenomenology but at different times. Initially, all sections have fcc structure (the peaks have a finite width because initially the system is at room temperature), then melt, as is appreciated at the times 3.3 ps, 6 ps and 8.5 ps for regions A, B and C, respectively. Finally, all these regions recover their crystalline structure, but at higher temperatures than the initial stage. In the case of the radial zone far from the bullet trajectory the situation is different because this part did not melt at any time, preserving the initial fcc structure but at higher temperatures, around 500 K.

Interestingly, the crystalline structure that the sample recovers after the passage of the bullet is a mixture between fcc and hcp structure. In fact, the high pressure resulting by the impact produce structural transformation, which at the end results in the coexistence of fcc and hcp phases. To quantify its relation, we perform a common neighbors analysis, CNA, for the the three region where the projectile pass, at the beginning (region A), the middle (region B) and the end (region C), with respect to the z direction. The CNA calculates the percentage of atoms with structure fcc, hcp, bcc and icosahedral, and the rest is considered as non-crystalline (amorphous) structure. Figure 15 displays the percentage of fcc and hcp atoms (the difference between their sum and 100% corresponds to atoms in amorphous structure). We can see that in the region A, for $t < 2$ ps, all the atoms are still in a fcc order, because the bullet is just hitting. After that, the percentage of fcc atoms decrease to 10% and the hcp atoms appear, reaching also almost 10%. The rest are atoms in a non-crystalline structure. At $t > 8.5$ ps, when the projectile has go out the sample, the region A start to recover its crystalline order,

most atoms in fcc order. Finally, at $t = 28$ ps, the region reach 70% of fcc atoms, 3% of hcp atoms and around 25% of non-crystalline atoms. For the others regions the situation is similar, except it occurs at longer times, when the perturbation and the bullet reach that regions. The only significant difference is that, in the case of region C, the percentage of atoms in a non-crystalline structure is greater than the previous regions, which can be also seen directly from the snapshot (Fig. 11(h)).

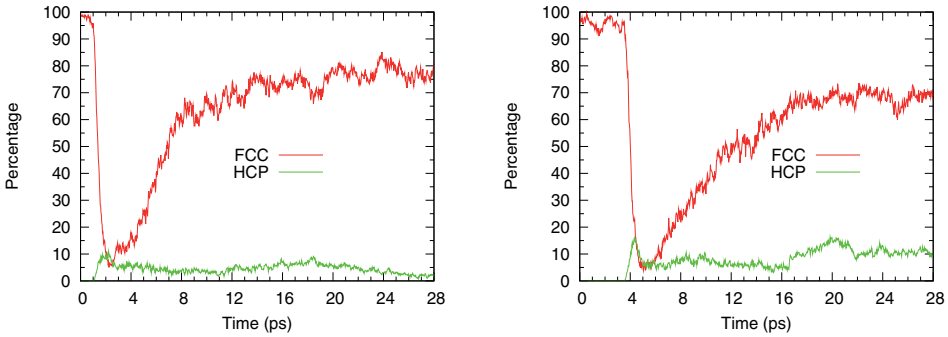

(a) Region A (b) Region B

(c) Region C

Fig. 15. Common neighbors analysis (CNA) at different times, for three region in the z direction.

In summary, molecular dynamics simulation of hypervelocity projectile impact has been done. The atomic level study allows us to describe several interesting features that are not possible to track by other methods. In particular, two regimes has been identified, in dependence of the projectile initial velocity. At high velocity, the passage of the projectile through the target leaves a hole in the sample, as well as produce structural phase transition. Al low temperature, the case that has been study in detail here, the projectile cause local melting and dislocations as it moves through the sample. At the end, the target recover its original fcc crystalline structure, but with a non-negligible percentage of atoms in hcp structure and amorphous phase.

6. Conclusions

Descriptions of phenomena far from equilibrium are not an easy task in physics: from the experimental point of view it is required to have both high spatial and temporal resolution in the different variables measured; even worse, often we have destructive experiments, such as

projectile impact. From a theoretical standpoint, it is known that there is not a formalism that allows generally treatment of these systems, except in the case of linear response. This is where computer simulation provides valuable services, allowing for an atomic description of the phenomenon, taking into account the entire trajectory of the system. This was precisely what we do here, using a comprehensive computer code developed by us, for two cases of interest, namely inelastic impact and hypervelocity impact. In the first case, we were able to separate the various contributions of energy and revealed how they are transferred between them. Our results show that the most important transferable energy is the one between the ball-surface atoms, which grows during the impact and is zero at the others cases. Thus, this energy allows us to define a time of impact, which is approximately 1/10 the time between bounces. For the case of hypervelocity impact, we showed that molecular dynamics simulation reveals that exist a thresholds of materials behavior respect to projectile velocity: beyond certain velocity, in our case 4 km/s, the sample left with a permanent structural damage, expressed as a permanent hole in the center of the sample.

7. Acknowledgments

This work was supported by the Anillo Project ACT-24 *Computer simulation lab for nano-bio systems.* G. Gutiérrez thanks ENL 10/06 VRID-Universidad de Chile. F. González-Cataldo thanks CONICYT-Chile Ph.D fellowship. S. Davis acknowledges Fondecyt grant 3110017.

8. References

Aguirregabiria, J., Hernández, A. & Rivas, M. (2008). A simple model for inelastic collisions, *American Journal of Physics* 76(11): 1071.

Alonso, M. & Finn, E. (1992). *Physics*, Addison Wesley.

Baranyai, A. (2000). Temperature of nonequilibrium steady-state systems, *Phys. Rev. E* 62: 5989–5997.

Barrat, J. & Bocquet, L. (1999). Large slip effect at a nonwetting fluid-solid interface, *Physical Review Letters* 82(23): 4671–4674.

Bridges, F., Hatzes, A. & Lin, D. (1984). Structure, stability and evolution of saturn's rings, *Nature* 309: 333–335.

Callen, H. (1985). *Thermodynamics and an Introduction to Thermostatistics*, Wiley.

Casas-Vásquez, J. & Jou, D. (2003). Temperature in non-equilibrium states: a review of open problems and current proposals, *Rep. Prog. Phys.* 66: 1937–2023.

Davis, S., Loyola, C., González, F. & Peralta, J. (2010). Las palmeras molecular dynamics: A flexible and modular molecular dynamics code, *Computer Physics Communications* 181(12): 2126 – 2139.
URL: *http://www.sciencedirect.com/science/article/pii/S001046551000336X*

Dewar, R. (2005). Maximum entropy production and the fluctuation theorem, *J. Phys. A* 38(21): L371.

Dewar, R. C. (2003). Information theory explanation of the fluctuation theorem, maximum entropy production and self-organized criticality in non-equilibrium stationary states, *J. Phys. A: Math. Gen.* 36: 631.

Eisberg, R. & Lerner, L. (1981). *Physics: Foundations and Applications*, McGraw-Hill Inc.

Evans, D. & Searles, D. (2002). The fluctuation theorem, *Advances in Physics* 51(7): 1529–1585.
URL: *http://www.tandfonline.com/doi/abs/10.1080/00018730210155133*

Falcon, E., Laroche, C., Fauve, S. & Coste, C. (1998). Behavior of one inelastic ball bouncing repeatedly off the ground, *Eur. Phys. J. B* 3: 45–57.

Goldsmith, W. (2001). *Impact*, Dover Publications.

Gutiérrez, G., Menéndez-Proupin, E., Loyola, C., Peralta, J. & Davis., S. (2010). Computer simulation study of amorphous compounds: structural and vibrational properties, *Journal of Material Science* 45: 5124–5134. DOI: 10.1007/s10853–010–4579–0.

Hatzes, A. P., Bridges, F. G. & Lin, D. N. C. (1988). Collisional properties of ice spheres at low impact velocities, *Mon. Not. R. Astr. Soc.* 231: 1091.

Holian, B. L. (1995). Atomistic computer simulations of shock waves, *Shock waves* 5: 149–157.

Honeycutt, J. & Andersen, H. (1987). Molecular dynamics study of melting and freezing of small lennard-jones clusters, *Journal of Physical Chemistry* 91(19): 4950–4963.

Hoover, W. & Hoover, C. G. (2007). Computational physics with particles, *Am. J. Phys.* 76: 481.

Hsieh, H., Averback, R. S., Sellers, H. & Flynn, C. P. (1992). Molecular-dynamics simulations of collisions between energetic clusters of atoms and metal substrates, *Physical Review B* 45: 4417.

Jacquet, D. & Beyec, Y. L. (2002). Cluster impacts on solids, *Nuclear Instruments and Methods in Physics Research B* 193: 227.

Jaynes, E. T. (1980). The minimum entropy production principle, *Annu. Rev. Phys. Chem.* 31: 579.

Johnson, K. (1987). *Contact Mechanics*, Cambridge University Press.

Kirkpatrick, A. (2003). Gas cluster ion beam applications and equipment, *Nuclear Instruments and Methods in Physics Research B* 206: 830.

Kittel, C. (2005). *Introduction to Solid State Physics*, eighth edn, John Wiley & Sons, Inc, University of California, Berkeley.

Kleidon, A., Lorenz, R. & Lorenz, R. D. (2005). *Non-equilibrium thermodynamics and the production of entropy: life, earth, and beyond*, Springer.

Lifshitz, J. & Kolsky, H. (1964). Some experiments on anelastic rebound, *Journal of the Mechanics and Physics of Solids* 12(1): 35–43.
URL: *http://www.sciencedirect.com/science/article/pii/0022509664900055*

Loyola, C. (2010). *Material Behavior at Atomic Level: A Computer Simulation Study*, PhD thesis, Departamento de Física, Facultad de Ciencias, Universidad de Chile, Chile.

Loyola, C., Davis, S., Peralta, J. & Gutiérrez, G. (2010). Onset of failure in solid argon by the effect of a shockwave: a molecular dynamics study, *Computational Materials Science* 49: 582–587. DOI 10.1016/j.commatsci.2010.05.052.

Lun, C. & Savage, S. (1986). The effects of an impact velocity dependent coefficient of restitution on stresses developed by sheared granular materials, *Acta Mechanica* 63: 15–44. 10.1007/BF01182538.
URL: *http://dx.doi.org/10.1007/BF01182538*

Popok, V. N. & Campbell, E. E. B. (2006). Beams of atomic clusters: Effect on impact with solids, *Reviews on Advanced Materials Science* 11: 19.

Prigogine, I. (1968). *Introduction to thermodynamics of irreversible processes*, Interscience Publishers.

Raman., C. V. (1918). The photographic study of impact at minimal velocities, *Phys. Rev.* 12: 442–447.
URL: *http://link.aps.org/doi/10.1103/PhysRev.12.442*

Reed, J. (1985). Energy losses due to elastic wave propagation during an elastic impact, *Journal of Physics D: Applied Physics* 18: 2329.

Refson, K. (2000). Moldy: a portable molecular dynamics simulation program for serial and parallel computers, *Computer Physics Communications* 126(3): 310 – 329.
URL: *http://www.sciencedirect.com/science/article/pii/S0010465599004968*

Smith, W. & Forester, T. (1996). Dl_poly_2.0: A general-purpose parallel molecular dynamics simulation package, *Journal of Molecular Graphics* 14(3): 136 – 141.
URL: *http://www.sciencedirect.com/science/article/pii/S0263785596000434*

Stock, G., Ghosh, K. & Dill, K. A. (2008). Maximum caliber: A variational approach applied to two-state dynamics, *J. Chem. Phys.* 128: 194102.

Supulver, K., Bridges, F. & Lin, D. (1995). The coefficient of restitution of ice particles in glancing collisions: Experimental results for unfrosted surfaces, *Icarus* 113: 188–199.

Tabor, D. (1948). A simple theory of static and dynamic hardness, *Proceedings of the Royal Society of London. Series A. Mathematical and Physical Sciences* 192(1029): 247–274.
URL: *http://rspa.royalsocietypublishing.org/content/192/1029/247.abstract*

Tillett, J. (1954). A study of the impact of spheres on plates, *Proceedings of the Physical Society. Section B* 67: 677.

Tsai, Y. & Kolsky, H. (1967). A study of the fractures produced in glass blocks by impact, *Journal of the Mechanics and Physics of Solids* 15(4): 263–278.
URL: *http://www.sciencedirect.com/science/article/pii/0022509667900166*

Zener, C. (1941). The intrinsic inelasticity of large plates, *Phys. Rev.* 59: 669–673.
URL: *http://link.aps.org/doi/10.1103/PhysRev.59.669*

Zukas, J., Nicholas, T., Swift, H., Greszczuk, L. & Curran, D. (1982). *Impact Dynamics*, John Wiley & Sons Inc.

Zwanzig, R. (2001). *Nonequilibrium Statistical Mechanics*, Oxford University Press.

Part 4

Dynamics of Molecules on Surfaces

13

Recent Advances in Molecular Dynamics Simulations of Gas Diffusion in Metal Organic Frameworks

Seda Keskin
Koç University, Department of Chemical and Biological Engineering
Turkey

1. Introduction

Over approximately the last decade, metal organic framework (MOF) materials have attracted a great deal of attention as a new addition to the classes of nanoporous materials. MOFs, also known as porous coordination polymers (PCPs) or porous coordination networks (PCNs), are hybrid materials composed of single metal ions or polynuclear metal clusters linked by organic ligands through strong coordination bonds. Due to these strong coordination bonds, MOFs are crystallographically well defined structures that can keep their permanent porosity and crystal structure after the removal of the guest species used during synthesis.(Eddaoudi et al., 2000; Li et al., 1999; Rowsell et al., 2005; Yaghi et al., 2003) MOFs typically have low densities (0.2-1 g/cm^3), high surface areas (500-4500 m^2/g), high porosities and reasonable thermal and mechanical stabilities. This combination of properties has made MOFs interesting materials for a wide range of potential applications, including gas storage, gas separation, catalysis and biomedical applications.(Eddaoudi et al., 2002; Keskin&Kizilel, 2011; Millward&Yaghi, 2005; Mueller et al., 2006; Pan et al., 2004)

MOFs have become attractive alternatives to traditional nanoporous materials specifically in gas storage and gas separation since their synthesis can be readily adapted to control pore connectivity, structure and dimension by varying the linkers, ligands and metals in the material.(Düren et al., 2004; Eddaoudi et al., 2002; El-Kaderi et al., 2007) Hundreds of MOF materials with various physical and chemical characteristics have been synthesized to date.(James, 2003; Kitagawa et al., 2004; Uemura et al., 2005; Yaghi et al., 2003) Most of the studies in the literature have focused on a few specific MOF groups such as IRMOFs (isoreticular MOFs)(Eddaoudi et al., 2002), ZIFs (zeolite imidazolate frameworks)(Park et al., 2006), CPOs (coordination polymers of Oslo)(Dietzel et al., 2005; Dietzel et al., 2006), MILs (Materials of the Institute Lavoisier)(Loiseau et al., 2004), CuBTC (Copper 1,3,5-benzenetricarboxylate) (Chui et al., 1999) and $Zn(bdc)(ted)_{0.5}$ (Zinc 1,4-benzenedicarboxylic acid-triethylenediamine) (Li et al., 1998). As an example Figure 1 shows the unit cell structure of one of the most widely studied MOFs, CuBTC (also known as HKUST-1). The figures from left to right represent an empty CuBTC structure, a CuBTC structure with CH_4 molecules in the pores at 100 bar, 298 K and a CuBTC structure with adsorbed CH_4 and H_2 molecules in the pores at 100 bar, 298 K for a bulk gas composition of CH_4/H_2:5/95.

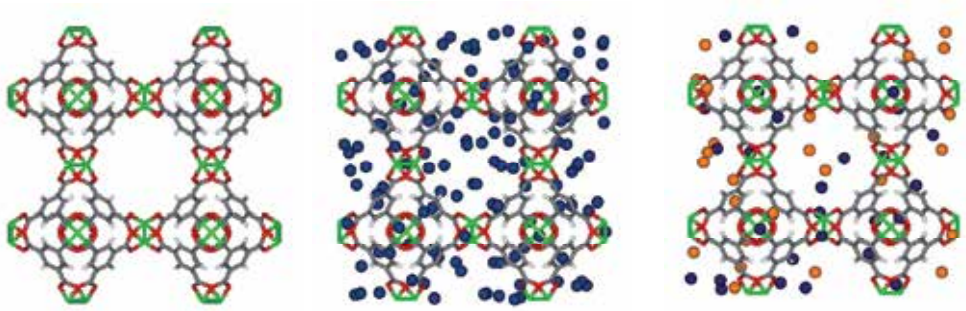

Fig. 1. Unit cell representation of a widely studied MOF, CuBTC. From left to right: Empty CuBTC, CuBTC with CH_4 molecules (blue spheres) in the pores, CuBTC with CH_4 and H_2 (orange spheres) molecules in the pores. The atoms in the unit cell are copper (green), oxygen (red), carbon (gray) and hydrogen (white).

The enormous number of different possible MOFs indicates that purely experimental means for designing optimal MOFs for targeted applications is inefficient at best. Efforts to predict the performance of MOFs using molecular modeling play an important role in selecting materials for specific applications. In many applications that are envisioned for MOFs, diffusion behavior of gases is of paramount importance. Applications such as catalysis, membranes and sensors cannot be evaluated for MOFs without information on gas diffusion rates. Most of the information on gas diffusion in MOFs has been provided by molecular dynamics (MD) studies. Figure 2 indicates that the idea of using MD simulations to assess the diffusivity of gases in MOFs is a new area and there is a rapid growth in the number of publications featuring the terms 'MOFs', 'MD' and 'diffusion' over the past decade.

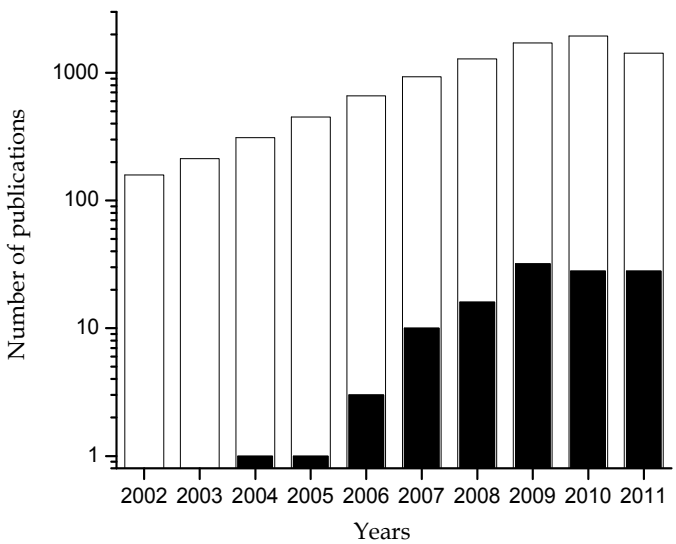

Fig. 2. Open bars represent the number of publications featuring the term 'metal organic framework', closed bars represent the number of publications featuring the terms 'metal organic framework' and 'molecular dynamics' and 'diffusion'. (Source: ISI Web of Science, retrieved August, 8 2011).

The objective of this chapter is to review the recent advances in MD simulations of gas diffusion in MOFs. In Section 2, the MD models used for gas molecules and MOFs will be introduced. Studies which computed single component and mixture gas diffusivities in MOFs will be reviewed in Section 3. The discussion of comparing results of MD simulations with the experimental measurements and with the predictions of theoretical correlations will be given in Sections 4 and 5, respectively. Finally, opportunities and challenges in using MD simulations for examining gas diffusion in MOFs will be summarized in Section 6.

2. Molecular dynamics models

Gas diffusion is an observable consequence of the motion of atoms and molecules as a response to external force such as temperature, pressure or concentration change. Molecular dynamics (MD) is a natural method to simulate the motion and dynamics of atoms and molecules. The main concept in an MD simulation is to generate successive configurations of a system by integrating Newton's law of motion.(Frenkel&Smit, 2002) Using MD simulations, various diffusion coefficients can be measured from the trajectories showing how the positions and velocities of the particles vary with time in the system. Several different types of gas diffusion coefficients and the methods to measure them will be addressed in the next section in details.

In accessing the gas diffusion in nanoporous materials, equilibrium MD simulations which model the behavior of the system in equilibrium have been very widely utilized. In equilibrium MD simulations, first a short grand canonical Monte Carlo (GCMC) simulation is applied to generate the initial configurations of the atoms in the nanopores. Initial velocities are generally randomly assigned to each particle (atom) based on Maxwell-Boltzmann velocity distribution.(Allen&Tildesley, 1987; Frenkel&Smit, 2002) An initial NVT-MD (NVT: constant number of molecules, constant volume, constant temperature) simulation is performed to equilibrate the system. After the equilibration, Newton's equation is integrated and the positions of each particle in the system are recorded at a pre-specified rate. Nosé-Hoover thermostat is very widely applied to keep the desired temperature and the integration of the system dynamics is based on the explicit N-V-T chain integrator by Martyna et al.(Martyna et al., 1992; Martyna et al., 1996) By keeping temperature constant, Newton's equations are integrated in a canonical ensemble (NVT) instead of a microcanonical ensemble (NVE: constant number of molecules, constant volume and constant energy). To describe the dynamics of rigid-linear molecules such as carbon dioxide the MD algorithm of Ciccotti et al.(Ciccotti et al., 1982) is widely used. The so-called order *N* algorithm(Frenkel&Smit, 2002) is implemented to calculate the diffusivities from the saved trajectories.

In order to perform classical MD simulations to measure gas diffusion in MOFs' pores, force fields defining interactions between gas molecules-gas molecules and gas molecules-MOF's atoms are required. Once these force fields are specified, dynamical properties of the gases in the simulated material can be probed. These force fields will be studied in two parts: models for gas molecules (adsorbates) and models for MOFs (adsorbents).

2.1 Models for gases

Diffusion of hydrogen, methane, argon, carbon dioxide and nitrogen are very widely studied in MOFs. For H_2, three different types of fluid-fluid potential models have been

used. In most of the MD simulations, spherical 12-6 Lennard-Jones (LJ) model (Buch, 1994) has been used for H_2. The Buch potential is known to reproduce the experimental bulk equation of state accurately for H_2. Two-site LJ models have also been used in the literature.(Yang&Zhong, 2005) The potential model of Darkrim and Levesque (Darkrim&Levesque, 1998) has been used to account for the quadrupole moment of H_2 molecules. This potential consists of a LJ core placed at the center of mass of the molecule and point charges at the position of the two protons and the center of mass.(Liu et al., 2008b)

Methane and argon diffusion simulations have been performed using single site-spherical LJ potentials. The CO_2 potential consists of three LJ sites with charges located on each site to represent the quadrupole moment of CO_2.(Potoff&Siepmann, 2001) In N_2 diffusion simulations, N_2 is generally represented as a three site model with two sites located at two N atoms and the third one located at its center of mass (COM) with partial point charges.(Potoff&Siepmann, 2001) For alkanes in MOFs, the TraPPE potential has been used.(Martin&Siepmann, 1997) As an example, the most widely used potential parameters (ε: energy parameter, k_B: Boltzmann constant, σ: size parameter) are listed in Table 1.

Atoms/Molecules	ε/k_B (K)	σ (Å)	References
H_2-H_2	34.20	2.96	Buch, 1994
Ar-Ar	119.8	3.4	Clark, 1998
CH_4-CH_4	148.20	3.73	Martin&Siepmann, 1997
C-C (in CO_2)	27.00	2.80	Potoff&Siepmann, 2001
O-O (in CO_2)	79.00	3.05	Potoff&Siepmann, 2001
N (in N_2)	36.4	3.32	Potoff&Siepmann, 2001
COM (N_2)	0.00	3.32	Potoff&Siepmann, 2001

Table 1. Potential parameters used for adsorbate molecules in MD simulations.

2.2 Models for MOFs

When the first MD simulations were performed to examine gas diffusion in MOFs at the beginning of 2004, there was no experimental data to validate the accuracy of MD studies. However, in general whenever experimental equilibrium properties such as adsorption isotherms have been reproduced by the molecular simulations, it has been observed that dynamic simulations based on the same interatomic potentials are also reliable. Therefore, many MD studies examining gas diffusion in MOFs first showed the good agreement between experiments and simulations for gas adsorption isotherms and then used the same potential models for gas diffusion simulations.(Skoulidas&Sholl, 2005) Here, it is useful to highlight that considering a wide gas loading range when comparing simulation results with experimental data is crucial.(Keskin et al., 2009b) It is unreasonable to compare outcome of simulations with the experimental measurements over a very narrow range of loading and assume that good (or poor) agreement with experiment will continue to high loadings.

The MD simulations have used general-purpose force fields such as the universal force field (UFF) (Rappe et al., 1992), DREIDING force field(Mayo et al., 1990) and optimized potential for liquid simulations all-atom (OPLS-AA)(Jorgensen et al., 1996) force field for representing the interactions between MOF atoms and adsorbates. A few studies have used quantum

mechanical calculations to develop new potentials for specific MOF-adsorbate interactions.(Bordiga et al., 2005; Sagara et al., 2004) There are studies where the parameters of the force fields are refined to match the predictions of simulations with the experimental measurements (in most cases experimental adsorption isotherm data exist whereas experimental diffusion data do not exist) or using first principles calculations.(Sagara et al., 2004; Sagara et al., 2005a; Sagara et al., 2005b; Yang&Zhong, 2005; Yang&Zhong, 2006). Of course, one must be careful in refining force field parameters to match the results of simulations with the experimental data since the accuracy of the experiments are significantly affected by the defects of as-synthesized MOFs or trapped residual solvent molecules present in the samples.(Keskin et al., 2009b)

Most MD simulations performed to date have assumed rigid MOF structures which means the framework atoms are fixed at their crystallographic positions. Generally, the crystallographic data for MOFs are obtained from X-ray diffraction experiments. In rigid framework simulations, only the nonbonding parameters, describing the pair wise interactions between the adsorbate and the adsorbent atoms of the particular force field, were used. It can be anticipated that the assumption of a rigid framework brings a huge computational efficiency yet the inclusion of the lattice motion and deformation is crucial for an accurate description of diffusion of large gas molecules since they fit tightly in the MOF pores, forcing the MOF to deform in order to allow migration from pore to pore.

In order to include the lattice dynamics in MD simulations of gas diffusion in MOFs, Tafipolsky and coworkers extended the MM3 (Molecular Mechanics) force field (Lii et al., 1989), which is well known to accurately describe structures and conformational energies of organic molecules, with parameters for the Zn_4O moiety based on the first principles of density functional theory (DFT) calculations of nonperiodic model systems.(Tafipolsky et al., 2007) After this force field accurately predicted the structure of MOF-5 (also known as isoreticular MOF-1, IRMOF-1), it was used in MD simulations to investigate the self diffusion of benzene in MOF-5.(Amirjalayer et al., 2007) The self diffusivity calculated from MD simulations, 2.49×10^{-9} m^2/s, corresponds well to the experimental value determined by Stallmach et al., who found values between $1.8\text{-}2\times10^{-9}$ m^2/s.(Stallmach et al., 2006) Under identical conditions, MD simulations performed with a rigid MOF lattice gave substantially higher diffusion coefficient, 19.5×10^{-9} m^2/s, which is almost one order of magnitude larger than the value obtained from MD simulations with flexible lattice.

Amirjalayer et al. later investigated the diffusion mechanism of benzene in MOF-5 using MD simulations based on fully flexible MM3 force field and computed the self diffusivity of benzene as a function of loading in MOF-5.(Amirjalayer&Schmid, 2009) The results were close to the experimentally determined self diffusivity for liquid benzene, therefore they concluded that MOF-5 is a very open structure with liquid like mobilities for benzene, $\sim2.49\times10^{-9}$ m^2/s. The third study including flexibility of MOFs in MD simulations used the modified MM3 force field to study hexane's self diffusion mechanism in IRMOF-1 and IRMOF-16 and concluded that the flexibility of IRMOF-16 is much larger than that of IRMOF-1 due to the nature of the organic linkers.(Xue&Zhong, 2009)

Greathouse and Allendorf developed a flexible hybrid force field for MD simulations of IRMOF-1(Greathouse&Allendorf, 2006) and the activation energy for benzene self diffusion calculated at low loadings using this force field was found to be in good agreement with previous MD simulations and nuclear magnetic resonance (NMR) results. (Greathouse

& Allendorf, 2008) In this force field, only nonbonded parameters were used to describe Zn−O interactions and the CVFF (consistent valence force field) was used with slight modifications to describe the benzene dicarboxylate linker. The magnitude of the diffusion constant was underestimated and this was attributed to the deficiencies in the CVFF portion of the force field.

The literature summary presented so far indicates that the number of MD simulation studies with flexible MOFs and flexible force fields is very limited. More research will sure be helpful to understand the importance of lattice dynamics on diffusivity of gas molecules in MOFs. Studies to date indicated that the lattice dynamics are specifically important in computing diffusivity of large gas molecules (such as benzene) in MOFs having relatively narrow pores. Studies on flexible force fields also suggested that a force field developed for a specific MOF can be adapted to similar MOF structures (as in the case of IRMOFs) with slight modifications for doing comparative studies to provide a comprehensive understanding of gas diffusion in flexible MOFs.

One major issue in carrying out MD simulations for MOFs is to assign partial charges to the MOF atoms that are required to calculate adsorbate-adsorbent interactions for some polar (including quadrupolar) adsorbates. Several MD studies computed the diffusivity of CO_2 in MOFs' pores and to do this, partial charges must be assigned to MOF atoms. Recent studies showed that the effects of inclusion of framework charges are crucial at low loadings. If the charge-quadrupolar interactions are not taken into account in MD simulations then the diffusivities can be significantly overestimated.(Rankin et al., 2009) Force field-based classical MD simulations of MOFs typically treat electrostatic interactions between adsorbates and MOF atoms by assigning fixed point charges to each atom. In this context an important role for quantum mechanics (QM) calculations is to assign the point charges that can later be used in force field calculations. Unfortunately, multiple methods exist for partitioning the net electron density determined in a QM calculation(Keskin et al., 2009b) and none of these methods give an unambiguous definition of the resulting point charges. Keskin and coworkers reviewed the partial charges assigned to IRMOF-1 on the basis of QM calculations and showed that there is a significant variation in the charge values based on the method used.(Keskin et al., 2009b) This variation may have a significant impact on the outcome of classical force field calculations in examples where electrostatic interactions are important. Since QM calculations are time consuming and the charges obtained from these calculations are method sensitive, a strategy called connectivity based atom contribution method (CBAC) with which the partial charges of framework atoms can be estimated easily was proposed.(Xu&Zhong, 2010) A recent study on two different MOFs showed that CO_2 adsorption isotherms and diffusivities computed using the charges from QM methods based on the ChelpG(Francl et al., 1996) DFT calculations are very similar to the ones computed using charges from CBAC method.(Keskin, 2011a)

3. Predicting gas diffusivity using molecular dynamics simulations

In the literature, MD simulations have been used to predict three different types of gas diffusivities in MOFs. These are transport diffusivity, corrected diffusivity and self diffusivity. The transport diffusivity, which is also known as Fickian diffusivity or chemical diffusivity, can be defined without approximation in terms of corrected diffusivity, D_o and a

thermodynamic correction factor, a partial derivative relating the adsorbate concentration, c and bulk phase fugacity, f

$$D_t(c) = D_o(c) \cdot \frac{\partial \ln f}{\partial \ln c}. \tag{1}$$

The thermodynamic correction factor is fully defined once the single component adsorption isotherm is known. Well developed approaches exist for calculating the corrected diffusion coefficient from MD simulations.(Kärger&Ruthven, 1992; Keil et al., 2000; Skoulidas&Sholl, 2003; Skoulidas&Sholl, 2005) For systems with a single adsorbed component, the corrected diffusivity is equivalent to the Maxwell-Stefan diffusion coefficient.(Kapteijn et al., 2000; Ruthven, 1984; Sholl, 2006) The corrected diffusivity includes information on the collective motion of multiple adsorbed molecules that is relevant to net mass transport and can be calculated using the following expression:(Kärger&Ruthven, 1992; Keil et al., 2000)

$$D_{o,i} = \lim_{t\to\infty} \frac{1}{6Nt} \left\langle \left(\sum_{l=1}^{N_i} \left[r_{il}(t) - r_{il}(0) \right] \right)^2 \right\rangle \tag{2}$$

Here, N is the number of molecules, $r_{il}(t)$ is the three dimensional position vector of molecule l of species i at time t and the angular brackets denote that the ensemble average. Using MD simulations, one can record the trajectory of the gas molecules in the pores of MOFs and calculate the corrected diffusivity. A more microscopic measure of diffusion is the self diffusion coefficient which describes the motion of individual, tagged particles. In an isotropic three dimensional material, the self diffusivity is related to the mean squared displacement of tagged particles by the Einstein relation:

$$D_{self,i} = \lim_{t\to\infty} \frac{1}{6t} \left\langle \frac{1}{N_t} \sum_{l=1}^{N_i} \left[r_{il}(t) - r_{il}(0) \right]^2 \right\rangle \tag{3}$$

This definition of self diffusivity is applicable to both single component and multi-component systems.(Sanborn&Snurr, 2000) In general, all three diffusion coefficients described here, transport, corrected and self diffusivities are the functions of concentration and they are only equal in the limit of dilute concentrations.(Sholl, 2006) In some extreme cases, the self and corrected diffusivities vary by orders of magnitude.(Ackerman et al., 2003; Skoulidas et al., 2002) This observation sometimes underscores the value of characterizing these two diffusivities independently. Applications such as modeling of membranes, pressure swing adsorption require the accurate description of net mass transfer and in these processes generally the transport diffusivity is of greatest interest.(Sholl, 2006)

Almost all applications of nanoporous materials in gas separations involve chemical mixtures; therefore it is important to describe the multi-component gas transport in nanopores. There are several mathematically equivalent formalisms such as Onsager, Fickian and Maxwell-Stefan to describe multi-component gas transport through nanoporous materials.(Krishna&van den Broeke, 1995; Wesselingh&Krishna, 2000) The Onsager formulation is based on irreversible thermodynamics and expresses the flux of each species in terms of chemical potentials. One can calculate the Onsager coefficient using MD simulations based on the method by Theodorou et al. (Theodorou et al., 1996):

$$L_{ij} = \frac{1}{6Vk_BT}\lim_{t\to\infty}\frac{1}{t}\left\langle \sum_{l=1}^{N_i}\left[r_{il}(t)-r_{il}(0)\right]\cdot\sum_{k=1}^{Nj}\left[r_{jk}(t)-r_{jk}(0)\right]\right\rangle \tag{4}$$

In this formulation, V is the subsystem volume, k_B is the Boltzmann constant, T is temperature, $r_{il}(t)$ is the three-dimensional position vector of molecule l of species i at time t and N_i is the number of molecules of species i. The Onsager coefficients and the matrix of Fickian coefficients are mathematically equivalent and they are related to each other without approximation by expressions involving derivatives of the mixture adsorption isotherm for the adsorbed species.(Skoulidas et al., 2003) The Onsager coefficients from MD simulations can be converted to Fickian diffusion coefficients using the followings:

$$D_{ii} = \frac{k_BT}{c_i}\sum_{j=1}^{N}L_{ij}\left(\frac{\partial\ln f_i}{\partial\ln c_i}\right) \tag{5}$$

$$D_{ij} = \frac{k_BT}{c_j}\sum_{k=1}^{N}L_{ik}\left(\frac{\partial\ln f_k}{\partial\ln c_j}\right) \tag{6}$$

In these equations, T is temperature, c_i is the concentration of species i, f_j is the fugacity of species j, k_B is Boltzmann constant, L_{ij} and L_{ik} are the Onsager coefficients and D_{ii} and D_{ij} are the Fickian diffusivity coefficients. Using Onsager or Fickian diffusivities, one can calculate the flux (J) of a binary gas mixture through a membrane as follows:

$$\begin{pmatrix}J_1\\J_2\end{pmatrix} = -\begin{pmatrix}D_{11} & D_{12}\\D_{21} & D_{22}\end{pmatrix}\cdot\begin{pmatrix}\nabla c_1\\\nabla c_2\end{pmatrix} \tag{7}$$

$$\begin{pmatrix}J_1\\J_2\end{pmatrix} = -\begin{pmatrix}L_{11} & L_{12}\\L_{21} & L_{22}\end{pmatrix}\cdot\begin{pmatrix}\nabla \mu_1\\\nabla \mu_2\end{pmatrix} \tag{8}$$

$$\vec{J} = -L\nabla\vec{\mu} = -D\nabla\vec{c} \tag{9}$$

In these expressions, ∇c_i and $\nabla\mu_i$ represent concentration gradient and chemical potential gradient of species i through the membrane, respectively. As Equation 9 suggests, gas fluxes in a MOF membrane can be calculated based on either of the formulations (Onsager or Fickian).

3.1 Single component diffusion

The transport rates of single component gas molecules inside the materials' pores are important in many potential applications of MOFs. For example, in equilibrium-based separations such as pressure swing adsorption, transport rates define limits on the cycle times that can be achieved. In these cases, molecular transport rates are mainly important if they are very slow. Since accurate characterization of molecular transport inside nanoporous materials using experiments is very challenging, most of the information that is currently available about single component gas diffusion in MOFs has obtained from MD simulations.

Skoulidas performed the first study of gas diffusion in a MOF material in the literature using equilibrium MD simulations and calculated the self, corrected and transport diffusivities of argon at 298 K as a function of pressure.(Skoulidas, 2004) Results showed that diffusion in CuBTC MOF is an activated process as in zeolites. The calculated diffusivities of Ar in CuBTC were similar to the diffusion in zeolites both in magnitude and concentration dependence. Sarkisov et al. used equilibrium MD simulations to calculate the self diffusivities of methane, n-pentane, n-hexane, n-heptane, cyclohexane and benzene in MOF-5 at 300 K at dilute loadings.(Sarkisov et al., 2004) They found that self diffusivities of n-alkanes in MOF-5 are comparable to those in the crystalline bipyridine system ($0.1\text{-}3\times10^{-8}$ m^2/s), but they show a stronger dependence on chain length because of the more open structure of MOF-5.

Skoulidas and Sholl(Skoulidas&Sholl, 2005) then used equilibrium MD simulations to probe the self, corrected and transport diffusivity of a number of gas species, Ar, CH_4, CO_2, N_2 and H_2 in MOF-5 as a function of pore loading at room temperature. They also calculated self, corrected and transport diffusivities of Ar in MOF-2, MOF-3, MOF-5, CuBTC and MFI to make a comparison among different MOFs and a zeolite. They concluded that diffusion of gas molecules in MOFs is mostly dominated by motions where the adsorbed species remain in close contact with the surfaces defined by the pore structure throughout their diffusion. At the time of their study, there was no experimental data for gas diffusion in MOFs. Therefore, Skoulidas and Sholl could not directly comment on the accuracy of the MD simulations, however, they pointed out that using similar molecular simulation methods for gas diffusion in zeolites they got excellent agreement with the experiments.

Yang and Zhong performed constant temperature equilibrium MD simulations by a momentum scaling method to calculate the self diffusivity of H_2 in isoreticular MOFs, IRMOF-1, IRMOF-8 and IRMOF-18 as a function of pressure.(Yang&Zhong, 2005) Their results showed that the diffusivity of H_2 in IRMOFs is slightly larger than in zeolites due to the larger pore volume of IRMOFs. The self diffusivity of H_2 in IRMOFs at 77 K at low pressures was around $1\text{-}3\times10^{-8}$ m^2/s whereas the self diffusivity of H_2 in various zeolites were experimentally measured to be around $0.1\text{-}1\times10^{-8}$ m^2/s. The activation energy of H_2 in IRMOFs was between 2-3 kJ/mol which is close to the values measured in zeolite NaX (4 kJ/mol(Bär et al., 1999)) and single walled carbon nanotubes (1.12 kJ/mol(Narehood et al., 2003)). This MD study examined the effects of framework topology on the diffusivity of H_2. For example, H_2 diffuses more rapidly in IRMOF-8 than that in IRMOF-1 because of the relatively larger pore sizes of the former. The diffusivity of H_2 in IRMOF-18 is much slower than diffusion in IRMOF-1 and IRMOF-8 due to the steric hindrance effects of the pendant CH_3 groups in IRMOF-18.

IRMOFs can be further categorized as catenated and non-catenated structures. In catenation, two or more identical frameworks are intergrown at the expense of pore volume. Early studies showed that catenated MOFs can give better adsorption properties compared to their counterparts.(Ryan et al., 2008) The first study about the effects of catenation on the gas diffusion used equilibrium MD simulations in the canonical ensemble to investigate H_2 diffusion.(Liu et al., 2008a) Nosé-Hoover chain thermostat as formulated by Martyna et al.(Martyna et al., 1996) was used to calculate room temperature self diffusivities of H_2 in catenated and non-catenated MOFs. The results showed that H_2 self diffusivity in the IRMOFs without catenation such as IRMOF-10, IRMOF-12, IRMOF-14, IRMOF-16 ($30\text{-}90\times10^{-}$

^{8} m^2/s) are two or three times of those (10-20×10^{-8} m^2/s) in their corresponding catenated counterparts IRMOF-9, IRMOF-11, IRMOF-13, IRMOF-15. This implied that the motion of H_2 molecules in these MOFs is restricted by their catenated structures.

Lee and coworkers also investigated the diffusion of H_2 in catenated MOFs, IRMOF-9, IRMOF-11 and IRMOF-13 at 77 K.(Lee et al., 2009) Diffusivities reported by Liu et al. were larger than the ones reported by Lee et al. by one order of magnitude since the former group performed the MD simulations at room temperature. The results of two studies were consistent; the diffusion rate of H_2 is dramatically reduced by the catenation of IRMOFs due to the interpenetrated chains of the catenated structures and/or by tighter binding of the H_2 molecules in catenated structures. Equilibrium MD simulation studies showed that the effect of catenation on CH_4 diffusivity is much larger than that on H_2 diffusivity at room temperature.(Xue et al., 2009) Xue and coworkers discussed that the motion of both CH_4 and H_2 is restricted by the catenated structures of IRMOF-11 and IRMOF-13 while the stronger interactions between CH_4 and atoms of the catenated frameworks lead to stronger confinement effects than that of H_2 in these IRMOFs.

Liu and coworkers(Liu et al., 2008b) investigated the influence of quantum effects on H_2 diffusivity using MD simulations. They used both the classical and the Feynman-Hibbs (FH)(Feynman&Hibbs, 1965) effective Buch potentials with UFF in their MD simulations to calculate self, corrected and transport diffusivities of H_2 in a MOF called Zn(bdc)(ted)$_{0.5}$ at 77 K. The inclusion of quantum effects increased the self diffusivity of H_2 at zero loading which was explained by the decrease in the diffusion energy barrier due to a non-uniform smearing of solid-fluid potential within the FH formalism. At higher loadings, inclusion of quantum effects decreased H_2 diffusivity which was attributed to the steric hindrance in narrow pores due to the increase in the effective size parameter for the solid-fluid and fluid-fluid interactions. In contrast to self diffusivity, transport diffusivity is not strongly influenced by the quantum effects at 77 K.

In order to compare the diffusivities of gases in MOFs with those in zeolites, MD simulations were performed to calculate self, corrected and transport diffusivities of CH_4 and CO_2 in silicalite, IRMOF-1 and C_{168} schwarzite.(Babarao&Jiang, 2008) The simulations were carried out in a canonical ensemble with a Nosé-Hoover thermostat and the equations of motion were integrated using a sixth order Gear predictor-corrector algorithm. (Allen&Tildesley, 1987) Both self and corrected diffusivities of CH_4 and CO_2 were found to be larger in IRMOF-1 ($D_{self\text{-}CH4}$:4-5×10^{-8} m^2/s, $D_{self\text{-}CO2}$:2-3×10^{-8} m^2/s) compared to the diffusivities in MFI and C_{168}. This was attributed to the large pore volume of the IRMOF-1. This work also showed that in the limit of infinite dilution the diffusivities at various temperatures exhibit a good Arrhenius relationship. In another MD study, NVT ensemble with Berendsen(Frenkel&Smit, 2002) thermostat was used to examine the self diffusivity of CH_4 in alkoxy functionalized IRMOF-1.(Jhon et al., 2007) As expected, CH_4 diffusion was hindered due to the constriction of the pores as the length of the alkoxy chains increases. Comparison of the results with the early MD studies of Sarkisov et al.(Sarkisov et al., 2004) revealed good agreement whereas there is an unexplained small discrepancy between the results of Jhon et al. and Skoulidas et al.(Skoulidas&Sholl, 2005) at higher loadings.

Zeolite imidazolate frameworks (ZIFs) are a subclass of MOFs with their tetrahedral networks that resemble those of zeolites with transition metals linked by imidazolate ligands.(Banerjee et al., 2008; Banerjee et al., 2009; Hayashi et al., 2007; Park et al., 2006)

Zeolites are known with the $Al(Si)O_2$ unit formula, whereas ZIFs are recognized by $M(Im)_2$ where M is the transition metal (zinc, cobalt, copper, etc.) and Im is the imidazolate-type linker. Recent MD simulations focused on gas diffusion in ZIFs. For example, self and corrected diffusivities of CO_2, CH_4 and H_2 were simulated using equilibrium MD in ZIF-68 and ZIF-70.(Rankin et al., 2009) That study underlined the importance of including charge-quadrupole interactions on the diffusivity of CO_2. Simulation results clearly revealed that addition of charge-quadrupole interaction terms results in almost one order of magnitude drop in the self and transport diffusivities of CO_2 at low loadings. At high loadings diffusivities calculated from MD simulations with or without charge-quadrupole interaction terms converge towards the same values. The diffusivities of CO_2, CH_4 and H_2 in ZIF-68 were found to be lower than the ones in ZIF-70 since ZIF-68 has narrower pores hence provides stronger confinement of the adsorbate molecules in the pores. Self diffusivity of CO_2 in ZIF-68 and ZIF-69 was also computed by MD simulations.(Liu et al., 2009) The diffusion of CO_2 in ZIF-68 and ZIF-69 was found to be nearly an order of magnitude slower than that in IRMOF-10 and IRMOF-14. This was attributed to the smaller pores of ZIFs and their structural characteristic that causes larger steric hindrance. Pantatosaki and coworkers computed H_2 self diffusion in ZIF-8 using both LJ and FH potentials at 77 and 300 K.(Pantatosaki et al., 2010) The diffusivity predictions showed that quantum mechanical description of H_2 at ambient temperatures is unimportant whereas MD simulations showed a marked difference between the values obtained from the classical and quantum mechanical description at 77 K. A recent MD study computed self diffusivities of H_2, CO_2, CH_4 and N_2 in ZIF-2, ZIF-4, ZIF-5, ZIF-8 and ZIF-9.(Battisti et al., 2011) Results showed that gases except H_2 do not diffuse appreciably in ZIF-5 at least within the time interval of the MD calculations which makes ZIF-5 promising in H_2 separations as a molecular sieve.

Self diffusivities of H_2, CH_4 and CO_2 in bioMOF-11 were computed from canonical ensemble MD simulations at 298 K.(Atci et al., 2011) BioMOFs are another subclass of MOFs that have been recently discovered. They incorporate simple biomolecules and biocompatible metal cations in their structures as linkers and metals.(An et al., 2009a; An et al., 2009b) Gas diffusion in bioMOFs was found to be similar to IRMOFs in terms of magnitude and loading dependence. As can be seen from the literature reviewed so far, most of the MD studies on MOFs computed self diffusivity of gases rather than corrected diffusivities since the calculation of the latter is computationally demanding. Keskin computed both single component self and corrected diffusivities of CH_4 and H_2 as a function of fugacity and pore loading in CPO-27-Ni.(Keskin, 2010a) The diffusivity of H_2 (4×10^{-3} cm^2/s) was faster than CH_4 (6×10^{-4} cm^2/s) as expected. Single component corrected diffusivities were found to be higher than the self diffusivities, since corrected diffusivity by definition includes information on the collective motion of multiple adsorbed molecules that is relevant to net mass transport.

Figure 3 represents the self diffusivity of CO_2 computed from MD simulations in the widely studied MOFs at room temperature. Gas diffusion in MOFs having large pores (IRMOF-1, CuBTC, $Zn(bdc)(ted)_{0.5}$) is higher than the one in MOFs having narrow pores ($Cu(hfipbb)(H_2hfipbb)_{0.5}$, MMIF). The CO_2 self diffusivity decreases with increased adsorbed loading in bioMOF-11, $Cu(hfipbb)(H_2hfipbb)_{0.5}$ and MMIF since CO_2 reaches saturation in these MOFs due to their small pore volumes. The diffusivities in large pore MOFs do not change significantly with increased loadings since CO_2 is further away from the saturation loading in MOFs having large pore volumes.

As the literature cited so far indicated most MD studies focused on diffusion of small gas molecules such as Ar, CH_4, CO_2, N_2, H_2 in MOFs. Limited number of studies investigated diffusion of larger gases. The self diffusivities of hexahydro-1,3,5-trinitro-1,3,5-triazine (RDX) were generated by MD in IRMOF-1, IRMOF-3, IRMOF-10.(Xiong et al., 2010) The trend for the self diffusivities of RDX in MOFs followed the pore sizes, highest in IRMOF-10 and lowest in IRMOF-3. The self diffusivity of ethane, n-butane, n-hexane and cyclohexane in a MOF with the organic linker tetrakis[4-(carboxyphenyl)oxamethyl]methane was studied using MD simulations.(Sun et al., 2011) For linear alkanes, the diffusivities decreased dramatically with increased chain length. The specific MOF studied in this work exhibited high selectivity towards n-hexane as a result of kinetics.

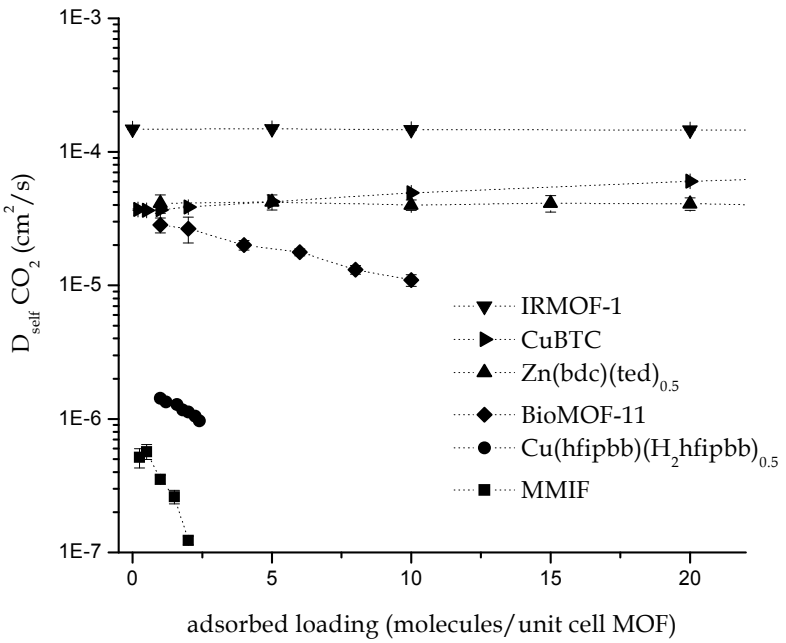

Fig. 3. The self diffusivity of CO_2 in IRMOF-1, CuBTC, Zn(bdc)(ted)$_{0.5}$, bioMOF-11, Cu(hfipbb)(H_2hfipbb)$_{0.5}$ and MMIF at 298 K computed from MD simulations.(Atci et al., 2011; Erucar&Keskin, 2011;Keskin, 2011b; Keskin&Sholl, 2009b;Watanabe et al., 2009)

In some cases, the adsorbate molecules cannot move in the MOF pores at a rate that can be measured by MD simulations. This case is generally observed when the kinetic diameter of the gas molecule is very similar in size to the pore diameter of the MOF. For example, initial MD simulations of adsorbed CH_4 in a rigid Cu(hfipbb)(H_2hfipbb)$_{0.5}$ indicated that CH_4 can not move between adjacent cages on the nanosecond time scales accessible using MD due to the large energy barrier.(Watanabe et al., 2009) The authors used a simple transition state expression to estimate the diffusivity of CH_4 in Cu(hfipbb)(H_2hfipbb)$_{0.5}$ by assuming that the CH_4 hopping rate between cages is,

$$k = \upsilon \cdot \exp(-E_{trans} / k_B T) \tag{10}$$

where υ is the pre-exponential factor (10^{12}-10^{13} s^{-1}), E_{trans} is the transition energy barrier computed using DFT calculations for a flexible MOF, k_B is the Boltzmann constant, T is temperature. These calculations resulted in a one-dimensional diffusivity,

$$D = 1/2 \cdot k \cdot a^2 \tag{11}$$

where a is the cage-to-cage distance along the pore. Keskin studied diffusion of CH_4 and CO_2 in a microporous metal-imidazolate framework and similarly observed that CH_4 diffusion in this MOF is not accessible by MD due to a very large energy barrier (95 kJ/mol) that exists for the adsorbate to move through the pore.(Keskin, 2011b) It is important to note that both Watanabe et al. and Keskin concluded that Cu(hfipbb)$(H_2hfipbb)_{0.5}$ and MMIF are very promising materials for separation of CO_2 from CH_4 since CO_2 diffuses several orders of magnitude faster than CH_4 in these MOFs.

3.2 Mixture diffusion

In most practical applications, gases exist as mixtures rather than single components. For example, in membrane-based separations, at least two gas components exist. The relative transport rates of these components inside the material of interest are crucial in determining the overall performance of a material. Therefore, understanding mixture diffusion in MOFs is essential to design these materials as separation devices. In this section, MD simulations which predicted multi-component mixture diffusion in MOFs will be reviewed. These studies have mostly focused on self diffusivities of CO_2/CH_4, CO_2/H_2, CO_2/N_2, CO_2/CO and CH_4/H_2 mixtures. The diffusion selectivities of MOFs for these gas mixtures have been computed using MD to understand the potential of MOFs in kinetic-based separations. It is important to highlight the fact that number of mixture MD simulations is limited compared to the number of single component MD simulations since characterizing diffusivity of gas mixtures is harder than studying a single species.

Keskin and coworkers provided the first gas mixture diffusivity data in a MOF material using MD simulations.(Keskin et al., 2008) They computed self and Fickian diffusivities of CH_4/H_2 mixtures at various compositions in CuBTC. Theoretical correlations that can estimate mixture self and Fickian diffusivities based on single component data were tested in that work and the predictions of the correlations were compared with the results of direct MD simulations. This will be discussed in detail in Section 5. Keskin and Sholl later showed that if MD (GCMC) simulations are used to compute the mixture diffusivities (adsorbed amounts of each species) in a MOF, one can simply estimate the selectivity of this MOF as a membrane using:(Keskin&Sholl, 2009b)

$$\alpha_{perm,1/2} = \frac{D_{1,self}(q_1,q_2)}{D_{2,self}(q_1,q_2)} \cdot \frac{q_1/q_2}{y_1/y_2} = \alpha_{diff,1/2} \cdot \alpha_{sorp,1/2} \tag{12}$$

where $\alpha_{perm,1/2}$, $\alpha_{diff,1/2}$ and $\alpha_{sorp,1/2}$ represent permeation selectivity, diffusion selectivity and sorption selectivity of species 1 over species 2, respectively. In this approximate expression, the diffusion selectivity is defined as the ratio of self diffusivities in a binary mixture ($D_{i,self}(q_i)$) and the sorption selectivity is described as the ratio of adsorbed molar loadings, q_i. This expression predicts a membrane's selectivity at a specified feed pressure and composition based on a single mixture GCMC simulation and an MD simulation performed

at the loadings determined from this GCMC calculation. Keskin and Sholl computed self diffusivities for CH_4/H_2, CO_2/CH_4 and CO_2/H_2 mixtures in several MOFs, IRMOF-1, IRMOF-8, IRMOF-9, IRMOF-10, IRMOF-14, COF-102, $Zn(bdc)(ted)_{0.5}$ using MD simulations and based on these diffusivities they estimated the membrane selectivity of these MOFs.

Mixture self diffusivities of CH_4/H_2 in CPO-27-Ni and CPO-27-Co were computed at 298 K for a wide pressure range and selectivity of these MOFs in CH_4/H_2 separations were predicted.(Keskin, 2010a) MD calculations were carried out to evaluate diffusion selectivities and permeation selectivities of ZIF-3 and ZIF-10 for CH_4/H_2, CO_2/CH_4 and CO_2/H_2 mixtures.(Keskin, 2011a) Figure 4 shows the diffusion selectivities for these mixtures in the pores of ZIF-3 and ZIF-10 as a function of pressure at room temperature. Using the same approach, Krishna and van Baten computed diffusion selectivities and permeation selectivities for equimolar CO_2/CH_4 and CO_2/H_2 mixtures as a function of total pore loading in CPO-27-Zn, CPO-27-Mg, IRMOF-1.(Krishna&van Baten, 2011) Atci and coworkers evaluated the mixture self diffusivities of CH_4/H_2, CO_2/CH_4 and CO_2/H_2 in bioMOF-11 at the adsorbed loadings calculated from GCMC simulations.(Atci et al., 2011)

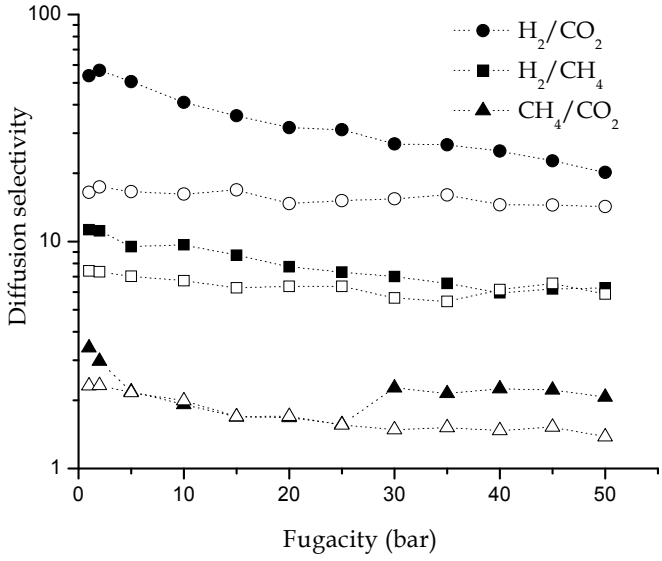

Fig. 4. The diffusion selectivities of ZIF-3 (closed symbols) and ZIF-10 (open symbols) computed from MD simulations. The first species on the label indicates the selected one. The compositions of the bulk gas mixtures are CH_4/H_2:10/90, CO_2/CH_4:10/90 and CO_2/H_2:1/99.(Keskin, 2011a)

The self diffusivities of adsorbed CH_4/H_2 mixtures were examined at different compositions in $Zn(bdc)(ted)_{0.5}$.(Keskin, 2010b) The self diffusivities of CH_4 (H_2) in the CH_4/H_2 mixture were larger (smaller) than pure component CH_4 (H_2) self diffusivity at the same loading. This observation is natural since the fast diffusing H_2 molecules in the mixture speeds up the slowly diffusing CH_4 molecules. Self diffusivities of CO_2/CH_4 and CH_4/H_2 mixtures were computed in ZIF-68 and ZIF-70 using NVT-MD simulations.(Liu et al., 2011) Results

indicated that diffusion of CH_4 is increased with increasing concentration of H_2 in the CH_4/H_2 mixture, while the diffusivity of H_2 decreases with increasing CH_4 concentration. In contrast, the diffusivity of CH_4 was essentially independent of the concentration of CO_2 in the CO_2/CH_4 mixture, while CO_2 diffusivity decreases with increased CH_4 loading, even though the diffusivity of CH_4 is substantially larger than that of CO_2. This unusual behavior was explained in terms of differences in adsorption site preferences due to charge-quadrupole interactions. Another recent MD study examined the self diffusivities of equimolar CO_2/ethane, CH_4/ethane and CO_2/methanol mixtures in Zn(tbip) including the flexibility effects.(Seehamart et al., 2011) Similar to previous observations, faster diffusing molecules accelerate the slower diffusing molecules whereas the slower ones slow down the faster ones through the channel of Zn(tbip).

4. Comparison of diffusivities from molecular dynamics with experiments

Measuring diffusivities of gas molecules in nanoporous materials is a challenging process, therefore experimentally measured diffusion data for gases in the pores of MOFs is still very limited. Stallmach and co-workers(Stallmach et al., 2006) carried out the first experimental study in the literature for diffusivity of hydrocarbons in MOF-5. They measured diffusion of methane, ethane, n-hexane, benzene by pulsed field gradient-nuclear magnetic resonance (PFG-NMR) which is a well-established technique for intra-crystalline diffusion studies in nanoporous materials. Diffusion of methane and ethane in MOF-5 was found to be faster than in NaX which was attributed to the larger pores of the former. This study supplied the first experimental data points for gas diffusion in MOFs for direct comparison between experiments and MD simulations. The measured diffusivity of n-hexane, $3.2\text{-}4.1\times10^{-9}$ m^2/s, was found to be in a good agreement with the value of 2.2×10^{-9} m^2/s predicted by earlier MD simulations(Sarkisov et al., 2004) for a slightly higher loading. However, the self diffusivity of CH_4 measured by PFG-NMR was about one order of magnitude higher than the value of 3.1×10^{-8} m^2/s reported in MD simulations.(Sarkisov et al., 2004; Skoulidas&Sholl, 2005) Stallmach and coworkers attributed this discrepancy to the imperfections that may exist in the MOF structure and loadings used in MD simulations which were lower than the ones considered in the experiments. Zhao and coworkers(Zhao et al., 2009) measured diffusivity of CO_2 in MOF-5 and reported a value (8×10^{-13} m^2/s) which is several orders of magnitude smaller than the one obtained by the MD simulations (4×10^{-9} m^2/s)(Skoulidas&Sholl, 2005) and also significantly smaller than the diffusivity of larger adsorbates such as n-hexane, benzene measured by other groups. This large difference between experiments and simulations can be again attributed to the imperfections in the synthesized MOF structure.

The first experimental exploration of the H_2 self diffusivity in MOFs was performed by quasielastic neutron scattering (QENS) measurements.(Salles et al., 2008) The QENS technique has proved to be very powerful to extract the loading dependence of the diffusivities for a wide range of adsorbates including H_2 diffusivity in zeolites.(Jobic et al., 1999) Combining QENS technique with molecular simulations has been successful in the past to characterize the diffusion mechanism of various adsorbates in nanoporous materials.(Jobic&Theodorou, 2007) The self diffusivities of H_2 in MOFs, MIL-47(V) and MIL-53(Cr) were extracted from QENS measurements and compared with the ones predicted by MD simulations performed in the NVT ensemble using the Evans isokinetic

thermostat.(Frenkel&Smit, 2002) Simulated data was in a good agreement with the experimentally measured data for both MILs. Experiments measured a diffusivity of 9×10^{-8} m^2/s (1.65×10^{-7} m^2/s) and simulations predicted 4.5×10^{-8} m^2/s (1.5×10^{-7} m^2/s) at a loading of 0.5 H_2 molecules per unit cell of MIL-53(Cr) (MIL-47(V)). In a similar study, QENS measurements were combined with MD simulations in NVT ensemble using either Berendsen or Evans thermostat to determine the self diffusivity of H_2 in the same MILs.(Salles et al., 2008) Two different force fields, spherical one site model(Frost et al., 2006) and explicit two atoms model(Yang&Zhong, 2005) were used in MD simulations of H_2. Comparisons between QENS data and MD simulations clearly showed that the two force fields lead to very similar diffusivity values that produce the experimental value. This observation suggests that H_2 diffusion is not significantly affected by the potential model.

A combination of MD and QENS measurements were used to examine the diffusivity of water in MIL-53(Cr).(Salles et al., 2011) The breathing of this MOF upon water adsorption induces a structural transition between narrow pore (NP) and large pore (LP) forms. The self diffusivity of water was faster in LP form (8×10^{-10} m^2/s) compared to the one in NP form (2.5×10^{-11} m^2/s) since the confinement degree was much higher in NP structure. As an extension of this work, self, corrected and transport diffusivities of CO_2 in MIL-47(V) were determined using MD and QENS.(Salles et al., 2010) While self and corrected diffusivities exhibited a decreasing profile with increased loading as expected, transport diffusivity presented an unexpected trend with a decrease at low loadings. This behavior was attributed to the unusual evolution of thermodynamic correction factor. This work was a good example of probing the transport diffusivity of gases in MOFs by combining MD and QENS.

Two experiments studied diffusion of alkanes in MOFs: The diffusivity of n-butane, iso-butane, 2-methylbutane and 2,2-dimethylpropane in CuBTC was investigated using infrared microscopy and MD simulations.(Chmelik et al., 2009) In another work, intracrystalline self diffusivities of propane, propene, n-butane, 1-butene, n-pentane and n-hexane in CuBTC were assessed using PFG-NMR and MD simulations.(Wehring et al., 2010) For the n-alkanes, measured diffusivities within the experimental uncertainty agreed with the values from the MD simulations. The different trends observed in diffusivities of alkanes remained as an unsolved issue.

5. Comparison of diffusivities from molecular dynamics with theories

The prediction of transport properties in chemical mixtures from data taken from single component studies has been a long standing goal in describing mass transport in nanoporous materials. The validation of methods for this task can have great practical significance, but this type of validation can only be considered when high quality mixture diffusion data is available from MD. This section will present the validity of theoretical correlations by comparing their predictions for self diffusivities and Fickian diffusivities with the ones derived from MD. In the literature, Krishna-Paschek's (KP) correlation (Krishna&Paschek, 2002) and Skoulidas, Sholl and Krishna (SSK) correlation(Skoulidas et al., 2003) have been widely used to predict the self diffusivities and Fickian diffusivities of a binary gas mixture, respectively.

Keskin and Sholl studied MOF-5 as a membrane for separation of CO_2/CH_4 mixtures.(Keskin&Sholl, 2007) As discussed in previous sections, in order to study transport

of gas mixtures in membranes mixture diffusivity data is required. However, at the time of that study there was no binary diffusion data available for MOF-5. Keskin and Sholl applied the SSK approach to quantify mixture diffusion of CO_2/CH_4 in MOF-5. This approach combines information from the loading dependence of the single component self diffusivities and corrected diffusivities (computed from MD simulations) with the binary adsorption isotherms (computed from GCMC simulations) to predict the loading and composition dependent matrix of binary diffusion coefficients. The SSK approach defines the mixture diffusivities for all loadings and compositions, an important feature of any description that will be used in examining a wide range of potential membrane operating conditions. Prior tests of this method by comparison with detailed atomic simulations of binary diffusion in silica zeolites and carbon nanotubes indicated that this approach is accurate for a wide variety of adsorbed mixtures.(Sholl, 2006)

A year later, Keskin and coworkers presented the validity of SSK approach in a MOF.(Keskin et al., 2008) They examined both KP and SSK approaches by comparing predictions of these methods with the results of MD simulations for mixture transport of H_2/CH_4 in CuBTC. In order to use SSK correlation, continuous functions describing the pure component self and corrected diffusivities were required. The self and corrected diffusivities of each species in H_2/CH_4 mixture were calculated by MD simulations. Based on these single component diffusivities, the SSK approach predicted the Fickian diffusivities. Mixture MD simulations in a Nosé-Hoover thermostat in the NVT ensemble calculated Onsager coefficients (Equation 4) for H_2/CH_4 mixture and these values were converted to Fickian diffusivities (Equations 5 and 6). The predictions of the SSK approach for the Fickian diffusivities were in good agreement with the direct MD simulations of binary diffusion, suggesting that this approach may be a powerful one for examining multi-component diffusion in MOFs. Mixture self diffusivities were predicted using KP correlations based on single component self diffusivities, corrected diffusivities and fractional loadings. Comparison between KP predictions and mixture MD simulations were also found to be in a good agreement. The SSK approach was also used to obtain Fickian diffusivities of CH_4/H_2, N_2/H_2, N_2/CH_4, CO_2/H_2, CO_2/N_2 mixtures in MOF-5 and CH_4/H_2, CO_2/CH_4 in CuBTC.(Keskin&Sholl, 2009a; Keskin et al., 2009a)

Babarao and Jiang calculated self diffusivities of CH_4 and CO_2 in IRMOF-1 as a function of total loading based on the adsorption of an equimolar mixture using MD simulations and compared their results with the predictions of KP correlation.(Babarao&Jiang, 2008) Theory predictions were found to be in a fairly good agreement with MD simulations particularly for CH_4 diffusivity in IRMOF-1 whereas the CO_2 diffusivity was slightly overestimated by the theory. No certain reasoning was given for this overestimation. The predictions of KP correlations for mixture self diffusivities of CH_4 and H_2 were in reasonable agreement with the results of MD simulations for ZIF-68 and ZIF-70. (Liu et al., 2011)

6. Conclusion and outlook

Because of the large number of different MOFs that exist, efforts to predict the performance of MOFs using molecular modeling play an important role in selecting materials for specific applications. The high number of publications on MOFs and the dense interest of academy and industry on these new nanoporous materials hint that MOFs have numerous potential applications. Since almost all of these applications require the knowledge of molecular

transport rates, MD studies become one of the most beneficial methods in studying MOFs. As is evident from the volume of literature cited, this area is growing rapidly. The development of quantitative information about mixture diffusion in MOFs is just beginning (section 3.2) whereas a significant number of studies have already considered single component gas diffusion in MOFs (section 3.1). Detailed understanding of mixture diffusion in MOFs will be very beneficial for design of MOF membranes, adsorbents, catalysts and sensors. Current opportunities and challenges of using MD simulations in assessing transport rates of gases in MOFs will be addressed below.

6.1 Opportunities

The most significant opportunity of employing MD simulations for obtaining gas diffusivity in MOFs lies in areas where experiments for transport property of interest (transport diffusivities, energy barrier to diffusion) are challenging, not in reiterating properties that have already been addressed experimentally. Measuring diffusivity at a wide range of loadings in the pores at extreme conditions such as infinite dilute loading and/or saturation loading is experimentally difficult. MD simulations can provide information about gas diffusion in MOFs' pores under these conditions. Getting diffusivity data as a function of gas loading is crucial to design membranes, adsorbents, catalysts from MOFs that will work under a wide range of operating conditions.

As addressed in Section 5, the development of quantitative information about mixture diffusion in MOFs is just beginning. Since performing mixture MD simulations for MOFs with large frameworks and for gas mixtures at high adsorbed loadings are computationally demanding, theoretical correlations that predict mixture diffusion based on single component diffusion data are very useful. Recent research search showed that these models yield accurate results for at least simple chemical mixtures in MOFs. Testing and validation of theoretical correlations for predicting gas diffusivity in various subclasses of MOFs will be useful to widely utilize these correlations for different structures.

A great advantage of using MD simulations is to test hypothetical MOF structures for particular applications if the metric describing the performance of a material for the application can be directly calculated. For example, Düren and coworkers used GCMC simulations to design materials with large adsorption capacities for CH_4.(Düren et al., 2004) In a similar way, MD simulations can be used to design materials with slow diffusivities for CH_4 and fast diffusivities for CO_2 to identify materials that will be promising in kinetic separation of CO_2 from CO_2/CH_4 mixtures.

6.2 Challenges

The development of accurate classical interatomic potentials for describing gas diffusion in MOFs remains challenging. From the modeling perspective, it is important to use experimental diffusion data from a broad range of conditions to parameterize interatomic potentials whenever this is practical. However, as discussed in Section 4, the number of experimental data on gas diffusion in MOFs is very limited. Furthermore, developing potentials specific to a MOF structure is not the solution since hundreds of different MOF structures are available. Therefore, efforts to test and improve the transferability of potentials among related families of MOFs will have a great value. One of the major

challenges in using MD simulations for MOFs was addressed in Section 2.2: absence of fully flexible force fields. Rigid framework assumption creates tremendous savings in computational effort. A handful of studies used flexible force fields to include the lattice dynamics effects on gas diffusivity in MOFs. These studies showed that there can be orders of magnitude difference between the diffusivity data from MD simulations using rigid framework and the one using flexible framework, specifically for large adsorbates. This issue indeed turns to be related with the challenge listed above, having accurate flexible interatomic potentials which can be applied to a family of MOF structures in a computationally meaningful time scale.

Another major challenge, especially in diffusivity simulations of CO_2 and N_2, is the choice of method to assign partial charges to MOF atoms. The QM calculations were used to define partial point charges in the literature, however there is no unique way to accomplish this task and different charge decomposition methods can give rather different results. Studies have shown that charge effects are important especially for computing diffusivities at low loadings. Careful studies that establish reliable approaches in charge assignment will be very useful in employing MD simulations for diffusion of polar and quadrupolar molecules in MOFs.

To date MD simulations have been used to compute the transport rates of adsorbates in MOFs. One remaining challenge is to predict the long term stability of MOFs since this is a serious issue in practical applications of these materials. Although stability issue sounds to be most likely addressed by experimental studies, one recent MD study which investigated the mechanism of water induced decomposition of IRMOF-1(Greathouse&Allendorf, 2006) showed that molecular simulations can be also helpful in this area.

7. References

Ackerman, D. M., Skoulidas, A. I., Sholl, D. S.&Johnson, J. K. (2003). Diffusivities of Ar and Ne in Carbon Nanotubes. *Mol. Simulat.*, 29, 677-684.

Allen, M. P.&Tildesley, D. J. (1987). *Computer Simulation of Liquids*. Oxford University Press,New York

Amirjalayer, S., Tafipolsky, M.&Schmid, R. (2007). Molecular Dynamics Simulation of Benzene Diffusion in MOF-5: Importance of Lattice Dynamics. *Angew. Chem. Int. Ed.*, 46, 463-466.

Amirjalayer, S.&Schmid, R. (2009). Mechanism of Benzene Diffusion in MOF-5: A Molecular Dynamics Investigation. *Micropor. Mesopor. Mater.*, 125, 90-96.

An, J., Geib, S.&Rosi, N. L. (2009a). Cation-Triggered Drug Release from a Porous Zinc-Adeninate Metal-Organic Framework. *J. Am. Chem. Soc.*, 131, 8376-8377.

An, J., Fiorella, R., Geib, S. J.&Rosi, N. L. (2009b). Synthesis, Structure, Assembly, and Modulation of the CO_2 Adsorption Properties of a Zinc-Adeninate Macrocycle. *J. Am. Chem. Soc.*, 131, 8401-8403.

Atci, E., Erucar, I.&Keskin, S. (2011). Adsorption and Transport of CH_4, CO_2, H_2 Mixtures in a Bio-MOF Material from Molecular Simulations. *J. Phys. Chem. C*, 115 6833-6840.

Babarao, R.&Jiang, J. (2008). Diffusion and Separation of CO_2 and CH_4 in Silicalite, C_{168} Schwarzite and IRMOF-1: A Comparative Study from Molecualr Dynamics Simulation. *Langmuir*, 24, 5474-5484.

Banerjee, R., Phan, A., Wang, B., Knobler, C., Furukawa, H., O'Keeffe, M.&Yaghi, O. M. (2008). High-Throughput Synthesis of Zeolitic Imidazolate Frameworks and Application to CO_2 Capture. *Science*, 319, 939-943.

Banerjee, R., Furukawa, H., Britt, D., Knobler, C., O'Keeffe, M.&Yaghi, O. M. (2009). Control of Pore Size and Functionality in Isoreticular Zeolitic Imidazolate Frameworks and Their Carbon Dioxide Selective Capture Properties. *J. Am. Chem. Soc.*, 131, 3875-3877.

Bär, N.-K., Ernst, H., Jobic, H.&Kärger, J. (1999). Combined Quasi-Elastic Neutron Scattering and NMR Study of Hydrogen Diffusion in Zeolites. *Magn. Reson. Chem.*, 37, 79-83.

Battisti, A., Taioli, S.&Garberoglio, G. (2011). Zeolitic Imidazolate Frameworks for Separation of Binary Mixtures of CO_2, CH_4, N_2 and H_2: A Computer Simulation Investigation. *Micropor. Mesopor. Mater.*, 143, 46-53.

Bordiga, S., Vitillo, J. G., Ricchiardi, G., Regli, L., Cocina, D., Zecchina, A., Bj.Arstad, Bjørgen, M., Hafizovic, J.&Lillerud, K. P. (2005). Interaction of Hydrogen with MOF-5. *J. Phys. Chem. B*, 109, 18237-18242.

Buch, V. (1994). Path-Integral Simulations of Mixed Para-D-2 and Ortho-D-2 Clusters - the Orientational Effects. *J. Chem. Phys.*, 100, 7610-7629.

Chmelik, C., Kärger, J., Wiebcke, M., Caro, J., van Baten, J. M.&Krishna, R. (2009). Adsorption and Diffusion of Alkanes in CuBTC Crystals Investigated Using Infra-Red Microscopy and Molecular Simulations. *Micropor. Mesopor. Mater.*, 117, 22-32.

Chui, S. S. Y., Lo, S. M. F., Charmant, J. P. H., Orpen, A. G.&Williams, I. D. (1999). A Chemically Functionalizable Nanoporous Material [Cu-3(Tma)(2)(H2O)(3)](N). *Science*, 283, 1148-1150.

Ciccotti, G., Ferrario, M.&Ryckaert, J.-P. (1982). Molecular-Dynamics of Rigid Systems in Cartesian Coordinates: A General Formulation. *Mol. Phys.*, 47, 1253-1264.

Clark, L. A., Gupta, A.&Snurr, R. Q. (1998). Siting and segregation effects of simple molecules in zeolites MFI, MOR, and BOG. *J. Phys. Chem. B* 102, 6720-6731.

Darkrim, F.&Levesque, D. (1998). Monte Carlo Simulations of Hydrogen Adsorption in Single-Walled Carbon Nanotubes. *J. Chem. Phys.*, 109, 4981-4985.

Dietzel, P. D. C., Morita, Y., Blom, R.&Fjellvag, H. (2005). An in Situ High-Temperature Single-Crystal Investigation of a Dehydrated Melal-Organic Framework Compound and Field-Induced Magnetization of One-Dimensional Metaloxygen Chains. *Angew. Chem. Int. Ed. Eng.*, 44, 6354-6358.

Dietzel, P. D. C., Panella, B., Hirscher, M., Blom, R.&Fjellvag, H. (2006). Hydrogen Adsorption in a Nickel Based Coordination Polymer with Open Metal Sites in the Cylindrical Cavities of the Desolvated Framework *Chem. Commun.*, 959-961.

Düren, T., Sarkisov, L., Yaghi, O. M.&Snurr, R. Q. (2004). Design of New Materials for Methane Storage. *Langmuir*, 20, 2683-2689.

Eddaoudi, M., Li, H.&Yaghi, O. M. (2000). Highly Porous and Stable Metal-Organic Frameworks: Structure Design and Sorption Properties. *J. Am. Chem. Soc.*, 122, 1391-1397.

Eddaoudi, M., Kim, J., Rosi, N., Vodak, D., Wachter, J., O'Keeffe, M.&Yaghi, O. M. (2002). Systematic Design of Pore Size and Functionality in Isoreticular MOFs and Their Application in Methane Storage. *Science*, 295, 469-472.

El-Kaderi, H. M., Hunt, J. R., Mendoza-Cortés, J. L., A.P. Côté, Taylor, R. E., M.O'Keeffe&Yaghi, O. M. (2007). Designed Synthesis of 3D Covalent Organic Frameworks. *Science*, 316, 268-272.

Feynman, R. P.&Hibbs, A. R. (1965). *Quantum Mechanics and Path Integrals*. McGraw-Hill,New York

Francl, M. M., Carey, C., Chirlian, L. E.&Gange, D. M. (1996). Charges Fit to Electrostatic Potentials. II. Can Atomic Charges Be Unambiguously Fit to Electrostatic Potentials? *J. Comput. Chem.* , 17, 367-383.

Frenkel, D.&Smit, B. (2002). *Understanding Molecular Simulation: From Algorithms to Applications*. Academic Press,San Diego

Frost, H., Düren, T.&Snurr, Q. (2006). Effects of Surface Area, Free Volume, and Heat of Adsorption on Hydrogen Uptake in Metal-Organic Frameworks. *J. Phys. Chem. B*, 110, 9565-9570.

Greathouse, J. A.&Allendorf, M. D. (2006). The Interaction of Water with MOF-5 Simulated by Molecular Dynamics. *J. Am. Chem. Soc.*, 128, 10678-10679.

Greathouse, J. A.&Allendorf, M. D. (2008). Force Field Validation for Molecular Dynamics Simulations of IRMOF-1 and Other Isoreticular Zinc Carboxylate Coordination Polymers. *J. Phys. Chem. C*, 112, 5795–5802.

Hayashi, H., Cote, A. P., Furukawa, H., O'Keeffe, M.&Yaghi, O. M. (2007). Zeolite A Imidazolate Frameworks. *Nat. Mater.*, 6, 501-506.

James, S. J. (2003). Metal Organic Frameworks. *Chem. Soc. Rev.*, 32, 276-288.

Jhon, Y. H., Cho, M., Jeon, H. R., Park, I., Chang, R., Rowsell, J. L. C.&Kim, J. (2007). Simulation of Methane Adsorption and Diffusion within Alkoxy-Functionalized IRMOFs Exhibiting Severely Disordered Crystal Structures. *J. Phys. Chem. C*, 111, 16618-16625.

Jobic, H., Kärger, J.&Bée, M. (1999). Simultaneous Measurement of Self- and Transport Diffusivities in Zeolites *Phys. Rev. Lett.*, 82, 4260-4263.

Jobic, H.&Theodorou, D. N. (2007). Quasi-Elastic Neutron Scattering and Molecular Dynamics Simulation as Complementary Techniques for Studying Diffusion in Zeolites. *Micropor. Mesopor. Mater.*, 102, 21-50.

Jorgensen, W. L., Maxwell, D. S.&Tirado-Rives, J. (1996). Development and Testing of the Opls All-Atom Force Field on Conformational Energetics and Properties of Organic Liquids. *J. Am. Chem. Soc.*, 118, 11225-11236.

Kapteijn, F., Moulijn, J. A.&Krishna, R. (2000). The Generalized Maxwell-Stefan Model for Diffusion in Zeolites: Sorbate Molecules with Different Saturation Loadings. *Chem. Eng. Sci.*, 55, 2923-2930.

Kärger, J.&Ruthven, D. (1992). *Diffusion in Zeolites and Other Microporous Materials*. John Wiley & Sons,New York

Keil, F. J., Krishna, R.&Coppens, M. O. (2000). Modeling of Diffusion in Zeolites. *Rev. Chem. Eng.*, 16, 71-197.

Keskin, S.&Sholl, D. S. (2007). Screening Metal-Organic Framework Materials for Membrane-Based Methane/Carbon Dioxide Separations. *J. Phys. Chem. C*, 111, 14055-14059.

Keskin, S., Liu, J., Johnson, J. K.&Sholl, D. S. (2008). Testing the Accuracy of Correlations for Multi-Component Mass Transport of Adsorbed Gases in Metal Organic Frameworks: Diffusion of H_2/CH_4 Mixtures in Cu-BTC. *Langmuir*, 24, 8254–8261.

Keskin, S.&Sholl, D. S. (2009a). Assessment of a Metal-Organic Framework Membrane for Gas Separations Using Atomically Detailed Calculations: CO_2, CH_4, N_2, H_2 Mixtures in MOF-5. *Ind. Eng. Chem. Res.*, 48, 914-922.

Keskin, S.&Sholl, D. S. (2009b). Efficient Methods for Screening of Metal Organic Framework Membranes for Gas Separations Using Atomically-Detailed Models. *Langmuir*, 25, 11786-11795.

Keskin, S., Liu, J., Johnson, J. K.&Sholl, D. S. (2009a). Atomically-Detailed Models of Gas Mixture Diffusion through CuBTC Membranes. *Micropor. Mesopor. Mater.*, 125, 101-106.

Keskin, S., Liu, J., Rankin, R. B., Johnson, J. K.&Sholl, D. S. (2009b). Progress, Opportunities, and Challenges for Applying Atomically Detailed Modeling to Molecular Adsorption and Transport in Metal-Organic Framework Materials. *Ind. Eng. Chem. Res.*, 48, 2355-2371.

Keskin, S. (2010a). Comparing Performance of CPO and IRMOF Membranes for Gas Separations Using Atomistic Models. *Ind. Eng. Chem. Res.*, 49, 11689-11696.

Keskin, S. (2010b). Molecular Simulation Study of CH_4/H_2 Mixture Separations Using Metal Organic Framework Membranes and Composites. *J. Phys. Chem. C*, 114, 13047-13054.

Keskin, S. (2011a). Atomistic Simulations for Adsorption, Diffusion, and Separation of Gas Mixtures in Zeolite Imidazolate Frameworks. *J. Phys. Chem. C*, 115, 800-807.

Keskin, S. (2011b). High CO_2 Selectivity of A Microporous Metal-Imidazolate Framework: A Molecular Simulation Study. *Ind. Eng. Chem. Res.*, 50, 8230-8236.

Keskin, S.&Kizilel, S. (2011). Biomedical Applications of Metal Organic Frameworks. *Ind. Eng. Chem. Res.*, 50, 1799-1812.

Kitagawa, S., Kitaura, R.&Noro, S. (2004). Functional Porous Coordination Polymers. *Angew. Chem. Int. Ed.*, 43, 2334–2375.

Krishna, R.&van den Broeke, L. J. P. (1995). The Maxwell-Stefan Description of Mass Transport across Zeolite Membranes. *Chem. Eng. J.* , 57, 155-162.

Krishna, R.&Paschek, D. (2002). Self-Diffusivities in Multicomponent Mixtures in Zeolites *Phys. Chem. Chem. Phys.*, 4, 1891-1898.

Krishna, R.&van Baten, J. M. (2011). In Silico Screening of Metal-Organic Frameworks in Separation Applications. *Phys. Chem. Chem. Phys.*, 13, 10593-10616.

Lee, T. B., Jung, D. H., Kim, D., Kim, J., Choi, K.&Choi, S.-H. (2009). Molecular Dynamics Simulation Study on the Hydrogen Adsorption and Diffusion in Non-Interpenetrating and Interpenetrating IRMOFs. *Catalysis Today*, 146, 216-222.

Li, H., Eddaoudi, M., Groy, T. L.&Yaghi, O. M. (1998). Establishing Microporosity in Open Metal-Organic Frameworks: Gas Sorption Isotherms for Zn(Bdc) (Bdc = 1,4-Benzenedicarboxylate). *J. Am. Chem. Soc.*, 120, 8571-8572.

Li, H., Eddaoudi, M., O'Keeffe, M.&Yaghi, O. M. (1999). Design and Synthesis of an Exceptionally Stable and Highly Porous Metal-Organic Framework. *Nature*, 402, 276-279.

Lii, J.-H., Allinger, N. L.&Yuh, Y. H. (1989). Molecular Mechanics. The MM3 Force Field for Hydrocarbons. *J. Am. Chem. Soc.* 111, 8551-8566.

Liu, B., Yang, Q., Xue, C., Zhong, C.&Smit, B. (2008a). Molecular Simulation of Hydrogen Diffusion in Interpenetrated Metal-Organic Frameworks. *Phys. Chem. Chem. Phys.*, 10, 3244-3249.

Liu, D., Zheng, C., Yang, Q.&Zhong, C. (2009). Understanding the Adsorption and Diffusion of Carbon Dioxide in Zeolitic Imidazolate Frameworks: A Molecular Simulation Study. *J. Phys. Chem. C*, 113, 5004-5009.

Liu, J., Lee, J. Y., Pan, L., Obermyer, R. T., Simizu, S., Zande, B., Li, J., Sankar, S. G.&Johnson, J. K. (2008b). Adsorption and Diffusion of Hydrogen in a New Metal Organic Framework Material:[Zn(Bdc)(Ted)$_{0.5}$]. *J. Phys. Chem. C*, 112, 2911-2917.

Liu, J., Keskin, S., Sholl, D.&Johnson, J. K. (2011). Molecular Simulations and Theoretical Predictions for Adsorption and Diffusion of CH_4/H_2 and CO_2/CH_4 Mixtures in ZIF-68 and ZIF-70. *J. Phys. Chem. C*, 115, 12560-12566.

Loiseau, T., Serre, C., Huguenard, C., Fink, G., Taulelle, F., Henry, M., Bataille, T.&Ferey, G. (2004). A Rationale for the Large Breathing of the Porous Aluminum Terephthalate (Mil-53) Upon Hydration. *Chem.-Eur. J.*, 10, 1373-1382.

Martin, M. G.&Siepmann, J. I. (1997). Predicting Multicomponent Phase Equilibria and Free Energies of Transfer for Alkanes by Molecular Simulation. *J. Am. Chem. Soc.*, 119, 8921.

Martyna, G. J., Tuckerman, M. E.&Klein, M. L. (1992). Nose-Hoover Chains: The Canonical Ensemble Via Continuous Dynamics. *J. Chem. Phys.*, 97, 2635-2643.

Martyna, G. J., Tuckerman, E., Tobias, D. J.&Klein, M. L. (1996). Explicit Reversible Integration Algorithms for Extended Systems. *Mol. Phys.*, 87, 1117-1157.

Mayo, S. L., Olafson, B. D.&Goddard, W. A. (1990). Dreiding: A Generic Force Field for Molecular Simulations. *J. Phys. Chem. C*, 94, 8897-8909.

Millward, A. R.&Yaghi, O. M. (2005). Metal-Organic Frameworks with Exceptionally High Capacity for Storage of Carbon Dioxide at Room Temperature. *J. Am. Chem. Soc.*, 127, 17998-17999.

Mueller, U., Schubert, M., Teich, F., Puetter, H., Schierle-Arndt, K.&Pastré, J. (2006). Metal Organic Frameworks-Prospective Industrial Applications. *J. Mater. Chem.*, 16, 626-636.

Narehood, D. G., Pearce, J. V., Eklund, P. C., Sokol, P. E., Lechner, R. E., Pieper, J., Copley, J. R. D.&Cook, J. C. (2003). *Phys. Rev. B*, 67, 205409-205415.

Pan, L., Sander, M. B., Huang, X. Y., Li, J., Smith, M., Bittner, E., Bockrath, B.&Johnson, J. K. (2004). Microporous Metal Organic Materials: Promising Candidates as Sorbents for Hydrogen Storage *J. Am. Chem. Soc.*, 126, 1308-1309.

Pantatosaki, E., Pazzona, E. G., Megariotis, G.&Papadopoulos, G. K. (2010). Atmic Simulation Studies on the Dynamics and Thermodynamics of Nonpolar Molecules within Zeolite Imidazolate Framework-8. *J. Phys. Chem. B*, 114, 2493-2503.

Park, K. S., Ni, Z., Cote, A. P., Choi, J. Y., Huang, R. D., Uribe-Romo, F. J., Chae, H. K., O'Keeffe, M.&Yaghi, O. M. (2006). Exceptional Chemical and Thermal Stability

of Zeolitic Imidazolate Frameworks. *Proc. Natl. Acad. Sci. U. S. A.*, 103, 10186-10191.

Potoff, J. J.&Siepmann, J. I. (2001). Vapor-Liquid Equilibria of Mixtures Contaning Alkanes, Carbon Dioxide, and Nitrogen. *AIChE J.*, 47, 1676-1682.

Rankin, R. B., Liu, J., Kulkarni, A. D.&Johnson, J. K. (2009). Adsorption and Diffusion of Light Gases in ZIF-68 and ZIF-70: A Simulation Study. *J. Phys. Chem. C*, 113, 16906-16914.

Rappe, A. K., Casewit, C. J., Colwell, K. S., Goddard, W. A.&Skiff, W. M. (1992). Application of a Universal Force Field to Organic Molecules. *J. Am. Chem. Soc.*, 114, 10035-10046.

Rowsell, J. L. C., Spencer, E. C., Eckert, J., Howard, J. A. K.&Yaghi, O. M. (2005). Gas Adsorption Sites in a Large-Pore Metal Organic Framework. *Science*, 309, 1350-1354.

Ruthven, D. M. (1984). *Principles of Adsorption and Adsorption Processes.* Wiley,New York

Ryan, P., Broadbelt, L. J.&Snurr, R. Q. (2008). Is Catenation Beneficial for Hydrogen Storage in Metal-Organic Frameworks? *Chem. Commun.*, 4132-4134.

Sagara, T., Klassen, J.&Ganz, E. (2004). Computational Study of Hydrogen Binding by Metal-Organic Framework-5. *J. Chem. Phys.*, 121, 12543-12547.

Sagara, T., Ortony, J.&Ganz, E. (2005a). New Isoreticular Metal-Organic Framework Materials for High Hydrogen Storage Capacity. *J. Chem. Phys.*, 123, 214707-214713.

Sagara, T., Klassen, J., Ortony, J.&Ganz, E. (2005b). Binding Energies of Hydrogen Molecules to Isoreticular Metal-Organic Framework Materials. *J. Chem. Phys.*, 123, 014701-014706.

Salles, F., Jobic, H., Maurin, G., Koza, M. M., Llewellyn, P. L., Devic, T., Serre, C.&Ferey, G. (2008). Experimental Evidence Supported by Simulations of a Very High H_2 Diffusion in Metal Organic Framework Materials. *Phys. Rev. Lett.*, 100, 245901-245904.

Salles, F., Jobic, H., Devic, T., Llewellyn, P., Serre, C., G.Ferey&Maurin, G. (2010). Self and Transport Diffusivity of CO_2 in the Metal−Organic Framework MIL-47(V) Explored by Quasi-Elastic Neutron Scattering Experiments and Molecular Dynamics Simulations. *ACS Nano*, 4, 143-152.

Salles, F., Bourrelly, S., Jobic, H., Devic, T., Guillerm, V., Llewellyn, P., Serre, C., G.Ferey&Maurin, G. (2011). Molecular Insight into the Adsorption and Diffusion of Water in the Versatile Hydrophilic/Hydrophobic Flexible MIL-53(Cr) MOF. *J. Phys. Chem. C*, 115, 10764-10776.

Sanborn, M. J.&Snurr, R. Q. (2000). Diffusion of Binary Mixtures of CF_4 and N-Alkanes in Faujasite. *Sep. Purif. Technol.*, 20, 1-13.

Sarkisov, L., Düren, T.&Snurr, R. Q. (2004). Molecular Modeling of Adsorption in Novel Nanoporous Metal-Organic Materials. *Mol. Phys.*, 102, 211-221.

Seehamart, K., Chmelik, C., Krishna, R.&Fritzsche, S. (2011). Molecular Dynamics Investigation of the Self Diffusion of Binary Mixture Diffusion in the Metal Organic Framework Zn/Tbip) Accounting for the Frameowrk Flexibility. *Micropor. Mesopor. Mater.*, 143, 125-131.

Sholl, D. S. (2006). Understanding Macroscopic Diffusion of Adsorbed Molecules in Crystalline Nanoporous Materials Via Atomistic Simulations. *Acc. Chem. Res.*, 39, 403-411.

Skoulidas, A. I., Ackerman, D. M., Johnson, J. K.&Sholl, D. S. (2002). Rapid Transport of Gases in Carbon Nanotubes. *Phys. Rev. Lett.*, 89, 185901-185904.

Skoulidas, A. I.&Sholl, D. S. (2003). Molecular Dynamics Simulations of Self-Diffusivities, Corrected Diffusivities, and Transport Diffusivities of Light Gases in Four Silica Zeolites to Assess Influences of Pore Shape and Connectivity. *J. Phys. Chem. A*, 107, 10132-10141.

Skoulidas, A. I., Sholl, D. S.&Krishna, R. (2003). Correlation Effects in Diffusion of CH_4/CF_4 Mixtures in MFI Zeolite. A Study Linking MD Simulations with the Maxwell-Stefan Formulation. *Langmuir*, 19, 7977-7988.

Skoulidas, A. I. (2004). Molecular Dynamics Simulations of Gas Diffusion in Metal-Organic Frameworks: Argon in CuBTC. *J. Am. Chem. Soc.*, 126, 1356-1357.

Skoulidas, A. I.&Sholl, D. S. (2005). Self-Diffusion and Transport Diffusion of Light Gases in Metal-Organic Framework Materials Assessed Using Molecular Dynamics Simulations. *J. Phys. Chem. B*, 109, 15760-15768.

Stallmach, F., Groger, S., Kunzel, V., Kärger, J., Yaghi, O. M., Hesse, M.&Muller, U. (2006). NMR Studies on the Diffusion of Hydrocarbons in the Metal-Organic Framework Material MOF-5. *Angew. Chem. Int. Ed.*, 45, 2123-2126.

Sun, X., Wick, C. D., Thallapallya, P. K., McGraila, B. P.&Danga, L. X. (2011). Molecular Mechanism of Hydrocarbons Binding to the Metal–Organic Framework. *Chem. Phys. Lett.*, 501, 455-460.

Tafipolsky, M., Amirjalayer, S.&Schmid, R. (2007). Ab Initio Parametrized MM3 Force Field for the Metal-Organic Framework MOF-5. *J. Comput. Chem.*, 28, 1169-1176.

Theodorou, D. N., Snurr, R. Q.&Bell, A. T. (1996). *Molecular Dynamics and Diffusion in Microporous Materials. In Comprehensive Supramolecular Chemistry*. Pergamon Press,New York

Uemura, K., Matsuda, R.&Kitagawa, S. (2005). Flexible Microporous Coordination Polymers *J. Solid State Chem.*, 178, 2420-2429.

Watanabe, T., Keskin, S., Nair, S.&Sholl, D. S. (2009). Computational Identification of a Metal Organic Framework for High Selectivity Membrane-Based Gas Separations. *Phys. Chem. Chem. Phys.*, 11, 11389-11394.

Wehring, M., Gascon, J., Dubbeldam, D., Kapteijn, F., Snurr, R. Q.&Stallmach, F. (2010). Self-Diffusion Studies in CuBTC by PFG NMR and MD Simulations. *J. Phys. Chem. C*, 114, 10527-10534.

Wesselingh, J. A.&Krishna, R. (2000). *Mass Transfer in Multicomponent Mixtures*. Delft University Press,Delft

Xiong, R., Odbadrakh, K., Michalkova, A., Luna, J. P., Petrova, T., Keffer, D. J., Nicholson, D. M., Fuentes-Cabrera, M. A., Lewis, J. P.&Leszczynski, J. (2010). Evaluation of Functionalized Isoreticular Metal Organic Frameworks (IRMOFs) as Smart Nanoporous Preconcentrators of RDX. *Sensors and Actuators B: Chemical*, 148, 459-468.

Xu, Q.&Zhong, C. (2010). A General Approach for Estimating Framework Charges in Metal Organic Frameworks. *J. Phys. Chem. C*, 114, 5035-5042.

Xue, C.&Zhong, C. (2009). Molecular Simulation Study of Hexane Diffusion in Dynamic Metal Organic Frameworks. *Chinese J. Chem.*, 27, 472-478.

Xue, C., Zhou, Z., Liu, B., Yang, Q.&Zhong, C. (2009). Methane Diffusion Mechanism in Catenated Metal Organic Frameworks. *Molecular Sim.*, 35, 373-380.

Yaghi, O. M., O'Keeffe, M., Ockwig, N. W., K.Chae, H., Eddaoudi, M.&Kim, J. (2003). Reticular Synthesis and the Design of New Materials. *Nature*, 423, 705-714.

Yang, Q.&Zhong, C. (2005). Molecular Simulation of Adsorption and Diffusion of Hydrogen in Metal-Organic Frameworks. *J. Phys. Chem. B*, 109, 11862-11864.

Yang, Q.&Zhong, C. (2006). Understanding Hydrogen Adsorption in Metal-Organic Frameworks with Open Metal Sites: A Computational Study. *J. Phys. Chem. B*, 110, 655-658.

Zhao, Z., Li, Z.&Lin, Y. S. (2009). Adsorption and Diffusion of Carbon Dioxide on Metal Organic Framework (MOF-5). *Ind. Eng. Chem. Res.*, 48, 10015-10020.

14

Molecular Dynamic Simulation of Short Order and Hydrogen Diffusion in the Disordered Metal Systems

Eduard Pastukhov, Nikolay Sidorov,
Andrey Vostrjakov and Victor Chentsov
Institute of Metallurgy, Russian Academy of Sciences, Ural division
Russian Federation

1. Introduction

Main concepts of Hydrogen permeability (HP) mechanism for the pure crystal metals are already stated. There are well-founded theoretical models and numerous experimental researches. As far as disordered systems (in which Hydrogen solubility is much more, than in crystal samples) are concerned, such works appear to be comparatively recent and rare. Particularly, they are devoted to Hydrogen interaction of with amorphous structures. Deficiency of similar researches is caused by thermo-temporal instability of amorphous materials structure and properties.

Unlike crystal alloy, where interstice volumes are presented discretely only by tetrahedron and octahedron cavities, small and big interstice cavities distribution in an amorphous alloy is close to Gaussian function (Polukhin and Vatolin, 1985, Polukhin et.al, 1984, 1986). Thus Hydrogen energy distribution function form in the amorphous alloys cavities is close to the main RDF peak which is approximated by Gaussian function. Inter-cavities transitions are strongly correlated, and the stationary states contribution to the Hydrogen atoms motion is negligible.

Amorfizator-elements (Si, B, C, etc.) insertion into the amorphous metals reduces number of large cavities (octahedrons) providing most energetically favourable Hydrogen migration path. It reduces metal absorption ability, as well as hydrogen diffusion motion intensity, reducing Hydrogen permeability.

Amorphous alloys absorption ability of hydrogen is defined by number and size of cavities for hydrogen insertion, as well as the hydride forming elements (Ti, Zr, Hf, etc.) content in an alloy. Hydrogen diffusion factor in the amorphous alloys depends on its concentration.

Crystal and amorphous Palladium alloys are widely used in membranes for high pure Hydrogen producing. Literary data analysis shows possibility of filtering alloys production for hydrogen based on less expensive metals: V, Nb, Zr, Ta, etc., characterized by high Hydrogen solubility, which defines alloy Hydrogen permeability by diffusion factors as well as Palladium. Negative effect of these elements hydrides formation should be inhibited

by the other metals additives. In the plasma-arc (PAM) and electron beam (EBM) refining melting of the Nb, Zr, Ta, etc. metals, the necessity of impurity elements (especially hydrogen and iron) transport research in such melts arises. Electric and magnetic fields affect to liquid metal and its impurities during melting have been indicated in the number of researches as well.

Therefore research of an electric field intensity affect to the impurity elements transport properties in the liquid metals is very urgent.

Amorphous and liquid systems based on Fe, Pd, Zr, Ta, Si with and without Hydrogen researches are presented in this work. Short order structure experimental results and molecular dynamics simulations are considered. Partial structure factors, radial distribution function of atoms, its mean square displacement and diffusion factors are calculated. Hydrogen concentration affect to its mobility and short order parameters in the system are analyzed. Electric field intensity affect to liquid metals are compared with literary data on impurities removal from Zr and Ta in plasma-arc melting in the Hydrogen presence.

2. Molecular dynamics calculation method

Molecular dynamics method (MD) had been primary proposed in (Alder & Wainwright, 1959). The method allows particles real-time motion analysis using classic equations. So far it's the only numeric method for dens medium dynamic research. Generally accepted nowadays MD calculation scheme is the following. A system consisting of several hundred particles with the given interparticle interaction potential is considered. Classic equations of the particles motion are numerically resolved using Verlet algorithm (Verlet, 1976). It calculates i-particle coordinate on the following (k+1)-step by coordinates on given k- and previous (k-1)-steps.

$$r_i(k+1) = 2r_i(k) - r_i(k-1) + \frac{F_i(k)(\Delta t)^2}{m} \tag{1}$$

Where r_i – radius-vector of particle, m - its mass, F_i – resultant force and Δt – time step. Velocity doesn't take part in calculation. Other algorithms of motion path calculation are considered in (Polukhin & Vatolin 1985). Periodic boundary conditions are used in motion equation solution, i.e. if some particle with p_i - momentum exits through cube face, then other particle with the same momentum enters through opposite face symmetric relatively plane in the center of cube. Interaction in the MD models is defined as the pair interaction potentials resultant force in the pair approximation models. Temperature of system is defined basing on its total kinetic energy. Diffusion factors are calculated from mean square displacement of the particles in model $\left\langle r_i^2(t) \right\rangle$ by the major of steps.

$$D = \frac{1}{6t} < r_i^2(t) >, \tag{2}$$

Where $<r^2(t)>$ – mean square displacement of Hydrogen atoms at t – time.

Disorder systems short order is characterized by of radial distribution function of atoms g (r) (RDF) and its Fourier transform – structure factor s(k). Radial distribution function RDF

determines location probability any atom at r distance from the chosen atom and described in MD model by the well-known formula:

$$g(r) = \frac{(\Delta N)L^3}{4\pi r^2 \Delta r N}, \tag{3}$$

Where ΔN — number of particles in a spherical layer thickness Δr on r distance from the chosen particle: L — cube edge length of basic cell and N — number of its particles. Structure factor s(k) is defined by following equation:

$$s(k) = 1 + \frac{4\pi N}{L^3} \int_0^{r_m} [g(r) - 1] \frac{Sin(kr)}{kr} r^2 dr, \tag{4}$$

Where k is wave vector, $k = (4\pi \text{ Sin } 2\Theta)/\lambda$ and r_m is RDF attenuation radius.

Minimum k value in the MD – experiment is inversely proportional to main cube edge and calculations for smaller k, have not physics sense. Final configuration for RDF in our calculation was chosen its constant value. This condition needs no less than 10000 steps. Coordination number had been calculated by following formula:

$$Z = \frac{4\pi N}{L^3} \int_0^{r_m} g(r) r^3 dr \tag{5}$$

Molecular dynamics calculation had been done using microcanonical (NVE) ensemble.

The particles of system were randomly distributed in the basis MD – cell. Interpartial potentials and its numerical value factors had been taken from works of (Varaksin & Kozjaychev, 1991, Zhou et.al, 2001, Rappe et.al, 1992). General questions of this method using had been considered in details by authors (Polukhin & Vatolin, 1985).

3. Hydrogen in amorphous and recrystallized Fe-Ni-Si-B-C-P alloy (experiment)

Experimental researches of Hydrogen absorption affect to structure and physical-chemical properties of transition metals (Palladium and Iron) alloys are presented by works (Pastukhov et.al, 1988). This researches indicated, that Hydrogen absorption leads to considerable shift of structure relaxation start and finish to the higher heating temperature interval. This process provokes significant modification of the amorphous (Iron based) material strength properties and leads to increased embrittlement. All mentioned changes are adequately displayed on the atoms distribution curves (fig. 1), obtained from diffraction experiment data (Vatolin et.al, 1989).

Hydrogen permeability of the amorphous and recrystallized Fe based ($Fe_{77.333}Ni_{1.117}Si_{7.697}B_{13.622}C_{0.202}P_{0.009}$) alloy membrane (25 micron thickness) was researched by stationary stream method (Pastuchov et.al, 2007). Recrystallized alloy was prepared by vacuum annealing at 400^0C from amorphous specimen.

Molecular Hydrogen injection to input side of degasified specimen at maximal acceptable temperatures (300°C for amorphous and 400°C for recrystallized specimens) didn't lead to

noticeable output stream increase. At 10 torr Hydrogen pressure the stream achieved $3.8 \cdot 10^{12}$ sm^{-2}/s value. Hydrogen medium glow discharge had been used in order to delete the specimen passivation layer. Hydrogen ions, formed in glow discharge, simply penetrate to the specimen bulk (Lifshiz, 1976). We observed significant penetrating stream in this procedure. All researches have been carried out at 2 torr Hydrogen pressure, when the discharge is most stable.

Temperature dependences of the stable (stationary) Hydrogen stream had been defined for amorphous and recrystallized specimens. Lower limit of the researched temperature interval was defined as reliable stream registration possibility which had been stated as 125^0C for amorphous and 200^0C for crystal specimens. Most impotent difference between two states of the researched alloy is observed as non-monotonic output stream increase at temperature expansion in amorphous state.

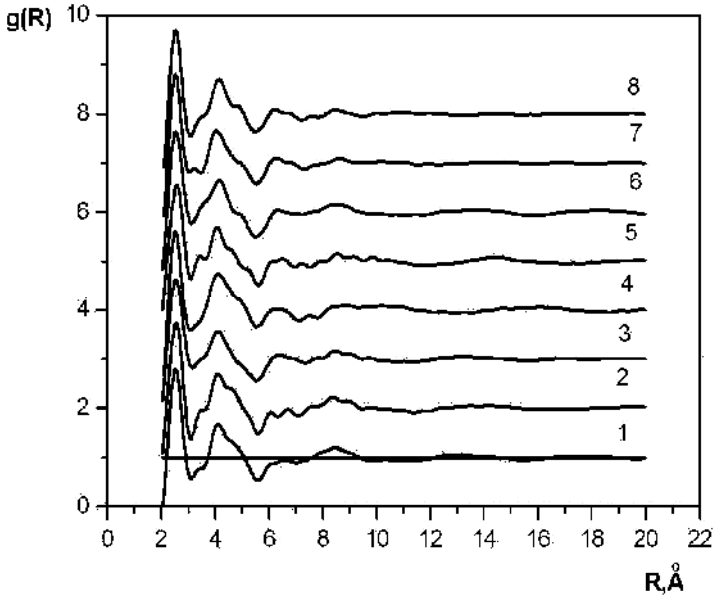

Fig. 1. Atoms radial distribution for amorphous ($Fe_{77.3}Ni_{1.1}Si_{7.7}B_{13.6}C_{0.2}P_{0.009}$) alloy with Hydrogen ($<H_2>$) and Hydrogen absence (1 - 275^0C; 2 - 300^0 + $<H_2>$; 3 - 425^0C; 4 - 425^0C + $<H_2>$; 5 - 450^0C; 6 - 475^0C +$<H_2>$; 7 - 550^0C; 8 - 575^0C +$<H_2>$).

Hydrogen stream stabilization has different nature in amorphous and recrystallized specimens. But both situations are characterized by rapid increase of output stream with characteristic 30÷60s stabilization times.

Amorphous membrane is characterized by very elongated hydrogen output with 6000s stabilizing time after rapid output increase at temperatures from 125^0 C up to 225°C. Hydrogen stream dependence on inverse temperature is illustrated by fig.2. The dependence isn't monotonous and has maximum in 200°C region.

The stream increases from 125^0C and achieves maximum $3.3 \cdot 10^{13}$ $sm^{-2}s^{-1}$ value at 200°C. Subsequent heating demonstrates anomalously sharp decrease. Second specimen follows to classic Arrhenius dependence with activation energy 17.9 kj/mol and maximum stream

value $2.7 \cdot 10^{13}$ $sm^{-2}s^{-1}$ at 375^0C (fig. 2). Amorphization of the alloys leads to considerable free volume increasing, which increases Hydrogen permeability, solubility and diffusion. Special attention should be directed to the Hydrogen permeability changing (by order) effect with comparatively low solubility increase. This effect is explained by competition from amorphization-elements, which occupy large Bernal polyhedron-cavities, first of all in the high amorphization-elements concentration region (Polukhin et.al, 1997). "Overextended" stream yield to the stationary value evidently related to reversible diffusant capture (Herst,1962). Thus Hydrogen escape probability from the traps increases faster than capture probability. It was experimentally showed, that at temperature increase up to 200^0C, low increase Hydrogen streams observed in reality. Its decrease begins after 200^0C. Such behavior is proper namely for the traps with activation energies of escape and capture $E_{esc}>E_{cap}$.

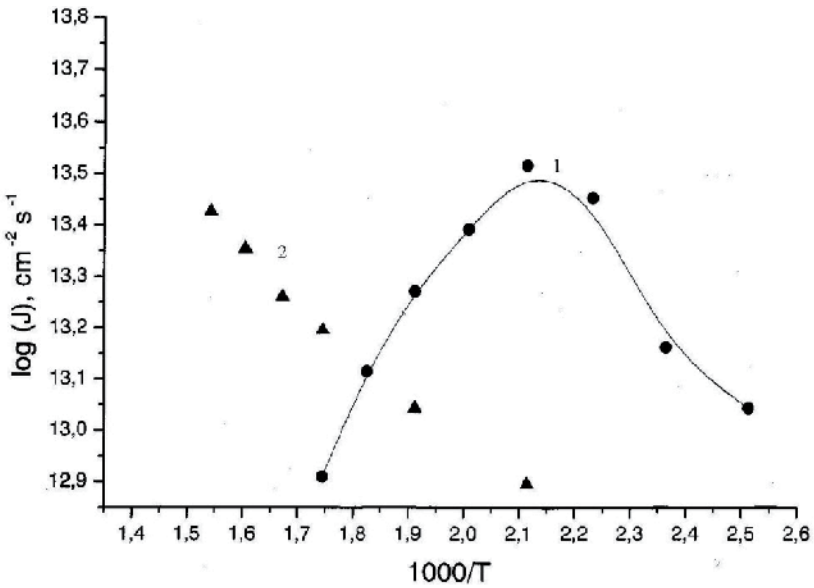

Fig. 2. Stationary Hydrogen stream (J) dependence on temperature. (1 – amorphous alloy, 2 – recrystallized alloy)

Penetrating stream decreasing in amorphous specimen for temperature interval from 200^0 C up to 300^0 C most probably is related to surface processes. Since penetrating stream is three orders less than incident stream to input surface ($V_f \approx 10^{16} cm^{-2}s^{-1}$), balance of streams is written as

$$V_f = V_T + V_r \tag{6}$$

where $V_T + V_r$

$$V_r = V_f C_i / C_{max} \quad \text{and} \quad V_T = b_i \cdot \exp(-E_i/RT) C_i \tag{7}$$

are streams of ion-induced reemission and thermal desorption on input side. Term C_i is Hydrogen concentration in no-violated alloy structure near input surface, b_i – pre-exponent factor. Maximal obtainable concentration in near-surface layer C_{max} at room temperature

(when thermal desorption is negligible) is estimated as 10^{18} at/cm^3 (Grashin et.al, 1982, Sokolov et.al, 1984). In assumption, that C_2 – concentration n on output side much less than C_i, for stationary penetrating stream, we obtain following expression

$$J = A \cdot \exp(-E_d/RT)/(1 + B \cdot \exp(-E_i/RT)) \quad (8)$$

where E_d – diffusion activation energy. The rates of diffusant capture and release are equal in stationary state and do not affect to stationary stream intensity. Thus equation (8) doesn't include interaction parameters of Hydrogen with traps. Approximation results are displayed by solid curves at fig. 3. Energy values E_d^{am} = 40.8, E_i^{am} = 86.7 kj/mol for amorphous, and E_d^{cr} = 71.2, E_i^{cr} = 51.7 kj/mol for crystal specimens give good agreement with experiment data.

Concentration calculation on input membrane side by (6) and (7) equations accounting thermodesorption activation energies is illustrated by fig. 4. Parameter C_{max} , used in calculation does not any effect to activation energies, but affects only to pre-exponent factors.

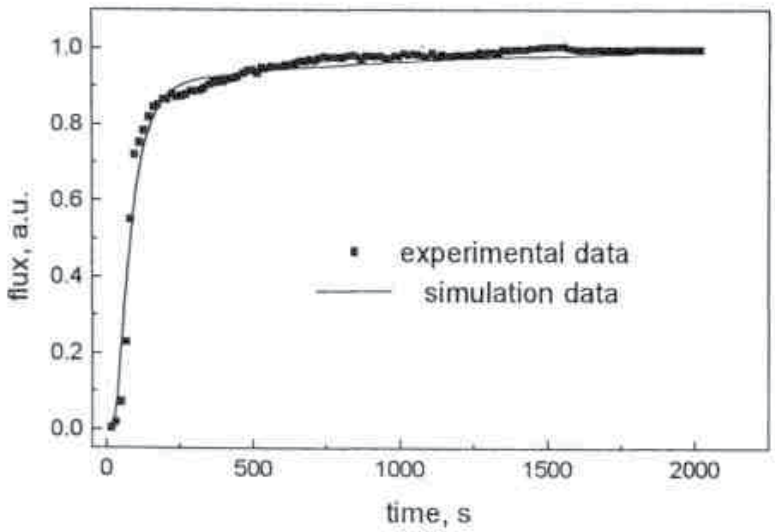

Fig. 3. Stable (stationary) Hydrogen stream through amorphous membrane.

Surface processes and correlation of E_d and E_i values define stationary stream temperature dependence. Concentration C_{am} for an amorphous alloy has C_{max} value up to 175°C temperature and penetration rate is defined by diffusion, at that stream increases. Following temperature increase leads to exponential C_i concentration decrease, and $E_d<E_i$ correlation leads to stream decreasing. Input C_{cr} concentration for recrysallyzed alloy decreases in all temperature interval (fig. 4, curve 2), and $E_d > E_i$ relation leads to classic Arrhenius dependence

$$J \approx \exp(-E_a/RT) \quad (9)$$

where $E_a=E_d-E_i$ ~ 19.6 kj/mol in our calculation, that is close to E_a = 17.9 kj/mol, obtained experimentally.

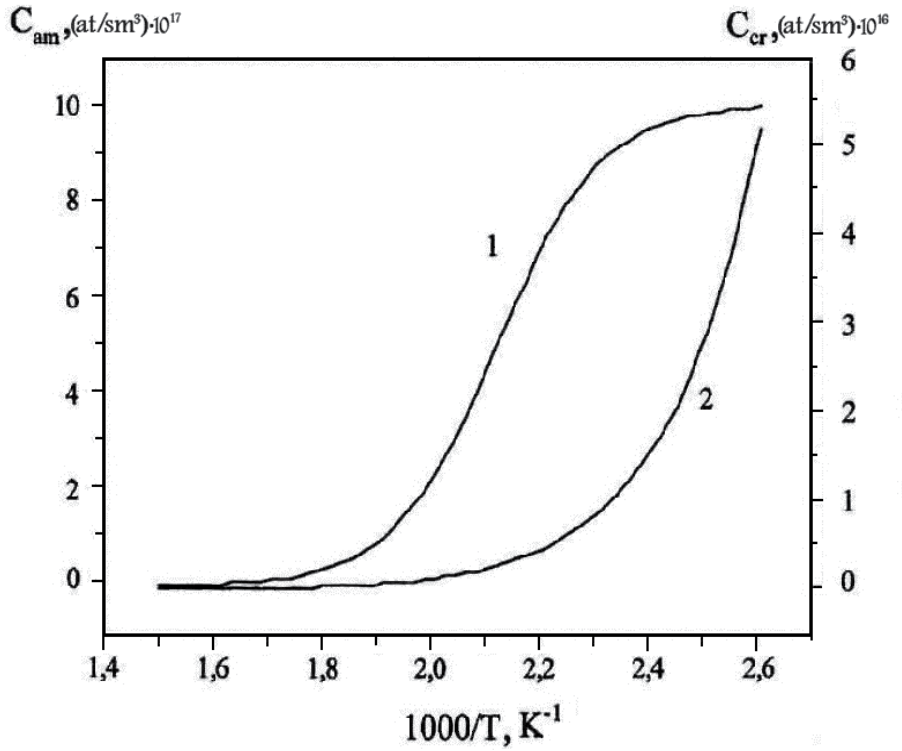

Fig. 4. Temperature Hydrogen concentration dependence at input side of membrane (1- amorphous alloy, 2- recrystallized alloy).

Diffusion activation energies related to specimens structure, obviously. Excess free volume presence in the amorphous alloy provides less energy consumption for the Hydrogen atom jumps from one interstice to another. Besides some part of interstices may perhaps be wrong Bernal cavities, i.e. be deformed. Thermodesorption activation energy in recrystallized alloy is less than in amorphous one $E_i^{cr} < E_i^{am}$. This fact could be explained by surface reconstruction and changing of the passivation layer to the Hydrogen desorption.

4. Hydrogen effect to the short order structure for liquid, amorphous and crystal silicon

Due to its semiconductor properties, Silicon had been found wide application in the recent microelectronics and electronic technique. Hydrogen has been generally recognized to play impotent function in the different complex formation in the amorphous Silicon. Attention to the Hydrogen behavior in Silicon is explained by its affect to physical-chemical properties, which gives opportunity of new materials with necessary properties development.

Hydrogen diffusion in crystal Si was researched by TBMD (tight binding molecular dynamics) method (Panzarini. & Colombo, 1994). The model considered single Hydrogen atom in 64-atoms super-cell of Silicon. On the TBMD data the authors supposed, that

Hydrogen diffusion mechanism in crystal Silicon acts according to Arrhenius low, and there are not other "anomalous" mechanisms but, for example, the single skips. Amorphous Silicon short order structure had been researched in the works of (Pastukhov et.al, 2003, Gordeev et.al, 1980). It had been found, that amorphous Silicon retains covalent bond type with coordination number Z=4.2, in difference with melt, where the bond has metallic character (Z=6.4).

The data of experimentally estimated values for Hydrogen diffusion factors in amorphous Si are limited, and published results are not in good agreement. The experimental research data on amorphous Silicon Hydrogen permeability are presented in the work (Gabis, 1997). For Hydrogen transfer through amorphous Silicon film the author used model, where besides diffusion, low rate of the processes on surface, as well as capture and temporal keeping of the Hydrogen diffusing atoms in traps had been taken into consideration. It's the author's opinion that Hydrogen transfer related to local bonds Silicon-Hydrogen reconstruction.

Physics-chemical properties of computer models (containing thousands atoms) for amorphous Silicon, could be described in terms of empiric potentials (Tersoff, 1986, Stillimger & Weber, 1985).

We used interparticle potential (Tersoff, 1986) and MD method to calculate structure parameters and diffusion factors of Si and H in crystal, amorphous and liquid Silicon (Pastukhov, 2008).

Calculations had been carried out for system, containing 216 Silicon and 1 Hydrogen atoms in basic cube using periodic boundary conditions. Cube edge length had been had been taken according to experimental density system under consideration at 298K temperature. Molecular dynamic calculation results are presented on fig. 5, 6 and in table 1. Valent angles mean values were found from first and second coordination sphere radii using following formula:

$$\varphi = 2\arcsin\left(\frac{r_2}{2r_1}\right) \tag{10}$$

Experimental data analysis obtains, that, in certain approximation, there is one metastable equilibrium configuration of atoms with coordination number 4 in the c-Si и a-Si materials with Hydrogen as well as without it. First peak sharpness of intensity curve (fig. 6) indicates comparatively large ordering in a-Si. First and second maxima of RDF curve practically coincide. Differences are observed in consequent part of curves. Third maximum of RDF for a-Si is practically absent.

Computer calculations for Si-H model found, that Hydrogen diffusion mechanism in crystal Si with n – conductivity type is realized by electro-neutral Hydrogen atoms migration through tetrahedral interstices according to the same principle as screened proton diffusion in the amorphous transition metals (Vatolin et.al, 1988). However Hydrogen atom moving path trough matrix nodes accompanied by Si-Si bond breakage due to Si atom 0.05nm shift from the node occupied and formation of chemical bond Si-H and free Si bond, left in the lattice node.

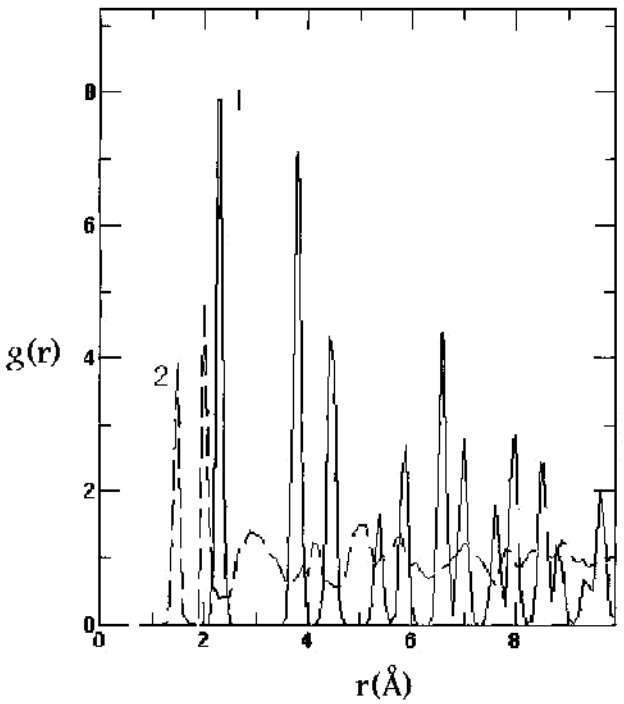

Fig. 5. RDF of the Si-Si (1) and Si-H atoms (2) for crystal Silicon with Hydrogen at 278K.

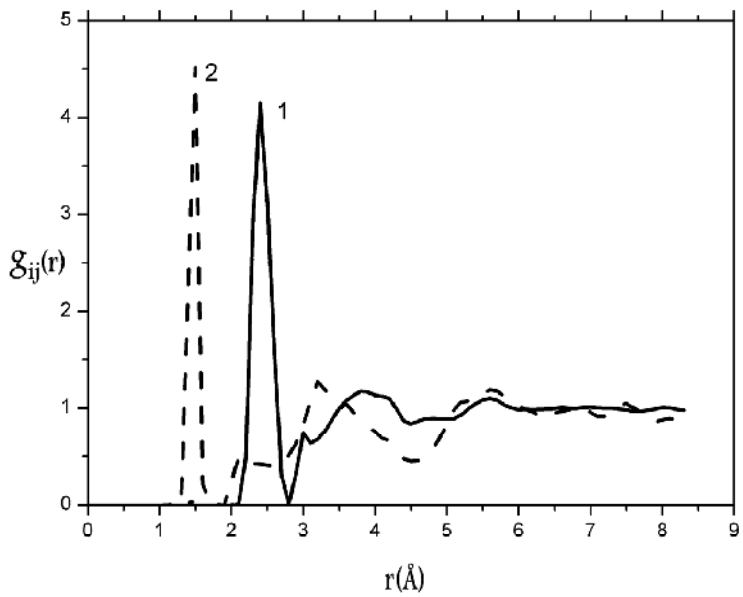

Fig. 6. RDF of the Si-Si (1) and Si-H atoms (2) for amorphous Silicon with Hydrogen at 278K.

Silicon phases structure	RDF Peaks positions, Nm.		Coord. numb. Z	Mean angle inter-bonds φ	Diff. factors D, cm^2/s	Density ρ, g/cm^3.
	r_1	r_2				
1	2	3	4	5	6	7
Diamond	0,236	0,384	4			
White Tin (calculation)	0,25	0,355; 0,42	6,3			
Liquid Si (1700K)			6,4	103,9±26,8	$6,4 \cdot 10^{-5}$	
a-Si (300K)	0.241		4.6	106.3±21		2.294
a-Si, (298K) Our data MD-model	0.240	0.386	4,2	106		2.10
a-Si+H, (298K) Our data MD-model	(Si-Si) 0,250 (Si-H) 0.15	(Si-Si) 0.450 (Si-H) 0.218	4,2	(φ_{Si-Si}) 180 (φ_{Si-H}) 90	D_{Si} $1.94 \cdot 10^{-5}$ D_H $4.83 \cdot 10^{-4}$	2.10
c-Si+H, (298K) Our data MD-model	(Si-Si) 0,231 (Si-H) 0.15	(Si-Si) 0,380 (Si-H) 0.215/0.27	4	(φ_{Si-Si}) 110 (φ_{Si-H}) 90	D_{Si} $2.45 \cdot 10^{-6}$	2.33

Table 1. Short order parameters for crystal (c-Si), liquid (l-Si) and amorphous Silicon (a-Si). (Pastukhov et.al, 2003, Gordeev et.al, 1980).

5. Hydrogen diffusion in the amorphous Pd-Si alloy

Model system (Pastukhov et.al, 2009), used in MD method for Hydrogen behavior research in the amorphous Pd-Si alloy at T=300K temperature, was presented by 734 Palladium particles, 130 Silicon particles and 8 Hydrogen particles in the cubic cell with 2.44869nm edge length. Motion equation integration was carried out with $1.8 \cdot 10^{-15}$s time steps. Short order structure analysis of the amorphous Pd materials (Sidorov & Pastukhov, 2006) and Pd-Si (15 ат.%) with Hydrogen had been carried out using partial functions $g_{ij}(r)$ of Pd-Pd, Pd-Si and Pd-H pairs (Pastukhov et.al, 2009) (fig. 7 and 8).

Second peak of $g_{ij}(r)$ curve for Pd-H (fig. 7) has change symmetry shoulder in comparison with $g_{ij}(r)$ curve for Pd-Pd.

Refer to (Herst, 1962), distances, related to second g(r) peak are formed by 3 types of contact: a) two Pd atoms through Pd atom ($r = 2r_0$); b) two Pd atoms trough через two Pd atoms ($r = 1.732r_0$); c) two Pd atoms through three Pd atoms ($r = 1.633r_0$). More easy Hydrogen affected turns contact of Pd-Pd atoms, realized by b) - type. Amorphous Palladium structure changes, due to Hydrogen presence, are caused by re-distribution of formed distances to its increasing (right sub-peak of RDF second peak). Observed second peak splitting inversion of $g_{ij}(r)$ for amorphous Palladium with Hydrogen obtains information about short order reforming of metal. Second peak differences of $g_{ij}(r)$ for Pd-Pd and Pd-H indicate strong Hydrogen affect to Palladium matrix structure.

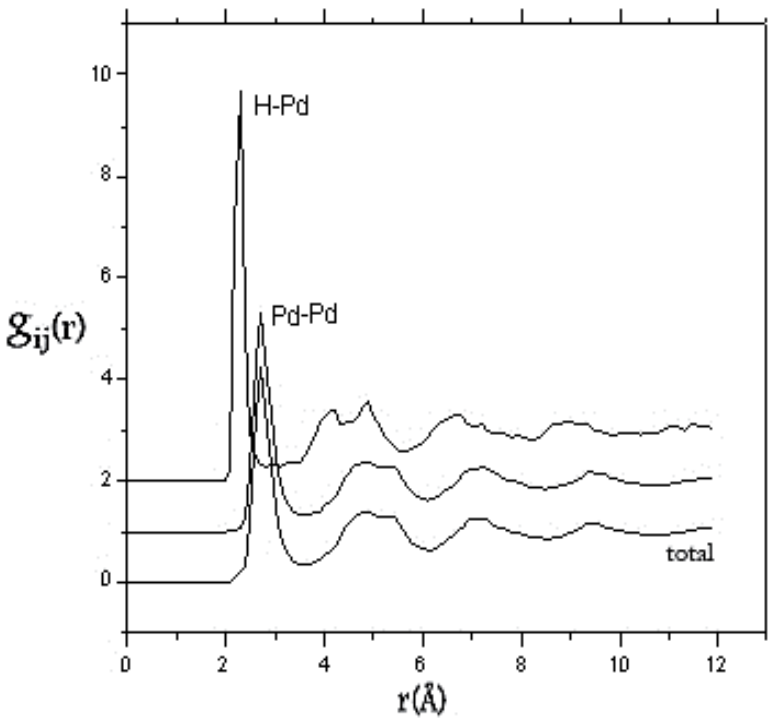

Fig. 7. Partial RDF in an amorphous Pd-H – system.

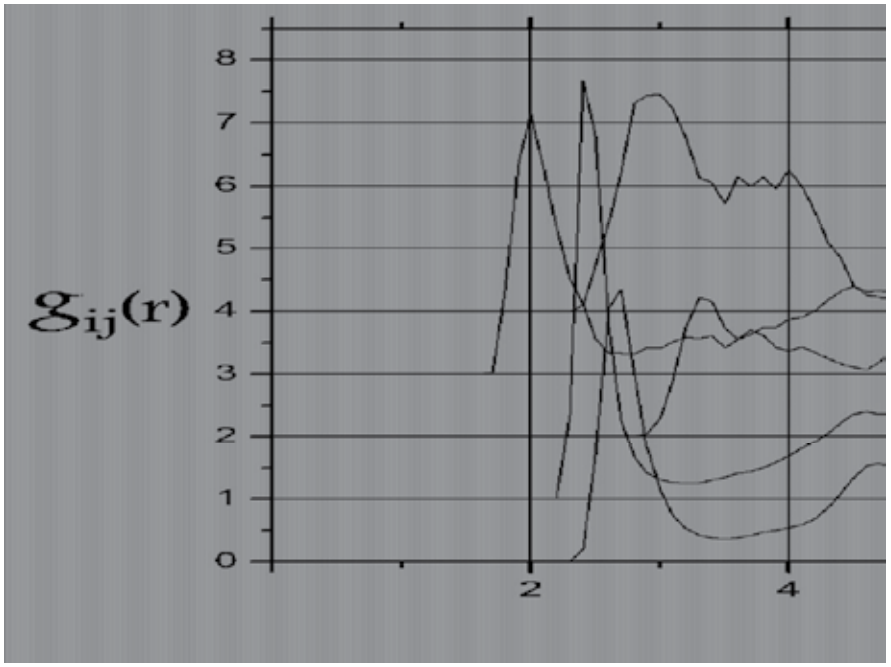

Fig. 8. Partial RDF for amorphous Pd-Si (15 at.%)-H alloy.

Partial RDF for Si-Si indicates to preferential Silicon atoms distribution relatively each other in the second coordination sphere, i.e. Palladium atoms cover Silicon atoms by the first coordination shell (fig. 8).

The effects observed in MD – model allow assumption about micro-grouping presence, which are identified as stable hydride structures, indicating to high degree of dissipative structures of Pd-H, Si-H - types presence (Ivanova et.al,, 1994, Avduhin et.al, 1999).

Hump, observed close to 3.44nm^{-1} (fig. 9) on our calculated and experimental (Polukhin 1984) structure factor curves for amorphous state with Hydrogen as well as its absence, hasn't so far interpretation. Authors (Polukhin & Vatolin, 1985) have shown by statistic geometry method, that most often Voronoy-polyhedrons occurred in the amorphous metals are recognized as polyhedrons with 12, 13, 14, 15 coordination numbers for given sties-atom.

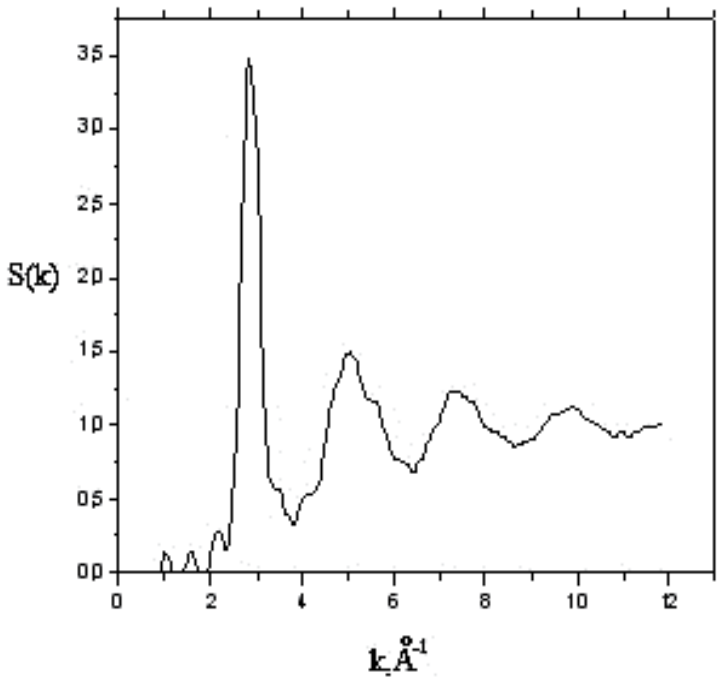

Fig. 9. Structure factor for amorphous Pd-Si with Hydrogen obtained by MD – model calculation.

Mixed type micro-groupings occurred, in $Pd_{85}Si_{15}$ alloy, are formed with most presence of BCC and FCC polyhedron type. Particles number does not exceed 13-14 in one cluster.

Amorphous Pd-Si alloy structure model is supposed to consist from Palladium micro-groupings, characterized by distorted triangle pyramid form with 2.5Å leg (Pd-Si) and regular 2.71Å leg (Pd-Pd) base triangle (Polukhin, 1984)

Separately chosen Pd, Si and H atoms motion in our model is different by its character.

Calculated diffusion factors values for Pd-H system were: $D_H = 18.8 \cdot 10^{-6}$ cm^2·s^{-1}, $D_{Pd} = 3.4 \cdot 10^{-6}$ cm^2·s^{-1}, and $D_H = 6.67 \cdot 10^{-6}$ cm^2·s^{-1}, $D_{Pd} = 2.0 \cdot 10^{-6}$ cm^2·s^{-1} for amorphous Pd-Si-H alloy.

As MD model calculation show, not only Silicon atoms can affect Hydrogen mobility, but Hydrogen itself can change considerably diffusion of the other components of alloy. For example, Pd-Si system without Hydrogen has $D_{Si} = 4.93 \cdot 10^{-6}$ cm^2·s^{-1}, but $D_{Si} = 2.53 \cdot 10^{-6}$ cm^2·s^{-1} with Hydrogen presence. There are different energy zones in an amorphous system, which lead to different time mode of Hydrogen diffusion.

Therefore low of defunding particle energy change in the amorphous metals should be statistic nature and be defined by the cavities type distribution type. Due to little part of the octahedron cavities, three types of diffusion process are possible in the amorphous metals. That are octahedron-octahedron, octahedron-tetrahedron-octahedron, octahedron-octahedron, tetrahedron-tetrahedron. Due to volume changing in the hydrogenization process for crystal is similar to that for amorphous alloys (Kircheim et.al, 1982), this fact indirectly proves, that hydrogen occupies similar Bernal polyhedrons (tetrahedrons and octahedrons). Interstice diffusion factors in disordered material can be calculated as temperature and concentration function with hydrogen energies distribution and constant saddle point energy according to Kircheim formalism (Kircheim et.al, 1985).

$$D = D_0^1 \frac{\partial}{\partial C}\left\{(1-C)^2 \exp\left(\frac{\mu}{RT}\right)\right\}, \qquad D_0^1 = D_0^* \exp\left(\frac{E_0}{RT}\right) \tag{11}$$

Here D_0^* - pre-exponent factor, E_0- mean activation energy, equal to difference between mean Hydrogen energy, calculated, from energy distribution function and saddle point constant energy $E_0 - E_g$, (if energy distribution is Gaussian).

Hydrogen diffusion factors are calculated from equation (11) dependent on its concentration for amorphous $Pd_{83}Si_{17}$ alloy at T=298K temperature. It was obtained, that D_H increases depending on its concentration increase.

For example D_H value is $7.85 \cdot 10^{-6}$cm^2·s^{-1} at T=298K and $C_H(H/Me)=10^{-3}$ for amorphous $Pd_{83}Si_{17}$ alloy.

Basing on D_H temperature dependence, diffusion activation energy value was estimated as E_0 = 18.9 kj/mol. It should be noted, that for crystal alloy activation energy is higher. It's equal to 26kj/mol independently on Hydrogen concentration.

According to Richards theory (Richards, 1983), there is Hydrogen probability to occupy low energy interstices, that are large faces polyhedrons.

Due to Hydrogen concentration increase, it occupies low energy interstices forcing H atoms to overcome higher energy potential barriers. Thus it neutralizes one of the factors, which decreases diffusion mobility.

On the other hand, Hydrogen atoms location in the higher energy interstices leads to activation energy decrease.

Described mechanism does not affect to diffusion, due to most part of Hydrogen atoms, absorbed by metal, have been found in low energy interstices (which are traps for H atoms). Sharp diffusion factor increase takes place only after traps saturation by Hydrogen.

6. Hydrogen diffusion in the amorphous Ni-Zr alloys

Computer calculation of the amorphous Ni-Zr and Ni-Zr-H alloys structure and properties are presented by fig. 10, 11 and table 2. The model system unlike (Pastukhov et.al, 2009, 2010) contained 640 (360)particles of nickel, 360 (640) particles of zirconium and 1(2) particles of hydrogen in the cubic cell. The movement equations integrating were carried out by time steps of $1.1 \cdot 10^{-15}$ s. General structure factors for $Ni_{64}Zr_{36}$ (alloy 1, curve 4) и $Ni_{36}Zr_{64}$ (alloy 2, curve 1), with Hydrogen and without it are presented on fig. 10. All curves have diffused interferential maxima proper to amorphous state, which indicates, that amorphous state is saved with Hydrogen absorption at low as well as at high hydrate-forming element and Hydrogen concentration in an alloy. Increasing the number of H - atoms in a MD model for 1- alloy initially results in structural factor peaks displacement to the low dispersion vectors (S) and in main peak height (h) increasing. Then the displacement vice versa results in the high S- and low h-values. It testifies to the quantity of H-atoms affects to amorphous alloys structure. All peaks of a(s) became more relief, oscillations extend to higher scattering vectors. The authors (Sadoc et.al, 1973, Maeda & Takeuchi 1979) proved, that icosahedrons type of atoms packing is dominating in amorphous metals structure, where high polyhedron concentration with coordination number 12 takes place. The main structural factor maximum height and form of the bifurcated second peak are determined by contacting polyhedrons quantity and their type of bond (Brine & Burton, 1979). The amorphous alloy short order therefore can be described with the help of a coordinating icosahedron cluster, which is the basic structural unit of $NiZr_2$ crystal.

Hydrogen in such a structure can be located in numerous tetra-cavities, formed by Ni and Zr atoms (Kircheim et.al, 1988). For 2 - alloy, that is close to $NiZr_2$ composition (curve 1), two first maxima location of a(s) curve corresponds to averaged location of the interference lines for crystal $NiZr_2$ compound. Hydrogen atom including in the MD-model (curve 2) leads to strong diffusion and height decreasing of relatively good resolved structure factor peaks due to Hydrogen penetration into numerous cavities of the amorphous structure. Hydrogen atoms probably form with Zr some kind of quasi crystal ZrH_2 lattice (Sudzuki et.al, 1987). This assumption reveals in a better resolution of short and long diffraction maxima (3, 6 curves) of structure factors for alloys with high contents of Zr and H atoms.

Partial $g_{ij}(r)$ radial distribution functions of model systems and short order parameters are presented in Fig. 11 and in the table 2. For all low and zero hydrogen alloys, the shortest inter-atomic distance of Ni-Ni pair remains constant (0.240nm), decreasing up to 0.230nm when H increases up to two atoms. Inter-atomic distances of N-Zr and Zr-Zr pairs considerably decrease with growth of Zr and H concentration. We note that rNi-Ni and rZr-Zr are close to Ni and Zr atoms diameters (0.244 nm and 0.324 nm) correspondently, and the distance between Ni-Zr atoms is somewhat less than the sum of the Ni and Zr atoms radii, that is confirmed by diffraction experiment results (Buffa et.al, 1992). This fact confirms bond formation between these elements due to hybridization of vacant 3d – electron band of Ni and 4d-band of Zr Hafiuer et.al, 1993). Calculated diffusion coefficients of hydrogen for amorphous Ni-Zr-H alloys are presented in the Table 2. The value of D_H varies from $2 \cdot 10^{-4}$ up to $1.2 \cdot 10^{-5} cm_2 \cdot s^{-1}$, in the same limits, as diffusion coefficients of H atoms in an icosahedron TiNiZr alloy (Morozov et.al, 2006). As it follows from the Table 2, D_H grows

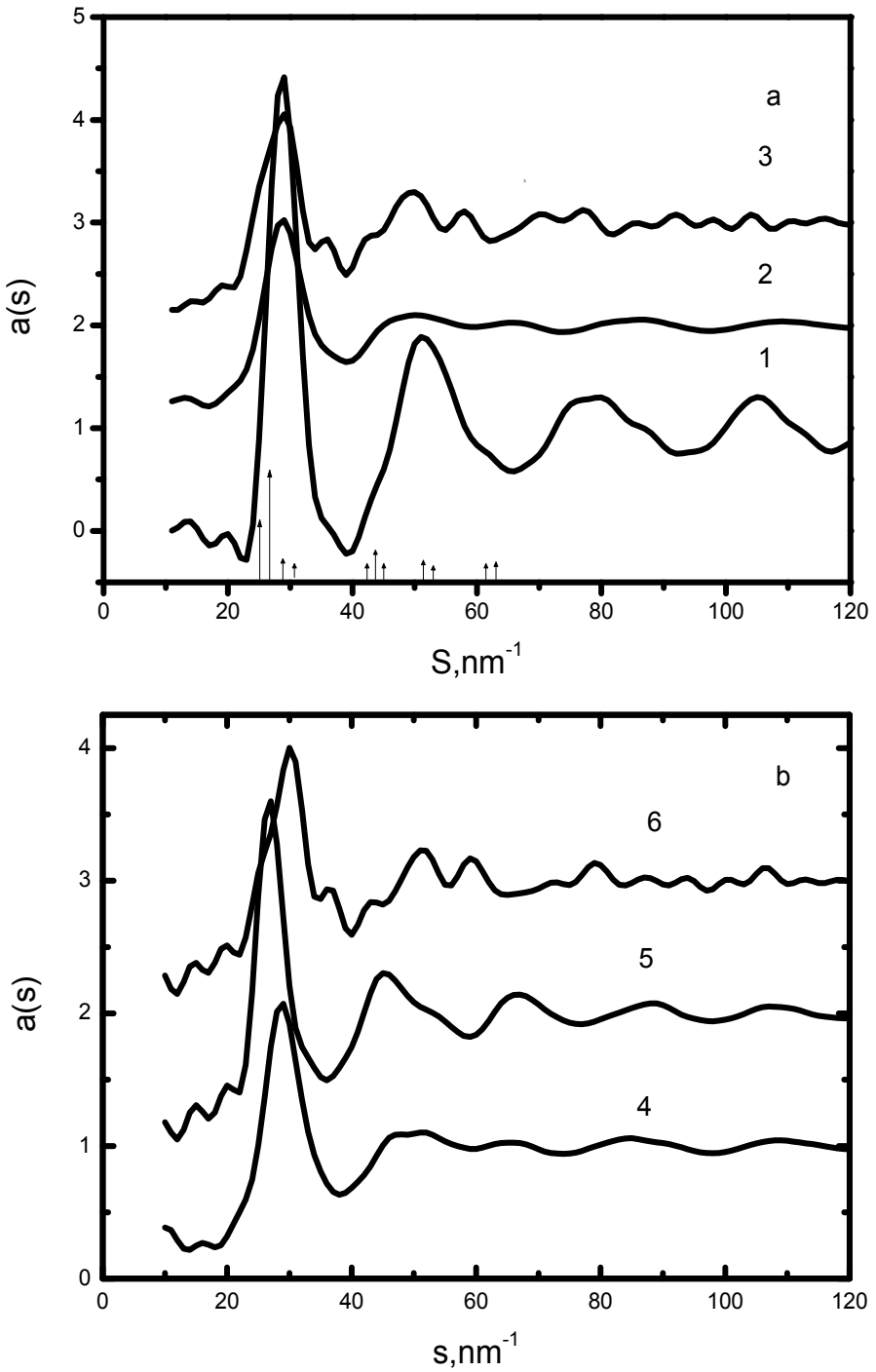

Fig. 10. Amorphous Ni-Zr alloys structure factors with hydrogen and without:
a) $Ni_{36}Zr_{64}$(1), $Ni_{36}Zr_{64}$+1H(2), $Ni_{36}Zr_{64}$+2H(3);
b)$Ni_{64}Zr_{36}$(4), $Ni_{64}Zr_{36}$+1H(5), $Ni_{64}Zr_{36}$+2H(6).

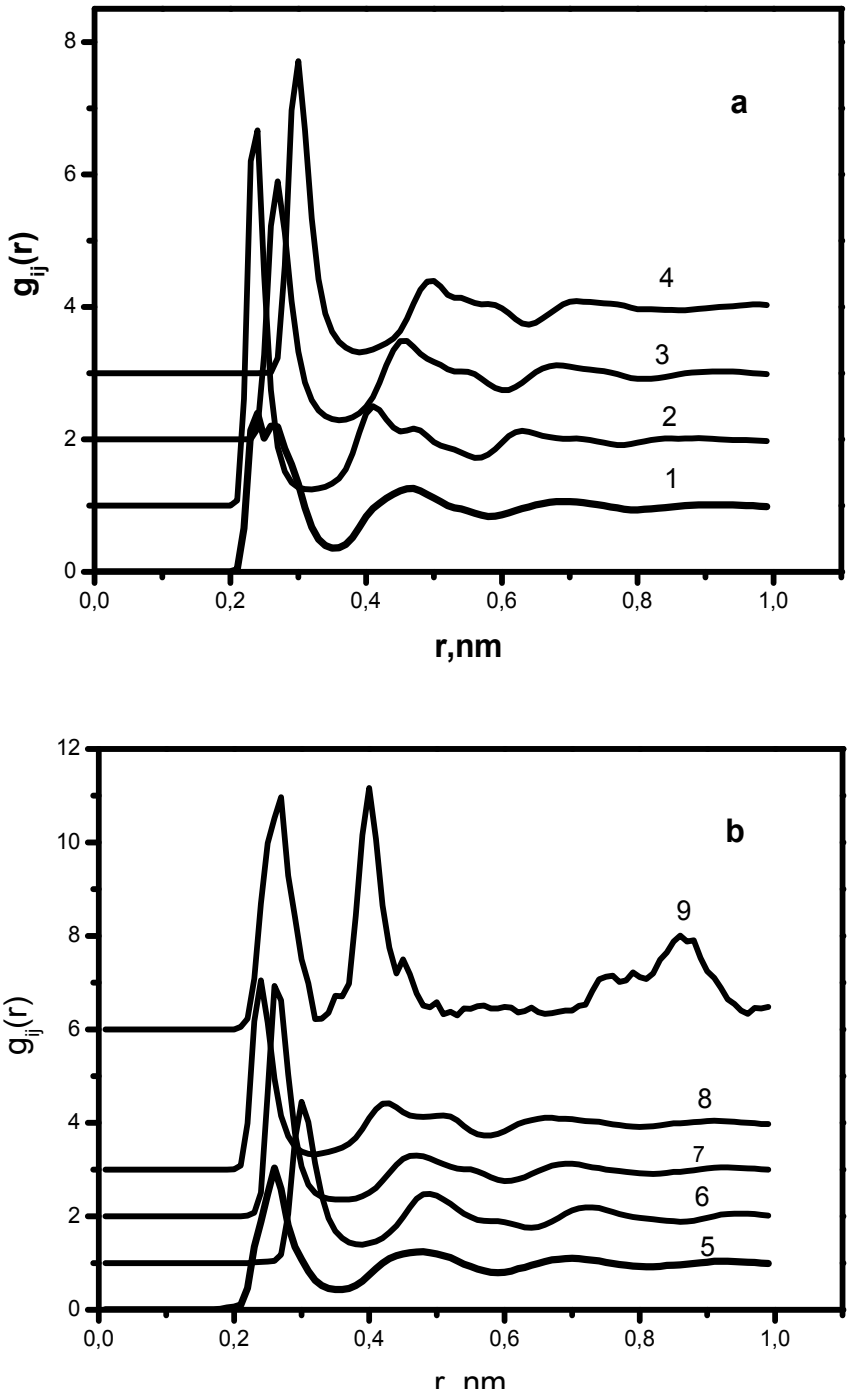

Fig. 11. Radial distribution functions g_{ij} (r) of $Ni_{64}Zr_{36}$ alloy: (a) - no hydrogen; (b) - one hydrogen atom. Partial g_{ij} (r): 1,5- general; 2,8 - Ni-Ni; 3,7 - Ni-Zr; 4,6 - Zr-Zr; 9 - H-H.

with increase of hydride forming element Zr concentration and H atoms in the MD-model. The activation energy of hydrogen diffusion for amorphous $Ni_{64}Zr_{36}$ alloy was estimated in the 298-768K temperature interval. A value of E=0.1eV was obtained. This result on H atoms diffusion may be explained by various energy position (Richards, 1983, Kircheim et.al, 1988) in the disordered materials. Deep potential wells acts like traps (octa-cavities) and are occupied by hydrogen initially. Then hydrogen occupies interstices with high energy values (tetra-cavities) and an abrupt increase of D_H is observed.

System	Partial RDF			D_H at 298K
	Ni-Ni	Ni-Zr	Zr-Zr	
	r, nm	r, nm	r, nm	cm^2s^{-1}
$Ni_{64}Zr_{36}$	0.238	0.270	0.301	
$Ni_{36}Zr_{64}$	0.240	0.261	0.290	
$Ni_{64}Zr_{36} < 1H_2 >$	0.240	0.266	0.310	$1.2 \cdot 10^{-5}$
$Ni_{64}Zr_{36} < 2H_2 >$	0.240	0.26	0.29	$1.7 \cdot 10^{-4}$
$Ni_{36}Zr_{64} <1H_2 >$	0.241	0.265	0.297	$8.9 \cdot 10^{-5}$
$Ni_{36}Zr_{64} < 2H_2 >$	0.230	0.250	0.280	$2.1 \cdot 10^{-4}$

Table 2. Short order parameters for amorphous alloy in the Ni-Zr and Ni-Zr-H systems.

7. Hydrogen and electric field effect to Iron impurities diffusion in the Zr-Fe melt

Iron and Zirconium diffusion factor dependence on electric field intensity and Hydrogen presence in the molten Zirconium had been analyzed in the terms of molecular dynamics (MD) method. Model system for research of Iron and Hydrogen ions behavior in the Zr-Fe-H melt at T=2273K temperature and electric field presence contained 516 Zirconium particles, 60 Iron particles and 1Hydrogen particle in cubic cell with a=2.44195 nm cube edge. Integration of the motion equation was carried out by $1.1 \cdot 10^{-15}$s time steps. Inter-particle potentials and its parameters had been taken from (Varaksin & Kozyaichev, 1991, Zhou et.al, 2001). Calculation results of impurities migration in the molten Zirconium are compared to experimental data (Lindt et.al, 1999, Ajaja et.al, 2002, Mimura et.al, 1995). Partial radial distribution functions $g_{ij}(r)$ for Zirconium-Iron melt are presented on fig. 12. Most probable inter-atomic distance in first coordination sphere is close to sum of atomic radii for Iron and Zirconium (r_{Zr-Fe}= 0.29nm, r_{Fe}= 0.130nm, r_{Zr}= 0.162nm).

This results comparison to computer simulation data for Ta-Fe melt (Pastukhov et.al, 2010, Vostrjakov et.al, 2010) reveals sufficiently close character of the radial distribution function for large dimension atoms, namely Ta-Ta (0.29 nm, r_{Ta} = 0.145nm) and Zr-Zr (0.324nm, r_{Zr}=0.162nm). Iron and Zirconium diffusion factors in the Zirconium melt in the presence, as well as absence of electric field and Hydrogen at 2273K had been calculated by means of MD method (fig. 13 and 14). Diffusion factor of Iron (D_{Fe}) in the Zirconium melts with Hydrogen linearly depends on electric field intensity (E) and Iron concentration (C_{Fe}). Hydrogen diffusion factor negligibly decreases from $2.16 \cdot 10^{-4}$ $cm^2 \cdot s^{-1}$ to $1.94 \cdot 10^{-4}$ $cm^2 \cdot s^{-1}$, if electric field intensity increases from 900 to 1020 v/m. Hydrogen inducing into system at $C_{Fe} \approx 0.1\%$ decreases D_{Fe} value from $7.86 \cdot 10^{-5}$ to $6.36 \cdot 10^{-5} cm^2 s^{-1}$, and electric field 1020 v/m intensity applying decreases D_{Fe} to $5.23 \cdot 10^{-5} cm^2 \cdot s^{-1}$ (fig.14).

Calculation results of D_{Fe} changing in dependence on E value had been compared to evaporation constant rate for the Fe-ions from Zr, calculated by equation (Pogrebnyak et.al, 1987, Vigov et.al, 1987)

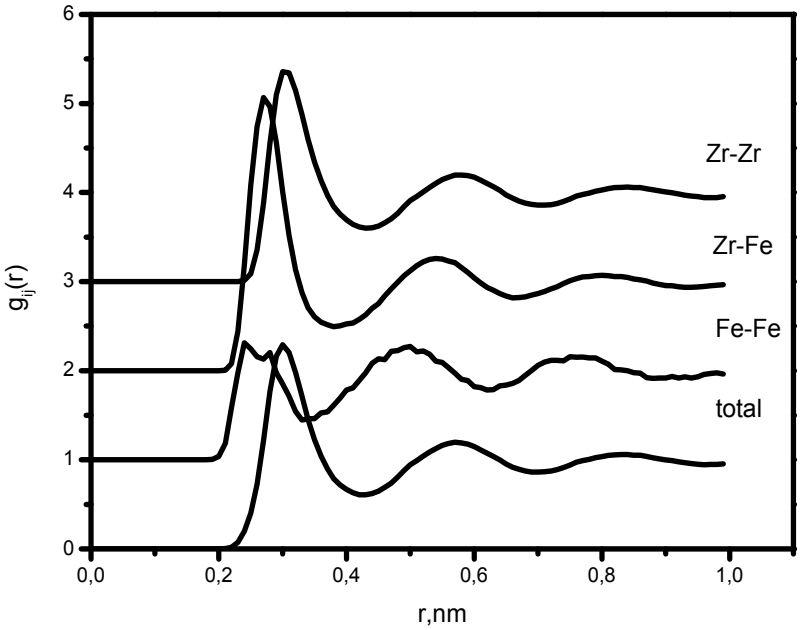

Fig. 12. Partial radial distribution functions $g_{ij}(r)$ for Zr-Fe melt at 2273K, calculated in terms of MD model.

$$k = \nu \cdot C_{Fe} \exp\left[-\frac{\lambda + I - W - (q^3 \cdot E)^{1/2}}{RT}\right], \tag{12}$$

where ν – ion vibration frequency (10^{13}·s^{-1}), C_{Fe} – impurity concentration, λ – Fe evaporation heat, I – first ionization potential (V/Å), E – electric field intensity, W – electron exit work, q – ion charge. Values of λ, I, W, R had taken in electron-volt, E – in volt per angstrom. Diffusion factor D directly depends on rate (k) and time (t) evaporation of main metal (Kuznetsov et.al, 1968). The log k and log D_{Fe} on E dependences (fig. 15) are relatively similar.

Thus assumption is possible, that limiting factor of Fe removal from the Zr melt is diffusion of Fe. The Hydrogen is considered as light intrusion impurity into metals with different cell type. Therefore Hydrogen diffusion is significant problem in researching of high temperature metals refining. Impurities have less action upon Incoherent diffusion. Therefore this kind of diffusion becomes dominating at high temperature (Maximov et.al, 1975).

We had compared Hydrogen diffusion factors in Ta at 3400K (Pastukhov et.al, 2010) and in Zr at 2273K (Ajaja et.al, 2002). This values are 1,7 10^{-5} and 5,01 10^{-4} cm^2·s^{-1} respectively. The authors (Maximov et.al, 1975) explain such difference due to Hydrogen diffusion activation energy (E_a) dependence on atomic metal mass, its Debye frequency, modulus of elasticity and volume change at Hydrogen addition.

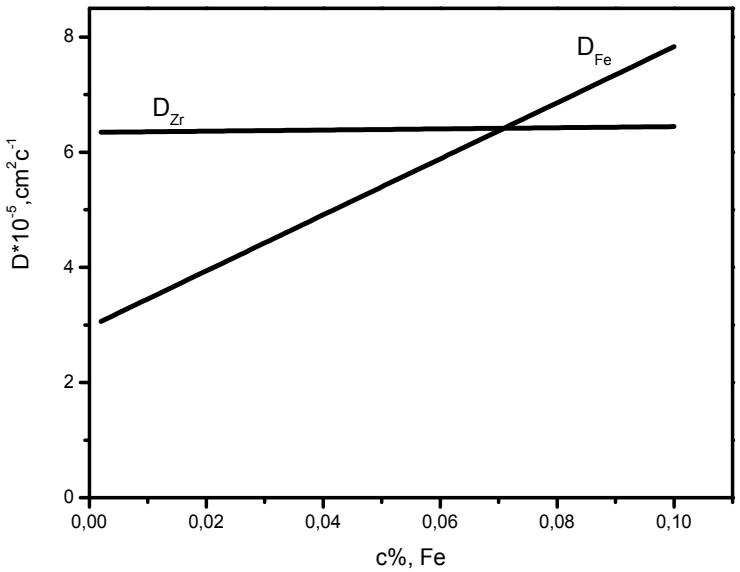

Fig. 13. Dependencies of D_{Fe} and D_{Zr} on Iron concentration at 2273K (MD - calculation).

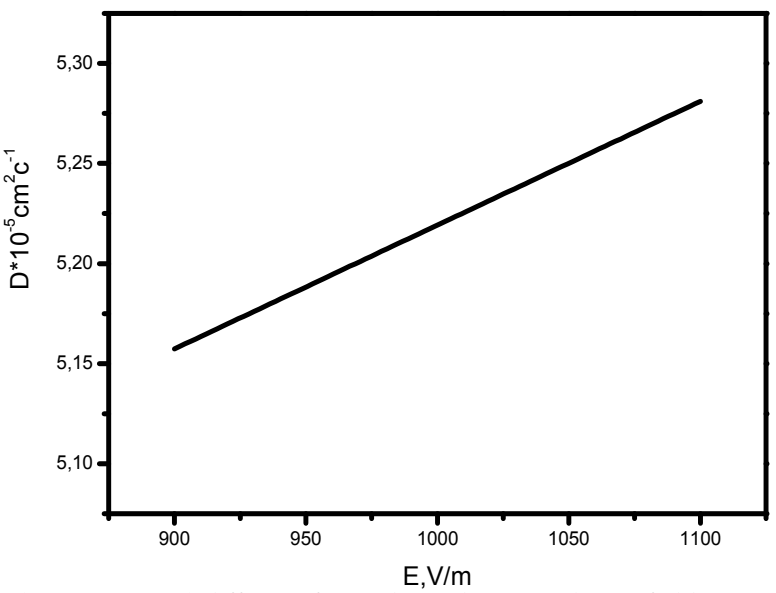

Fig. 14. Iron (C_{Fe} =0.1mas.%) diffusion factor dependence on electric field intensity at 1173K temperature (MD – calculation).

Calculated values of E_a for different metals (Flynn et.al, 1970) are in quantity agreement with experimental data. Temperature dependence D_H at high temperatures is described in the term of theory (Flynn et.al, 1970). Authors (Shmakov et.al, 1998) calculated D_H in Zirconium at 2273K without electric field influence as $3.862 \cdot 10^{-4} cm^2 \cdot s^{-1}$, which low differ from our calculated value $D_H = 5.01 \cdot 10^{-4} cm^2 \cdot s^{-1}$.

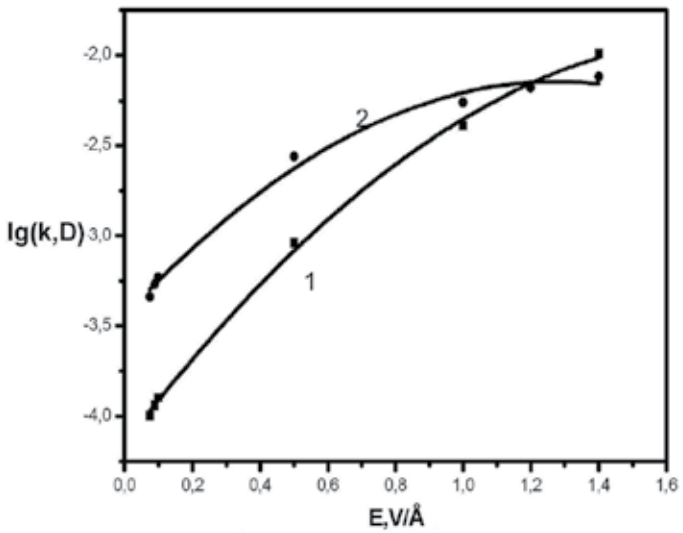

Fig. 15. Dependence of lgD_{Fe} (curve 1) and lgk (curve 2) on electric field intensity.

We have estimated diffusion layer thickness (x) by (13) equation (Flynn et.al, 1970). Calculation were carried out basing on C_{Fe} - experimental time – dependence (Mimura et.al, 1995). Value of D_{Fe} we calculated by MD – method.

$$C_{(x,t)} = C_0 erfc\left(\frac{x}{2\cdot\sqrt{D_{Fe}\cdot t}}\right), \tag{13}$$

In the equation C_0 and $C_{(x,t)}$ are impurity concentrations in initial and refined Zirconium (Flynn et.al, 1970) and t is time of refining. Calculated (*x)* value is equal $7\cdot10^{-2}$cm. By the order of value it's close to data on Silicon borating (Filipovski et.al, 1994), which is $1.6\text{-}1.8\cdot10^{-2}$cm. It should be noted, that zone thickness of Zirconium shell interaction with molten Uranium is $0.2\cdot10^{-2}$cm (Belash et.al, 2006).

We carried out calculation of Iron removal rate (G) from Zirconium by Iron concentration decrease during matched time intervals of plasma-arc-melting (PAM) with Hydrogen basing on the experimental data of (Mimura et.al, 1995) for 9.5 Pa and 50% of Hydrogen concentration in residual Argon. The data are shown in table 3. Mean residual Iron concentration at 15, 90 and 165 minutes of melting compiled 0.46, 0.01 and $2.2\cdot10^{-4}$ mas.% respectively. These calculations had been compared with Iron evaporation rate from Zirconium melt obtained from Langmuir equation:

$$L = 0.0583\gamma C_{Fe} cp\sqrt{\frac{M}{T}} \tag{14}$$

This equation parameters are following: Iron activity coefficient in Zirconium (γ) is equal to 0.052 from [43], (C_{Fe}) - concentration of Iron in Zr, (p) – Iron vapor pressure at 2273K, (M) – Iron atomic mass, (T) – Kelvin temperature. Temperature of melting [46] is indicated in the 2350 – 2450K limits. Calculation of L by these temperatures founds L < G in both cases. Ratio

G/L decreases at temperature increase. Obtained G/L ≈ 1.15 value at C_{Fe}= 0.46 and T = 2450K may indicate, that close to 15% of Iron is being removed due to electro-magnetic forces affect, rather than evaporation.

T,K	C_{Fe}, mas.%	logG	logL	G/L	Remark	Issue
2350	0.46	-4.572	-5.066	3.115	L<G	[4]
	0.01	-6.09	-6.728	4.348		
	$2.2\cdot10^{-4}$	-7.902	-8.386	3.047		
2450	0.46	-4.572	-4.755	1.153	L<G	[4]
	0.01	-6.09	-6.418	2.128		
	$2.2\cdot10^{-4}$	-7.902	-8.076	1.491		
2900	$7.82\cdot10^{-3}$	-6.967	-5.406	0.027	L>G	[2]
	$2.68\cdot10^{-3}$	-7.44	-5.871	0.027		
	$0.92\cdot10^{-3}$	-7.903	-6.335	0.028		
2450	$7.82\cdot10^{-3}$	-6.967	-6.525	0.361	L >G	[2]
	$2.68\cdot10^{-3}$	-7.44	-6.990	0.355		
	$0.92\cdot10^{-3}$	-7.903	-7.454	0.356		
2300	$7.82\cdot10^{-3}$	-6.967	-7.001	1.081	L < G	[2]
	$2.68\cdot10^{-3}$	-7.44	-7.466	1.062		
	$0.92\cdot10^{-3}$	-7.903	-7.930	1.065		

Table 3. Dependences of L and G on mean residual Iron content in Zirconium for PAM process. C_{Fe} – mean Iron concentration: initial (15min.), middle (90min.), and final (165min.) stage of melt.

8. Hydrogen and electric field effect to Iron impurities diffusion in Ta-Fe melt

Hydrogen and Iron atoms radial distribution functions and diffusion constants had been found by MD method in the Tantalum melt at 3400K in the presence and absence of outer electric field (fig. 16).

The model system was presented by 486 tantalum, 1 iron and 1hydrogen atoms in a cubic cell of 2.13572 nanometers cube edge length. Computer experiment data have found short order of Ta-Fe-H system at 3400K is close to Tantalum structure: first maximum at R_{Ta-Ta} ≈ 0.29 nm corresponds to Tantalum atom radius ≈ 0.292 nm. All RDF maxima diffusion is observed at electric field and Hydrogen in the Ta-Fe system. This fact may indicate liquid transition to more disordered structure.

Unusual kind of RDF curve for Ta-H atoms pairs obtained at electric field 1020v/m intensity (fig. 17): first maximum of the curve is bifurcated, besides first sub-peak at r_1 = 0.22nm corresponds to one of most probable distance Ta-H and second sub-peak at r_2 = 0.24nm corresponds to Ta-Fe without electric field.

Dynamics and local structure of the close to Hydrogen surrounding for the ternary interstitial alloy should depend on Hydrogen concentration, temperature and solvent structure short order. There is no conventional opinion about Hydrogen location in such systems. Since the Hydrogen atom radius is 0.032 nm, it can occupy octahedron (0.0606 nm), as well as tetrahedron (0.0328нм) (Geld et.al, 1985) location. System Ta – H particularity is

that starting from the concepts of geometry, distance between Tantalum atom and octahedron interstice centre in Tantalum cell more, than Ta (0.146nm) and H (0.032nm) radii sum. Distance Ta – H remains less than equilibrium distance, and Hydrogen not always occupies interstice centre.

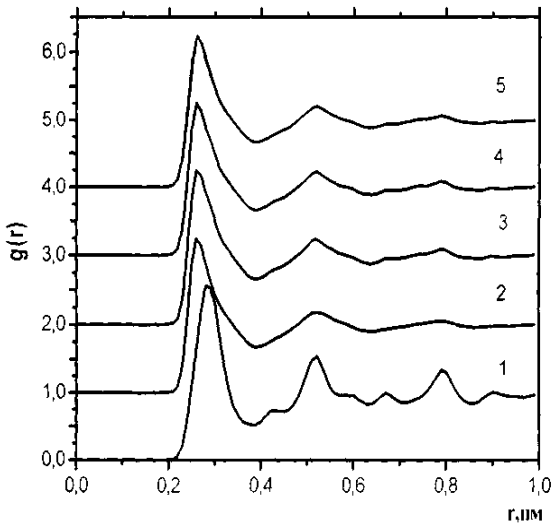

Fig. 16. Radial distribution function g (r) for Ta-Fe melt at 3400 K temperature, obtained in MD model at 15.4 g/sm^3 liquid Ta density. 1. No electric field, no hydrogen, 2. Electric field 85 [V/m], no hydrogen, 3. Hydrogen, no electric field, 4. Electric field 85 [V/m], Hydrogen, 5. Electric field 1020 [V/m], Hydrogen.

At the same time, distance from the octahedron interstice centre to the second neighbors, $R_2=a/\sqrt{2}=0.234$nm is more than Tantalum plus Hydrogen distance. That leads to Hydrogen atoms shift from octahedron centre to whatever neighbor of Tantalum atom.

Dynamics and local structure of the close to Hydrogen surrounding for the ternary interstitial alloy should depend on Hydrogen concentration, temperature and solvent structure short order. There is no conventional opinion about Hydrogen location in such systems. Since the Hydrogen atom radius is 0.032 nm, it can occupy octahedron (0.0606 nm), as well as tetrahedron (0.0328нм) (Geld et.al, 1985) location. System Ta – H particularity is that starting from the concepts of geometry, distance between Tantalum atom and octahedron interstice centre in Tantalum cell more, than Ta (0.146nm) and H (0.032nm) radii sum. Distance Ta – H remains less than equilibrium distance, and Hydrogen not always occupies interstice centre.

At the same time, distance from the octahedron interstice centre to the second neighbors, $R_2=a/\sqrt{2}=0.234$nm is more than Tantalum plus Hydrogen distance. That leads to Hydrogen atoms shift from octahedron centre to whatever neighbor of Tantalum atom.

Hydrogen shift from geometric centre of octahedron position during heating of researched system is possible. According to computer experiment data, distance between nearest Tantalum and Hydrogen atoms changes at electric field and Hydrogen presence, but Ta-Fe remains constant (table 4).

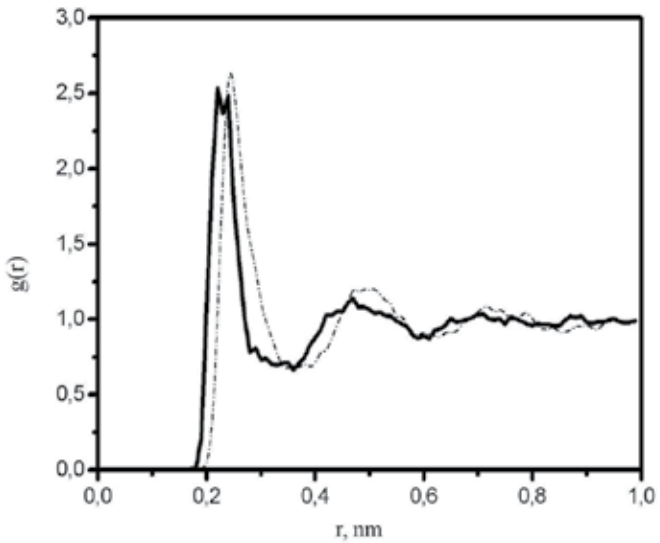

Fig. 17. Partial distribution function of the atomic Ta-H pair in electric field 1020 v/m (dashed curve) and Ta-Fe without electric field (solid curve), obtained by MD model.

After Hydrogen induction into MD cell, Tantalum diffusion constant increases from $1.7 \cdot 10^{-4}$ до $7. \cdot 10^{-4}$ cm^2 s^{-1}, which some less, than Iron diffusion constant increase: from $1.3 \cdot 10^{-5}$ to $1.5 \cdot 10^{-4} cm^2$ s^{-1}.

Thus, Hydrogen increases Iron atoms mobility more than electric field. This fact is in god agreement with Ta-H and Ta-Fe bonds strength.

System	T, K	E,V/m	PRDF (nm)		
			rTa-Ta	rFe-Fe	rTa-H
Ta-Fe	3400		0.29		
Ta-Fe-H	3400	85	0.26	0.25	
Ta-Fe-H	3400		0.26	0.24	0.22
Ta-Fe-H	3400	85	0.26	0.24	0.235
Ta-Fe-H	3400	1020	0.26	0.24	0.22/0.24

Table 4. Partial inter-atomic distances in the Ta-Fe by MD calculation.

9. Conclusion

Amorphous and liquid systems structure for Fe, Pd, Zr, Ta, Si with presence and absence of Hydrogen atoms had been researched by means of x-rays diffraction and molecular dynamic methods. Strong affect of H atoms to amorphous matrixes Fe-Ni-Si-b-C-P, Pd-Si and Ni-Zr structure had been obtained.

Observed RDF changing at Hydrogen presence had been revealed in better resolution of the close and distant maxima could indicate to stable hydride bonds like Pd-H, Si-H, Zr-H formation.

Calculated by MD model Hydrogen diffusion constants increase on H concentration and hydride forming element presence in alloy (system Ni-Zr-H). Not only amorphous alloy

component (Pd-Si-H) affects to H atoms mobility, but Hydrogen atoms can considerably change other components (Si) diffusion. Refining processes of the liquid high-melting metals, like Zr, Ta, containing Fe impurities can be analyzed by MD method for PAM and EBM melting technologies. The method gives opportunity to estimate limiting stage of process, electric field affect and Hydrogen presence in system to Fe diffusion constant in the melts.

The researches had been carried out with financial support of Minobrnayka. Federal contract 16.552.11.7017, science equipment of CKP "Ural-M" had been used.

10. References

Ajaja, V.; Vugov, P. & Lavrinenko, S. et. al. (2002). Electron-beam melting of Titanium, Zirconium and Hafnium. *Voprosi atomnoi nauki I tehniki*. (2002). No. 6. pp. 95-99

Alder, B. & Wainwright, T. (1959). Studies in Molecular Dynamics. I. General Method - *J. Chem. Phys.* Vol.31, No.2, pp. 459-469.

Avduhin, V.; Katsnelson, A. & Revkevich, G. (1999). Oscillatory phase transformations in the initial relaxation stage of Pd-Er-H alloy *Crystallography* (1999), Vol.44. No.1.p.49; (1999). Non equilibrium phase transformations of oscillatory type in Pd-Er alloy, relaxing after Hydrogen saturation. *Vectnik Moscow Univercity* Ser.3 (1999). Vol.40. No.5. p.44.

Belash, N.; Tatarinov, V. & Semenov, N. (2006). Complex alloying of Uranium in centrifugal casting in Zirconium form. *Voprosi atomnoy nauki i tehniki. Seriya «Fizika radiatsionnih povrejdeni I radiatsionnoe materialovedenie».* (2006). No. 4. pp. 123-127

Brine, C. & Burton, Y. (1978). Icosahedral Microclusters. A Possible Structural Unit in Amorphous Metals. *Phys.Stat. Sol.(b).* (1978). Vol. 85. No.1. pp.393-402

Buffa, F.; Corrias, A.: Licheri, G.; Navarra, G. & Raoux, D. (1992). Short range structure of mechanically alloyed amorphous Ni_2Zr investigated anomalous X-ray scattering. *J. Non-Cryst. Solids*, Vol.150. Issues 1-3, 2 November (1992). pp. 386-390

Filipovski, F. & Nasarenko, I. (1994). Method for removing suicide coatings in a medium of low-melting Metals. *Materials Science.* (1994).Vol.30. No.3. pp.368-370

Flynn, C. & Stoneham, A. (1970). Quantum Theory of Diffusion with Application to Light Interstitials Metals. *Phys Rev* (1970). B1. pp. 3966-3978.

Gordeev, V.; Popov, A. & Filikov, V.(1980). Structure of amorphous Silicon, obtained by high frequency ion-plasma spraying. *Izv. AN.USSR. Neorgan. materiali.* 1980. Vol.16. No.10, pp. 1733-1736.

Gabis, I. (1997). Transfer of Hydrogen in the graphite films, amorphous Silicon and Nickel oxide. *Phizika* i tehnika *Poluprovodnikov*. 1997. Vol.31. No. 2, pp. 145-151.

Geld, P.; Ryabov, R. & Mokhracheva. (1985). Vodorod I fizicheskie svoystva metallov I splavov. Nauka. (1985), Moscow. Russia.

Grashin, S.; Sokolov, U. & Gorodetsky, A. et. al. (1982). Hydrogen interaction with material of discharge tokamak chamber. *Preprint IAE (rus.)* No.3622/7. Moscow. 1982.

Hafiuer, J.; Krajci, M. & Hausleitner, C. (1993). Methods in the determination of partial structure factors. *Scientific Publishing.* (1993). Singapore

Herst, D. (1962) Diffusion of fusion gas. Calculated diffusion from sphere taking into account trapping and return from the traps. *In CRRP -1124. Atomic Energy of Canada Inst. Conf.* Oct.-Nov., 1962, Balk River. pp. 129- 135

Ivanova, V.; Balankin, A.; Bunin, I. & Oksogoev, A. (1994). *Sinergetica i fractali v materialovedenii*. Nauka. (1994).Moscow, Russia

Kirchheim, R.; Sommer, F. & Schluckebier, G. (1982). Hydrogen in amorphous metals. *J. Acta Metall.* (1982) Vol.30. No.6. pp. 1059-1068

Kichheim, R.; Szokefalvi-Nagy.; Stolz, A. & Spelling, A. (1985). Hydrogen in deformed and amorphous palladium – silicon ($Pd_{80}Si_{20}$) compared to hydrogen in deformed and crystalline palladium. *J. Non-Cryst. Solids*. (1985). Vol. 70. No.2. pp. 323-329

Kircheim, R. et al. (1988). Hydrogen in amorphous and nanocrystalline metals. *Mat. Sci. Eng.* (1988). Vol.99. No.2, pp. 457-462

Kuznetsov, V.; Loginova, R.; Ovsyanikov, M. & Postnikov, V. (1968). *Growth and structure processes of mono-crystal Semiconductors.* Part I. Nauka. (1968). Novosibirsk. Russia.

Lifshits, A. (1976). Interaction of the membranes with nonequilibrium gases in the case of adsorption with dissociation. *JTF (Jurnal Teoreticheskoy Fiziki (rus.)).* Vol.46, No.2, pp. 328 – 338.

Lindt, K.; Muhachev, A.; Shatalov, V. & Kotsar, M. (1999). Perfection of process of calcium-thermal reduction of Zirconium tetra-fluoride. *Voprosi atomnoy nauki i tehmiki. Seriya «Fizika radiatsionnih povrejdeni I radiatsionnoe materialovedenie».* (1999). No. 2. pp. 3-8

Maeda, K. & Takeuchi, S. (1979). Geometrical characterization of Computer Constructed Metallic Amorphous Structure *Techn.,Rep. ISSP(a)*. (1979). No.54. pp.1-17

Maksimov, E. & Pankratov, O. (1975). Hydrogen in metals. *Uspehi fizicheskih nauk. (UFN).* (1975). Vol. 116. Issue 3. pp. 385-412.

Mimura, K.; Lee S. & Isshiki M. (1995). Removal of alloyng elements from zirconium alloys by hydrogen plasma-arc Melting. *Journal of Aloys and Compounds.* (1995). Vol. 221. pp. 267-273

Morozov, A.; Isaev, E. & Vekilov, U. (2006). *Fizika tverdogo tela (rus.).* (2006). Vol. 48. Issue 9. pp. 1537-1540

Pastukhov, E.; Sidorov, N.; Belyakova, R. & Polukhin, V. (1988). Hydrogen affect to electric resistance of amorphous films Pd-Si and Fe-B in crystallization temperature interval. *Abstracts of III Vsesouznoy conference "Problems of amorphous metallic alloys researches"(rus.)*. Moscow, pp. 27-28.

Pastukhov, E.; Vatolin, N. & Lisin, V. et. al. (2003). *Diffractsionnie issledovaniya stroeniya visokotemperaturnix Rasplavov*. UrO RAN. Ekaterinburg. Russia.

Pastuchov, E.; Sidorov, N. & Chentsov, V. (2007). Diffusion permeability of hydrogen in amorphous Fe-Ni-Si-B-C-P alloy The optimization of the composition, structure and properties of metals, oxides, composites, nano-and amorphous materials. *Proceeding of the VII International Russia-Israeli Conference*, June 24-28, Jerusalem 2007, pp. 85-94.

Pastukhov, E.; Sidorov N. & Chentsov, V. (2008). Hydrogen affect to short order structure of liquid amorphous and crystal Silicon. *Proceedings of IX Russian seminar "Computer simulation of glasses and melts physical-chemical properties."* Kurgan. Russia. (2008). pp.25-26.

Pastukhov, E.; Sidorov,V.; Polukhin, V. & Chentsov, V. (2009). Short Order and Hydrogen Transport in Amorphous Palladium Materials. *Defect and Diffusion Forum.* Vols.283-286 (2009) pp.149-154

Pastukhov, E.; Vostrjakov, A.; Sidorov,V.; & Chentsov, V. (2010). Molecular Dynamic Calculation of Hydrogen and Iron Diffusion in molten Tantalum under Electric Field. *Defect and Diffusion Forum*. Vols.297-301 (2010) pp.193-196

Pogrebnyak, A.; Kulmentyeva, O. & Kshnyakin, V. et. al. (2002). Strengthening and mass transport in impulse-plasma-detonation of steel treatment. *Fizika i himiya obrabotki materialov*. (2002). No. 2. pp. 40-48

Polukhin, V.; Pastukhov, E. & Sidorov, N. (1984). Structure of $Pd_{1-x}Si_x$ and $Fe_{1-x}P_x$ alloys in liquid and amorphous states. *Phizika metallov i metallovedenie (rus.),* Vol.57, No.3, pp. 621-624.

Polukhin, V. & Vatolin, N. (1985). *Modelirovanie Amorfnih Metallov (rus.),* Nauka, Moskow, USSR

Polukhin, V.; Vatolin, N.; Belyakova, R. & Pastukhov, E. (1985). Hydrogen affect to amorphous Iron distribution function from molecular dynamic simulation. *Dokladi AN SSSR (rus.)*. Vol.287, No.6, pp. 1391-1394.

Polukhin, V.; Sidorov, N. & Vatolin, N. (1997). Statistic models of diffusion and permeability of Hydrogen in the membrane amorphous alloys. *Melts (Rasplavi (rus.))* No.3, pp. 3-27

Panzarini, G. & Colombo, L. (1994). Hydrogen Diffusion in Silicon from Tight-Binding Molecular Dynamics. *Phys. Rev. Lett.* (1994), No.73, p. 1636

Rappe, A.; Cascwit, C. & Cowell, K. (1992). UFF, a full periodic Table force field for molecular mechanics and molecular dynamics simulations. *J. Am. Chem. Soc*, Vol.114, No.25, pp. 10024-10035.

Richards, P.; (1983). Distribution of activation energies for impurity hopping in amorphous metals. *Phys.Rev.* (1983). Vol.27. No. 4. pp. 2059-2072

Sadoc, J.; Dixmier, J. & Guiniter, A. (1973). Theoretical Calculation of Dense Random Packing of Equal and Non-equal Size Hard Spheres. Application to Amorphous Metallic Alloys. *J.Non-Cryst.Solids*. Vol.12. No.1.(1973). pp.46-60

Shmakov, A. & Singh, R. (1998). Some peculiarities of Hydrogen behavior and related hydride cracking in zirconium based reactor alloys. *Atomic Energy*.(1998). Vol.85. No.3. pp.675-678

Sidorov, N. & Pastukhov, E. (2006). Hydrogen diffusion in an amorphous Palladium: molecular-dynamic model. *Proceedings of the Third Russian conference "Physical problems of Hydrogen energetics"*. Sanct-Peterburg. Russia. 20-22 November. (2006). pp. 39-41.

Sokolov, U.; Gorodetsky, A.& Grashin, S. et. al. (1984). Interaction of hydrogen with the material of discharge chamber of tokamak TM-4

Stillimger, F. & Weber, T. (1985). Computer simulation of local order in condensed phases of silicon. *Phys.Rev.* B31, (1985). pp. 5262-5271.

Sudzuki, K.; Fudzinori, H. & Hasimoto, K. (1987).*Amorfnie metalli.* (1987). Metallurgiya. Moskow. Russia

Tersoff, J. (1986). New empirical model for the structural properties of silicon. *Phys. Rev., Lett.* No.56. (1986) .pp. 632-638

Varaksin, A.; Varaksin, A. & Kozyaichev, V. (1991). Diffusion of Hydrogen in Palladium: Molecular dynamics Simulation. *Phizika metallov i metallovedenie (rus.),* Vol.57, No.2, pp. 45-51.

Vatolin, N.; Poluhkin, V.; Belyakova, R. & Pastukhov, E. (1988). Simulation of the Influence of Hydrogen on the Structural Properties of Amorphous Iron. *Mater. Science and Eng*. (1988). No.99. pp. 551-554.

Vatolin, N.; Polukhin, V.; Belyakova, R.; Pastukhov, E. & Sidorov, N. (1989).The properties and thermostability of the hydrated glasses based on Iron and Palladium. *Abstracts of international congress on glass.* Leningrad. Nauka. pp. 378-381.

Verlet, L. (1976). Computer experiments in classical fluids. – *Phys. Rev*. Vol.159, No.1, pp.98-103.

Vigov, P.; Goncharov, K. & Kuzmenko, V. et.al. (1987). *Poly-elements activation analysis by means of (p,n)-reactions*. HFTI. (1987).Kharkov. AN Ukr.SSR.

Vostriakov, A.; Sidorov, N.; Pastukhov, E. & Lisin, V. (2010). Influence of the Electric Field Strength and Hydrogen on the Rate of Removal of Iron Atom Impurites in Refinig Remelting of Tantalum. *Russian Metallurgy (Metalli).* Vol. 2010, pp.124-127

Zhou, X.; Wadly, H.; & Johnson, R. (2001). Atomic scale structure of sputtered metal multilayers. *Acta mater*. No.49, pp. 4005-1015.

15

Molecular Simulation of Dissociation Phenomena of Gas Molecule on Metal Surface

Takashi Tokumasu
Institute of Fluid Science, Tohoku University
Katahira, Aoba-ku, Sendai, Miyagi
Japan

1. Introduction

Dissociative adsorption phenomena often occur in various fields of engineering, such as oxidation-reduction reactions, cleaning, adhesion, plating, plasma etching, sputtering, and tribology. These phenomena that involve surface reactions have attracted much attention and are analyzed both experimentally and numerically. However, when the surface has structures on the molecular scale, and the scale is not small enough compared to the system, the characteristics of a surface reaction cannot be sufficiently expressed macroscopically, for example by the rate equation. It is extremely difficult to analyze the characteristics of a nanoscale system experimentally due to the scale. Therefore, analysis by numerical calculation, in which the system structure and its electronic state are treated comprehensively, is more effective.

To analyze the surface reaction of these systems accurately, it is necessary to solve the electronic state by the first principle calculation based on quantum mechanics and to then obtain the energy state. The Molecular Orbital (MO) method is most accurate one. However it takes much calculation time and it is impossible to analyze the dissociation phenomena of gas molecule on metal surface because metal has many electrons. Recently, density functional theory (DFT) is one of the most commonly used methods for this process (Parr & Yang, 1989; Satoko & Onishi,1994). Based on the theory that the state of a system is expressed by the functional of the density distribution of the electron, this method can calculate a system state faster than methods that calculate the wave functions of each electron like MO. In the process of surface reaction analysis, this method is applied in various situations, such as specifying the reaction paths from the potential energy surface obtained by the method and calculating the reaction probability at the surface by the value of the absorption/activation energy and the transition state theory (Steinfeld et al., 1989). However, the effects of the motion of gas molecules impinging on the surface and the motion of surface atoms on the surface reaction cannot be considered because this method is applied under the assumption that the temperature is 0 K (fixed atom). , In order to analyze the flow dynamics, including the surface reaction, accurately, a method that considers the interaction between the electronic state of the system and the motion of atoms or molecules for which the time/space scale is distant, must be used.

Molecular Dynamics (MD) is one of the most suitable method for simulating the motion of atoms. In this method, the force between atoms is first obtained, and then the positions or velocities of the atoms are simulated by a time marching scheme. The quantum molecular dynamics (QMD) method, in which the interaction between atoms of a system is obtained according to the quantum calculation mentioned above, is the most precise method. In particular, the Car-Parrinello method (Car & Parrinello, 1985), in which the potential force of a system is calculated using the DFT to calculate the electronic state, is applied to analyze the process of oxidation-reduction reaction at the platinum surface (Wang & Balbuena, 2004; Jinnouchi & Okazaki, 2003). In general, the Car-Parrinello method is known as a first principle quantum molecular dynamics method. However, despite its precision, the Car-Parrinello method is not practical for analyzing a flow phenomenon as a statistical behavior of numerous motions of atoms or molecules because of the enormous calculation load. For the analysis of flow phenomena with surface reaction, the application of the multi-scale method, in which only smaller-scale systems are analyzed by precise quantum calculation and the characteristics that affect surface reaction are modeled, is more appropriate. Flow phenomena with larger-scale surface reactions can then be analyzed by the MD method using this model, rather than treating the entire system using quantum calculation.

The tight binding (TB) method, which greatly improves the computation speed, is contrived by simplifying the first principle quantum molecular dynamics method. Regarding this method, as mentioned later, it has been reported that the computation speed was improved 5,000 times beyond that of the first principle quantum molecular dynamics method by calculating the electronic state using the extended Hückel method (Yonezawa et al, 2001a, 2001b). Since this method enables faster computation and still has the characteristics of calculating the electronic state of a system according to quantum theory, the tight binding method is often applied within the field of chemistry for analyzing the surface reaction dynamics of relatively large systems. Using the tight binding method, the process of the production reaction of water in a fuel cell at the solid-gas interface has been simulated (Ishimoto et al., 2006). In addition, a hybrid method, which combines the tight binding method and the classical molecular dynamics method, is also being developed.

The tight binding method is still not sufficient for large-scale calculations that deal with the "flow" of a system because the calculation procedure is complicated because the electronic state of a system is calculated according to quantum theory. For calculations that deal with the statistical quantity of atomic motion, another method that determines the potential function, which is used in the classical molecular dynamics method using the results of the density functional theory, is also applied frequently. For instance, the potential, which is a function of the position or the orientation of an impinging molecule, is contrived by fitting the potential energy surface of a diatomic molecule on a transient metal surface at various orientations obtained by the density functional theory using an analytic function. The potential is often used to analyze the dissociation phenomena of hydrogen on a Pt or Pd surface (Beutl et al., 1995; Olsen et al., 1999, 2002). In this method, however, the motion of surface atoms cannot be considered, and therefore the effect of thermal motion of surface atoms on dissociation phenomena cannot be analyzed using this method. Owing to this defect, it has often been reported that the dissociation probability obtained by this method cannot be used to reproduce experimentally obtained data (Vincent et al., 2004).

The embedded atom method (EAM) is a scheme that treats the interaction between gas atoms and a metal surface by considering the effects of the surface electrons (Daw & Baskes, 1983; 1984). The method is based on DFT, and the potential energy of the system is expressed as a sum of the energy embedded an atom in the electron density of the surface and pair-interaction energy. In EAM, the electron density of the system can be reflected in the interaction potential, and therefore the motion of an atom on a metal surface can be simulated accurately. Moreover, the method has the advantage of a smaller computational load than quantum molecular dynamics (QMD), which is also based on DFT. EAM has often been used to analyze the motion of atoms on a transient metal surface (Baskes, 1992; Baskes et al., 2007). However, there has been little research of the application of EAM to dissociation phenomena. To apply EAM to the analysis of dissociation probability, incorporating the motion of the metal surface atoms, brings the simulations closer to the real system. Moreover, this method can be easily expanded to a more complicated surface.

In this chapter, the methods used for multi-scale analysis of flow phenomena including a surface reaction are described, and a typical example in which these methods are applied to the analysis of flow phenomena including a surface reaction is presented. In Section 2, the simulation method of Density Functional Theory and Embedded Atom Method are described. In Section 3, the analysis of dissociation phenomena by the EAM is discussed. Section 4 summarized the chapter.

2. Simulation methods

This section describes the simulation method which was used in this chapter. Especially Density Functional Theory (DFT) and Embedded Atom Method (EAM) are described.

2.1 Density Functional Theory (DFT)

The density functional theory (DFT) is the method in which various values obtained by wave functions of a system and operators are expressed by the functional of electron density of the system. In this method, the energy of the system is obtained exactly. In the analysis of the surface reaction, macroscopic values such as dissociation probability are obtained from the potential energy surface of the system obtained by this method. Moreover, this method is effective for obtaining the database necessary to determine the parameters for the tight binding method or the embedded atom method mentioned below. In this subsection, the outline of the theory of the method is explained below. For details, the reader should refer to some references (Parr & Yang, 1989; Satoko & Onishi,1994).

Let us consider the system that consists of M nuclei and N electrons. Thus, the nuclei are fixed and only the state of the electron is considered (Born- Oppenheimer approximation). The Schrödinger equation, which expresses the ground state of a system, is given by:

$$H\Psi_o = E_o\Psi_o \tag{1}$$

where Ψ_o and E_o denote a wave function that expresses the ground state of a system without degeneracy and the energy of electron at this state, respectively, and H denotes an operator, called the Hamiltonian, that expresses the total energy of the system. The operator is expressed using the kinetic energy of the electron, K, the Coulomb interaction between electrons, V_{ee}, and the interaction with the external force field, V_{ex}, as

$$H = K + V_{\mathrm{ee}} + V_{\mathrm{ex}} \tag{2}$$

The external force field, V_{ex}, in Eq. (2) is expressed as the sum of a function of only the position of each electron, $v(\boldsymbol{r})$. The formula of the function, for instance, is expressed in atomic units as

$$v(\mathbf{r}_i) = \sum_{k=1}^{M} \frac{-Z_k}{|\mathbf{r}_i - \mathbf{R}_k|} \tag{3}$$

assuming that $v(\boldsymbol{r})$ is a Coulomb interaction from the nuclei of the system. In Eq. (3), $\boldsymbol{r}_i$ and $\boldsymbol{R}_k$ denotes the position of electron i and that of nucleus k reduced by the Bohr radius, respectively, and Z_k denotes the charge of nucleus k reduced by elementary electric charge (e=1.602×10^{-19} C). The Coulomb interaction between electrons is expressed as the sum of the Coulomb interaction between electron i and j as

$$V_{\mathrm{ee}} = \sum_{i=1}^{N} \sum_{j>i}^{N} \frac{1}{|\mathbf{r}_i - \mathbf{r}_j|} \tag{4}$$

The solution of Eq. (1) satisfies the equation below:

$$E_o[\Psi_o] = \underset{\Phi \to \Psi_o}{\mathrm{Min}} \langle \Phi | H | \Phi \rangle \tag{5}$$

where <Φ | Φ>=1, Φ is an eigenfunction of H, Ψ_o is a function that minimizes the total energy of the system among the eigenfunctions of H. As mentioned above, when the formula of the interaction from the external force field, $v(\boldsymbol{r})$, is determined, the Hamiltonian is obtained by Eq. (2), and therefore the wave function Ψ_o and the total energy E_o of the system are obtained by Eq. (5). Namely, the state of the system is a functional of the interaction with the external force field, $v(\boldsymbol{r})$. Moreover, the electron density at position $\boldsymbol{r}$ is obtained by

$$\rho(\mathbf{r}) = |\Psi_o|^2(\mathbf{r}) \tag{6}$$

The basic principle of the density functional theory is that an interaction with the external force field, $v(\boldsymbol{r})$, corresponds to a certain electron density, $\rho(\boldsymbol{r})$, and vice versa, at the ground state without degeneracy. That is, an interaction from the external force field, $v(\boldsymbol{r})$, is obtained by a functional of electron density, $\rho(\boldsymbol{r})$ (Parr & Yang, 1989). The electron density at the ground state, $\rho(\boldsymbol{r})$, is obtained as described below, rather than by Eq. (5), so as to minimize the total energy of the system.

$$E[\rho] = \underset{\rho' \to \rho}{\mathrm{Min}} \left(K[\rho'] + V_{\mathrm{ee}}[\rho'] + V_{\mathrm{ex}}[\rho'] \right) \tag{7}$$

In density functional theory, the electron density is obtained by Eq. (7). The total energy of the system, $E[\rho]$, is expressed as

$$E[\rho] = F[\rho] + \int \rho(\mathbf{r}) v(\mathbf{r}) d\mathbf{r} \tag{8}$$

where the sum of the kinetic energy, $K[\rho]$, and the interaction between electrons, $V_{ee}[\rho]$, is expressed by $F[\rho]$. The electron density at the ground state, $\rho(\boldsymbol{r})$, minimizes $E[\rho]$ in Eq. (8) and satisfies the following Euler equation:

$$\mu = v(\mathbf{r}) + \frac{\delta F[\rho]}{\delta \rho(\mathbf{r})} \tag{9}$$

while considering the conservation of the number of electron as

$$\int \rho(\mathbf{r}) d\mathbf{r} = N \tag{10}$$

where μ is Lagrange's undetermined multiplier. In other words, it is necessary to solve the electron density, $\rho(\boldsymbol{r})$, that satisfies Eq. (9) in the density functional theory. However, it is difficult to solve Eq. (9) because the interaction between electrons is included in the functional $F[\rho]$. In the density functional theory, the electron density of the system, $\rho(\boldsymbol{r})$, is obtained by solving formula of a virtual system in which a certain effective potential, v_{eff}, affects electrons, and an interaction between electrons is not considered in the self-consistent field method.

Let us consider a system that consists of N electrons without interaction between electrons. The Hamiltonian of the system is expressed as

$$H = K + V_{ex} = \sum_{i=1}^{N} \left(-\frac{1}{2} \nabla_i^2 \right) + \sum_{i=1}^{N} v_v(\mathbf{r}_i) \tag{11}$$

where $v_v(\boldsymbol{r})$ denotes an interaction from an external force field and is a function of only the electron position. The wave function of the system at the ground state is expressed by the Slater determinant of the one-electron wave function, φ_i, as

$$\Psi_o = \frac{1}{\sqrt{N!}} \det[\varphi_1 \varphi_2 \cdots \varphi_N] \tag{12}$$

The one-electron wave function, φ_i, corresponds to the function in which the eigenenergy is lowest among all of the wave functions satisfying Eq. (13).

$$\left[-\frac{1}{2} \nabla_i^2 + v_v(\mathbf{r}_i) \right] \varphi_i = \varepsilon_i \varphi_i \tag{13}$$

The electron density of the system at the ground state, $\rho(\boldsymbol{r})$, is obtained by Eq. (6) using the wave functions obtained by Eq. (12). According to the theory mentioned above, the total energy of the system is a functional of electron density, $\rho(\boldsymbol{r})$, and is obtained by

$$E_v[\rho] = K_v[\rho] + \int \rho(\mathbf{r}) v_v(\mathbf{r}) d\mathbf{r} \tag{14}$$

However, the electron density, $\rho(\boldsymbol{r})$, obtained from the wave function in Eq. (12) is that which minimizes the energy of Eq. (14) and satisfies the following Euler equation:

$$\mu = v_{\mathrm{v}}(\mathbf{r}) + \frac{\delta K_{\mathrm{v}}[\rho]}{\delta\rho(\mathbf{r})} \tag{15}$$

because the electron density is that at the ground state, where $K_{\mathrm{v}}[\rho]$ in Eq. (14) or Eq. (15) shows the term of the kinetic energy of the virtual system. Namely, if Eq. (9), which includes the interaction between electrons in the functional $F[\rho]$, can be changed to Eq. (15), the electron density of the system can be obtained by Eqs. (6), (12), and (13) using an interaction with the external force field of the virtual system, $v_{\mathrm{v}}(\boldsymbol{r})$.

The functional in Eq. (9), $F[\rho]$, is expressed as

$$F[\rho] = K_{\mathrm{v}}[\rho] + J[\rho] + E_{\mathrm{xc}}[\rho] \tag{16}$$

where $J[\rho]$ denotes a classical Coulomb interaction between electrons and is expressed as

$$J[\rho] = \frac{1}{2}\int\int \frac{\rho(\mathbf{r})\rho(\mathbf{r}')}{|\mathbf{r}-\mathbf{r}'|} d\mathbf{r}d\mathbf{r}' \tag{17}$$

and the functional,

$$E_{\mathrm{xc}}[\rho] = F[\rho] - K_{\mathrm{v}}[\rho] - J[\rho] = \left(K[\rho] - K_{\mathrm{v}}[\rho]\right) + \left(V_{\mathrm{ee}}[\rho] - J[\rho]\right) \tag{18}$$

denotes the sum of the non-classical terms of interactions between electrons, ($V_{\mathrm{ee}}[\rho]$-$J[\rho]$) and the difference in kinetic energy between the real system and virtual system, ($K[\rho]$-$K_{\mathrm{v}}[\rho]$). The functional, $E_{\mathrm{xc}}[\rho]$, is called the exchange-correlation energy. Using Eqs.(9) and (16), we obtain

$$\mu = v(\mathbf{r}) + \frac{\delta K_{\mathrm{v}}[\rho]}{\delta\rho(\mathbf{r})} + \frac{\delta J[\rho]}{\delta\rho(\mathbf{r})} + \frac{\delta E_{\mathrm{xc}}[\rho]}{\delta\rho(\mathbf{r})} = v(\mathbf{r}) + \phi(\mathbf{r}) + v_{\mathrm{xc}}(\mathbf{r}) + \frac{\delta K_{\mathrm{v}}[\rho]}{\delta\rho(\mathbf{r})} \tag{19}$$

where

$$\phi(\mathbf{r}) = \int \frac{\rho(\mathbf{r}')}{|\mathbf{r}-\mathbf{r}'|} d\mathbf{r}' \tag{20}$$

denotes the Coulomb interaction of the electrons and

$$v_{\mathrm{xc}}(\mathbf{r}) = \frac{\delta E_{\mathrm{xc}}[\rho]}{\delta\rho(\mathbf{r})} \tag{21}$$

denotes the exchange-correlation energy. Assuming the value in Eq. (19), $v(\boldsymbol{r})+\phi(\boldsymbol{r})+v_{\mathrm{xc}}(\boldsymbol{r})$, to be an interaction with the external force field in the virtual system, $v_{\mathrm{v}}(\boldsymbol{r})$ in Eq. (15) (referred to as effective potential, $v_{\mathrm{eff}}(\boldsymbol{r})$), namely,

$$v_{\mathrm{eff}}(\mathbf{r}) = v_{\mathrm{v}}(\mathbf{r}) = v(\mathbf{r}) + \varphi(\mathbf{r}) + v_{\mathrm{xc}}(\mathbf{r}) \tag{22}$$

Equation (19) is the same as Eq. (15), and the electron density of the real system can be obtained using Eqs. (6), (12), and (13). In order to obtain the effective potential, $v_{\mathrm{eff}}(\boldsymbol{r})$, in Eq. (22), the term of the exchange-correlation energy, $v_{\mathrm{xc}}(\boldsymbol{r})$, must be determined. The values are

given as a functional of electron density. Several types of functional have been proposed in previous studies. The local density approximation (LDA), which is the most well known of these functionals, is obtained by assuming that the electron is uniformly distributed at a small region of the system. Other functionals, such as the generalized gradient approximation (GGA), which includes the information of the gradient of the electron density, or the local spin density approximation (LSDA), which is applied to the case of spin polarization, are developed considering the compensation between the accuracy and the calculation time. After the exchange-correlation energy is determined, the electron density is obtained by Eqs. (6), (12), (13), (20) and (22). However, it is necessary to obtain the electron density by the convergence scheme because $\phi(\boldsymbol{r})$ and $v_{xc}(\boldsymbol{r})$ are functionals of electron density. A flowchart of this scheme is shown in Fig. 1.

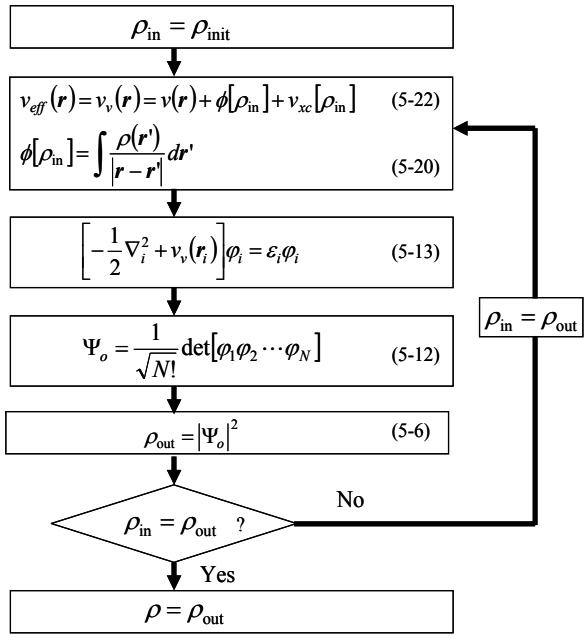

Fig. 1. Flowchart for the calculation of electron density by the density functional theory.

The advantage of this method is the dramatic decrease in the calculation time needed to directly calculate the energy from the electron density without solving the wave functions of the system. Namely, the exact solution can be obtained from the electron density of an independent N-electron system without solving the Schrödinger equations of the $3N$ space including the interaction between electrons by including the interaction between electrons in the empirical exchange-correlation energy.

2.2 Embedded Atom Method (EAM)

DFT can calculate the energy barrier accurately and the dissociation probability can be obtained from the information of energy barrier. However, it is based on static transition state theory (TST), while in real system atoms and molecules move. To consider the motion of atoms, the FPMD must be used. However it costs too much calculation load to analyze

the statistical characteristics of dissociation phenomena. It is necessary to use a faster method to analyze flow phenomena obtained as the statistical characteristics of the motion of atoms of the system. In this subsection, an outline of the embedded atom method is presented. The theory of this method is based on density functional theory, and this method is often applied to the analysis of the motion of atoms on a metal surface (Daw and Baskes, 1984).

In the embedded atom method, the energy of a system is expressed as the sum of the energy necessary to embed an atom into the background electron density and interaction between nuclei. The former corresponds to the energy from the electrons of the system, and the latter corresponds to the energy from the nuclei of the system. The energy of a system is then expressed as

$$E = \sum_{i=1}^{N} F_i\left(\rho_i\right) + \frac{1}{2}\sum_{i=1}^{N}\sum_{j\neq i}\phi_{ij}\left(R_{ij}\right) \tag{23}$$

where $F_i(\rho)$ denotes the energy necessary to embed atom i into the background electron density ρ, and $\phi_{ij}(R_{ij})$ denotes the core-core pair repulsion between atoms i and j separated by the distance R_{ij}. In addition, ρ_i denotes the electron density at atom i due to the remaining atoms of the system. The electron density is expressed by the superposition of the electron density of each atom as

$$\rho_i = \sum_{j\neq i}^{N} \rho_j^a\left(R_{ij}\right) \tag{24}$$

where ρ_j^a is the electron density contributed by atom j. It is necessary to determine the functions, $F_i(\rho)$, $\phi_{ij}(R_{ij})$, and ρ_j^a (R_{ij}) included in Eqs. (23) and (24) in order to use the embedded atom method. An example of how to determine these functions or parameters is described below.

The electron density can be obtained by a quantum chemical calculation, such as the DFT or molecular orbital calculation. McLean and Clementi calculated the wave functions of various atoms by the Roothaan-Hartree- Fock method and generated a data table (Clementi & Roetti, 1974; McLean & McLean, 1981). The reader can obtain the electron density by the data table and Eq. (6). With respect to the function, $F_i(\rho_i)$, the energy of various atoms embedded in a homogeneous electron density as a function of electron gas density have been obtained by the density functional theory (Puska et al, 1981; Norskov, 1982). The core-core pair-repulsion, $\phi_{ij}(R_{ij})$, is often determined such that the crystal structure of the bulk system can be reproduced by the EAM using the determined values of ρ_j^a (R_{ij}) and $F_i(\rho_i)$. These functions are determined for every type of atom.

The force acting on atom i is obtained by differentiating Eq. (23), as follows:

$$F = -\frac{\partial E}{\partial \mathbf{R}_i} = -\sum_{i=1}^{N}\frac{dF_i\left(\rho_i\right)}{d\rho_i}\frac{\partial \rho_i}{\partial \mathbf{R}_i} - \frac{1}{2}\sum_{i=1}^{N}\sum_{j\neq i}\frac{\partial \phi_{ij}\left(R_{ij}\right)}{\partial R_{ij}}\frac{\partial R_{ij}}{\partial \mathbf{R}_i} \tag{25}$$

3. Results and discussion

In this section the example of the analysis of dissociation phenomena of gas molecule on metal surface is introduced. We use the dissociation of H_2 molecule on Pt(111) surface, which is important not only for the fundamental system of dissociation phenomena but also for the reaction at anode side in Polymer Electrolyte Fuel Cell.

3.1 Potential energy surface

Analysis of the potential energy surface is important when discussing dissociation phenomena on a metal surface. From this potential energy surface, the values of the dissociation path or the dissociation barrier are calculated, and the dissociation probability is then obtained. In this subsection, a method for calculating the potential energy surface of a platinum-hydrogen system according to the density functional theory and the above-described analysis will be shown. All the calculations were conducted using the commercial density functional theory (DFT) program, DMol^3. LDA/VWN and GGA/PBE were used as exchange-correlation functionals for geometry optimization and energy calculations, respectively. The double-numerical plus polarization functions (DNP) were used as the basis sets for all atoms. All electrons were considered in the calculation. The convergence tolerance for the self-consistent field (SCF) calculation was set at 1.0×10^{-6} Ha and the convergence tolerance for geometry was set at 1.0×10^{-5} Ha. Smearing was set at 5.0×10^{-3} Ha for both calculations to improve convergence of the calculations. Spin was unrestricted during calculations.

Figure 2 shows the calculation model. In the calculation of the typical density functional theory, the surface is often expressed by three molecular layers in order to have a reasonable calculation load. At each layer, a platinum atom is placed at a location to its Miller indices correspond. Figure 2 shows the arrangement of the (111) surface. Because the calculation load determines the number of atoms representing one layer of the surface, the calculation of the direction of the surface is generally performed under the assumption of the periodic boundary condition, expressing the surface with $2\times2 = 4$ atoms. In the same figure, the basic cell is denoted by the white line. In the density functional theory, calculation is performed with periodic boundary condition in all directions. Figure 2 shows the technique used to avoid interactions normal to the surface by setting a long vacuum region.

Sometimes the calculation model that passed through the process described above is applied as a metal surface, but this causes instability when using the structure of bulk as is for the surface. At the actual surface, the structure changes slightly, causing surface relaxation. In the case of calculating a more realistic surface, reconstruction of the surface atom arrangement to achieve the most stable state after geometry optimization is one option. The LDA method is usually used for geometry optimization.

The orientation of molecule toward the surface is determined by locating the center of the molecule on a particular site on the surface (location of the molecule on a surface) and then defining the Euler angle of the molecular axis (ϕ, θ) in the space coordinate system. For the determined orientation, the energy of a system is calculated by changing the distance between nuclei, r, and the distance between the first surface layer and the center of the molecule, Z. The GGA method is most commonly used for the energy calculation. Repeated energy calculation while changing the values of r and Z enables the contour of the energy

(potential energy surface) to be drawn under the condition that the lateral axis is r and the longitudinal axis is Z. Examples are shown in Fig. 3. The left-hand side represents the PES at ϕ=0° and θ=90° of top site, and the right-hand side represents that at ϕ=0° and θ=90° of brg site. In this calculation, r is changed at 0.5 Å intervals in the range between 0.5 Å and 2.5 Å, and Z is changed at 0.5 Å intervals in the range between 0.5 Å and 2.5 Å.

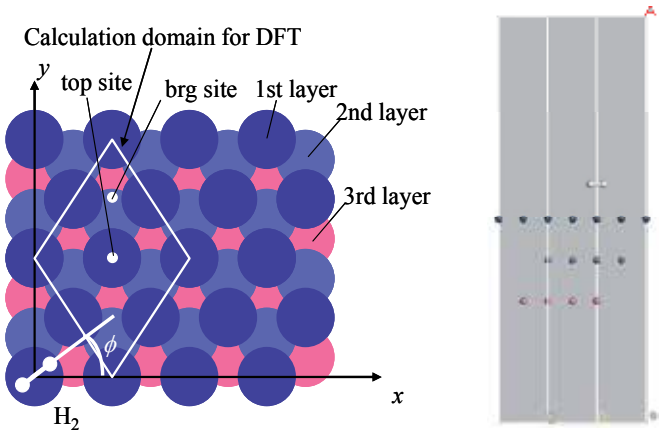

Fig. 2. Simulation system for the potential energy surface.

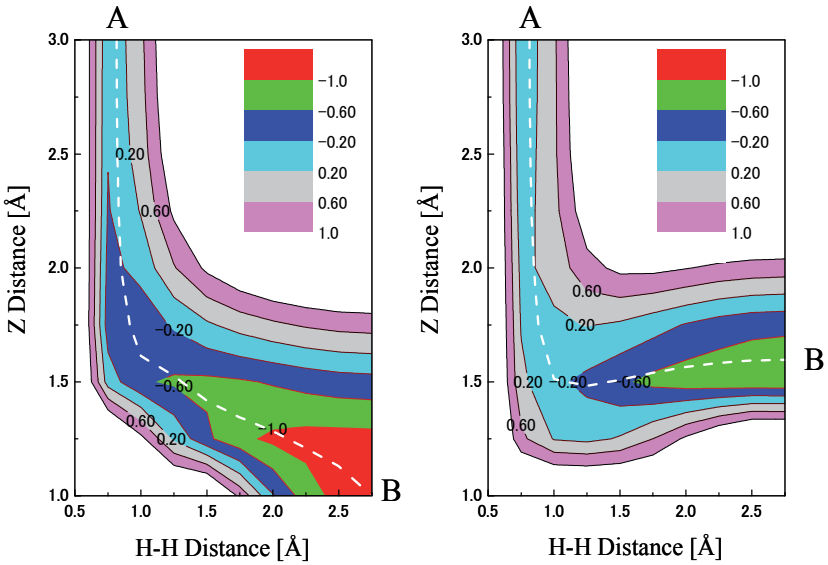

Fig. 3. Contour of the potential energy surface. The contour is plotted at 0.2 eV intervals. The white dashed lines show the dissociation path.

From the PES, the dissociation path or the height of the dissociation barrier is obtained as described below. Assuming that the hydrogen molecule passes through the route of lowest

energy from the state before dissociation (State A) to that after dissociation (State B) in Fig. 3, the route corresponds to a ridge of the potential energy surface. Therefore, the route of reaction is determined by obtaining the ridge from State A to State B. The white dashed lines in Fig. 3 show the dissociation path of each potential energy surface. The energy on the dissociation path is calculated by defining the energy of State A as 0. The potential energy increases as the molecule approaches the surface. The maximum energy on the dissociation path is called the "dissociation barrier". Molecules of less energy than the dissociation barrier cannot dissociate.

In the transient state theory, the dissociation probability is obtained from the height of the dissociation barrier. The probability that the kinetic energy of molecules impinging on the surface is in the range of $[e_{tr}, e_{tr}+de_{tr}]$ is obtained by Boltzmann distribution as

$$f(e_{tr})de_{tr} = 2\left(\frac{1}{kT}\right)^2 e_{tr}\exp\left[-\frac{e_{tr}}{kT}\right]de_{tr} \tag{26}$$

where k denotes the Boltzmann's constant. In this theory, all of the molecules that have a more energy than the dissociation barrier are considered to dissociate. This probability is obtained by integrating Eq. (26) in the range of $[E_b, \infty]$, as follows:

$$P = 2\left(\frac{1}{kT}\right)^2 \int_{E_b}^{\infty} e_{tr}\exp\left[-\frac{e_{tr}}{kT}\right]de_{tr} \tag{27}$$

3.2 Energy transfer between gas molecule and solid atoms

In the analysis of dissociation probability by the transient state theory and the density functional theory mentioned above, the molecules that are reflected from the surface without dissociation after passing over the dissociation barrier are not considered when obtaining the dissociation probability because in this theory all molecules that have an energy greater than the dissociation barrier are considered to dissociate. Moreover, the effect of the direction of the motion or the rotational energy of molecules on the dissociation probability is not considered because the dissociation probability is determined by only the magnitude of the translational energy of the molecule. However, the potential energy surface is likely to change due to the motion of surface atoms. It is necessary to consider these motions of atoms in order to make the analysis more real. In this subsection, the method used to obtain the dissociation probability while considering the motion of atoms is described. The embedded atom method is used as the simulation method. The method used to determine the embedded function or the core-core pair-repulsion function is also described.

In the EAM, the potential energy, E_{pot}, of the system, which consists of a Pt surface of N atoms and an H_2 molecule, is obtained by

$$E_{pot} = \sum_{i=1}^{N} F_{Pt}(\rho_i) + \sum_{k=1}^{2} F_H(\rho_k) + \sum_{i=1}^{N}\sum_{j>i}^{N} \phi_{Pt-Pt}(R_{ij}) + \sum_{i=1}^{N}\sum_{k=1}^{2} \phi_{Pt-H}(R_{ik}) + \phi_{H-H}(R_{12}) \tag{28}$$

where subscripts i and j denote the given number of Pt atoms, subscript k denotes the given number of H atoms, and R denotes the distance between atoms. The functions $F_{Pt}(\rho_i)$ and

$F_H(\rho_i)$ denote the energy necessary to embed a Pt atom or an H atom, respectively, into the background electron density, ρ_i, and $\phi_{Pt\text{-}Pt}(R_{ij})$, $\phi_{H\text{-}H}(R_{12})$ and $\phi_{Pt\text{-}H}(R_{ik})$, denote the core-core pair-repulsion potential between Pt atoms, between H atoms, and between a Pt atom and an H atom, respectively. In addition, ρ_i and ρ_k denote the electron density at Pt atom i or H atom k, respectively, by the remaining atoms. By defining these functions such that the results obtained by the EAM reproduce those obtained by the DFT, calculation by the EAM is faster, and the accuracy in the EAM is sufficient. The details of the form of the function are omitted herein. For these details, the reader should refer to some references (Tokuamsu and Ito, 2007; 2011).

Next, an example of simulating the dissociation phenomena of H_2 on the Pt surface by the EAM potential determined mentioned above is described. A schematic diagram is shown in Fig. 4. The Pt(111) surface consists of 10×10×3 = 300 Pt atoms in the x, y, and z direction, respectively. A periodic boundary condition is imposed in the x and y directions. The initial position of atoms is the same as that of a bulk crystal structure of Pt. The lattice constant of Pt is set at 3.92 Å.

When the temperature of the surface is controlled, it is often used to control the velocity of the atoms of the system. However, this method affects the motion of dissociating molecules because the velocity of atoms that directly interact with the dissociating molecules is changed artificially. For this reason, in this example, the temperature of the surface is controlled by phantom molecules (Blomer and Beylich, 1996). The initial velocities of the Pt atoms and the phantom atoms are given at random, according to the Boltzmann distribution at the temperature of T [K], and the system is relaxed toward the equilibrium state when the temperature of the system is controlled. The spring constant for phantom atoms, k, was set at 46.8 N/m, and the coefficient of the dumper, α, was set at 5.184×10^{-12} kg/s. The cutoff distance of the interaction was set at 15 Å. Time integration was calculated by the leap-frog method(Allen & Tildesley, 1986) with a time interval, Δt, of 1 fs.

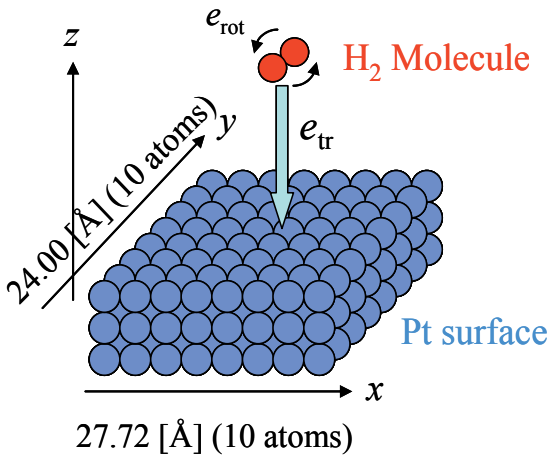

Fig. 4. Schematic diagram of simulation system.

Before simulating the dissociation of H_2 molecules, the relaxed Pt(111) surface, whose temperature was controlled to a target temperature, had to be obtained. The simulation was

performed until the system reached equilibrium at the target temperature. In this simulation, the target temperature was set at T=350 K.

H_2 molecules impinged upon the top, brg, or fcc sites of the relaxed Pt(111) surface from a height of 5 Å. An initial translational energy, E_{tr}, was given to the H_2 molecule normal to the surface as the impinging energy. Neither rotational nor vibrational energy was given to the H_2 molecule. The orientation of the impinging H_2 molecule was given at random.

A typical example of the difference from the initial energy of kinetic energy of Pt atoms, kinetic energy of the impinging H_2 molecule, potential energy obtained in Eq. (28) and total energy are shown in Fig. 5. Bold line shows the total energy of the system and square, circle and triangle denotes the E_{pot} obtained in Eq. (28), kinetic energy of Pt atoms and that of the impinging H_2 molecule, respectively. As shown in this figure, the energy transfers between each degree of freedom but total energy of the system was well conserved relative to the difference from initial energy of each degree of freedom. Simulations were performed for 40,000 steps or 10,000 steps, depending upon whether the impinging energy was smaller or larger than 0.1 eV, respectively, because an H_2 molecule with a smaller impinging energy takes more time to reach the surface. Typical examples of the behavior of an H_2 molecule on a Pt(111) surface upon collision are shown in Fig. 6. Fig. 6 (a) and (b) show the dissociation case and no dissociation case, respectively. Both the distance of the center of mass of the H_2 molecule from the surface and the distance between H atoms in the H_2 molecule are shown.

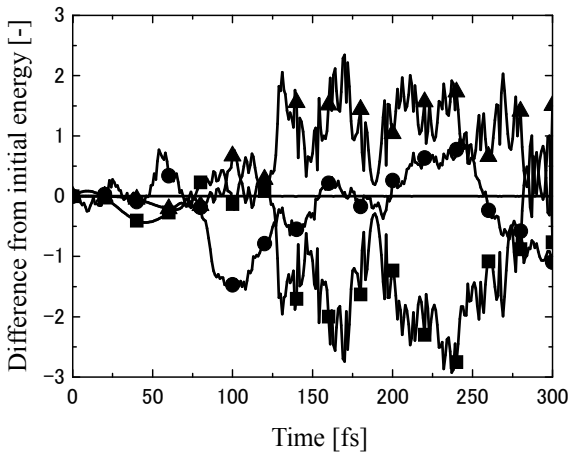

Fig. 5. Typical example of differential from initial energy of degree of freedom. Bold line denotes the difference of initial energy of total energy. Square, circle and triangle denote those of potential energy, kinetic energy of Pt atoms and kinetic energy of H_2 molecule, respectively.

In Fig. 6 (a), the impinging energy was set at E_{tr}=0.25 eV. In this case, the velocity of impinging molecule decreases during t=50~60 fs and the molecule collide with the Pt surface, which implies that the molecule passes over a dissociation barrier. The distance between H atoms becomes longer while the H_2 molecule migrates on the surface. In the present simulations, H_2 molecules having a distance between H atoms larger than 3.5 Å

were considered to dissociate. Figure 6 (b) shows the case not dissociating after collision. The impinging energy was set at E_{tr}=0.1 eV. As shown in this figure, the molecule can pass over the dissociation barrier and collides with the surface. However, the molecule reflects and departs again directly. In this case the vibrational energy is excited because of the strong interaction to the surface.

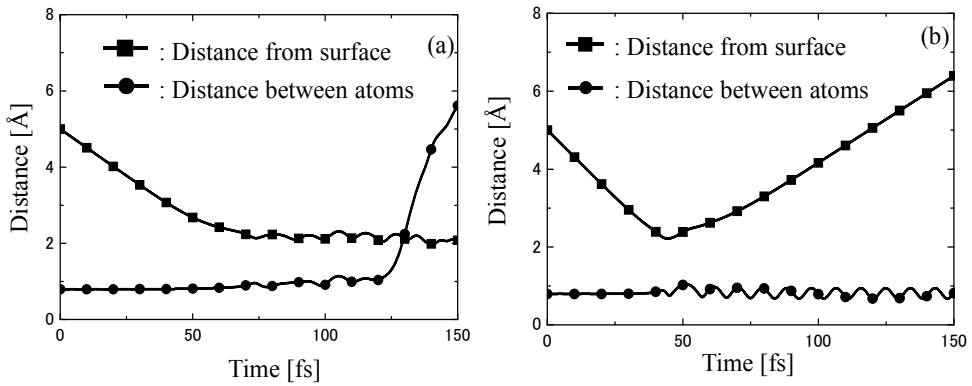

Fig. 6. Distance from surface of the center of mass of the H_2 and the distance between H atoms. (a) the impinging H_2 molecule dissociates. (b) the impinging H_2 molecule does not dissociate.

3.3 Dissociation probability

The simulations mentioned in Sec. 3.2 were performed 640 times, fixing the impinging energy and the site on the Pt(111) surface, and changing the orientation of the H_2 molecule at random. The dissociation probability was obtained against impinging energy at top, brg, and fcc sites from the ratio of dissociated to all cases. The initial configuration of the Pt(111) surface was changed in every simulation. The impinging energy was varied from 0.01 to 0.5 eV. The "dynamic" dissociation probabilities, P_d, against impinging energy are shown in Fig. 7 (a).

By the way, the "static" dissociation probabilities, P_s, can be obtained from the interaction potential between an H_2 atoms and a Pt surface. The detailed method was described in a reference (Tokumasu and Ito, 2011). The static dissociation probability is shown in Fig. 7 (b). Fig. 7 (a) shows that at brg and fcc sites, the dynamic dissociation probability increases with increasing impinging energy of the H_2 molecule, and becomes nearly constant at higher impinging energy. The tendency is similar to the static dissociation probability shown in Fig. 7 (b), implying that dynamic effects are not important to the dissociation at brg or fcc sites. The dissociation probability at top site, however, decreased with increasing impinging energy. This tendency is very different from the static dissociation probability shown in Fig. 7 (b). Moreover, Fig. 7 (b) shows that the dissociation probability when the impinging energy is near 0 is about 25 %, which means that 75 % of the impinging molecules cannot pass over the dissociation barrier. However, Fig. 7 (a) shows that 90 % of the impinging molecules dissociates when the impinging energy is near 0. This contradiction shows the

"dynamic effects" on the dissociation probability (Tokumasu & Ito, 2011), and therefore the effects at the top site are larger than that at brg or fcc sites. This contradiction was analyzed in detail.

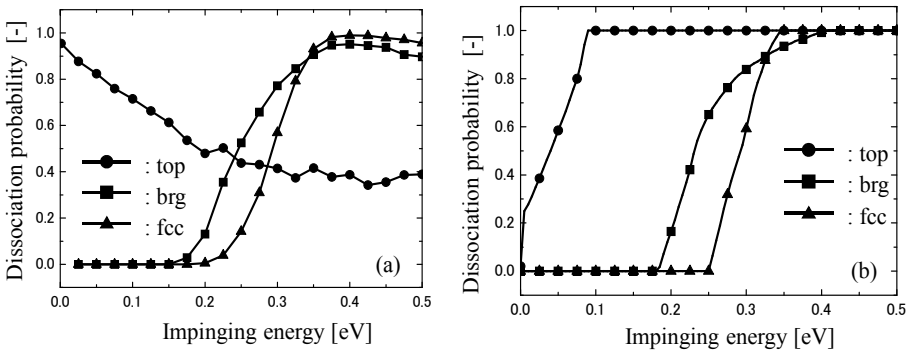

Fig. 7. The dissociation probabilities at each site. Circles, squares, and triangles show the results at top, brg, and fcc sites, respectively. (a) Dynamic dissociation probability, (b) Static dissociation probability.

Initially, the probability that an impinging H_2 molecule reaches the chemisorption layer, P_c, was obtained for the top site. The result is shown in Fig. 8. As shown in this figure, all impinging molecules reach the chemisorption layer, even at very low impinging energy, unlike the results shown in Fig. 7 (b). The behavior of the impinging H_2 molecules clearly shows that H_2 molecules with very low impinging energy can reach the chemisorption layer by changing their orientation via interaction with the Pt(111) surface. These impinging molecules have no dissociation barrier, even if they have an initial orientation at which the dissociation barrier is large. The change in orientation of an impinging molecule via interaction with the surface to reduce the dissociation barrier is called the "steering effect (Darling & Holoway, 1994; Darling et al, 1998; Gross et al. 1995). Previous research indicated that an impinging molecule is easier to dissociate than expected in a static manner due to this effect when the impinging energy and rotational energy of the impinging molecule is very small (Darling et al, 1998). The steering effect is also observed at brg and fcc sites. The impinging molecules with very low impinging energy, however, cannot pass over the dissociation barrier regardless of orientation at brg or fcc sites, because the minimum dissociation barrier is more than 0.1 eV at these sites. For this reason, the steering effect is unimportant to dissociation phenomena at brg or fcc sites. The steering effect becomes remarkable only at sites where a molecule can reach the chemisorption layer with a very small dissociation barrier (or no dissociation barrier) at specific orientations, such as at the top site.

The dissociation probability, however, decreases rapidly with increasing impinging energy, although all impinging molecules reach the chemisorption layer. The tendency is different from that of brg and fcc sites, where almost all molecules that reach the chemisorption layer dissociate. The distribution of orientation of impinging molecules at the top site, when the molecules pass over the dissociation barrier and when the molecules dissociate, were

investigated at very low impinging energy. The results showed that the orientation of the impinging molecule at which the dissociation barrier is very low is normal to the surface, and the orientation at which the molecules dissociate is parallel to the surface at the top site. Almost all the molecules can dissociate at the top site when the impinging energy is very low, because the molecules can change their orientation by the steering effect to easily pass over the dissociation barrier to reach the chemisorption layer (by aligning normal to the surface). They can then readjust their orientation, again by the steering effect, such that they can easily dissociate (by aligning parallel to the surface). With increasing impinging energy, however, the molecules have sufficient energy to reach the chemisorption layer without the steering effect, and do not have time to change their orientation to one in which they can easily dissociate. Therefore, they depart from the surface without dissociation after collision. In dissociation at the top site, two steering effects are important: once when the molecule reaches the chemisorption layer, and again when the molecule dissociates. Therefore, the dominant factor in dissociation at the top site is the motion of the H_2 molecule at the chemisorption layer by steering effect, not the probability that the H_2 molecule reaches the chemisorption layer. The dynamic effects on dissociation probability are very important when dissociation phenomena at the top site are considered.

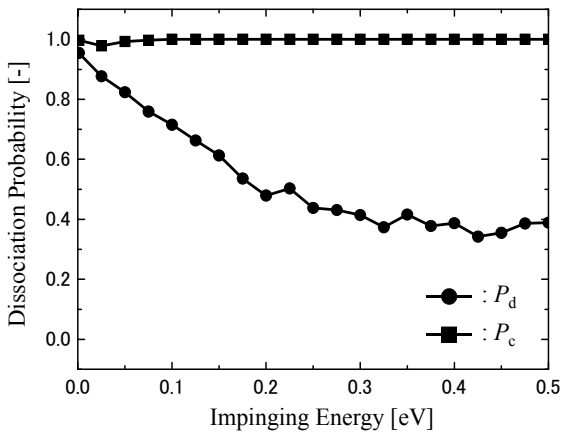

Fig. 8. Dissociation probability at brg and fcc sites, P_d, and the probability of reaching the chemisorption layer, P_c (top site). Circles and squares show P_d and P_c, respectively.

3.4 Comparison with experimental results

To check the valildity of the simulation, the dissociatino probability against the impinging angle was simulated and the resuts were compared with experimental results (Luntz et al., 1990). In this study, D_2 molecules were used as impinging gas molecules because in the experimental study with which we compared our results, D_2 molecules were used. The EAM potential constructed for the H_2 molecule was used for the D_2 molecule since the state of electrons can be regarded as the same for both of these molecules. Simulation system were almost the same as that obtained in Sec. 3.1, but the incident angle was given to the impinging molecule. The incident polar angle was varied from 0^o (normal to the surface) to 60^o and the incident azimuthal angle was varied in a uniform random manner. Moreover, the initial position of H_2 molecule is given at random. The rotational energies were given

according to Boltzmann distribution. The detailed method was described in a reference (Koido et al., 2011).

The results of MD simulations are shown in Fig. 9. The dissociation probability, P_d, for each incident angle against initial translational energy is shown. It shows that P_d increases along with the initial translational energy at all level of polar angle of incidence. When the angle is normal to the surface (θ_i = 0°), even at very low translational energy, P_d has a certain value and it increases along with the initial translational energy. This shows that there is no obvious translational energy threshold for dissociation probability to rise. It means that there is no energy barrier for dissociation when a gas molecule approaches to the surface with the orientation that takes the minimum potential among its possible potential energy surfaces. At a larger initial translational energy than E_{tr} = 0.25 eV, P_d does not increase.

At larger angles of incidence, P_d increases more slowly with initial translational energy similar to the normal incidence case and stops increasing at higher initial translational energy. It should be noted that when the polar angle of incidence is off normal to the surface, at the lowest initial translational energy calculated (E_{tr}=0.0025 eV), P_d is a little higher than the value at little higher translational energy. The rise at very low translational energy suggests that the "Steering Effect" at the top site (Tokumasu and Ito, 2011) is important. When translational energy is very low, the possibility of a molecule to have both low translational energy and low rotational energy is relatively high. Moreover, it allows good chance for a molecule to rotate to the orientation that experiences low energy barrier to dissociate near the surface. It can be said that even though the result is the average of collisions on all the surface area, the “Steering Effect” at a particular site cannot be neglected.

These MD results are compared with experimental data (Luntz, 1990) at each incident polar angle. Although the MD results and the experimental data do not agree very well, they both show the following trends: P_d increases along with initial translational energy, P_d decreases along with increasing polar angle of incidence, and no initial translational energy threshold for dissociation probability is observed when the molecules approach along the surface normal.

If we see the hydrogen dissociation on other metal surfaces, the trends may be quite different. It was reported that hydrogen dissociation on Cu(111) surface requires at least around 0.5 eV of large activation energy (Luntz, 2009; Gross, 1998). Moreover, it was also reported both theoretically and experimentally that the dissociation probability is high at 0 translational energy and decreases along with the translational energy and increases at higher energy again on Pd(100) surface (Luntz, 2009; Gross, 1998). From the above discussion, MD simulations using the constructed EAM potential are capable of simulating molecular beam experiments to a certain degree.

The rise in the dissociation probability observed at low translational energies in the MD results cannot be compared with the experiments due to lack of experimental data.

4. Summary

In order to analyze the dissociation phenomena of gas molecule on metal surface which includes chemical reactions, it is necessary to perform quantum mechanical calculations

considering the electronic states of materials. However, since this is not practical due to the large calculation time and therefore the analysis based on molecular dynamics, which needs dramatically small calculation time than quantum calculation, is desired. Therefore, a quantum mechanical method is first used to analyze the (nanoscale) electronic state, which dominates the reaction phenomena, and, using the obtained information, the empirical parameter applied to molecular dynamics is determined. The behavior of the molecule or its statistical (micro-scale) quantity is then analyzed. This analysis is referred to as "multi-scale analysis". In multi-scale analysis, it is important to properly understand the nanoscale phenomena that dominate the micro-scale phenomena.

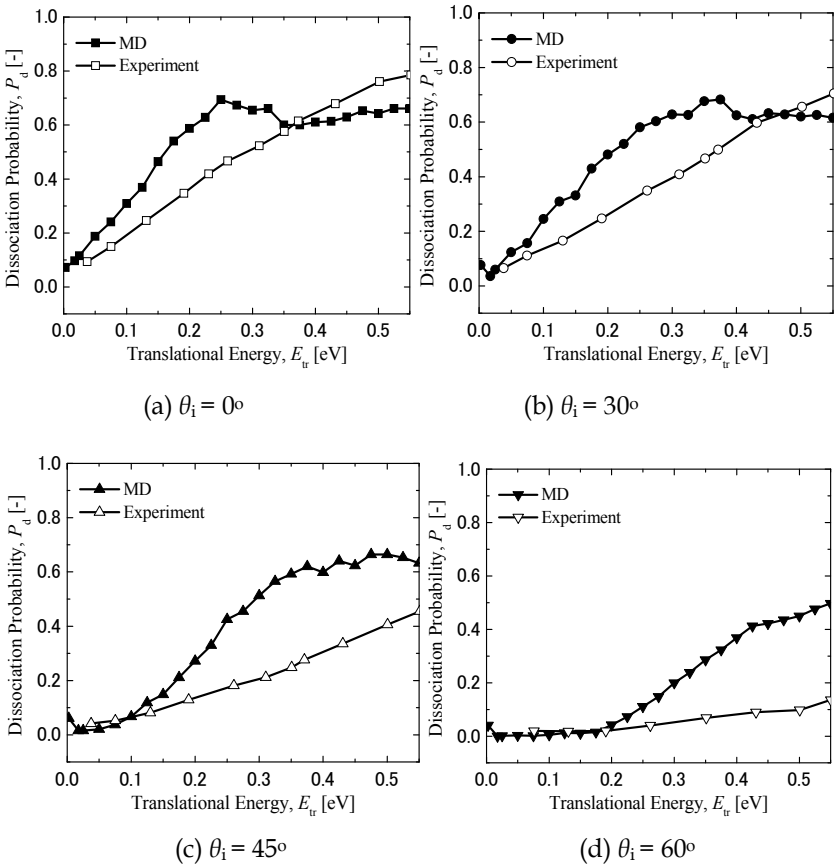

Fig. 9. Dissociation probability predicted by MD simulations (black symbols) as a function of initial translational energy, E_{tr} for surface temperature, T_s = 295 K, for different incident polar angles ((a) θ_i=0°, (b) θ_i=30°, (c) θ_i=45°, (d) θ_i=60°) are compared with experimental results by Luntz et al. (white symbols).

5. Acknowledgment

I am very grateful to Dr. Koido for his results of comparing MD simulation with experimental data. All the simulations of this chapter were performed by a supercomputer system of Institute of Fluid Science, Tohoku University.

6. References

Allen, M. P. and Tildesley, D. J. (1986). Computer Simulation of Liquids, Oxford University Press, (1989), pp.80-81.

Baskes, M. I. (1992). Modified embedded-atom potentials for cubic materials and impurities, *Physical Review B*, Vol. 46, pp.2727-2742.

Baskes, M. I. ; Srinivasan, S. G. ; Valone, S. M. & Hoagland, R. G. (2007), Multistate modified embedded atom method, *Physical Review B*, Vol. 75, 094113.

Beutl, M.; Riedler M. & Rendulic K. D. (1995). Strong Rotational Effects in the Adsorption Dynamics of H_2/Pd(111): Evidence for Dynamical Steering, *Chemical Physics Letters*, Vol. 247, pp.249-252.

Blömer, J and Beylich, A. E. (1997). MD-Simulation of Inelastic Molecular Collisions with Condensed Matter Surfaces, *Proceedings of Rarefied Gas Dynamics*, pp.392-397, Beijing, China, August 19-23, 1996.

Car, R. & Parrinello, M. (1985). Unified Approach for Molecular Dynamics and Density-Funtional Theory. *Physical Review Letters,* Vol. 55, pp.2471-2474.

Clementi, E. & Roetti, C. (1974). Roothaan-Hartree-Fock Atomic Wavefunctions Basis Functions and Their Coefficients for Ground and Certain Excited States of Neutral and Ionization Atoms, Z < 54, *Atomic Data and Nuclear Data Tables*, Vol. 14, pp.177-478.

Darling, G. R. & Holloway, S. (1994). Rotational motion and the dissociation of H_2 on Cu(111), Journal of Chemical Physics, Vol. 101, No. 4, pp.3268—3281

Darling, G. R.; Key, M. & Holloway, S. (1998). The steering of molecules in simple dissociation reactions, *Surface Science*, Vol. 400, pp.314--328

Daw, M. S. & Baskes, M. I. (1983). Semiempirical, Quantum Mechanical Calculation of Hydrogen Embrittlement in Metals, *Physical Review Letters*, Vol. 50, pp.1285-1288.

Daw, M. S. & Baskes, M.I. (1984). Embedded--atom method: Derivation and application to impurities, surfaces, and other defects in metals, *Physical Review B*, Vol. 29, pp.6443-6453.

Gross, A. ; Wilke, s. & Scheffler, M. (1995). Six-Dimensional Quantum Dynamics of Adsorption and Desorption of H2 at Pd(100): Steering and Steric Effects, Physical Review Letters, Vol. 75, pp.2718—2721

Gross, A. (1998). Hydrogen Dissociation on Metal Surface - A Model System for Reactions on Surface, *Applied Physics A*, Vol. 67, No. 6, pp.627-635.

Ishimoto, R.; Jung. C. H.; Tsuboi, H.; Koyama, M.; Endou, A.; Kubo, M.; Del Carpio, C. A. & Miyamoto, A. (2006). Periodic Density Functional and Tight-Binding Quantum Chemical Molecular Dynamics Study of Catalytic Properties on Gamma-Al_2O_3 Supported Pt Catalysts, *Applied Catalysis A-General*, Vol. 305, (2006), pp.64-69.

Jinnouchi, R. & Okazaki, K. (2003), New Insight into Microscale Transport Phenomena in PEFC by Quantum MD, *Microscale Thermophysical Engineering*, Vol. 7, pp.15-31.

Koido, T., Tomarikawa, K., Yonemura, S. & Tokumasu, T. (2011), Molecular Dynamics Study of the Effects of Translational Energy and Incident Angle on Dissociation Probability of the H_2/D_2-Pt(111) System, Journal of Applied Physics, Vol. 110, No. 2, pp. 024301

Luntz, A. C.; Brown, J. K. & Williams, M. D. (1990), Molecular beam studies of H_2 and D_2 dissociative chemisorption on Pt(111), Journal of Chemical Physics, Vol. 93, No. 7, pp.5240—5246

Luntz, A. C. (2009). The Dynamic of Dissociative Adsorption on Metal Surface: "First Principles" theory - Experiment Confrontations, *Surface Science,* Vol. 603, pp.1557-1563.

Mclean, A. D. & Mclean, R. S. (1981). Roothaan-Hartree-Fock Wave Functions Slater Basis-Set Expansions for Z=55-92, Atomic Data and Nuclear Data Tables, Vol. 26, pp.197-381.

Norskov, J. K. (1982). Covalent Effects in the Effective-Medium Theory of Chemical Binding: Hydrogen Heats of Solution in the 3d Metals, *Physical Review B*, Vol. 26, (1982), pp.2875-2885.

Olsen, R. A.; Kroes, G. J. & Baerends, E. J. (1999). Atomic and Molecular Hydrogen Interacting with Pt(111), *Journal of Chemical Physics*, Vol. 111, pp.11155-11163.

Olsen, R. A.; Busnengo, H. F.; Salin, A.; Somers, M. F.; Kroes, G. J. & Baerends, E. J. (2002). Constructing Accurate Potential Energy Surfaces for a Diatomic Molecular Interacting with a Solid Surface: H_2+Pt(111) and H_2+Cu(100), *Journal of Chemical Physics*, Vol. 116, pp.3841-3855.

Parr, R. G. & Yang, W. (1989). *Density-Functional Theory of Atoms and Molecules*, Oxford University Press

Puska, M. J., Nieminen, R. M. & Manninen, M. (1981). Atoms Embedded in an Electron Gas: Immersion Energies, *Physical Review B*, Vol. 24, pp.3037-3047.

Satoko, T. & Onishi, S. (1994). *Density-Funcional Theory and its application, 6th Ed.* Kodansha, (in Japanese)

Steinfeld, J. I. ; Francisco, J. S. & Hase, W. L. (1989). *Chemical Kinetics and Dynamics*, Prentice-Hall, pp.287-319.

Tokumasu, T. & Ito, D. (2007). The Dependence of Molecular Motion on the Dissociative adsorption of H_2 on Pt(111), *Proceedings of 2007 ASME-JSME Thermal Engineering Summer Heat Transfer Conference*, HT2007-32590 (CD-ROM), Vancouver, Canada, July 8-12, 2007

Tokumasu, T. & Ito, D. (2011). The Dynamic Effects of Dissociation Probability of H_2-Pt(111) System by Embedded Atom Method, *Journal of Applied Physics*, Vol.109, No.6, 063509.

Vincent, J. K.; Olsen, R. A.; Kroes, G. J. & Baerends, E. J. (2004) Dissociation Chemisorption of H2 on Pt(111): Isotope Effect and Effects of the Rotational Distribution and Energy Dispersion, *Surface Science*, Vol. 573, pp.4376-4384.

Wang, Y. & Balbuena, P. B. (2004). Roles of Proton and Electron Field in the Electroreduction of O_2 on Pt(111) Surfaces: Results of an Ab- Initio Molecular Dynamics Study, *Journal of Physical Chemistry B*, Vol. 108, pp.4376-4384.

Yonezawa, T.; Nagata, T.; Kato, H. & Imamura, A. & Morokuma, K. (2001), *Introduction of Quantum Chemistry, 14th Ed.*, Vol. 1, Kagaku-Dojin, (in Japanese)

Yonezawa, T.; Nagata, T.; Kato, H. & Imamura, A. & Morokuma, K. (2001), *Introduction of Quantum Chemistry, 14th Ed.*, Vol. 1, Kagaku-Dojin, (in Japanese)

16

A Study of the Adsorption and Diffusion Behavior of a Single Polydimethylsiloxane Chain on a Silicon Surface by Molecular Dynamics Simulation

Dan Mu[1] and Jian-Quan Li[2]
[1]*College of Chemistry Chemical Engineering and Materials Science, Zaozhuang University, Shandong*
[2]*Photoelectric Engineering College, Zaozhuang University, Shandong China*

1. Introduction

In three dimensions, polymer dynamics exhibits a rich and complex behavior which depends on the solvent conditions and polymer concentration (1; 2). That the dynamics of polymer chains at and near solid interfaces differs profoundly from that in the bulk is intuitively expected. Polymer adsorption on the surface is of technological and scientific importance in the field of colloids and biomolecules. Examples include the two-dimensional (2-D) diffusion of DNA oligonucleotides confined to biological interfaces such as cell membranes (3; 4). The diffusion of confined polymers at surface is always a fundamental, yet problematical topic in polymer physics (1; 2; 5–8). The behavior of polymers at the liquid-solid interface is crucial to technologies involving molecular surface placement (9; 10). Polymers adsorbed onto a surface to form thin films is an emerging topic of modern materials science (11; 12). They can be applied, for example, in the fields of biosensors, light-emitting diodes, nonlinear optical devices, and permeation-selective gas membranes (13–18). The fabrication of the thin films always takes place in vacuum or dilute solutions. The adsorption of the polymer chains can be controlled by varying multiple parameters such as the polymer-surface interaction, the solvent quality, surface nano-roughness, temperature, polymer chain length and so on. The knowledge about the adsorption dynamics and the thermodynamics of the equilibrium adsorption is crucial to understand and furthermore improve the property of the final product. Experimentally it is difficult to control well the above influences separately, thus, clear information on the exact effect of a specific environmental parameter is hard to obtain. Due to the fast-growing computation power nowadays, it is possible to utilize the computer as an "experimental apparatus" to solve the problem, with the aid of various simulation techniques. It has attracted attention for decades already.

Granick and co-workers studied poly(ethylene glycol) molecules adsorbed on solid surface by means of fluorescence microscopy (19–22). They found that the diffusion coefficient (D) of such chains scales with the degree of polymerization (N) as $N^{-3/2}$, which is characteristic for

2-D chain models. On the other hand, Maier and Rädler found much weaker scaling, namely N^{-1}, when studying adsorbed DNA in a lipid bilayer (3; 4). In the simulations, Milchev and Binder (23) showed that D scales with the chain length as $N^{-1.1}$; Azuma and Takayama (24) obtained $D \sim N^{-3/2}$; but Falck et al. (25) found that D should scale as N^0. Therefore, the dynamics behavior of a confined polymer on a surface is still an interesting research topic.

Computer simulations for the mechanism of a single polymer chain adsorbed and diffusing on a surface are important, as experimental studies on an isolated polymer chain are difficult in most cases. Many simulations had been performed for different polymeric systems with multiple chains (or a single chain) adsorbing and diffusing on the surface (24–27).

Binder and coworkers successfully studied polymer films in different conditions via computer simulations (28–31). Lu and Kim observed the surface pattern of a thin polymer film by using a three-dimensional electrostatic model. The competition between the electrostatic energy and the surface energy leads to a characteristic pillar size. Furthermore, the film thickness significantly influences the growth rate and the distance between pillars (32). Recently, Kumar and coworkers found that a non-wetting solvent aids adsorption of the polymer chain at low sticking energies compared to wetting solvent by the aid of molecular dynamics simulations (33). However, there was no literature about the adsorption and diffusion of the PDMS (polydimethylsiloxane) single chain on the silicon surface. In this research, our main objective is to study the adsorption and diffusion processes of a hydrophobic chain on a hydrophobic surface. The similar hydrophobic-hydrophobic systems usually appears in the wetting, surface adhesion and flow in confined geometries are examples of such systems. Because we have completed some research about the poly (vinyl alcohol) adsorbing on the hydroxylated β-cristobalite (34), polyethylene chain adsorbing on the hydroxylated β-cristobalite (35), and the polyethylene chain adsorbing on the silicon (111) surface (36), then the results of the polydimethylsiloxane adsorbing on the silicon (111) surface may be helpful and enriching for further understanding of the configuration change and the dynamics of the hydrophobic polymer chain adsorbed on a hydrophobic surface.

We consider a single PDMS chain adsorbed on the rigid (111) silicon surface in a vacuum and in mimetic good solvent condition. The adsorption and diffusion processes of the chain are investigated through energy minimizations and molecular dynamics simulations with all the molecular degrees of freedom being taken into account. Only one single chain is adopted in a simulation because it relates directly to 2-D polymer diffusion in very dilute solution. In addition, PDMS is a widely available polymeric material, comes in a range of molecular weights, and is easy to use. The hydrophobic silicon is chosen because of its relative simplicity and rigidity, so it can be treated as a fully rigid body for our purposes. We follow a two-step strategy: first, we carry out direct energy minimizations of the PDMS chain close to the silicon surface with different initial configurations in order to relax the model; second, we use the most stable configuration after minimization to perform MD (Molecular Dynamics) simulation. In the theory of dynamical scaling the two key quantities are the radius of gyration (R_g) and the center-of-mass diffusion coefficient D of the chain. We thus use them to describe the characteristics for the system in this paper. We also change the effective dielectric constant to 78.0 to mimic good solvent condition. The results are compared with the systems in a vacuum (which can be taken as in bad solvent condition). The chain configurations show

similar, but the diffusion coefficients vary greatly, showing strong dependence on the solvent condition.

2. Models and simulation details

The MD simulation is carried out in a box with 3-D periodic boundary conditions. The PDMS chain is embedded into the simulation box with a fixed (111) silicon surface parallel to the XY plane. We choose N for the chain as 10, 20, 30, 40, 50 and 60. The thickness of the surface is around 12 Å. The length of the simulation box in the Z direction is 80 Å, which is large enough so that the interactions between the adsorbed PDMS chain and the periodic images of silicon in the top plane can be ignored. In this way, the 3-D periodicity inherent in the model is transformed into an actual 2-D periodicity thus simulating an infinitely extended surface.

A high-quality force field COMPASS (condensed-phase optimized molecular potentials for atomistic simulation studies) (37; 38) is adopted in the simulation. In contrast to early force fields which were mostly parameterized based on gas-phase data or ab initio calculations, COMPASS combines ab initio and empirical parametrization procedures. In addition, it adds cross terms to potential in order to consider the influence of all atoms close-by and distortions of bond length or bond angle. It enables accurate and simultaneous prediction of structural, conformational, vibrational and thermophysical properties for a broad range of molecules in isolation and in condensed phases. The energy calculation with COMPASS is a combination of bonding and non-bonding terms. The bonding terms include stretching, bending and torsion energy as well as the diagonal and off-diagonal cross coupling terms. The van der Waals interactions are truncated at r_c=12 Å by using a spline function from 11 Å. The Coulomb interactions are calculated via Ewald summation (39). Before the MD simulations, energy minimizations are performed to relax the local unfavorable structure of the chain. Subsequently, MD simulations with 5 ns are performed under NVT thermodynamics ensemble. Every simulation is performed three times to ensure the reliability of the results. The equations of motion are integrated with a time step of 1 fs. The constant temperature T=300 K is controlled through the Berendsen thermostat (40) with a relaxation time of 0.1 ps.

In these simulations, the total and potential energies show an initial decrease, possibly with a few separate kinetic stages, and then fluctuate around a constant value, indicating the achievement of the equilibrium state. This process corresponds to the adsorption and diffusion dynamics of the PDMS chain from the initial configuration. We then change the dielectric constant to 78.0 to mimic the good solvent condition. Of course in this way the explicit solvation effects cannot be considered. Nevertheless, we can directly study the effects by simply changing the bad to the good solvent condition on the chain configurations and dynamics.

3. Simulation results and discussion

In this section, we show the simulation results, such as the chain configurations, the diffusion coefficient and the adsorption energy. All simulations are run until the chain reaches its equilibrium structure, i.e., until the simulated chain lost its memory of the initial configuration, and running the program further results in no discernible changes in the structural properties and energy beyond natural fluctuations.

3.1 In vacuum (or bad solvent)

3.1.1 Configuration change of PDMS during adsorption

Fig.1 shows the simulation snapshots of the PDMS chains with N=40. Furthermore, it shows good adsorption during the simulation time on the silicon (111) surface. Interestingly, the sequent configurations present curved not straight, and they all present 2-D adsorption configuration from the side view when the single chain has adsorbed well on the surface. With time evolution, the chain configuration changes from initially isolated "random-coil" in a

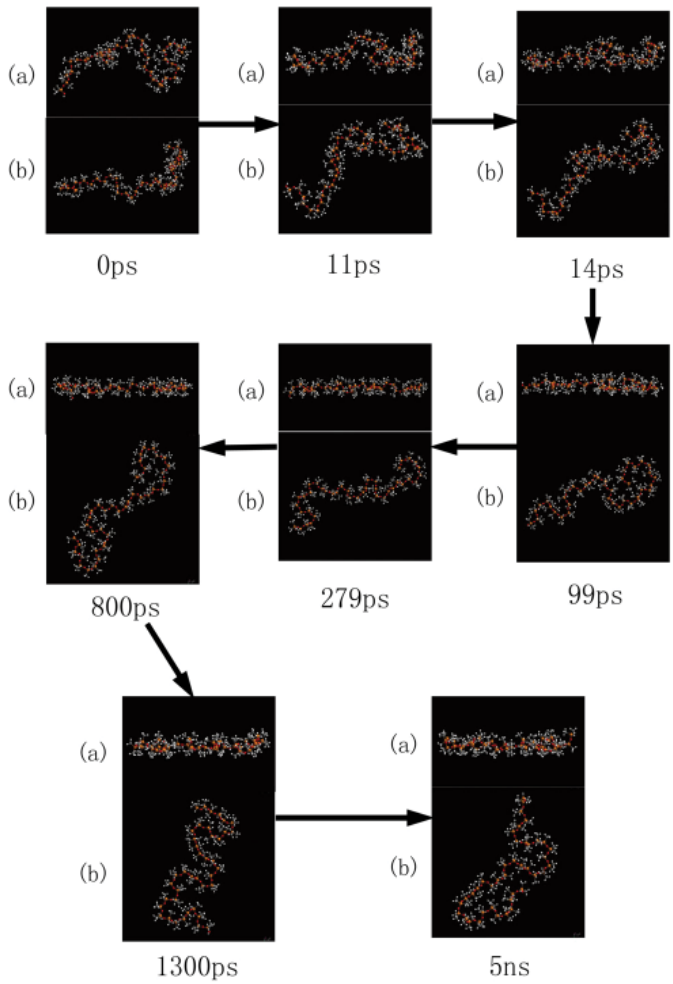

Fig. 1. We take the case of N=40 for example, extract the snapshots of the configurations during its adsorption process.

vacuum to a compact form adsorbed on the surface. In the first several hundred picoseconds, chain adsorption occurs accompanied by diffusion. When the energy dynamically reaches constant, the chain dynamics is mainly dominated by the diffusion process. Fig.2 shows the simulation snapshots of the PDMS chains with N=10, 40, 50 and 60 in equilibrium, but the configurations of longer chain like N=50 and 60 present partial arched part. However,

it shows good adsorption of no matter short or long PDMS single chain on this silicon surface. Interestingly, these configurations present curved, especially the long chains. Finally, they all present 2-D adsorption configuration from the side view when they reach both thermodynamic and kinetic equilibrium state. To show the chain configuration change during

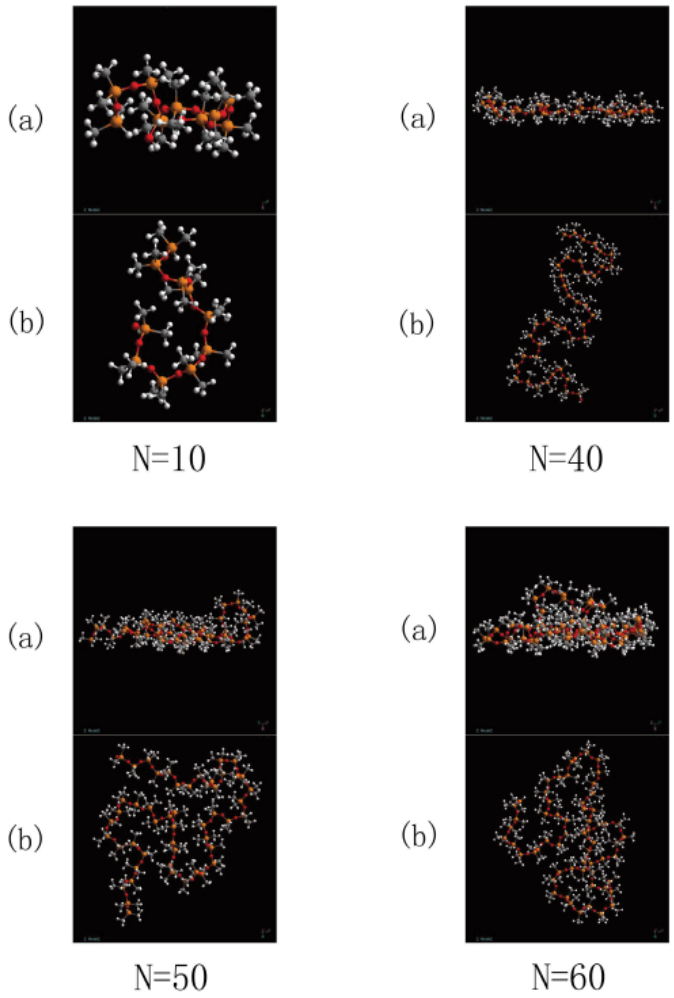

Fig. 2. Snapshots for PDMS chains adsorbed on the silicon surface with N=10, 40, 50 and 60 are displayed. The gray color denotes carbon and the white denotes hydrogen. Red denotes oxygen, orange denotes silicon.

the adsorption, we calculate the mean radius of gyration which is defined as

$$< R_g >= \sqrt{< \frac{1}{A} \sum_{i=1}^{N} (r_i - r_{cm})^2 >} \tag{1}$$

where r_i and r_{cm} denote the position vector of each atom in a chain and the center-of-mass for the whole chain, respectively, and A represents the number of atoms. Fig.3 shows the change

of calculated $< R_g >$ with increasing A. We fit this curve with the first order exponential decay function as $R_g = A_1 exp(-x/t_1) + y_0$, therein $y_0 = 6.82 \pm 0.35, A_1 = -9.62 \pm 0.55$ and $t_1 = 18.76 \pm 2.9$.. By seeing the simulation snapshots, we can find that all the PDMS chain are ultimately well-adsorbed on the silicon surface with 2-D configurations. It appears increasing trend of $< R_g >$ during the increase in the N values, then it's amplitude becomes smaller and smaller, especially for the longer chains. For the sake of characterizing the

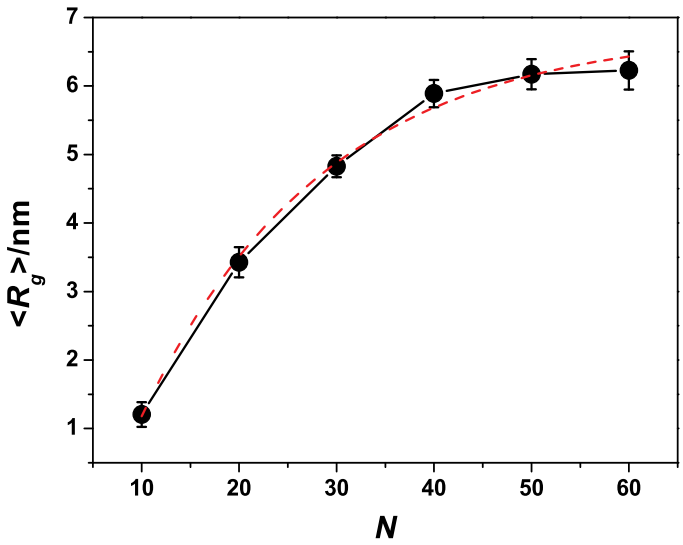

Fig. 3. The mean radius of gyration R_g vs the chain length N. The symbols are MD simulation results. The error bars are the standard deviation measured in three parallel simulations.

anisotropic configuration of the polymer and interpreting the configuration change during adsorption, we calculate two ratios such as $(R_x^2 + R_y^2)/R_z^2$ and R_{max}/R_{min}. R_x, R_y and R_z are the components in three principal directions of R_g. R_{max} and R_{min} correspond to the large and small magnitude between R_x and R_y, respectively. The results are shown in Fig.4, panels a and b. The component of R_g along the Z axis that is perpendicular to the surface is strongly reduced during the adsorption. The components of R_g along the X and Y axes display significant increase due to the chain spreading on the surface. All the chains are well adsorbed on the surface and therefore present 2-D configurations. Thus R_x and R_y are larger and R_z is very small.

3.1.2 Diffusion of PDMS chain on the surface

After the adsorption process, which is monitored by the interaction energy between the chain and the surface starting to fluctuate only around a constant value, the dynamics of PDMS is mainly dominated by the chain diffusion on the surface. We calculate the diffusion coefficients of the chains via the Einstein relation. Fig.5 shows the change of D with the varying degree of polymerization. There is apparent scaling between D and N, that is, $D \sim N^{-3/2}$. The dependence of D on N can be explained by the change of interaction energy between the chain and surface with increasing N. This adsorption energy can be calculated via

$$E_{int} = E_{tot} - (E_{frozen} + E_{plane}) \tag{2}$$

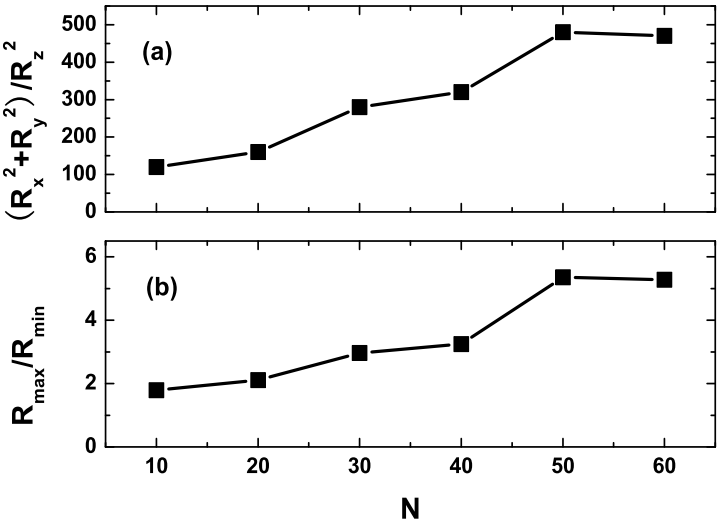

Fig. 4. These two ratios are calculated from the three principal components of R_g. Panel a shows the ratio of $(R_x^2+R_y^2)/R_z^2$ vs N and panel b shows the ratio of R_{max}/R_{min} vs N, where R_{max} denotes the larger one of R_x or R_y, and R_{min} denotes the other.

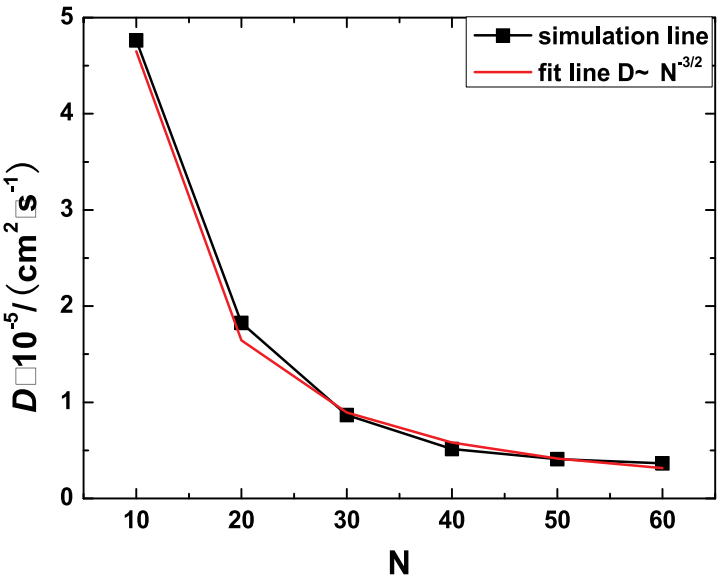

Fig. 5. Diffusion coefficients, D, are plotted against degree of polymerization of the PDMS chain, N.

where E_{tot} is the potential energy of the chain plus the surface system in equilibrium, E_{frozen} is the potential energy of the adsorbed chain isolated in a vacuum with the geometry unchanged, and E_{plane} is the potential energy of the surface. Larger molecular configuration deformation allows for better adsorption of the chain onto the surface; however, this will break the intramolecular interaction which causes a free energy penalty. Therefore such an interaction competition results in all the adsorption energy with increasing N, which can be seen in Fig.6.

We fit this curve with the linear function, and the average adsorption energy per segment (E_{int}/N) is -0.42 kcal/mol.

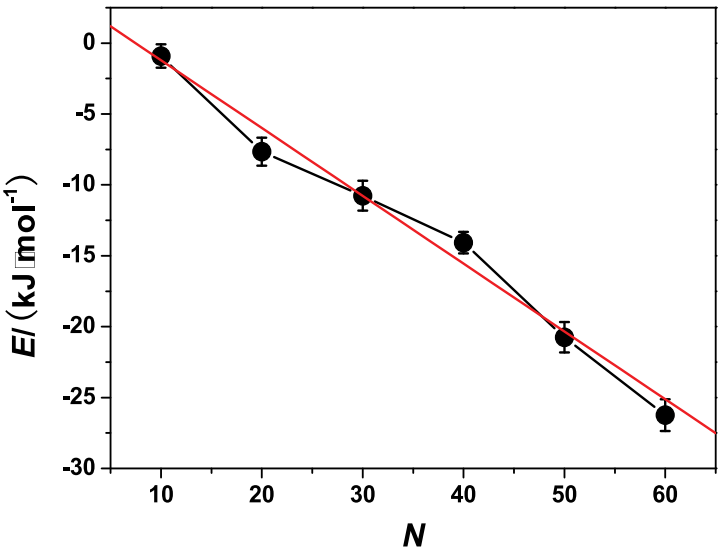

Fig. 6. Adsorption energy E_{int} vs chain length N.

3.2 In good solvent

We change the dielectric constant to 78.0 to mimic the good solvent condition (41). Of course in this way the explicit solvation effects cannot be considered. Nevertheless, we can directly study the effects by simply changing the bad to the good solvent condition on the chain configurations and dynamics.

The PDMS chain also can be adsorbed onto the hydrophobic surface in good solvent environment, showing 2-D configurations, no matter how many monomers the chain contains. The adsorption takes place very fast and the equilibrium is attained around about 200 ps. Sequentially, 2-D chain configurations are always retained in the successive diffusion process. At last, the chain possesses the most stable configuration as one layer on the surface. For saving time and avoiding repetitious work, we have only chosen one special chains with the same length as $N = 10$. Compared to the relative results in a vacuum, we can find that the contact area between the chain and the surface decrease, also the interaction energy increases, which results the data of E_{int} and diffusion coefficients both increase. The results are shown in Table 1. Also the configurations are both changed: the configuration of $N = 10$ turns from "coil pancake" to more extended configuration; and the configuration from the side view can be seen contains stacking part, which can be attributed to its lower diffusion coefficient value in good solvent compared with it in bad solvent. The equilibrium configuration of these two cases are present in Fig.7. In summary, it is clear that solvent effect has an important influence on the configurations and the dynamics of the hydrophobic-hydrophobic system from the discussion above. It can change not only the equilibrium chain configuration after the adsorption, but also the dynamics behavior of the chain on the surface.

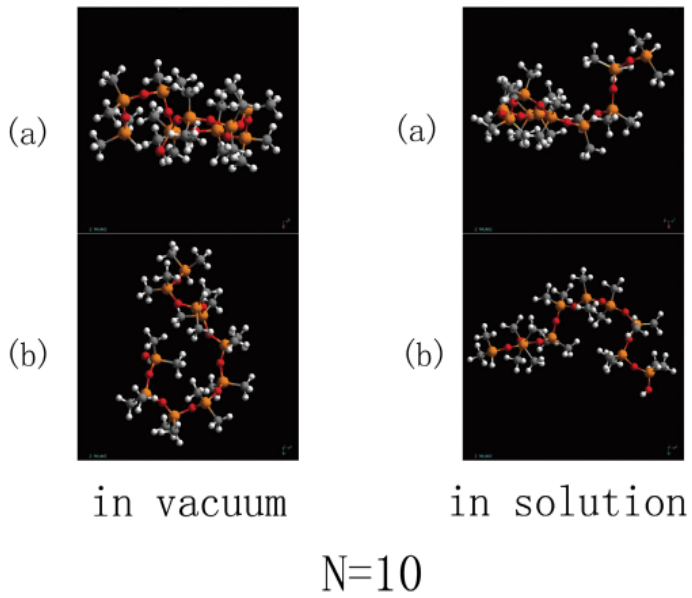

Fig. 7. Snapshots for PDMS chains adsorbed on the silicon Surface with N=10 are displayed in bad (in vacuum) and good (in solution) solvent environment, respectively. The gray color denotes carbon and the white denotes hydrogen. Red denotes oxygen, orange denotes silicon.

	E_{int}(kcal/mol)	D(cm^2/s)
in vacuum	-0.91	4.76 $\times 10^{-5}$
in good solvent	-0.85	7.42 $\times 10^{-5}$

Table 1. Details of Adsorption Energy and Diffusion Coefficient for the Adsorption Behavior of N=10 PDMS Single Chain on Silicon surface.

4. Conclusions

In this paper, MD simulations are used to investigate the adsorption and diffusion behavior of a single flexible hydrophobic PDMS chain on a hydrophobic silicon surface. Because of their similar characteristics, the PDMS chains are all adsorbed well onto the surface and possess 2-D configurations.

In a vacuum (or bad solvent), the PDMS chains are well adsorbed onto the hydrophobic surface and displays 2-D configuration. The calculated results of mean radius of gyration and two ratios such as $(R_x^2 + R_y^2)/R_z^2$ and R_{max}/R_{min} manifest the chain length dependence of the adsorption configuration. The adsorption energies are linearly scaled with N, therein the average E_{int}/N value is -0.42 kcal/mol. In addition, the data of their diffusion coefficient obey scaling law with $N^{-3/2}$ for the considered chain lengths, which is the same as polyethylene on Si (111) surface (45).

In good solvent, the PDMS chain also can be adsorbed very well on the surface and displays 2-D configuration, especially for the chains with less monomers; when the chains become longer, it would present quasi 2-D configurations, owing to its larger adsorption energy and larger diffusion coefficient in good solvent environment, compared with that in bad solvent

environment with the same chain length. Owing to the decrease of adsorption energy and diffusion coefficients, the configuration of $N = 10$ in good solvent changes to be more extended with less folded number, compared with that in a vacuum environment. The lower adsorption energy determines the larger diffusion coefficient, which means the higher diffusion rate.

The above results show that a single PDMS chain can be adsorbed onto the hydrophobic surface well. This is affected by the solvent conditions. By changing from the bad to good solvent, the chain can be worse adsorbed, which means it is good for desorption in good solvent environment, accordingly, it is good for adsorption in bad solvent enviroment. Thus by fine-tuning the solvent quality, one can manipulate the behavior of the chain.

5. Acknowledgment

The project is supported by the Science-Technology Foundation for Middle-aged and Young Scientist of Shandong Province (BS2010CL048), Shandong Province Higher School Science & Technology Fund Planning Project (J10LA61) and Zaozhuang Scientific and Technological Project (200924-2).

6. References

[1] de Gennes, P.G.(1979) *Scaling Concepts in Polymer Physics*, Cornell University Press, Ithaca, NY.
[2] Doi, M.; Edwards, S.F. (1986) *The theory of Polymer Dynamics*, Clarendon Press, Oxford, UK.
[3] Maier, B.; Rädler, J.O. (1999) Conformation and Self-Diffusion of Single DNA Molecules Confined to Two Dimensions *Phys. Rev. Lett.*, 82, 1911-1914.
[4] Maier, B.; Rädler, J.O. (2000) DNA on Fluid Membranes: A Model Polymer in Two Dimensions *Macromolecules*, 33, 7185-7194.
[5] Yethiraj, A. (2002) Polymer Melts at Solid Surfaces *Adv. Chem. Phys.*, 121, 89-139.
[6] Sheiko, S.S.; Möller, M. (2001) Visualization of moleculesąła first step to manipulation and controlled response *Chem. Rev.*, 101, 4099-4123.
[7] Granick, S. (2002) Kinetic and Mechanical Properties of Adsorbed Polymer Layers *Eur. Phys. J. E.*, 9, 421-424.
[8] Granick, S.; Kumar, S.K.; Amis, E.J.; Antonietti, M.; Balazs, A.C.; Chakraborty, A.K.; Grest, G.S.; Hawker, C.; Janmey, P.; Kramer, E,J.; Nuzzo, R.; Russell, T.P.; Safinya, C,R. (2003) Macromolecules at Surfaces: Research Challenges and Opportunities from Tribology to Biology *J. Polym. Sci. Part B: Polym. Phys.*, 41, 2755-2793.
[9] Haynes, C.A.; Norde, W. (1994) Globular Proteins at Solid/Liquid Interfaces *Colloids Surf. B.*, 2, 517-566.
[10] Malmsten, M. (1998) Formation of Adsorbed Protein Layers *J. Colloid Interface Sci.*, 207, 186-199.
[11] Decher, G. (1997) Fuzzy Nanoassemblies: Toward Layered Polymeric Multicomposites *Science*, 277, 1232-1237.
[12] Esker, A.R.; Mengel, C.; Wegner, G. Ultrathin Films of a Polyelectrolyte with Layered Architecture (1998) *Science*, 280, 892-895.
[13] Caruso, F.; Caruso, R.A.; Mohwald, H. (1998) Nanoengineering of Inorganic and Hybrid Hollow Spheres by Colloidal Templating *Science*, 282, 1111-1114.

[14] Shiratori, S.S.; Rubner, M.F. (2000) pH-Dependent Thickness Behavior of Sequentially Adsorbed Layers of Weak Polyelectrolytes *Macromolecules*, 33, 4213-4219.
[15] Clark, S.L.; Hammond, P.T. (1998) Engineering the Microfabrication of Layer-by-Layer Thin Films *Adv. Mater.*, 10, 1515-1519.
[16] Husemann, M.; Morrison, M.; Benoit, D.; Frommer, J.; Mate, C.M.; Hinsberg, W.D.; Hedrick, J.L.; Hawker, C.J. (2000) Manipulation of Surface Properties by Patterning of Covalently Bound Polymer Brushes *J. Am. Chem. Soc.*, 122, 1844-1845.
[17] Xia, Y.N.; Whitesides, G.M. (1998) Soft lithography *Annu. Rev. Mater. Sci.*, 28, 153-184.
[18] Huck, W.T.S.; Strook, A.D.; Whiteside, G.M. (2000) Synthesis of Geometrically Well Defined, Molecularly Thin Polymer Films *Angew. Chem. Int. Ed.*, 39, 1058-1061.
[19] Sukhishvili, S.A.; Chen, Y.; Müller, J.D.; Gratton, E.; Schweizer, K.S.; Granick, S. (2000) Materials science: Diffusion of a polymer pancake *Nature*, 406, 146-146.
[20] Bae, S.C.; Xie, F.; Jeon, S.; Granick, S. (2001) Single isolated macromolecules at surfaces *Curr. Opin. Solid. State. Mater.*, 5, 327-332.
[21] Sukhishvili, S.A.; Chen, Y.; Müller, J.D.; Gratton, E.; Schweizer, K.S.; Granick, S. (2002) Surface Diffusion of Poly(ethylene Glycol) *Macromolecules*, 35, 1776-1784.
[22] Zhao, J.; Granick, S. (2004) Polymer lateral diffusion at the solid-liquid interface *J. Am. Chem. Soc.*, 126, 6242-6243.
[23] Milchev, A.; Binder, K. (1996) Static and Dynamic Properties of Adsorbed Chains at Surfaces: Monte Carlo Simulation of a Bead-Spring Model *Macromolecules*, 29, 343-354.
[24] Azuma, R.; Takayama, H. (1999) Diffusion of single long polymers in fixed and low density matrix of obstacles confined to two dimensions *J. Chem. Phys.*, 111, 8666-8671.
[25] Falck, E.; Punkkinen, O.; Vattulainen, I.; Ala-Nissila, T. (2003) Dynamics and scaling of two-dimensional polymers in a dilute solution *Phys. Rev. E.*, 68, 050102.
[26] Cavallo, A.; Müller, M,.; Binder, K. (2005) Unmixing of Polymer Blends Confined in Ultrathin Films: Crossover between Two-Dimensional and Three-Dimensional Behavior *J. Phys. Chem. B*, 109, 6544-6552.
[27] Wang, Y.; Mattice, W.L. (1994) A Comparison between Monte Carlo Simulation and the Scheutjens-Fleer Mean-Field Lattice Theory *Langmuir*, 10, 2281-2288.
[28] Milchev, A.; Binder, K. (1997) Dewetting of thin polymer films adsorbed on solid substrates: A Monte Carlo simulation of the early stages *J. Chem. Phys.*, 106, 1978-1989.
[29] Pandey, R.B.; Milchev, A.; Binder, K. (1997) Semidilute and Concentrated Polymer Solutions near Attractive Walls: Dynamic Monte Carlo Simulation of Density and Pressure Profiles of a Coarse-Grained Model *Macromolecules*, 30, 1194-1204.
[30] Varnik, F.; Baschnagel, J.; Binder, K.; Mareschal, M. (2003) Confinement effects on the slow dynamics of a supercooled polymer melt: Rouse modes and the incoherent scattering function *Eur. Phys. J. E.*, 12, 167-171.
[31] Lin, Y.-C.; Müller, M.; Binder, K. (2004) Stability of thin polymer films: Influence of solvents *J. Chem. Phys.*, 121(8), 3816-3828.
[32] Kim, D.-C.; Lu, W. (2006) Three-dimensional model of electrostatically induced pattern formation in thin polymer films *Phys. Rev. B*, 73, 035206.
[33] Desai, T.; Keblinski, P.; Kumar, S. (2006) Computer simulations of the conformations of strongly adsorbed chains at the solidÍCliquid interface *Polymer*, 47, 722-727.
[34] Mu, D.; Lu, Z.-Y.; Huang, X.-R. (2008) The adsorption of poly (vinyl alcohol) on the hydroxylated β-cristobalite *Molecular Simulation*, 34(6), 611-618.

[35] Mu, D.; Lu, Z.-Y.; Huang, X.-R.; Sun, C.-C. (2008) Ordered Adsorption of Polyethylene on Hydroxylated β Cristobalite (100) Surface *Chem. J. Chinese Universities*, 29(10), 2065-2069.
[36] Mu, D.; Zhou, Y.-H. (2011) Molecular Dynamics Simulation of the Adsorption and Diffusion of a Single Hydrophobic Polymer Chain on a Hydrophobic Surface *Acta Phys. -Chim. Sin.*, 27(2), 374-378.
[37] Sun, H. (1998) COMPASS: An ab Initio Force-Field Optimized for Condensed-Phase Applications - Overview with Details on Alkane and Benzene Compounds *J. Phys. Chem. B*, 102, 7338-7364.
[38] Sun, H.; Ren, P.; Fried, J.R. (1998) The compass force field: parameterization and validation for phosphazenes *Comput. Theor. Polym. Sci.*, 8, 229-246.
[39] Allen, M.P.; Tildesley, D.J. (1987) *Computer Simulation of Liquids*, Clarendon, Oxford, UK.
[40] Berendsen, H.J.C.; Postma, J.P.M.; van Gunsteren, W.F.; Dinola, A.; Haak, J.R. (1984) Molecular-dynamics with coupling to an external bath *J. Chem. Phys.*, 81, 3684-3690.
[41] Raffaini, G.; Ganazzoli, F. (2004) Molecular dynamics simulation of the adsorption of a fibronectin module on a graphite surface *Langmuir*, 20, 3371-3378.
[42] Rouse, P.E. (1953) A theory of the visco-elastic properties of dilute solutions of coiling polymers *J. Chem. Phys.*, 21, 1272-1280.
[43] Shannon, S.R.; Choy, T.C. (1997) Dynamical Scaling Anomaly for a Two Dimensional Polymer Chain in Solution *Phys. Rev. Lett.*, 79, 1455-1458.
[44] Ala-Nissila, T.; Herminghaus, S.; Hjelt, T.; Leiderer, P. (1996) Diffusive spreading of chainlike molecules on surfaces *Phys. Rev. Lett.*, 76, 4003-4006.
[45] Mu, D.; Zhou, Y.-H. (2011) Adsorption and Diffusion Processes of Polyethylene on Silicon (111) Surface Studied by Molecular Dynamics Simulation *J. Theor. Comput. Chem.*, 10(4), 411-421.

Part 5

Dynamics of Ionic Species

17

The Roles of Classical Molecular Dynamics Simulation in Solid Oxide Fuel Cells

Kah Chun Lau[1] and Brett I. Dunlap[2]
[1]*Department of Chemistry, George Washington University, Washington D.C.*
[2]*Code 6189, Chemistry Division, Naval Research Laboratory, Washington D.C.*
USA

1. Introduction

1.1 Solid state ionics and SOFC

Solid ionic compounds normally form insulating compounds because each ion usually has a closed-shell electronic configuration, which prevents delocalization of electrons and thus electronic conduction in the system. In an appropriate temperature regime, charge can be transported in these solid materials, however, by the motion of highly mobile ionic species (e.g. Li^+, Na^+, O^{2-}, etc.) (Fig. 1 Top) (Chu et al., 2006). This phenomenon is termed "ionic conductivity". Such ionic compounds exhibit liquid-like conductivities whilst still in the solid state, i.e. at temperatures are well below their melting points (Hull, 2004). Exploiting this unusual property, considerable progress has been made in recent years in fuel cells and batteries, which are promising key technologies to meet our rising energy and environmental needs.

Using "superionic conductivity" (e.g. typically ~ 10^{-1} Scm^{-1}) (Fig. 1 Top), high temperature fuel cells, e.g. solid oxide fuel cells (SOFC) operate between 600° and 1200° C. Compared to batteries which are electrochemical energy storage devices, SOFC's are energy conversion device that produces electricity by electrochemically combining fuel (e.g. H_2, CH_4, CO, hydrocarbon etc.) and oxidant (e.g. air, O_2) chemical reactions at anode and cathode respectively (Fig. 1 Middle), with high thermodynamic efficiency and low environmental impact (Andersson et al., 2010; Etsell et al., 1970; Lashtabeg et al., 2006). A SOFC is a complex ceramic-solid-based electrochemical device consisting of three main components: an anode, electrolyte and cathode. The main component requiring fast ion transport and diffusion is the solid electrolyte. With external electron transfer, oxygen is reduced to oxygen ions (O^{2-}) at the cathode side through the oxygen reduction reaction (ORR): $\frac{1}{2}\ O_2 + 2e^- \rightarrow O^{2-}$. Then the oxygen ions are incorporated into the oxygen ion conductor, the SOFC electrolyte. The oxygen ions (O^{2-}) are transported through the electrolyte, but electrons are not. An ideal electrolyte in a SOFC is an electronic insulator, but an ionic conductor, and therefore permits only the oxygen ions to pass through to the anode. At the anode, the oxygen ions will combine with the fuel (e.g. H_2) to form water: $H_2 + O^{2-} \rightarrow H_2O + 2e^-$.

Through this oxidation process, electrons are released and lead via an external circuit to the cathode where the ORR occurs again, and thus electrical power is generated (Andersson et

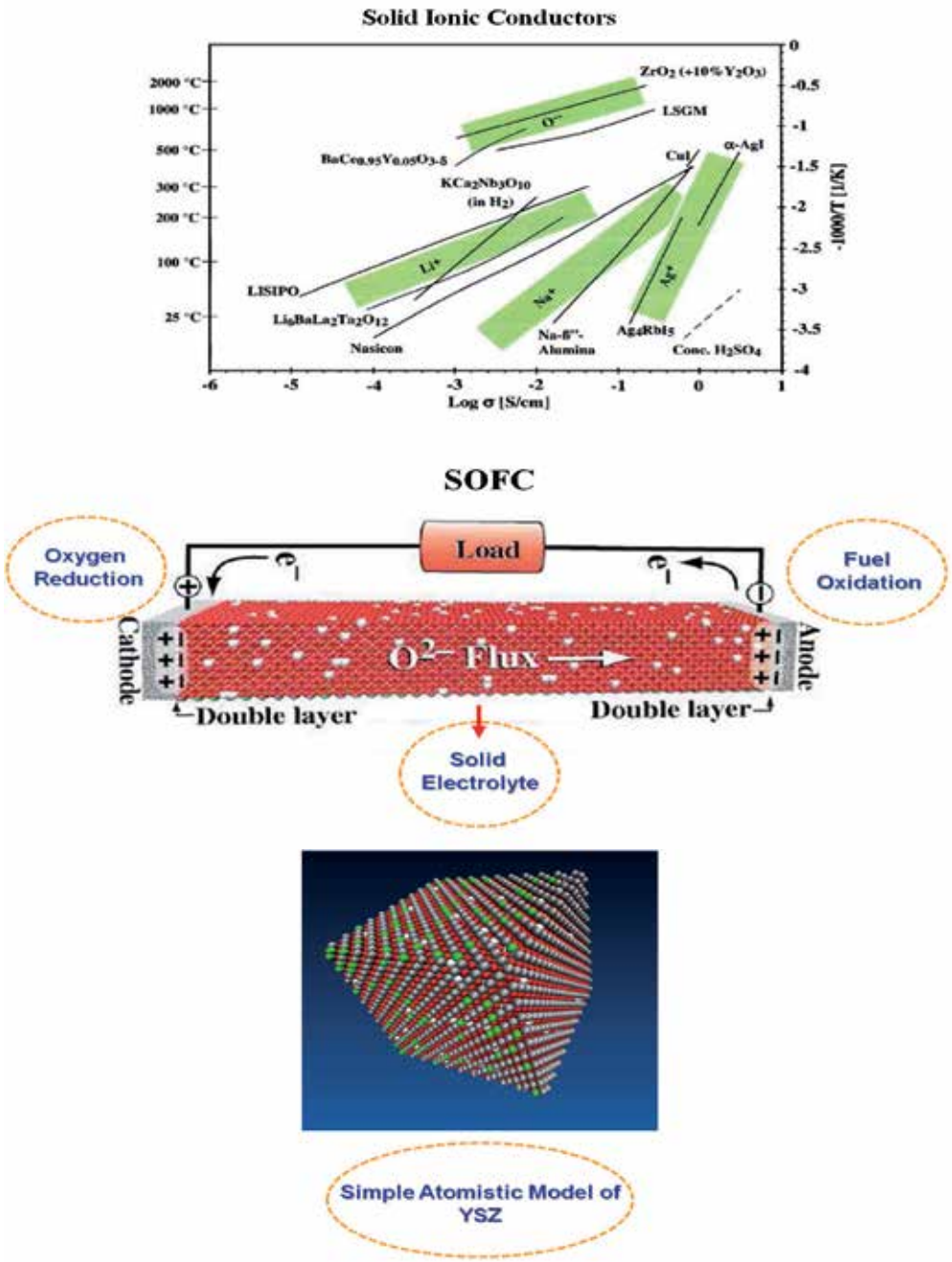

Fig. 1. (Top) Temperature dependence of the best solid ionic conductors of Ag^+, Na^+, Li^+, and O^{2-} ions (adapted from Chu et al., 2006). The ionic conductivities fall within ranges which are highlighted by the shaded areas. (Middle) A simple atomistic model of SOFC that consists of three basic components: anode, cathode and electrolyte. (Bottom) The basic properties of solid electrolyte of SOFC can be simulated using standard atomistic modeling.

al., 2010). In short, the overall electrochemical cell reaction is built upon the chemical potential difference between the cathode and anode sides, which is given by the Nernst equation in the simplest approach.

To maximize this superionic conductivity in a SOFC, alloying zirconia (ZrO_2) with various metal oxides (e.g. Y_2O_3, Sc_2O_3, La_2O_3, MgO, CaO, etc) is a plausible approach (Lashtabeg et al., 2006). In certain regimes, alloying can stabilize the highly symmetric cubic-fluorite phase of zirconia, which consequently facilitates the ionic conductivity through the introduction of oxygen vacancies as the host Zr^{4+} cations are replaced by dopant aliovalent cations. Above all, yttria-stabilized zirconia, YSZ (i.e. the $Zr_{1-x}Y_xO_{2-x/2}$ system, with $x/2$ being the Y_2O_3 dopant concentration), is the most common choice for the electrolyte (Fig. 1 Top), due to its good oxide ion conductivity over a wide range of oxygen partial pressures, its stability under oxidizing and reducing conditions, and its good high-temperature mechanical properties (Ralph et al., 2001). This versatility ultimately arises from atomic defects (i.e. oxide ion vacancies) in the cubic zirconia crystalline lattices. The vacancies, through the coupled interactions among the vacancies and ions in these different alloys can dramatically affect the structural, thermal, mechanical and electrical properties of the system. Furthermore, the optimum ionic conductivity of each alloy varies with synthesis route and sintering conditions due to the resultant diverse local morphologies and microstructures (Badwal et al., 1992; Butz et al., 2006; Chen et al., 2002; Fukui et al., 2004; Ioffe et al., 1978; Korte et al., 2008; Zhang et al., 2007; Zhu et al., 2005). Thus a variety of different morphologies and microstructures of YSZ can be found in experiments (Badwal et al., 1992; Butz et al., 2006; Chen et al., 2002; Cheng et al., 2011; Etsell et al., 1970; Fukui et al., 2004; Ioffe et al., 1978; Korte et al., 2008; Lashtabeg et al., 2006; Zhang et a., 2007; Zhu et al., 2005). Non-cubic crystalline phases, grain boundaries, and disordered lattices of amorphous features can commonly be found. To understand how the local microstructures and system morphologies affect the ionic conductivity and degradation of the electrolyte (YSZ) upon SOFC operation, theoretical simulation can provide detailed *in situ* atomistic information that is difficult to obtain experimentally.

To increase the basic understanding of the scientific phenomena that underlie current experimental findings, which could most dramatically affect engineering design, atomistic modeling based on quantum mechanics (e.g. first-principles or *ab initio* methods), molecular dynamics and Monte Carlo simulation (Fig. 2) are particularly useful. They provide relevant predictions of crystal structure, energetics, and vibrational frequencies through detailed atomistic descriptions that complement the standard analytical continuum model of ion diffusion at the macroscopic scale (Andersson et al., 2010; Cheng et al., 2011). Furthermore, various fundamental physical processes and chemical reactions can be described via quantum mechanics. The most accurate quantum mechanical atomistic descriptions, first-principles or *ab initio* methods, however are limited to small system size (less than about 1000 atoms) and short times (less than a few nanoseconds). For long-time-scales and larger length scales in atomistic modeling, recent sophisticated studies use kinetic Monte Carlo (KMC) (Gatewood et al., 2011; Lau et al., 2008, 2009; Pornprasertsuk et al., 2007; Turner et al., 2010; Wang et al., 2010, 2011) simulations. KMC can treat the longest time scales for chemical reactions, because reactants are not followed to products in time. Instead, chemical reactions are stochastically chosen to occur at the assigned rates. This is important for SOFC modeling, because charge-separating electrochemical reactions tend to have slower rates. KMC has modeled the ionic transport in a SOFC under various operating conditions

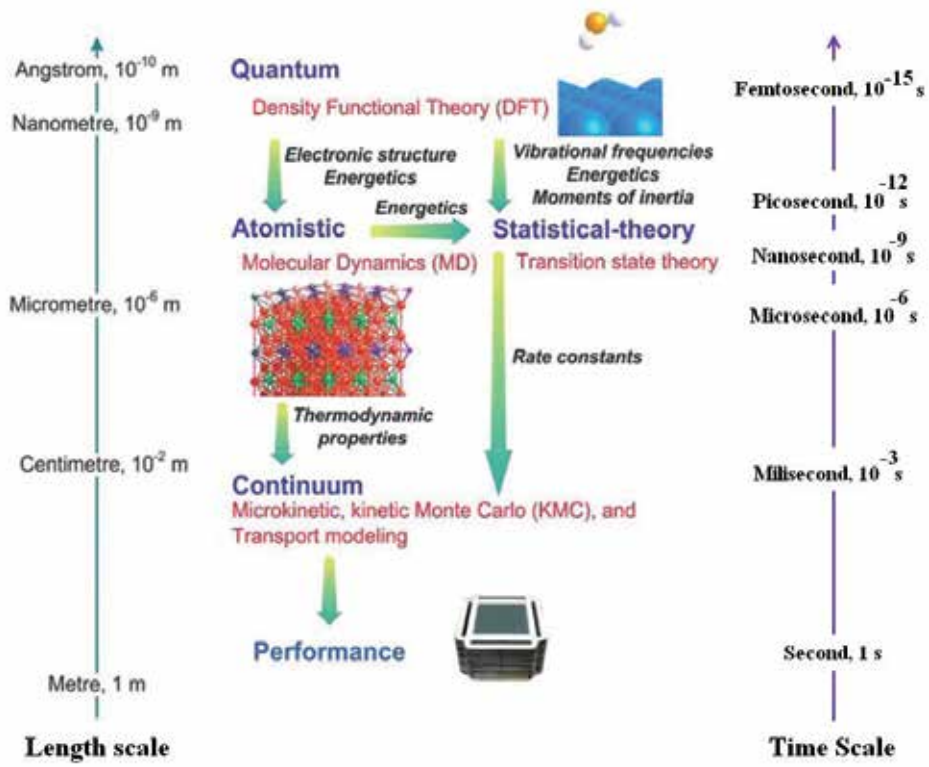

Fig. 2. Computational methods at different length and time scales to model a SOFC material adopted from Cheng et.al. 2011. (Adapted figure reproduced from Cheng et.al. 2011. Copyright 2011 RSC Publishing.)

(Gatewood et al., 2011; Lau et al., 2008, 2009; Pornprasertsuk et al., 2007; Turner et al., 2010; Wang et al., 2010, 2011). Specifically, KMC can probe SOFC performance by simultaneously capturing various reaction pathways of electrochemical and physicochemical reactions in the electrolyte and at the three-phase boundary (TPB), i.e. the interface where the gas reactants, electrolyte, and electrode meet. The electrical current through the YSZ is simulated in direct current (dc) and alternating current (ac), as electrochemical impedance spectra under various operating conditions using a minimal set of uniform chemical reaction rates on an assumed cubic YSZ lattice via KMC (Gatewood et al., 2011; Lau et al., 2008, 2009; Pornprasertsuk et al., 2007; Turner et al., 2010; Wang et al., 2010, 2011). Despite the robustness of KMC simulation, this approach is based on a rigid lattice gas model and can not predict the experimentally observed ionic conductivity maximum as a function of Y_2O_3 dopant concentration (Hull, 2009). Beyond the kinetics driven atomic motion as implemented in minimal KMC models, the complex dynamics of real lattices and the real-time multi-particle ion-vacancy interactions at a finite temperature can be computed 'on-the-fly' in simulation. However simple or complex, the ionic conductivity of any atomistic model of solid YSZ is, the conductivity can accurately be derived from standard equilibrium classical MD simulation (Frenkel & Smit, 1996). Thus to explore and understand the nature of unique ionic conductivity in the solid electrolytes of SOFC's, YSZ solids have been

intensively studied using classical MD simulations (Devanathan et al., 2006; Fisher et al., 1998, 1999; Khan et al., 1998; Kilo et al., 2003; Lau et al., 2011; Li et al., 1995; Okazaki et al., 1994; Sawaguchi et al., 2000; Schelling et al., 2001; Shimojo et al., 1992; van Duin et al., 2008; Yamamura et al., 1999) in the past few years.

1.2 Basic justification of classical MD

In crystalline solids, ionic conductivity is fundamentally different from electronic conductivity. Electronic conduction in a metal, for example, occurs on a three-dimensional array of ion cores whose excess valence electrons have dissociated to form a continuous "sea of free electrons" partially filling the electronic bands around the Fermi-level. Because the electron has a small mass, its de Broglie wavelength is large and therefore quantum mechanical effects force the electrons into those bands. As ions are much heavier than electrons, their motion is far less governed by quantum mechanics. Below the typical atomic vibrational frequencies (< 100 GHz), ionic motion is best described by thermally activated hopping between (usually) charge-compensating sites (Dyre et al., 2009).

The dynamics of mobile ions in a disordered inorganic ionic conductor (e.g. amorphous YSZ) is clearly a complex multi-particle problem. Unlike a perfect crystal, the potential-energy landscape experienced by an ion in a disordered solid is irregular and contains a distribution of depths and barrier heights. The ions' interaction with the dynamic atomic lattice network is fundamental: first, because the lattice supplies a persistent disordered potential energy landscape for the mobile anions and second, because the local fluctuations of the lattice atoms promote anionic jumps. Additional multi-particle behavior stems from the interaction among the mobile ions and vacancies. All these distinct coupled interactions contribute to the complete theoretical description of ionic conductivity in amorphous solids (Dyre et al., 2009; Lammert et al., 2010). A complete analytical microscopic theory is not available by now and, due to the complexity of the problem, would be extremely difficult to formulate without some basic understanding at the atomistic level. The direct approach to ionic conduction in the YSZ electrolyte of the SOFC is via molecular dynamics (MD) simulations. From the time-evolved atomic trajectories detailed microscopic information about the underlying mechanisms is available. Understanding them would make theoretical prediction possible.

2. The model of classical MD for YSZ

2.1 Interatomic potentials

It is possible to model a few thousands to millions of particles in classical MD using phenomenological interatomic and intermolecular potentials. They are obtained by using the phenomenological approach of selecting a parameterized mathematical form for the interaction between atoms, and fitting its unknown parameters to various experimental or higher-level theoretical (e.g. *ab initio* quantum mechanics simulation) properties. In general, the flexibility, accuracy, transferability, and computational efficiency of the interatomic potentials each have to be carefully considered (Frenkel & Smit, 1996).

For the YSZ electrolyte in a SOFC, the simplest, relevant interatomic potentials are those commonly used to describe rigid ionic compounds (Lewis et al., 1985). Under the rigid ion model, the potential energy is a simple function of the distance between the ions. It consists

of a Coulomb term to describe the long-range electrostatic interactions between the ions of YSZ (i.e. Zr^{4+}, Y^{3+}, and O^{2-}), and a Born–Meyer–Buckingham (BMB) potential to describe the short-ranged interactions between the ions. The potential energy between ions i and j separated by a distance r_{ij} with ionic charges Q_i and Q_j is then given by:

$$E_{ij} = Q_i Q_j / r_{ij} + A_{ij} \exp(-r_{ij}/\rho_{ij}) - (C_{ij}/r^6_{ij}) \quad (1)$$

The exponential term of the short-ranged BMB potential takes account of Pauli repulsion, whereas the r^{-6} term takes account of the attractive dispersion or van der Waals interaction. To calculate the long-range Coulomb interactions between the ions in the 3D periodically repeated simulation cell, Ewald summations must be used. To maximize the accuracy of these interatomic potentials and have more reliable energy landscape features, these parameters are usually fitted empirically to more accurate *ab initio* quantum mechanical calculations, i.e. density functional theory (DFT) or quantum chemistry methods, and relevant experimental findings on some known physical properties (Gale et al., 2003).

Of the several sets of interatomic potential parameters available in the literature (Bush et al., 1994; Dwivedi et al., 1990; Lewis et al., 1985; Minervini et al., 2000; Schelling et al., 2001; Zacate et al., 2000), the parameters proposed by Lewis *et al* (Lewis et al., 1985) and Minervini *et al* (Minervini et al., 2000; Zacate et al., 2000) were chosen for the initial guess potential functions in the fitting of interatomic potentials for ZrO_2 and Y_2O_3 crystals. To better capture the correct dielectric constants and lattice vibrational frequencies as described in the system (Gale et al., 2003; Lindan et al., 1993), the effects of environment-dependent electronic polarizability of the ions (Lau et al., 2009) can be included in the fiting of the interationic potential through the shell model (Gale et al., 2003; Lau, 2011; Lindan et al., 1993). In the core-shell model, the ionic core and shell are coupled through harmonic spring force constants, k (Gale et al., 2003; Lau et al., 2011) which take into account interactions of different types: between ions, between ions and outer shell electrons, and between outer electrons. Such an approach allows one to take into account the electronic polarizability of ions that is caused by the forces acting between the ion cores and shells. However to probe the basic structural properties and ionic motion at high temperatures at a reasonable cost of computation, the electronic polarizability within the core-shell model mentioned can be ignored (i.e. all the core–shell spring constants k_{Zr}, k_Y and k_O mentioned are set to zero). This is appropriate in MD simulations in which no electric field is applied, as in the case of superionic conduction at high temperature in SOFC. The explicit effect of the core-shell model was found to be small (Lindan et al., 1993), and therefore the approximate description of rigid ions (Eq. 1) without core–shell interaction in molecular dynamics should be sufficient.

Stabilized YSZ in its cubic fluorite structure has cations occupying an fcc lattice and oxygen anions occupying its tetrahedral interstices. A finely tuned ZrO_2 and Y_2O_3 interatomic potential that describes the entire $Zr_{1-x}Y_xO_{2-x/2}$ system, with $x/2$ being the Y_2O_3 dopant concentration of YSZ has to be established. According to the reported literature (Bush et al., 1994; Devanathan et al., 2006; Dwivedi et al., 1990; Fisher et al., 1998, 1999; Khan et al., 1998; Kilo et al., 2003; Lau et al., 2011; Lewis et al., 1985; Li et al., 1995; Minervini et al., 2000; Okazaki et al., 1994; Sawaguchi et al., 2000; Schelling et al., 2001; Shimojo et al., 1992; ; van Duin et al., 2008; Yamamura et al., 1999; Zacate et al., 2000), the typical "semi-empirically" fitted properties of ZrO_2 and Y_2O_3 crystals that are chosen for the fitting dataset can be the

lattice parameters, lattice elastic properties, dielectric constants, defect formation energies (e.g. vacancies and interstitials), and phonon frequencies of cubic (*c*-ZrO_2, space group *Fm*3*m*), tetragonal (*t*-ZrO_2, space group *P*42/*nmc*) (Ackermann et al., 1975; Aldebert et al., 1985; Boysen et al., 1991; Dash et al., 2004; Howard et al., 1988; Smith et al., 1965; Zhao et al., 2002;), monoclinic (*m*-ZrO2, space group $P2_1/c$), and yttria (Baller et al., 2000; Lau et al., 2009) (Y_2O_3, space group *Ia*3).

Compared to determining the geometry and energetics of the competing phases of ZrO_2 polymorphs, searching for ground state atomic arrangements across a composition range of ZrO_2–Y_2O_3 is definitely more complicated. The YSZ solid inherits the complexity of the competing phases of ZrO_2 and adds the possiblility that any Zr atom can be replaced by a Y atom and half of a vacancy. The structures and lattices are not merely determined by different composition at different ambient condition, but also dictated by intrinsic long- and short-range order in the system (Bogicevic et al., 2001). Fortunately, under normal conditions, the cubic fluorite scaffold is found to be stable for yttria (Y_2O_3) content in the range of ~8 – 40 mol% (Bogicevic et al., 2001; Ostanin et al., 2002, 2003; Predith et al., 2008). For the SOFC application, the ionic conductivity (and oxygen self-diffusivity) of YSZ does not increase monotonically with increasing vacancy concentration; rather, it exhibits a maximum between 8 and 15 mol% Y_2O_3. These unique characteristics must also determine the basic parameter "tune-up" of the interatomic potential for the MD simulation of YSZ. To ensure neutrality of the simulation cell and that it obeys chemical stoichiometry, the cations and anions of YSZ are typically chosen to be Zr^{4+}, Y^{3+} and O^{2-} ions.

To simplify the simulation further, the interaction of Zr^{4+}–Y^{3+} in YSZ is assumed to be governed by the Coulomb interaction of the two ionic charges. This assumption is based on the fact that at the low Y_2O_3 dopant concentrations of this study, a very strong first-neighbor interaction between Zr^{4+} and Y^{3+} in the lattice is very unlikely compared to the first-neighbor interactions between oxygen anions and vacancies (Pietrucci et al., 2008; Schelling et al., 2001; Stapper et al., 1999). This approach has been widely adopted in previous studies literature (Bush et al., 1994; Devanathan et al., 2006; Dwivedi et al., 1990; Fisher et al., 1998, 1999; Khan et al., 1998; Kilo et al., 2003; Lau et al., 2011; Lewis et al., 1985; Li et al., 1995; Minervini et al., 2000; Okazaki et al., 1994; Sawaguchi et al., 2000; Schelling et al., 2001; Shimojo et al., 1992; ; van Duin et al., 2008; Yamamura et al., 1999; Zacate et al., 2000) In this dilute Y_2O_3 concentration limit of YSZ, the local environments of oxygen atoms in cubic YSZ crystals are assumed to be more like that in ZrO_2 than in Y_2O_3, therefore the O–O potential adopted throughout the simulation can be approximated to be identical to the O–O potential of ZrO_2 (Lau et al., 2011). As one of the "semi-empirical fitted" BMB potentials that can be found in the literatures, the relevant interatomic potentials (Lau et al., 2011) is shown in Table 1. Besides describing the cubic ZrO_2 phase (i.e. *c*-ZrO_2) well, these potentials can also describe the tetragonal phase of ZrO_2 (i.e. *t*-ZrO_2) and the Y_2O_3 crystalline phase well, as pointed out in a recent paper (Lau et al., 2011).

2.2 Atomistic models for YSZ solids

For SOFC, the challenges that delay the full commercialization include materials degradation, materials selection, materials function, and coupled interactions with other cell components. For the ion-conducting electrolyte like YSZ, the main problems can be attributed to the need for chemical, mechanical, and thermodynamic stability over a wide

range of operating conditions. In addition, the optimum ionic conductivity of the electrolyte varies with different synthesis routes and sintering conditions due to the resultant diverse local morphologies, grain boundaries, and microstructures. To facilitate the engineering design, determine materials functionality, and extend experimental findings, classical MD simulation has a unique role within the multi-scale atomistic modeling to provide the relevant predictions that complement standard continuum modeling. One example is its ability to generate a large-scale atomistic structure exhibiting different morphologies and microstructures precisely with reasonable computation cost.

Interaction	A_{ij} (eV)	ρ_{ij} (Å)	C_{ij} (eV Å^6)
Zr^{4+}–O^{2-}	1.29285x10^3	3.58388x10^{-1}	1.93646x10^1
Y^{3+}–O^{2-}	1.642724x10^3	3.53197x10^{-1}	1.04180x10^2
O^{2-}–O^{2-}	1.30989x10^4	2.19670x10^{-1}	4.92998x10^1
System	Property	This Work	DFT
Ω-YSZ	a (Å)	6.26	6.40
	b (Å)	6.30	6.20
	c (Å)	6.29	6.30
	α (deg)	100.71	99.96
	β (deg)	100.13	100.75
	γ (deg)	99.69	98.57
	ω_{min} (cm^{-1})	101	114
	ω_{max} (cm^{-1})	696	719
Δ-YSZ	a (Å)	6.23	6.37
	b (Å)	6.29	6.28
	c (Å)	6.37	6.48
	α (deg)	81.23	81.53
	β (deg)	99.49	99.59
	γ (deg)	80.59	79.98
	ω_{min} (cm^{-1})	146	115
	ω_{max} (cm^{-1})	678	707

Table 1. Short-range interatomic BMB potential for the YSZ solids and their predicted properties compared to *ab initio* DFT planewave calculations within the Local Density Approximation (LDA) (Lau et al., 2009). Here, the Ω-YSZ (i.e. $Zr_5Y_2O_{13}$ solid) consists of 17 mol% yttria, whereas the Δ-YSZ (i.e. $Zr_3Y_4O_{12}$) consists of 40 mol% yttria. The ω_{min} and ω_{max} refer to the lowest and highest vibration frequency of phonons for the corresponding YSZ system.

Within the rigid-ion approximation validated in Table 1, various types of YSZ solids that arise from different experimental synthesis routes and sintering conditions can be modeled using the appropriate spatial boundary conditions under realistic thermodynamic conditions (Sect. 2.1). Those include the perfect crystal, amorphous structures, grain boundaries, thin-film surfaces, and nanocrystals of Fig. 3. For the YSZ systems shown in that figure, the number of Zr^{4+}, Y^{3+}, and O^{2-} ions depends on the chosen Y_2O_3 dopant concentration. Initially, the cubic fluorite lattice of ZrO_2 was constructed, and yttrium Y^{3+} ions were generated by random replacements of zirconium Zr^{4+} ions according to the predefined chemical composition. To keep stoichiometry and the neutrality of the

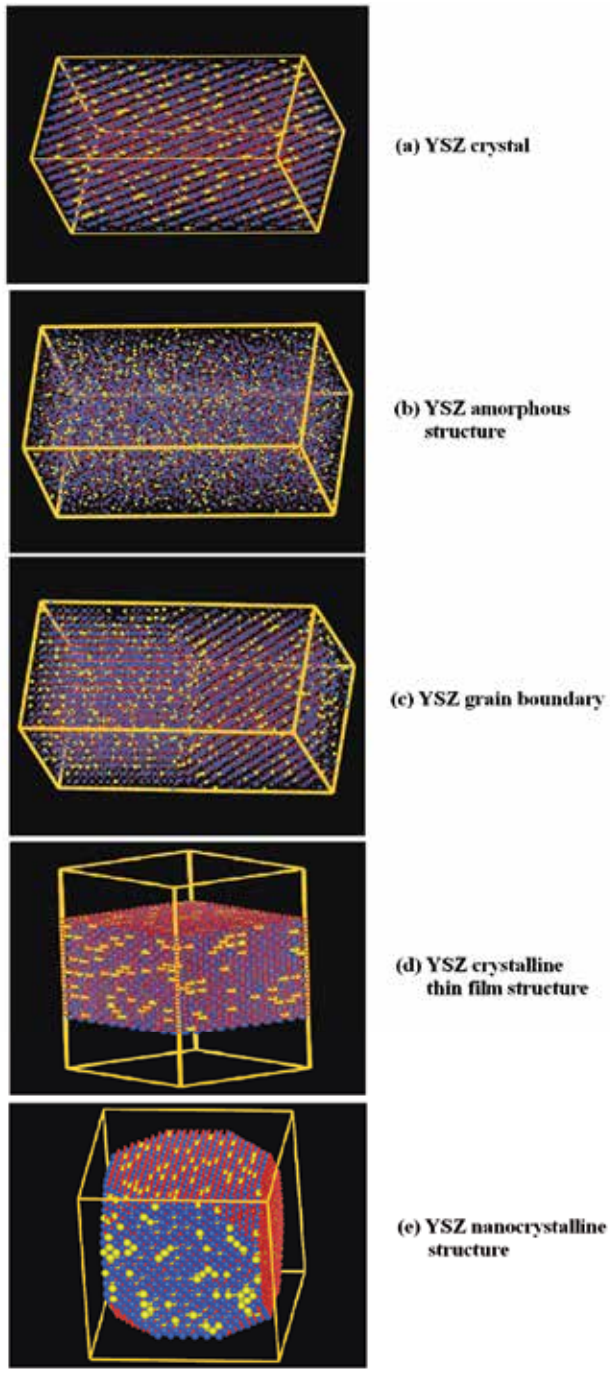

Fig. 3. Various morphologies of YSZ solids (i.e. Zr^{4+} is blue, Y^{3+} is yellow and O^{2-} is red ion) that can be modeled using classical MD simulation (a) crystal, (b) amorphous structure, (c) grain boundary, (d) crystalline thin film structure, and (e) the finite nanocrystalline structure.

simulation box, an O^{2-} ion was removed from randomly selected anion sites for every two Y3+ dopant ions in the system. An amorphous structure, which is different from crystalline YSZ, was generated via standard structural relaxation, the "amorphization and recrystallization (A&R) strategy" proposed by Sayle et al. (Sayle et al., 1999, 2002, 2005). By adopting the standard MD techniques that are implemented in the standard classical MD codes e.g. LAMMPS and DL_POLY, a thermal well-equilibrated amorphous solid of YSZ as shown in Fig. 3b can be obtained (Lau et al., 2011).

3. Static and dynamic properties of YSZ bulk solids

In this section, we present a brief discussion of the principal static and dynamic properties of the YSZ bulk solids that primarily focuses on the unique characteristics of YSZ in crystalline (Fig. 3a) and disordered bulk lattices (Fig. 3b). In particular, the accuracy of the simple atomic potential (Table 1) will be validated, and the implications of these MD predictions will be discussed. For abbreviation, all YSZ crystals will be termed *n*-YSZc, where *n* gives the mol% doping (e.g. 8-YSZc is a crystal with 8.0 mol% Y_2O_3 dopant). The corresponding amorphous YSZ structures will be termed *n*-YSZa. Both the crystal and amorphous structures referred to together will be termed *n*-YSZ systems

3.1 Static properties

3.1.1 Lattices

In contrast to the disordered lattice of the amorphous structure, the YSZ crystals that are typically found in the cubic fluorite structure can be fully characterized by a single lattice constant, *a*. From Fig. 4, the computed lattice parameters of cubic YSZ as a function of doping and temperature are generally consistent with experimental observation (Hayashi et al., 2005; Pascual et al., 1983). This further validates the interatomic potentials we employed in Table 1. Because of the larger size of the dopant Y^{3+} cation, which yields larger Y-O bond distances in the lattice, the cell volume of YSZ crystals generally increase with increased doping with Y_2O_3. However at low temperature, this trend is not uniform. From Fig. 4, the lattice constant *a* of 3-YSZc is ~ 5.125 Å, is larger than 8-YSZc (*a* ~ 5.121 Å), but less than 12-YSZc (*a* ~ 5.128 Å). These discrepancies might be a signature of mixing the low-temperature tetragonal ZrO_2 ground state and high-temperature cubic structures for the 3-YSZc (or any other low mol% of Y_2O_3 YSZ crystals in the dilute regime) at low temperature or of the limitation of the current fitted atomic potential used (Table 1), which is unable to capture accurately the phase stability of all YSZ polymorphism at low mol% of Y_2O_3 dopant in the low-temperature regime.

Within the linear response regime, the thermal expansion of a cubic crystal lattice can be described as $a(T) = a(300)[1 + \alpha (T - 300)]$, where $a(300)$ is the lattice constant for YSZ solid at 300 K and α is the linear thermal expansion coefficient of the system. From a linear fit of MD results, the coefficients of linear thermal expansion are found to lie in the range ~ 6.0–7.0x10^{-6} K^{-1} (Lau, 2011), close to the reported experimental (Hayashi et al., 2005; Ingel et al., 1986; Pascual et al., 1983) values of ~9.6–10.8x10^{-6} K^{-1} and other theoretical values (Devanathan et al., 2006) of 6.8–8.0x10^{-6} K^{-1} for other Y_2O_3 doping. For the amorphous YSZ, the low symmetry yields the irregularity in local structure that gives distinct lattice properties (i.e. *a*, *b* and *c*). Under the homogeneous quenching via Hoover barostats and

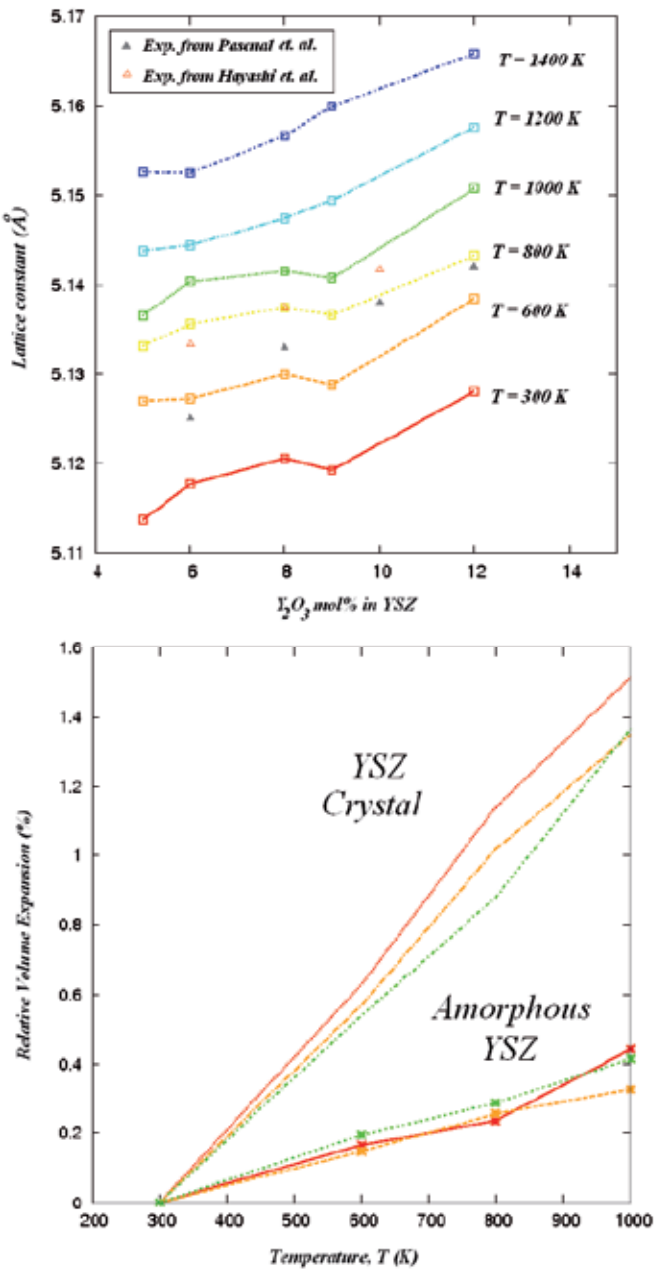

Fig. 4. (Top) Lattice constant (in Å) of YSZ crystals with various Y_2O_3 mol% dopant concentrations as a function of temperature (Lau et al., 2011) , compared with reported experimental values (Hayashi et al., 2005; Pascual et al., 1983) (in triangles) at 300 K. (Bottom) Relative volume expansion (in %) referenced to 300 K of 3-YSZc (green dots), 8-YSZc (yellow dashes), 12-YSZc (red lines) systems and corresponding amorphous solids (lines with points) over the temperature range 300–1000 K.

thermostats (*NPT*) for further solidification and recrystallization, the MD simulation will generally yield a cubic structure (Lau et al., 2011). In the case of 8.0% Y_2O_3 doping in amorphous YSZ (i.e. 8-YSZa), the temperature dependence of the 8-YSZa lattice can be fitted to the expression $a(T)=a(300)[1+a_a(T-300)]$, and $c(T)=c(300)[1+a_c(T-300)]$, with a_a and a_c corresponding to linear thermal expansion coefficients along the *a* and *c* lattice directions. The a_a and a_c are found to be nearly identical for each *n-YSZa* system. Overall, the *a* for the 3-YSZa, 8-YSZa and 12-YSZa solids are found to be ~1.5–2.2x10^{-6} K^{-1}, which are significantly smaller than for the corresponding YSZ crystals (Lau et al., 2011). The amorphous YSZ solids generally have a much smaller volume expansion over the temperature range shown in Fig. 4, which might be attributed to extra flexibility in spatial rearrangements for the ions in disordered solids.

3.1.2 Structural features

i. Crystallographic direction views

Besides the different thermal responses of the lattices, a more illuminating way of exhibiting the qualitative differences between the YSZ crystals and amorphous YSZ solids can be shown by the structural features determined by the ion distribution within the lattices of these solids.

Bulk YSZ is a solid solution on a cubic fluorite lattice with yttrium and zirconium distributed on a face-centered cubic cation lattice and oxygen and vacancies distributed on a simple-cubic anion lattice. Its fully dense solid features are revealed at the top of Fig. 5. To differentiate a dense crystalline lattice with a disordered solid lattice, the Miller index that defines a crystallographic direction for the planes and directions in the crystal lattice can be very useful. By randomly distributing the Y^{3+} within a cubic $Zr_{(1-x)}Y_xO_{(2-x/2)}$ phase, the distribution of the Y^{3+} ions in both the YSZ crystals (e.g. 8-YSZc) and the amorphous solids (e.g. 8-YSZa) are found to be nearly isotropic as shown in Fig. 5. For 8-YSZc in its cubic fluorite structure, the ionic distributions in all three cubic (001), (010), and (001) directions are found to be equivalent in all cases. These directions for the amorphous cases correspond to those directions in the original crystal that was made amorphous by heating in vacuum and then repeatedly heating and cooling under hydrostatic pressure. In contrast to the YSZ amorphous systems, the YSZ crystals (e.g. 8-YSZc in Fig. 5) exhibit comparatively clear Zr^{4+} (cation), O^{2-} (anion) crystalline planes in both directions shown in Fig. 5 for the crystal lattice. The dopant (Y^{3+}) ions have a similar distribution to that of the Zr^{4+} ions that they replace in the crystal of YSZ (Fig. 5). For both systems (i.e. the crystal and amorphous structure), the ratio of Zr^{4+}/O^{2-}~ 1/2 can be found in all crystallographic planes, analogous to the ZrO_2 stoichiometry which acts as a host lattice. In addition, these similar features are also found in the YSZ systems with other Y_2O_3 concentrations (i.e. ~ 3.0 - 12.0 mol%) and for elevated temperatures, as long as there is no grain boundary in the crystal.

ii. Radial distribution function

We analyze the bonding features of the simulated n-YSZc and n-YSZa systems. Even for ions in a disordered-network of an amorphous solid with no long range order, the short range order, however, can be obtained from the distribution of coordination number, bond length, and bond angles. Interpreting the static equilibrium structural features of these YSZ systems in another way, we calculated the radial distribution function (RDF), *g(r)* of the

constituent ions, which describes the average spatial organization of cations and anions in the lattice. A Fourier transform of the radial distribution function results in the structure factor $S(q)$, which is experimentally measurable from X-ray or neutron scattering. Therefore, it is an important result from the predicted static structure of a material. Based on the prominent peaks within the short-range order (i.e. < 6 Å), the average local connectivity of the Zr^{4+}, Y^{3+} and O^{2-} ions in the system can be determined. From the RDF, the successive peaks correspond to the nearest-, the second- and the next-neighboring atomic distributions inside a YSZ system. The distinct RDFs of the YSZ crystal and YSZ amorphous solid (Fig. 6) are due to their unique local ion distributions and system densities.

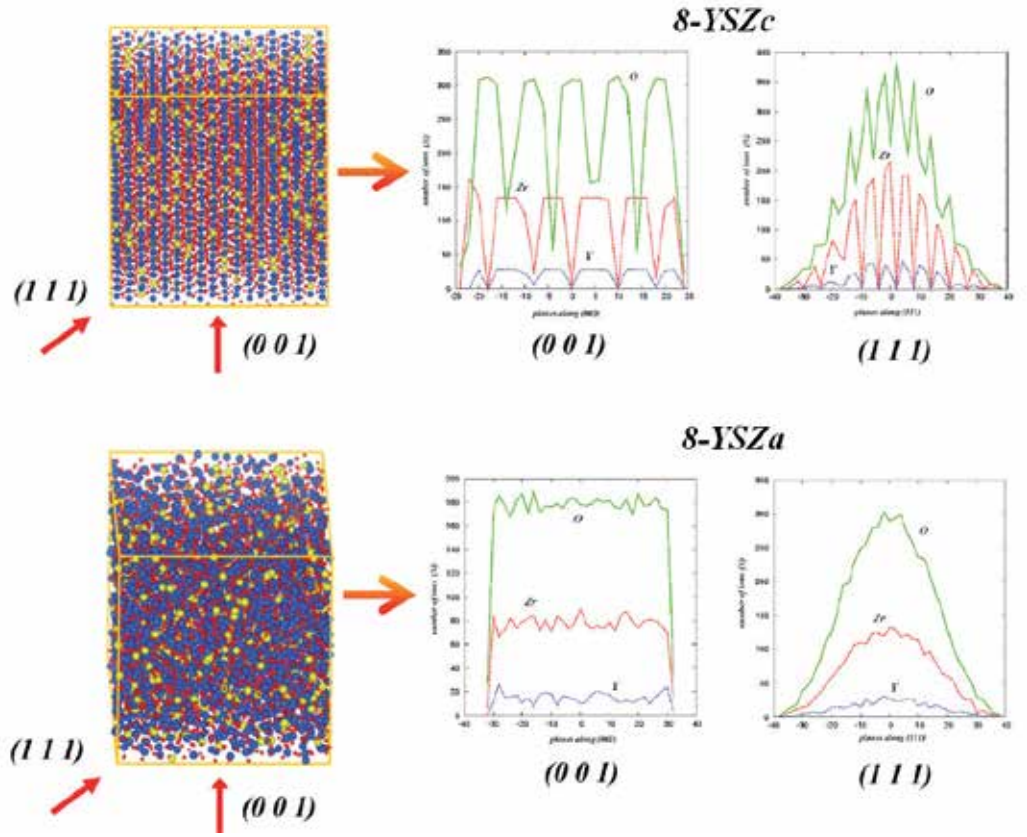

Fig. 5. The 8-YSZc crystal (top) and the 8-YSZa amorphous structure (bottom). Arrows show the projection vectors in the (001) and (111) directions of these simulation cells. The right two columns of figures give the distribution of the three ions binned by atomic planes, every two angstroms, along these two crystallographic directions (Lau et al., 2011).

For 8-YSZc at ~ 300 K, the average nearest-neighbor Zr-O, Y-O, O-O, and Zr-Y bond distances are ~ 2.08, 2.33, 2.58, and 3.58 Å, respectively (Fig. 6a). These features generally are very similar to the RDF features of 14-YSZc computed using the more sophisticated ReaxFF Reactive Force Field method (van Duin et al., 2008) (Fig. 6b). For the prediction of the Zr-O distance in YSZ crystals, both interatomic potentials yield excellent agreement with EXAFS (i.e. 2.13 Å) and neutron diffraction (i.e. 2.08 Å) for the 15-YSZ crystal (van Duin et al., 2008).

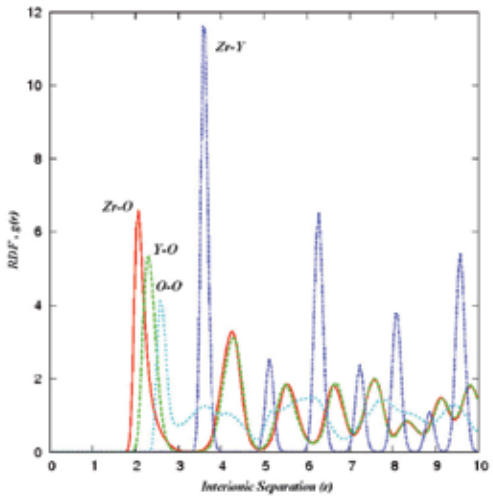

(a) Buckingham Potential
(8-YSZc at T = 300 K)

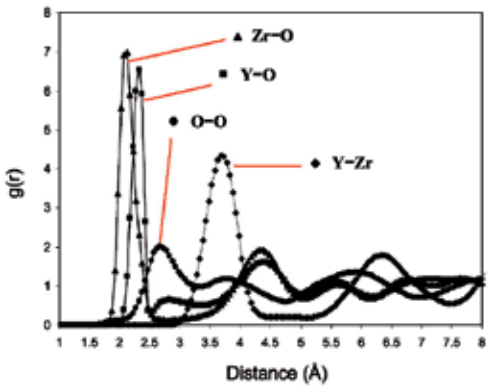

(b) ReaxFF Reactive Force Field
(14-YSZc at T = 1000 K)

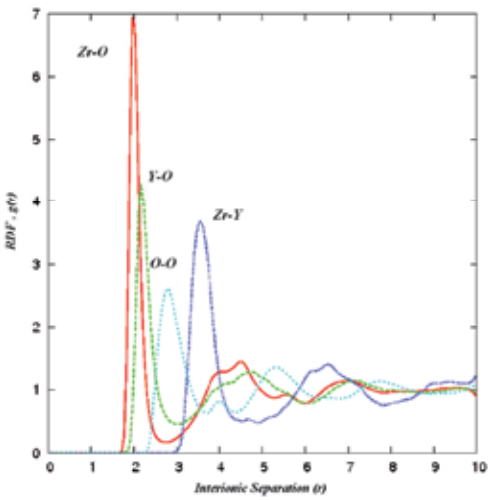

(c) Buckingham Potential
(8-YSZa at T = 300 K)

Fig. 6. (a) The RDF of 8-YSZc at 300 K based on the Buckingham (BMB) potential as defined in Eq. 1 using parameters from Table 1. (b) The RDF of 14-YSZc at 1000 K based on the ReaxFF Reactive Force Field adopted from van Duin et al. (van Duin et al., 2008). (c) The RDF of 8-YSZa at 300 K based on the BMB potential from Table 1.

Integrating the Zr-O RDF up to the first minimum ~ 3.27 Å past the peak at 2.08 Å, gives an average coordination number N_{Zr} = 7.6, in between that of N_{zr} = 7 for the monoclinic ZrO_2, and N_{Zr} = 8 for the tetragonal ZrO_2 phase. From ReaxFF computed 14-YSZc, the RDF for the Y-O indicates an average Y-O distance to be ~ 2.32 Å (Fig. 6b), which is close to Y-O distance of 8-YSZc (i.e. ~ 2.33 Å) computed based on the BMB potential and experimental

EXAFS data, 2.32 Å (Ishizawa et al., 1999). Integrating the Y-O RDF to its first minimum (~3.22 Å), gives coordination number N_Y = 6.6, slightly larger than the N_Y = 6 of the cubic Y_2O_3 crystal.

For the O-O pair distribution, its more diffusive behavior compared the heavier cations yields a broader pair distribution over the range of O-O distances of *g(r)* that is plotted (Fig. 6a). With its O-O average distance found to be ~ 2.58 Å at T = 300 K, the average oxygen atom has N_O = 6.24 (integrating up to the first O-O minimum at 2.98 Å), which is almost the same as in both ZrO_2 and Y_2O_3. As the temperature rises, all the ions tend to move on average farther away from their equilibrium positions which give the thermal volume expansion of the system. All the peaks of *g(r)* in the RDF are generally lowered relative to room temperature for all the ionic pairs in a system, as a result of thermal broadening and increased mobility.

Similar observations are found in the ReaxFF-computed RDF of 14-YSZc (Fig. 6b). For the O-O pair distributions in 14-YSZc at T =1000 and 2000 K, the average O-O bond distance is ~ 2.67 Å at T = 1000 K, increasing to ~ 2.77 Å at T = 2000 K. Thus this suggested that for both the Buckingham potential and the ReaxFF Reactive Force Field, the description of static structural features is found to be equivalent for heavy ions (Zr^{4+} and Y^{3+}) and mobile ions (O^{2-}). As shown from Fig. 6a and Fig. 6b, for different Y_2O_3 compositions (from 3.0 to 14.0 mol% Y_2O_3), their ion pair distributions generally remain similar, as the cubic crystal lattice features are preserved. However, higher concentration of the Y^{3+} dopant means more Zr^{4+} ions were substituted; hence, the heights of the Zr-Zr *g(r)* peaks are reduced with increasing Y^{3+} concentration. Consistent with N_O ~ 6.24 for both ZrO_2 and Y_2O_3, the first peak height for the O-O *g(r)* profile is independent of dopant concentration, but higher Y^{3+} concentration requires more oxygen vacancies in the system, and therefore lowers the height of *g(r)* for more distant O-O pairs.

For the YSZ amorphous solid, disordered structural features are reflected in its RDF. In general, the peaks of the RDF spectrum for all ion pairs at small interatomic separations are broadened relative to the crystal. This broadening increases with separation, and structure almost disappears at the largest separations plotted. This is a clear indication of disorder, which increases with distance. Instead of having several pronounced peaks which preserve long-range order in a perfect crystal, there is no significant structure beyond ~ 8.0 Å for the Zr-O, Y-O, Zr-Y, and O-O pair separations (Fig. 6c). The broad profile of these ion pairs indicates that these amorphous solids have no long-range order for ions separated beyond ~ 8.0 Å. Based on the discrete peaks within the short-range order (i.e. < 8.0 Å), the local connectivity of these ions however can be examined. For these ion pairs, the average nearest-neighbor Zr-O, Y-O, O-O, and Zr-Y bond distances are found to be 1.98, 2.18, 2.78, and 3.53 Å, respectively, for the 8-YSZa solid. Despite having the same Y^{3+} composition as 8-YSZc in Fig. 6a, the substantial increase in volume (i.e. 8.6% volume swelling) together with loss of long-range order cause the average coordination number of Zr, N_{Zr} to be ~ 5.9, substantially less than N_{Zr} = 7.6 for the crystal represented by 8-YSZc. Similarly for N_Y (i.e. by integrating the Y-O RDF to the minimum at ~3.03 Å), the N_Y is 5.6, less than both N_Y ~ 6.6 in 8-YSZc and N_Y = 6 in the cubic Y_2O_3 crystal, which also might attributed to the slight expansion in the volume of amorphous YSZ. However, with increased temperature the peaks of *g(r)* for the amorphous state broaden as they do in the perfect crystal.

3.2 Dynamic properties

From MD simulation, the time-dependent trajectories of the ions of a system within a time interval often provide a lot of useful information, e.g. ion diffusion patterns, ion hopping mechanisms, vibrational frequencies, transport properties (e.g. ionic and thermal), etc., that govern the diverse phenomena and the evolution of the dynamic properties of a system. For the YSZ, the most useful property is the ionic transport property that determines the electrical conductivity of an operating SOFC. The method to compute this property will be discussed in this section.

3.2.1 Ion diffusion and ionic transport in YSZ solids

i. Temperature-dependent self diffusion and ionic conductivity of O^{2-} ions

As we know, diffusion means "spreading". This quantity can be either observable (physical) or abstract and probabilistic (stochastic) in nature. In the context of YSZ, diffusion refers to the basic dynamic properties of the collective motion of its different constituent ions in response to temperature, which are governed by the self-diffusion of the ions. In general, the self-diffusion of each type of ion is governed by thermally activated random walks in the local structure, which for oxygen ions are primarily determined by the surrounding occupied and vacant sites. At low frequencies, the existence of direct-current (dc) conductivity implies that the mean square displacement (MSD) of ions is linear, i.e. $\langle r^2(t)\rangle_{dc} \sim Dt$ (Sidebottom, 2009). Linear time-dependent behavior is just a reflection of random diffusion of the ions as they migrate from site to site stochastically, which is a hallmark of uncorrelated motion. To relate experimental observation and computed atomic trajectories, MSD is a key quantity of interest in quantifying the motion of ions, and it is defined as follows:

$$\langle r^2_i(t)\rangle = \Sigma^{N_i}[r_i(t)-r_i(0)]^2/N \quad (2)$$

Within the linear response regime (Dyre et al., 2009) for an isotropic medium such as a cubic lattice of YSZ, one can extract the diffusion constant D_i for species i from the MSD using the Einstein relation, $\langle r^2_i\ (t)\rangle = 6D_it+C$. Thus, the diffusion coefficients can be evaluated from the slope of the MSD curves versus elapsed time in a steady-state MD simulation. The direct current (dc) ionic conductivity, σ_i, of ion species i can be estimated using the Nernst–Einstein relation: $\sigma_i = N_iq^2_iD_i/H_rk_BT$, where N_i is the charge density of charge carriers, q_i, per unit volume, H_R is the Haven ratio (March, 1982) (for simplicity, we chose $H_R = 1.0$ in this work), k_B is the Boltzmann constant, and T is the system temperature.

At low temperature (e.g. $T \ll 300$ K), all constituent ions within the YSZ lattices (i.e. both crystalline and amorphous solids) are mostly found to be 'frozen' at a metastable lattice sites with negligible hopping. However, the thermally activated ionic hopping within the lattices is essentially governed by the kinetic energy, which in turn is determined by system temperature and ionic mass. At a given temperature the heavier species (e.g. cations like Zr^{4+}, Y^{3+}) are less mobile than the anions (e.g. O^{2-}, or equivalently its vacancy). As an oxygen-ion conductor at elevated temperatures, the basic feature of oxygen-ion transport within YSZ is generally well described by the Arrhenius relationship for activated processes, relationship $D_i = D_0\exp(-\Delta E_{act}/kT)$. Based on the simple BMB potential (Table 1), the least-squares linear fit to the computed self-diffusion of oxygen in the 8-YSZc system over the

temperature range is found consistent with the reported experimental data (Kilo et al., 2003), as highlighted in Fig. 7a. From the data points of the present MD simulations for a period up to 2.5 ns for 300–1400 K, the pre-exponential diffusion constant, D_0, and activation energy, ΔE_{act}, for oxygen-ion diffusion in 8-YSZc are found to be ~5.83±0.47x10^{-5} cm^{2}s^{-1} and 0.59±0.05 eV, respectively, in close agreement with previously reported 6.08x10^{-5} cm^{2}s^{-1}, and 0.60 eV theoretical results (Devanathan et al., 2006), but slightly smaller than ~ 1.0 eV for 10.0 mol% Y_2O_3 YSZ reported from experiment (Kilo et al., 2003). Similarly for the other YSZ crystals in the range of 3.0-12.0 mol% Y_2O_3 of this study, the predicted activation energy, ΔE_{act}, for oxygen ions is ~0.57–0.68 eV, within the range ~0.2–1.0 eV of those reported in previous theoretical studies (Devanathan et al., 2006; Khan et al., 1998; Kilo et al., 2003; Li et al., 1995; van Duin et al., 2008) at various Y_2O_3 concentrations, including the prediction obtained from the more accurate ReaxFF Reactive Force Field (van Duin et al., 2008). From Fig. 7b our ionic conductivity is maximal at 8 mol% Y_2O_3.

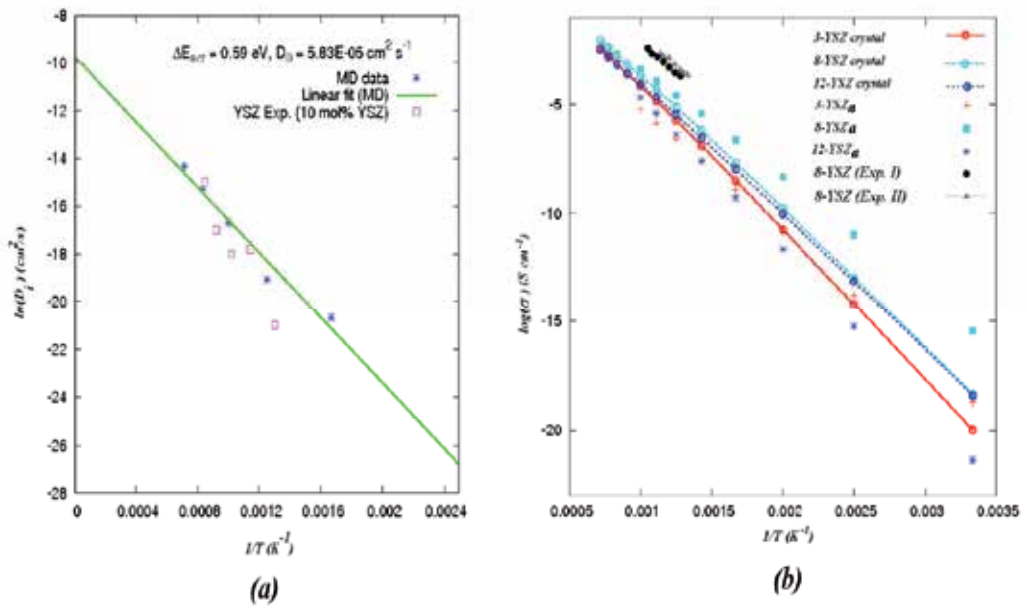

Fig. 7. The predicted oxygen ion transport properties of YSZ crystals and amorphous solids within the range ~ 300-1400 K based on the simple interatomic potential (BMB potential) from Table 1. (a) The self-diffusion coefficient D_i (in cm^{2}s^{-1}) of O^{2-} for 8-YSZc as a function of reciprocal temperature, *1/T* (in K^{-1}) compared to the reported experimental observation for 10.0 mol% Y_2O_3 YSZ. (b) The temperature-dependent ionic conductivity, σ (in Scm^{-1}) of YSZ-a and YSZ-c compared to experimental values of dc electrical conductivity measured on 8.0 mol% YSZ amorphous (i.e. 8-YSZ Exp. I) and crystalline YSZ thin films (i.e. 8-YSZ Exp. II) (Lau et al., 2011).

Based on the MD simulations for periods up to the same 2.5 ns for 300–1000 K, the oxygen-ion conductivity in amorphous YSZ solids is generally found to be comparable to that of the corresponding YSZ crystals. This trend is also found to be consistent with the reported temperature-dependent dc-electrical conductivity measured on the YSZ crystalline and

amorphous thin films (Heiroth et al., 2008). Fitting to the Arrhenius relationship over the temperature range, a pre-exponential D_0 for the 8-YSZa of ~3.56±0.29x10^{-5} cm^{2}s^{-1} is obtained, whereas ~5.83±0.47x10^{-5} cm^{2}s^{-1} was found for crystalline 8-YSZc (Lau et al., 2011). In general, the pre-exponential D_0 of amorphous YSZ solids are found to be slightly less compared to their respective perfect crystals. This might be attributed to their distinct local structural properties, which subsequently affect the underlying random walks of the mobile O^{2-} ions. Specifically, the Zr^{4+} and Y^{3+} ions are found to be lower in coordination number to the O^{2-} ions in the irregular structural geometries (Sect. 3.1.2.II). Thus the effective probability of an oxygen ion finding a vacant site, relative to these reduced cation coordination numbers, in the amorphous lattices is increased relative to a highly coordinated, compact perfect cubic YSZ crystal. The effective activation energy, ΔE_{act}, of these YSZ amorphous (3.0, 8.0 and 12.0 mol% Y_2O_3) solids is ~ 0.45–0.61 eV, comparable to YSZ crystals with the same Y_2O_3 concentration. For the 8-YSZa solid, the ΔE_{act} is slightly smaller (i.e. 0.45±0.03 eV) compared to its crystal counterpart. The differences might be due to a slight variation in ionic transport within the lattices. For YSZ crystals, the ion diffusion is mainly dominated by thermally activated hopping processes of the mobile anions and vacancies, whereas for YSZ amorphous solids, there is an additional, non-negligible mutual diffusion that involves cations and anions moving together in the expanded lattices (Sect. 3.2.3).

ii. Y_2O_3-dopant concentration dependent self diffusion and ionic conductivity of O^{2-} ions

As anticipated in Fig. 7, the high ionic conductivity in YSZ solids (both crystalline and amorphous) generally occur at rather elevated temperatures. Facilitated by increasing temperature, the isolated anion and its vacancy become mobile at T > 800 K. At very high temperatures ~1000 K or above, all the YSZ crystals exhibit exceptionally high values of ionic conductivity (σ) and reach the order of ~0.1 S cm-1 (Fig. 7), consistent with the range of reported ionic conductivity in experiment (Hull, 2004; Nakamura et al., 1986) at T ~ 1000–1250 K. As an anion-deficient fluorite, the oxygen ion and its vacancy migration kinetics in YSZ crystal, however, cannot be described solely by a simple vacancy assisted diffusion model (Hull, 2004; Krishnamurthy et al., 2004). At elevated temperature, the vacancy diffusion rate is not always simply proportional to fractional vacancy concentration, $D_i \propto x$ (with x defining Y_2O_3 dopant concentration) in the $Zr_{1-x}Y_xO_{(2-x/2)}$ system. The MSD of oxygen ions cannot increase proportional to molar concentration of the mol% Y_2O_3 because Y_2O_3 is an insulator. An optimal concentration of Y_2O_3 dopant exists and it is not predicted by a simple vacancy assisted diffusion mechanism. In many cases, maximum ionic conductivity occurs between ~ 8 and 15.0 mol% Y_2O_3 (Fig. 8) (Casselton, 1970; Hull, 2004; Krishnamurthy et al., 2004). Interestingly, this trend in ionic conductivity/diffusivity is also commonly observed in a wide range of oxide materials having the same fluorite structure.

Several investigations have addressed the origin of this unusual trend in ionic conductivity/diffusivity. Casselton, et al., (Casselton, 1970) attributes this conductivity anomaly to Coulomb attraction between dopant cations (i.e. Y^{3+}) and oxygen vacancies. They propose that at higher dopant (and vacancy) concentrations, vacancies will be trapped in defect complexes, thus resulting in a decrease in the conductivity. Experimental studies of dopant–vacancy interactions were not unambiguous. X-ray and neutron scattering studies (Morinaga et al., 1979, 1980; Steele et al., 1974) indicate that the

oxygen vacancy preferentially occupies interstitial sites adjacent to the dopant ions, implying significant dopant–vacancy attraction. However the extended X-ray absorption fine structure spectroscopy (EXAFS) and electron microscopy (Allpress et al., 1975; Catlow et al., 1986; Veal et al., 1988) studies indicates that oxygen vacancies (i.e. positively charged) have a greater preference for sitting in the first neighbor shell of Zr^{4+} ions than Y^{3+} ions. Hence, the dopant ion has a higher oxygen coordination number than the host Zr^{4+} ions. This argument suggests that the oxygen vacancy–Y-ion interaction is also dominated by size effects rather than a simple Coulomb interactions (note, the vacancy is positively charged and the Y^{3+}-ion is negatively charged, relative to the host lattice, Zr^{4+}-ion). Therefore to capture the Y_2O_3-dopant dependent ionic conductivity behavior, a small simulation cell might not be sufficient. In the meantime for YSZ, when an oxygen vacancy is formed, the lattice contracts in the vicinity of the vacancy. Because Zr^{4+} ions are smaller than Y^{3+} ions, Zr^{4+} ions can better accommodate this contraction. In this case, a simple lattice statics calculations based on a Born–Mayer interatomic potential also support this view (Dwivedi et al., 1990).

As shown in Fig. 8c, the simple interatomic potential from Table 1 can provide a consistent qualitative feature, a conductivity maximum, which is observed in experiments (Arachi et al., 1999; Badwal et al., 1992; Hull, 2009; Ioffe, 1978) and Kinetic Monte Carlo simulation in Fig. 8a (Krishnamurthy et al., 2004). For all three temperatures in the range 800–1200 K, the variation of conductivity, σ, with dopant concentration shows a maximum close to 8.0 mol% Y_2O_3 (or x ~0.16 in $Zr_{(1-x)}Y_xO_{(2-x/2)}$), consistent with finding the maximum close to the lower limit of the amount of doping required to stabilize the cubic YSZ phase (i.e. *c**-YSZ) (Arachi et al., 1999; Hull, 2009; Nakamura et al., 1986).

For YSZ amorphous solids, a similar trend of the optimal Y_2O_3 concentration governing ionic conductivity is also supported by a recent MD simulation (Lau et al., 2011). Of the 3.0, 8.0 and 12.0 mol% Y_2O_3 systems (i.e. n-YSZa) studied; it was found that σ_{max} occurs at ~ 8.0 mol% Y_2O_3 similar to the maximum found for the YSZ crystals. To account for this intriguing result, one simple, yet direct explanation can be the local Y^{3+} aggregation within the system (Lau et al., 2011). The diffusion pathways of an ion are essentially determined by the local interactions with the surrounding ions in YSZ at a given temperature. Due to the cooperative effects of larger attractive terms (A_{ij} and ρ_{ij} in Tables 1) in the BMB potential, larger bond length (i.e. R_{Y-O} from RDF at Fig. 6) and larger Y^{3+} ion relative to Zr^{4+} ion in the lattice, steeper potential wells among Y^{3+}–O^{2-} relative to Zr^{4+}–O^{2-} are expected. Thus, this will hinder the mobility of O^{2-} (or its vacancy), if the local Y^{3+} aggregation is large enough. At a given temperature, the local Y^{3+} aggregation can be defined qualitatively by comparing to the degree of Y^{3+}-clustering, η (Table 2), based on the thermal equilibrium structures of each system. For each of the N_Y atoms, we count the number of other Y atoms less than 3.7Å away. If N_c is the number of these Y atoms that have four or more neighboring Y atoms, then $\eta = N_c/N \times 100.0\%$. As shown in Table 2, η increased as the mol% of Y_2O_3 increased regardless of crystal or amorphous geometry. As the system temperature goes up, η generally decreases due to thermal expansion of the lattice. Despite this change with temperature, the relative comparison of each system remains the same. Therefore, this suggests that YSZ ionic conductivity is a thermally activated process as shown in Fig. 7 and 8, but the subtle interplay between the vacancy concentration and the intrinsic ionic diffusion pathways that are defined by local structures and local orderings cannot be ignored.

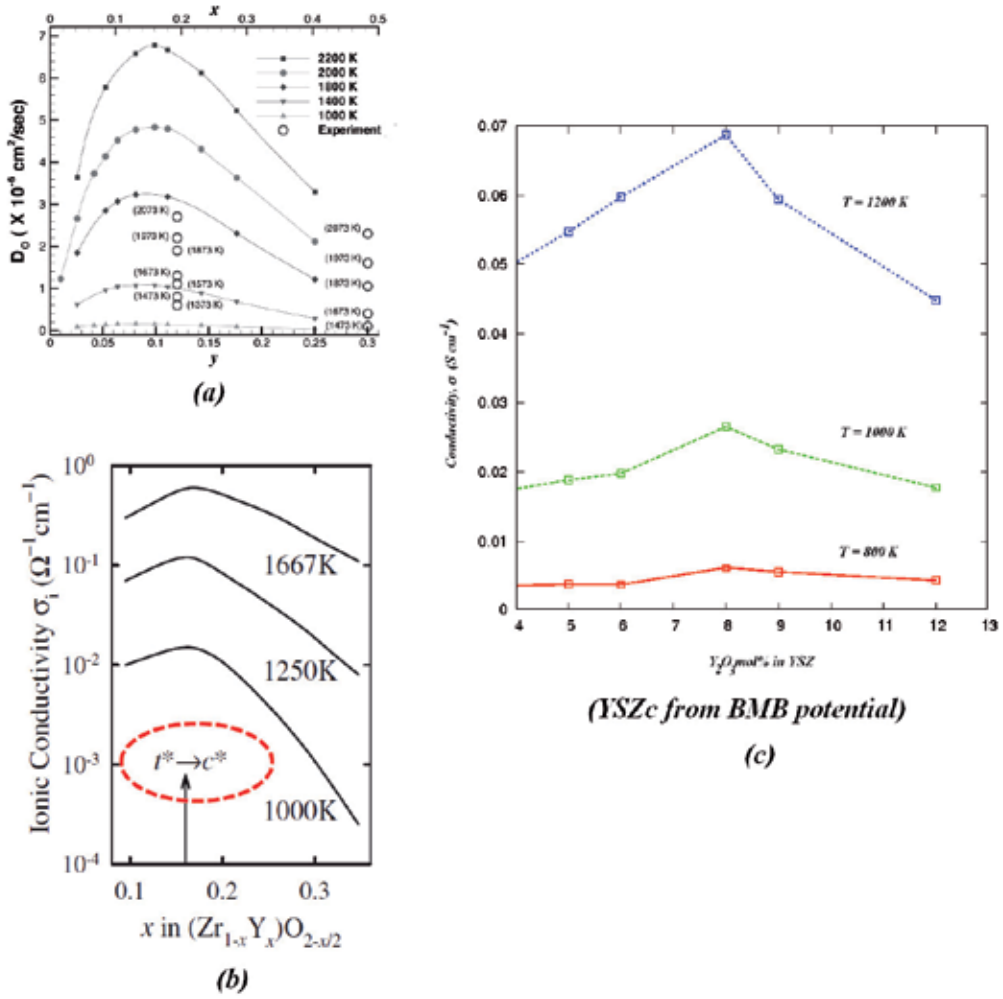

Fig. 8. (a) Oxygen diffusivity as a function of the Y_2O_3 mole fraction, y, and yttrium ion concentration, x, in YSZ at different temperatures, adopted from Krishnamurthy et. al. (Krishnamurthy et al., 2004). (b) The variation of the ionic conductivity σ_i of $Zr_{1-x}Y_xO_{(2-x/2)}$ with dopant concentration x at three different temperatures. The maximum in σ_i occurs close to the lower limit of stability of the stabilized cubic form (c^*), adopted from Hull, 2009. (c) The predicted ionic conductivity, σ (in Scm^{-1}), of 3.0–12.0 mol% Y_2O_3 YSZ crystal over 800–1200 K, with the conductivity maxima as a function of Y_2O_3 concentration based on the simple interatomic potential (Lau et al., 2011) of Table 1.

3.2.2 Why can ionic transport in YSZ crystal and YSZ amorphous be different?

As we have seen from previous sections, the basic static structural features and dynamics of ions in both YSZ crystals (n-YSZc) and amorphous solids (n-YSZa) can be well-described through the simple BMB potentials (Table 1). For both systems, the key-elements are almost the same: the system consists of a rigid ordered (i.e. crystalline lattice) or disordered (i.e.

amorphous lattice) matrix through which the ions travel together. The charge-compensating cation sites are fixed to the matrix about which the ions are loosely bonded by the weaker-than covalent ionic bonds. Because of these ionic bonds, often the thermal energy in the solids can provide the energy needed for the ion to dissociate from its site and "hop" to an adjacent site. These phenomena lead to a so-called "activation energy" (i.e. ΔE_{act} in Fig. 7), which defines the mean effective energy associated with the hop of an ion between adjacent sites. The rate of hopping is mostly controlled by the temperature and is given by the Boltzmann factor (or Arrhenius law) as anticipated in Fig. 7. MD simulations enable us to understand in depth this interesting mechanism. We can track the position of these ions over time, but we may need to utilize some ensemble-averaged quantities such as the mean-square displacement $<r^2(t)>$ (MSD) as a key to understanding these motions, and elucidating the slight differences of ionic motion between the YSZ-c (crystals) and YSZa (amorphous) structures as we found in Fig. 7.

System	η (T = 300K)	η (T = 1000K)
Crystal (mol%)		
3.0	2.46	3.36
8.0	20.52	15.26
12.0	25.93	17.69
Amorphous (mol%)		
3.0	1.37	0.73
8.0	16.67	12.82
12.0	22.62	24.44

Table 2. The degree of Y^{3+}-clustering, η (in %), of 3.0, 8.0 and 12.0 mol% Y_2O_3 YSZ crystals and amorphous solids at T = 300 and 1000 K. (Note: only the Y^{3+}-clusters with the size ≥ 4 ions are counted. By assuming the cluster cut-off radius [$R(Y^{3+}-Y^{3+})$] to be ~ 3.7 Å as found by RDF, we define $\eta = N_c/N \times 100.0\%$, where N_c is the number of clusters with ≥ 4 Y^{3+}-ions and N is the total number of Y^{3+}-clusters in a system adopted from Lau et al. (Lau et al., 2011).

i. Information given by the mean-square displacement

As we suspected, diffusion in atomistic scale in a lattice can be mainly determined by the internal structure of a material. Thus the elements of the underlying random walks are often biased on the detailed local microstructure of the material, and the strength of the interatomic forces. In the high-temperature regime, the MSD corresponding to the diffusion of the dominant charge carriers (i.e. oxygen ions O^{2-}) will grow linearly in time, analogous to ionic transport in a liquid (Fig. 9). This linear diffusive regime typically can also be found in other reported literature, which used interatomic potentials (Bush et al., 1994; Devanathan et al., 2006; Dwivedi et al., 1990; Fisher et al., 1998, 1999; Khan et al., 1998; Kilo et al., 2003; Lau et al., 2011; Lewis et al., 1985; Li et al., 1995; Minervini et al., 2000; Okazaki et al., 1994; Sawaguchi et al., 2000; Schelling et al., 2001; Shimojo et al., 1992; ; van Duin et al., 2008; Yamamura et al., 1999; Zacate et al., 2000) different from those of Table 1. For the much heavier cations (Zr^{4+} and Y^{3+}) in YSZ crystals, the MSD generally decays and saturates over a period of time, as the kinetic energy is not sufficient to reach monotonic diffusive behavior, and therefore the path is bounded in the fixed crystal lattice (Fig. 9). This unique feature, however, is not found in YSZ amorphous solids. In the

YSZ amorphous phase, the heavy cations are not simply bound to a rigid crystal lattice as in YSZ crystals (Fig. 9).

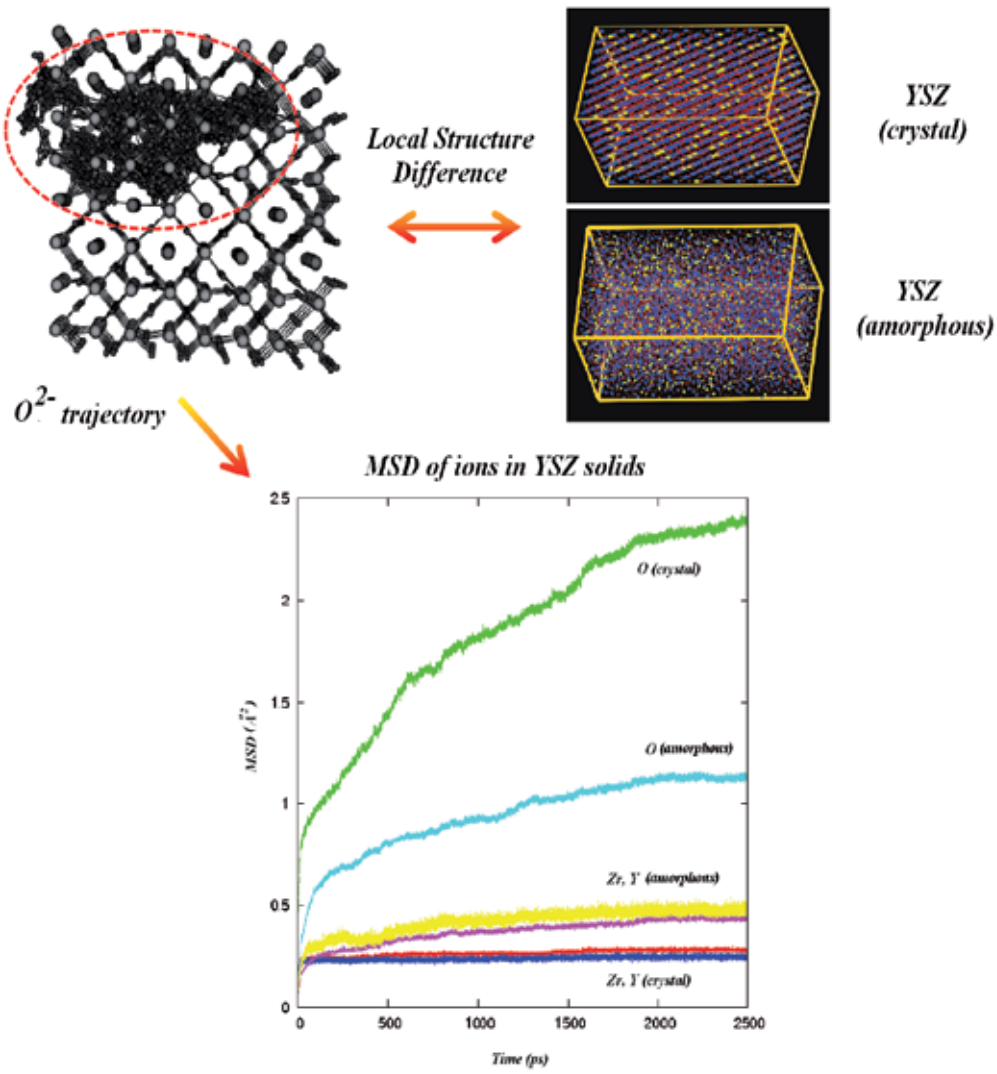

Fig. 9. The MSD of different ions (Zr^{4+}, Y^{3+}, O^{2-}) in YSZ system (crystal and amorphous) that were obtained from MD simulation through the averaging over the ensemble of the trajectories of respective ions. The systems shown are 3-YSZc and 3-YSZa at 800 K for 2.5 ns trajectories from Lau et al. (Lau et al., 2011). Representative superposed pictures of the different motions are shown to the upper left (van Duin et al., 2008).

Instead of fixed in the rigid "stationary" lattices, substantial motions can be observed through the MSD. Comparable to the negligible motion of the cations in YSZ crystals (i.e. $\langle r^2 \rangle \sim 0.2$ Å^2), the displacements of Zr^{4+} and Y^{3+} ions are rather substantial (i.e. $\langle r^2 \rangle \sim 0.5$ Å^2 at 800 K within 2.5 ns), are almost as diffusive (Fig. 9) as the mobile O^{2-} anions. For YSZ

amorphous structure from MD trajectories, the three constituent ions (Zr^{4+}, Y^{3+}, O^{2-}) have similar slopes over a long period of simulation time, indicating that mutual diffusion driven by correlated motion between anions and cations might be substantial in the YSZ amorphous structure.

In this case, the difference can become more evident if temperature is raised. Here it is noteworthy to point out a limit due to finite computer resources. This subtle phenomenon can also attributed to the fact that the simulated YSZ amorphous systems are mostly metastable and are continuously crystallizing at a slow rate even at elevated temperatures, analogous to crystallization of amorphous YSZ film which was reported in a recent experiment (Heiroth et al., 2008). Unlike that of a perfect crystal, the potential-energy landscape experienced by an ion in a disordered amorphous solid is irregular, containing a distribution of stationary points, wells, barrier heights, and saddle point energies. Thus, the residence sites for an ion in an amorphous system are more vulnerable to thermal fluctuations, and possibly are even metastable. Thus, a much longer simulation time might be needed to achieve thermal equilibrium for an amorphous YSZ structure compared to YSZ crystals as pointed out in a recent study (Lau et al., 2011). In real experiments, the stability of amorphous YSZ often depends on the crystallization process and is directly correlated to grain size and different local environments (Heiroth et al., 2008). This suggests that besides short-distance thermal vibrations, the dynamics of both the cation and anion can be responsible for the observed slow crystallization process and related ionic conductivity fluctuation seen in experiments (Heiroth et al., 2008).

ii. Information given by van hove correlation functions

To capture the intriguing observation as shown in MSD (Fig. 9), the physics behind the time-dependent mutual diffusion and structural variations observed particularly in YSZ amorphous structure can be analyzed based on the van Hove correlation function, *G(r,t)* (Frenkel, 1996; Lau, 2011, Rapaport, 2004). By following the definition (Frenkel & Smit, 1996; Rapaport, 2004), *G(r,t)* can be represented separately by the self:

$$G_s(r,t) = <\Sigma_j \delta(r+r_j(0)-r_j(t))>/N_j \quad (3)$$

and the distinct part:

$$G_d(r,t) = <\Sigma_{i\neq j} \delta(r+r_i(0)-r_j(t))>/N_i \quad (4)$$

which are determined by the space- and time-dependent density correlations of the constituent ions in the system. As defined, $G_s(r,t)$ compares the position of a particle to its position within a time interval. In thermal equilibrium, $G_s(r,t)$ depends only on the time difference, and provides information about the hopping and diffusion processes of the separated ions. Whereas $G_d(r,t)$ compares the positions of a particle to the position of another particle at different time, and yields information about the correlated motions within a time interval.

As expected for a diffusion process, $G_s(r,t)$ decreases generally with increasing distance at each time and reflects the nature of Brownian motion, which is proportional to the system temperature. For a mobile ion, the width of $G_s(r,t)$ generally are broader than the stationary ion. At low temperature, the $G_s(r,t)$ are generally found to be more localized, with longer residence time for the individual ions. Thus for a YSZ crystal (YSZc) and a YSZ amorphous

(YSZa) structure, their differences in MSD over a simulation time can also be highlighted in the van Hove correlation as shown in Fig. 10. To capture the time-evolution of ions' hopping and diffusion process in both the YSZ crystals and amorphous structures, a direct comparison of $G_s(r,t)$ with a Gaussian form of diffusive motion can be very useful (Lau et al., 2011).

For a diffusion process, Fick's laws apply when there is a concentration gradient in a system. However as a typical thermodynamic equilibrium system, these MD calculations have no long-range gradient. To better analyze the features in $G_s(r,t)$, a comparison of $G_s(r,t)$ with the diffusion transport character in Gaussian form is particularly useful. By applying the Laplace transform to Fick's second law ($D\nabla^2 C = \partial C/\partial t$), subject to the initial condition at time $C(x, y, z, t = 0)$ for all $x, y, z = 0$ and the boundary condition $C(\pm\infty, t) = 0$ so that a finite number of diffusive ions cannot alter the charge composition of the system, the diffusion process is subject to the diffusion solution in Gaussian form, with concentration field

$$C(x,y,z,t) = \exp(-(x^2+y^2+z^2)/4Dt)/(4\pi Dt)^{3/2} = \exp(-r^2/4Dt)/(4\pi Dt)^{3/2} \quad (5)$$

where $r^2 = x^2+y^2+z^2$. Assuming that the time response of the van Hove self-correlation function $G_s(r, t)$ of ions in the YSZ crystal and amorphous solid (i.e. 3-YSZc and 3-YSZa in Fig. 10) is reminiscent of $C(x, y, z, t)$ [or $C(r, t)$], the evolution of the self-part of the van Hove function $4\pi r^2 G_s(r, t)$ as a function of r with time (i.e. 10 and 2500 ps shown in Fig. 10) at 800 K can be compared with an ideal Gaussian distribution of diffusive motion of ions, $4\pi r^2 C(r, t)$ with $C(r, t) = \exp(-r^2/4Dt)/(4\pi Dt)^{3/2}$ where $\langle r^2 \rangle \sim 6Dt$ is assumed and D is the diffusion coefficient of the corresponding ion.

As shown by $C(r, t)$, its normal distribution is essentially governed by the ionic motion under thermal equilibrium at a given temperature that is analogous to a 'drifting wave-packet' under the thermal motion. Basically, the drifting 'wave-packet' of charged carriers is determined by the mobility of the ions in the ensemble, which can be captured by $\langle r^2 \rangle$. As time develops, the Gaussian-shaped wave-packet widens as it travels due to the ion diffusion about the mean (Fig. 10). Compared to the Gaussian form diffusive motion, $4\pi r^2 C(r, t)$ in Fig. 10, the decay of the profile and variation found in $4\pi r^2 G_s(r, t)$ of the YSZ system is prominent as time develops. From its initial localized 'impulse-like' distribution (e.g. $4\pi r^2 G_s(r, t)$ at 10 ps in Fig. 10a) analogous to a localized δ-function (Frenkel & Smit, 1996; Rapaport, 2004), the variation of $G_s(r, t)$ for the ions is obviously less uniform compared to $C(r, t)$ in Gaussian form. Here neither of the ionic motions in the two YSZ systems is fitted perfectly by a Gaussian distribution, and strong deviation from the Gaussian form is prominent as time develops (Fig. 10). In this case, the both YSZ crystals and amorphous solid share similar features in $G_s(r, t)$ up to 2500 *ps*, yet are not perfectly identical. In both cases, the non-Gaussian features of the mobile O^{2-} in $G_s(r,t)$ can be attributed to a non- uniform distribution of the mobility of the carriers which varies over a wide range of velocity caused by the coexistence of hopping processes and 'liquid-like' diffusivity. As time evolves, the multiple satellite peaks which represent the hopping processes are evident in both YSZ systems for all the constituent ions. For YSZ crystal (e.g. 3-YSZc in Fig. 10), we can see only the mobile anions attain the significant diffusive features, namely a decaying peak accompanied by a tail part of the $G_s(r, t)$ function that develops with time. The long tail at large r is related to the long-range motion found in the time-dependent trajectory, i.e. by fast mobile anions with successive hopping motions. For YSZ

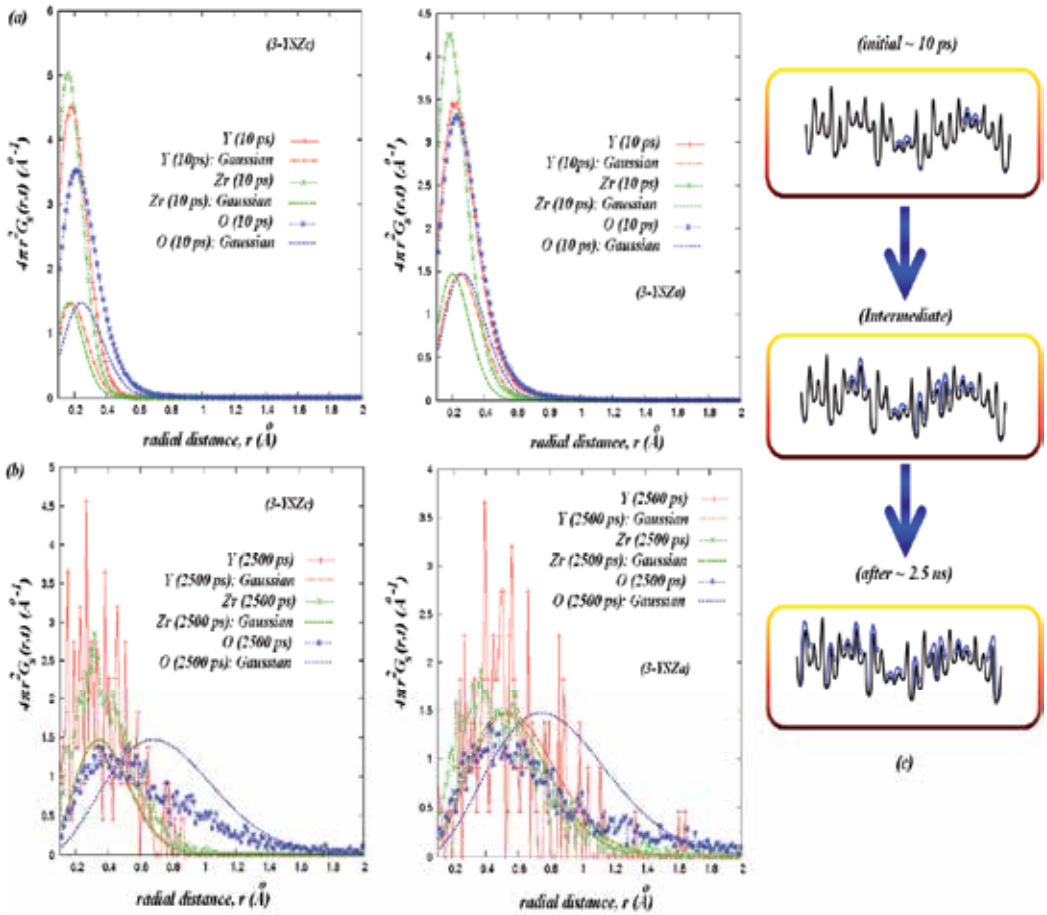

Fig. 10. The self-part of the van Hove correlation function $4\pi r^2 G_s(r, t)$ (lines with symbols) for both 3-YSZc (crystal) and 3-YSZa (amorphous) at 800 K. The functions develop from top to bottom with time, and are compared with Gaussian diffusion motion $4\pi r^2 C(r,t)$ with $C(r,t)$ (plane lines) determined by the steady-state diffusion constant D at 10 ps (a) and at 2500 ps (b) for crystal (left) and amorphous solid (center). (c) A schematic figure that illustrates a time-evolving ion's hopping (large fluctuations) and diffusion (small fluctuations) processes in both YSZ crystal and amorphous solid that can be captured through the van Hove correlation function.

amorphous solids (e.g. 3-YSZa in Fig. 10), the coexistence of the 'liquid-like' features of diffusive cations (Zr^{4+}, Y^{3+}) and anions (O^{2-}) however is more obvious, with the long dispersive tails of $G_s(r,t)$ spreading to large r. Instead of the localization of the maximum at the origin as the initial stage, substantial drifting (Δr ~ 0.4–0.7 Å) of the maximum for both cations and anions in YSZ amorphous solids after 2500 ps can be seen (Fig. 10b). This suggests that the residence sites in a metastable disordered amorphous solid of YSZ are

always influenced by interactions with the migrating cations, and therefore change with time. By involving the mutual diffusion (i.e. sites previously occupied by cations can be visited by anions and vice versa), the hopping processes of ions will therefore be influenced greatly by the changing intermediate surroundings, which makes fast diffusive ions with successive hopping jumps less probable. Therefore the MSD of the mobile O^{2-} in the amorphous solid will be less compared to the crystal (Fig. 9).

4. Conclusion

During recent decades, it has become feasible to simulate a complicated system on a computer due to rapid progress in parallel computing. Within the scale of atomistic and molecular simulation, the application of the classical molecular dynamics (MD) simulation method covers a vast variety of systems undergoing current scientific development. The method of MD solves the classical equations of motion for an ensemble of atoms. It results in time-dependent trajectories for all atoms in a system. From these atomistic trajectories, MD can provide detailed *in situ* atomistic information that is difficult to obtain experimentally. As one of the robust and well-developed simulation techniques, MD simulation is an ideal scientific tool to complement experimental observations to properly characterize a complicated system. Those that involve a vast time and spatial dimension, and heterogeneous materials interfaces can be modeled using a multi-scale framework. One of the best such examples that are becoming appropriate for MD is the study of the inner workings of a solid oxide fuel cell (SOFC), which is important as an electrochemical energy conversion and clean energy storage.

SOFC is a new alternative clean energy device that converts the energy of combustion and electrochemical interactions into electricity, which utilizes the superionic conductivity ($> 10^{-1}$ Scm^{-1}) of special materials at high temperature. Despite the advantages over conventional power generation technologies, there remain a number of challenges that delay the full commercialization of the SOFC and one of the challenges is to understand the basis of ionic transport in its solid electrolyte (e.g. YSZ, the $Zr_{1-x}Y_xO_{2-x/2}$ system, with $x/2$ being the Y_2O_3 dopant concentration). For YSZ, the optimum ionic conductivity can vary with different synthesis routes and sintering conditions due to the resultant diverse local morphologies, grain boundaries, and microstructures.

Within the rigid ion model approximation, we have shown a systematic study of the static and dynamic properties of YSZ crystals and amorphous solids within the typical dilute Y_2O_3 concentration limit (i.e. 3.0 – 12.0 mol% Y_2O_3) in the temperature range 300 – 1400 K based on a simple semi-empirical Born–Meyer–Buckingham (BMB) interatomic potential through the standard techniques in classical MD. The results suggest that the vacancy assisted ion conductivity of YSZ as a function of mol% of Y_2O_3 at a given temperature seems to be a universal feature of YSZ electrolytes, regardless of varying local structures. Whether it is an amorphous or a crystal, the oxygen ionic conductivity shows a maximum at ~8.0mol%Y_2O_3, close to the lower limit of the cubic YSZ phase stability that is confirmed by experiments. For YSZ amorphous solids, their lower absolute ionic conductivity relative to YSZ crystals is consistent with the trends observed in YSZ crystalline and stabilized amorphous thin films reported from experiments. For the YSZ

amorphous solids, the mobile anions and the slowly migrating cations are strongly coupled in their motion. This mutual diffusion (cations and anions) found in the amorphous phases contributes considerably to the dynamics as seen through the time-dependent van Hove correlation functions. This reduces the effective oxygen-ion conductivity. These moving ions carry charges, and thus produce an electrical response. It is expected that the intriguing features of mutual diffusion found in amorphous YSZ solids can therefore be detected by current experimental techniques at frequencies below the typical vibrational frequencies (>100 GHz). To gain further insight into the different correlated motions in various YSZ system and its interfaces, richness in morphologies, longer equilibration, better statistical methods and better atomic potentials are highly desirable.

5. Acknowledgements

This work was supported and by the Office of Naval Research, both directly and through the Naval Research Laboratory.

6. References

Ackermann, R J; Rauh, E G. & Alexander, C A. (1975) High Temp. Sci. Vol. 7, pp. 305.

Aldebert, P. & Traverse, J P. (1985) J. Am. Ceram. Soc. Vol. 68, pp. 34.

Allpress, J. G. & Rossell, H. J. J. Solid State Chem. Vol. 15, pp. 68–78.

Andersson, M.; Yuan, J. & Sundén, B. (2010) Applied Energy, Vol. 87, pp. 1461-1476.

Arachi, Y; Sakai, H; Yammoto, O; Takeda, Y. & Imanishai, N. (1999) Solid State Ion. Vol. 121, pp. 133.

Badwal, S. P. S. (1992) Solid State Ion. Vol. 52, pp. 23.

Baller, J; Krüger J K; Birringer, R. & Prousi, C. (2000) J. Phys.:Condens. Matter Vol. 12, pp. 5403.

Bogicevic, A; Wolverton, C; Crosbie, G M. & Stechel E B. (2001) Phys. Rev. B Vol. 64, pp. 014106.

Boysen, H; Frey, F. & Vogt, T. (1991) Acta Crystallogr. B Vol. 47, pp. 881.

Butz, B.; Kruse, P.; Störmer, H.; Gerthsen, D.; Müller, A.; Weber, A. & Ivers-Tiffée, E. (2006) Solid State Ion. Vol. 177, pp. 3275.

Bush, T.S.; Gale, J.D.; Catlow, C.R.A. & Battle, P.D. (1994) J. Mater. Chem. Vol. 4, pp. 831.

Casselton, R. E. W. (1970) Phys. Status Solidi A Vol. 2, pp. 571–585.

Catlow, C. R. A.; Chadwick, A. V.; Greaves, G. N. & Moroney, L. M. J. Am. Ceram. Soc. Vol. 69, pp. 272–277 .

Chen, X. J.; Khor, K A.; Chan, S H. & Yu, L G. (2002) Mater. Sci. Eng. A, Vol. 335, pp. 246.

Cheng, Z.; Wang, J-H.; Choi, Y.; Yang, L; Lin, M.C. & Liu, M. (2011) Energy Environ. Sci. Vol. DOI: 10.1039/c1ee01758f.

Chu, W-F; Thangadurai, V. & Weppner, W. (2006). Ionics, Vol. 12, pp. 1-6.

Dash, L K; Vast, N; Baranek, P; Cheynet M C. & Reining, L. (2004) Phys. Rev. B Vol. 70, pp. 245116.

Devanathan, R; Weber, W J; Singhal, S C. & Gale, J D. (2006) Solid State Ion. Vol. 177, pp. 1251.
Dwivedi, A. & Cormack, A N. (1990) Phil. Mag. A Vol. 61, pp. 1.
Dyre, J.C.; Maass, P.; Roling, B. & Sidebottom, D.L. (2009) Rep. Prog. Phys. Vol. 72, pp. 046501.
Etsell, T H. & Flengas S N. (1970) Chem. Rev. Vol. 70, pp. 339.
Frenkel, D. & Smit, B. (1996) Understanding Molecular Simulation: From Algorithms to Applications (New York: Academic).
Fisher, C A J. & Matsubara, H. (1998) Solid State Ion. Vol. 115, pp. 311.
Fisher, C A J. & Matsubara, H. (1999) Comput. Mater. Sci. Vol. 14, pp. 177.
Fukui, T; Murata, K.; Ohara, S.; Abe, H.; Naito M. & Nogi, K. (2004) J. Power Sources, Vol. 125, pp. 17.
Gale, J. & Rohl, A.L. (2003) Mol. Simul. Vol. 29, pp. 291.
Gatewood, D.S.; Turner, C.H. & Dunlap, B.I. (2011) ECS Transactions, Vol. 35, "Solid-Oxide Fuel Cells 12", pp. 1055–1063.
Hayashi, H; Saito, T; Maruyama, N; Inaba, H; Kawamura, K. & Mori, M. (2005) Solid State Ion. Vol. 176, pp. 613.
Heiroth, S; Lippert Th; Wokaum, A. & Döbeli M. (2008) Appl.Phys. A Vol. 93 pp. 639.
Howard, C J; Hill, R J. & Reichert B E. (1988) Acta Crystallogr. B Vol. 44, pp. 116.
Hull, S. (2004) Rep. Prog. Phys. Vol. 67, pp. 1233-1314.
Ingel, R P. & Lewis D. (1986) J. Am. Ceram. Soc. Vol. 69, pp. 325.
Ioffe, A. J; Rutman, D. S. & Karpachov, S.V. (1978) Electrochim. Acta Vol. 23, pp. 141.
Ishizawa, N.; Matsushima, Y.; Hayashi, M. & Ueki, M. (1999) Acta Crystallogr., Sect. B Vol. *55*, pp. 726.
Khan, M S; Islam, M S. & Bates, D R. (1998) J. Mater. Chem. Vol. 8, pp. 2299.
Kilo, M; Argirusis, C; Borchardt, G. & Jackson, R A. (2003) Phys. Chem. Chem. Phys. Vol. 5, pp. 2219.
Korte, C.; Peters, A.; Janek, J.; Hesse, D. & Zakharov, N. (2008) Phys. Chem. Chem. Phys. Vol. 10, pp. 4623.
Krishnamurthy, R.; Yoon, Y G.; Srolovitz, D J. & Car, R. (2004) J. Am. Ceram. Soc. Vol. 87 pp. 1821.
Lammert, H. & Heuer, A. (2010) Phys. Rev. Lett. Vol. 104, pp. 125901.
Lau, K. C.; Turner, C.H. & Dunlap, B. I. (2008) Solid State Ion. Vol. 179, pp. 1912.
Lau, K. C.; Turner, C.H. & Dunlap, B. I. (2009) Chem. Phys. Lett. Vol. 471, pp. 326.
Lau, K. C. & Dunlap, B. I. (2009) J. Phys.: Condens. Matter Vol. 21, pp. 145402.
Lau, K. C. & Dunlap, B. I. (2011) J. Phys.: Condens. Matter Vol. 23, pp. 035401.
Lashtabeg, A. & Skinner, S J. (2006) J. Mater. Chem. Vol. 16, pp. 3161.
Lewis, G V. & Catlow, C R A. (1985) J. Phys. C: Solid State Phys. Vol. 18, pp. 1149.
Li, X. & Hafskjold, B. (1995) J. Phys.: Condens. Matter Vol. 7, pp. 1255.
Lindan, P J D. & Gillan, M J (1993) J. Phys.: Condens. Matter Vol. 5, pp. 1019.
March, G E. (1982) Solid State Ion. Vol. 7 pp. 177.
Minervini, L; Grimes, R W. & Sickafus, K E. (2000) J. Am.Ceram. Soc. Vol. 83, pp. 1873.
Morinaga, M.; Cohen, J. B. & Faber, J. Jr. (1979) Acta Crystallogr. Vol. A35, pp. 789–795.

Morinaga, M.; Cohen, J. B. & Faber, J. Jr. (1980) Acta Crystallogr. Vol. A36, pp. 520–530.
Nakamura, A. & Wagner, J B Jr. (1986) J. Electrochem. Soc. Vol. 133 pp. 1542.
Okazaki, H; Suzuki, H. & Ihata, K. (1994) Phys. Lett. A Vol. 188, pp. 291.
Ostanin, S; Salamatov E; Craven, A J; McComb, D W. & Vlachos D. (2002) Phys. Rev. B Vol. 66, pp.132105.
Ostanin, S. & Salamatov E. (2003) Phys. Rev. B Vol. 68, pp. 172106.
Pascual, C. & Duran, P. (1983) J. Am. Ceram. Soc. Vol. 66 pp. 23.
Pornprasertsuk, R.; Cheng, J.; Huang, H. & Prinz, F. B. (2007) Solid State Ion. Vol. 178, pp. 195.
Pietrucci, F; Bernasconi, M; Laio, A. & Parrinello, M. (2008) Phys. Rev. B Vol. 78, pp. 094301.
Predith, A; Ceder, G; Wolverton, C; Persson K. & Mueller T. (2008) Phys. Rev. B Vol. 77, pp. 144104.
Ralph, M.; Schoeler, A. C. & Krumpelt, M. (2001) J. Mater. Sci. Vol. 36, pp. 1161.
Rapaport, D.C. 2004 The Art of Molecular Dynamics Simulation 2nd Edn (Cambridge: Cambridge University Press).
Sayle, D C. (1999) J. Mater. Chem. Vol. 9, pp. 2961.
Sayle, D C; Doig, J A; Parker, S C; Watson, G W. & Sayle, T X T. (2005) Phys. Chem. Chem. Phys. Vol. 7 pp. 16.
Sayle, D C; Maicaneannu, S A. & Watson, G W. (2002) J. Am. Chem. Soc. Vol. 124, pp. 11429.
Sidebottom, D.L. (2009) Rev. Mod. Phys. Vol. 81, pp. 999.
Turner, C.H.; W. An.; Dunlap. B.I.; Lau, K.C. & Wang, X. (2010) Annual Reports in Computational Chemistry, Vol. 6, pp. 201-234.
van Duin, A C T.; Merinov, B V; Jang, S S. & Goddard, W A III. (2008) J. Phys. Chem. A Vol. 112, pp. 3133.
Veal, B. W.; McKale, A. G.; Paulikas, A. P.; Rothman, S. J. & Nowicki, L. J. Physica B. Vol 150, pp. 234–240.
Wang, X.; Lau, K. C.; Turner, C. H. & Dunlap, B.I. (2010) J. Electrochem. Soc. Vol. 157, pp. B90–8.
Wang, X.; Lau, K. C.; Turner, C. H. & Dunlap, B.I. (2010) J. Electrochem. Soc. Vol. 195, pp. 4177.
Sawaguchi, N. & Ogawa, H. (2000) Solid State Ion. Vol. 128 pp. 183.
Schelling, P K; Phillpot, S.R. & Wolf, D. (2001) J. Am. Ceram. Soc. Vol. 84, pp. 1609.
Shimojo, F.; Okabe, T.; Tachibana, F.; Kobayashi, M. & Okazaki, H. (1992) J. Phys. Soc. Japan Vol. 61, pp. 2848.
Smith, D K. & Newkirk, H W. (1965) Acta Crystallogr. Vol. 18 pp. 983.
Stapper, G; Bernasconi, M; Nicoloso, N. & Parrinello, M. (1999) Phys. Rev. B Vol. 59, pp. 797.
Steele, D. & Fender, B. E. F. (1974) J. Phys. C: Solid State Phys. Vol. 7, pp. 1–11.
Yamamura, Y; Kawasaki, S. & Sakai H. (1999) Solid State Ion. Vol. 126 pp. 181.
Zacate, M.O.; Minervini, L.; Bradfield, D J.; Grimes, R W. & Sickafus, K E. (2000) Solid State Ion. Vol. 128, pp. 243.
Zhang, C; Li, C J.; Zhang, G.; Ning, X J.; Li, C X.; Li, H. & Coddet, C. (2007) Mater. Sci. Eng. B Vol. 137, pp. 24.

Zhao, X. & Vanderbilt, D. (2002) Phys. Rev. B Vol. 65, pp. 075105.
Zhu, Q. & Fan, B. (2005) Solid State Ion. Vol. 176, pp. 889.

18

Molecular Dynamics Simulation and Conductivity Mechanism in Fast Ionic Crystals Based on Hollandite $Na_xCr_xTi_{8-x}O_{16}$

Kien Ling Khoo[1,2] and Leonard A. Dissado[2]
[1]*Invion Technologies Sdn Bhd*
[2]*Engineering Department, University of Leicester, Leicester*
[1]*Malaysia*
[2]*UK*

1. Introduction

Fast ion conductors are keystone materials in the development of high performance solid oxide fuel cells and solid electrolytes. In spite the significant contributions in this area a fundamental understanding of the correlation between crystal structure and ionic conductivity is still lacking. In this chapter we report our recent computer simulation results on Hollandite ionic crystals. The objective of this work is to provide the structural parameters which will lead to the design and synthesis of high performance ionic conductors.

Hollandites are ionic crystals of a rather unusual kind, in which the ions of one type are in a disordered and highly mobile state (Dixon & Gillan, 1982). Such materials often have rather special crystal structures in that there are open tunnels or layers through which the mobile ions may move (West, 1988). Their crystal structure corresponds to a family of compounds of general formula $A_xM_{4-x}N_yO_8$. The basic formula of the Hollandite structure used in the research is $Na_x(Ti_{8-x}Cr_x)O_{16}$, (Michiue & Watanabe, 1995a, 1996). The chromium and titanium ions are randomly placed in unit cells according to the relative proportions of titanium and chromium ions with a corresponding amount of sodium ions to compensate for the smaller charge on the chromium ions (+3) compared to the titanium ions (+4).

The main interest of this Na-priderite is its structure as a promising (1-D) Na ion conductor (Michiue & Watanabe, 1995b). Priderites, titania-based hollandites, are typical one-dimensional ion conductors in which the 1-D tunnels are available for transport of cations in the tunnel (hereafter the "tunnel ion") (Michiue & Watanabe, 1995a). Priderites are generally represented by $A_xM_yTi_{8-y}O_{16}$, where A is the alkali or alkaline earth ions and M, di- or trivalent cations (Michiue & Watanabe, 1995a; A. Byström & A.M. Byström, 1950). The host structure for the hollandite being used mainly consists of titanium ions and oxygen ions. These titanium ions are each octahedrally bonded to six oxygen ions. Two such octahedra are joined by sharing an edge, and these doubled groups share further edges above and below to form extended double strings parallel to the growth axis. Four such double strings are joined by corner sharing to form a unit tunnel. The sodium ions are situated in the

tunnels, and each is ionically bonded to eight oxygen ions of the host structure at the corners of a slightly distorted cube. These cubes form a string of ion cages along the axis of a tunnel, and since not all cages have a chromium ion in the place of a titanium ion not all cages contain a sodium ion. The availability of vacant sites into which the sodium ion can move is what allows ion transport to be possible. A typical hollandite structure is shown in figure 1.

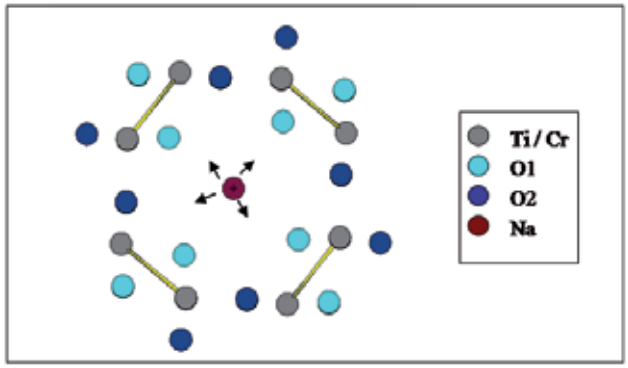

Fig. 1. A typical hollandite structure projected along the c-axis.

The behaviour of the tunnel ion is usually complicated because it interacts not only with the ions in the lattice sites but also with the other tunnel ions. The main two interactions are Lennard-Jones potential for the short range and Coulomb potential for the long range. Although the ions at the lattice sites give a potential surface for the tunnel ions, which the sodium ions move on, the interactions with other sodium ions in the tunnel is a many body problem like a liquid.

Herein, we investigate the response of the sodium ions under the effect of electric field. The dielectric behaviour of the hollandites is typically studied in the low frequency region [10^2-10^9 Hz]. Dryden and Wadsley (Dryden & Wadsley, 1958), in the first publication on the structure and electrical properties of a hollandite, reported the existence of a dielectric relaxation in several BaMg hollandites, which had a maximum absorption at room temperature in the radio frequency region of the spectrum (10^5-10^8 Hz). They reported that the dielectric absorption was only detected when the electric field was in the direction of the tunnel. The activation energy for the peak frequency representing the energy barrier to be overcome for ion displacement was found to be 0.17eV. Cheary and Dryden (Cheary & Dryden, 1991) reported that the mobility of the tunnel ion in Ba hollandite is very low except in limited regions and the activation energy that they obtained is 0.24eV. Activation energies of the order 0.05eV claimed by others was only detected in some samples with the presence of impurity TiO_2 as a second phase. Since then there have been further experimental work on the dielectric properties of hollandites published by Singer et al (Singer et al., 1973). Yoshikado et al (Yoshikado et al., 1982) emphasize the loss factor (ε'') at low frequencies which increases with decreasing frequency and usually depends on frequency as f^{-n} where $n<1$. Jonscher (Jonscher, 1983) concluded that the response of fast ion conductors follows the "universal law" for the charge carriers. He showed that strong low-frequency dispersion occurs at high temperature, 373K, in the hollandite ($K_{1.8}Mg_{0.9}Ti_{7.1}O_{16}$). The behaviour in the high frequency region is not well understood. Michiue and Watanabe (Michiue & Watanabe, 1999) reported that the strong response observed for the imaginary part of the dielectric

permittivity for K-hollandites around 100-300 cm^{-1} ($3x10^{12}$ – $9x10^{12}$ Hz) is due to the vibration of the framework structure. Not much work has been done in investigation for the frequency range around 1.2-70 cm^{-1} ($3.6x10^{10}$ – $2.1x10^{12}$ Hz).

Dissado and Hill (Dissado & Hill, 1983) predicted that particles moving in a flexible local environment experienced a cooperative interaction between the particle and their environment leading to a specific form of dielectric response, the constant phase angle response, $C'(f) \propto C''(f) \propto f^{-p}$. Dissado and Alison (Dissado & Alison, 1993) showed that this form of response included a Poley absorption peak in the far infra-red region of the spectrum. This form of absorption peak was observed by Poley (Poley, 1955), Davies (Davies et al, 1969) and some others (Johari, 2002; Chantry, 1977) in both liquids and solids and was named after Poley. The "liquid-like" hollandite structure is similar in form to the materials in which the Poley peak is observed, and hence such a peak can be expected. The theories (Dissado & Alison, 1993; Poley, 1955) suggest that this peak will be caused by the cooperative librations of the dipole produced by the sodium ions and their environmental counter-charges as the sodium ions displace under the many-body interactions of one another. It is the intention here to use molecular dynamics simulations to see if the predicted Poley absorption will be produced by such motions even in the absence of vibrations and flexible displacement in the surrounding crystal.

2. Molecular dynamics (MD) simulation

Molecular dynamics (MD) simulations technique has been used in this research to perform the atomistic calculations, of frequency dependent electrical conductivity in $Na_x(Ti_{8-x}Cr_x)O_{16}$, (x = 1.7). MD simulation is generally carried out to compute the motions of individual molecules in models of solids, liquids and gases. The key idea is motion, which describes how positions, velocities, and orientation change with time (Haile, 1992). The MD simulation method is carried out in such a way that atoms are represented by point particles and the classical (Newton) equations of motion, "force equals mass times acceleration or F = ma" are integrated numerically. The motions of these large numbers of atoms are governed by their mutual interatomic interaction. MD simulations are limited largely by the speed and storage constraints of available computers. Hence, simulations are usually done on system containing 100-1000 particles, with a time step of $1x10^{-15}$ s. This technique for simulating the motions of a system of particles when applied to biological macromolecules gives the fluctuations in the relative positions of the atoms in a protein or in DNA as a function of time. Knowledge of these motions provides insights into biological phenomena. MD is also being used to determine protein structure from NMR, to refine protein X-ray crystal structures faster from poorer starting models, and to calculate the free energy changes resulting from mutation in proteins (Karpus & Petsko, 1990).

The construction of the molecular dynamics model involved mainly model development and the use of the Molecular Dynamics simulation technique to solve the equation of motion iteratively. In model development, firstly the interaction between ions and the interaction between ion and environment have to be defined. The interaction between ions comprises three components: Lennard-Jones potential, Coulomb potential and Van der Waals' attraction. The rigid lattice approximation is being used in the simulation. This describes the interaction between the ions and the environment. In the rigid lattice approximation only the tunnel ions are allowed to displace from their equilibrium position. The environment

ions still give an interaction with the tunnel ions, i.e. they produce a constant potential surface for the tunnel ions. The tunnel ions interact with one another and are allowed to displace. After this has been done, the equations of motion are developed. A program, Gretep (LMGP-Suite Suite of Programs for the interpretation of X-ray Experiments) is used to generate the positions of all the ions by keying in parameters such as space group, unit cell dimensions, atomic parameters and etc. Then titanium ions are replaced by chromium ions randomly placed in unit cells along the tunnel according to the relative proportions of titanium and chromium. A tunnel ion, which is the sodium ion, is added to the model structure for every chromium ion, in order to preserve charge neutrality.

2.1 Modeling of ion-ion interactions

The molecular interactions are based on the intermolecular potential energy function. The total potential energy between two ions is the sum of the Lennard-Jones potential and Coulomb potential (West, 1988),

$$V(r) = \frac{\lambda}{r^p} \pm \frac{e^2}{4\pi\varepsilon_0 r} \tag{1}$$

where p is about 10 and the values for λ are different for different ion-pairs, e is the electron charge and r is the distance between two ions. The values for lambda for each ion-pair have to be found for the calculations of the equations of force. The method used is presented elsewhere (Khoo, 2003; Dissado and Khoo, 2006; Khoo et al., 2004, 2007). The relationship between the tunnel system and its surroundings is defined by using boundary conditions. These describe the interactions between the molecules with their surroundings. Rigid lattice approximation has been used in the simulation to simplify the simulation process and to reduce the simulation executable time. Rigid lattice approximation is done in such a way that only the tunnel ions, which are the sodium ions, are free to displace. All other ions in the lattice sites would remain static. However, there will still be interaction between sodium ions and the ions in the lattice sites.

Reflective boundary conditions are used at the two ends of the tunnel. Rebound is a special type of collision involving a direction change; the result of the direction change is a large velocity change. Collisions in which particles rebound with the same speed are known as elastic collisions. Thus, the velocity of the ion that bounds back from the boundary should have the opposite sign and equal in magnitude with that velocity of ion which hits the boundary. The angle of the velocity hitting the boundary is the same as the angle leaving the boundary. Force is the derivative of potential energy. Therefore, the component of the force along the a-axis is given by equation 2.

$$F_a = -\frac{dV(r)}{da} = \frac{dr}{da}\frac{\lambda p}{r^{p+1}} \mp \frac{dr}{da}\frac{e^2}{4\pi\varepsilon_0 r^2} \tag{2}$$

$$r = \sqrt{(Aion1 - Aion2)^2 + (Bion1 - Bion2)^2 + (Cion1 - Cion2)^2} \tag{3}$$

$$\frac{dr}{da} = \frac{|Aion1 - Aion2|}{r} \tag{4}$$

where |Aion1 – Aion2| is the absolute value of the displacement in a-axis for ion1 and ion2 and r is the distance between ion1 and ion2. The expressions for the component of forces in the b and c-axes are equivalent in form. The tunnel wall is made up by alternate stacking of two different oxygen-square layers which consist of four oxygen atoms denoted O1 at z = 0 (square-plane) and four oxygen atoms denoted O2 at z = 0.5 (cavity). The number and the positions of the basic tunnel ions are obtained from the x-ray analysis (Michiue & Watanabe, 1995a). There will be six sodium ions in the seven cavities, in other words in the 14 oxygen-square layers. This is shown in figure 2. The position of the sodium ion will depend on the position of the chromium ion.

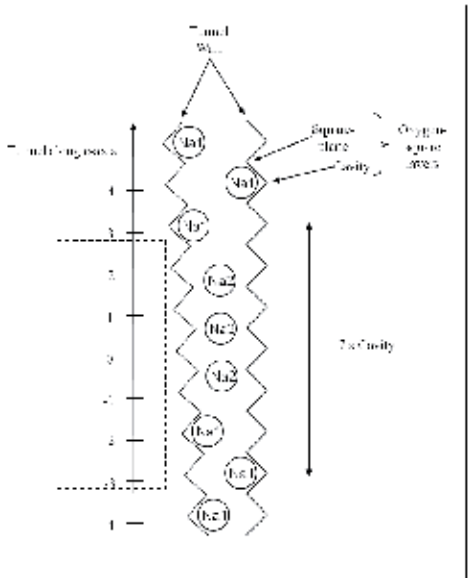

Fig. 2. Schematic representation of a probable local arrangement for sodium ions in the tunnel of $Na_xCr_xTi_{8-x}O_{16}$. In the 7 x Cavity (indicated by the rectangular box), there are six sodium ions.

From figure 2, it is clearly shown that there are three possible equilibrium positions for the sodium ions, Na1 (0.72,0.14,0.5), Na2 (0,0,0.2) and Na3 (0,0,0) (Michiue & Watanabe, 1995a). The three positions are very close to each other and therefore it is impossible for Na ions to occupy these positions simultaneously. The positions for the sodium ion are dependent on the position of the chromium ion. When a titanium ion in the square-plane is substituted by a chromium ion, a sodium ion (either Na2 or Na3) will be placed in the hollandite model as shown in the figure 3. The site of the chromium ion is chosen randomly from the titanium ions in the four corners, A, B, C or D. The Na2 and Na3 differ slightly in their position along the c-axis. The atomic parameters for Na2 and Na3 in c-axis or z-axis shown in figure 3 are 0.2 and 0 respectively. When a titanium ion in the cavity is substituted by a chromium ion, there will be four possible positions for the sodium ion (Na1). The chromium ion is chosen randomly from the titanium ions in the four corners, A, B, C or D. The sodium ion preferentially resides at an interstitial site within the same unit cell that contains a chromium ion (Michiue & Watanabe, 1996) shown by the arrow in figure 3. In this work, 24 sodium ions have been considered. Therefore, four sets of the six sodium ions shown in figure 2 are stacked up together to form a

longer tunnel. C++ is used as a tool to carry out the molecular dynamics simulation, to perform the complicated calculations and to store the required results in the specified text files. A total of five C++ programs have been written and the flow chart is shown in figure 4. Details of the calculations can be found in reference (Khoo, 2003).

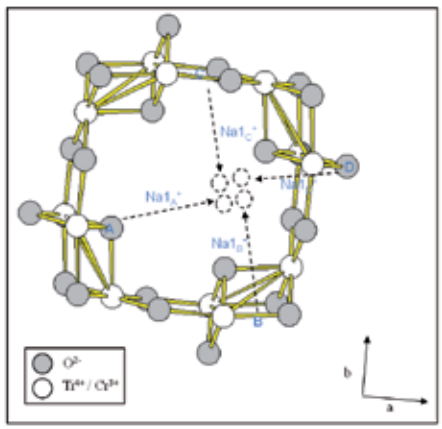

Fig. 3. Hollandite model projected slightly off the c-axis to give a clearer view of the 3-dimensional structure. When Ti_A^{4+} is replaced by Cr^{3+}, the preferable location for the $Na1_A^+$ ions is shown by the arrow, a similar situation is found for Ti_B^{4+}, Ti_A^{4+} & Ti_D^{4+} as shown by $Na1_B^+$, $Na1_C^+$ and $Na1_D^+$.

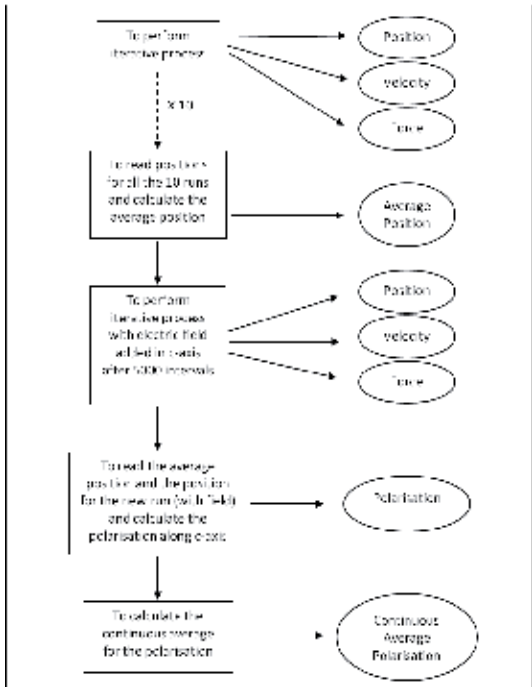

Fig. 4. Flow chart showing the five program codes written to perform the MD simulation, to carry out the complicated calculations and to generate the data required in text files.

3. Results

3.1 Position of sodium ions in c-axis without applied field

After ten runs have been carried out with different initial velocities for the individual sodium ions with their average value being set by the defined temperature, the average positions for each of the sodium ions in the c-axis are then calculated. Figure 5a shows the average position for the first six sodium ions along the c-axis with the initial conditions of 273K, 100000 intervals and time step=10^{-15}s. This gives a good comparison of the positions of the sodium ions throughout the 100000 intervals. The sodium ions only vibrate in their equilibrium positions depending upon where their equilibrium positions were. For example, the sixth sodium ion (pink) only vibrates around the cavity it belongs to.

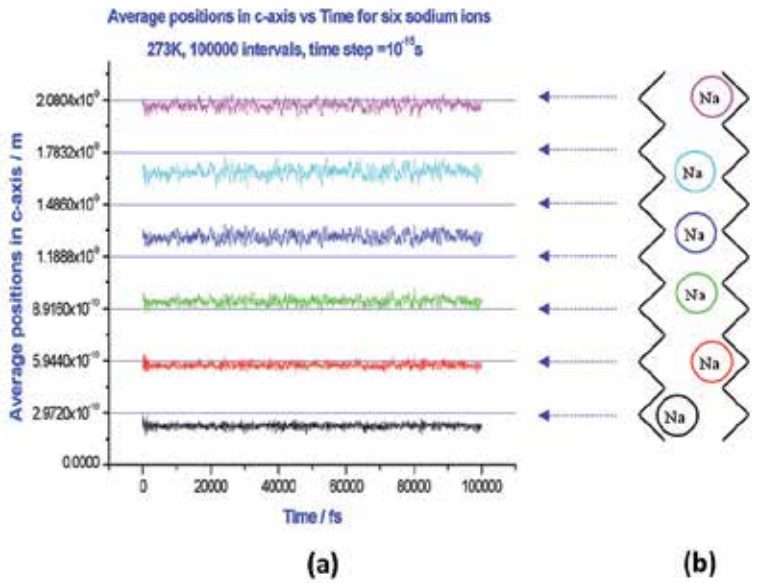

Fig. 5. (a) The average position along the c-axis for the first six sodium ions (b) The arrangement for the first six sodium ions in the tunnel. The arrows show the alignment of the cavities in the tunnel and the graphs.

3.2 Position of sodium ions in c-axis with applied field

An electric field in the range of 7.43MV/m to 74.3GV/m was applied along the c-axis to the hollandite model at the 5001th time interval. The initial conditions for the results shown below were temperature=273K, time step=10^{-15}s, 100,000 intervals and electric field=743MV/m. Figure 6 shows the positions of the first six sodium ions as a function of time. Over the initial 5000 intervals, which was in the absence of the electric field, the sodium ions just vibrate around their equilibrium positions. Starting from 5001th intervals, the positions of the sodium ions change dramatically. For example, the sixth sodium ion (pink) moved to the next cavity at some points and then back to the original cavity and then to the next cavity again.

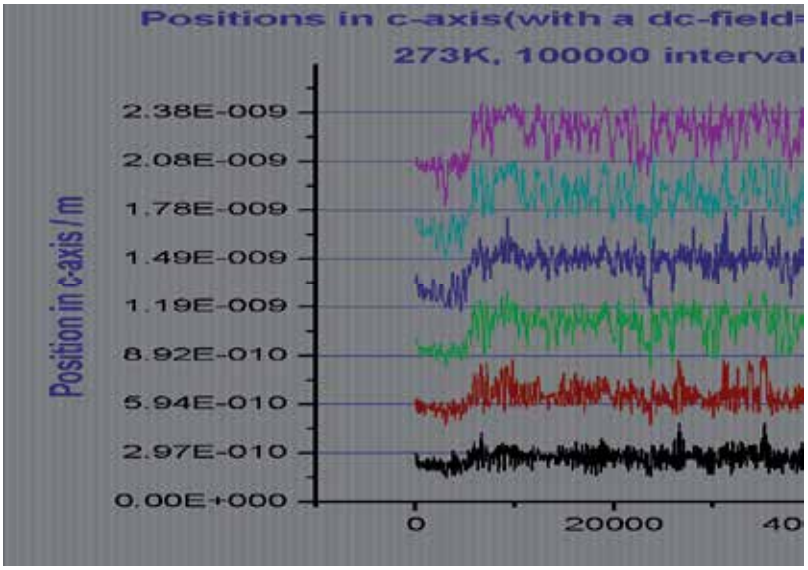

Fig. 6. Position of the first six sodium ions in c-axis when electric field of 743MV/m was applied along the c-axis to the hollandite model at 5001th time interval.

3.3 The polarisation

The polarisation along the c-axis was calculated for a range of electric fields and temperatures. Figure 7 shows the polarisation as a function of time. Over the initial 5000

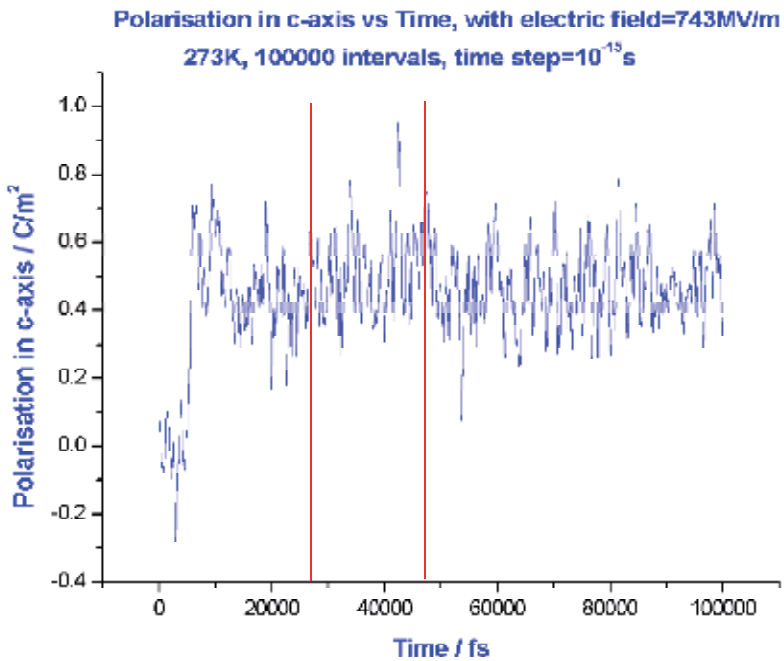

Fig. 7. The polarisation in c-axis with an applied field of 743MV/m as a function of time.

intervals, the polarisation tends to fluctuate around zero. Once the electric field is applied at 5001th interval, the polarisation increases rapidly to around 0.7 C/m² and after that sudden increase, the polarisation remains at an average of that value for the rest of the time intervals. The results under different electric field are similar, but a smaller field gives a smaller polarisation. A running average of the polarisation was taken over 100 intervals and only the results starting from 5001th intervals are taken into account. This is because the results of interest are those under the effect of electric field.

Figure 8 gives the continuous average for the polarisation as a function of time. The plot obtained was not as noisy as the polarisation plot shown in figure 7, as the running average over 100 intervals eliminates vibration periods at 10^{-13} s and shorter.

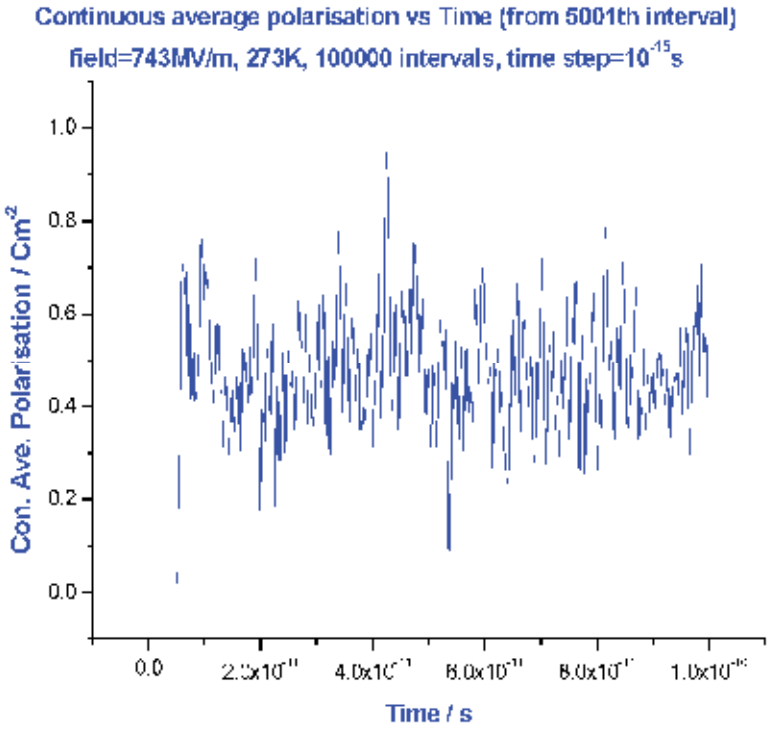

Fig. 8. Continuous average for the polarisation with an applied field of 743MV/m as a function of time.

3.4 Fast Fourier Transform (FFT) – Susceptibility

The Fast Fourier Transform (FFT) is performed in order to calculate the behaviour of the hollandite model in the frequency domain. The continuous average of the polarisation is imported to "Origin" program. A graph of polarisation versus time is plotted. Only the data between the 5001th and 100000th gives the polarisation since the electric field is switched on at the 5000th interval. The time derivative of the polarisation is then obtained via the program, and is plotted. The one-sided Fourier Transform of $(dP/dt)/Ee_0$ gives the frequency dependent dielectric susceptibility for comparison with experiment. The easier way to carry out the FFT in "Origin" software is by performing FFT on the dP/dt, the

results obtained are then divided by electric field, E and permittivity of free space, ε_0 to give the real and imaginary parts of the susceptibility. The FFT mathematical description is shown as follows:

$$X[k] = \sum_{n=0}^{N-1} x[n] \exp(-i2\pi F_k n) \tag{5}$$

with $F_k = k / N$, where FFT transforms x[n] into X[k]. The input data set is x[n] with index n in the range $0 \le n \le N-1$. It is easy to convert the index into "time" $t = n\tau$, where τ is the (time) interval, and $F_k = k / N$ into "frequency" $f_k = k / N\tau$.

Curve fitting is important, as it will give the best curve fit to the graph obtained. Firstly, the Real and Imaginary part of the susceptibility (the results generated by the FFT from the previous section) are plotted against frequency in two different graphs. This is to ease the fitting procedure as the two graphs are of different shape hence two different fitting functions are defined. If the results exhibit relaxation behaviour, then we would expect the loss peak to be characterised by power law frequency dependencies above and below the peak frequency.

If the results show a resonance character then we have to fit them to an appropriate expression. Two types of expressions are commonly used.

1. A Gaussian absorption function. This relates to a superposition of oscillator resonances with each oscillator vibrating independently of one another at a specific frequency, with the probability of a given frequency being defined by the Gaussian function. In our case the vibrations are those of the sodium ions, and these are not independent of one another, so the Gaussian form should not apply.
2. A Lorentzian function. This relates to an oscillator whose oscillations are damped by interaction with its surroundings. In our case we can think of a chosen sodium ion oscillator as being damped by its interaction with the other sodium ions. So the function may approximate to our situation. However, the other sodium ions also contribute to the response via group motions, so the Lorentzian is at the best an approximation to our hollandite model. Nonetheless the Lorentzian will be fitted to the data to see how good an approximation it is, and to determine in what respect it fails.

The real part of the susceptibility given in term of x (frequency) and w (damping factor) is shown in equation 6:

$$y = \frac{4A}{\pi} \frac{x_c - x}{4(x_c - x)^2 + w^2} \tag{6}$$

The imaginary part of the susceptibility given in term of x and w is shown in equation 7:

$$y = \frac{2A}{\pi} \frac{w}{4(x_c - x)^2 + w^2} \tag{7}$$

x_c, w and A are the parameters used for the resonant frequency, full width at ½ maximum and amplitude factor respectively.

The real part of the susceptibility, $\chi'(f)$ and the imaginary part of the susceptibility, $\chi''(f)$ were then obtained by dividing the results generated from the FFT by the applied field and

permittivity of free space. The χ' (f) and χ''(f), obtained from the FFT, are plotted as a function of frequency (f) as shown in figure 9.

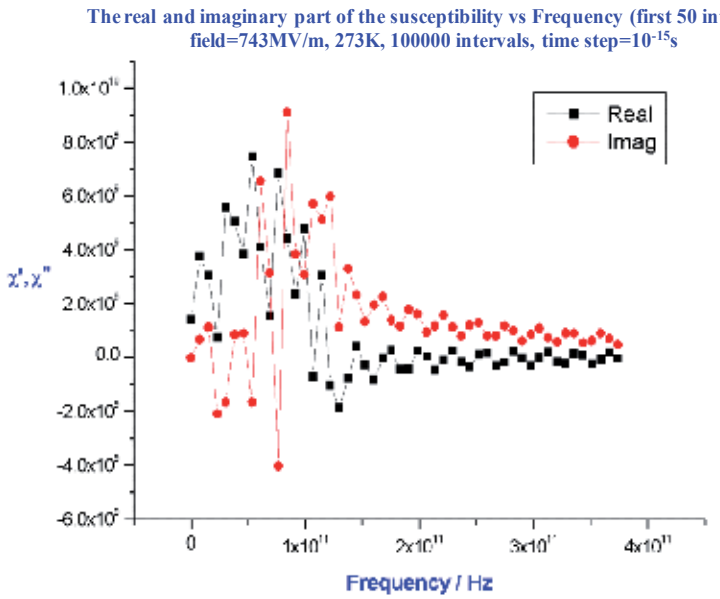

Fig. 9. The real and imaginary parts of the susceptibility as a function of frequency with an electric field of 743MV/m.

The simulation was run for 100ps (100000 x 10^{-15}s), which correspond to 10^{10} Hz. The susceptibility at frequencies below $4x10^{10}$Hz is unreliable as it relates to FFT extrapolations to regions, which are not consistent with the largest time (10^{-10}s) reached by the computation. At the higher frequency range, the smoothing process has removed the frequency higher than $2x10^{11}$ Hz; hence, frequency higher than $2x10^{11}$ Hz is similarly unreliable. Figure 9 shows χ'(f) and χ''(f) as a function of frequency. χ'(f) goes to a positive value, then drops to a negative value and then starts to fluctuate around a smaller negative value. χ''(f) shows a peak at about $1x10^{11}$ Hz and the frequency of the peak lies about half way along the slope of the χ'(f). From the overall non-monotonic behaviour of χ'(f), it is clear that the response is not that of a dielectric relaxation; hence the curve fitting to the Lorenzian function which is the resonance response would have to be carried out.

3.5 Depolarisation

An electric field was applied to the hollandite model at the start of the simulation for 5000 intervals. Then the field was switched off at 5001th interval. The depolarisation, continuous average for the depolarisation, FFT and curve fitting were obtained similarly to the procedures outlined above. Depolarisation was carried out with initial conditions of temperature=297K, time step=10^{-15}s, 100000 intervals and electric field=7.43GV/m. The results of the curve fitting to equations 6 and 7 for χ'(f) and χ''(f) (obtained from the depolarisation) respectively as a function of frequency are shown in the figure 10 and 11 below.

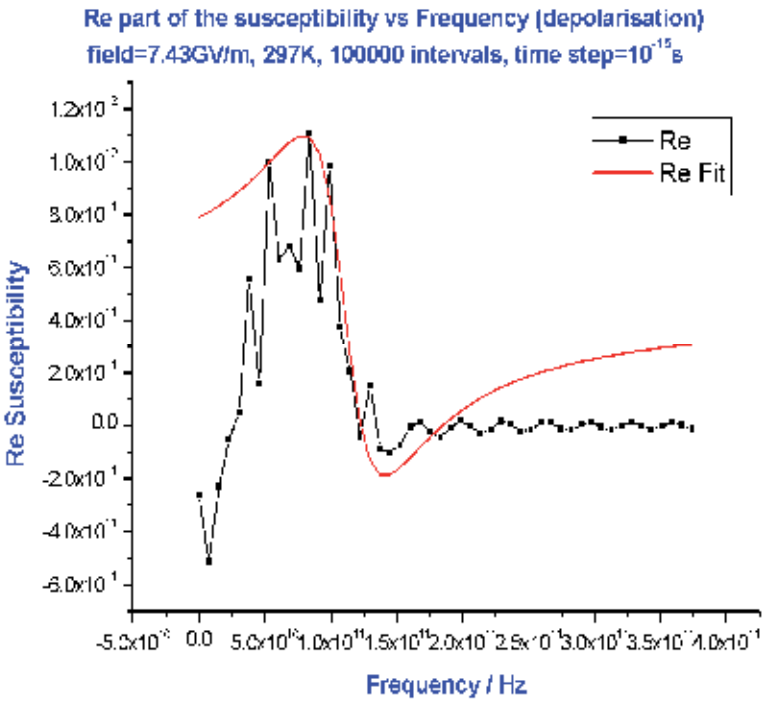

Fig. 10. The $\chi'(f)$ plot with the best fitting curve (red) to equation 6 as a function of frequency.

From figure 10, it is clearly shown that the equation 6 does not fit well to $\chi'(f)$ at all. For a resonance response, the magnitude for the lower frequency range should not be lower than the magnitude in the higher frequency range. Figure 11 shows that the equation 7 does not fit well with the simulation values of $\chi''(f)$ either. The fitted curve fits nicely in the higher frequency range but in the lower frequency range, the gradient of $\chi''(f)$ is much bigger than the fitting curve. It seems that the hollandite model had not reached an equilibrium state when the electric field was taken off. From the figure 12, the $\chi'(f)$ and the $\chi''(f)$ for the polarisation and the depolarisation were different although they should be identical for a linear response. Both the magnitude of the $\chi'(f)$ and $\chi''(f)$ for the depolarisation are bigger than the $\chi'(f)$ and $\chi''(f)$ of the polarisation. The resonance frequency of $\chi''(f)$ for the polarisation is lower compared to the resonance frequency of $\chi''(f)$ for the depolarisation.

3.6 Results obtained at the temperatures of 200K to 373K and with electric fields between 7.43MV/m and 74.3GV/m

The simulation has also been carried out with initial conditions of temperature between 200K and 373K, which were 200K, 250K, 273K, 297K and 373K. At each temperature, six different electric fields were investigated between 7.43MV/m and 74.3GV/m, which were 7.43MV/m, 74.3MV/m, 371.5MV/m, 743MV/m, 7.43GV/m and 74.3GV/m. On each of the results the procedures described in section 3.4 were carried out for the data analysis. The

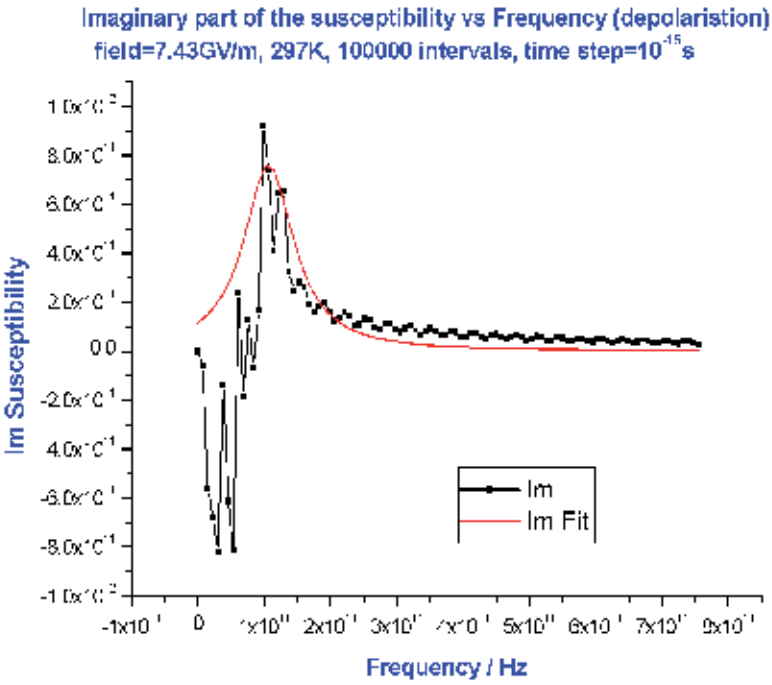

Fig. 11. The $\chi''(f)$ plot with the best curve fitting (red) to equation 7 as a function of frequency.

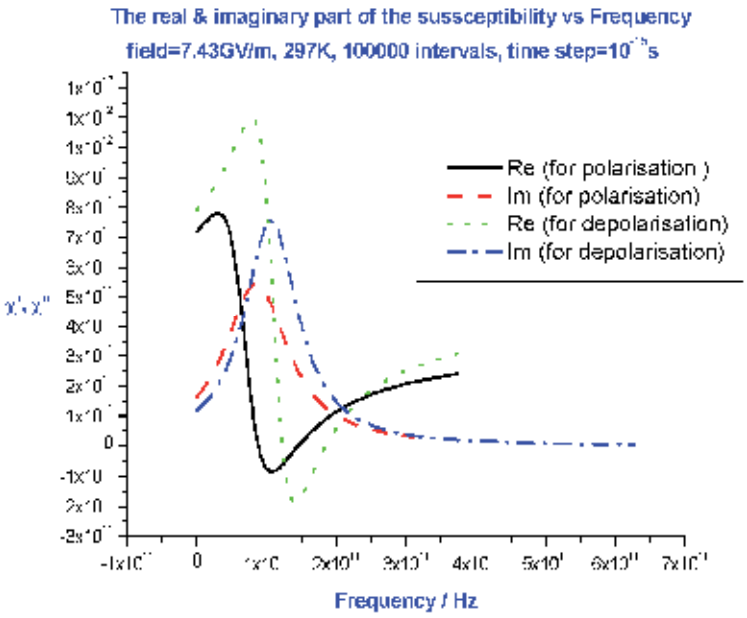

Fig. 12. The results of the curve fitting to equation 6 and 7 for both the $\chi'(f)$ and the $\chi''(f)$ of polarisation and the depolarisation respectively with an electric field of 7.43GV/m.

real part of the susceptibility does not fit well with equation 6. Hence, only the values for the parameters used (x_c, w, A_0) for the imaginary parts of the susceptibility are shown in table 1.

For all five temperatures (200K to 373K), the imaginary parts of the susceptibility (fitted to equation 7) for the electric field in the range of 7.43MV/m to 7.43GV/m show an absorption peak. The magnitude of the absorption peak differs with temperature and electric field. At an electric field of 74.3GV/m the polarisation was found to oscillate between two values. The time period can be determined from the polarisation plot. An example of the polarisation plot at 200 K is given in figure 13 which is just a part of the polarisation plot (5500^{th}-5530^{th} intervals) with initial conditions of 200K, 74.3GV/m and time step=10^{-15}s. The polarisation plot of 100000 intervals is the replication of the plot shown above. There are two and a half oscillations highlighted between the two red lines in the figure and the period of the oscillation is $4x10^{-15}$s. The time step for the simulation is 10^{-15}s, and the period of the oscillation is four times the time step. Therefore, at high electric field, all the sodium ions were driven by this force field to move as a group and they show a single frequency vibration caused by reflections from the tunnel boundaries according to the input boundary conditions.

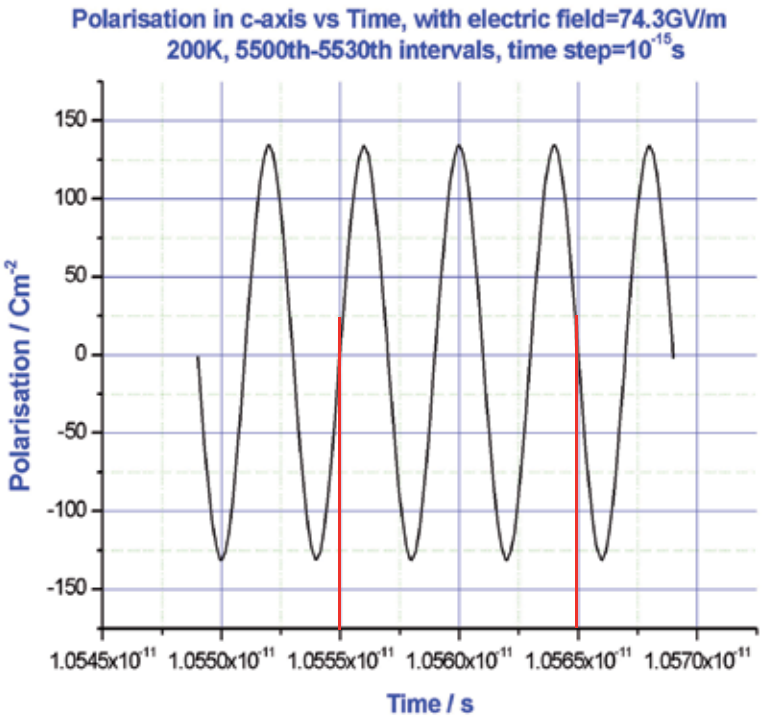

Fig. 13. The polarisation in c-axis (5500^{th}-5530^{th} intervals) with an applied field of 74.3GV/m and at temperature=200K.

Temperature	*Field*	x_c/*Hz*	*w*	*A*
200K	7.43MV/m	4.9725×10^{10}	9.5740×10^{10}	1.2542×10^{25}
	74.3MV/m	7.6060×10^{10}	7.6709×10^{10}	1.4691×10^{24}
	371.5MV/m	8.2752×10^{10}	8.1569×10^{10}	3.1800×10^{23}
	743MV/m	6.0352×10^{10}	1.4819×10^{11}	3.0551×10^{23}
	7.43GV/m	6.8566×10^{10}	1.6000×10^{11}	1.6091×10^{23}
	74.3GV/m	X	X	X
250K	7.43MV/m	6.8981×10^{10}	6.0862×10^{10}	1.5521×10^{25}
	74.3MV/m	7.7697×10^{10}	4.5186×10^{10}	1.5553×10^{24}
	371.5MV/m	7.2492×10^{10}	1.2669×10^{11}	5.1734×10^{23}
	743MV/m	9.0780×10^{10}	1.3829×10^{11}	3.1967×10^{23}
	7.43GV/m	6.2830×10^{10}	2.6115×10^{11}	2.2998×10^{23}
	74.3GV/m	X	X	X
273K	7.43MV/m	8.0000×10^{10}	8.5186×10^{10}	1.0223×10^{25}
	74.3MV/m	6.8439×10^{10}	5.0805×10^{10}	8.7585×10^{23}
	371.5MV/m	2.6842×10^{10}	1.5083×10^{11}	5.9509×10^{23}
	743MV/m	8.6971×10^{10}	7.0597×10^{10}	1.5142×10^{23}
	7.43GV/m	7.7340×10^{10}	1.1147×10^{11}	1.3679×10^{23}
	74.3GV/m	X	X	X
297K	7.43MV/m	4.9078×10^{10}	6.2072×10^{10}	7.0296×10^{24}
	74.3MV/m	8.3584×10^{10}	8.0137×10^{10}	1.7449×10^{24}
	371.5MV/m	4.4657×10^{10}	1.0050×10^{11}	4.5638×10^{23}
	743MV/m	8.8021×10^{10}	8.5461×10^{10}	1.3662×10^{23}
	7.43GV/m	7.8825×10^{10}	1.2695×10^{11}	1.2511×10^{23}
	74.3GV/m	X	X	X
373K	7.43MV/m	3.1715×10^{10}	2.0310×10^{11}	3.7451×10^{25}
	74.3MV/m	7.5239×10^{10}	8.1134×10^{10}	1.9478×10^{24}
	371.5MV/m	6.5725×10^{10}	9.5740×10^{10}	5.4199×10^{23}
	743MV/m	7.9450×10^{10}	1.3905×10^{11}	2.8229×10^{23}
	7.43GV/m	8.2974×10^{10}	8.7608×10^{10}	1.4814×10^{23}
	74.3GV/m	X	X	X

Table 1. The values for the parameters used (x_c, w and A) for the curve fitting for the imaginary part of the susceptibility.

4. Discussion

4.1 Position and trajectories of movement for the sodium ions

Five different temperatures (200K to 373K) have been set as an initial condition but even at the highest temperature 373K, the sodium ions still have not gained enough energy to leave the equilibrium positions for the next available sites in the absence of an electric field. A comparison of the average position for the first and second sodium ions at 200K and 373K is shown in the figure 14. At 373K, the sodium ions have more energy as the fluctuations are bigger compared to the average positions at 200K, but the sodium ions still do not have enough energy to go into the next available site.

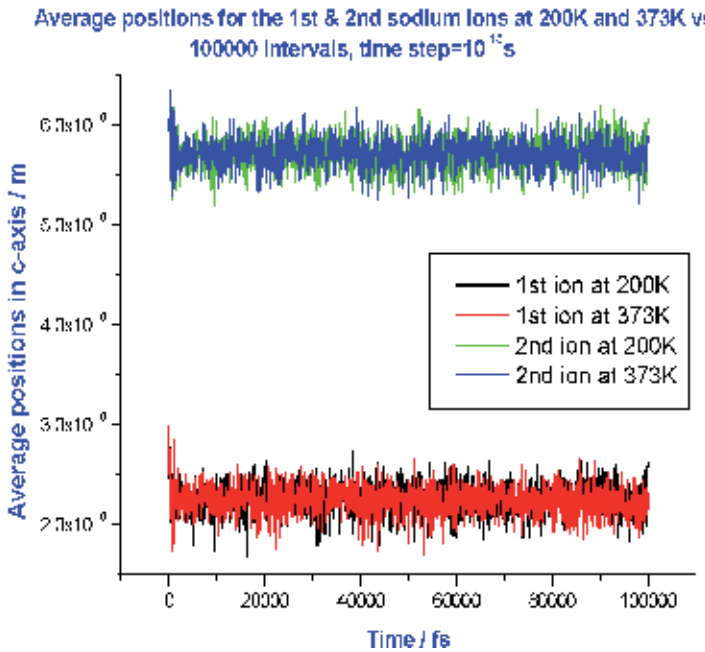

Fig. 14. A comparison of the average positions along c-axis for the first and second sodium ions at 200K and 373K as a function of time.

The next part of the research was to introduce the electric field to the hollandite model. The field was applied from 5001th interval to 100000th interval; it was clearly shown in figure 6 that the fluctuations of the sodium ions increase dramatically at 5001th interval. This is due to the extra energy obtained by the sodium ions from the applied field. In figure 6, take the sixth sodium (pink) for example; it gained enough energy from the applied field to hop into the next available site, which is the next cavity. It then vibrates in this new site for about 2000 intervals until it gained enough energy to hop back to the original cavity. This can be seen in figure 15. From the conservation of energy, in a closed system; the total energy is constant although energy may be transferred between kinetic and potential energy and from one group of sodium ions to another. In the case of the hollandite model, the energy is being swapped around between the sodium ions and this is clearly shown in the figure 16. Only three sodium ions have been shown here, the rest of the sodium ions would behave in a similar way.

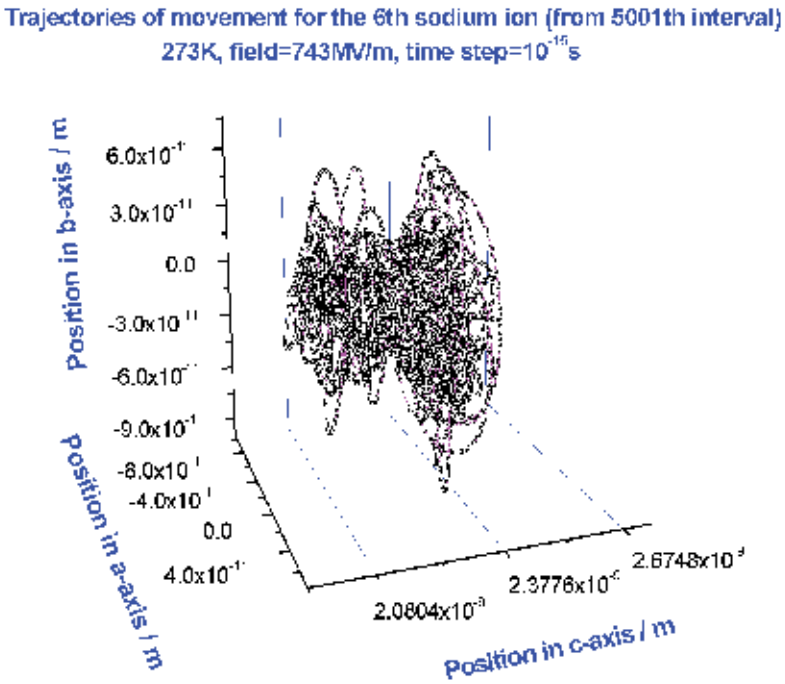

Fig. 15. Trajectories of movement in three-dimensions of the 6th sodium ion in the hollandite model with field of 743MV/m.

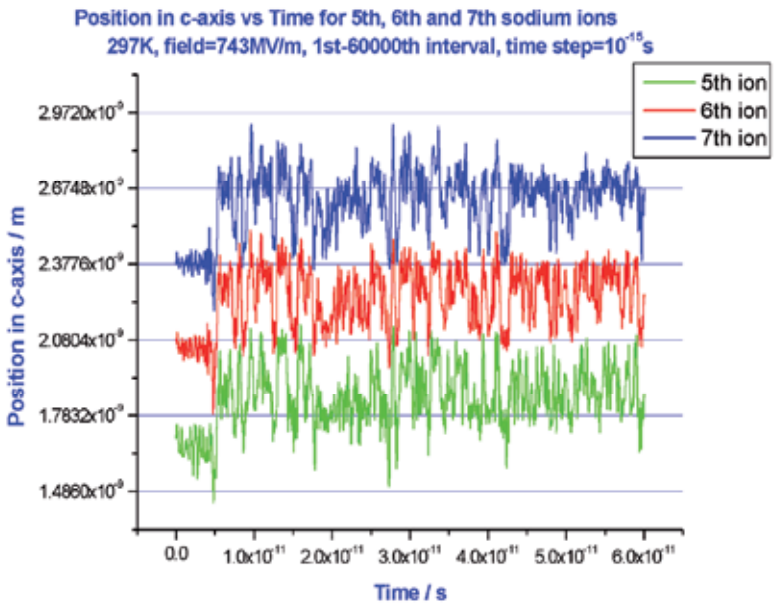

Fig. 16. A comparison of the position in c-axis for the 5th, 6th and 7th sodium ions with field of 743MV/m. The light blue line represents the position of the cavity.

Figure 17 shows that when the dc-field was applied at 5001th interval, the sixth sodium ion starts to gain energy to move into the next empty site. With the applied field of 743MV/m, the sodium ion hops into the next cavity almost as soon as the field is applied, whereas with a lower applied field which is 7.43MV/m, about 9×10^{-12} s is needed for the first hop of the sodium ion. As the electric field increases, the number of hops into the neighbouring sites increases as well.

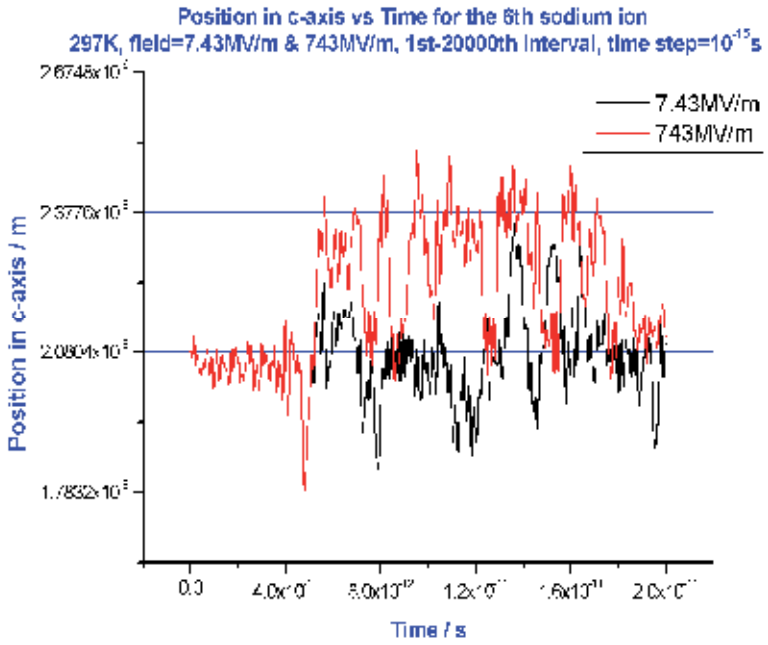

Fig. 17. A comparison of the position in c-axis for the 6th sodium ion with field of 7.43MV/m and 743MV/m. The light blue line represents the cavity.

This movement of the sodium ion is like a dipole moving around, as the sodium ion represents the positive part and the ions at the lattice site that formed the cage is the negative part. A relaxation behaviour would usually be expected to be obtained as the sodium ions hopping between equilibrium positions are like re-orienting dipoles.

4.2 Frequency dependence of χ' and χ"

Frequency dependence of χ′ and χ″ for a range of temperature and a range of field were obtained from the FFT procedure. The values for the frequency χ′(f) and χ″(f) obtained in our simulations are too high and this is because the hollandite model used (1 tunnel with 60 layers) is only a small section of the whole crystal. If a bigger model had been considered, the average displacement of the ions would be much smaller because the movement of the sodium ions are affected by the sodium ions in the other tunnels, and a smaller polarisation and smaller value of χ′(f) and χ″(f) would be obtained.

From the χ′(f) obtained (figure 9); it is clearly shown that χ′(f) is not a relaxation response as part of χ′(f) gives negative values. Hence the results obtained for χ′(f) and χ″(f) would be more

likely to relate to a resonance response. The peak frequency for $\chi''(f)$ is in the range of ($2.7x10^{10}$ – $8.8x10^{10}$ Hz). Ions hopping between equilibrium sites usually give a relaxation response, whereas in the case of hollandite model, a resonance response is obtained. What seems to be happening is that the movement of the sodium ions between sites change the vibration of the other sodium ions, so that the vibrations of each sodium ion in a group is coupled together and the hopping of one them to a new site destroys the group motion and acts like a damping effect on the resonance that is due to it, i.e. the motion of the system of dipoles behaves like a damped libration. This gives a good agreement to the prediction by Fröhlich (Fröhlich, 1958) who suggested that the absorption due to displacement of charges bound elastically to an equilibrium position is of resonance character, although in our case the ability of the sodium ions to displace from site to site adds a visco-elastic dimension to the situation.

In order to fit $\chi'(f)$ an additional resonance of amplitude y_0 can be added in equation 6. y_0 relates to the isolated higher frequency oscillations which had been removed by the smoothing process. Figure 18 below shows the real and imaginary parts of the susceptibility with a smoothing level of 2000 (that is 2000 points have been used as the number of data points considered to be smoothed at a time). It is clearly shown that adding a higher frequency resonance improves the fit to the data, and hence that oscillations in the form of additional resonance absorptions are present. The lowest resonance absorption was at the same position as in the results shown in figure 9.

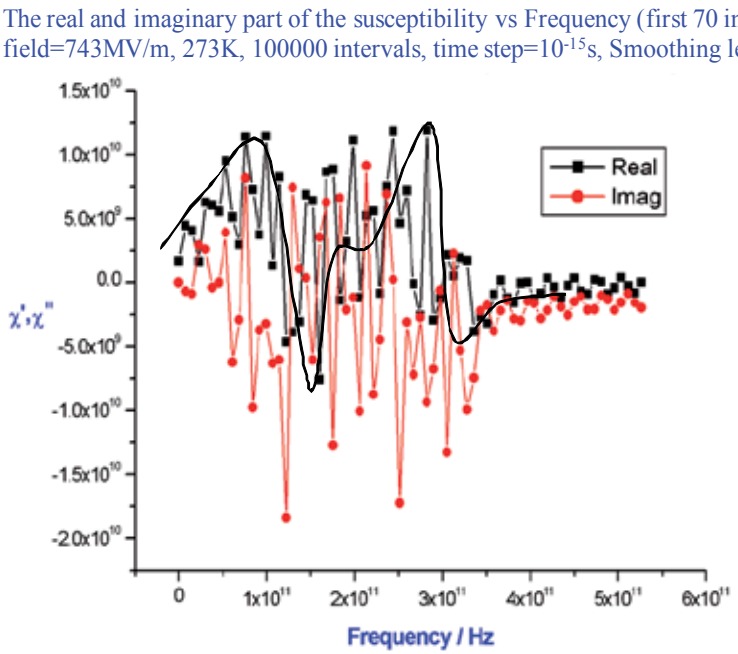

Fig. 18. The real and imaginary parts of the susceptibility as a function of frequency with an electric field of 743MV/m.

A single Lorentzian function does not fit both $\chi'(f)$ and $\chi''(f)$ well. Equation 7 does not fit $\chi''(f)$ well as it gives a symmetrical peak curve whereas $\chi''(f)$ is not symmetrical. The simulated $\chi''(f)$ data shows a steeper gradient at frequencies below the resonance absorption compared to the

fitted curve (equation 7). Similarly, equation 6 would not fit $\chi'(f)$ as equation 6 would give a symmetrical plot in magnitude where the maximum and the minimum points have the same value in magnitude but different sign. This is understandable as the Lorentzian function is generated when a single oscillator is damped by the surroundings whereas in the hollandite model the movement of the sodium ions between sites depend on the other sodium ions. The hopping of any of the sodium ions would damp the libration of the rest of the sodium ions. Hence, there is no specific frequency, which can be considered as a resonance since the number of sodium ions taking part in a group oscillation can change, with each number involved having a different group-oscillator frequency and hence different resonance frequency. However, the Lorenzian function has been used because there is no general non-linear frequency dependent expression available and we have to try to find some ways of expressing the results. As shown in figure 18 increasing the number of resonances improves the fit and hence we can expect when enough resonances have been included a good fit will be obtained within the limitations imposed by the time window of the simulation.

4.3 Temperature dependence

Simulations have been carried out for a range of electric field between 7.43MV/m and 7.43GV/m and temperatures between 200K and 373K. The absorption peak frequency, which is also the resonance frequency, and the resonance peak height, has been plotted as a function of temperature for a range of electric field in figures 19 and 20.

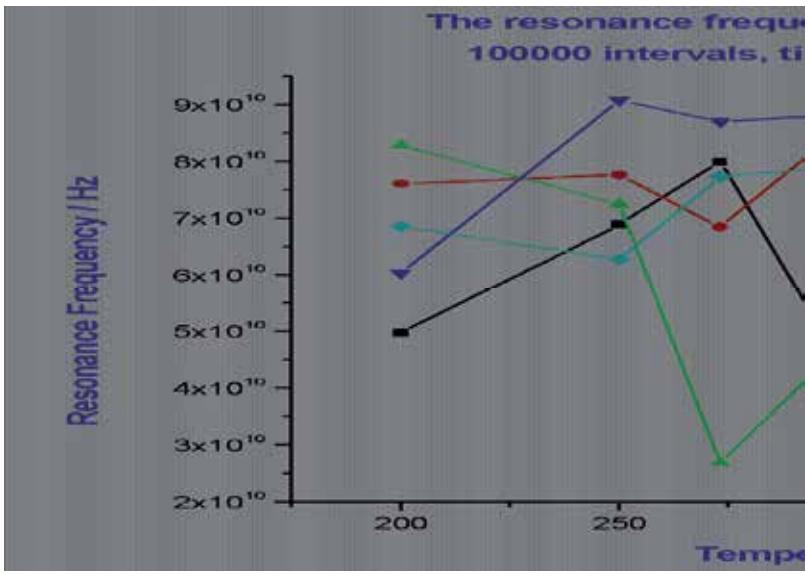

Fig. 19. The resonance frequency as a function of temperature for a range of electric field (7.43MV/m – 7.43GV/m).

From figure 19 the resonance frequency is independent of temperature for all the different electric field applied, and from figure 20 the resonance peak height does not change significantly as the temperature increases. This behaviour is not what would be expected of a dielectric relaxation but is what would be expected from the oscillatory behaviour of groups of sodium atoms whose vibrations are coupled together, where the temperature

would affect the lifetime of the group oscillation and hence the half-width of the peak but not the frequency of the group oscillation.

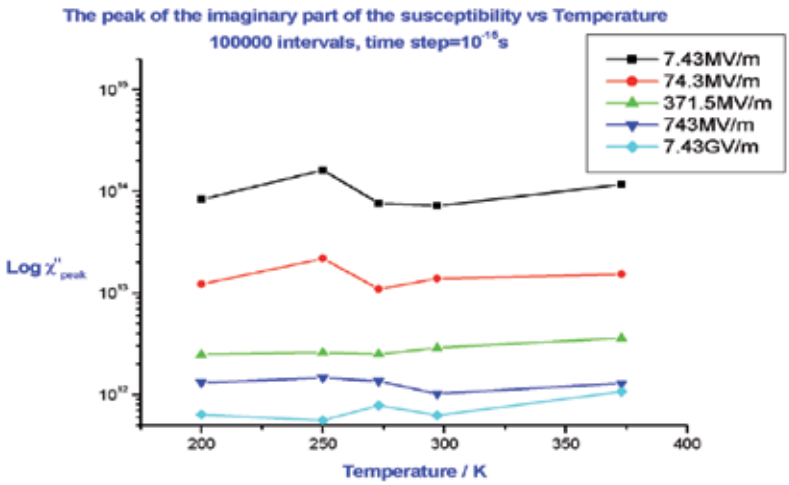

Fig. 20. The peak of the imaginary part of the susceptibility as a function of temperature for a range of electric field (7.43MV/m – 7.43GV/m).

4.4 Poley absorption

The imaginary part of the susceptibility has been plotted for a range of electric field (7.43MV/m – 7.43GV/m) at 297K as shown in figure 21 below. When the applied field gets higher, χ'' becomes smaller. This indicates that the higher the field, the less ions are involved in the group site-libration modes and more in damping (i.e. hopping between sites). The hopping of the sodium ions damp the libration of other sodium ions similar to the friction between the disc and annulus damps the libration in the Itinerant Oscillator (IO) model (Coffey et al., 1987).

This IO model does not explain the process that happens in the hollandite model well enough as the IO model is a harmonic model and does not take into account the effect of molecular translations upon the potentials and forces controlling the motion, a factor that our molecular dynamics simulation have shown to be important. The periodic potential model (Vij & Hufnagel, 1985; Praestgaard & van Kampen, 1981) is also not a good approximation for the same reason. On the other hand, the process in the hollandite model has a good agreement with the cluster model presented by Dissado and Alison (Dissado & Alison, 1993), where the cluster model takes into account the translations of the dipole. The displacements (translations) of the solute molecule was affected by the positions of its surrounding solvent molecules (solvent cage) and vice versa to bring the group (cluster) into an equilibrium configuration. This will cause the deformation of the solvent cage so that reorientations of the solute dipole will also involve reorganisation of the solvent cage deformations. A parameter n was defined such that when n=0 the solute did not deform the cage and its dipole reorientation was overdamped giving a relaxation peak with the vibrations of the solvent providing the viscous damping. When n=1 the solute and solvent formed a single cooperative system giving a Poley absorption and no relaxation peak. When

0<n<1, the solute motions were partitioned between the Poley absorption and relaxation peak. In our model the sodium ion system forms both solute (with ions able to hop to new sites) and solvent (with ions vibrating around their equilibrium sites). The surrounding lattice is held rigid and cannot be involved in the cage motions.

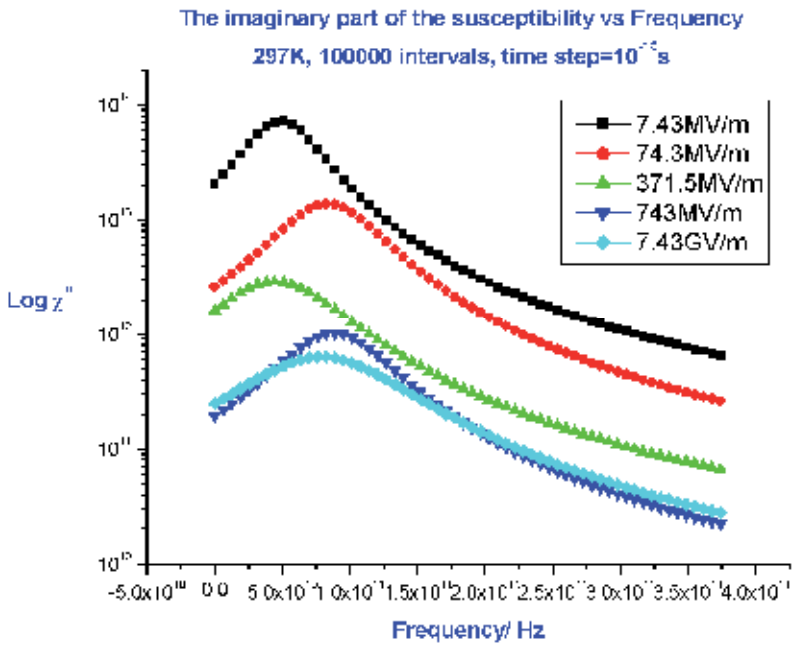

Fig. 21. The imaginary part of the susceptibility has been plotted for a range of electric field (7.43MV/m – 7.43GV/m) at 297K.

The kinetic energy of the sodium ions (defined by the temperature) would initially cause the librations of the sodium ions under the action of the forces from the ions in the fixed lattice sites. Forces from the environment (which is the other sodium ions with respect to a particular sodium ion, and the ions in the lattice sites) causes the sodium ions themselves to produce a force acting on each other, so that the displacement of each sodium ion would be adjusted according to the new equilibrium configuration at each interval, and hence translations changing the potentials occurs on top of the librations. The cluster model would suggest that since all sodium ion motions act cooperatively the parameter n≈1 and there would be a Poley peak with either a weak relaxation peak or none at all. Although the simulations have not been carried through to times longer than ~10^{-10}s, this seems to be what is happening, as the ion motions include both hopping and vibration and give just a damped resonance without any evidence of a relaxation peak.

At 297K, the resonance frequency is in the range of about $4.5x10^{10}$ – $8.8x10^{10}$ Hz for a range of electric field (7.43MV/m – 7.43GV/m). Poley (Poley, 1955) predicted that there is a significant power absorption in dipolar liquids at the ambient temperature in the 1.2 - 70 cm^{-1} ($3.6x10^{10}$ – $2.1x10^{12}$ Hz) region and Davies (Davies et al, 1969) named the broad peak as 'Poley absorption'. The absorption peaks obtained for the hollandite model lie at the lower end of Poley's prediction range. This absorption is due to the libration of the sodium

ions confined to the host structure undergoing displacement under the effect of electric field. The absorptions calculated lie below the resonance frequency of a single sodium ion, which defines the edge of the quantum region. They correspond to coupled displacements of sodium ion groups. It would be reasonable to assume that our calculated absorption corresponds to what would be the Poley absorption for this material. A similar process happens in ice clathrate materials as shown by Johari (Johari, 2002), where an absorption peak was seen in the far-infrared region ($7.5x10^{11}$ and $1.14x10^{12}$ Hz) and was contributed by the rotational oscillation of the tetrahydrofuran molecule, while confined to the cages of the ice clathrate crystal.

From figure 19, the resonance frequency is independent of temperature for all the different electric field applied. This is different from the deduction made by Johari (Johari, 2002) on the ice clathrate crystal and Nouskova et al (Novskova et al., 1986) on the model of a restricted rotator where the resonance frequency decreases with the increase in temperature due to the increase of the libration magnitude. From figure 20, the resonance peak height does not change much as the temperature increases. This is also different from the deduction made by both Johari (Johari, 2002) and Nouskova (Novskova et al., 1986). Johari reported that the resonance peak height increases with the increase in temperature whereas Nouskova said that the resonance peak height decreases with the increase in temperature. In our hollandite model, the sodium ion group motions take place in a rigid lattice unlike the experimental situation for ice clathrates. Therefore the libration amplitude of an individual sodium ion dipole is unaffected by temperature and the oscillation frequency of a specific group should not be affected unlike the situation in (Johari, 2002; Novskova et al., 1986). The resonance peak magnitude will be dependent upon the number of sodium ions taking part in a coupled group oscillation at a specific frequency and this will not be affected by temperature. The effect of temperature in our model is expected to lie in the half-width of the absorption peaks, since this is due to the hopping of sodium ions between oscillating groups.

4.5 Group oscillation at very high field

From figure 13, it is clearly shown that at high electric field, which is 74.3GV/m for the hollandite model, all the sodium ions were driven by the field to move as a group and show a single frequency vibration. The period of the oscillation is $4x10^{-15}$s. Since we use specular boundary conditions for the tunnel (i.e. the tunnel ends are reflective) this oscillation period is what would be expected if the sodium ions moved as a whole and were reflected from the boundaries after the first and third time-steps (i.e at 90 degree and 270 degree phases in the cycle). In the case of a smaller field, the sodium ion would just hop between empty sites next to the original site where it belongs. At bigger fields the sodium ions would have enough energy to move to the empty sites located furthest away. Figure 22 shows an example of three sodium ions in a tunnel. When the applied field is small, the sodium ions will hop between the available empty sites next to them. The only available site for Ion1 is the one on its right, whereas Ion2 and Ion3 will have two available sites to go to and this depends on the direction of the force acting on that particular sodium ion at that moment. As shown in Figure 21 increasing the field reduces the number of sodium ions taking part in coupled local group site-motions (reduced peak amplitude) in favour of sodium ion hopping between sites. For this reason a trend towards higher resonance frequencies and broader

peaks (i.e. higher damping) can be expected. When the applied field is high enough all the sodium ions will take part in hopping between sites, and the field will force all the sodium ions to move to the furthest available sites as shown in figure 22c. The reflective boundary condition at the two ends of the tunnel cause the sodium ions to vibrate between the two ends and this coherent group oscillation was generated. It can be speculated that this behaviour corresponds to a flow of sodium ions (i.e. a sodium ion dc current) when the boundaries regenerate the sodium ion concentration as would an ion exchange membrane.

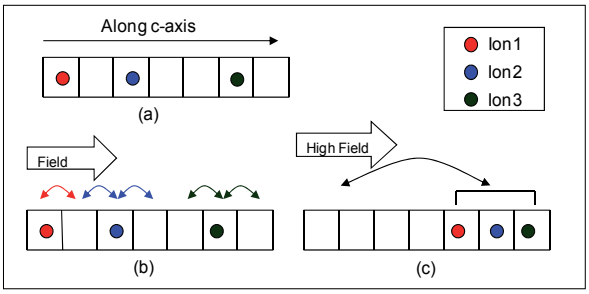

Fig. 22. The position of three sodium ions along c-axis (a) without electric field (b) with low electric field (c) with high electric field. The square denotes the available sites for the sodium ions to move to.

The oscillatory motion is of frequency 2.5x10^{14} Hz and this falls into the infrared frequency region. With a longer tunnel, a higher electric field would be needed to give a coherent group oscillation, as higher force is required to push all the sodium ions to the furthest distance. When all the sodium ions move to one end of the tunnel under the high field, it is just like ALL the dipoles being forced to align in one direction by the electric field, i.e. it is a state of motion that cannot exist without the presence of the field and is thus a non-linear response.

The motion of a group of charges as a whole in the Coulomb field of their counter charges defines a plasma oscillation, and it has a natural frequency that would apply for the sodium ions in an infinitely long tunnel. This plasma oscillation frequency is given in equation 8 below (Ziman, 1960),

$$\omega_p = 2\pi f_p = \sqrt{\frac{ne^2}{m_{Na}\varepsilon_0}} \tag{8}$$

where m_{Na} is the mass for the sodium ion, which is 3.81361x10^{-26} kg, e is the electron charge, ε_0 is the permittivity of free space and n is the concentration of sodium ions (number of sodium ions in a volume of 1m^3). The plasma oscillation frequency that we could expect for our Hollandite model in the absence of the reflective boundaries can be obtained by calculating n as follows: The Hollandite model consists of 60 layers with 24 sodium ions, the volume 1.54475x10^{-27} m^3 is the volume for the 24 sodium ions (Khoo, 2003). The average *volume* for one sodium ion is:

$$volume = \frac{1.54475 \times 10^{-27}}{24} = 6.4365 \times 10^{-29}\ m^3 \tag{9}$$

and n becomes

$$n = 1 / volume = 1.5536 \times 10^{28}\ m^{-3} \tag{10}$$

Substituting equations 9 and 10 into equation 8, the obtained f_p is 5.469x10^{12} Hz. This value is the upper limit for the group oscillations that our simulations show occur in the Hollandite system. The estimated plasma frequency is much lower than the high-field group oscillation frequency (~1/46), but is ten times higher than the frequency of the χ''_{peak} calculated for lower field. This is consistent with an interpretation of the simulations at low fields in which local site vibrations of the sodium ions (equivalent to dipole librations) are coupled together but cannot extend to all the sodium atoms because hopping of an ion between sites destroys the coupled motion, thus giving oscillation frequencies below the plasma oscillation limit. High fields produce a field driven coupled hopping that oscillates the ions between the reflective boundaries at higher frequencies than the plasma oscillation frequency.

5. Conclusions

We have presented a detailed description of the molecular dynamics computational methods applied to the fast-ion conductor Hollandite together with the fundamental concepts needed for interpreting our results. This study focused on the calculation of the sodium ion positions at a range of temperature and electric fields and the resulting frequency dependence of the conductivity mechanism and susceptibility. In the simulation the lattice surrounding the tunnel was held rigid and only the sodium ions in the tunnel were allowed to move. The ac dielectric response was calculated from the rate of change of polarisation, dP/dt, under the action of a dc step-field (i.e. dielectric response function) of 7.43MV/m to 74.3GV/m, at temperatures between 200K and 373K. Our hollandite model shows that the dielectric response due to the motion of the sodium ions in the tunnels behaves approximately like that of polar liquids in the far-infrared frequency region. The susceptibility shows an absorption peak $\chi''(f)_{peak}$ in the frequency region between 4.5x10^{10} and 8.8x10^{10} Hz at 297K. This fitted very well with Poley's prediction of an absorption typically observed in polar liquids in the 1.2 - 70 cm^{-1} (3.6x10^{10} – 2.1x10^{12} Hz) region at room temperature. The frequency dependence of the real and imaginary susceptibility components χ' and χ'' obtained show resonance behaviour. This is due to the vibration of sodium ions coupled together in groups in which the motion of each sodium ion is centred around a local site. This mode of motion is equivalent to the coupled libration of a group of dipoles. Transfer of a sodium ion between sites destroys the coupling for any particular group and acts as a damping on the resonance behaviour associated with its group oscillation. This is in agreement with the prediction by Fröhlich who suggested that the absorption due to displacement of charges bound elastically to an equilibrium position is of resonance character. The absorption peaks in χ'' at the resonance frequency lie between 4.5x10^{10} and 8.8x10^{10} Hz at 297K which matches very well with the Poley absorption which is typically observed in polar liquids in the 1.2 - 70 cm^{-1} (3.6x10^{10} – 2.1x10^{12} Hz) region at room temperature. The resonance frequency and the resonance peak height are independent of temperature. The absorption peak was associated with cooperative motions of the sodium ions

as suggested by the cluster model. The itinerant oscillator model does not allow for such many-body motions. On increasing the applied field χ'' becomes smaller and, more switches of sodium ions between sites are obtained. This indicates that the higher the field, the fewer ions are involved in coupled libration motions and more in damping through hopping between sites. At very high field, which is 74.3GV/m in our simulation, all the sodium ions were driven by the field to move as a group i.e. to transfer collectively from site to site giving a single frequency vibration due to our reflective boundary conditions.

6. References

Byström, A. & Byström, A.M. (1950). The Crystal of Hollandite, the Related Manganese Oxide Minerals, and αMnO_2. *Acta Crystallographica,* Vol.3, pp. 146-154

Chantry, G.W. (1977). Dielectric Measurements in the Submillimeter Region and a Suggested Interpretation of the Poley Absorption. *IEEE Transactions on Microwave Theory and Technique,* Vol.MTT-25, No.6, pp. 496-501

Cheary, R.W. & Dryden, J.S. (1991). Dielectric Relaxation in Hollandite and Rutile. *Philosophical Magazine B,* Vol.64, pp. 709-722

Coffey, W.T.; Corcoran, P.M. & Evans, M.W. (1987). On the Role of Inertial Effects and Dipole-Dipole Coupling in the Theory of the Debye and Far-Infrared Absorption of Polar Fluids. *Proceedings of Royal Society,* Vol.A410, pp. 61-88

Davies, M.; Hill, N.E.; Vaughan, W.E. & Price, A.H. (1969). *Dielectric Properties and Molecular Behaviour,* van Nostrand and Reinhold, London, UK, pp 306

Dissado, L.A. & Alison, J.M. (1993). The Relationship Between the Poley Absorption and Fractional Power Law Relaxation in the Cluster Model. *Journal of Molecular Liquids,* Vol.56, pp. 295-316

Dissado, L.A. & Hill, R.M. (1983). A cluster approach to the structure of imperfect materials and their relaxation spectroscopy. *Proceedings of The Royal Society of London*, Vol. A390, pp131-180

Dissado, L.A. & Khoo, K.L. (2006). The Nature of Terahertz Motions in a One-Dimensional Disordered Structure. *J. Phys. D: Appl. Phys.,* Vol.39, pp. 3882-87

Dixon, M. & Gillan, M.J. (1982). *Computer Simulation in Solids,* Vol.166, pp. 275, Springer-Verlag, Berlin, Germany

Dryden, J.S. & Wadsley, A.D. (1958). The Structure and Dielectric Properties of Compounds with the Formula $Ba_x(Ti_{8-x}Mg_x)O_{16}$. *Transaction Faraday Soc.,* Vol.54, 1574-1580

Fröhlich, H. (1958). *Theory of Dielectrics,* (2^{nd} edition), pp. 131, Clarendon Press, Oxford, UK

Haile, J.M. (1992). *Molecular Dynamics Simulation, Elementary Methods,* John Wiley & Son Inc., Canada

Johari, G.P. (2002). Molecular Inertial Effects in Liquids: Poley Absorption, Collision-Induced Absorption, Low Frequency Raman Spectrum and Boson Peaks. *Journal of Non-Crystalline Solids,* Vol.307-310, pp. 114-127

Jonscher, A.K. (1983). *Dielectric Relaxation in Solids,* Chelsea Dielectric Press Ltd, London, UK

Karpus, M. & Petsko, G.A. (1990). Molecular Dynamics Simulations in Biology. *Nature,* Vol.347, pp. 631-639

Khoo, K.L. (December 2003). *The Construction of Molecular Dynamics Model for the Response of $Na_xCr_xTi_{8-x}O_{16}$ (x=1.7) to Electric Fields of up to 100ps Duration,* PhD Thesis, Department of Engineering, University of Leicester

Khoo, K.L.; Dissado, L.A.; Fothergill, J.C. & Youngs, I.J. (2004). Molecular Dynamics Simulation of High Frequency (10^{10} to 10^{12} Hz) Dielectric Absorption in the Hollandite $Na_x(Ti_{8-x}Cr_x)O_{16}$, *International Conference on Solid Dielectrics,* pp. 550-553, Toulouse, France, July 5-9, 2004

Khoo, K.L.; Dissado, L.A. & Fothergill, J.C. (2007). Molecular Dynamics Simulation on Hollandite $Na_x(Ti_{8-x}Cr_x)O_{16}$: Dependence of DC Conductivity upon Temperature and Concentration, *International Conference on Solid Dielectrics,* pp. 47-50, Winchester, UK, July 8-13, 2007

LMGP-Suite Suite of Programs for the interpretation of X-ray Experiments, by Jean Laugier and Bernard Bochu, ENSP/Laboratoire des Matériaux et du Génie Physique, BP 46. 38042 Saint Martin d'Hères, France, http://www.inpg.fr/LMGP and http://www.ccp14.ac.uk/tutorial/lmgp/

Michiue, Y. & Watanabe, M. (1995a). X-ray Analysis of Sodium Ion Distribution in the One-Dimensional Tunnel of Priderite. *Solid State Ionics,* Vol.79, pp. 116-119

Michiue, Y. & Watanabe, M. (1995b). $Na_x(Ti_{8-x}Cr_x)O_{16}$, Priderite with Sodium Ions in the Tunnel-Structural Study for Stability and Na Ion Transport. *Journal of Solid State,* Vol.116, pp. 296-299

Michiue, Y. & Watanabe, M. (1996). Molecular Dynamics Simulation of Sodium Ions in One-Dimensional Tunnel Structure of Hollandite-Type. *Journal Physics Chemistry Solids,* Vol.57, pp. 547-551

Michiue, Y. & Watanabe, M. (1999). Atomistic Simulation Study of K-Hollandite: Ionic and Dynamics of the Linearly Disordered Solid. *Physical Review B,* Vol.59, No.17, pp. 11298-11302

Novskova, T.A.; Kukebaev, A.M. & Gaiduk, V.I. (1986). One Parameter Model of Dielectric Relaxation in Polar Liquids. *Institute of Radio Engineering and Electronics,* Academy of Sciences of USSR, Vol.29, No.1, pp. 41-54

Poley, J.Ph. (1955). Microwave Dispersion of some Polar liquids. *Journal Applied. Science,* Vol.4, pp. 337-387

Praestgaard, E. & van Kampen, N.G. (1981). A Model for Rotational Relaxation and Resonance. *Molecular Physics,* Vol.43, pp. 33-45

Singer, J.; Kautz, H.E.; Fielder, W.L. & Fordyce, J.S. (1973). *Fast Ion Transport in Solids,* pp. 653-663, Amsterdam, Holland

Vij, J.K. & Hufnagel, F. (1985). Advances in Microwave and Submillimeter Wave Dielectric Spectroscopic Techniques and their Application, in *Advances in Chemical Physics: Dynamical Processes in Condensed Matter,* Evans, M.W. (Ed.), Vol.LXIII, pp. 775-837, J. Wiley and Sons, NY

West, A.R. (1988). *Basic Solid State Chemistry,* Wiley, Chichester, UK

Yoshikado, A.; Ohachi, T.; Taniguchi, I.; Onoda, Y.; Watanabe, M. & Fujiki, Y. (1982). AC Ionic Conductivity of Hollandite Type Compounds from 100 Hz to 37.0 GHz. *Solid State Ionics,* Vol.7, pp. 335-344

Ziman, J.M. (1960). *Electron and Phonons. The theory of Transport Phenomena in Solids,* pp. 161-162, Clarendon Press, Oxford, UK

19

MD Simulation of the Ion Solvation in Methanol-Water Mixtures

Ewa Hawlicka and Marcin Rybicki
Institute of Applied Radiation Chemistry, Technical University of Lodz
Poland

1. Introduction

Sodium, calcium and magnesium ions are essential for the biological activity of many polyelectrolytes. This activity depends on a condensation of the metal ions. There are several clues, which suggest that interactions between the polyelectrolyte and metal ions depend on a hydration of the ion. This accounts for the great interest in the hydration of metal ions, particularly in the systems containing hydrophobic groups. In aqueous solutions the hydration of Na^+, Mg^{2+} and Ca^{2+} differs. The first hydration shells of Na^+ and Mg^{2+} consists of six water molecules and have octahedral symmetry (Dietz et al, 1982; Hawlicka & Swiatla-Wojcik, 1995). The first shell of Ca^{2+} is larger; it contains eight or more water molecules and does not show any regularity (Owczarek et al., 2007). X-ray diffraction studies (Tamura et al., 1992, Megyes et al., 2004) have suggested that all these cations are six-coordinated in methanolic solutions thus their shells are octahedral.

Various experimental techniques can be employed to gain insight into a coordination shell of the ion, but a lack of theory renders even a term 'preferential solvation' misleading. The concept of the preferential solvation has been introduced to explain non-linear changes of solution properties, but now this term is commonly used to emphasise a difference of the compositions of the coordination shell and the bulk solvent. Preferential solvation is usually expected if the ion interacts stronger with one of the solvent components. There are however experimental clues that the selective solvation might be due to a microheterogeneity of the binary solvent.

Methanol-water mixture is a suitable model to study structural aspects of solvation in binary systems, particularly when hydrophobic effects may occur. Both net components are highly associated liquids, but their hydrogen-bonded networks are inconsistent. Water molecules form a 3-dimensional, tetrahedrally coordinated structure, where cavities are filled with monomers (Soper & Phillips, 1986). Extension of the hydrogen bonds over 1 nm causes that liquid water, even at room temperature, behaves like a gel (Dore et al., 2000). Hydrogen-bonded molecules of methanol form zig-zag polymer chains (Narten & Habenschuss, 1984). Though in binary mixture the molecules of methanol and water may form a common hydrogen-bonded network the bulky methyl group causes that methanol molecule cannot simply replace the water molecule in the tetrahedral structure. In consequence the methanol-water mixture may become heterogeneous on the molecular level. Neutron diffraction (Dughan et al., 2004) and X-ray spectroscopy (Guo et al. 2004)

have confirmed that supposition. Despite apparent miscibility of both components, methanol and water clusters are observed over whole concentration range. At particular concentration, near 25-27 mol% of methanol, where transport and thermodynamic properties exhibit extrema, water and methanol form separate, percolating structures (Dughan et al. 2004).

Several experimental techniques were employed to investigate solvation of ions in methanol-water mixtures. Results are, however, inconsistent and lead to contradict conclusions. Therefore both a preferential hydration (Convington & Dunn, 1989; Hawlicka, 1995), as well as a lack of preferences (Holtz et al., 1977) have been postulated for alkali and halide ions in methanol-water mixtures. Though X-ray and neutron scattering measurements should provide a direct insight into the ion coordination shell, their results cannot be decisive for methanol-water mixture, because distances between these ions and the oxygens of either water (Neilson & Enderby, 1979; Licheri et al, 1975) or methanol (Megyes, 2004) are almost the same. Moreover a direct correlation between the alkali earth cations and the methyl group is lacking (Radnai et al., 1995). In such case the scattering techniques are not enough sensitive to investigate the preferential solvation in methanol-water mixture. Thus a molecular dynamics simulation seems to be a useful tool to provide additional information concerning the structure of the ion shell.

A quality of the simulation results depends on the methods used to describe all interactions in the solutions. *Ab initio* quantum mechanics would be the most accurate method, but its application to systems containing ions and a few hundred water molecules could not be expected for the near future. Therefore QM/MM MD simulation seems to be an elegant approach for investigating the aqueous solutions of electrolytes. The ion and its nearest water molecules are treated quantum mechanically. Such approach includes many-body interactions between particles within the solvation shell. QM/MM MD simulations were carried out for aqueous solutions of various ions (Tongraar & Rode, 2003, Rode et al., 2004, Öhrn & Karlström, 2004; Tongraar & Rode, 2005, Payaka et al., 2009; Tongraar et al., 2010). Their results evidenced a significant role of the many-body interactions on structural and dynamical properties of the hydrated ions. These simulations concerned, however, the systems, which contain only one ion, either cation or anion, and a few water molecules. Thus this technique is useless for studies more concentrated solutions, where an association of the ions occurs. The formation of the various types of the ionic pairs, solvent separated, solvent shared and contact pairs, is frequently observed in binary solvents. This phenomenon may affect significantly the solvation of ions.

Classical MD simulations are usually carried out for NVE or NVT ensembles. The volume is fixed and it depends on a number of the particles, temperature, composition of the system. Particles are placed into a periodic cube. The size of the periodic box results from the experimental density of the simulated system. Initial coordinates of particles are frequently chosen from the crystal lattice (Heyes, 1998), however the random distribution of the particles in the cube is better, because it reduces a time of equilibration.

In classical simulations the interactions between molecules are represented by a sum of the pair potentials and many-body interactions are neglected. Usually the pair potential consists of Coulomb term, for which the Ewald summation is applied, and of short-range parts, for which shifted-force potential method (Allen & Tidesly, 1987) is used.

2. Effective pair potentials

Several potentials have been proposed to describe the interaction of the water molecules, but this molecule still remains 'a challenge to model, because it is polar, polarizable, has light H atoms and is flexible' (Heyes, 1998). Only a few of the models consider the water molecule as a flexible body and permit internal vibrations. Most of them are a modification of the simple point charge potential of Berendsen *(*Berendsen et al., 1981) They use a potential of the spectroscopic type (Zhu & Wong, 1993; Ferguson, 1995) to describe an intramolecular interaction. Unfortunately SPC model neglects non-Coulomb interactions of hydrogen atoms, which seem to be important in hydrogen-bonded systems.

In simulations presented here the interactions of the water molecules has been described by the BJH potential (Bopp et al., 1983; Jancso & Bopp, 1983) which treats the intermolecular interactions of oxygens and hydrogens by mean of the central force model (CF) (Stillinger & Rahman, 1978) and uses a three body description of intermolecular interactions. This model has been frequently employed to simulate aqueous solutions of electrolytes, both in classical (Dietz et al., 1982; Jancso et al. 1985; Probst et al., 1985, Probst et al., 1991; Hawlicka & Swiatla-Wojcik, 1995, Lavenstein et al. 2000; Ibuki & Bopp, 2009) and in QM/MM MD (Tongraar & Rode, 2003, Rode et al., 2004, Öhrn & Karlström, 2004; Tongraar & Rode, 2005, Payaka et al., 2009; Tongraar et al., 2010) simulations. The BJH potential is appropriate to simulate the methanol-water mixtures, because it is fully consistent with the PHH flexible model (Palinkas et al. 1987) of the methanol molecule. The BJH and PHH, potentials reproduce properly the structure, energies and dynamic properties of the methanol-water mixtures (Palinkas et al., 1991a; Palinkas et al., 1991a, Hawlicka & Swiatla-Wojcik, 2000). An advantage of the flexible models is, that they permit a distortion of the solvent molecules from their equilibrium geometry. In consequence a molecular polarizability is incorporated.

The BJH and PHH potentials consist of two parts, which describe the inter- and intramolecular interactions respectively:

$$V(\rho_i, r_{\alpha\beta}) = V^{\text{intra}}(\rho_i) + V^{\text{inter}}(r_{\alpha\beta}) \tag{1}$$

The intermolecular parts are the sum of Coulombic and non-Coulombic terms. The Coulombic terms result from the partial charges of the interacting sites. In water molecule the partial charges are located on oxygen (-0.66 e) and hydrogen (+0.33 e) atoms. Methanol molecule consists of the charged oxygen (-0.6 e), hydroxyl hydrogen (+0.35 e) and the methyl group (+0.25 e), considered as the pseudo-atom. Non-Coulombic intermolecular O-O, O-H and H-H interactions of the water and methanol molecules are the same as in CF2 model for water (Stillinger & Rahman, 1978) The non-Coulomb interaction of the methyl group with the hydroxyl hydrogens has been neglected and that with oxygens and methyl groups has been represented by the Lennard-Jones potential (Jorgensen, 1981).

Intramolecular potentials for water and methanol are based on the formulation proposed by Carney et al. (Carney et al, 1976). They are expressed as power series of the internal coordinates, ρ_i, 'stretch' and 'bend' and the three-body interactions are included:

$$V(\rho_i) = \sum L_{ij}\rho_i\rho_j + \sum L_{ijk}\rho_i\rho_j\rho_k + \sum L_{ijkl}\rho_i\rho_j\rho_k\rho_l \tag{2}$$

Usually in classical MD simulations the ion potentials are represented by the Coulomb and the Lennard-Jones terms. These potentials overestimate, however, the number of the solvent

molecules in the ion shells (Hawlicka & Swiatla-Wojcik, 2002) and underestimate a stability of the ion shells (Hawlicka & Swiatla-Wojcik, 2002, Bujnicka & Hawlicka, 2006). Moreover such potentials are inconsistent with flexible models of the solvent molecules. Therefore the ion-water and ion-methanol potentials were evaluated from *ab initio* calculations and fitted to the BJH and PHH models.

The potential energy for the complexes of the ion and the solvent molecule was computed for several hundred configurations of the complexes. Then the potential surfaces were fitted to the analytical form:

$$V_{i\alpha}(r) = \sum_{\alpha=1}^{3}\left[\frac{Q_{i\alpha}}{r} + \frac{A_{i\alpha}}{r^{n}} + B_{i\alpha}\cdot\exp(-C_{i\alpha}\cdot r)\right] \tag{3}$$

where $Q_{i\alpha}$ represents the Coulombic interactions, which are defined by the ion charge and partial charges of the water or methanol molecules. The energies of the Coulombic interactions were subtracted from the potential surfaces. Parameters $A_{i\alpha}$, $B_{i\alpha}$ and $C_{i\alpha}$, were adjusted to the non-Coulomb part of the energy surface. They have no physical meaning. Parameters derived for ions, Na^+(Marks et all, 1991; Hawlicka & Swiatla-Wojcik, 1995), Mg^{2+} (Dietz et al., 1982; Tamura et al., 1992), Ca^{2+}(Probst et al., 185; Owczarek & Hawlicka, 2006), Cl^- (Marks et all, 1991; Hawlicka & Swiatla-Wojcik, 1995) and the flexible molecules of BJH water and PHH methanol are summarized in Table 1.

The pair potentials for ions and solvent molecules are displayed in Figure 1 as a function of the ion-oxygen distance for the coplanar orientation shown in the insertion.

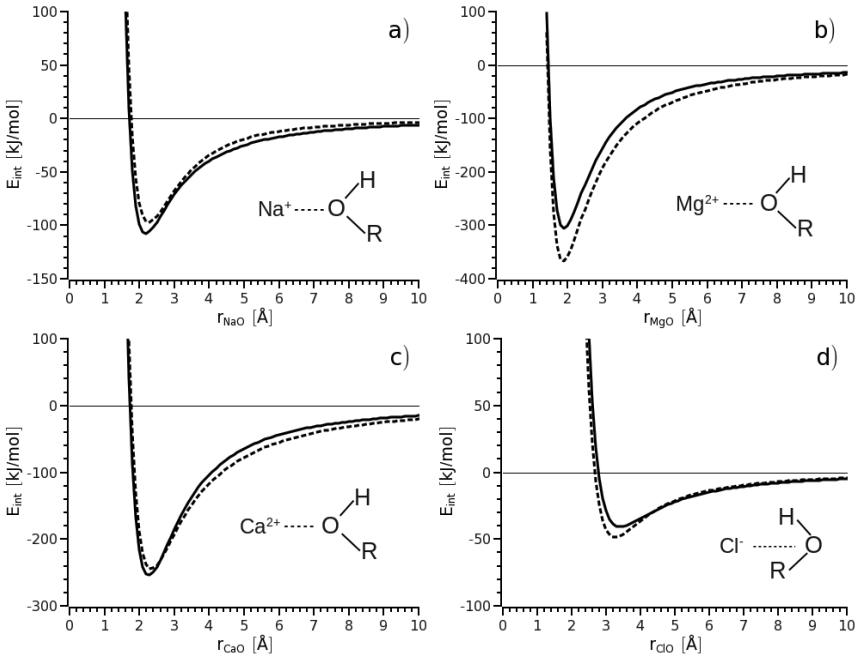

Fig. 1. Fitted pair potentials for the ion-water (solid) and ion-methanol (dashed) as function of the ion-oxygen distance for the orientation shown in the insertion.

i	α	$Q_{i\alpha}$ [kJ Å mol^{-1}]	$A_{i\alpha}$ [kJ Å^n mol^{-1}]	$B_{i\alpha}$ [kJ mol^{-1}]	$C_{i\alpha}$ [Å^{-1}]
Na	O_m	-833.61	-172.23	2.5328× 10^5	4.1501
Na	H_m	486.27	593.40	-8.3289× 10^2	0.9591
Na	Me	347.34	-274.90	5.1674× 10^4	2.7930
Na	O_w	-916.28	-352.20	3.5555× 10^5	4.2988
Na	H_w	458.14	151.60	5.1867× 10^4	5.3919
Ca	O_m	-1667.30	-1372.63	2.5971× 10^5	3.4900
Ca	H_m	972.58	933.29	8.3277× 10^2	0.9600
Ca	Me	694.70	-474.95	5.1666× 10^4	2.7930
Ca	O_w	-1832.56	-1572.66	2.5972× 10^5	3.4900
Ca	H_w	916.28	626.41	1.2022× 10^5	6.7900
Mg	O_m	-1667.30	-721.86	4.0778× 10^5	4.3937
Mg	H_m	972.58	-7.21	4.2904× 10^1	0.2749
Mg	Me	694.70	-232.28	1.8277× 10^4	2.6485
Mg	O_w	-1832.56	-890.83	2.6954× 10^5	4.0800
Mg	H_w	916.28	82.04	7.3844× 10^1	0.3490
Cl	O_m	833.61	127.02	1.4532× 10^5	3.1999
Cl	H_m	-486.27	-193.41	2.5091× 10^4	3.3082
Cl	Me	-347.34	6.77	5.9262× 10^5	3.2984
Cl	O_w	916.28	9.34	1.1750× 10^5	2.6727
Cl	H_w	-458.14	-68.27	9.0210× 10^4	4.5420

Table 1. Parameters $Q_{i\alpha}$, $A_{i\alpha}$, $B_{i\alpha}$ and $C_{i\alpha}$ in equation (3) for the interactions of ions with PHH methanol and BJH water.

As seen the interactions of the ion with molecules of the solvent components are similar. The lowest binding energies for ion-water and ion-methanol complexes are observed at the same distances. This position of the energy minimum is shifted to larger distance as the ionic radius increases (Marcus & Hefter, 2004) As might be expected the energy minimum becomes deeper when the charge density increases. The binding energy of Na^+ and Ca^{2+} ions with water is about 3% lower than that with methanol. An opposite features are found for of Mg^{2+} and Cl^- ions, because their interactions with methanol are stronger than those with water. For Mg^{2+} ions the difference is about 10%, but for Cl^- ions is less than 2%.

The pair potentials for interactions between ions were also derived from ab initio calculations. The potential energy surfaces were constructed from hundred configurations. Then they were fitted to the equation (3). Parameters were summarized in Table 2.

i	α	$Q_{i\alpha}$ [kJ Å mol^{-1}]	$A_{i\alpha}$ [kJ Å^n mol^{-1}]	$B_{i\alpha}$ [kJ mol^{-1}]	$C_{i\alpha}$ [Å^{-1}]	n
Na	Na	1389.4	-9.9154× 10^2	1.0180× 10^6	5.5909	6
Na	Cl	-1389.4	-7.9000× 10^1	1.7172× 10^5	3.1940	2
Ca	Ca	5557.6	-1.5198× 10^4	2.6010× 10^6	4.4870	6
Ca	Cl	-2778.8	-3.5301× 10^2	3.6608× 10^5	3.0100	2
Mg	Mg	5557.6	-1.4799× 10^3	1.8226× 10^6	6.3600	6
Mg	Cl	-2778.8	-2.0069× 10^3	1.1854× 10^5	2.6500	2
Cl	Cl	1389.4	-2.8672× 10^4	9.1704× 10^5	3.3863	6

Table 2. Parameters $Q_{i\alpha}$, $A_{i\alpha}$, $B_{i\alpha}$ and $C_{i\alpha}$ in equation (3) for the ion-ion interactions.

3. Radial distribution functions for the ions

Radial distribution function $g_{ion\text{-}\alpha}(r)$ represents the probability of finding the ion and α-site of the solvent molecule in a distance r, relative to the probability expected for a random distribution with the same density. These functions provide clear information about a structure of the ion surrounding. At room temperature the order is short-range thus the pair distribution function exhibits no more than two peaks. Positions of these peaks reflect average distances of neighbours in the first and second coordination shells.

Though the peak area is proportional to the number of the molecules in the shell, its height and width depend on a balance between the ion-solvent attraction and thermal motions of the solvent molecules. The first peak of the pair distribution functions increases with the increasing charge density, therefore it is generally higher and sharper for the cations than that for the anions and for the divalent ions than for the monovalent ions (Yu et al., 2010)

A surrounding of the ion in the methanol-water mixtures can be described by five radial distribution functions, two of them for the sites of water (O_w and H_w) and three for the sites of methanol (O_m, H_m and Me). The characteristic parameters of these functions are listed in Tables 3 and 4. There are positions of the first (R_{max1}) and second (R_{max2}) maxima, the positions of the first (r_{min1}) and second (r_{min2}) minima and the numbers of the particles in the first (n_1) and second (n_2) coordination shells.

The radial distribution functions of cation-oxygen in water, methanol and equimolar methanol-water mixture are shown in Figure 2. In aqueous solutions of $MgCl_2$ and $CaCl_2$ the cation-oxygen functions exhibit a sharp first peak, followed by broad second maximum. Positions of the first and second peaks coincide with the average distances of the first and second neighbours deduced from diffraction experiments (Ohtaki & Radnai, 1993). The $g_{NaOw}(r)$ function shows only one peak. As might be expected the position of the first peak is shifted to larger distances as the radius of the cation increases. The peak height depends on the charge density and the $Mg^{2+}O_w$ radial distribution function shows the highest peak.

Addition of methanol does not affect the position of the first maximum of the $g_{ionOw}(r)$ function. However the methanol addition increases the first peak, particularly that of the

x_M	ion	R_{max1}	$g(R_{max1})$	r_{min1}	n_1	R_{max2}	$g(R_{max2})$	r_{min2}	n_2
					oxygen				
0.0	Na	0.232	8.66	0.320	6.05	-	-	-	-
	Ca	0.237	15.65	0.340	10	0.430	2.82	0.552	27
	Mg	0.199	21.14	0.270	6.2	0.452	1.75	0.512	16
	Cl	0.335	2.98	0.398	8	-	-	-	-
0.1	Na	0.230	8.54	0.297	4.76	-	-	-	-
	Ca	0.240	18.67	0.300	9.70	0.440	2.80	0.564	23
	Mg	0.199	24.04	0.270	5.40	0.452	1.34	0.507	10
	Cl	0.337	2.23	0.410	5.80	-	-	-	-
0.5	Na	0.231	10.37	0.297	2.27	-	-	-	-
	Ca	0.237	35.88	0.305	6.80	0.450	2.38	0.558	7
	Mg	0.199	38.33	0.270	3	0.394	1.29	0.504	3
	Cl	0.344	1.10	0.386	1.04	-	-	-	-
0.9	Na	0.230	24.19	0.295	0.75	-	-	-	-
	Ca	0.232	105.93	0.310	2.30	-	-	-	-
	Mg	0.199	46.67	0.270	0.60	0.397	1.86	0.500	0.6
	Cl	-	-	-	-	-	-	-	-
					hydrogen				
0.0	Na	0.300	3.41	0.375	13.3	-	-	-	-
	Ca	0.307	5.93	0.380	20.0	0.500	1.41	0.620	59
	Mg	0.274	6.42	0.337	12.5	0.492	1.05	0.575	40
	Cl	0.242	2.50	0.310	7.38	-	-	-	-
0.1	Na	0.295	3.27	0.367	9.96	-	-	-	-
	Ca	0.312	7.57	0.382	19.4	0.512	2.28	0.620	51
	Mg	0.274	7.03	0.337	10.8	0.497	1.10	0.575	22
	Cl	0.242	1.86	0.310	4.96	-	-	-	-
0.5	Na	0.301	4.08	0.374	4.6	-	-	-	-
	Ca	0.312	30.69	0.382	13.6	0.518	3.50	0.623	15
	Mg	0.274	11.11	0.337	6.2	0.496	0.90	0.567	7
	Cl	0.251	0.87	0.306	1.06	-	-	-	-
0.9	Na	0.300	9.38	0.392	1.52	-	-	-	-
	Ca	0.310	42.35	0.370	4.5	-	-	-	-
	Mg	0.274	15.48	0.339	1.2	0.472	1.22	0.557	1
	Cl	-	-	-	-	-	-	-	-

Table 3. Characteristic parameters of the ion-water radial distribution functions: positions (in nm) of the first (R_{max1}) and second (R_{max2}) maxima, the first (r_{min1}) and second (r_{min2}) minima, heights of the first $g(R_{max1})$ and second $g(R_{max2})$ maxima and the first (n_1) and second (n_2) coordination numbers.

$Mg^{2+}O_w$ and $Ca^{2+}O_w$ functions. This may suggest that in mixed solvent the interactions of the cations with water molecules are favoured, despite similar binding energies of Ca^{2+} and Na^+ ions with methanol and water. This preference for water is observed also for Mg^{2+} ion, despite its stronger interactions with methanol than with water (see Figure 1 b). Moreover the first peak of the $g_{ionOw}(r)$ function increases, when the water content decreases. This is particularly remarkable for the Ca^{2+} ions and in the water deficit mixture, when the water

x_M	ion	R_{max1}	$g(R_{max1})$	r_{min1}	n_1	R_{max2}	$g(R_{max2})$	r_{min2}	n_2
					oxygen				
0.1	Na	0.237	15.46	0.317	1.25	-	-	-	-
	Ca	-	-	-	-	0.652	1.90	0.760	~5
	Mg	0.202	26.66	0.270	0.7	0.397	7.33	0.519	5
	Cl	0.325	14.09	0.410	2.25	-	-	-	-
0.5	Na	0.234	14.24	0.316	3.56	-	-	-	-
	Ca	0.252	5.75	0.332	1.7	0.478	3.05	0.555	8
	Mg	0.202	34.57	0.270	2.92	0.392	3.55	0.495	8
	Cl	0.324	9.84	0.414	6.10	-	-	-	-
0.9	Na	0.235	13.72	0.312	5.61	-	-	-	-
	Ca	0.250	15.60	0.347	5.7	0.480	3.47	0.565	~10
	Mg	0.202	46.67	0.270	5.4	0.399	3.17	0.472	7
	Cl	0.325	6.84	0.418	7.1	-	-	-	-
1.0	Na	0.238	15.90	0.340	5.8	-	-	-	-
	Ca	0.247	22.03	0.362	7.6	0.488	3.05	0.565	9
	Mg	0.202	50.22	0.270	6	0.397	3.35	0.472	7
	Cl	0.328	7.00	0.430	7.2	-	-	-	-
					hydroxyl hydrogen				
0.1	Na	0.282	7.29	0.380	1.25	-	-	-	-
	Ca	-	-	-	-	0.732	1.58	0.825	~5
	Mg	0.259	9.81	0.259	0.7	0.444	4.74	0.580	5
	Cl	0.227	27.12	0.312	2.20	-	-	-	-
0.5	Na	0.300	4.07	0.380	4.60	-	-	-	-
	Ca	0.337	2.96	0.419	1.7	0.545	2.38	0.623	~6.5
	Mg	0.262	11.91	0.262	2.92	0.492	2.28	0.574	9
	Cl	0.231	18.26	0.326	5.32	-	-	-	-
0.9	Na	0.290	5.86	0.385	5.59	-	-	-	-
	Ca	0.335	8.46	0.440	5.7	0.550	2.41	0.635	~12
	Mg	0.262	16.73	0.262	5.4	0.510	2.16	0.530	8
	Cl	0.235	13.56	0.335	6.70	-	-	-	-
1.0	Na	0.295	6.90	0.380	5.90	-	-	-	-
	Ca	0.332	11.90	0.400	7.6	0.562	2.19	0.635	~11
	Mg	0.262	17.98	0.262	6	0.505	2.19	0.522	8
	Cl	0.235	12.70	0.340	7.00	-	-	-	-

Table 4. Characteristic parameters of the ion-methanol radial distribution functions: positions (in nm) of the first (R_{max1}) and second (R_{max2}) maxima, the first (r_{min1}) and second (r_{min2}) minima, heights of the first $g(R_{max1})$ and second $g(R_{max2})$ maxima and the first (n_1) and second (n_2) coordination numbers.

content does not exceed 10 mol%, the first peaks of the $Ca^{2+}O_w$ function is about 7 times higher than that in aqueous solution (see Table 3). This suggests that in methanol rich solvents the Ca^{2+} shell contains several water molecules. The second maximum of the $g_{CaOw}(r)$ function shows also a distinct behaviour. In aqueous solution it is split into two peaks of similar heights, at 0.43 and 0.49 nm, respectively. When the methanol is added this splitting becomes less visible and vanishes in equimolar mixture.

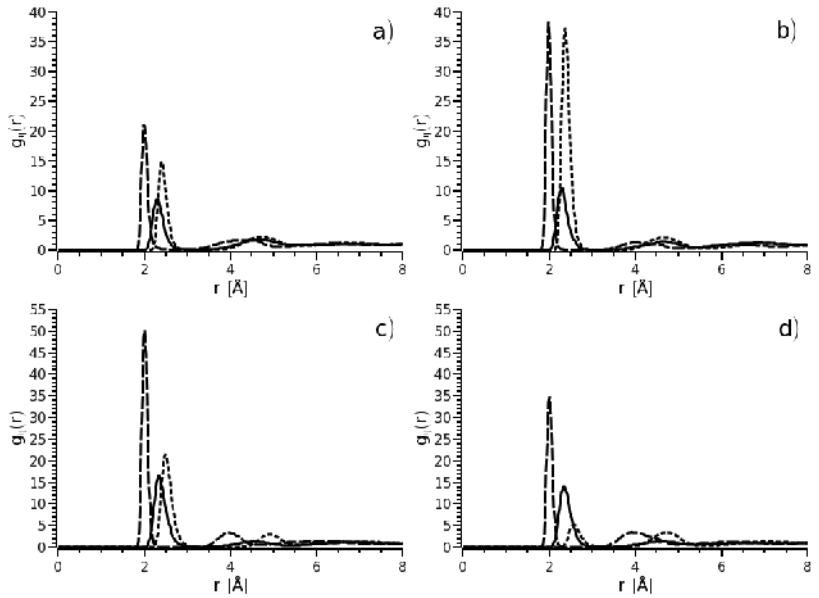

Fig. 2. Cation-oxygen radial distribution functions in solutions of NaCl (solid), $MgCl_2$ (dashed) and $CaCl_2$ (dotted) in water (a), methanol (c) and equimolar water-methanol mixture: oxygen of water (b) and methanol (d).

A comparison of the radial distribution functions for the cations in aqueous and methanolic solutions shows that the average distance to the methanol's oxygen is almost the same as to the water's oxygen. Such feature is in good agreement with the experimental results (Megyes et al., 2004; Neilsen & Enderby, 1979). The first peaks of all ion-oxygen functions in methanolic solutions are higher that those in aqueous solutions. This suggests that positions of the methanol molecules in the cation shells are more restricted than those of water molecules. As seen from Table 4 the height of the $g_{ionOm}(r)$ peak decreases when the methanol content decreases. A striking behaviour has been notice for calcium ions. In water rich mixture, for the methanol content 10 mol%, the first and second maxima of the $g_{CaOm}(r)$ function, expected at 0.25 and 0.49 nm, are absent. This suggests that the methanol molecules do not enter the first and even the second coordination shell of Ca^{2+} ions, despite very similar energy of interactions (see Figure 1c).

Radial distribution functions of the cations and the hydroxyl hydrogens of water and methanol are shown in Figure 3.

The cation-hydroxyl hydrogen functions coincide with the cation-oxygen pair distribution functions. Therefore is not surprising that the positions of the sharp first peak of $g_{ionH}(r)$ do not depend on the methanol content. As seen from Tables 3 and 4 the cation-hydroxyl hydrogen distance is longer, by about 0.07 nm, than that of the water's and methanol 's oxygen. This suggests an antidipole orientation of the solvent molecules in the first coordination shells of the cations. The radial distribution functions for the cations and the methyl group are not shown, because a direct correlation between these sites is lacking.

Radial distribution functions computed for chloride ions in the solutions of NaCl, $MgCl_2$ and $CaCl_2$ are very similar, therefore the pair distribution functions, computed for $CaCl_2$

solutions are displayed in Figure 4 as the example of the Cl^- -oxygen and Cl^- -hydroxyl hydrogen pair distribution functions.

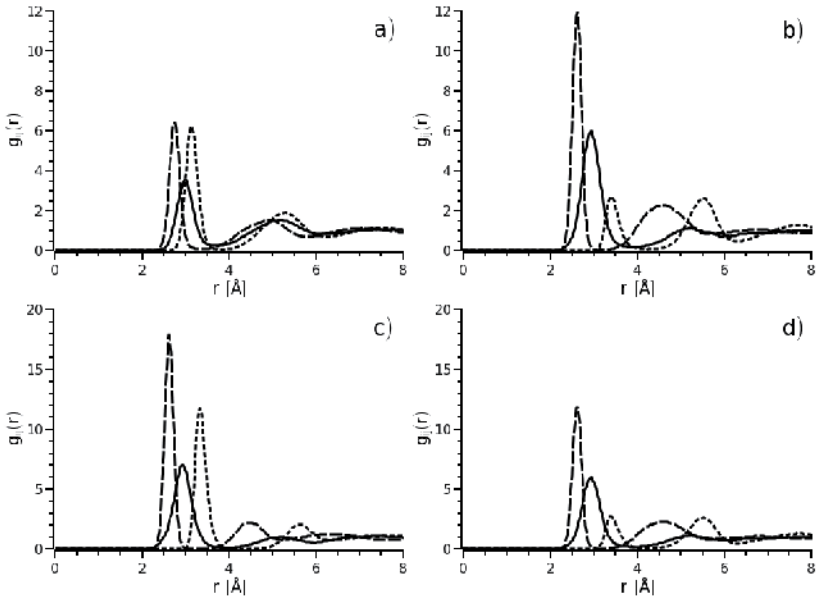

Fig. 3. Cation-hydroxyl hydrogen radial distribution functions in solutions of NaCl (solid), $MgCl_2$ (dashed) and $CaCl_2$ (dotted) in water (a), methanol (c) and equimolar water-methanol mixture: oxygen of water (b) and methanol (d).

In aqueous and methanolic solutions of NaCl, $MgCl_2$ and $CaCl_2$ the first peak of the Cl^- O_w and Cl^- O_m functions is centred at 0.33 nm. This agrees with the average distance, deduced from X-ray diffraction, from the Cl^- ion to oxygens in aqueous (Yu et al., 2010) and methanolic (Megyes et al., 2004; Neilsen & Enderby, 1979) solutions. Position of the $g_{ClHw}(r)$ and $g_{ClHm}(r)$ functions, at 0.242 nm, coincides with the anion-oxygen distance. This shorter, by about 0.09 nm, distance suggests almost linear hydrogen bond between the anion and the solvent molecules. In aqueous solutions the first peaks of the $g_{ClOw}(r)$ and $g_{ClHw}(r)$ functions are not distinctly separated from the bulk. This evidences a high flexibility of the hydrated anion and suggests an easy exchange of the water molecules between the coordination shell and the bulk solvent. In methanolic solutions the peaks of the $g_{ClOm}(r)$ and $g_{ClHm}(r)$ functions are higher and better pronounced. This may indicate that the coordination shell of the anion in methanolic solutions is more stable.

The composition of the mixed solvent does not affect the peak positions, but it influences remarkably the peak height. The changes of the peak height follows the changes of the solvent components, therefore the $g_{ClOm}(r)$ and $g_{ClHm}(r)$ peaks increase and the $g_{ClOw}(r)$ and $g_{ClHw}(r)$ peaks should decrease with the increasing methanol content. However the influence of the solvent composition on the Cl^- -water radial distribution function is more dramatic. In equimolar mixture the first peaks of the $g_{ClOw}(r)$ $g_{ClHw}(r)$ functions, expected at 0.33 and 0.242 nm, respectively, are absent. This means that the coordination shells of the anions do not contain the water molecules. This is observed despite the very similar energy interactions of the Cl^- ion with water and methanol molecules (see Figure 1d).

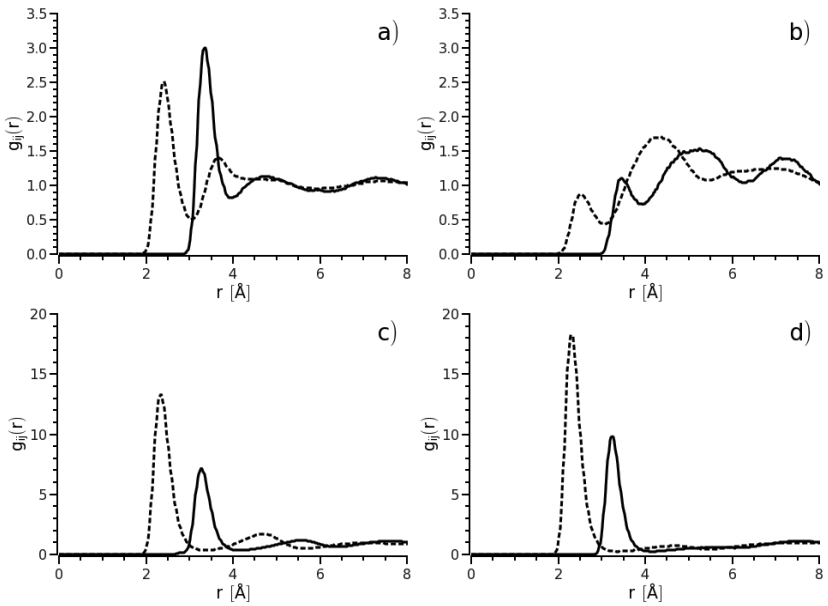

Fig. 4. Radial distribution functions for Cl^- and water and methanol sites: oxygen (solid) and hydroxyl hydrogen (dotted). Solutions of $CaCl_2$ in water (a), methanol (c) and equimolar water-methanol mixture: water's (b) and methanol's (d) sites.

4. Coordination numbers of the ions

The numbers of the α-sites in the coordination shells are equal to the running integration numbers, which have been computed by the integration of the $g_{ion\alpha}(r)$ function within the boundaries of the shell, r_1 and r_2, respectively.

$$n_\alpha = 4\pi\rho_\alpha \int_{r_1}^{r_2} g_{ion\alpha}(r) r^2 dr \tag{4}$$

where ρ_α denotes the number density of the α-sites. The boundaries of the shells correspond to the minima of the g(r) functions. Well-separated peaks of the radial distribution functions for the cations permit to compute unambiguously the number of the molecules in the first and even in the second shell. The number of the solvent molecules in the Cl^- shell is not certain, because the peaks are badly pronounced.

Diffraction experiments have shown that sodium and magnesium ions are six-coordinated both in aqueous (Ohtaki&Radnai,1993) and methanolic (Megyes et al., 2004) solutions. The hydration number of Ca^{2+} is greater, it strongly depends on the salt concentration and covers a wide interval, from 10.7 to 5.5 (Yamagouchi et al., 1989). The salt concentration influences also the number of the methanol molecules coordinated by Ca^{2+}, but this dependence is weaker (Megyes et al., 2004).

Coordination numbers of Na^+ and Mg^{2+}, obtained from MD simulations, agree with the experimental results. Despite higher charge density of Mg^{2+} both cations, Na^+ and Mg^{2+}, are

six-coordinated in aqueous and methanolic solutions. Thus the coordination number should be independent of the solvent composition. Though the charge density of Ca^{2+} is smaller than that of Mg^{2+} , the first shell of Ca^{2+} is larger. In aqueous solution the Ca^{2+} shell consists of 10 water molecules. In methanolic solution the Ca^{2+} shell contains less molecules. The coordination number is 7.6. This means that the Ca^{2+} shells contain either seven or eight methanol molecules. Thus one may expect that the methanol addition will slightly reduce the coordination number of Ca^{2+}.

In aqueous solutions of NaCl, $MgCl_2$ and $CaCl_2$ the chloride ion coordinates about eight water molecules. Smaller hydration number, about 6, was deduced from the X-ray experiments (Yu et al., 2010) Such discrepancy can be understood, because the hydration shell of the anion is badly pronounced. In methanolic solution the Cl^- ion coordinates less molecules, about 7. Different coordination numbers of Cl^-, six (Megyes et al., 2004) and more than seven (Yamagouchi et al., 1989) have been deduced from X-ray scattering in methanol solutions of $CaCl_2$ and $MgCl_2$. The discrepancy might be due to the higher concentration of the experimentally examined solution.

Interactions of the ions with water and methanol are very similar (see Figure 1) therefore a selective solvation of the ions has been not expected. The inspection of the results listed in Tables 3 and 4 shows, however, that the influence of the methanol addition on the composition of the ion shells can be dramatic. To describe this effect the real composition of the ion shells has been compared with the expected composition.

The 'real' methanol mole fraction in the first and second coordination shells of the ions has been computed as follows:

$$(x_m)_{obs} = \frac{(n_m)_k}{(n_m)_k + (n_w)_k} \tag{5}$$

where $(n_w)_k$ and $(n_m)_k$ are the running integration numbers of the methanol and water molecules, respectively, computed for the first or second coordination shells.

The number density of the methanol and water molecules in the mixture depends nonlinearly on the methanol mole fraction. Therefore even when the preferential solvation of ions does not occur, the methanol concentrations in the coordination shell and the bulk solvent are not the same. Assuming a lack of the selective solvation, the expected mole fraction of methanol in the ion shell can be calculated as follows (Hawlicka & Switla-Wojcik, 2000):

$$(x_m)_{exp} = \frac{(n_m)_o \frac{\rho_m(x_m)}{(\rho_m)_o}}{(n_m)_o \frac{\rho_m(x_m)}{(\rho_m)_o} + (n_w)_o \frac{\rho_w(x_m)}{(\rho_w)_o}} \tag{6}$$

$(n_w)_o$ and $(n_m)_o$ are the numbers of the coordinated solvent molecules in pure water and methanol, $(\rho_w)_o$ and $(\rho_m)_o$ denote the number densities of the solvent components in the aqueous and methanolic solutions of the salts, while $\rho_w(x_m)$ and $\rho_m(x_m)$ are the number densities of water and methanol, respectively, in ternary systems: salt-methanol-water.

The non-linear changes of the mixed solvent density should give a slight excess of methanol in the primary coordination shells of the ions. The results of MD simulation show, however, significant deviations of the real composition of the ion shells. This suggests a selective solvation of the ions. To demonstrate the preferences of the ions the observed methanol mole fraction, $(x_m)_{obs}$, is shown as the function of the expected methanol mole fraction $(x_m)_{exp}$ in Figure 5.

The content of methanol in the first coordination shells of Ca^{2+} and Mg^{2+} ions is remarkably smaller than expected. Thus the Ca^{2+} and Mg^{2+} ions favour water molecules in their shells. As seen from Figure 5 the preferential hydration of these cations is observed over whole range of the mixture composition. The Na^{+} ion also favours the water molecules in its primary shell, but this inclination is weaker, therefore the preferential hydration occurs only in the water deficit mixtures. This agrees with experiments, which have shown the equality of the self-diffusion coefficients of water and Na^{+} ions in water deficit mixtures (Hawlicka, 1986). The self-diffusion experiments have also shown that the addition of $CaCl_2$ to the methanol water-mixture does not influence the methanol self-diffusion coefficient, but it reduces strongly the water self-diffusion coefficient (Palka & Hawlicka, 2004) . This means that translations of the cation and water molecules are correlated, because these species form an aggregate.

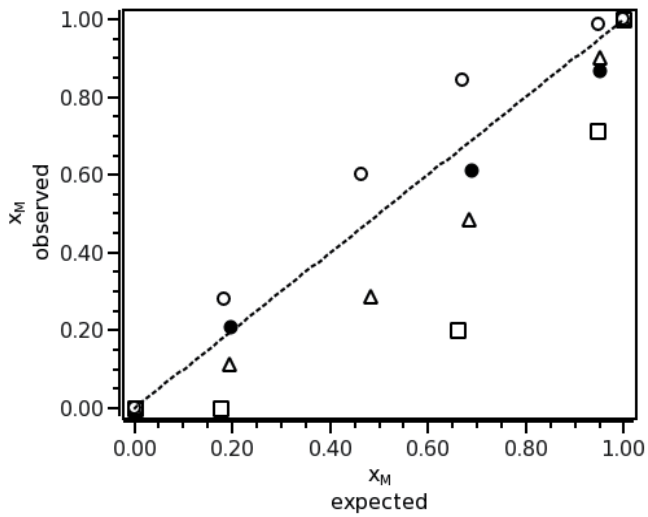

Fig. 5. The dependence of the observed methanol mole fraction in the primary shell of Na^{+} (●), Mg^{2+} (Δ), Ca^{2+} (□) and Cl^{-} (○) ions on the expected methanol mole fraction.

Though all cations favour water molecules in the nearest surrounding, some difference should be noticed. The Mg^{2+} shells contain about 10% more water than expected, the significant excess is observed only in equimolar mixture. The Ca^{2+} ions exhibit the stronger preference for water, because in the water deficit region the calcium ion coordinates most of the water molecules. Moreover the Ca^{2+} ion favours the water molecules also in its second shell. In water rich mixture both shell of the Ca^{2+} ions consist only of the water molecules. Preferences of the Mg^{2+} and Na^{+} ions in their second shells are opposite and an excess of the methanol content is observed.

Interactions of the chloride ions with methanol and water are weaker than those of cations. The coordination shell of Cl^- is flexible, but its composition differs significantly from that of the bulk solvent. The chloride ions favour methanol molecules in their coordination shells. This preference is observed in solutions of NaCl, $CaCl_2$ and $MgCl_2$, over the whole range of the composition of the mixed solvent. The preferential solvation of Cl^- by methanol has been postulated from self-diffusion coefficients. The diffusion experiments have shown that in methanol rich solvents translations of the chloride ions and methanol molecules are strongly correlated (Hawlicka, 1986). The Cl^- ion favours the methanol molecules in its primary shell despite very similar binding energies of the anion with the solvent components.

5. Orientation of the solvent molecules in the first coordination shell

Orientation of the molecules around the ion can be characterised by an angle θ between the vector connecting the ion with the oxygen and the dipole moment of the solvent molecule. The angular distribution functions are shown in Figure 6.

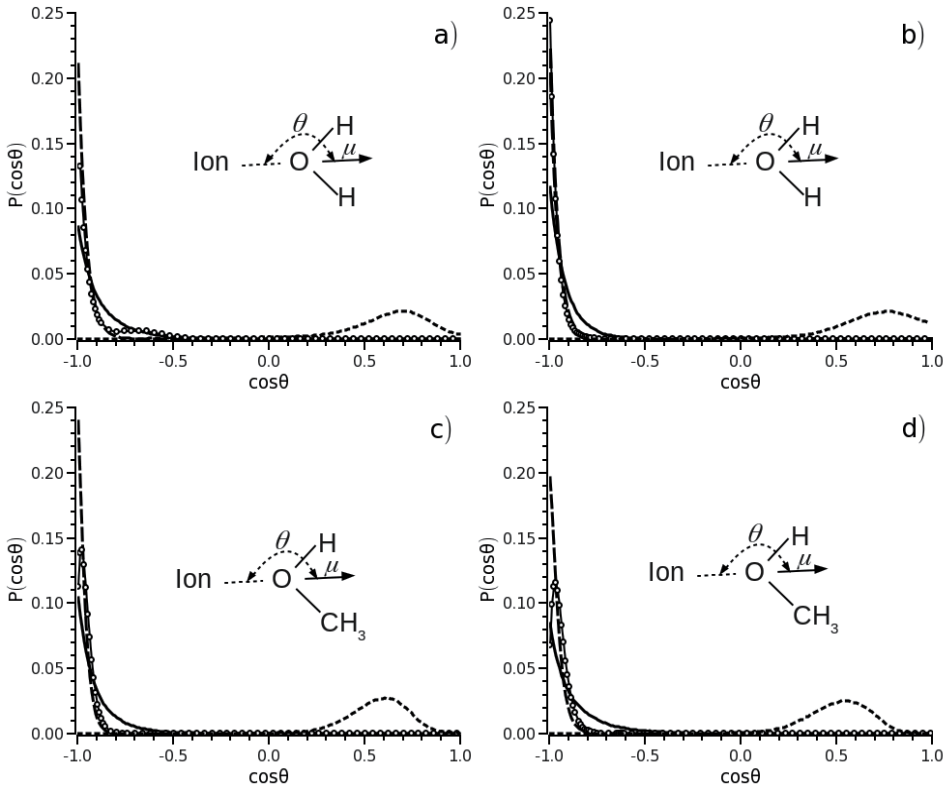

Fig. 6. Distribution functions of angular orientation of the nearest neighbours of Na^+ (solid), Mg^{2+}(dashed), Ca^{2+} (○) and Cl^- (dotted) in water (a), methanol (c) and equimolar mixture (b, d). The angle θ defined in the inset.

Distribution functions of the angular orientation of the water molecules in the primary shells of Na^+, Mg^{2+} and Ca^{2+} ions show the peak centred at cosθ = -1. This indicates that the

antidipole orientation of the water molecules in the cation shells dominates. The distribution of the θ angle for Mg^{2+} is narrower than those for Na^{+} and Ca^{2+}. This is not surprising that the water molecules are better oriented in the field of Mg^{2+}, which is stronger than the fields of Na^{+} and Ca^{2+}. The primary shell of Ca^{2+} contains more water molecules than the shells of the six-coordinated Na^{+} and Mg^{2+}ions, therefore the angular distribution for Ca^{2+} shows a shoulder for $\cos\theta \cong -0.7$. This means that the dipole moments of a few water molecules in the Ca^{2+} shell are tilted, by about 45°, from the antidipole orientation. This 'improper' orientation vanishes in equimolar mixture when the coordination number decreases from 10 to 7. This suggests that the coordination shell of Ca^{2+} is compact.

The antidipole orientation of the methanol molecules is also observed in the Na^{+} and Mg^{2+} shells. A different orientation has been noticed for the methanol molecules in the Ca^{2+} shell. The distribution of the O-Ca^{2+}O angles, shows the dominant peak at $\cos\theta = -0.9$. Thus the dipole moments of the methanol molecules in the Ca^{2+}vicinity are tilted by about 25°.

As might be expected the orientation of the solvent molecules in the vicinity of chloride ions is different. The distance from the anion to oxygen is longer than that to hydrogen. This suggests a hydrogen bond between the anion and the nearest solvent molecules. In aqueous and methanolic solutions the dominant peaks of the angular distributions are centred at $\cos\theta = 0.68$. This confirms that H-bond between the anion and solvent molecules is almost linear. As might be expected the orientation of the solvent molecules in the anion shell for all studied solutions is independent of the solvent composition.

To describe a geometrical arrangement of the solvent molecules in the solvation shells two angles can be defined. The φ angle is the angle between two vectors pointing from the ion to the nearest oxygens. The ψ angle, which is the angle between the three oxygens, permits to deduce a difference between the order of the water molecules in the coordination shells and the tetrahedral structure of water. The distributions of the φ angles have been computed without any distinction between oxygens belonging to water and methanol molecules. The results are displayed in Figure 7.

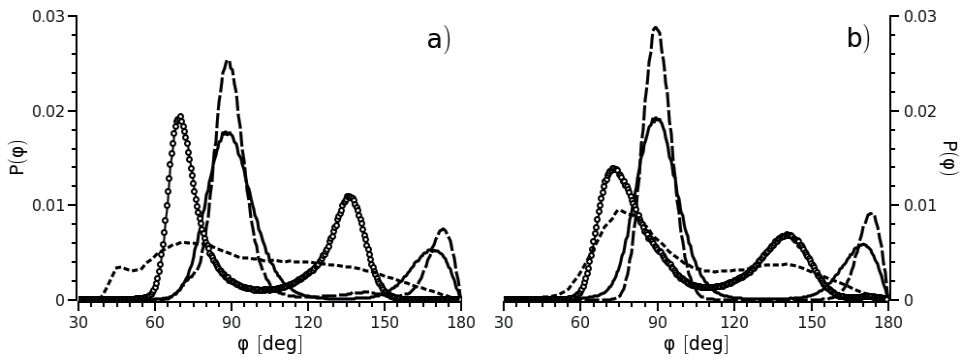

Fig. 7. Distribution of φ angles, for the water (a) and methanol (b) molecules in the primary shells of Na^{+} (solid), Mg^{2+}(dashed), Ca^{2+}(○) and Cl^{-} (dotted).

The distribution of φ angles computed for the coordination shells of the Na^{+} and Mg^{2+} ions is independent of the solvent composition. Two peaks, centred at 90° and 180°, indicate that the water and methanol molecules form an octahedron around the cation. The distribution

of the angles between three oxygens of the solvent molecules in the Na^+ and Mg^{2+} shells shows two peaks at 60 and 90°, respectively. This confirms the octahedral arrangement of the coordination shells.

The Ca^{2+} shell, which contains more molecules, does not show any symmetry. As seen from Figure 7 in aqueous solution the distribution of O-Ca^{2+}-O angles exhibits two peaks, around 67° and 135°, respectively. The former angle is close to the value, which can be expected for tetrahedral or hexahedral symmetry, but the latter angle cannot be correlated with any of the polyhedra. This means that the Ca^{2+} shell is irregular. When the coordination number of Ca^{2+} decreases with the increasing methanol content, the most probable O-Ca^{2+}-O angle increases. In methanolic solution the distribution of φ angles shows two peaks around 75° or 145°, respectively. This means that the cation shell remains irregular. The distribution of the O-O-O angles confirms a lack of symmetry of the Ca^{2+} shell, because in all studied solutions these angles are either 55° or 107°.

The O-Cl^--O angles, computed for the solutions of NaCl, $MgCl_2$ and $CaCl_2$, are very similar. As seen from Figure 7 the distribution of the O-Cl^--O angle is almost uniform. This means that the coordination shell does not show any symmetrical arrangement. A lack of the symmetry of the Cl^- shell causes that in aqueous solution the distribution of the O-O-O angles is almost uniform, except a small peak at about 54°. It is worthy to notice that such peak is believed to be a distinctive feature of the tetrahedral arrangement of pure water (Gallanger & Sharp, 2003). This means that in the coordination shell of Cl^- the water structure partially remains.

6. Residence time of the solvent molecules in the coordination shells

An important feature of ions in solutions is a persistence of the coordination shell, because a dynamics of an exchange process may determine a reaction rate. A residence time of the solvent molecules in the coordination shells of the ions has been calculated from a time correlation function R(t), proposed previously (Impeay et al., 1983). The time correlation function is defined as follows:

$$R(t) = \frac{\sum_{i=1}^{N\alpha}\sum_{j=1}^{N_\beta} \kappa_{ij}(t)\cdot\kappa_{ij}(t+\Delta t)}{N_\alpha \cdot N_\beta} \tag{7}$$

where N_α and N_β denote the number of ions and the solvent molecules in the sphere of the radius defined by the first minimum of the $g_{ionO}(r)$ function, respectively. $\kappa_{ij}(t)$ is the step function; $\kappa_{ij}(t)=1$, if the solvent molecule j is in the ion shell and $\kappa_{ij}(t)=0$ otherwise. The calculations of the R(t) functions were performed for at least 500 randomly chosen initial configurations. The calculations were done for several time intervals Δt within the range 0.01-0.5 ps.

The solvent molecules could leave the ion shell for a period, which was shorter than Δt, otherwise they were neglected in further calculations. Variations of Δt and the solvent composition do not influence the character of R(t) functions. For all simulated systems the time correlation functions for Mg^{2+} and Ca^{2+} ions decrease rapidly in the period shorter than

1 ps, afterward, independently of the time interval, they reach a constant value close to 0.95. This means that about 95% of the solvent molecules do not leave the coordination shells of the cations during the whole simulation time. The coordination shells of the divalent cations are very stable, with the lifetime remarkably exceeding 150 ps, and being independent of the solvent composition. The long lifetime of the primary hydration shells has been reported previously for Ca^{2+}, about 700 ps, and Mg^{2+} , about 422 ps (Konesham et al., 1998). The long residence time of the solvent molecules has been expected, because the hydrodynamic radii of both cations noticeably exceed the ion radii in crystal (Hawlicka, 1995). This means that the cations move with their coordination shells together, because the ion filed controls the translations of all nearest neighbours.

The R(t) functions for the Na^+ and Cl^- ions decrease monotonously and they can be fitted to a second-order exponential decay:

$$R(t) = A_1 \exp(-\frac{t}{\tau_1}) + A_2 \exp(-\frac{t}{\tau_2}) \tag{8}$$

The first term describes an escape of the solvent molecules located close to the border of the coordination shell, whereas the second term concerns the persistence of the shell. Parameters A_1 and A_2 reflect fractions of the solvent molecules involved in both processes. The first process is rather fast and its characteristic time τ_1 is shorter than 1 ps. The residence time τ_2 of the solvent molecules in the Cl^- shell and the methanol molecules in the Na^+ shell increase with the time interval Δt. Such dependence it is shown in Figure 8.

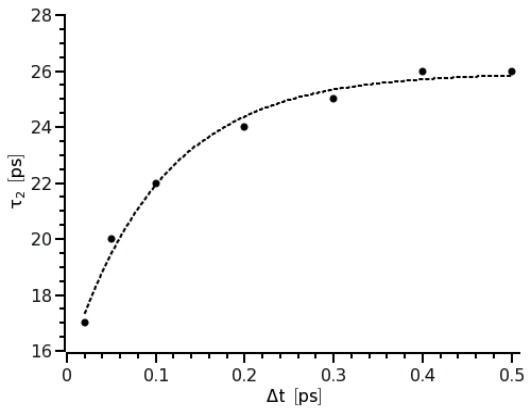

Fig. 8. Influence of the time interval Δt. on the residence time τ_2 of the methanol molecules in the Cl^- shell.

As seen the residence time reaches the constant value when Δt is not shorter than 0.2ps. Thus the τ_2 values discussed below were computed for Δt=0.2 ps. This means that the solvent molecules leaving the ion shell for the time longer than 0.2 ps were neglected in further calculations.

In aqueous solution the lifetime of the coordination shell of Na^+ is long, more than 170 ps, but in methanolic solution this time is much shorter, about 45 ps. Therefore is not surprising that the lifetime of the Na^+ shell decreases when the methanol content increases.

The exchange of the water molecules between the Cl^- shell and the bulk is fast. Though the size and composition of the anion shell in solutions of $CaCl_2$, $MgCl_2$ and NaCl are the same, the persistence of the shells is different. In solutions of $CaCl_2$ and $MgCl_2$ the anion shells are more flexible than those in NaCl solutions. In solutions of the alkali earth chlorides about 85% of the water molecules stay in the primary shell of the anion less than 5 ps. This means that the water residence time is shorter than the characteristic time of the water translations, about 6 ps (Hawlicka & Switla-Wojcik, 2000). This explains why the hydrodynamic radius of Cl^- in aqueous solution is like its radius in crystal (Hawlicka, 1986). In NaCl solution the lifetime of the anion shell is longer. About 75% of the water molecules stay in the shell about 19 ps.

The residence time of the methanol molecules in the Cl^- shell is longer than that of the water molecules. In methanolic solutions of $CaCl_2$ and $MgCl_2$ the lifetime of the Cl^- shell exceeds 50 ps. Shorter lifetime, about 25 ps, has been found for the methanolic solution of NaCl. However even this shortest residence time, 25 ps, exceeds significantly the characteristic time of methanol translations, about 9 ps (Hawlicka & Switla-Wojcik, 2000). This explains why the hydrodynamic radius of Cl^- in net methanol is greater than the radius in crystal (Hawlicka, 1986).

7. H-bonds of the solvent molecules in the first coordination shell

Comparison of the number of the solvent molecules in the first and second coordination shells suggests that in aqueous solutions and water rich mixtures, almost any water molecule in the primary shell of Mg^{2+} has at least two neighbours in the second shell. Such result seems to be consistent with the antidipole orientation of these molecules. The orientation of the water molecules in the first shell of Ca^{2+} is less restricted therefore it is not surprising that they have three neighbours in the second shell. Number of the second neighbours of Na^+ is difficult to determine, because the second shell is not stable and the second peak of the Na^+O radial distribution function is lacking.

With increasing methanol content the number of the neighbours in the second shells of Mg^{2+} and Ca^{2+} decreases rapidly and in equimolar mixture the water or methanol molecule in the first shell has only one neighbour in the second shell. A question is whether the molecules in the primary shell are hydrogen bonded with those in the second shell or in the bulk.

In MD simulation all pair interactions change continuously as a function of the separation and orientation of the molecules therefore there is no unambiguous definition of the hydrogen bond. Usually two definitions, either energetic or geometric, of the H-bond are considered. The energetic criterion of H-bond, based on the pair interaction energy, treats two molecules as H-bonded, if their interaction energy is less than –8 $kJ \cdot mol^{-1}$. This criterion coincides with the geometric definition, which considers two molecules as H-bonded, if the distances between two oxygens and between the hydrogen and oxygen of the H-bond acceptor do not exceed 0.350 and 0.250 nm, respectively, and if the angle between the OH intramolecular bond of the H-donor and the line connecting the oxygens is less than 30^o (Hawlicka & Swiatla-Wojcik, 1998).

The average numbers of the H-bonds were computed in 0.001 ps intervals over the whole simulation runs. The average number of H-bonds per water molecule in pure water is $\langle n_{HB} \rangle_w = 3.5$. Addition of electrolytes, NaCl, $MgCl_2$ and $CaCl_2$, reduces slightly this number.

In all studied solutions the H-bond numbers are the same, $<n_{HB}>_w$=3.1. Thus this influence is slight and only in $CaCl_2$ solutions it extends beyond the first coordination shells of the ions (Owczarek et al., 2007).

Differences between the electrolyte solutions appear when the H-bonds of the molecules in first coordination shell of the cations are compared. The Mg^{2+} and Na^{2+} ions are six-coordinated and the angular distributions show, that all water molecules are properly oriented to form two H-bonds as H-donors. Though the average number of H-bonds per the water molecule in the Na^+ shell is two, $[<n_{HB}>_w]_{Na^+}$=2, a detailed analysis shows that about 65% of the water molecules in the Na^+ shell form 2 H-bonds, whereas the reminder of them has either one, about 15%, or three, about 20%, H-bonded neighbours. Most of the water molecules in the Mg^{2+} shell, about 70%, have two H-bonded neighbours, but 30% of the molecules form only one H-bond. Though both cations coordinate six water molecules the radius of Mg^{2+} shell is smaller, about 0.27 nm, than that of the Na^+ shell, about 0.32 nm. Thus the Mg^{2+} shell must be more compact and there is probably not enough space for H-bonded neighbours of all water molecules. The water molecules in the Ca^{2+} shell have also less H-bonded neighbours. Most of them, about 80%, has only one H-bonded neighbour and only 20%of the molecules form two H-bonds with their neighbours in the second shell. The radii of Ca^{2+} and Na^+ ions in crystal, 0.096 and 0.102 nm (Marcus & Hefter, 2004) and their shells, 0.34 and 0.32 nm respectively (see Table 3), are similar. The first shell of Ca^{2+} consists however of 10 water molecules. Though most of them are oriented properly to have the H-bonded neighbours the shell is compact and only 20% of the molecules have enough space for two H-bonded neighbours in the second shell.

In mixed solvent the number of H-bonds per water molecule in the shells of Na^+ and Mg^{2+} ions remains unchanged. Such behaviour might be expected, because neither the coordination number nor the orientation of the molecules depends on the solvent composition. In methanol-water mixtures the water molecules from the first shells of Na^+ and Mg^{2+} prefer the methanol molecules as H-bonded neighbours in the next sphere. Such preference can be understood, because the H-bond between the H-donor water molecule and the H-acceptor methanol molecule is energetically favourable (Palinkas et al. 1991).

As seen from Tables 3 and 4 the number of the molecules in the first and second shells of Ca^{2+} decrease with the increasing methanol content. The radii of both shells are, however, independent of the mixture composition. Thus the first shell becomes less compact. This improves the orientation of the water molecules as H-donors. In consequence all water molecules have two H-bonded neighbours. However they have water molecules as the H-bonded neighbours despite the unfavourable energy of H-bond between two water molecules. The methanol molecules appear in the first shells of Ca^{2+} in methanol rich solvents, when there is a lack of water to form the coordination shell. Their antidipole orientation causes that they have only one H-bonded neighbour.

The chloride ion is H-bond acceptor and in aqueous solution the water molecules form almost linear H-bond with Cl^- shell. About 80% of the water molecules coordinated by the anion form three H-bonds with the neighbours in the bulk solvent. In mixed solvent the methanol molecules replace the water molecules in the anion shell. The molecules form the linear H-bond with Cl^- therefore they are H-acceptors and have only one H-bonded neighbour in the bulk solvent.

An interesting question is how does the ionic field influence a strength and persistency of the H-bonds. To describe this effect the average H-bond energy of the molecules in the ion shells was calculated and it was compared with the average H-bond energy computed for the mixed solvent. The average energy of two H-bonded molecules in liquid BJH water, $\langle E_{HB} \rangle_w$= -17.3 kJ·mol^{-1}, is of about 10% higher than the energy of two H-bonded molecules in liquid PHH methanol, $\langle E_{HB} \rangle_w$= -19.2 kJ·mol^{-1}. Such feature agrees with the difference of the binding energies of water and methanol dimers (Palinkas et al. 1991). In gas phase the binding energies for the dimer of unlike molecules depends on the configuration of the water and methanol molecules. The H-bond between the H-acceptor methanol molecule and H-donor water molecule is energetically favourable (Palinkas et al., 1991). Therefore the average energy of the H-bond in the methanol-water mixtures decreases with the increasing methanol content (Owczarek et al., 2009). In liquid mixtures the energies of two different configurations are slightly different and the energy of the H-acceptor methanol and H-donor water is lower by about 7%.

The influence of the anionic field on the strength of H-bonds is negligible and the H-bond energy of the water and methanol molecules, coordinated by the Cl^- ions, does not differ from the H-bond energy in the bulk solvent. A lack of the influence can be understood, because the charge density of the chloride ion is small, therefore the anion field does not polarise the solvent molecules.

The charge densities of the cations are higher, particularly of Mg^{2+}, and their field polarises the solvent molecules. In such case a strengthening of the H-bonds might be expected. Indeed the energies of the H-bonds of the water molecules coordinated by the cations are lower than the energy of the H-bonds in the bulk solvent. As might be expected the influence of the Mg^{2+} field is the strongest one and the H-bond energy is lower by about 20%, than that in the bulk. The H-bond energy of the water molecules coordinated by Na^+ and Ca^{2+} ions is lower, by about 10%, as compared with that in the bulk solvent. The influence of the Ca^{2+} and Na^+ fields seems to be very similar, despite different charge densities, but it is worthy to stress that the second neighbours of these cations are different. The Ca^{2+} ion favours the water molecules in both shells and such H-bonds are weaker as compared with those between the water molecules in the Na^+ shell and its second neighbours, the methanol molecules.

To describe an influence of the ionic field on a persistence of the H-bonds a lifetime of H-bonds of the molecules in the first shells was computed and compared with that in binary solvent. From among various concepts of the H-bond lifetime an approach proposed previously (Rappaport, 1983) was adopted. The concept of so-called 'continuous lifetime' takes into account only the unbroken H-bonds. This means that the H-bond once broken and then renewed is neglected. The lifetime of H-bonds was computed from the time correlation function R(t), defined above by the equation (7). In these calculations N_α and N_β denote the number of ions and the H-bonds, respectively, and $\kappa_{ij}(t)$ is the step function. If the solvent molecule *j* was H-bonded than $\kappa_{ij}(t)=1$ and otherwise $\kappa_{ij}(t)=0$. The calculations of the R(t) functions were performed for at least 500 randomly chosen initial configurations. The H-bonds were monitored in 0.001 time intervals. This short time interval is consistent with hindered rotations of the solvent molecules (Roberts et al., 2009), which may destroy the H-bond. The R(t) functions can be fitted to the first-order exponential decay.

At room temperature the continuous lifetime of H-bonds in pure water is about 0.3 ps, it increases linearly with the increasing methanol content and reaches about 1.5 ps in pure

methanol. The influence of the ionic field on the H-bond lifetime is minor. The cationic field slightly stabilizes the persistence of the H-bonds. The lifetime of the H-bonds of the water and methanol molecules in the cation shells is by about 20% longer. The influence of the anion filed is opposite and the lifetime of the H-bonds is slightly shorter than in the bulk solvent.

8. Influence of the ions on intramolecular vibrations

Total spectral densities S(ω) of water and methanol have been calculated as the sum of partial densities $S^{\alpha}(\omega)$ of sites α (α= O, H, H for water and O, H, Me for methanol):

$$S(\omega) = \sum_{\alpha=1}^{3} S^{\alpha}(\omega) \tag{9}$$

where ω denotes the frequency of vibrations given in wave number (cm^{-1}). The partial densities $S^{\alpha}(\omega)$ have been obtained via Fourier transform of the normalized velocity autocorrelation function:

$$S(\omega) = \frac{2m_{\alpha}c}{kT} \int_{0}^{\infty} C_{vv}^{\alpha}(t) \cos(2\pi c\omega t) dt \tag{10}$$

where m_{α} is mass of the α site, c and k denote the light velocity and Bolzmann's constant, respectively. The normalized velocity autocorrelation function is defined as follows:

$$C_{vv}^{\alpha}(t) = \frac{1}{N_t N_{\alpha} C_{vv}^{\alpha}(0)} \sum_{i=1}^{N_t} \sum_{j=1}^{N_{\alpha}} \vec{v}_j^{\alpha}(t_i) \cdot \vec{v}_j^{\alpha}(t_i + \Delta t) \tag{11}$$

where N_t and N_{α} denote the numbers of the time averages and sites, respectively, $v_j^{\alpha}(t_i)$ is the velocity of the site j of the kind α at the time t_i and $C_{vv}^{\alpha}(0)$ represents the normalization factor.

Basic frequencies obtained from MD simulation for the liquid BJH water are 1716 cm^{-1} and 3533 cm^{-1} for the HOH bending and OH stretching modes. These results agree reasonably with the experimental frequencies of bending, 1670 cm^{-1}, and stretching, 3557 cm^{-1} (Falk & Walley, 1961). MD simulation reproduces correctly the shape of the density profile. As expected the sharper maximum, with the half-width about 200 cm^{-1}, has been obtained for the bending vibrations. A broader band has been found for the OH stretching. Its half-with, about 300 cm^{-1} (Hawlicka & Swiatla-Wojcik,1997), is in good agreement with the experimental half-width, about 260 cm^{-1} (Roberts et al. 2009).

MD simulations of the liquid PHH methanol yielded accurate frequencies of the basic modes; 1055 cm^{-1} for the CO stretching, 1407 cm^{-1} for the bending of the COH angle and 3342 cm^{-1} for the OH stretching. These results are in very good agreement with the experimental frequencies, 1029, 1420 and 3337 cm^{-1}, respectively (Lindgren et al, 1993).

Addition of electrolytes does not affect the CO stretching mode of methanol and their influence on bending modes, of methanol COH and water HOH, is minor (Stangret &

Gampe, 2002). Only stretching OH vibrations of water and methanol are very sensitive to the local environment of the molecules. These modes have been used to investigate the ionic solvation. The experimental spectra are composed, however, of several components. Even in the diluted solution of the electrolyte three components of the OH band must be considered: vibrations of molecules coordinated by cations and anions, as well as the vibrations of the bulk molecules. In concentrated solutions the spectra become more complex, because a solvent shared ion pair cannot be neglected. Therefore it is difficult to interpret the experimental spectra and to deduce the contributions of the anions and cations without additional assumptions. The MD simulation may provide additional information, because the frequency of the OH stretching can be computed independently for the solvent molecules in the ion coordination shells.

Density profiles of the OH stretching bands of water and methanol in the coordination shells of the ions in aqueous and methanolic solutions are displayed in Figure 9. For comparison the OH bands computed for pure water and pure methanol are also shown.

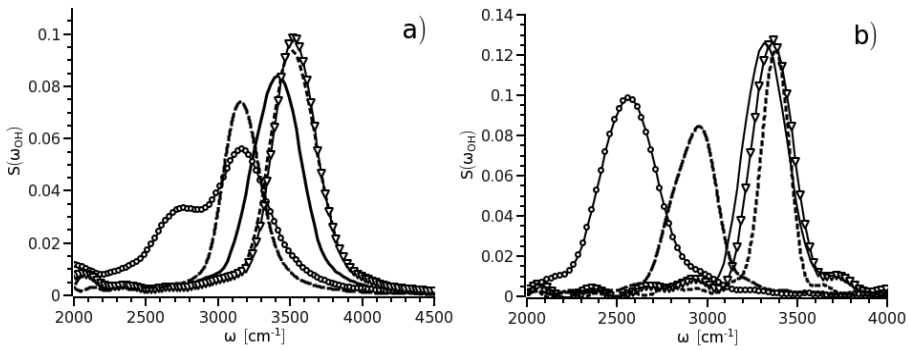

Fig. 9. Density profile of the OH stretching band of water (a) and methanol (b) in net solvents (▽) and coordination shells of Na^+ (solid), Mg^{2+} (dashed), Ca^{2+}(O) and Cl^- (dotted).

As seen the influence of the Cl^- ion on the OH frequency of water and methanol is minor. Despite almost linear H-bond between the anion and water molecule the red-shift of the OH frequency, observed for the water molecules in the Cl^- shell, is minor ($\Delta\omega_{OHw}$ = -27 cm^{-1}). Moreover the influence of the Cl^- ion on the OH frequency of the methanol is opposite and a small blue-shift ($\Delta\omega$= +25 cm^{-1}) is found.

The influence of the cations on the OH vibrations of the water and methanol molecules is remarkable. The frequencies of the OH stretching of the water and methanol molecules in the cation shells are shifted to lower wave numbers. This agrees with the red-shift of the molecules in the cation shells, deduced from experimental infrared spectra in HDO (Kristiansson & Lindgren, 1995; Roberts et al., 2009) . As seen from Figure 9 the OH bands of water molecules in the Na^+ and Mg^{2+} shells are broader than in pure water and the basic modes are shifted to lower wave numbers by – 125 and 265 cm^{-1}, respectively. Usually the broad OH mode, observed in pure water, is ascribed to large distribution of the configurations of the H-bonds (Lindgren et al, 1993).

The change of the OH band of the water molecules coordinated by the calcium ions is dramatic. The OH density profile is very broad; moreover it consists of two bands, centred at 3200 and 2740 cm^{-1}, respectively. As mentioned above the water molecules in the Ca^{2+} shell show two different orientations: most of 10 water molecules in the Ca^{2+} shell exhibit the antidipole orientation, but the dipole moment of some molecules is tilted by about 45^{o}. Probably the split of the OH band reflects the vibrations of the water molecules differently orientated towards Ca^{2+}.

The cation field affects remarkably the stretching OH of the methanol molecules. The OH stretching bands, computed for the cation shells, are broader than that in pure methanol and shifted to lower frequencies. The red-shifts increases in order Na^{+} ($-57cm^{-1}$) > Mg^{2+} ($-432cm^{-1}$) > Ca^{2+}($-800\ cm^{-1}$). One should notice that the OH band for the Ca^{2+} shell is not split, because all methanol molecules prefer similar orientation (see Figure 6 c).

The water and methanol molecules, coordinated by the cations, favoured the antidipole orientation towards the ion therefore they form less H-bonds than the molecules in net liquid component. This means that in aqueous solution about 14% of the water molecules in the Na^{+} shell, more than 40% of the molecules in the Mg^{2+} shell and about 80% of molecules in the and Ca^{2+}shell have one non-bonded OH group. In methanolic solutions most of the molecules coordinated by the cations have also non-bonded OH group. The frequencies of the non-bonded OH groups of water and methanol are higher. Thus the observed red-shift of the OH frequency of the molecules coordinated by the cations is usually ascribed to the strengthening of the H-bonds (Lindgren et al, 1993; Stangret & Gampe, 2002; Kristiansson & Lindgren, 1995). This might be the consequence of a polarisation (Collahan et al. 2010) of the solvent molecules.

The BJH water and PHH methanol molecules are flexible thus their geometry and, in consequence, their dipole moments can be changed. Indeed the dipole moments of the water and methanol molecules coordinated by the cations are greater of about 10% than that of the molecules in the net solvents. However the increase of the dipole moment does not influence remarkably the H-bond energy. The Na^{+} filed does not influence the H-bond energy, whereas the field of Ca^{2+} and Mg^{2+} lowers the H-bond energy, but this decrease, by about 20%, thus it cannot be responsible for the large red-shifts observed in MD simulation.

9. Conclusions

MD simulations of the electrolyte solutions improve the understanding of a nature of the solvation in methanol-water mixtures. Despite very similar interactions of the ions with both solvent components the compositions of the ion shells and the bulk solvent may be different. This leads to the conclusion that the solvation of ions does not depend only on the ion-solvent interactions, but it is affected by the interactions between the solvent molecules. Particularly in highly associated solvents a strong tendency to prevent the H-bonded network of the solvent competes with the ion-solvent interactions and it may lead to a selective solvation of the ions.

The H-bonds between the H-donor water and H-acceptor methanol molecules are energetically favourable. The molecules in the cationic shells exhibit the antidipole orientation, which favours the H-donor water molecules, whereas the almost linear H-bond

between the Cl^- ions and the solvent molecules favours the H-acceptor methanol molecules. In consequence the preferential hydration of the Mg^{2+} and Ca^{2+} ions and the selective solvation of Cl^- by methanol are observed over the whole range of the methanol concentration.

The first coordination shells of Mg^{2+} and Ca^{2+} are very stable. Though the residence time of the solvent molecules in the cationic shells is long their H-bonds are short living. It is worthy to notice than most of the molecules in the cation shells have less H-bonded neighbours than expected. Moreover the influence of the ionic field on the H-bond strength is minor. Therefore the observed red-shift of the OH-stretching frequency for water and methanol molecules reflects neither the strengthening nor stabilizing of the H-bonds. This red-shift results probably from the increase of the dipole moment of the solvent molecules.

10. References

Allen M. P., Tidesley D. J., Computer Simulation of Liquids, Oxford University Press, Oxford, 1987.

Berendsen H. J. C., Postma J. P, van Gunstern W. F., Hermans J., Intermolecular Forces, Pullman Ed. Dodrecht, 1981.

Bopp P., Jancso G., Heinzinger K., Chem. Phys. Lett., 98 (1983) 129-133.

Bujnicka K., Hawlicka E., J. Mol. Liquids, 125 (2006) 151-157.

Carney G. D., Curtiss L. A., Langhoff S. R., J. Mol. Spectr. 61 (1976) 371- 381.

Collahan K. M., Casillas-Ituarte N. N., Roeselova M., Allen H. C., Tobias D. J., J. Phys. Chem. A, 114 (2010) 5141-5148.

Convington A. K., Dunn M., J. Chem. Soc. Faraday Trans. I, 85 (1989) 2825-2834.

Dore J. C., Sufi A. A. M., Bellisent-Funnel M.-C., Phys. Chem. Chem. Phys., 2 (2000) 1599-1602.

Dietz W., Riede W. O., Heinzinger K., A. Naturforsch. A, 37 (1982) 1038-1048.

Dughan L., Bates S. P., Hargreaves R., Fox J. P., Crain J., Finney., J. L., Reat, V., Soper A. K, J. Chem. Phys., 121 (2004) 6456-6462.

Ferguson D. M., J. Comp. Chem., 16 (1995) 501-511.

Falk W., Walley E., J. Chem. Phys., 34 (1961) 1555.

Gallangher, K. R., Sharp, K. A., J. Am. Chem. Soc., 125 (2003) 9853-9860.

Guo J.-H., Luo Y., Augustsson A., Kashtanov S., Rubensson, J.-E. Shuh D., Zhuang V., Ross P., Ågren H., Nordgren J., J. Electron Spectroscopy, 137-140 (2004) 425-428.

Hawlicka E., Z. Naturforsch. 41 (1986) 939-943.

Hawlicka E., Z. Naturforsch., 42 (1986) 1014-1016.

Hawlicka E., Chem. Soc. Rev., (1995) 367-337.

Hawlicka E., Swiatla-Wojcik D., Chem. Phys. 195 (1995) 221-233.

Hawlicka E., Swiatla-Wojcik D., Chem. Phys. 218 (1997) 49-53.

Hawlicka E., Swiatla-Wojcik D., Chem. Phys., 232 (1998) 361-369.

Hawlicka E., Swiatla-Wojcik D., Phys. Chem. Chem. Phys., 2 (2000) 3175-3180.

Hawlicka E., Swiatla_ D. Wojcik, J. Phys. Chem. A, 106 (2002) 1336-1345.

Heyes D. M., *The Liquid State. Application of Molecular Simulation*. John Wiley & Sons, NY 1998

Holtz M., Waingartner H., Hertz H. G., J. Chem. Soc. Faraday Trans I, 73 (1977) 71-83.
Ibuki K., Bopp P. A., J. Mol. Liquids, 147 (2009) 56-63.
Impey R. W., Madden P.A., McDonald I. R., J. Phys. Chem., 87 (1983) 5071-5083.
Jansco G., Bopp P., Z. Naturforsch. A, 38 (1983) 206-213.
Jancso G., Heinzinger K., Bopp P., Z. Naturforsch. A, 40 (1985) 1235-1247.
Jorgensen W. L., J. Am. Chem. Soc., 103 (1981) 341-345.
S. Konesham, J. C. Rasaiah, R. M. Lynden-Bell, J. Phys. Chem. B, 102 (1998) 4193-4204.
Kristiansson O., Lindgren J., J. Phys. Chem., 95 (1995) 1488-1493.
Lavenstein A., Hermansson K., Lindgren J., Probst M., Bopp P. A., Inter. J. Quant. Chem., 80 (2000) 892-906.
Licheri G., Piccalunga G., Pinna G., J. Phys. Chem., 63 (1975) 4412.
Lindgren J., Hrmansson K., Wojcik M. J., J. Phys. Chem., 97 (1993) 5254-5259
Marcus Y., Hefter G., Chem. Rev. 104 (2004) 3405-3452.
Marx D., Heinzinger K., Palinkas G., Bako I., Z. Naturforsch. 46a (1991) 887-897.
Megyes T., Gross T., Radnai T., Bako I., Palinkas G., J. Phys. Chem. A, 108 (2004) 7261-7271.
Narten A. H., Habenschuss A., J. Chem. Phys. 80 (1984) 3387-3391.
Neilson G. W., Enderby J. E., Annu. Rep. Prog. Chem. C, 76 (1979) 185-220.
Ohtaki H., Radnai T., Chem. Rev., 93 (1993) 157-1204.
Owczarek E., Rybicki M., Hawlicka E., J. Phys. Chem. B, 111 (2007) 14271-14278.
Owczarek E., Rybicki M., Hawlicka E., Chem. Phys. 363 (2009) 78-87.
Öhrn A., Karlström G., J. Phys. Chem. B, 108 (2004) 8452-8459.
Payaka A.,. Tongraar A, Rode B. M., J. Phys. Chem. A, 113 (2009) 3291-3298.
Palinkas G., Hawlicka E., Heinzinger K., J. Phys. Chem., 91 (1987) 4343-4341.
Palinkas G., Hawlicka E., Heinzinger K., Chem. Phys., 158 (1991) 65-76.
Palinkas G., Bako I., Heinzinger K., Bopp P., Mol. Phys., 73 (1991) 897.
Pałka K., Hawlicka E., J. Mol. Liquids, 122 (2004) 28-31.
Probst M. M., Radnai T., Heinzinger K., Bopp P., Rode R. M., J. Phys. Chem., 89 (1985) 753-759.
Probst M. M., Spohr E., Heinzinger K., Bopp P., Molecular Simulation, 7 (1991) 43-57.
Radnai T., Bako I., Palinkas G., ACH, Models in Chemistry, 132 (1995) 159-178.
Rappaport D. C., Mol. Phys. 50 (1983) 1151.
Roberts S.T., Ramasesha K., Tolmakoff A., Acc. Chem. Res., 42 (2009) 1239-1249.
Rode B. M., Schwenk C. F., Tongraar A., J. Mol.Liquids, 110 (2004) 105-122.
Stillinger F. H., Rahman A., J. Chem. Phys. 68 (1978) 666-670.
Soper A. K., Phillips M. G., Chem. Phys., 107 (1986) 47-60.
Stangret J., Gampe T., J. Phys. Chem. A, 106 (2002) 5393-5402.
Tamura Y., Spohr E., Heinzinger K., Palikas G., Bako I., Ber. Bunsenges. Phys. Chem., 96 (1992) 147-158.
Tongraar A., Rode B. M., Phys. Chem. Chem. Phys., 5 (2003) 357-362.
Tongraar A., Rode B. M., Chem. Phys. Letters, 403 (2005) 314 -319.
Tongraar AThienprasert., J. T., Rujirawat S., Limpijunong S., Phys. Chem. Chem. Phys.,12 (2010) 10876-10887.
Yu H., Whitfield T. W., Harder E., Lamoureus G., Vorobyov I., Anisimov V. M., MacKerell A. D., jr., Roux B., J. Chem. Theor. Comp., 6 (2010) 774-786.

Yamagouchi T., Hayashi S., Ochiai H., Inorg. Chem., 28 (1989) 2434-2439.
Zhu S. B., Wong C. F., J. Chem. Phys., 99 (1993) 9047-9053.

Edited by Lichang Wang

Molecular Dynamics is a two-volume compendium of the ever-growing applications of molecular dynamics simulations to solve a wider range of scientific and engineering challenges. The contents illustrate the rapid progress on molecular dynamics simulations in many fields of science and technology, such as nanotechnology, energy research, and biology, due to the advances of new dynamics theories and the extraordinary power of today's computers. This first book begins with a general description of underlying theories of molecular dynamics simulations and provides extensive coverage of molecular dynamics simulations in nanotechnology and energy.

ISBN 978-953-51-4306-2

Photo by sakkmesterke / iStock

IntechOpen